

AD-A259 236



COMPUTER-AIDED STRUCTURAL  
ENGINEERING (CASE) PROJECT



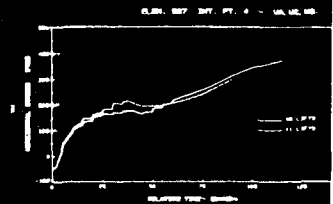
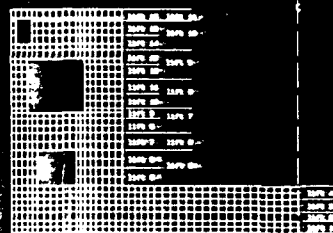
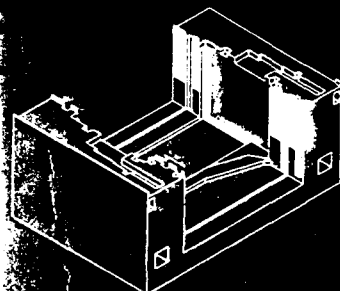
CONTRACT REPORT ITC-92-3

**EVALUATION OF THERMAL AND INCREMENTAL  
CONSTRUCTION EFFECTS FOR MONOLITHS  
AL-3 AND AL-5 OF THE MELVIN PRICE  
LOCKS AND DAM**

by

Kevin Z. Trumac, David L. Petruska, Abdelhader Ferhi

Department of Civil Engineering  
Washington University  
St. Louis, Missouri



92-33036

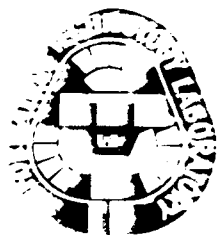
DTIC  
ELECTE  
DEC 29 1992  
S A D



September 1992

Final Report

Approved For Public Release; Distribution Is Unlimited



Prepared for DEPARTMENT OF THE ARMY  
US Army Corps of Engineers  
Washington, DC 20314-1000

Destroy this report when no longer needed. Do not return  
it to the originator.

The findings in this report are not to be construed as an official  
Department of the Army position unless so designated  
by other authorized documents.

The contents of this report are not to be used for  
advertising, publication, or promotional purposes.  
Citation of trade names does not constitute an  
official endorsement or approval of the use of  
such commercial products.

REPORT DOCUMENTATION PAGE			Form Approved OMB No. 0704-0188	
Public reporting burden for this collection of information is estimated to average 1 hour per response, including the time for reviewing instructions, searching existing data sources, gathering and maintaining the data needed, and completing and reviewing the collection of information. Send comments regarding this burden estimate or any other aspect of this collection of information, including suggestions for reducing this burden, to Washington Headquarters Services, Directorate for Information Operations and Reports, 1215 Jefferson Davis Highway, Suite 1204, Arlington, VA 22202-4302, and to the Office of Management and Budget, Paperwork Reduction Project (0704-0188), Washington, DC 20503.				
1. AGENCY USE ONLY (Leave blank)	2. REPORT DATE September 1992	3. REPORT TYPE AND DATES COVERED Final report		
4. TITLE AND SUBTITLE Evaluation of Thermal and Incremental Construction Effects for Monoliths AL-3 and AL-5 of the Melvin Price Locks and Dams		5. FUNDING NUMBERS DACW39-87-K-0065		
6. AUTHOR(S) Kevin Z. Truman David J. Petruska Abdelkader Ferhi				
7. PERFORMING ORGANIZATION NAME(S) AND ADDRESS(ES) Department of Civil Engineering Washington University St. Louis, Missouri		8. PERFORMING ORGANIZATION REPORT NUMBER Contract Report ITL-92-3		
9. SPONSORING/MONITORING AGENCY NAME(S) AND ADDRESS(ES) US Army Corps of Engineers Washington, DC 20314-1000 and USAE Waterways Experiment Station, Information Technology Laboratory, 3909 Halls Ferry Road, Vicksburg, MS 39180-6199		10. SPONSORING/MONITORING AGENCY REPORT NUMBER		
11. SUPPLEMENTARY NOTES Available from National Technical Information Service, 5285 Port Royal Road, Springfield, VA 22161				
12a. DISTRIBUTION/AVAILABILITY STATEMENT Approved for public release; distribution is unlimited		12b. DISTRIBUTION CODE		
13. ABSTRACT (Maximum 200 words) Two monoliths, a gate monolith and a chamber monolith, from the auxiliary lock at Melvin Price Locks and Dam near Alton, Illinois, are used to explore and evaluate the effects of creep, shrinkage, thermal loads, and construction sequence on massive concrete structures. The material and structural modelling, analysis procedures and software, and results are thoroughly discussed. The nonlinear material subroutines used to model aging modulus, autogenous shrinkage, creep, and smeared crack capabilities are described and discussed with regards to their use in modelling the structure and analyzing structural behavior. These parameters were used to perform a thorough parametric evaluation of their effects on massive concrete structures. The structural models for each monolith and its pile/soil foundation for both the thermal and mechanical analyses are provided. A detailed discussion regarding incremental construction for simulating construction is presented. The incremental analysis procedure was (Continued)				
14. SUBJECT TERMS Aging modulus Creep Incremental construction		Parametric Shrinkage		15. NUMBER OF PAGES 389
				16. PRICE CODE
17. SECURITY CLASSIFICATION OF REPORT UNCLASSIFIED	18. SECURITY CLASSIFICATION OF THIS PAGE UNCLASSIFIED	19. SECURITY CLASSIFICATION OF ABSTRACT	20. LIMITATION OF ABSTRACT	

13. ABSTRACT (Concluded).

that the lift heights in the gate monolith could be extended in various regions resulting in a minimum savings of \$720,000. Each aspect of the modelling and the results are thoroughly discussed and documented through the use of time history plots of critical location temperatures, stresses and strains.

## PREFACE

The analyses and research described in this report were conducted by the Department of Civil Engineering, College of Engineering, Washington University, in St. Louis, Missouri, for Headquarters, US Army Corps of Engineers. The study was performed under Contract No. DACW39-87-K-0065 to the Information Technology Laboratory (ITL), US Army Engineer Waterways Experiment Station (WES). This study was conducted as part of the Phase II Thermal Studies funded through the Melvin Price Locks and Dam project. The Technical Monitor for the Phase II Thermal Studies was Mr. Barry Fehl, Structural Engineer in the Structural Section of the St. Louis District.

This report was prepared by Dr. Kevin Z. Truman, Mr. David J. Petruska, and Mr. Abdelkader Fehri. Funds for publication of the report were provided from those available for the Computer-Aided Structural Engineering (CASE) Project managed by ITL. Dr. N. Radhakrishnan, Director, ITL, is Project Manager for the CASE Project.

At the time of publication of this report, Director of WES was Dr. Robert W. Whalin. Commander and Deputy Director was COL Leonard G. Hassell, EN.

Accession For	
NTIS CRA&I	<input checked="checked" type="checkbox"/>
DTIC TAB	<input type="checkbox"/>
Unannounced	<input type="checkbox"/>
Justification	
By	
Distribution/	
Availability Codes	
Dist	Avail and/or Special
A-1	

DTIC QUALITY INSPECTED 5

## CONTENTS

	<u>Page</u>
PREFACE . . . . .	1
CONVERSION FACTORS, NON-SI TO SI (METRIC) UNITS OF MEASUREMENT . . . . .	4
PART I: INTRODUCTION . . . . .	5
Introduction . . . . .	5
Objective and Scope . . . . .	10
PART II: MODELLING AND MATERIAL PROPERTIES FOR MONOLITH AL-5 . . . . .	12
Introduction . . . . .	12
Basic Concrete Properties . . . . .	12
Modelling for Heat Transfer Analysis . . . . .	12
Modelling for Elastic Stress Analysis . . . . .	20
Mesh and Element Selection and Time Frame . . . . .	25
PART III: TWO DIMENSIONAL USER MATERIAL MODEL FOR TIME DEPENDENT EFFECTS OF CONCRETE FOR MONOLITHS AL-3 AND AL-5 . . . . .	30
Introduction . . . . .	30
Shrinkage . . . . .	30
Creep . . . . .	31
Cracking Criteria . . . . .	33
PART IV: RESULTS FROM HEAT TRANSFER ANALYSIS FOR MONOLITHS AL-5 . . . . .	38
Introduction . . . . .	38
Discussion of the Heat Transfer Analysis Results . . . . .	38
PART V: STRESS ANALYSIS RESULTS VARYING THERMAL LOADINGS FOR MONOLITH AL-5 . . . . .	59
Introduction . . . . .	59
Discussion of Stress Analysis Results Varying the Degree of Thermal Loading . . . . .	60
PART VI: STRESS ANALYSIS RESULTS SHOWING OF CREEP AND SHRINKAGE FOR MONOLITH AL-5 . . . . .	77
Introduction . . . . .	77
Effect of Shrinkage on Resulting Stresses . . . . .	77
Effect of Creep on Resulting Stresses . . . . .	92
Combined Effect of Creep and Shrinkage . . . . .	107
Effect of Creep and Shrinkage on Strains . . . . .	122
Locations of High Tensile Stresses . . . . .	137
Summary . . . . .	141
PART VII: STATIC AND PARAMETRIC SERVICE LOAD ANALYSIS FOR MONOLITH AL-5 . . . . .	145
Introduction . . . . .	145
Stress Distributions . . . . .	145
Pile Forces . . . . .	154

	<u>Page</u>
PART VIII: OVERVIEW INTERPRETATION, AND VERIFICATION OF RESULTS FOR MONOLITH AL-5 . . . . .	157
Introduction . . . . .	157
Overview, Significance and Interpretation of Calculated Tensile Stress Results . . . . .	157
Verification of Results . . . . .	159
PART IX: MODELLING FOR MONOLITH AL-3 . . . . .	163
Introduction . . . . .	163
Finite Element Mesh . . . . .	163
Soil Depth . . . . .	163
Initial Soil Temperature Distribution . . . . .	174
Concrete - Soil Interface . . . . .	174
Lift Heights . . . . .	183
Heat Transfer Analysis . . . . .	183
Stress Analysis . . . . .	185
Material Properties . . . . .	188
PART X: RESULTS FROM THE HEAT TRANSFER ANALYSIS FOR MONOLITH AL-3 . . . . .	189
Introduction . . . . .	189
General Trends . . . . .	189
Temperature Comparison Between the 11 and 16-Lift Procedures . . . . .	207
PART XI: RESULTS FROM THE STRESS ANALYSIS FOR MONOLITH AL-3 . . . . .	231
Introduction . . . . .	231
Incremental Construction . . . . .	231
Comparison Between the 16 and 11-Lift Schedules . . . . .	275
PART XII: OVERVIEW, INTERPRETATION, AND CONCLUSIONS FOR MONOLITH AL-3 . . . . .	351
Introduction . . . . .	351
Overview and Significance of the Results . . . . .	351
REFERENCES . . . . .	353
TABLES 1-11	
APPENDIX A: DEVELOPMENT OF TWO- AND THREE-DIMENSIONAL AGING AND CREEP MODEL FOR CONCRETE . . . . .	A1

CONVERSION FACTORS, NON-SI TO SI (METRIC)  
UNITS OF MEASUREMENT

Non-SI units of measurement used in this report can be converted to SI (metric) units as follows:

<u>Multiply</u>	<u>By</u>	<u>To Obtain</u>
Fahrenheit degrees	5/9	celsius degrees or kelvins*
feet	0.3048	metres
inches	2.54	centimetres
kips (force) per inch	175.1268	kilonewtons per metre
pounds (force)	4.448222	newtons
pounds (force) per square inch	6.894757	kilonewtons per metre

---

\* To obtain Celsius (C) temperature readings from Fahrenheit (F) readings, use the following formula:  $C = (5/9) (F - 32)$ . To obtain Kelvin (K) readings, use:  $K = (5/9) (F - 32) + 273.15$ .

EVALUATION OF THERMAL AND INCREMENTAL CONSTRUCTION  
EFFECTS FOR MONOLITHS AL-3 AND AL-5 OF THE  
MELVIN PRICE LOCKS AND DAM

PART I: INTRODUCTION

Introduction

1. A state-of-the-art numerical method is used to study the significance of thermal loads, creep, shrinkage, and incremental construction on mass concrete structures, specifically U-frame lock monoliths. Mass concrete can be defined as: "Any large volume of cast-in-place concrete with dimensions large enough to require that measures be taken to cope with the generation of heat and attendant volume changes to minimize cracking," Mass Concrete Committee (1973). An incremental analysis formulation is employed to determine what effect the material parameters will have on the structural response both during the construction process and under service load conditions. A major concern is the prediction of cracking and the locations where it will occur.

2. Cracking in mass concrete structures has been detected as early as when the forms are being removed. Such cracking at early time is commonly accepted to be caused by thermal loads. Thermal loads arise from the fact that the reaction of cement with water is an exothermic reaction, thus a considerable amount of heat is liberated during the curing process. The laws of heat transfer state that heat can escape from a structure at a rate proportional to the inverse of the least dimension (Fintel 1974). Consequently, thermal loads are usually insignificant for small concrete members. However, for mass concrete structures, the volume to surface ratio is increased, thus the heat is dissipated gradually with time, and heat "build-ups" in the structure, producing thermal gradients resulting in thermal induced strains.

3. Concrete is a widely used material in structural engineering applications because, among other things, it is relatively inexpensive and performs well in compression. However, concrete does have disadvantages--two of these being that (a) concrete is not very efficient for transmitting tensile loads and (b) volume changes will occur when the temperature of moisture content changes (Hughes and Ghunaim 1982). Consequently, steel reinforcement is most

often used to control the effect that these properties will have on cracking. Nevertheless, even with steel reinforcement, cracks will still initiate leading to structural damage and costly repairs. This was the case with both the Dworshak Dam in Idaho and the Richard B. Russel Dam on the Georgia-South Carolina border. Both dams were built in the last 20 years, and verified computer programs were employed in the design process. In both cases, the serious cracking that did occur is believed to have been caused by thermal effects (Fehl 1987).

4. The mass concrete structures being analyzed here are two-dimensional sections from the auxiliary lock chamber to be constructed at Melvin Price Locks and Dam Replacement on the Mississippi River at Alton, Illinois. Figure 1 is an isometric view of the chamber monolith AL-5, and Figure 2 shows a

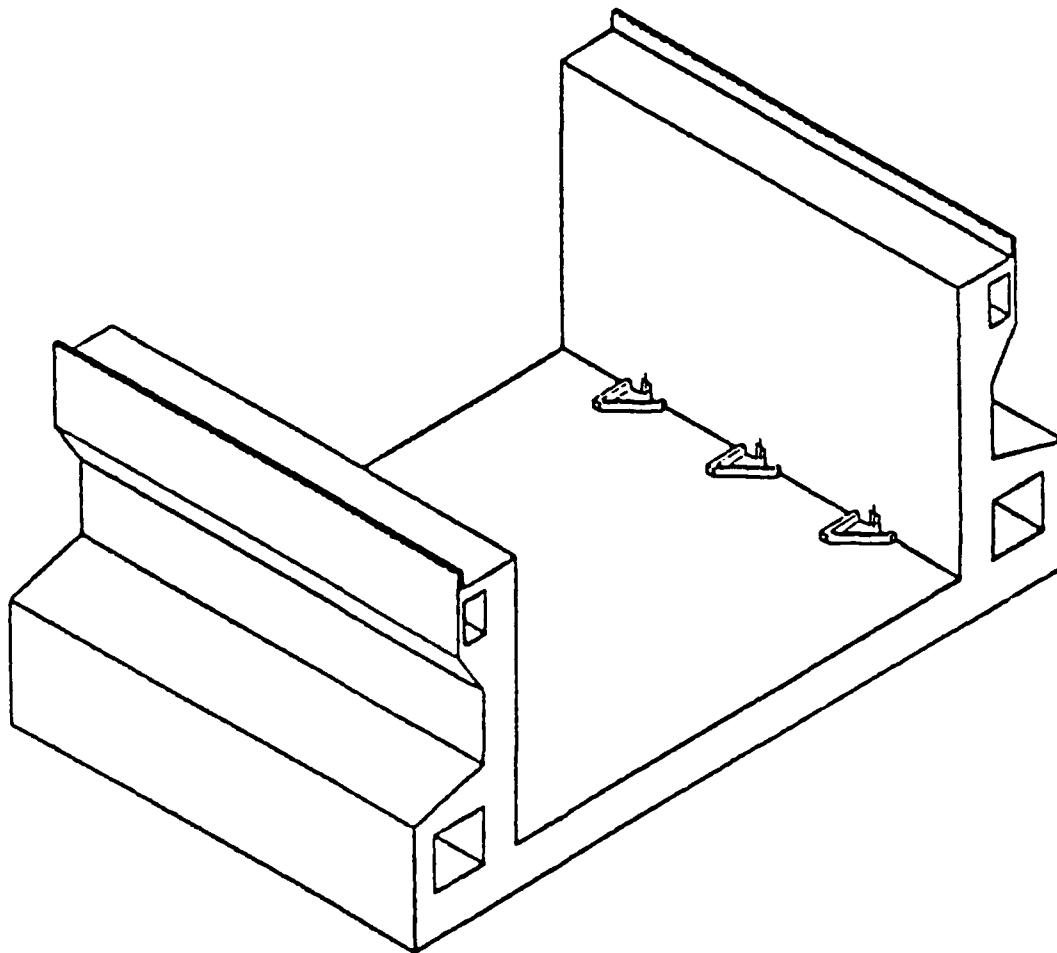


Figure 1. Three-dimensional view of auxiliary lock chamber for Lock and Dam 26R

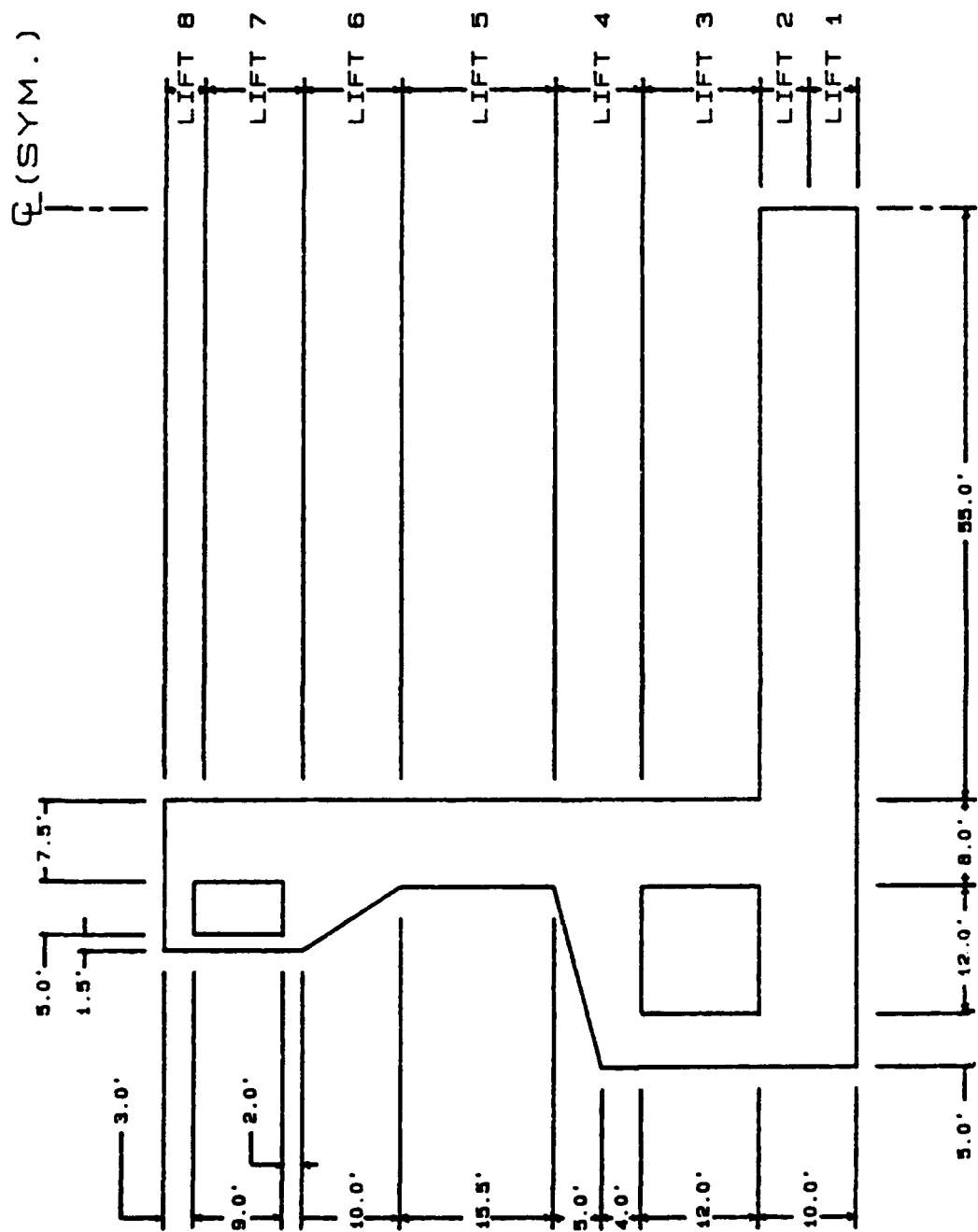


Figure 2. Two-dimensional view of auxiliary lock chamber for Lock & Dam 26R

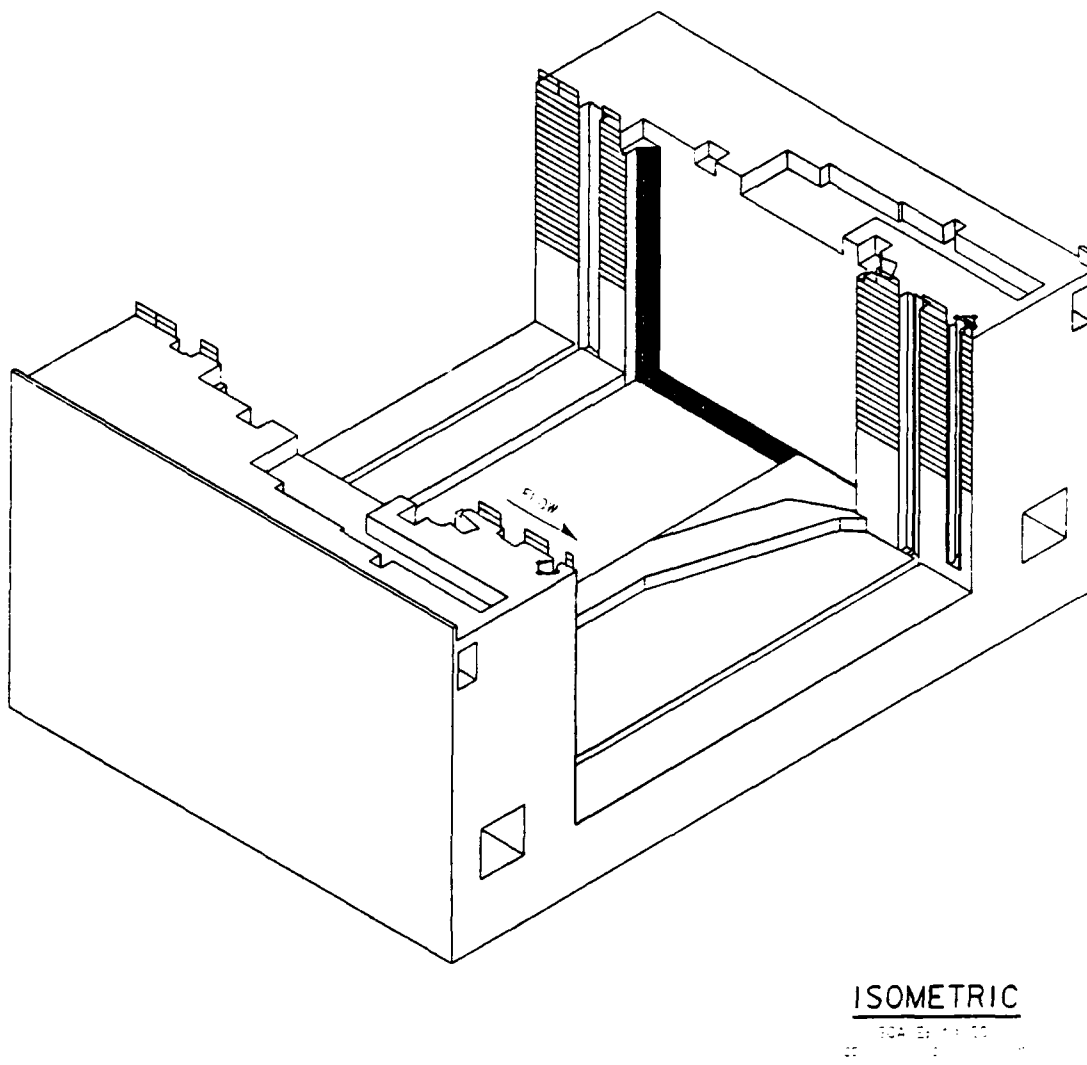


Figure 3. Three-dimensional view of lock monolith AL-3 for Lock and Dam 26R

two-dimensional view with dimensions and lifts indicated. Figures 3 and 4 show an isometric and a two-dimensional view of gate monolith AL-3. Time analyses are performed to model the incremental construction as closely as possible. The analytical method used to analyze the effects of creep, shrinkage, and thermal loads on the chamber monolith is a finite element solution. The finite element code used is ABAQUS (Hibbitt, Karlsson, and Sorenson, Inc. 1987).

5. Since this is an incremental analysis, the constitutive model takes into account the aging effects of the concrete. This is accomplished by using a two-dimensional user defined material model (UMAT) developed by Anatech, Inc. The model is capable of calculating the time-dependent parameters

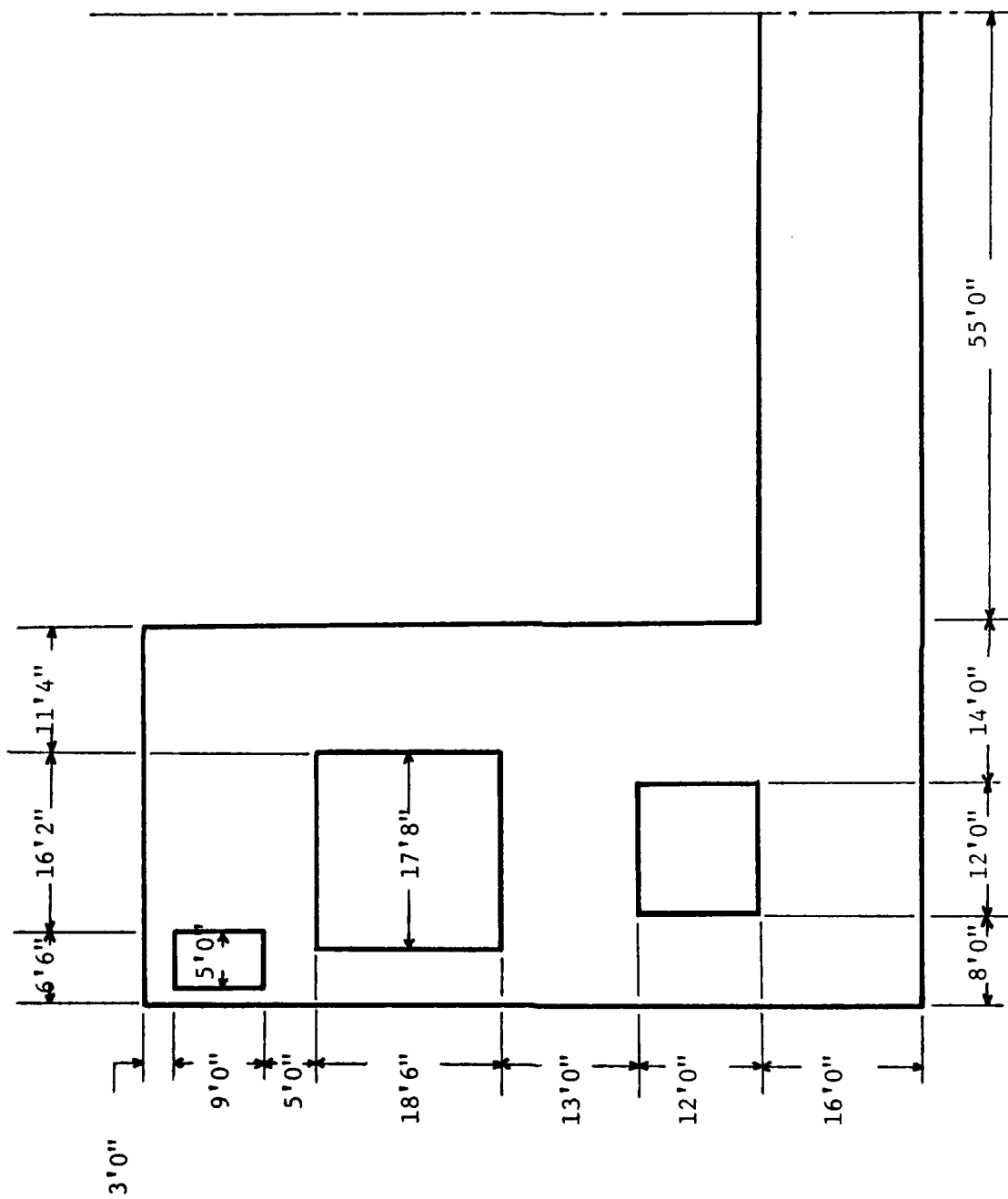


Figure 4. Two-dimensional view of gate monolith AL-3 for Lock & Dam 26R

important to the analysis. Thus, the effect of creep and shrinkage is accounted for in the analysis with the creep and shrinkage functions being based on laboratory test results. Also, the change in Young's Modulus with time is calculated to update the stiffness matrix for each increment. Finally, the subroutine is capable of determining when a crack occurs, and then updates the stiffness matrix.

### Objective and Scope

6. The primary objective of this study was to gain a better understanding of the effects of creep, shrinkage, thermal loads, incremental construction, and their effects on mass concrete structures. This was accomplished by performing a parametric study using upper and lower bounds on the creep and shrinkage functions as well as the adiabatic curve used to produce the heat of hydration as a function of time. Several load cases were run varying the three parameters among the upper and lower bounds in order to determine critical loading conditions. In addition, several load cases were run in which some of the parameters were isolated by neglecting their effects in the analysis process.

7. When the analyses were complete, the results of the various load cases were analyzed to determine which of these parameters had a significant effect on the structure. The worst realistic load case was determined so that the analysis could be extended to service load conditions and used as the primary load case for monolith AL-3. Also, a static analysis was performed applying only gravity and service loads. An assessment was made on the effects of the residual stresses from the incremental analysis process, with creep, shrinkage, and thermal loading included, compared with gravity turn-on coupled with service loads.

8. This report is basically divided into three sections. Parts I-III provide basic information on modelling and material properties. Parts IV-VIII are related to parametric studies performed on monolith AL-5 to assess the effects of thermal loads, creep, shrinkage, incremental construction, and their short and long term effects. Parts III and IX are related to the modelling and incremental construction of monolith AL-3. This monolith was targeted as a place where potential savings could be found through increased lift heights. Prior to analyzing this structures for both 11 and 16 lift

construction schedules, several other parameters were studied as shown in Parts IX through XI.

9. The results obtained are a first step in developing guidelines that can be used by the engineer when performing the design and analysis of mass concrete structures. Also, from the work performed, improvements can be made in the thermal stress analysis procedure. This includes modelling techniques and the implementation of such techniques.

### Introduction

10. Modelling and computer implementation to represent what physically occurs to the structure onsite is extremely important, if accurate results are to be obtained from an analysis. This requires both an accurate model of both the chamber monoliths, the construction procedure, and the material properties.

### Basic Concrete Properties

11. The input data used for the thermal and mechanical properties of concrete were obtained from previous studies for Melvin Price Locks and Dam by the US Army Corps of Engineers (Norman, Bombich, and Jones 1987). The concrete is assumed to have a nominal compressive strength of 3,000 psi\* using Type II cement with a maximum heat of hydration limit (70 cal/gm) and 25 percent replacement by solid volume of pozzolan (fly ash).

### Modelling for Heat Transfer Analysis

12. The convection coefficient used at the exposed surfaces in this analysis is based on a forced convection mode. This is a result of the fact that as the fluid (air) flows over the surface with some velocity, heat is carried away producing a temperature gradient (Holman 1981). Thus, the coefficient is approximated, for exposed surfaces, by using an equation that is a function of the mean wind speed velocity.\*\* Radiation heat transfers due to solar effects were neglected.

13. The convection coefficient for external surfaces is based on a mean velocity speed of 10 mph. For the unenclosed culvert and access void, a velocity of 1 mph was used since it was assumed that the unenclosed void would be exposed to and ventilated by ambient air; however, the air flow would be

---

\* A table of factors for converting non-SI to SI (metric) units of measurement is presented on page 4.

\*\* Personal Communication, July 1987, Tony Bombich, US Army Engineer Waterways Experiment Station, Vicksburg, MS.

reduced (Norman, Bombich, and Jones 1987). In addition, inside the voids, air elements were used to simulate the effect of air fair actually being there. To simulate the effect of the forms on external, vertical surfaces and for the culvert walls and roofs, a coefficient was calculated based on the type and thickness of the forms used. The coefficient used was based on the insulating effect caused by 3/4-in. plywood forms. An inch of wood is equivalent in insulation value to about 20 in. of concrete. The forms were assumed to be removed 2 days after the lift was placed. The forms are not actually removed at 2 days on the job site; however, this should result in a greater probability of surface cracking since the peak temperature at the surface is obtained near the same time as when the forms are being removed. This will cause a sudden cooling at the surface by the environment. Thus, a steeper gradient is produced causing higher tensile stresses.

14. The temperature of the convective medium was the mean ambient temperature as a function of time representative of the project site conditions (see Figure 5). The curve represents a sinusoidal curve with the highest temperature in August and the lowest in January. Daily variations in temperature were not used in this analysis since it would further complicate the analysis and the fact that daily variations are difficult to predict. All computer runs were based on a construction starting date of 1 July. This starting construction date was used because, when concrete is placed in cooler ambient temperatures, the maximum concrete temperature obtained will not be much greater than the final equilibrium temperature. The opposite extreme of starting construction in January could be as or more severe as starting in July and should be considered in future studies.

15. Concrete placement temperature was constant for all lifts of the structure. The temperature specified was 65° F. This placement temperature can be achieved during summer construction by using ice as a substitute for a portion of the water in the mix.

16. The initial starting temperature of the soil is dependent on depth. Figure 6 shows the temperature distribution used at start of construction. The distribution was obtained by performing a thermal analysis using only the soil elements exposed to the mean ambient temperature curve shown in Figure 5. The distribution shown is the soil temperature after a 1-year cycle. The depth of the soil used was 10 ft. A prior analysis has shown that only an

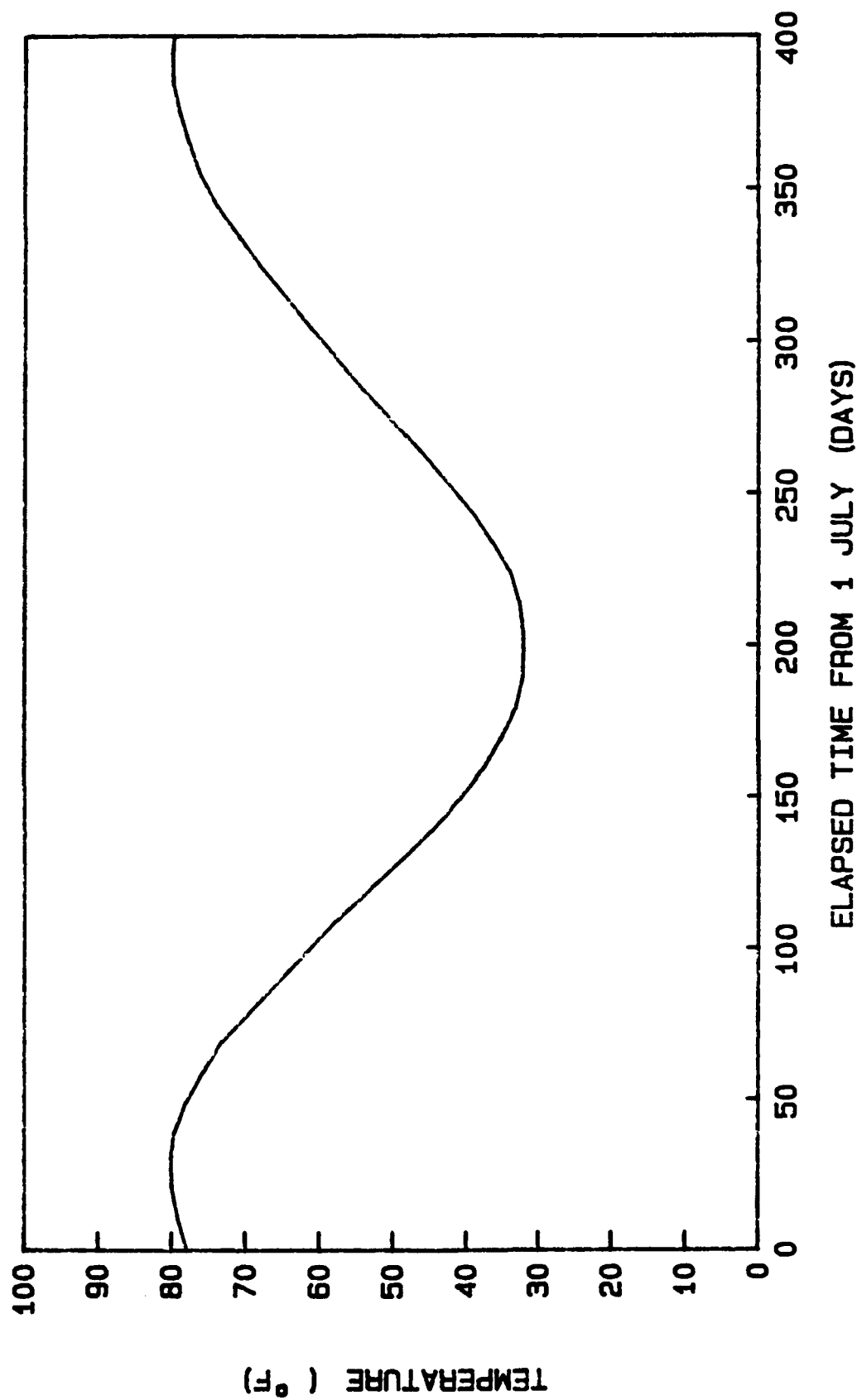


Figure 5. Mean daily ambient temperature for Alton, Illinois

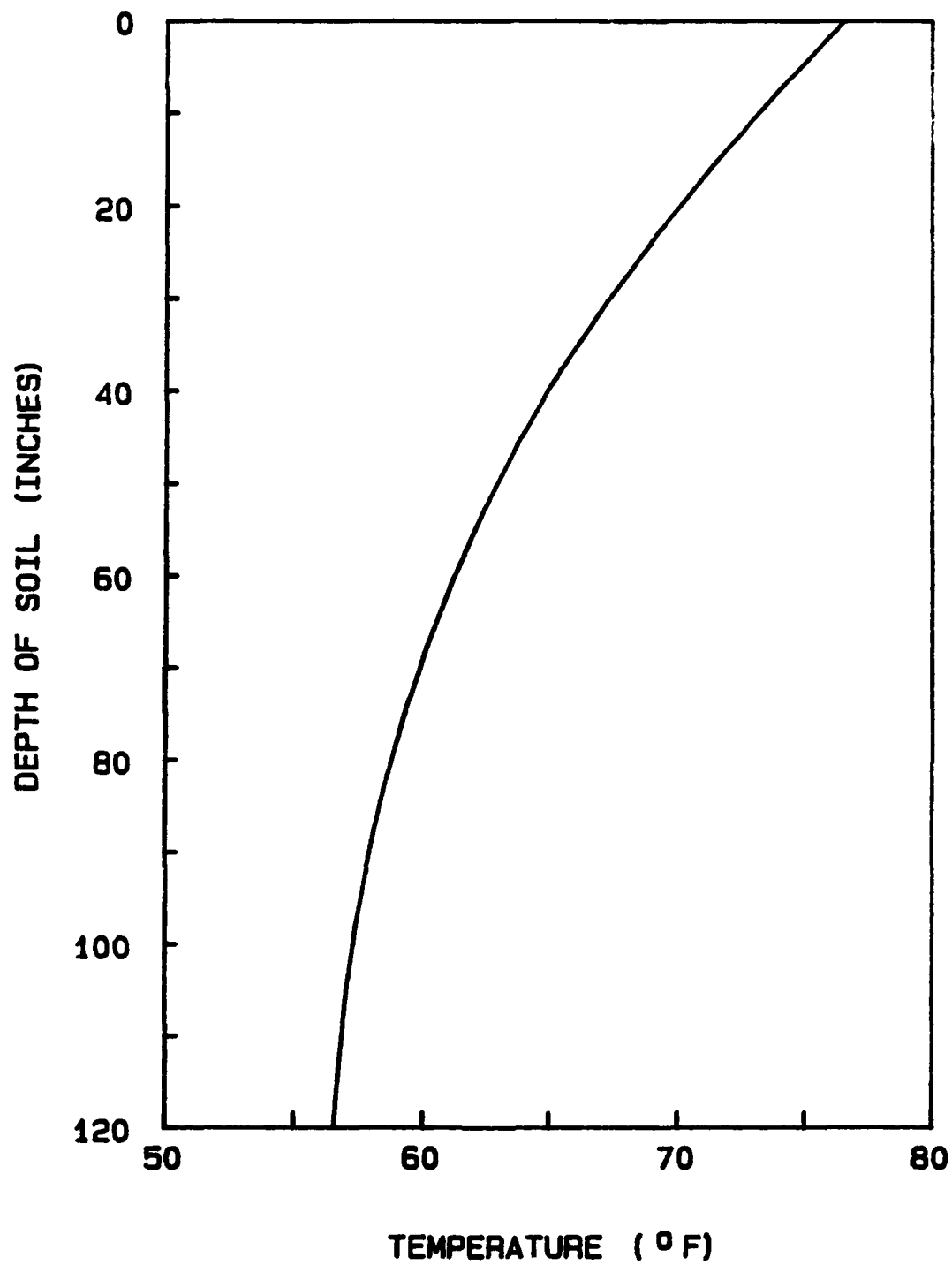


Figure 6. Soil temperature at start of construction

insignificant amount of heat flowed past this depth. The initial temperature of the air was 75° F.

17. A placement rate of 5 days was assumed for each lift with the form work being removed after 2 days, as previously stated. This rate is the maximum allowed by the specifications; whereas, actual lift placements proceed much slower. However, this rate will produce higher stresses especially near lift surfaces since this is the time when peak temperatures are obtained. Consequently, a higher thermal gradient is obtained producing higher stresses.

18. Lift heights used were provided by the US Army Engineer District, St. Louis. There are 8 lifts in the monolith. Lift heights for the base slab are 5 ft; whereas, heights for the chamber wall vary from 4 up to 15.5 ft. Higher lifts are obtained in the wall since the thickness of the members decreases. The actual lift arrangement is shown in the finite element mesh in Figure 7.

19. The heat of hydration as a function of time was obtained by determining the adiabatic temperature rise for a laboratory test specimen. The upper bound adiabatic curve is for a mixture having heat generation due to hydration of cement of 70 cal/gm; whereas, the lower bound is 53 cal/gm (see Figure 8). Note that most of the temperature rise occurs in the first 5 days. The heat of hydration can be calculated by:

$$Q = C\rho\Delta T/\Delta t \quad (1)$$

where

C = specific heat

$\rho$  = density

$\Delta T$  = change in temperature

$\Delta t$  = change in time

The upper and lower bound heat of hydration curves are shown in Figure 9.

20. Looking at Figures 1 and 3, we can see that the structures are geometrically symmetric. Obviously, the results for the thermal analyses will be the same for the right half and the left half of each structure for the assumptions used (i.e. neglecting solar effects, and assuming wind speed is constant over all exposed surfaces for calculating the convection coefficient). Thus, only one-half of the monoliths needs be modelled. For a heat transfer analysis, a boundary condition is invoked that allows no heat flow in the horizontal direction across the line of symmetry.

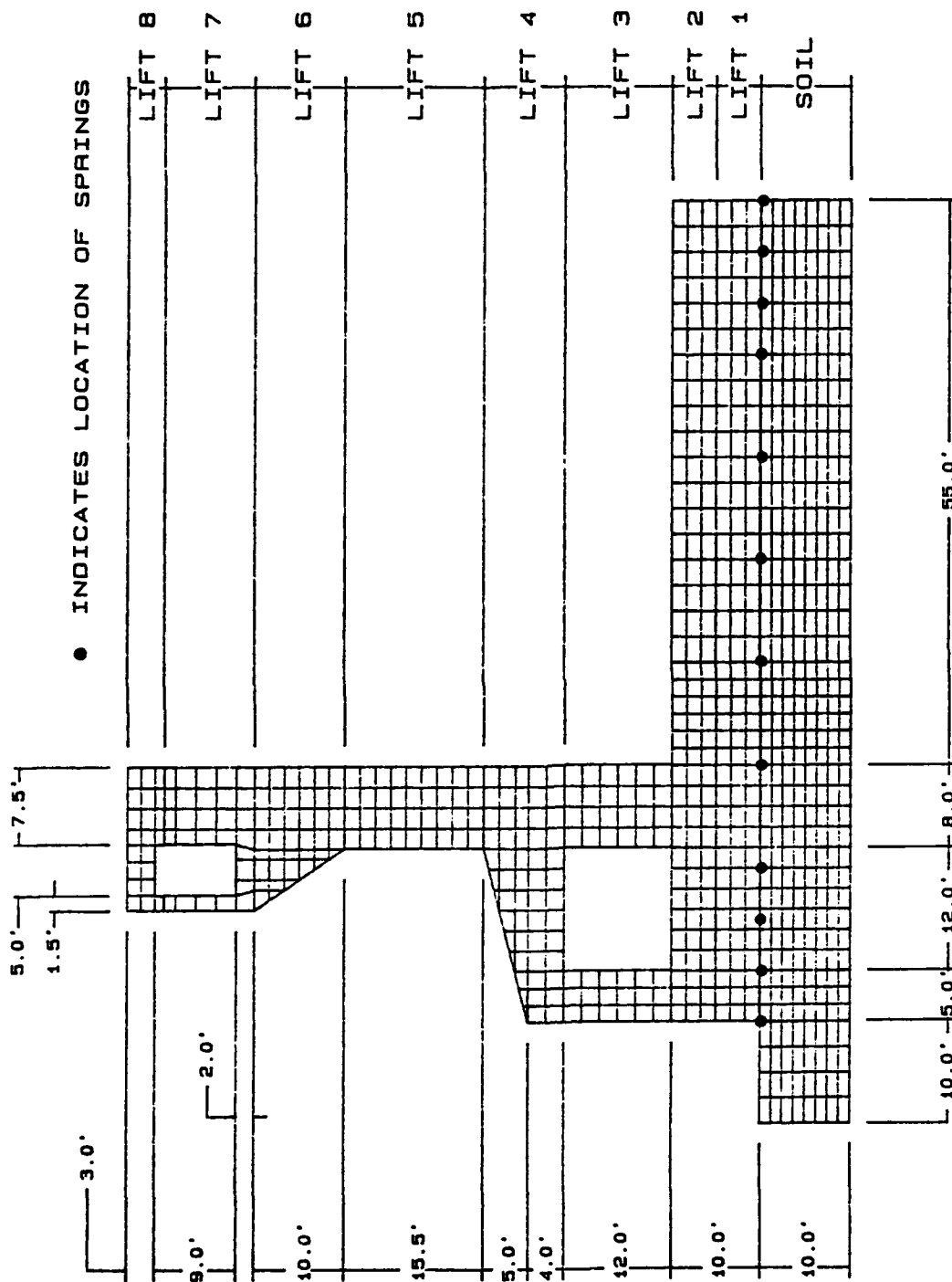


Figure 7. Finite element mesh used for heat transfer and stress analysis

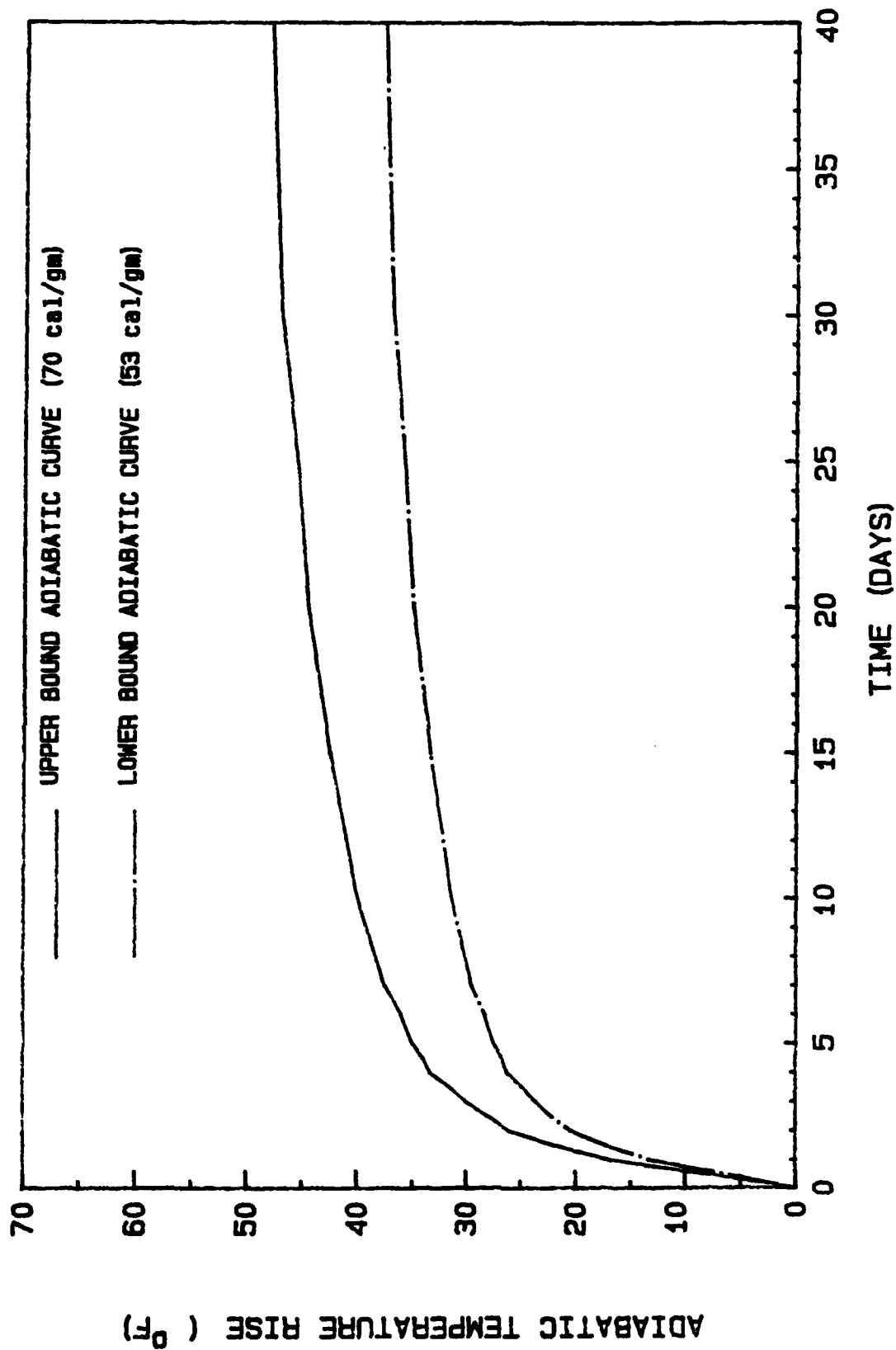


Figure 8. Upper and lower bound adiabatic temperature rise

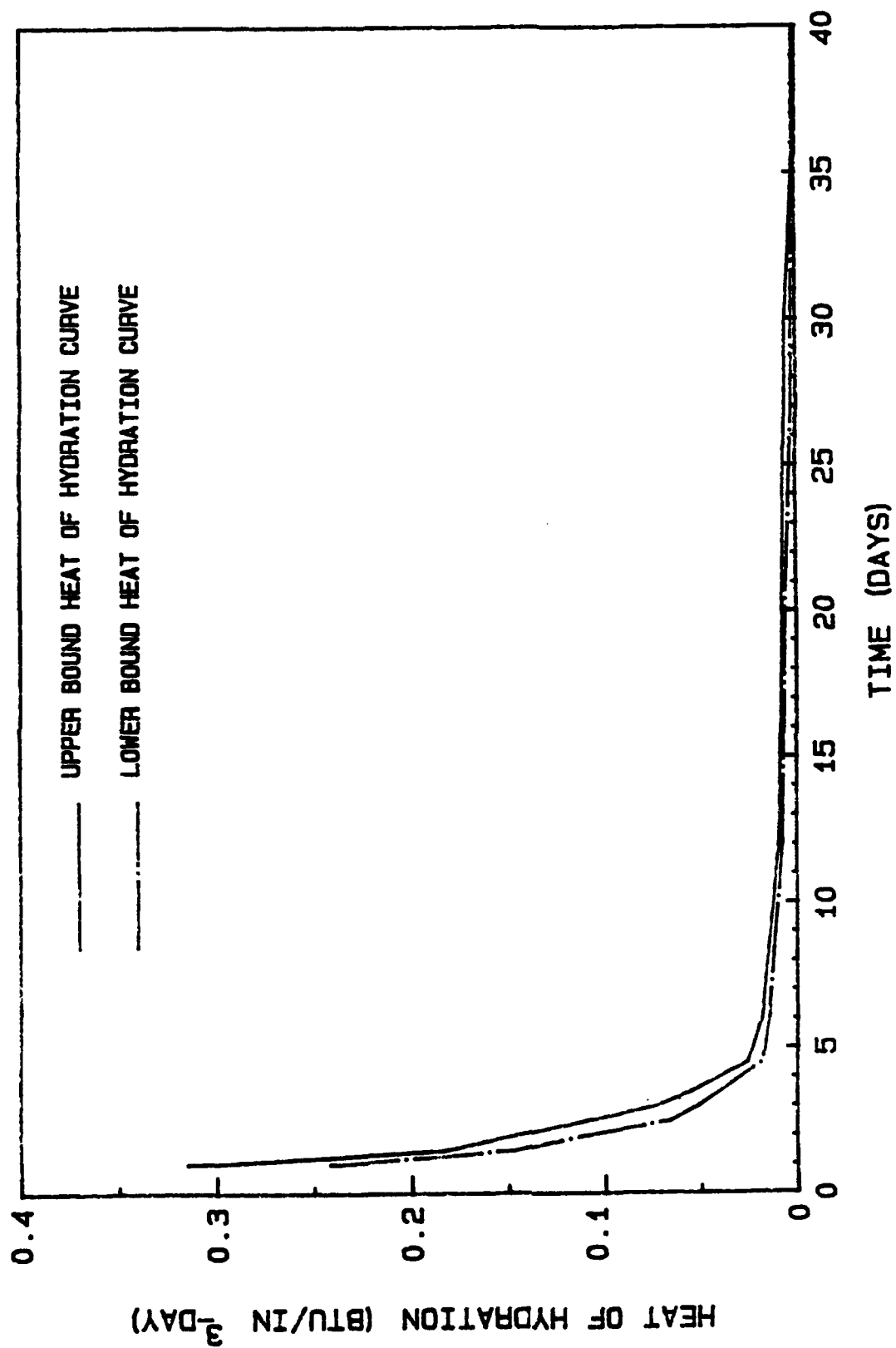


Figure 9. Upper and lower bound heat of hydration

21. The values of the material properties and convection coefficients used in the thermal analysis are given in Table 1. All of the above mentioned properties and parameters are capable of being modelled by ABAQUS. The heat of hydration for each time increment was calculated using a subroutine called DFLUX. This subroutine was written explicitly to handle the incremental construction process.

#### Modelling for Elastic Stress Analysis

22. The entire Melvin Price Locks and Dam structure is founded on H-piles. The pile arrangement and stiffness for the chamber monolith were supplied by the US Army Engineer District, St. Louis, and are shown in Figure 10 and Table 2. Pile stiffnesses for a strong soil pile support were used since greater restraint would be provided (Headquarters, US Army Corps of Engineers 1983). The actual finite element model is a section perpendicular to the direction of flow and was analyzed as a plane strain problem. As we can see from the figure, piles are arranged in rows parallel to the direction of flow, and the number of piles in the row varies. The piles were modelled in the analyses by using linear springs. The spring stiffness was obtained by finding the average stiffness of each row of piles per inch thickness. The spring stiffnesses used in the analyses are given in Table 3. Note that the value of the spring stiffness at the symmetric boundary condition is reduced by one-half.

23. Previous thermal studies by WES were performed with the soil elements removed during the stress analysis. At early times, this analysis showed excessive displacements at the bottom of the structure that do not actually exist. The large displacements are a result of the concrete's low strength after placement and thus its inability to effectively distribute the loads between the piles. However, during construction, the site is dewatered; thus, the soil does provide some restraint both horizontally and vertically. Consequently, the soil elements were included in the analysis performed here. The material properties used are representative of the soil found on the site. The value of Young's modulus used is 3,000 psi, and Poisson's ratio is 0.35. When service loads were applied, the soil elements were removed since Young's modulus would be greatly reduced due to saturation of the soil.

24. Accurately modelling the roof of the voids is extremely important since internal galleries are a main source of cracking in mass concrete

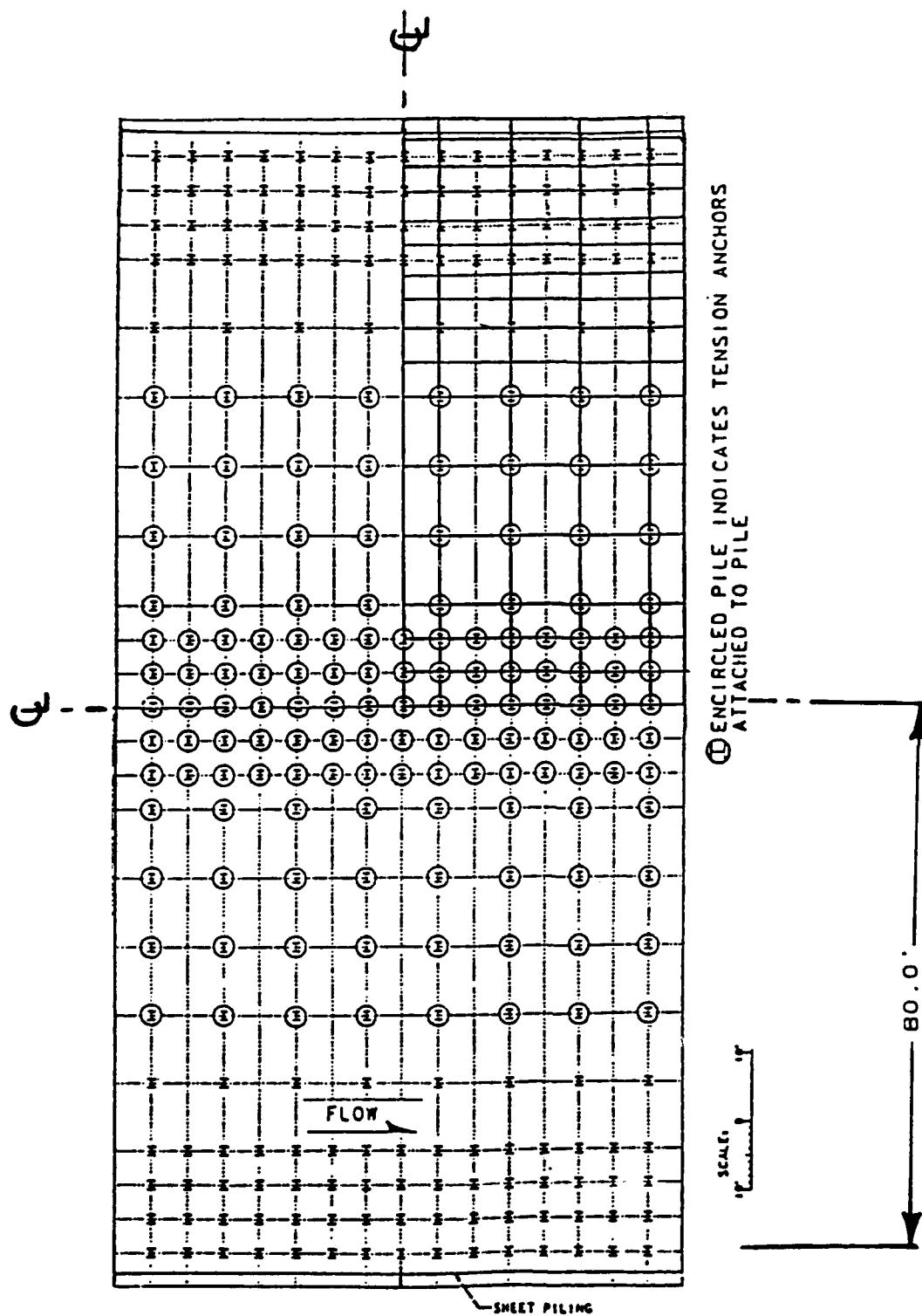


Figure 10. Pile layout for chamber monolith

(Rawhouser 1945). To leave the roof unsupported at early times after placement would result in unrealistic displacements and high stresses. Applying a fixed boundary condition would provide more restraint than actually exists and would force the walls into an erroneous state of stress. Thus, a subroutine was written called multiple point constraint (MPC) which allows individual constraints to be imposed on an arbitrary degree of freedom with the displacement being specified by some function with respect to two referenced degrees of freedom. When the constraint is imposed, the associated degrees of freedom are removed from the system matrix. In addition, the subroutine also calculates an array of derivatives required in order to redistribute the loads. The displacement function used produces a linear displacement in the vertical direction between the nodes at the top of the walls of the culvert and gallery. The constraint was removed 7 days after the lift was placed. When constructing the monoliths, a rigid box frame is placed to form and support the voids.

25. At the symmetric boundary condition, a restraint was applied to prevent movement in the horizontal direction but was left free to move in the vertical direction. The bottom of the soil was also prevented from moving in both the horizontal and vertical direction.

26. Thermal loads primarily depend on the change in temperature, the coefficient of thermal expansion, and Poisson's ratio when plane strain conditions are assumed. The value for the coefficient of thermal expansion used in the analysis was  $4.5 \times 10^{-6}$  in./in. ° F (Fintel 1974 and US Army Corps of Engineer District, St. Louis 1988). The value of Poisson's ratio used was 0.17. This value was assumed to be constant.

27. Gravity loads (body forces) were turned on 1 day after the lift was placed. Prior to 1 day, a distributed load was placed on the lift below to simulate the effect of the new lift. The loads were applied in this manner because of the low strength of concrete before 1 day and because time of set does not occur until about 12 hr. If the loads were applied when the lift was placed, the concrete would flow out the vertical face. During the actual construction process, the forms would provide the restraint to prevent this since a body force truly exists.

28. The service loads applied are shown in Figures 11 and 12. Service loads were applied 102 days after start of construction or 67 days after the last lift was placed. This amount of time was chosen since the thermal loads

**Figure 11. Normal service load conditions**

# EQ LOADING CONDITION

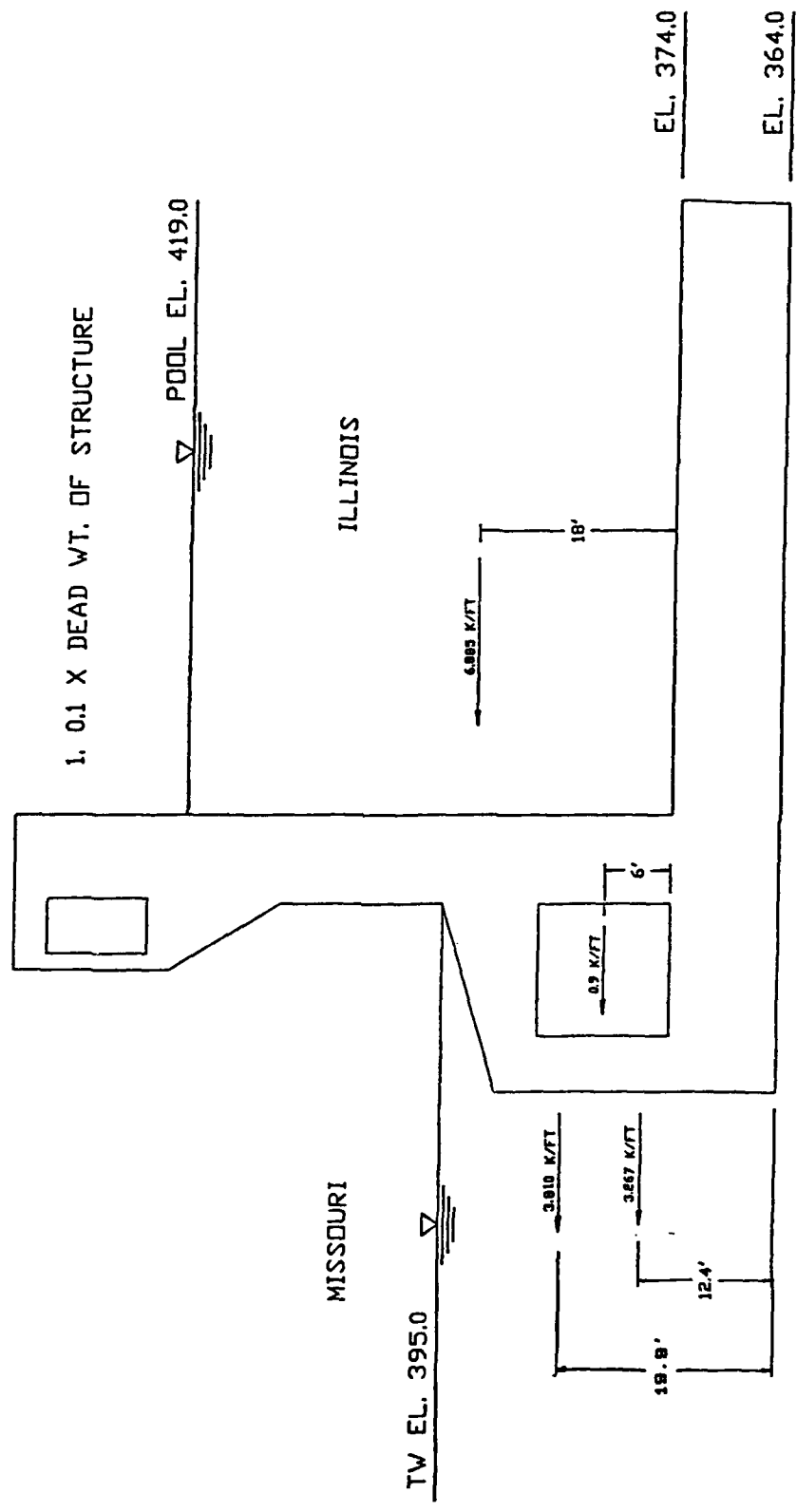


Figure 12. Earthquake service load conditions

had dissipated and any residual effects were considered to have stabilized. The loads represent backfill in place, upper pool at el 419 ft above sea level, upper pool elevation in lock, tailwater at el 395, minimum uplift pressure, 0.1-g earthquake force directed toward the Missouri side, and an equivalent concentrated force due to the effect of the water and backfill during an earthquake. The concentrated forces shown in the figures were actually applied as a uniform pressure over two of the element faces to avoid a stress concentration.

#### Mesh and Element Selection and Time Frame

29. As stated previously, the size of the elements and time step will determine how fast the solution process will proceed and the amount of error in the solution. For the finite element method, the error in the solution decreases as the size of the largest element goes to zero. Thus, proper mesh refinement and using a suitable time step is important to assure the quality of the results and also to minimize computing time and space.

30. In addition to choosing the element size, the element type also had to be selected. ABAQUS element library includes both eight noded and four noded quadrilateral elements for both heat transfer and plane strain stress analysis. Eight noded elements are generally preferred for linear analyses because larger elements can be used, thus reducing the number of elements in the mesh, while still producing good results. Four noded elements are preferred for nonlinear analyses if the size of the element is sufficiently small enough to capture the nonlinearity. The same mesh and element type was used for both the thermal and stress analyses, because the stress analysis uses the temperatures calculated in thermal analysis to determine the thermal induced stresses. The eight noded element was preferred in this study since fewer elements could be used to generate the mesh and because studies previously and currently being performed by the US Army Corps of Engineers also used the eight noded elements; thus, comparing results would be simpler. The eight noded element can also be used with either nine or four Gaussian quadrature points for the stress analysis. Earlier studies by WES showed that nearly the same results were obtained when the reduced integration option was used. Therefore, the reduced integration was used in the analysis performed here so as to reduce computing time and space.

31. ABAQUS also offers interface elements for both heat transfer and stress analysis. The one-dimensional heat transfer interface element allows the user to prescribe the conductance between different materials placed against each other. These elements can be useful at the soil-concrete interface and lift interfaces. The elements were, however, only used between the soil-concrete interface. The reason for this was due to the fact that the common node shared by the top of the soil element and the bottom of the concrete element can only be prescribed one initial temperature. However, with the interface element, the soil and concrete nodes, at the interface, can be given their respective starting temperature. The interface elements were not used between the lift interfaces.

32. The time step established by Waterways Experiment Station (WES) was also used in this analysis. The time increment used was one-fourth day for the first 2 days and one-half day for the next 3 days after a lift was placed. A 5-day time step was used to run the analysis to service loads. This time step works well to achieve the basic tolerance measure for the solution of the equilibrium equations at each increment without requiring an excessive number of iterations (Hibbitt, Karlsson, and Sorenson, Inc. 1987). The program allows the user to specify the tolerance level, the number of iterations allowed in an increment, and the ability to have the solution continue even though the tolerance level was not achieved in the allowed number of iterations. The tolerance level used was 10 lb with 20 iterations allowed in an increment. After lift 4 was placed, only the first increment did not converge. Note, however, that this occurred when the MPC was first applied, and that the program calculated the residual force to be approximately 15 lb. It was estimated that 10 more iterations would be required to achieve convergence.

33. The numerical stability of the heat transfer analysis can be assured by following a simple prederived stability criterion. With the time step being established, the element size can be determined by equation:

$$\Delta t > (\rho C / 6k) \Delta L^2 \quad (2)$$

where

$\rho$  = density in lb/ft<sup>3</sup>

C - specific heat in Btu/lb °F

k - thermal conductivity in Btu/(h • ft °F)

$\Delta L$  - element dimension in the direction considered in feet

$\Delta t$  - time step in h (hr)

The maximum element size for concrete material is 27.76 in. and for soil material is 16.70 in. when the eight noded element is used. Preliminary analyses were performed with the element size violating this equation which provided unusual oscillations in the results from the heat transfer analysis. Consequently, several analyses were made using an 8 ft thick by 80 ft long flat slab founded on 10 ft of soil with the various elements and sizes shown in Figure 13. For mesh IV, the interface element was also used between the soil and the concrete. The same material properties and parameters were used as outlined above but a different adiabatic curve was used which produced higher temperatures, and the initial soil temperature was constant throughout the depth at a value of 55° F. The results are shown in Figure 14.

34. The results shown are at the center line of the slab, 6 hr after the lift is placed. The results show that the element size should not violate Equation 2 in the direction of heat flow to prevent unrealistic oscillations. However; toward the middle of the slab, the element size can be increased in the horizontal direction since heat is flowing only in the vertical direction. It was found that an aspect ratio of two is acceptable in this area. The finite element mesh used for the chamber monolith was shown in Figure 7. The mesh has 328 soil elements, 37 interface elements and 51 air elements (used in heat transfer analysis only), and 445 concrete elements.

# CONCRETE ELEMENT

# SOIL ELEMENT

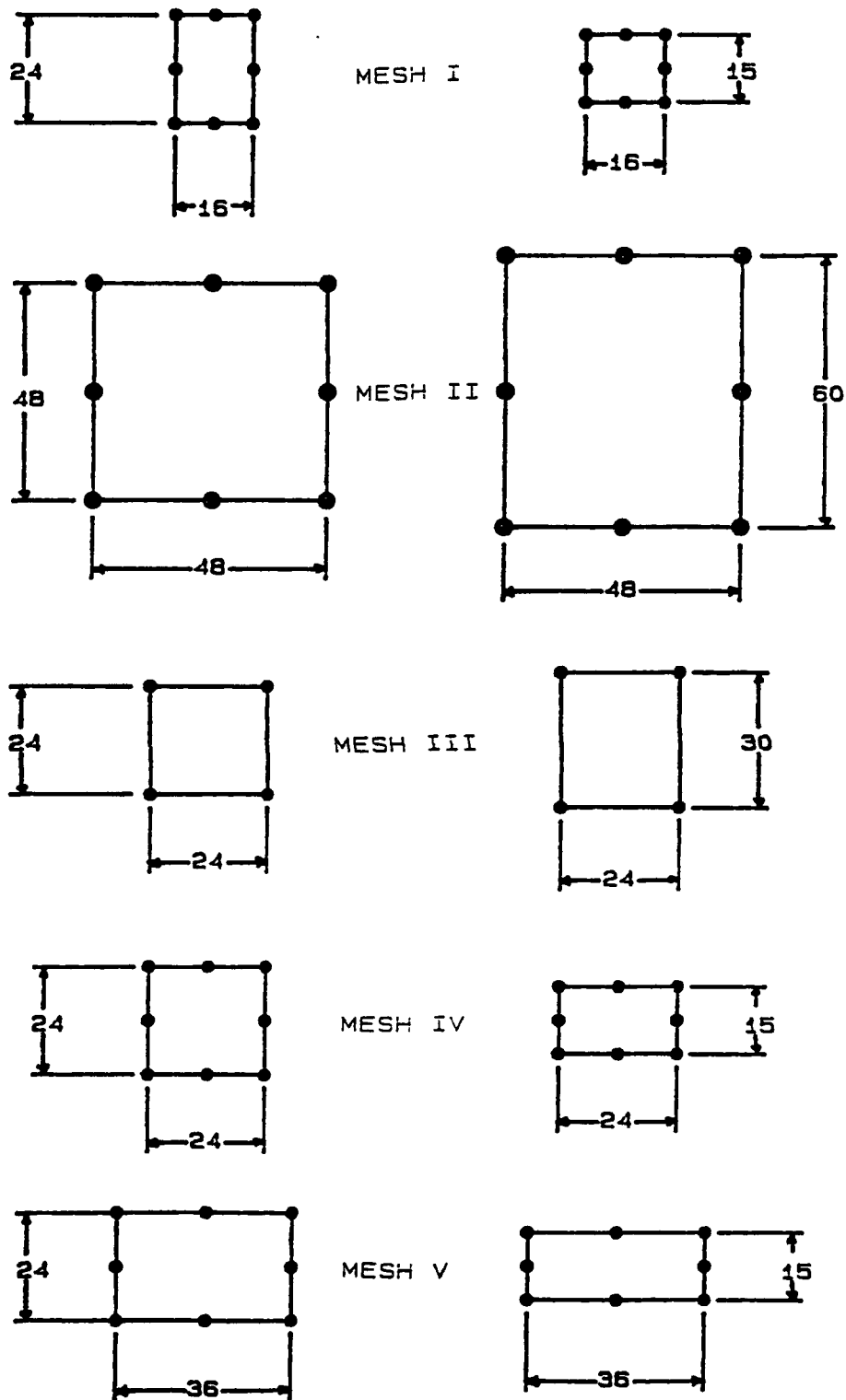


Figure 13. Element dimensions used to select mesh layout, in.

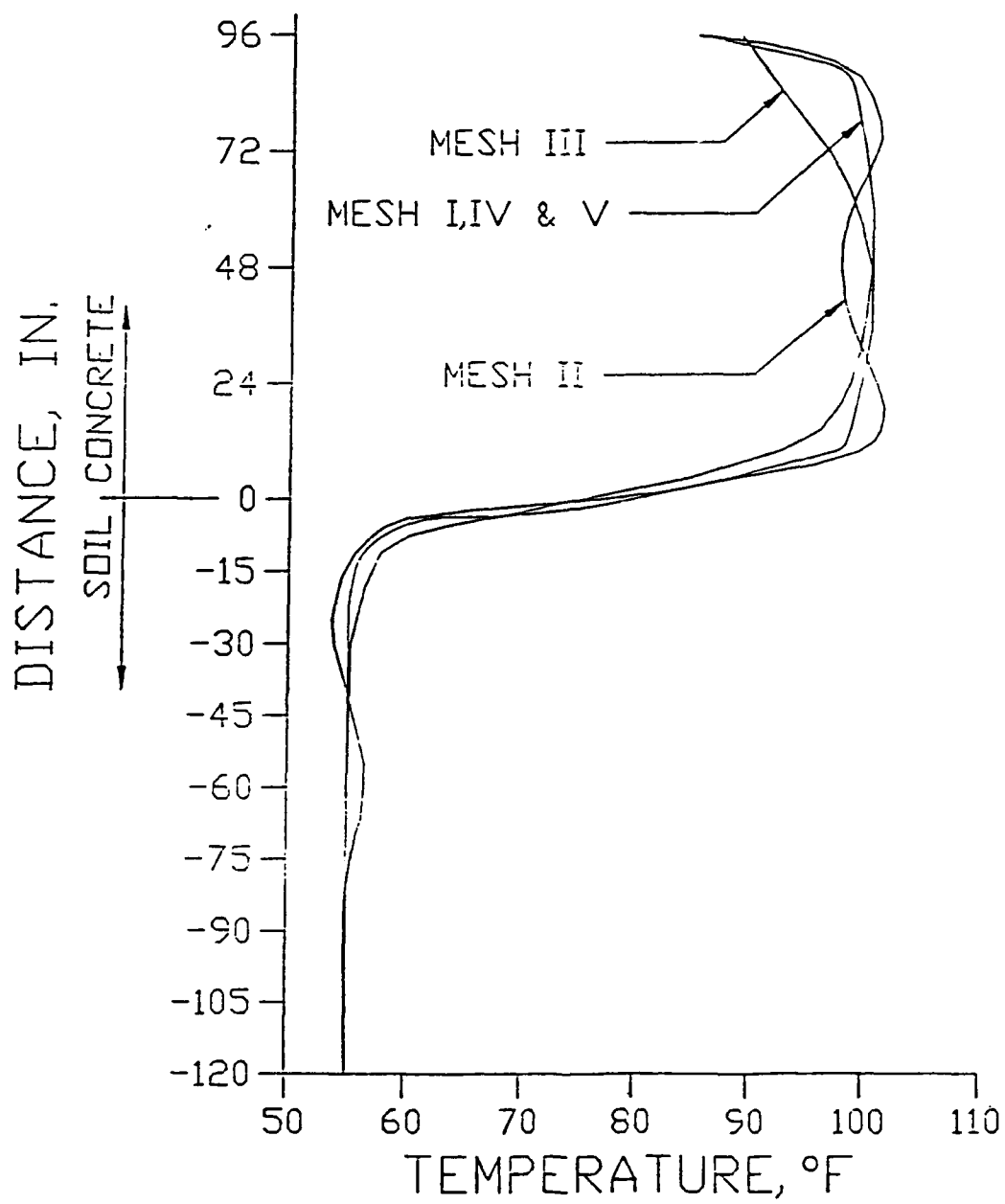


Figure 14. Temperature distribution for 8-ft slab using various meshes

PART III: TWO-DIMENSIONAL USER MATERIAL MODEL FOR TIME DEPENDENT  
EFFECTS OF CONCRETE FOR MONOLITHS AL-3 and AL-5

Introduction

35. The important time dependent effects include creep, shrinkage, Young's modulus, and cracking. One of the reasons for performing these analyses is to predict the significance of creep and shrinkage on mass concrete structures. Thus, how the creep and shrinkage functions are modelled is a major concern. The equations presented here were generated by WES (see Norman, Bombich, and Jones (1987) for a more detailed description). The two-dimensional user material subroutine UMAT was developed by Anatech, Inc., under the direction of WES. The values for the upper and lower bound of creep and shrinkage were decided upon at the Thermal Stresses in Mass Concrete Structure meeting in July 1987 to account for variability in test results.

Shrinkage

36. The type of shrinkage used in the model is autogenous shrinkage. Autogenous shrinkage is internal drying due to heat of hydration and may account for up to 95 percent of shrinkage effects in mass concrete. Drying shrinkage, however, was neglected in this analysis.

37. Autogenous shrinkage is largely a result of the chemical process that occurs during curing of concrete. This process occurs over a long period of time, up to several years. Much of the effect of autogenous shrinkage occurs in a short time after the lift is placed. The shrinkage process is also a volumetric process since curing is assumed to take place at the same rate throughout the lift, then shrinkage results equally in all directions.

38. The shrinkage strain equation in UMAT is given by:

$$\epsilon^s(t) = C_1(1 - e^{-s_1 t}) + C_2(1 - e^{-s_2 t}) \quad (3)$$

where

$$C_1 = 102.5 \times 10^{-6}$$

$$C_2 = 72.5 \times 10^{-6}$$

$$s_1 = -0.15$$

$$s_2 = -0.02263$$

Figure 15 shows shrinkage strains plotted against time for the upper and lower bound values that were used in the analysis.

### Creep

39. Creep of concrete is the dimensional change or increase in strain with time due to a sustained stress (Fintel 1974). In freshly placed concrete, volume changes due to creep are largely unrecoverable; whereas, creep that occurs in old or dry concrete is largely recoverable and appears to be independent of temperature and stress. Creep is generally a linear function up to a stress-strength ratio of 50 percent of the ultimate strength of the concrete. Beyond that point, creep becomes nonlinear (Fintel 1974). In addition, the rate of creep is high during the initial period of loading.

40. Creep is related to the age of the concrete and the elastic modulus at the time of loading, size and shape of the member, duration of the load, modulus and volumetric percent of aggregate, temperature, and the amount of steel reinforcement. The effect of the aggregate and reinforcement is to reduce the overall creep effect by restraining volume changes.

41. The creep relation in UMAT as a function of time, loading age, and temperature is given by:

$$J(t, \tau, T) = \sum_{i=1}^2 A_i(\tau, T) (1 - e^{-r_i(t-\tau)}) + D(\tau, T)(t-\tau) \quad (4)$$

where

$$A_1(\tau, T) = A_{01} e^{-Q/RT} \left[ \frac{E(3)}{E(\tau)} \right]^2$$

$$D(\tau, T) = D_{0e} e^{-Q/RT} \left[ \frac{E(3)}{E\tau} \right]^2$$

$$E(\tau) = E_0 + E_1(1 - e^{-n_1(\tau-1)}) + E_2(1 - e^{-n_2(\tau-1)})$$

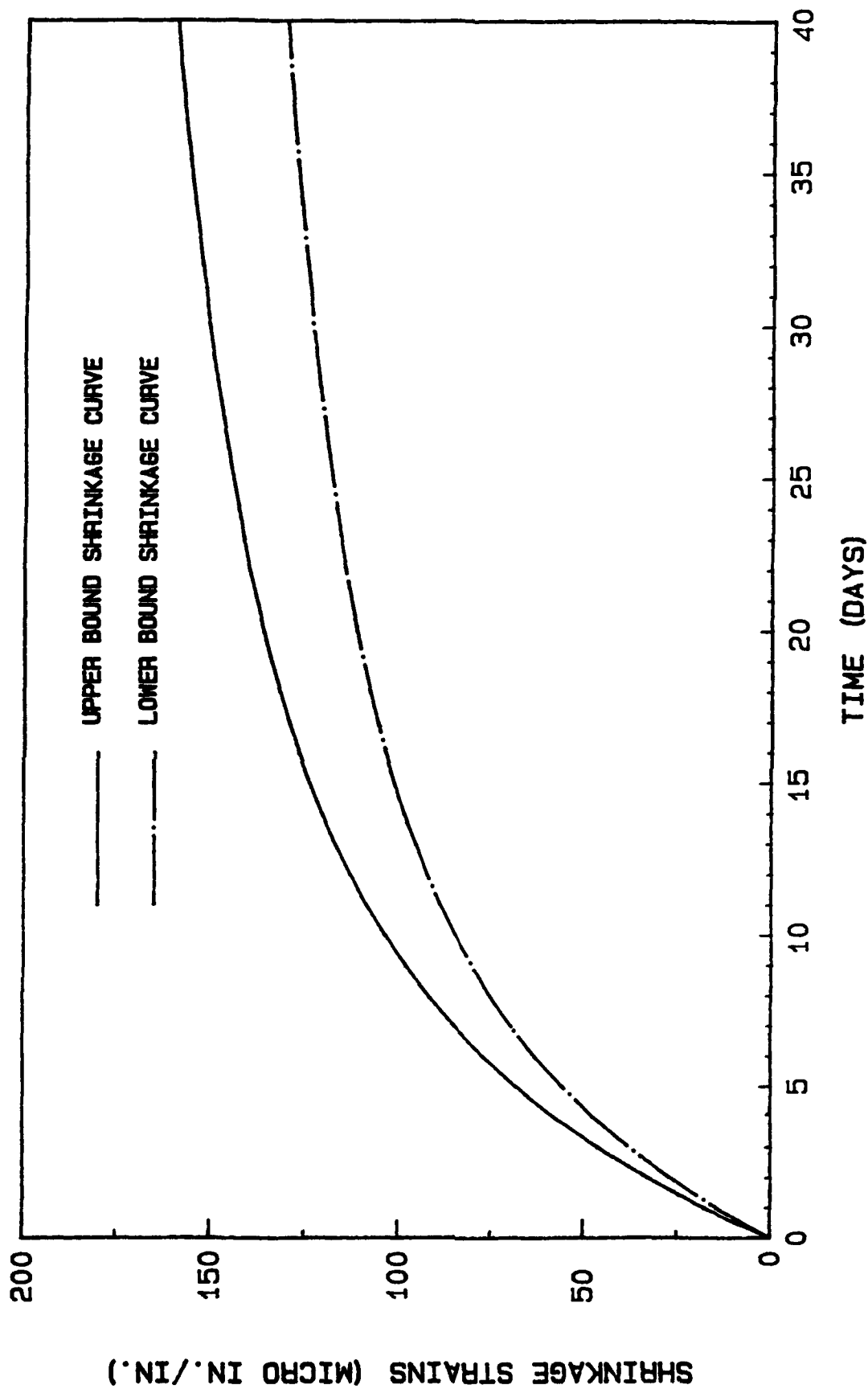


Figure 15. Upper and lower bound shrinkage strains versus time

where

$E(\tau)$  = Young's modulus as a function of time

$T$  = temperature

$R$  = gas content

Remaining values are material constants obtained from tests (Norman, Bombich and Jones 1987). The term involving the square of Young's modulus in the Coefficient A and D is the creep aging factor. The upper and lower bound specific creep curve used is shown in Figure 16. The first term in Equation 3-2 controls the short term creep for the first day. The second term governs the intermediate creep, up to 30 days, and the last term gives the creep behavior after 30 days (Anatech, Inc. 1987). The plot of Young's modulus versus time is shown in Figure 17.

42. With the specific creep and shrinkage function specified, the uniaxial strain can be calculated by:

$$\epsilon(t) = \int_0^t [1/E(\tau) + J(t, \tau, T)] \partial \sigma(\tau) / \partial \tau + \alpha \Delta T + \epsilon^s \quad (5)$$

Thus, the stresses can also be calculated and the stress analysis is near complete. With both stresses and strains calculated, the cracking criteria can now be implemented.

### Cracking Criteria

43. The cracking criterion that must be satisfied for a crack to be initiated into the model is as follows. The criterion is strain driven but is modified by the stress. For isotropic material, the principal strain and principal stress direction coincide (Anatech, Inc. 1987). The two-dimensional failure surface is shown in Figure 18. The tensile strength is calculated using an interactive criterion since a stress or a strain criterion alone is not general enough for a time dependent, nonlinear analysis including creep and shrinkage effects (Anatech, Inc. 1987). Thus, Figure 19 is used to relate cracking stresses and strains based on experimental data. For simplicity, a linear relationship is assumed. The factor of 2 is arbitrary but is used to expand the curve above and below the midpoint (uniaxial tension test) so as to accommodate cracking at high stresses and low strains and vice versa. Note

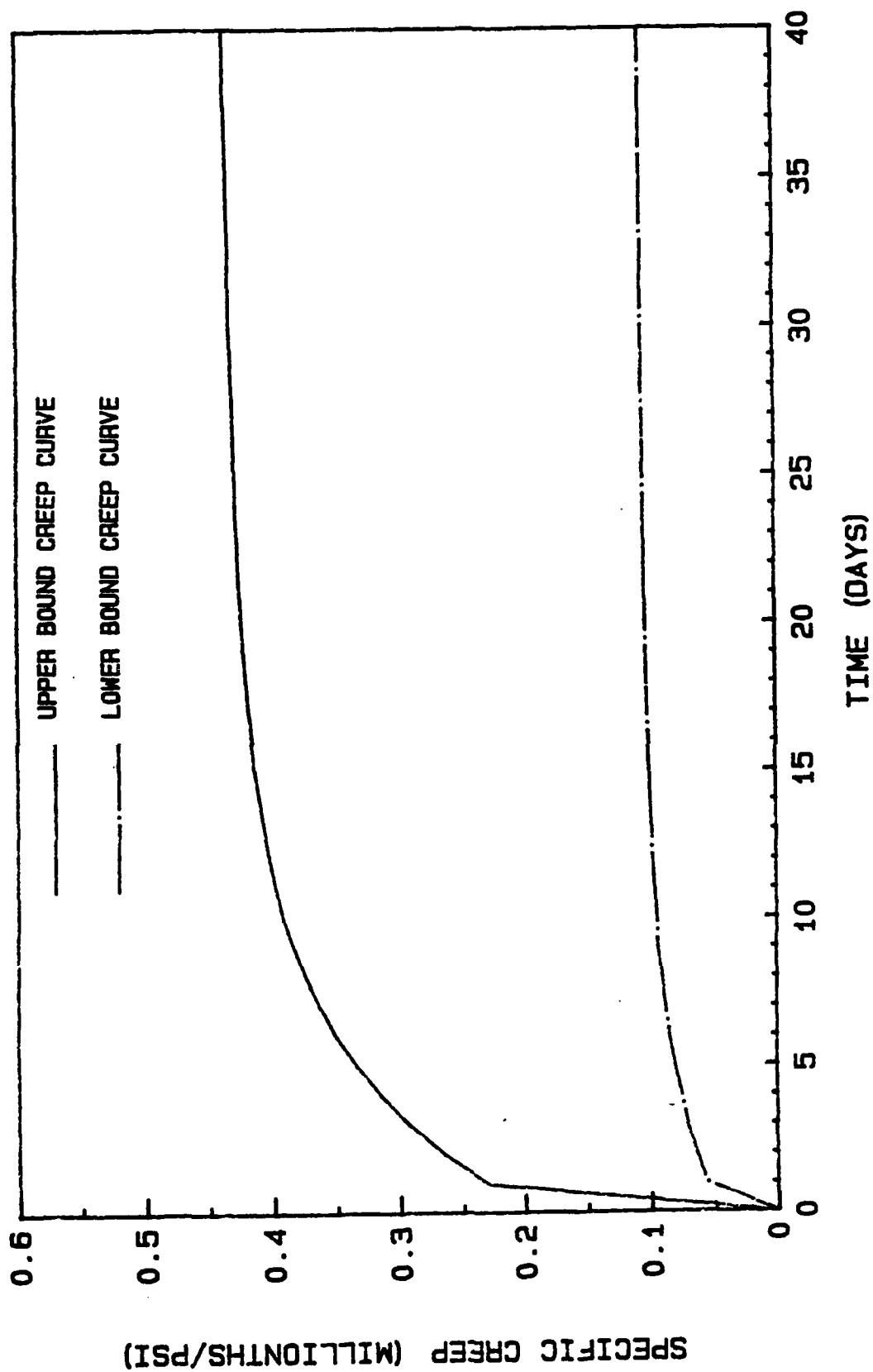


Figure 16. Upper and lower bound specific creep versus time

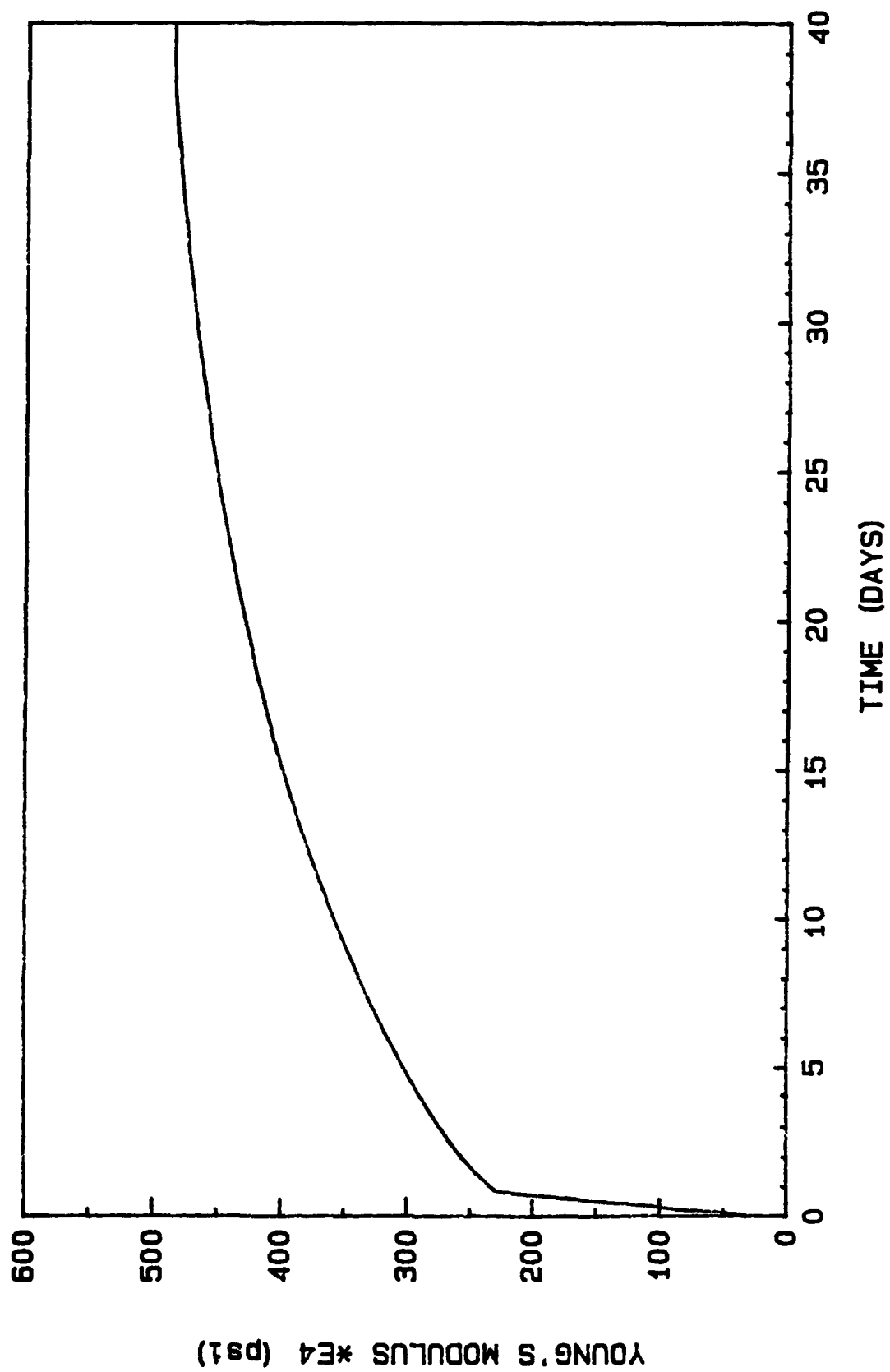


Figure 17. Young's modulus versus time

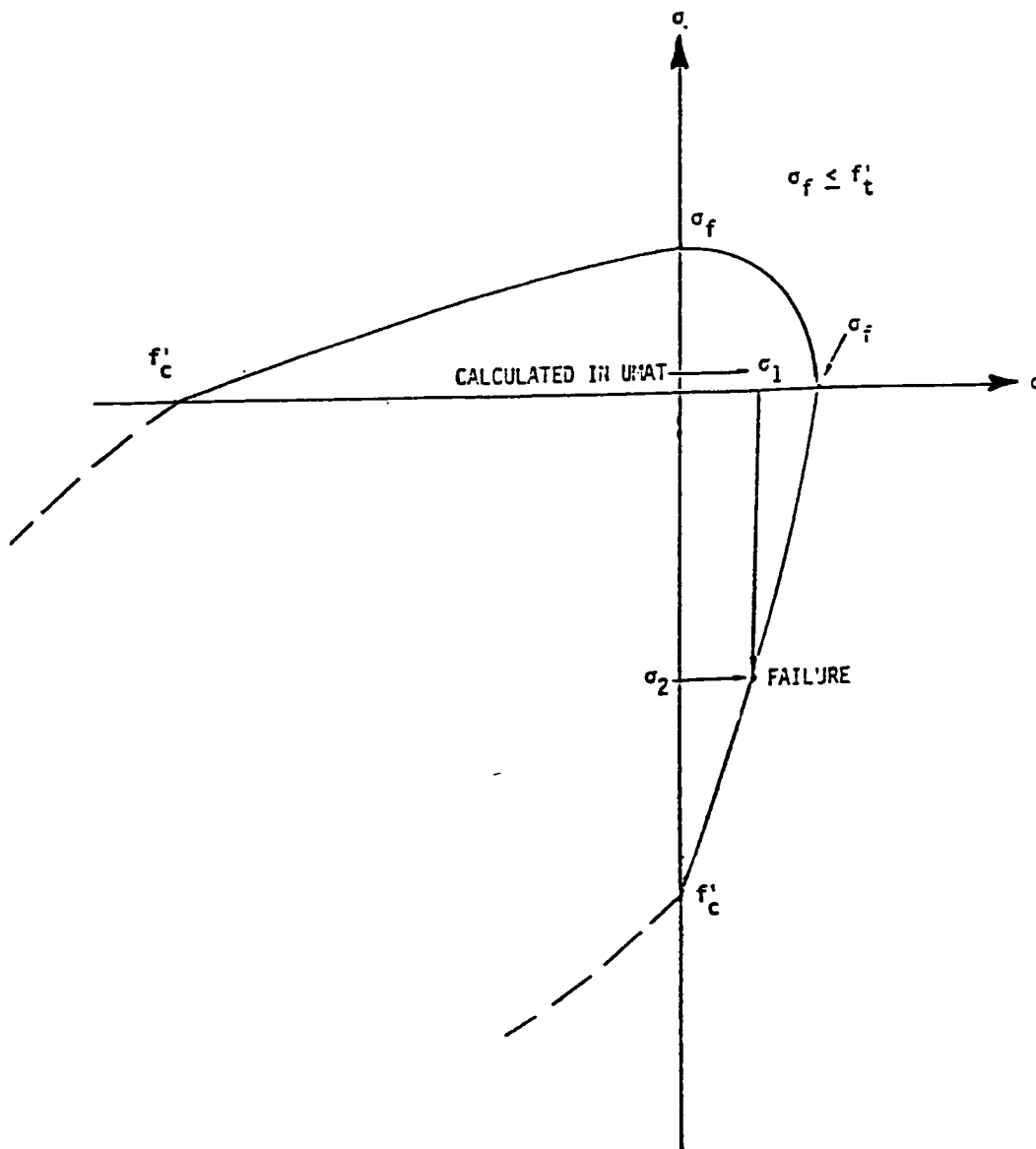
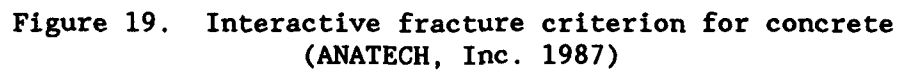


Figure 18. Concrete fracture surface (Anatech, Inc. 1987)

that from the theory of elasticity, cracking is impossible for strains less than zero for compressible material (i.e. Poisson's ratio  $< 0.5$ ) (Anatech, Inc. 1987).

44. To check the cracking criterion, the maximum principal strain  $\epsilon_1$  is first found. Next, Figure 19 is entered with  $\epsilon_1$  to find  $\sigma_t$  which is used to adjust Figure 18. If the point  $(\sigma_1, \sigma_2)$ , the principal stress components, lie outside the failure surface, a crack is initiated in the direction of the principal strain direction. The constitutive matrix is reformulated so that the crack can be taken into account when calculating nodal forces and in



37

### Introduction

45. The temperatures at selected nodes in the finite element mesh will be presented and discussed. The nodal temperatures are plotted against time. The time scale is relative to when the node is activated in the analysis process, or time zero corresponds to when the lift is placed. The solid lines are the results from the analysis using the upper bound adiabatic temperature rise curve (70 cal/gm), and the solid-dashed lines are the results when the lower bound adiabatic temperature rise curve (53 cal/gm) is used to determine the heat of hydration. The small circle on the monolith indicates the approximate location of the node and the top of a lift is indicated by the horizontal lines. Figure 20 shows the finite element mesh again with some of the nodes and elements numbered for reference of exact locations of the nodes. Figures 21-34 are temperature versus time plots at locations near the Gauss points where stresses were investigated. Figures 35-37 are presented because of their significance to the heat transfer analysis.

### Discussion of the Heat Transfer Analysis Results

46. Figures 21-34 are broken into three groups. Figures 20-25 are at nodes that are at the top of a lift when placed but become imbedded in the model when the next lift is placed. Figure 25 is a node at the soil-concrete interface. The nodes in Figures 26-34 are on the surface and always remain exposed to ambient conditions.

47. From Figures 21-24, the following patterns can be identified. After the lift is placed, a large temperature rise occurs in the first day due primarily to convection since the temperature of the surroundings during placement of all lifts is approximately 80° F. The temperature then remains constant at a temperature just slightly above 80° F until, at 5 days, another temperature rise occurs due to the placement of the next lift. This temperature rise is primarily a conduction process due to the heat liberated from the newly placed lift. The peak temperature is obtained at approximately 9-10 days after the lift is placed. The peak temperature is around 95° F. After the peak temperature is obtained, the temperature decreases in an

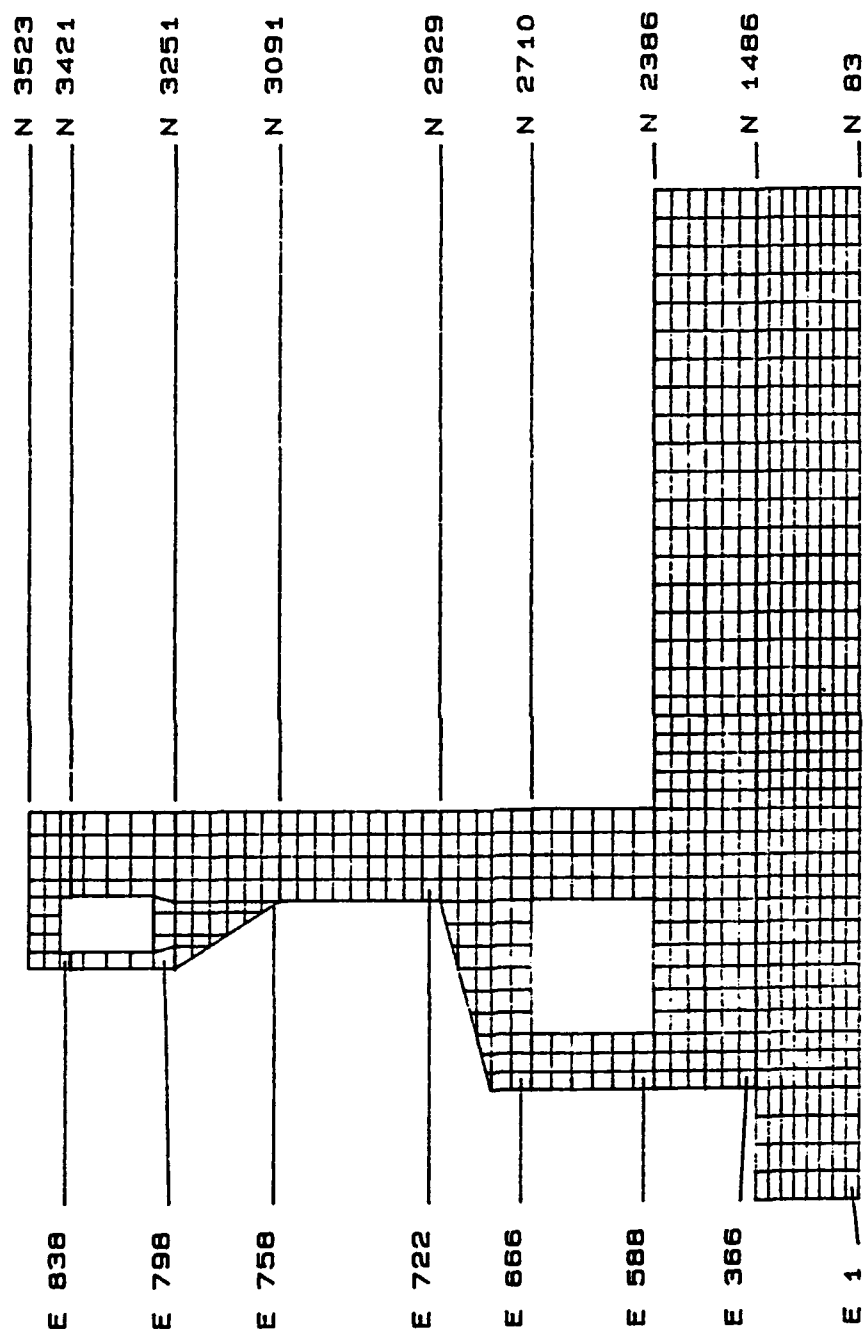


Figure 20. Mesh with nodal and element numbering

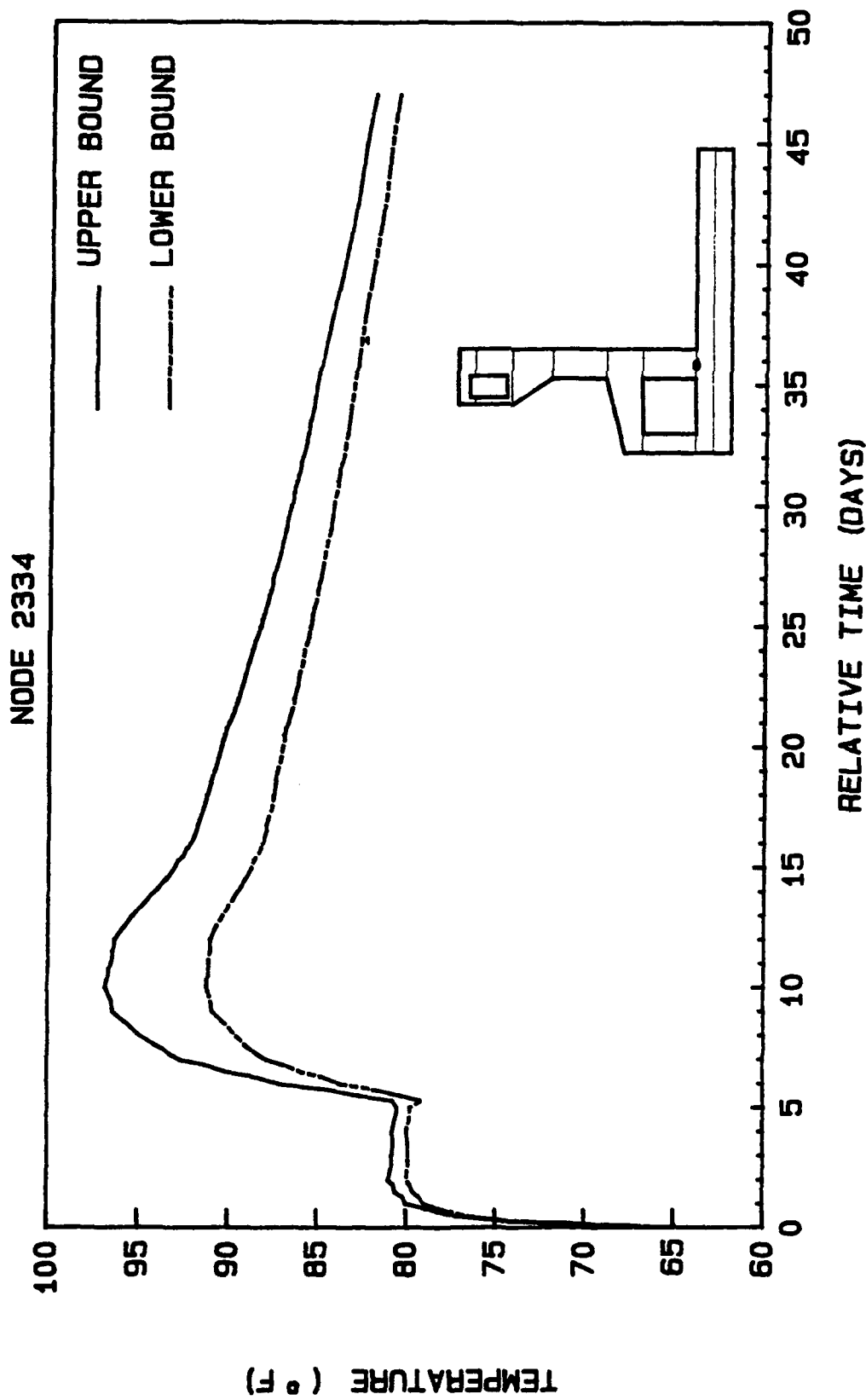


Figure 21. Temperature versus time for upper and lower adiabatic curve for node 2334

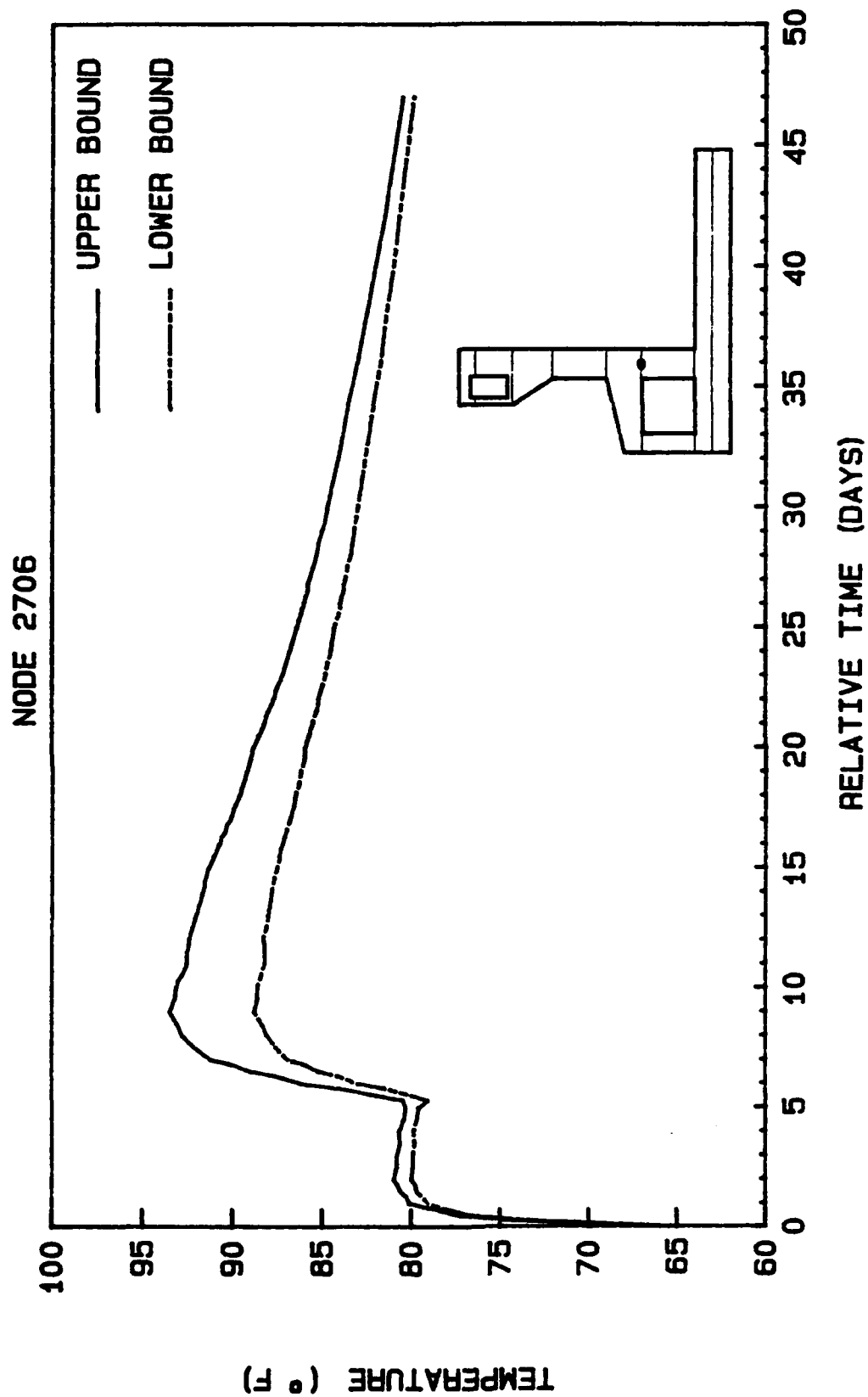


Figure 22. Temperature versus time for upper and lower adiabatic curve for node 2706

# NODE 2923

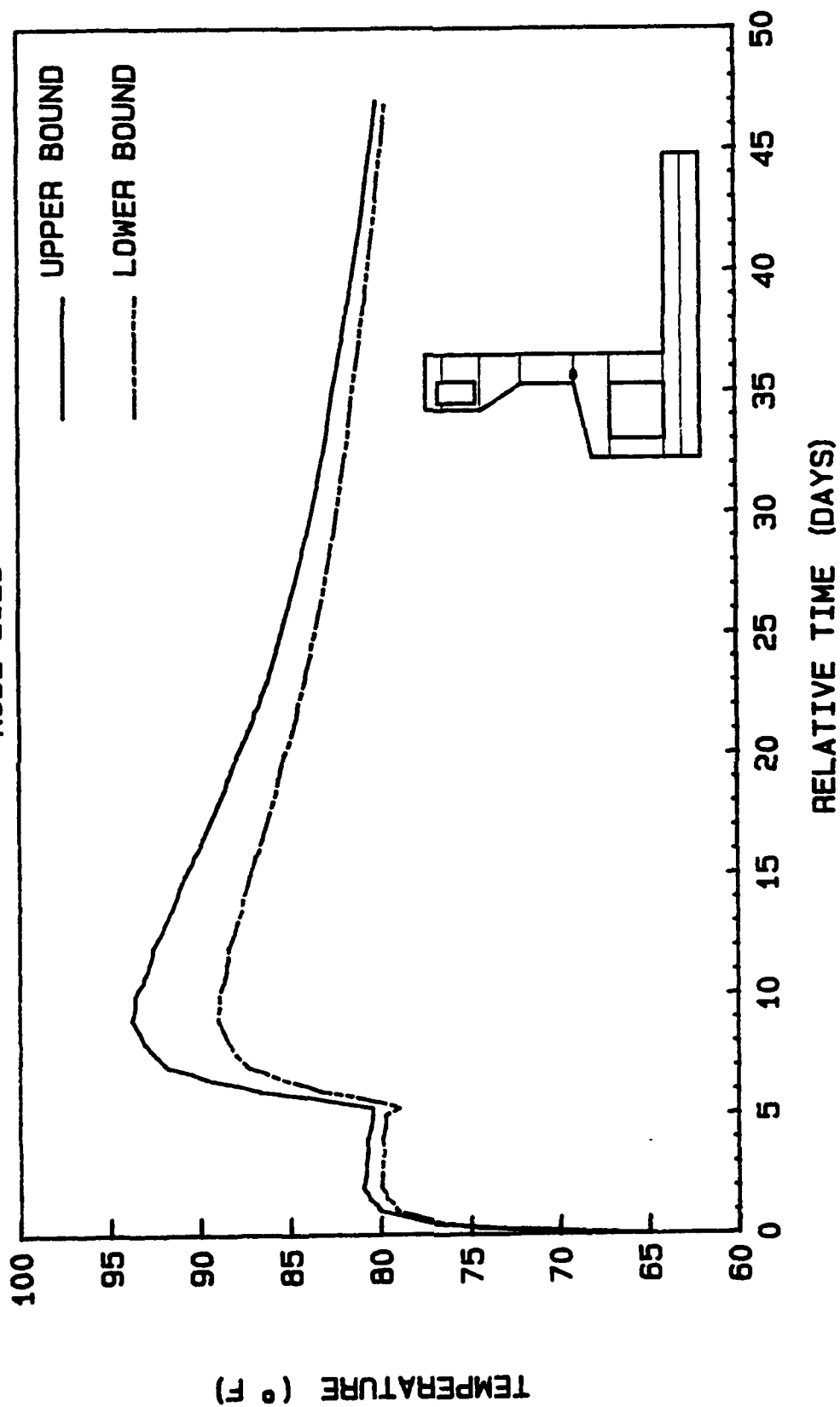


Figure 23. Temperature versus time for upper and lower adiabatic curve for node 2923

NODE 3447

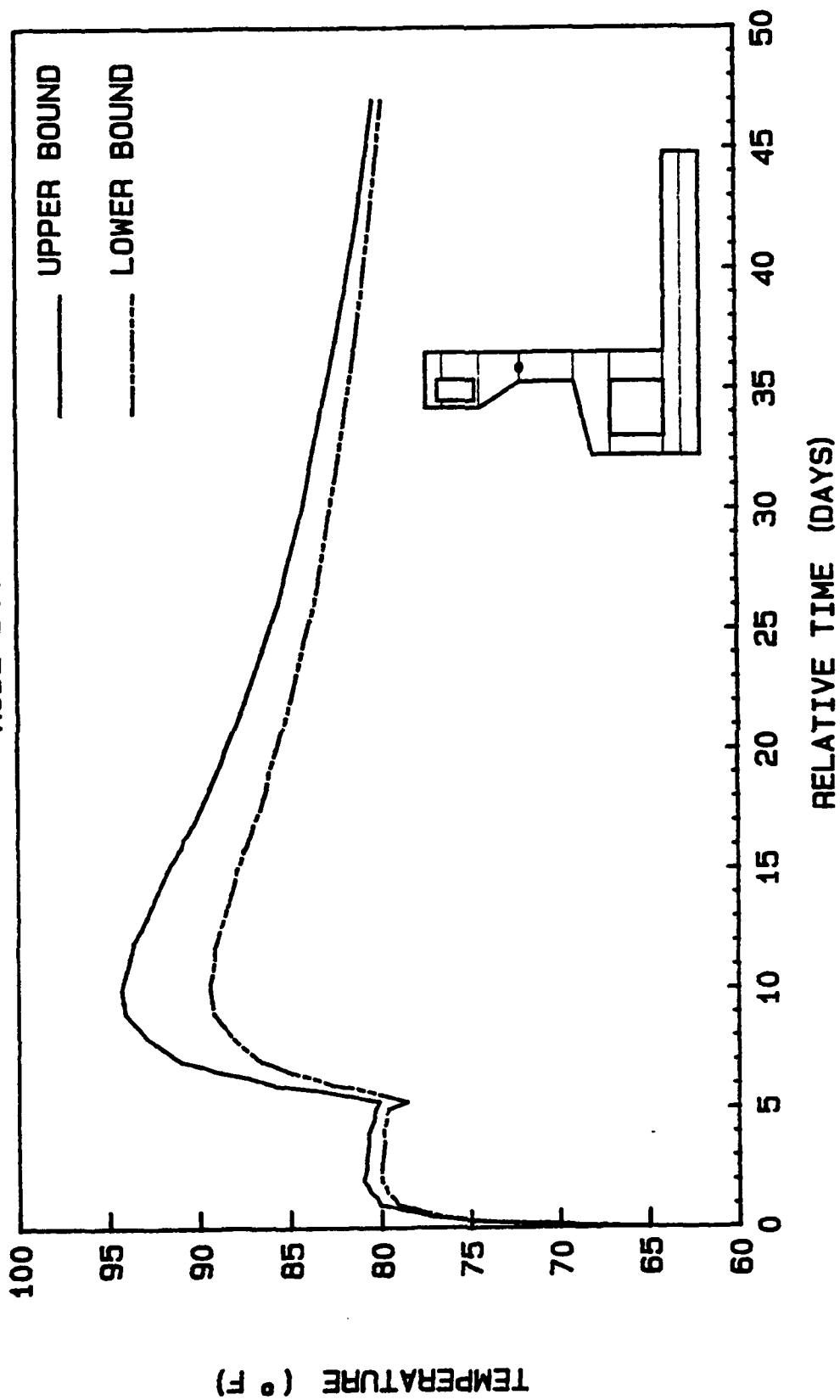


Figure 24. Temperature versus time for upper and lower adiabatic curve for node 3447

# NODE 1434

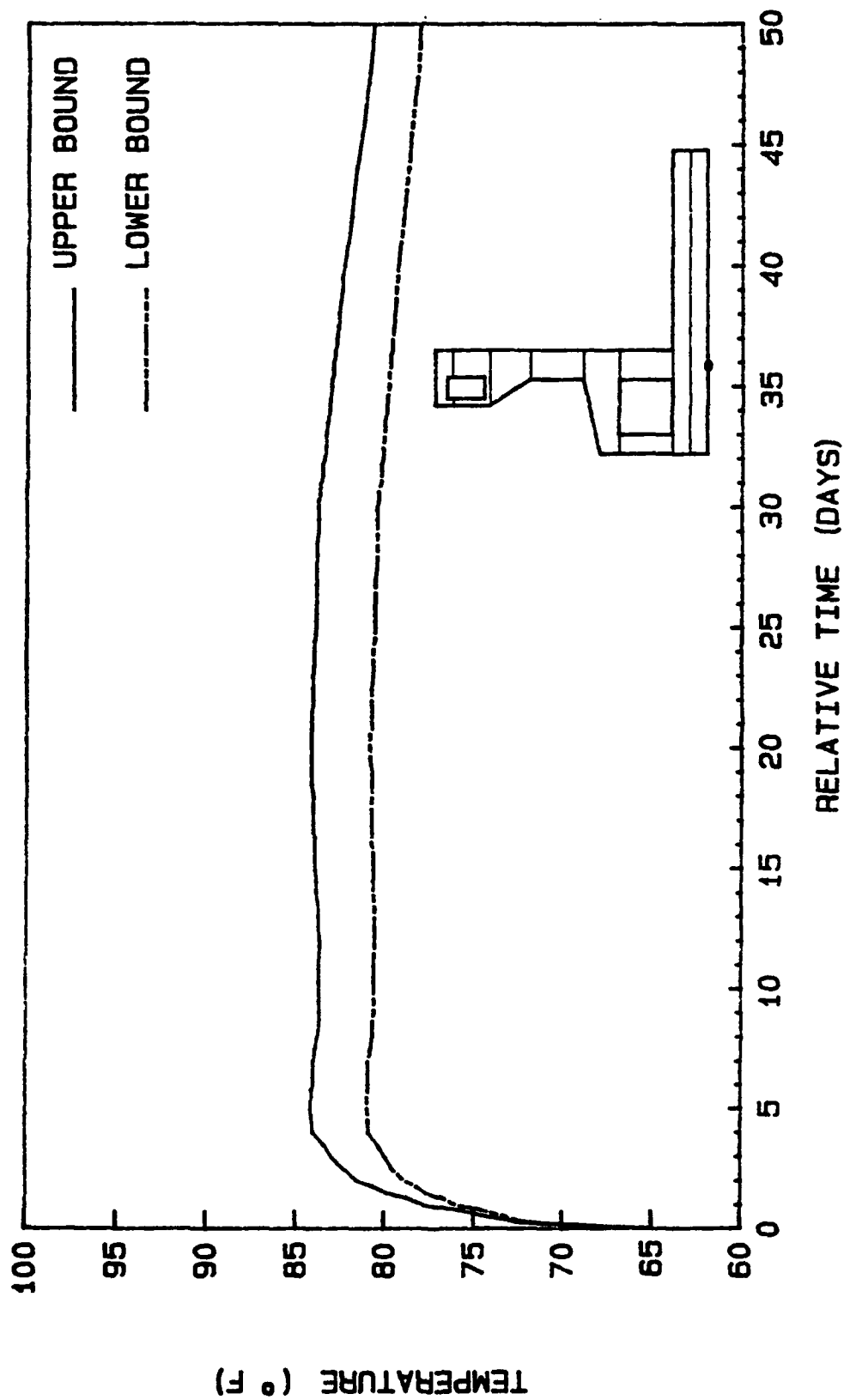


Figure 25. Temperature versus time for upper and lower adiabatic curve for node 1434

NODE 2324

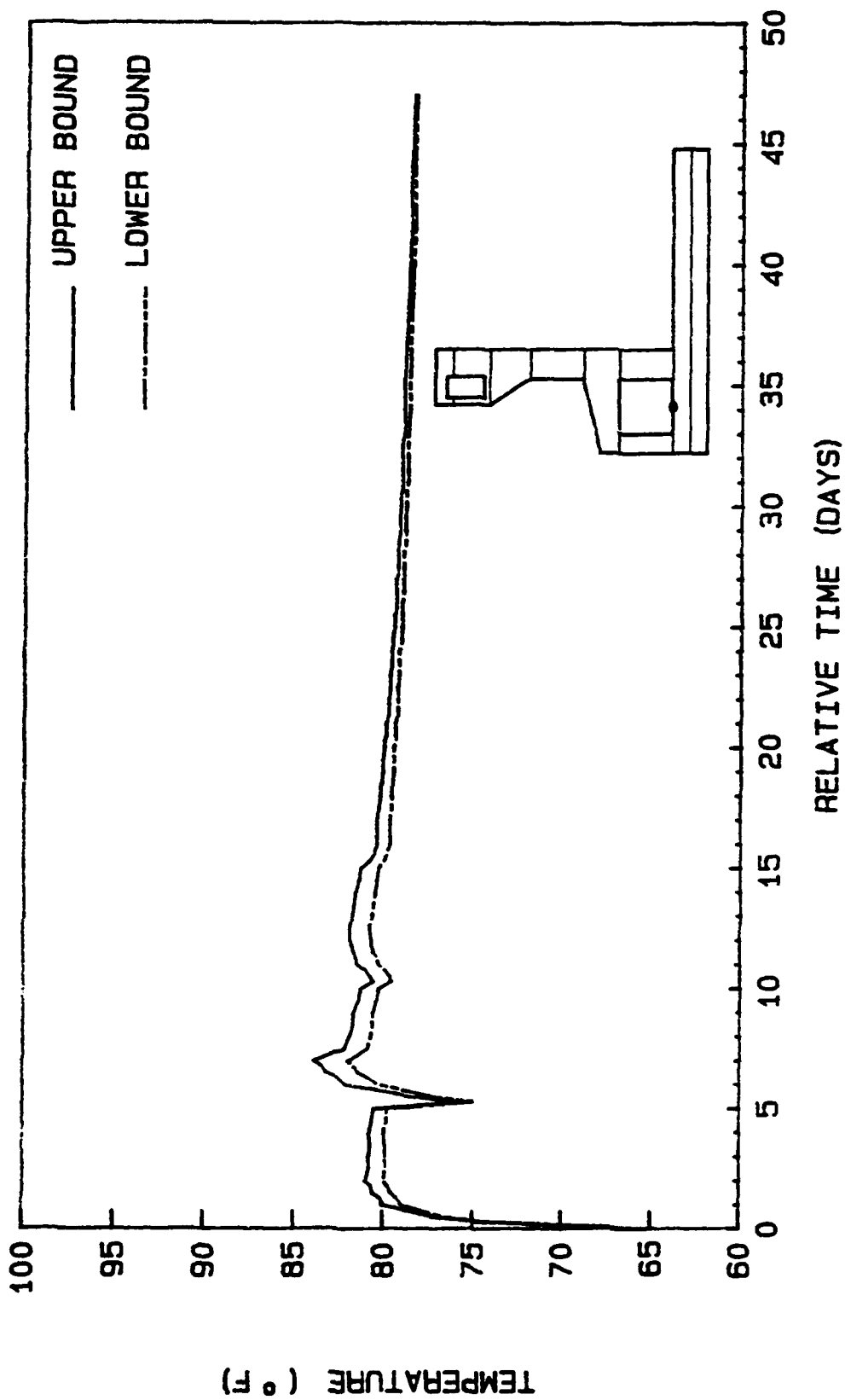


Figure 26. Temperature versus time for upper and lower adiabatic curve for node 2324

NODE 2386

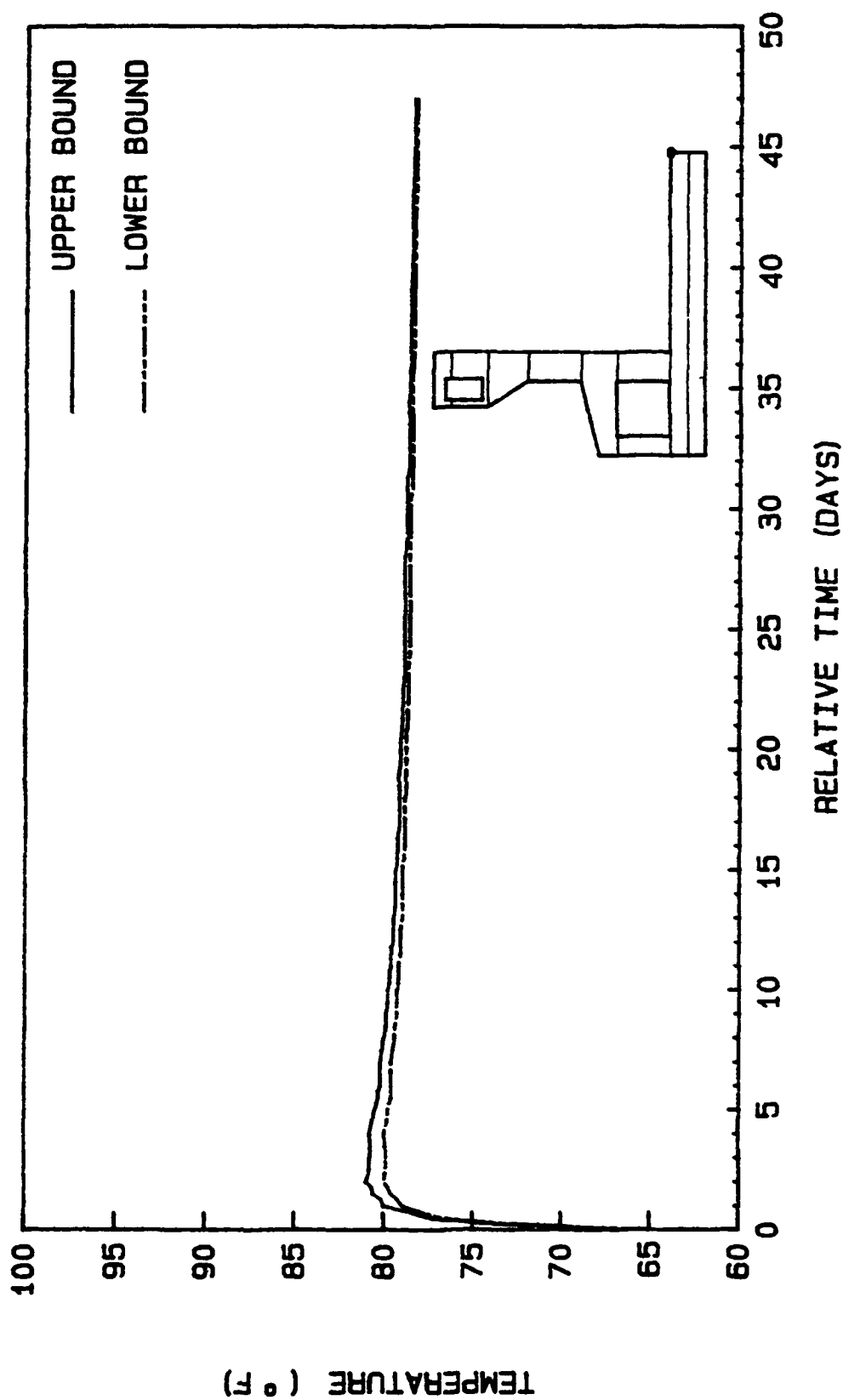


Figure 27. Temperature versus time for upper and lower adiabatic curve for node 2386

NODE 2486

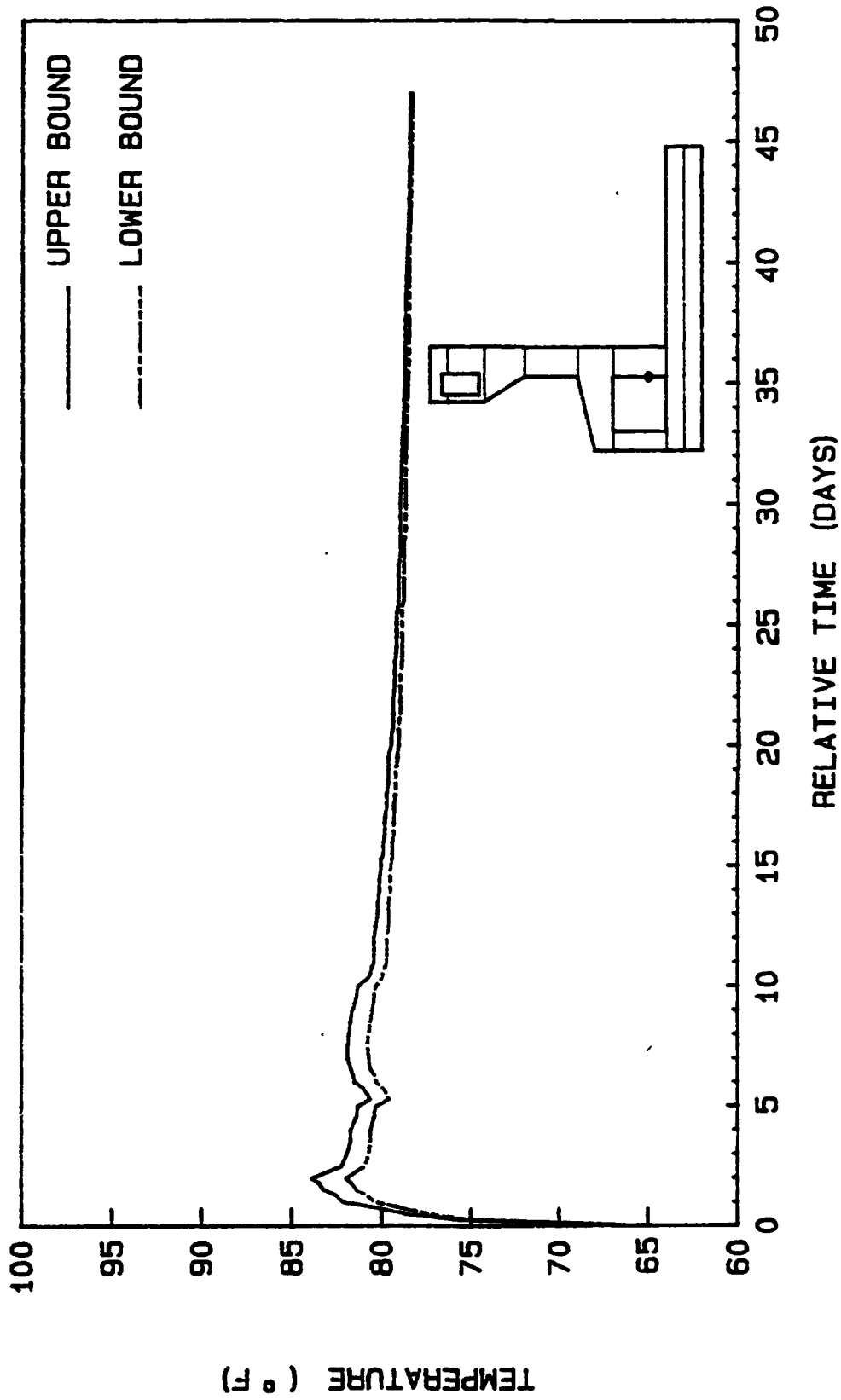


Figure 28. Temperature versus time for upper and lower adiabatic curve for node 2486

# NODE 2702

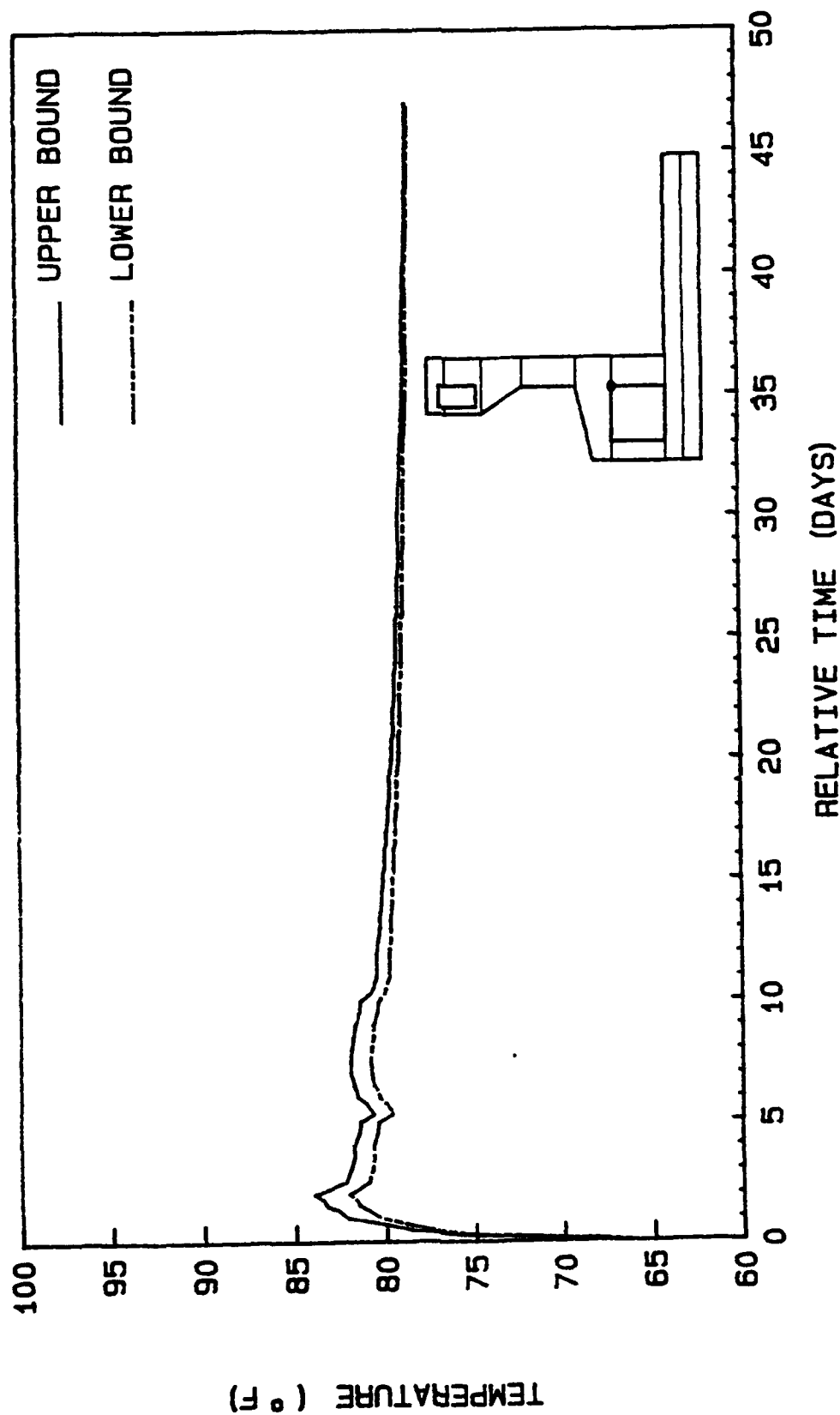


Figure 29. Temperature versus time for upper and lower adiabatic curve for node 2702

# NODE 2886

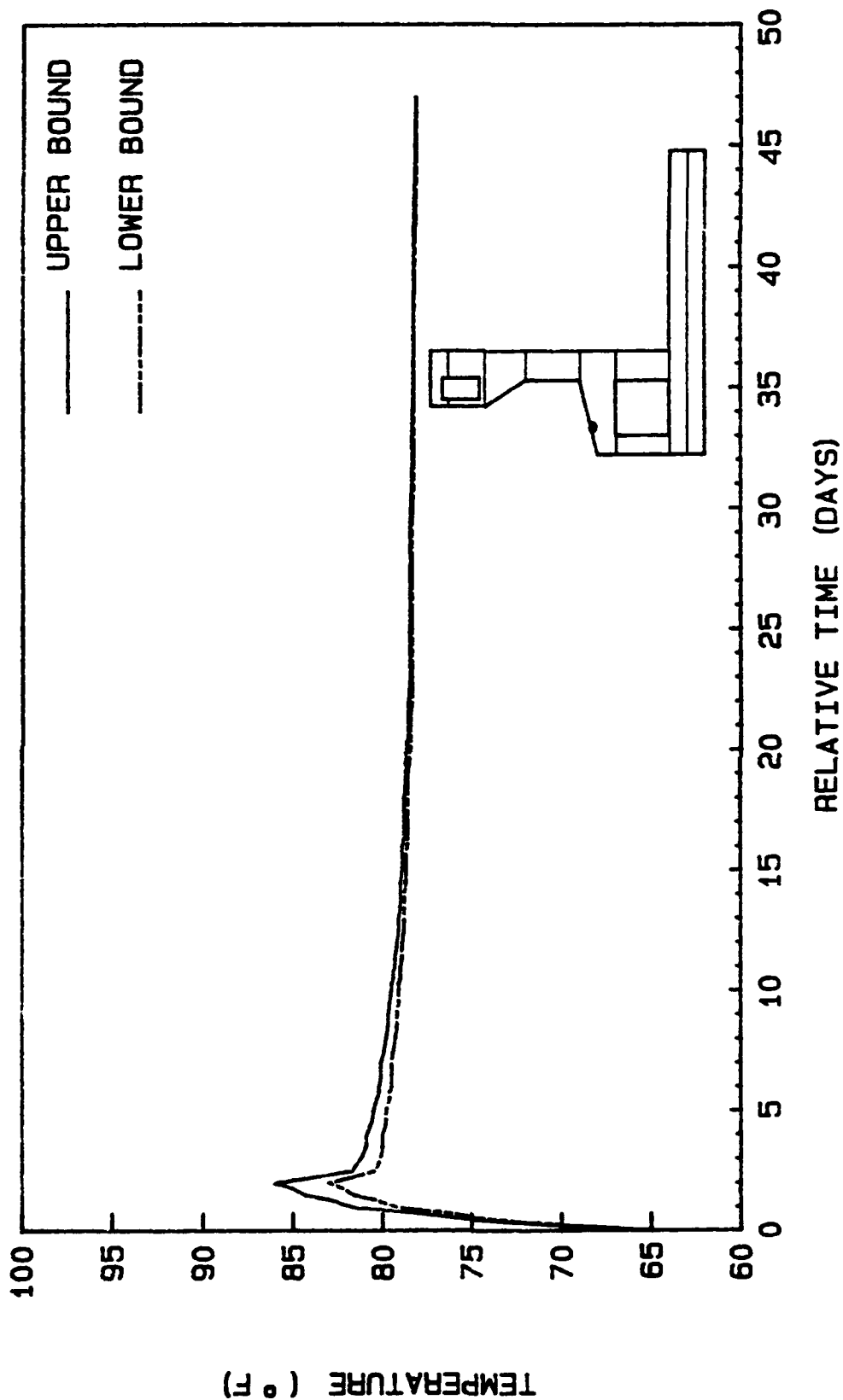


Figure 30. Temperature versus time for upper and lower adiabatic curve for node 2886

# NODE 3112

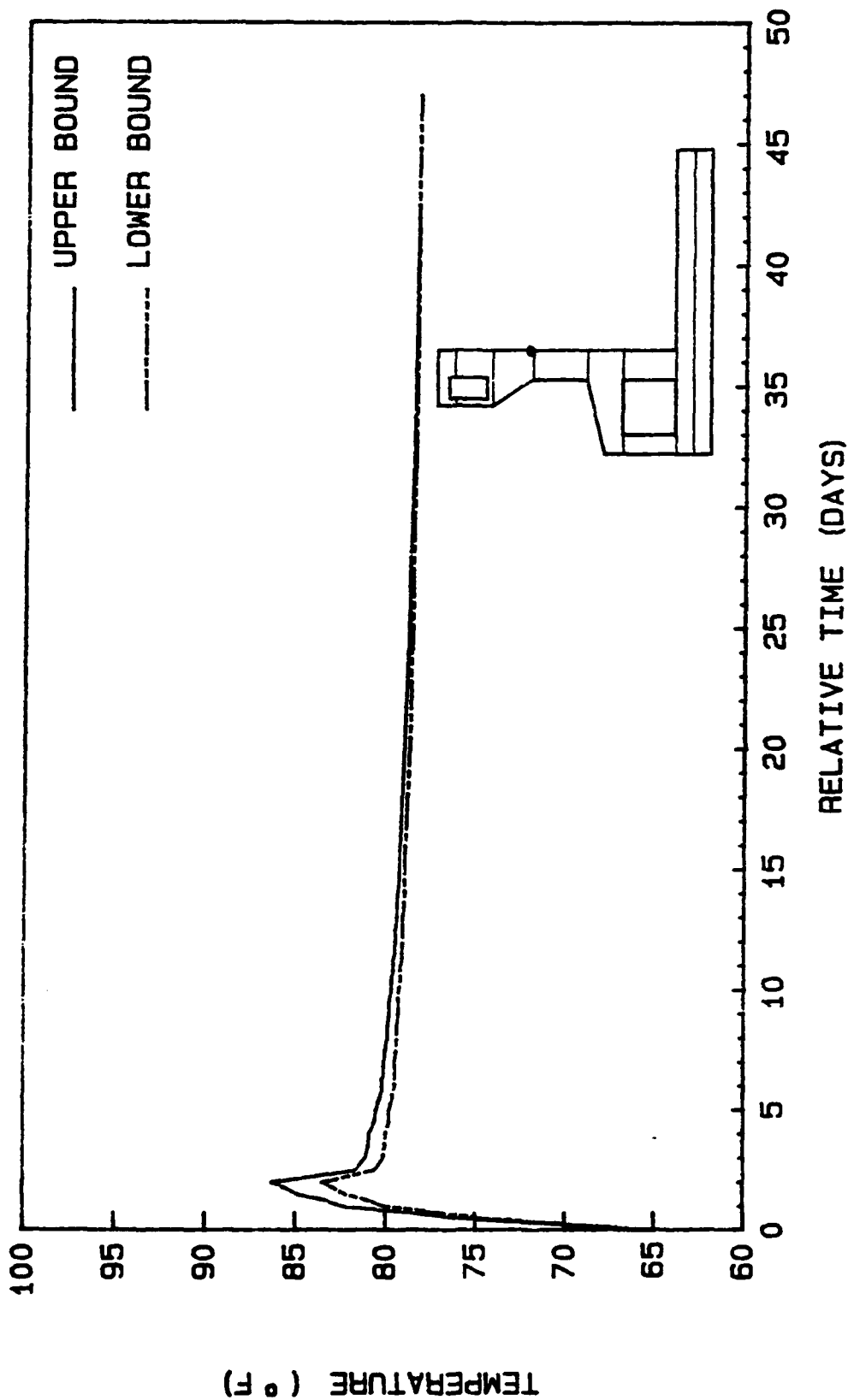


Figure 31. Temperature versus time for upper and lower adiabatic curve for node 3112

# NODE 3311

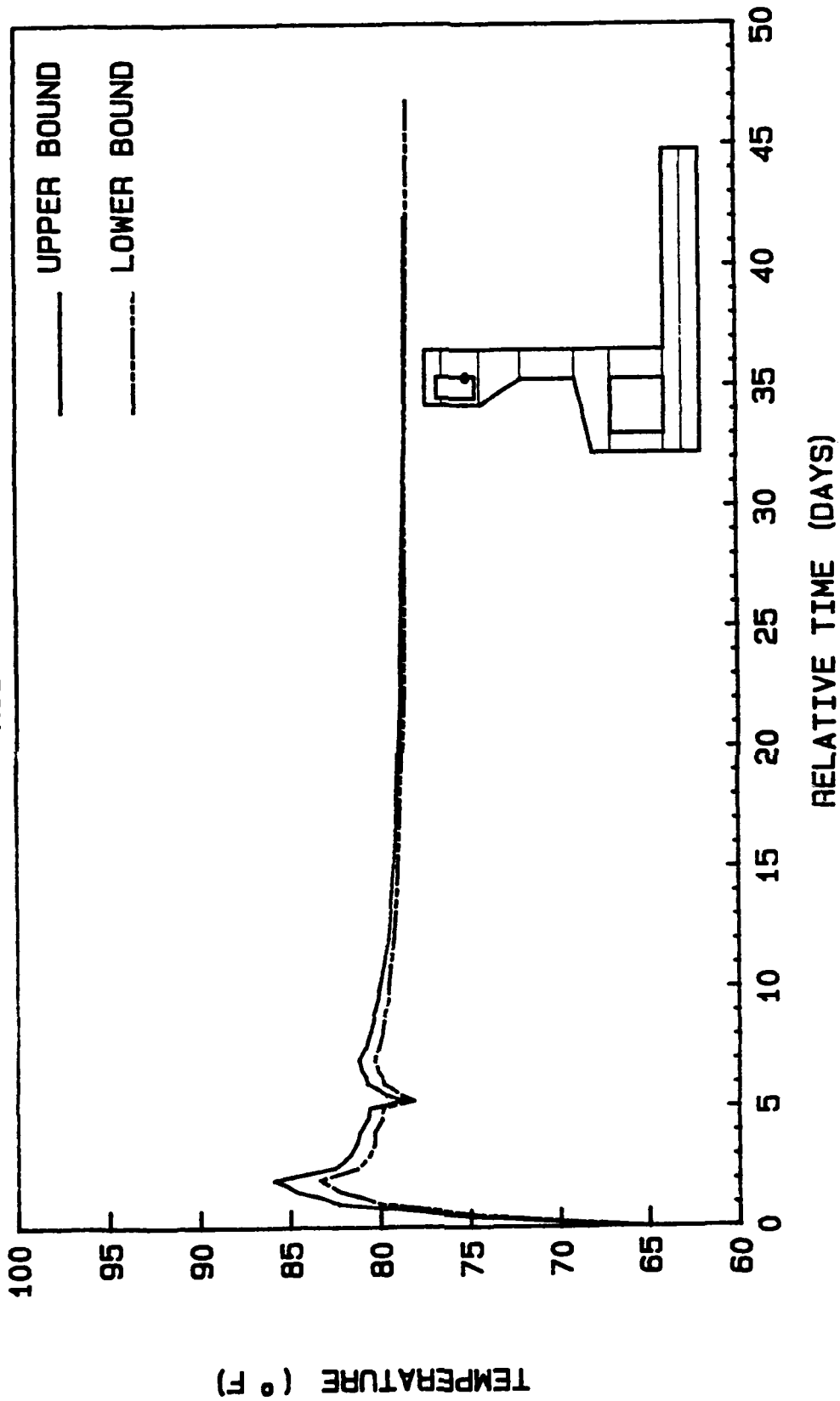


Figure 32. Temperature versus time for upper and lower adiabatic curve for node 3311

NODE 3447

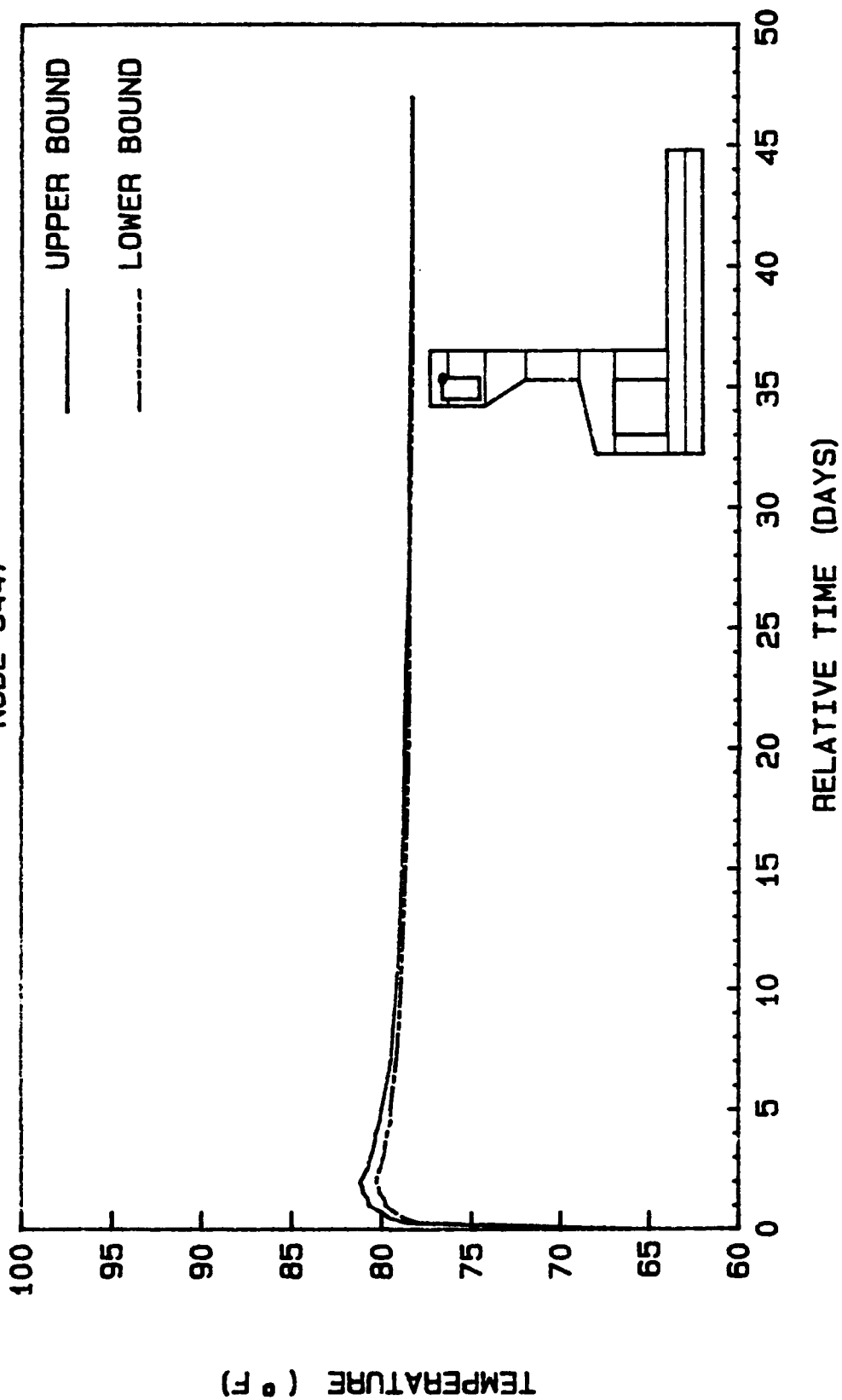


Figure 33. Temperature versus time for upper and lower adiabatic curve for node 3447

NODE 3521

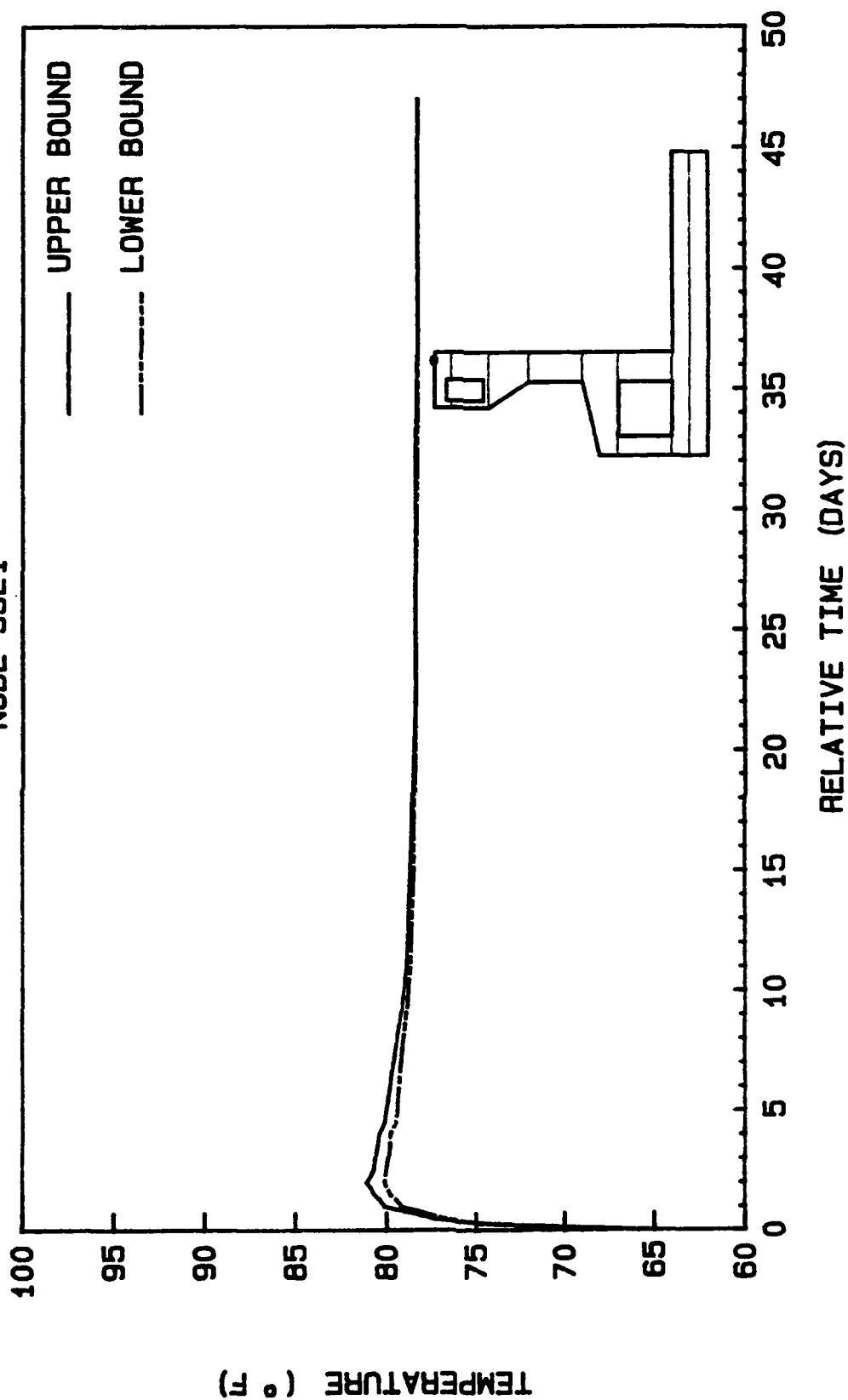


Figure 34. Temperature versus time for upper and lower adiabatic curve for node 3521

NODE 2525

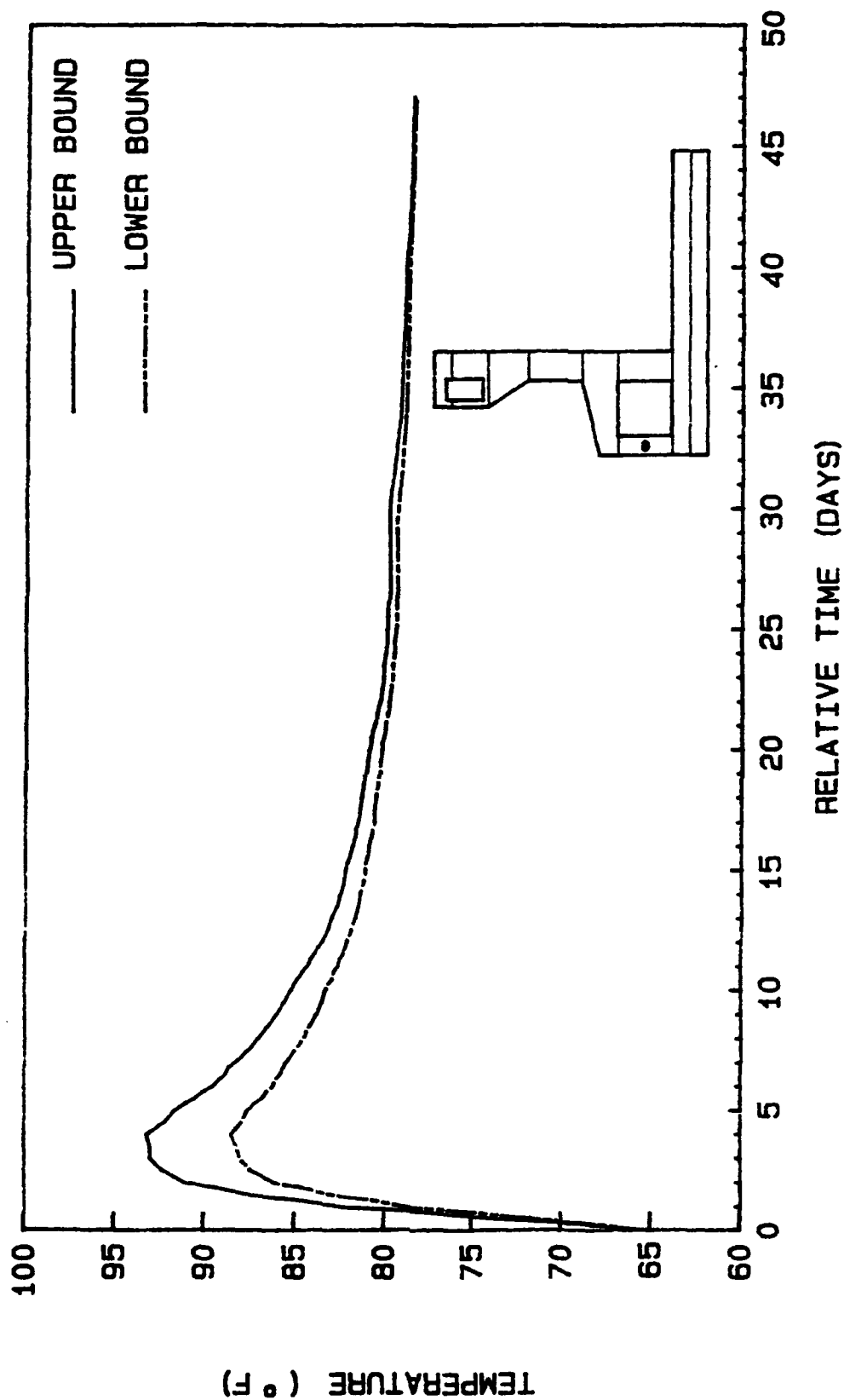


Figure 35. Temperature versus time for upper and lower adiabatic curve for node 2525

NODE 2544

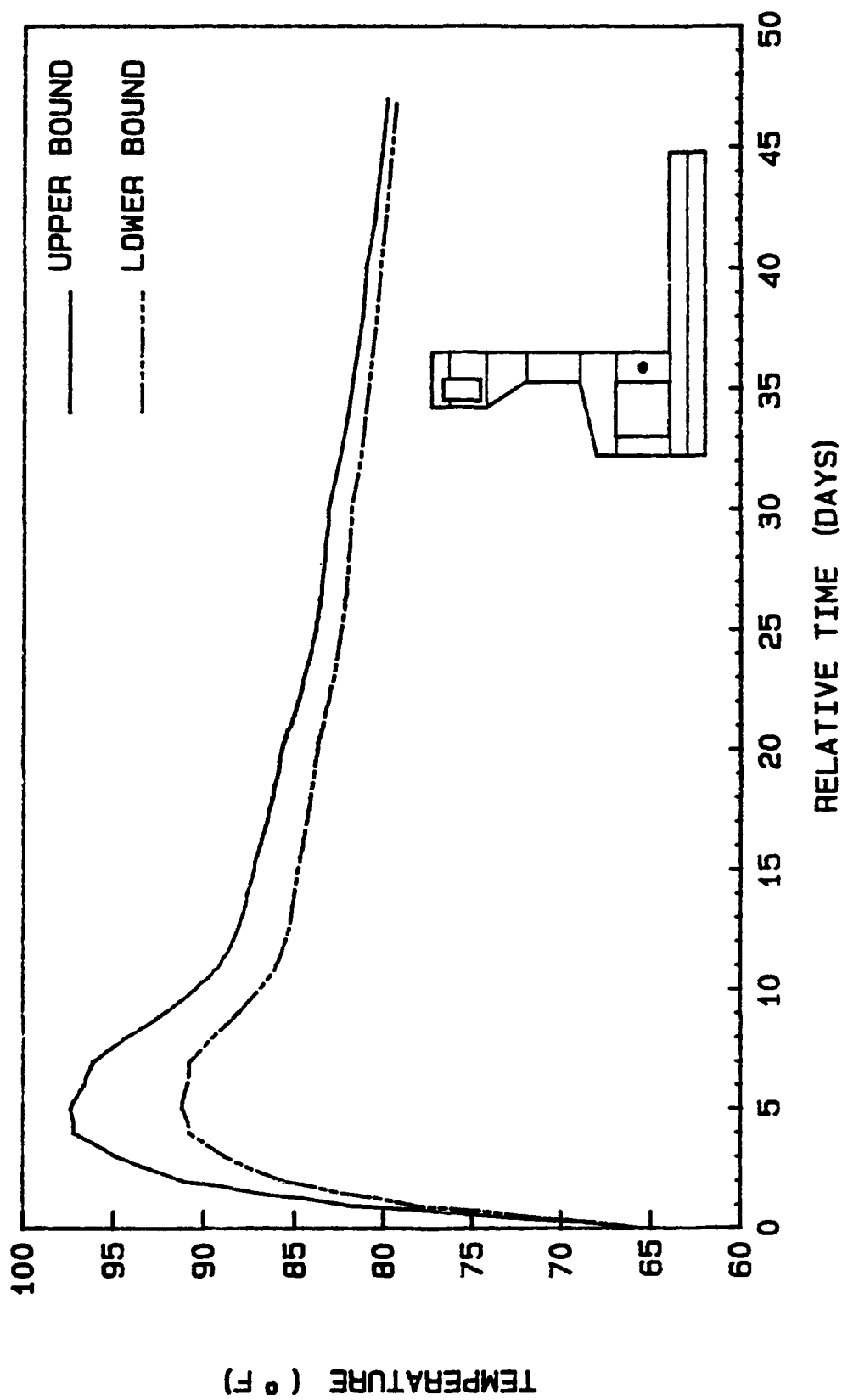


Figure 36. Temperature versus time for upper and lower adiabatic curve for node 2544

# NODE 3155

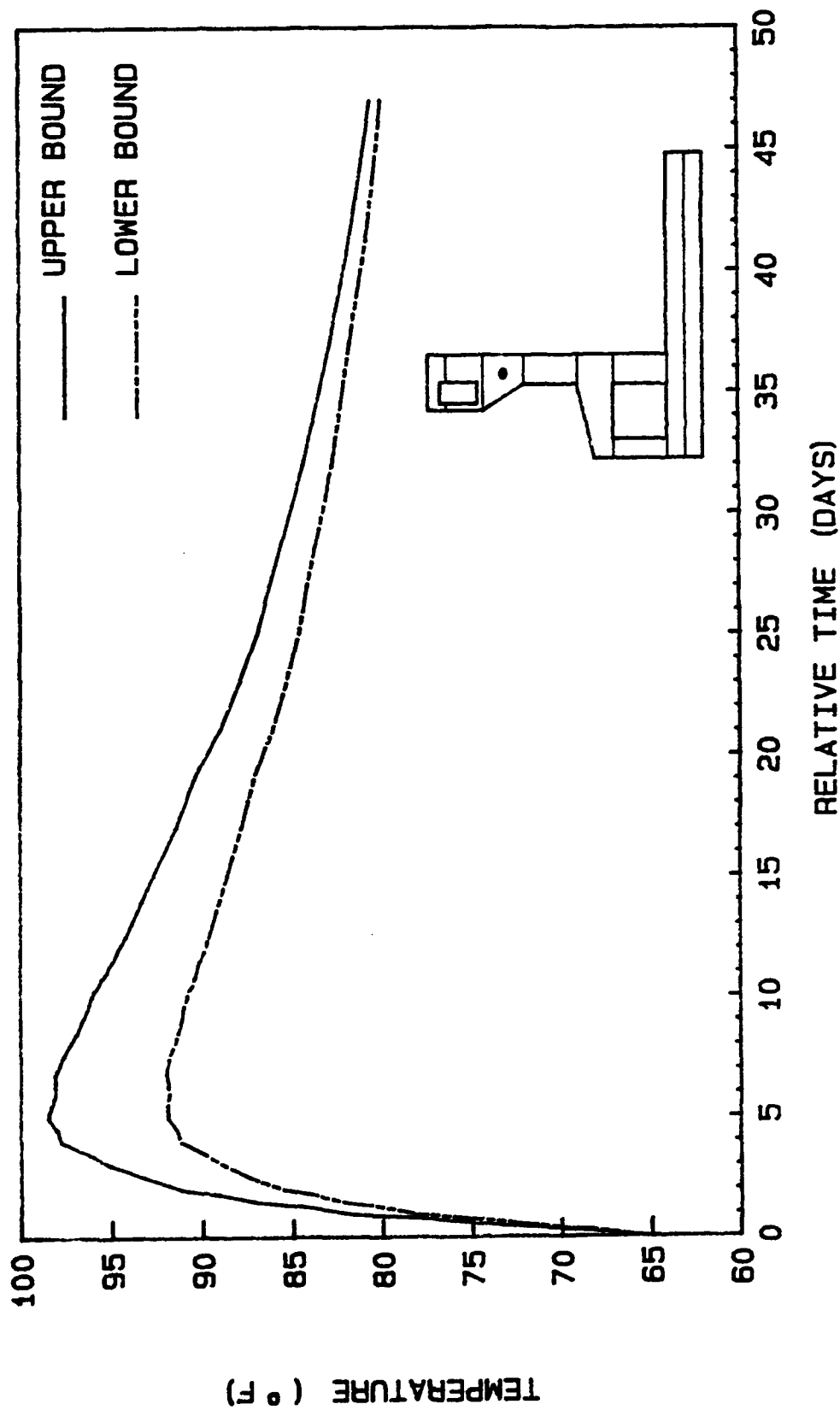


Figure 37. Temperature versus time for upper and lower adiabatic curve for node 3155

exponential fashion until thermal equilibrium is obtained. Obviously, the analysis using the upper bound heat of hydration produces higher temperatures in the structure. Also note that, for the lower bound temperature graphs, just after the next lift is placed (after 5 days) a small decrease in temperature occurs. This is a result of placing cooler concrete (recall that concrete placement temperature is 65° F) on top of the older concrete and also since enough heat is not liberated initially to produce an increase as in the upper bound temperatures.

48. The temperature increase shown in Figure 25 is predominantly a conduction process. Since this is at the soil-concrete interface, part of the initial increase in temperature of the concrete is due to placing the cooler concrete on the warmer top soil (Figure 21). The remaining temperature increase is due to the heat liberated by the concrete. Note that after the peak temperature is reached, the temperature remains fairly stable since the soil acts as an insulator but not a good insulator--otherwise, the peak temperature would be about 10° higher.

49. Figures 26-34 show a predominate convection process since the nodes lie on the exposed surfaces. In Figure 26, a decrease in temperature occurs after 5 days. This is a result of activating air elements when lift 3 is placed. The initial temperature of the air elements is 75° F, and it can be seen that the concrete elements take on the same value. Note also that the same node is shared by the concrete and air elements. The use of air elements and convection coefficients inside the culverts proved to be an inaccurate way to model what happens in this area. It can be seen that after the air elements are activated, they draw heat out of the system at a rate that is not realistic. If air elements are to be used, the material properties need to be reconsidered. The use of gap elements between the air and the concrete may also be required instead of using convection coefficients. However, this would only complicate the analysis while the use of convection coefficients alone at these surfaces should model what occurs there well enough. The decrease in temperature at 7 days is due to removal of the form work placed around the entire culvert. The decrease at 10 days is related to completely closing of the void. With lift 4 being added to the system, (with a 65° F placement temperature) the temperature of the air elements inside the void decrease thus causing the surface of the concrete to decrease slightly in temperature also.

50. In Figure 27, the node quickly takes on the temperature of the air and remains the same as the ambient air temperature. In Figures 28-32, the decrease in temperature at 2 days is again due to removing the form work, thus more heat can flow across the surface. The decrease in temperature in Figures 29 and 32 at 5 days is again related to using the air elements.

51. Looking at Figure 33, only a slight drop in temperature occurs when the form work is removed. This is again a result of the air elements. Since the void is much smaller than the culvert, there is less air to be heated, and it takes on a higher temperature. When the forms are removed (after the void is completely closed), heat flows back from the air into the concrete producing a smaller decrease in temperature. Again, this indicates that the use of the air elements may be need to be reconsidered in future studies.

52. Figures 35, 36, and 37 are presented because they show the temperature variation for nodes imbedded within a lift and they show the difference in the peak temperature will depend on the member size. From Figures 35 and 36 we can see that both nodes are in the center of the member and that both lifts are 12 ft high (Figure 28). However, node 2525 is in the center of a 5 ft thick member; whereas, node 2544 is in the center of a 8 ft thick section. Thus, node 2544 obtains a temperature approximately 4° F higher than node 2525 since the thicker member generates more heat and dissipates it slower. In Figure 37, the temperature for the node that obtained the highest temperature is shown. This temperature was reached 5 days after the lift was placed and the temperature was 98.5° F. This maximum temperature compares well with analyses performed by other people in this area of work (for example, see Fehl 1987). It should also be noted, that it took approximately 80 to 90 days to dissipate most of the heat generated within the monolith during the construction process.

## PART V: STRESS ANALYSIS RESULTS VARYING THERMAL LOADINGS

### Introduction

53. The nodal temperatures, generated from the thermal analysis, are stored in a file so that during the stress analysis, the program ABAQUS, can access this data to calculate the thermal induced strains. In addition, the time dependent material properties are made available for the stress analysis by calling a FORTRAN subroutine, UMAT, prior to assembling the stiffness matrix which is then used to determine the thermal, creep, and shrinkage strains. Thus, two separate nodal temperature files were created during the heat transfer analysis by using the upper and lower bound adiabatic curves shown in Figure 8. Therefore, two stress analyses were made with creep and shrinkage fixed at their respective lower bounds while the two temperature files were used so as to select the adiabatic curve which produces higher tensile stresses. This adiabatic curve was then used in the remaining stress analyses where the degree of creep and shrinkage was varied.

54. In this section, the results that were used to select the adiabatic curve and also the results of analysis made where thermal loads were neglected to show the significance of performing a time dependent thermal analysis simulating the construction process of a mass concrete structure will be presented. In the following part, the results of the various analyses with the different load cases (i.e. creep and shrinkage) will be discussed. Table 4 shows the various load cases that will be examined. It should be clearly noted that the location of the stresses presented are at the integration (Gauss) points and not at the nodes as were the temperatures shown in Part IV. Thus, the actual temperatures used to compute the thermal strains are not exactly the same since the integration point is located at a distance X from the edge of the element where X is given by:

$$X = L/2 - (L/2)/(\sqrt{2}) \quad (6)$$

where L is the dimension of the element. Note also that the sign convention used is that positive is tensile and negative is compression.

### Discussion of Stress Analysis Results Varying the Degree of Thermal Loading

55. Figures 38-51 show the results for loads cases 1, 2, and 3. In all the figures, we can see that for load cases 2 and 3, just after the lift is placed, the stress is compressive. This is due to the heat increase, thus the element wants to expand but internal restraints prevent it from freely expanding, and compressive stresses result. However, quickly the stress becomes tensile due to subsequent cooling of the concrete. In all the figures except Figure 41, neglecting thermal loads produces significantly lower stresses and most of the figures show for load case 1 that the stresses are predominantly compressive.

56. Figure 38 shows a situation where the stresses are mostly due to bending. Looking at Figure 10, we can see that the location is between two piles. The bottom of the slab acts like a continuous beam, transferring the loads into the piles. The soil does provide some support; however, it carries a small amount of the load (from the analysis, it was found that the soil carried about 25 percent of the load). The increase in stress at every 5 days is a result of placing new lifts.

57. The increase in the stress in Figure 39 for load case 2 and 3 at 5 days is a result of the drop in temperature due to activating the air elements (see Figure 24). The stress then decreases due to the increase in temperature, and then the stress increases again due to cooling. Looking at Figure 40, the stress decreases at every 5 days due primarily to a bending effect and also partially due to a Poisson effect of adding the weight of the new lift. For load case 2 and 3, an increase in the stress occurs after 5 days due to the additional heat being added to the element from the new lift.

58. Figure 41 shows the stress at the symmetric boundary condition. At this location in the structure, the thermal loads aid in reducing the stress. This is a result of the thermal loads causing the element to expand but the center-line support prevents the element from expanding to the right, providing a greater compressive stress initially which reduces the tensile stresses that result later. Looking at Figure 27, we note that the tensile stresses resulting are not related to the thermal effects since no significant drop in temperature occurs. The stress increases every time a new lift is placed

ELEMENT 377 INT. PT. 1

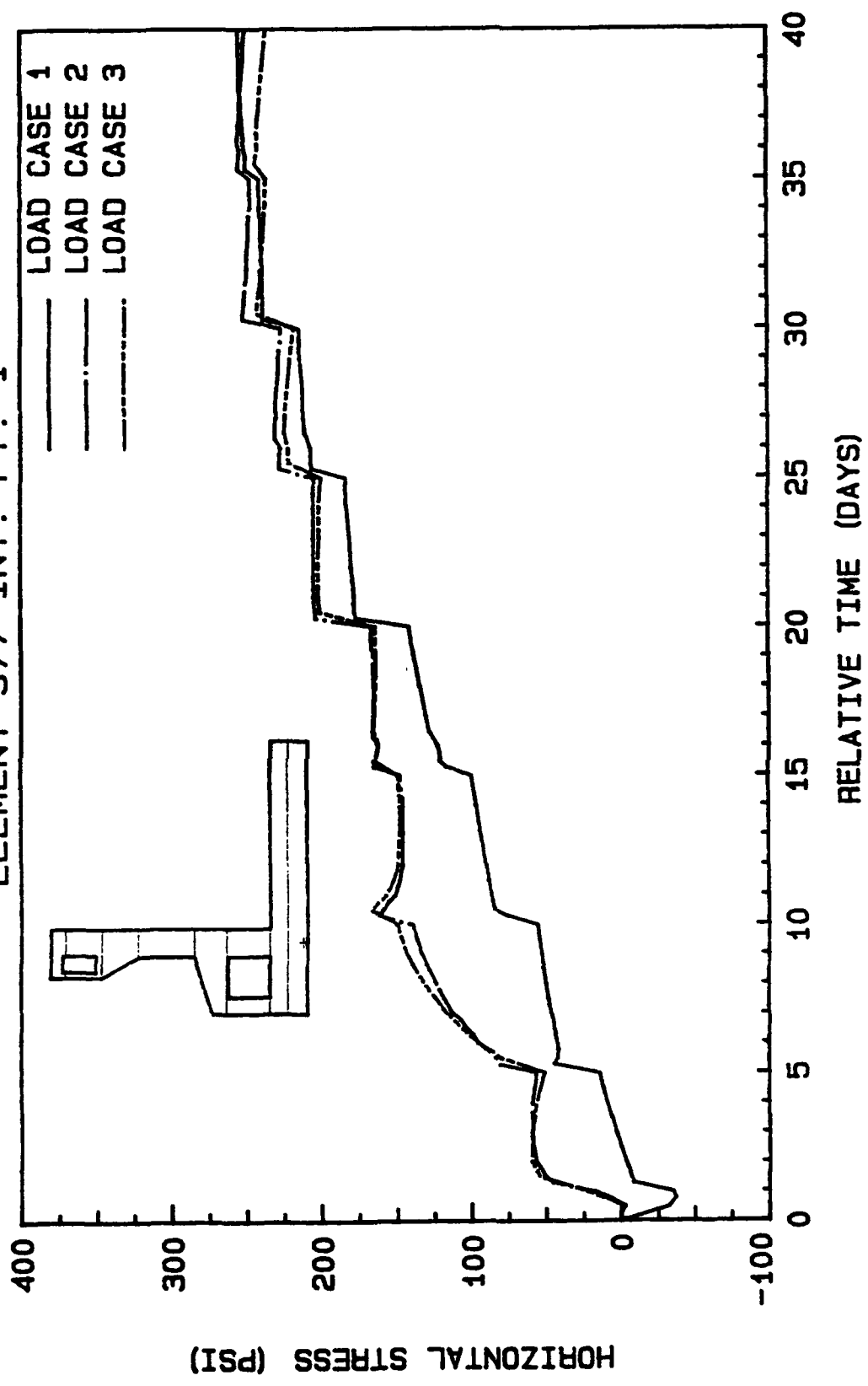


Figure 38. Stress versus time plot varying thermal loading for element 377

# ELEMENT 556 INT. PT. 4

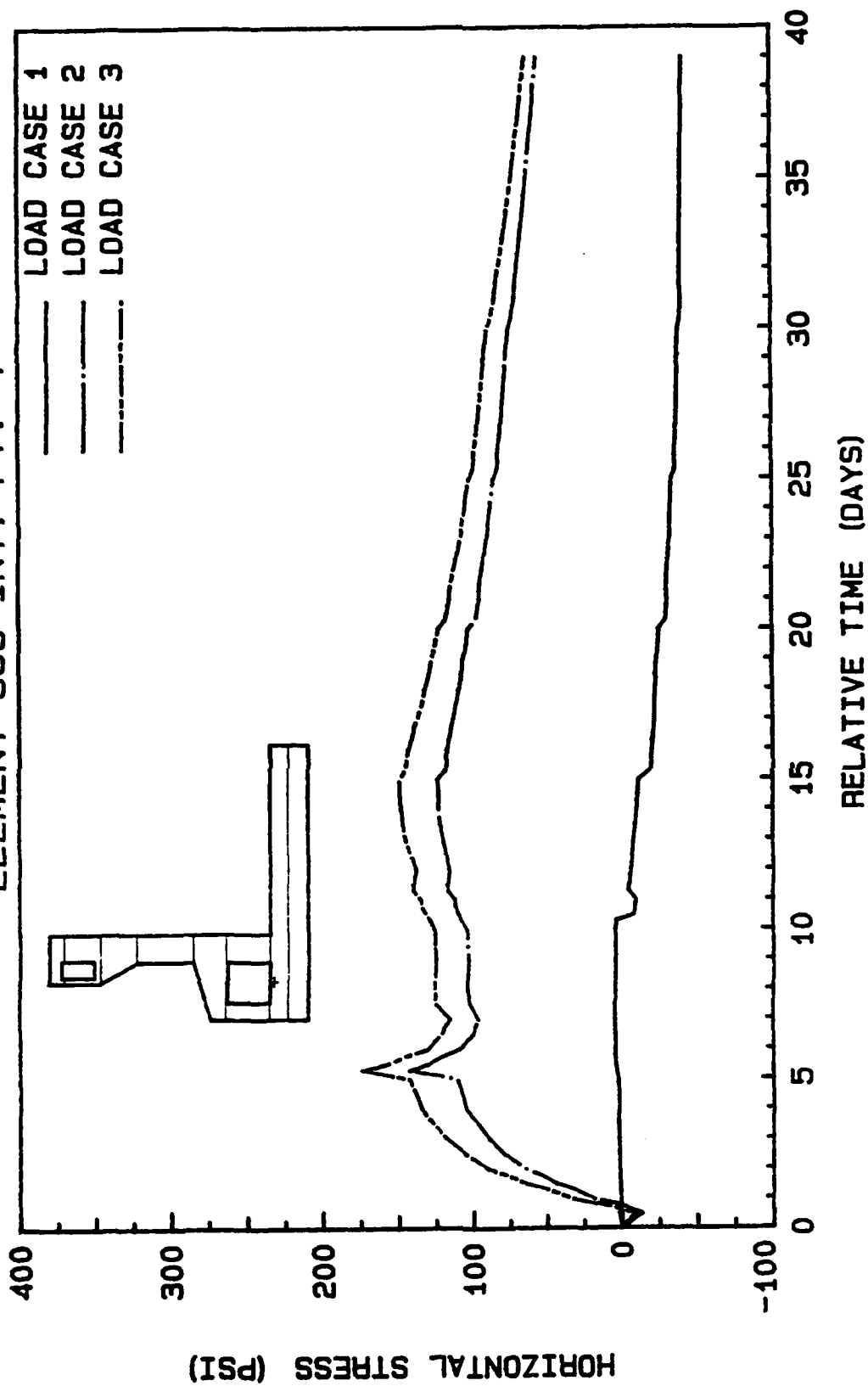


Figure 39. Stress versus time plot varying thermal loading for element 556

# ELEMENT 561 INT. PT. 4

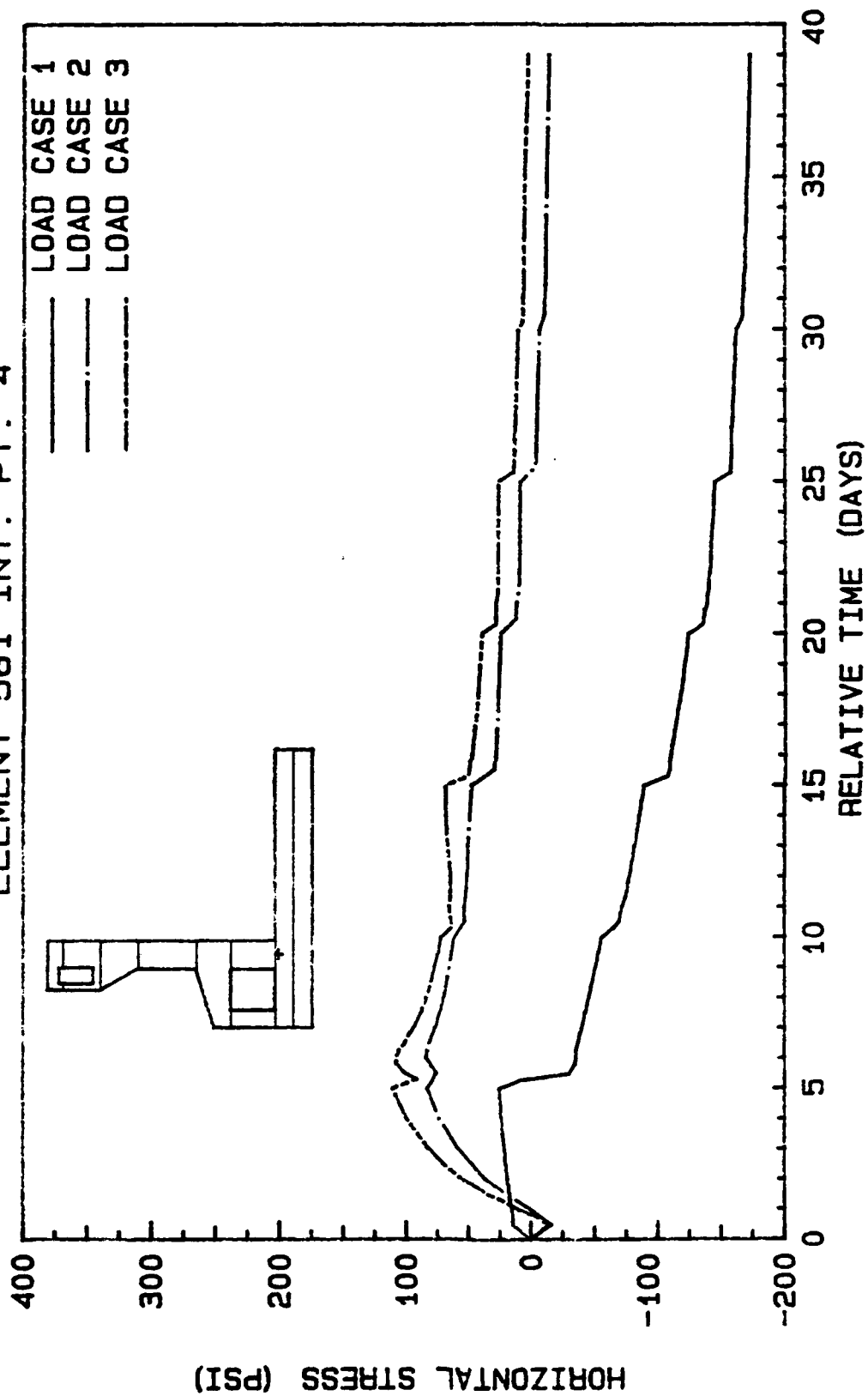


Figure 40. Stress versus time plot varying thermal loading for element 561

# ELEMENT 587 INT. PT. 4

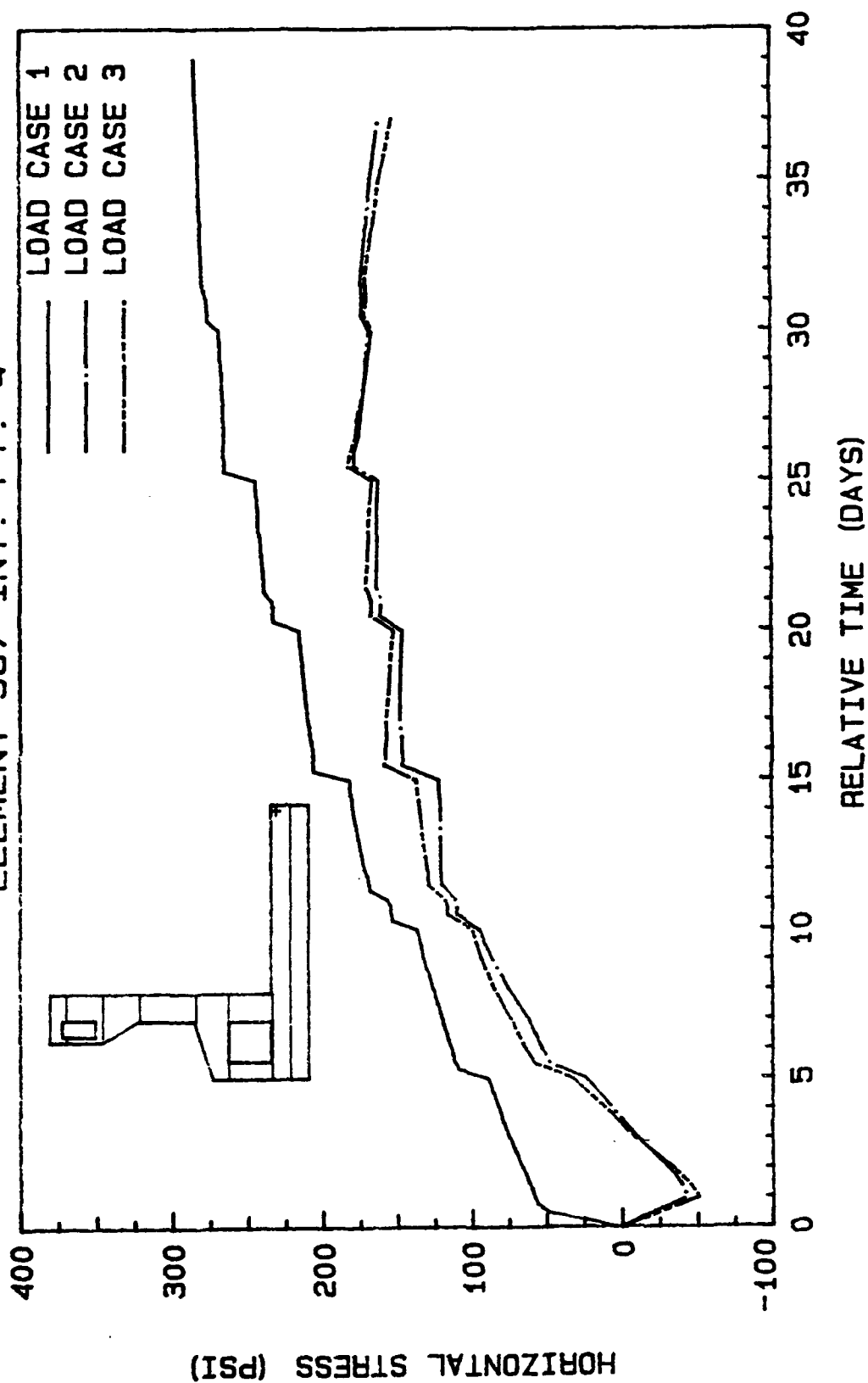


Figure 41. Stress versus time plot varying thermal loading for element 587

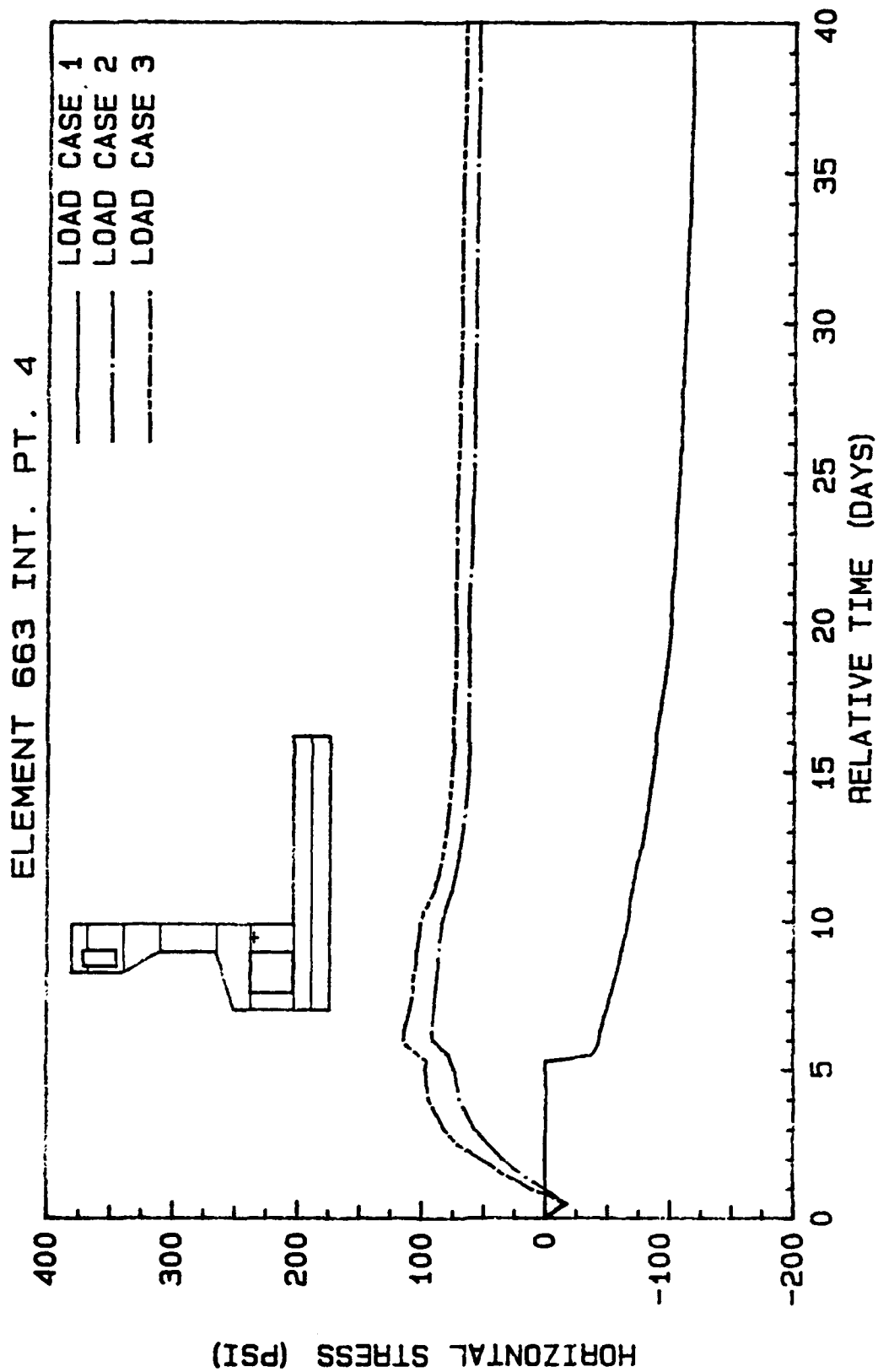


Figure 42. Stress versus time plot varying thermal loading for element 663

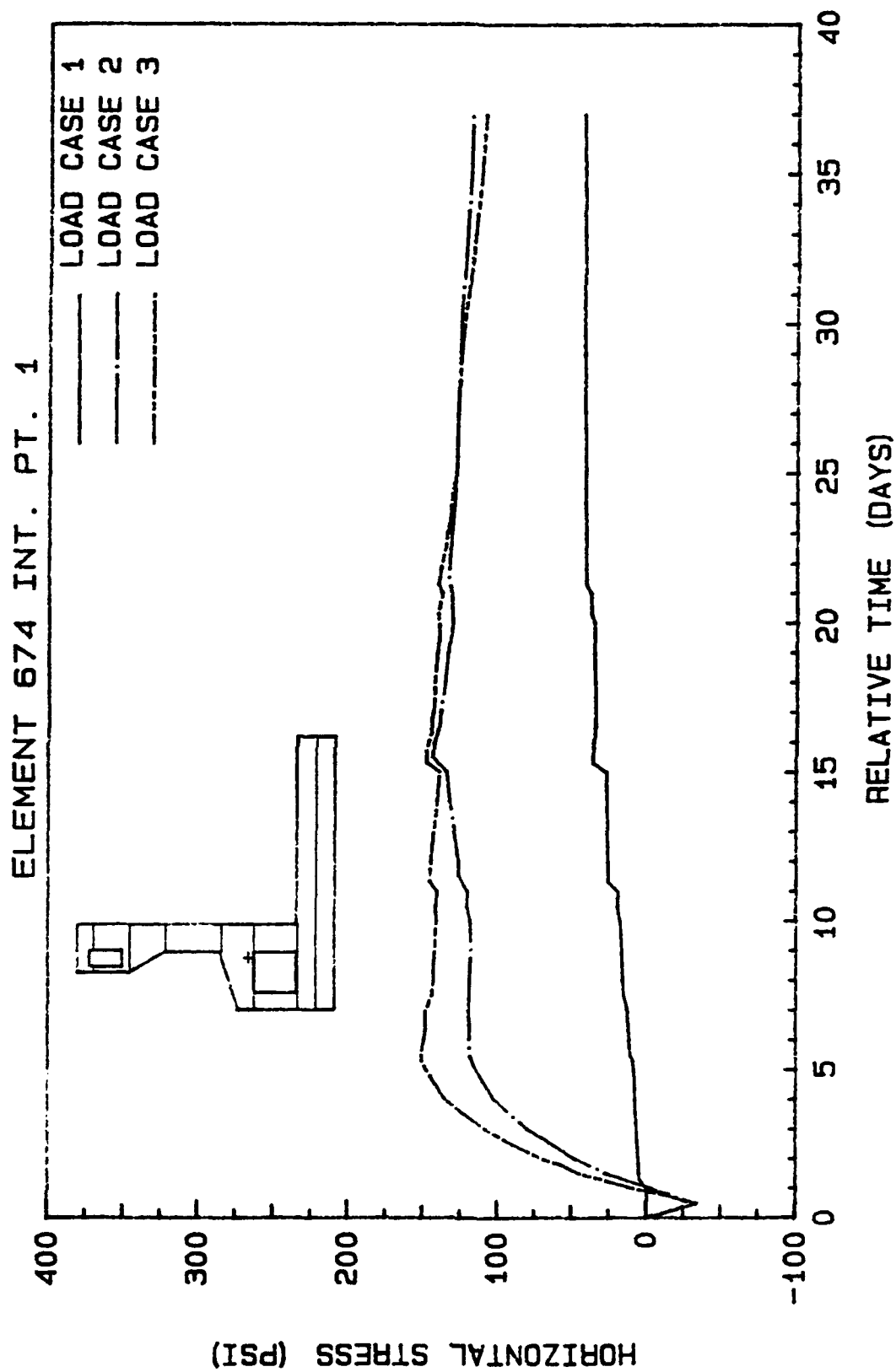


Figure 43. Stress versus time plot varying thermal loading for element 674

# ELEMENT 705 INT. PT. 4

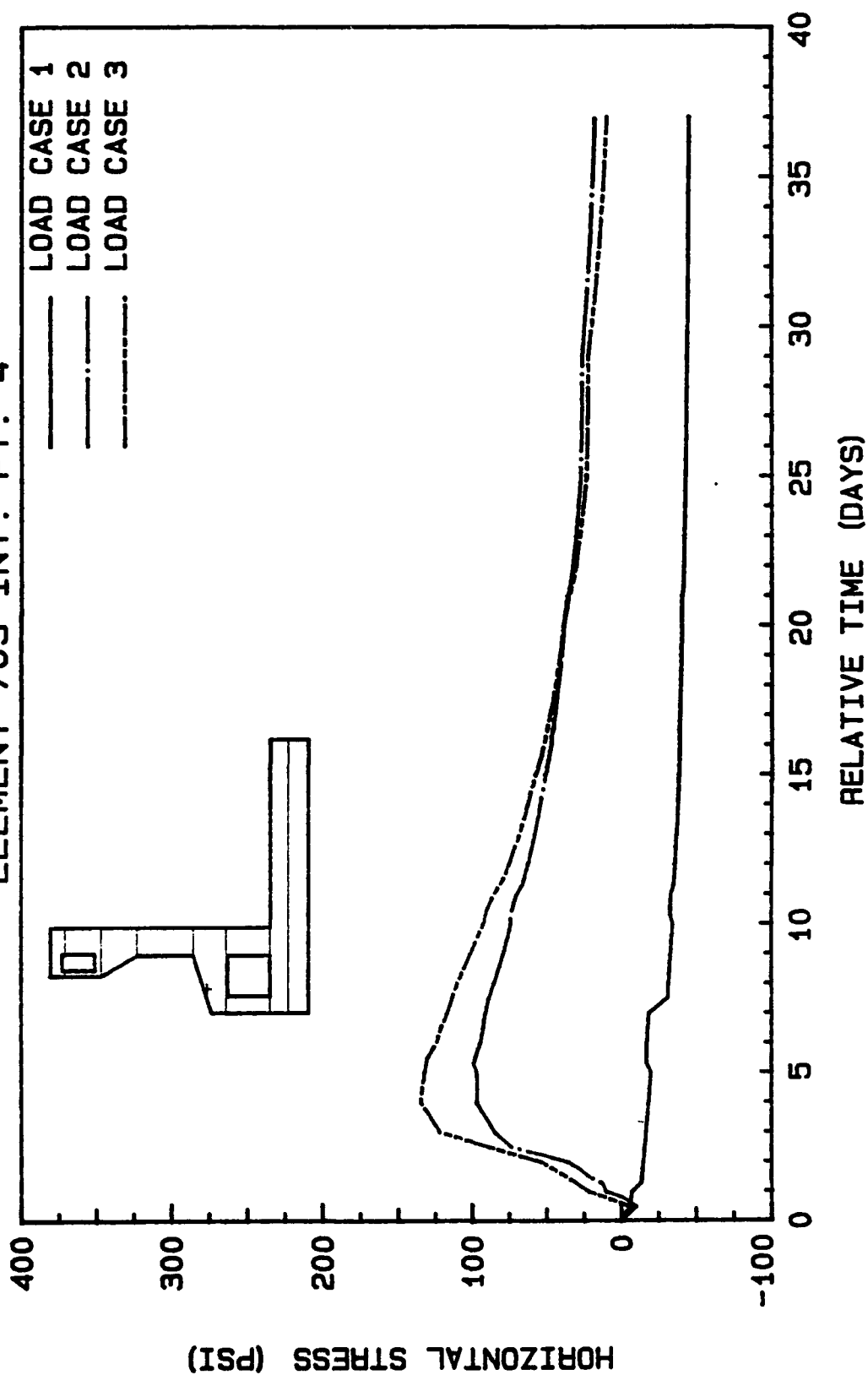


Figure 44. Stress versus time plot varying thermal loading for element 705

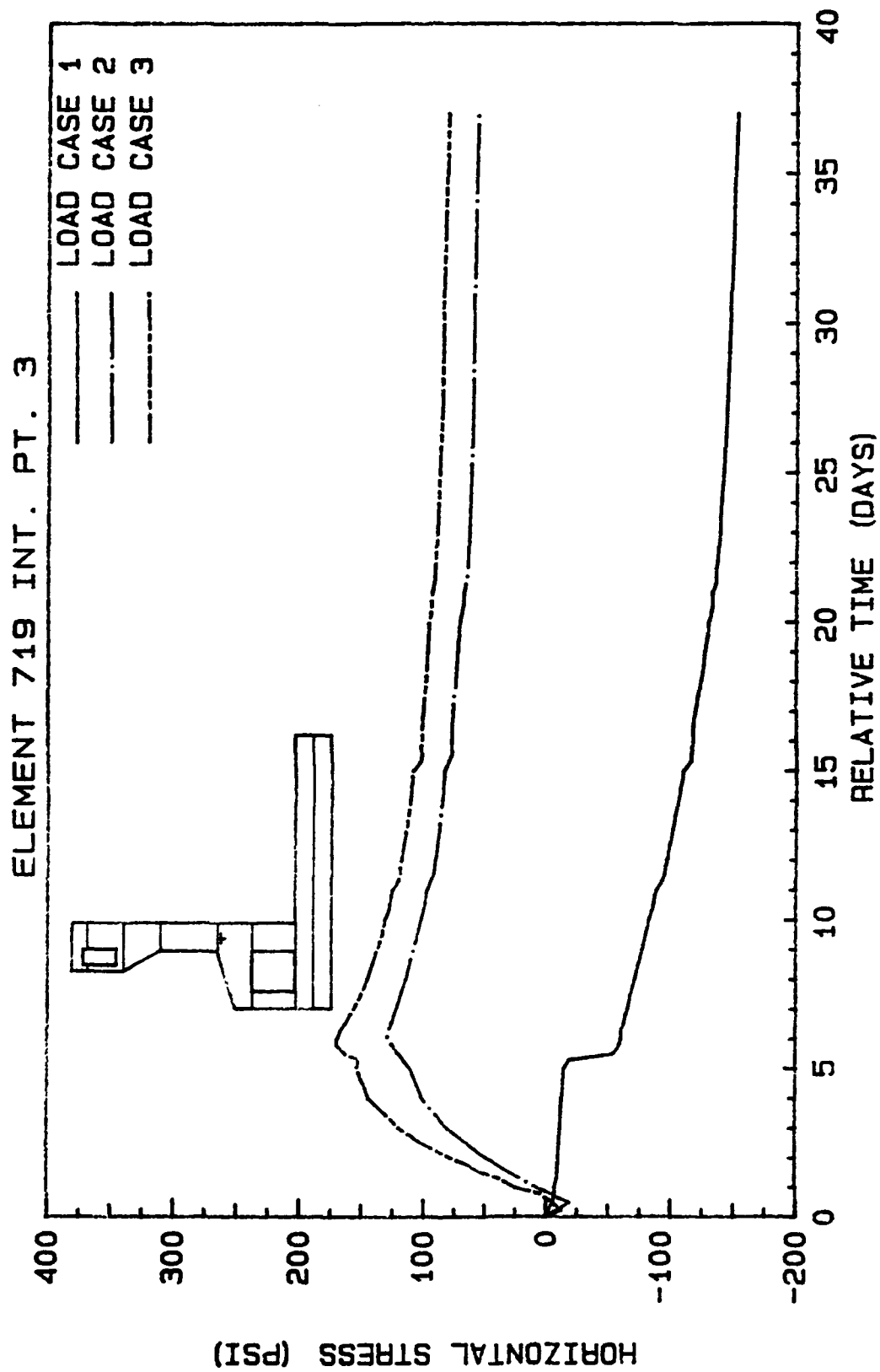


Figure 45. Stress versus time plot varying thermal loading for element 719

# ELEMENT 755 INT. PT. 4

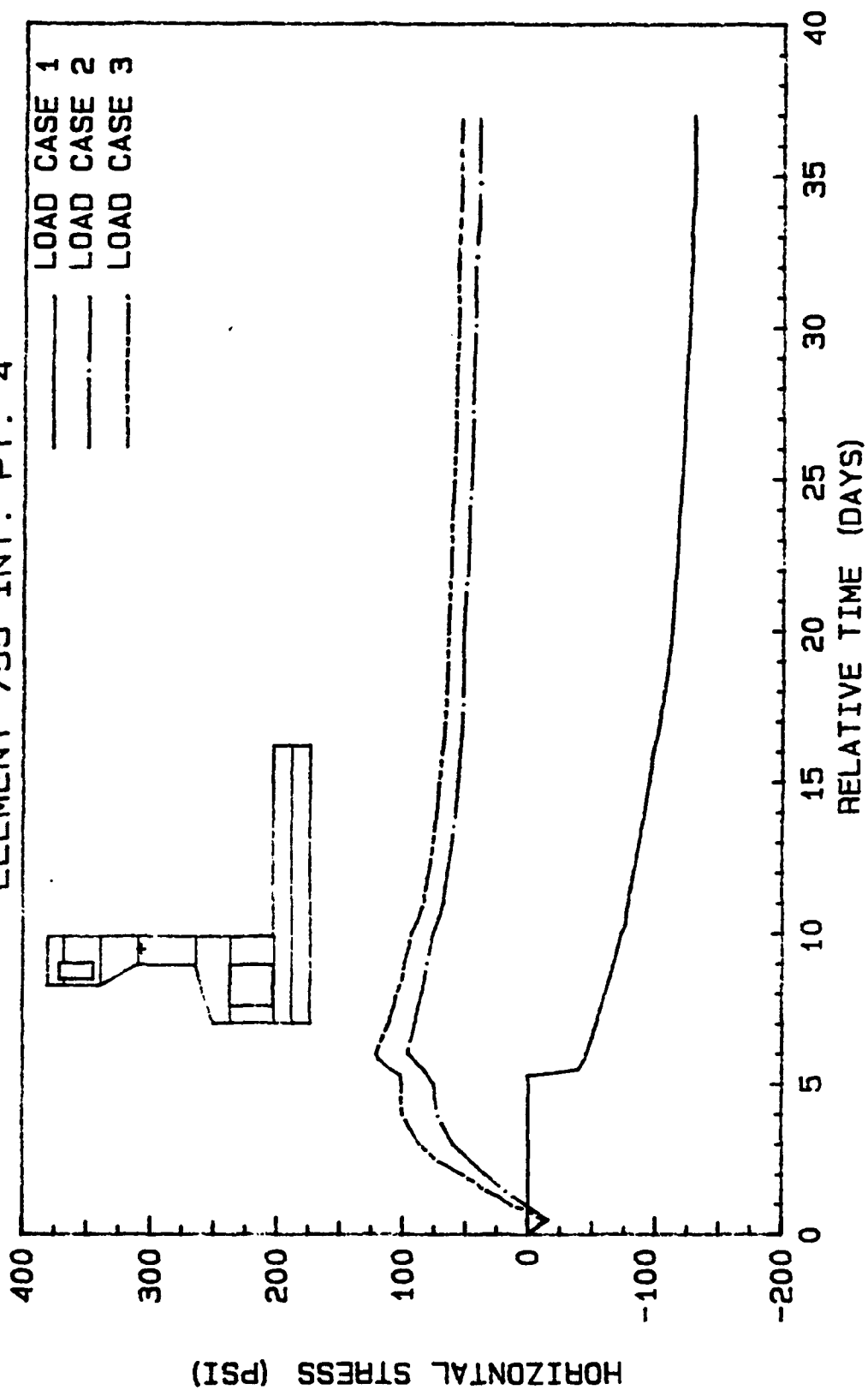


Figure 46. Stress versus time plot varying thermal loading for element 755

# ELEMENT 849 INT. PT. 2

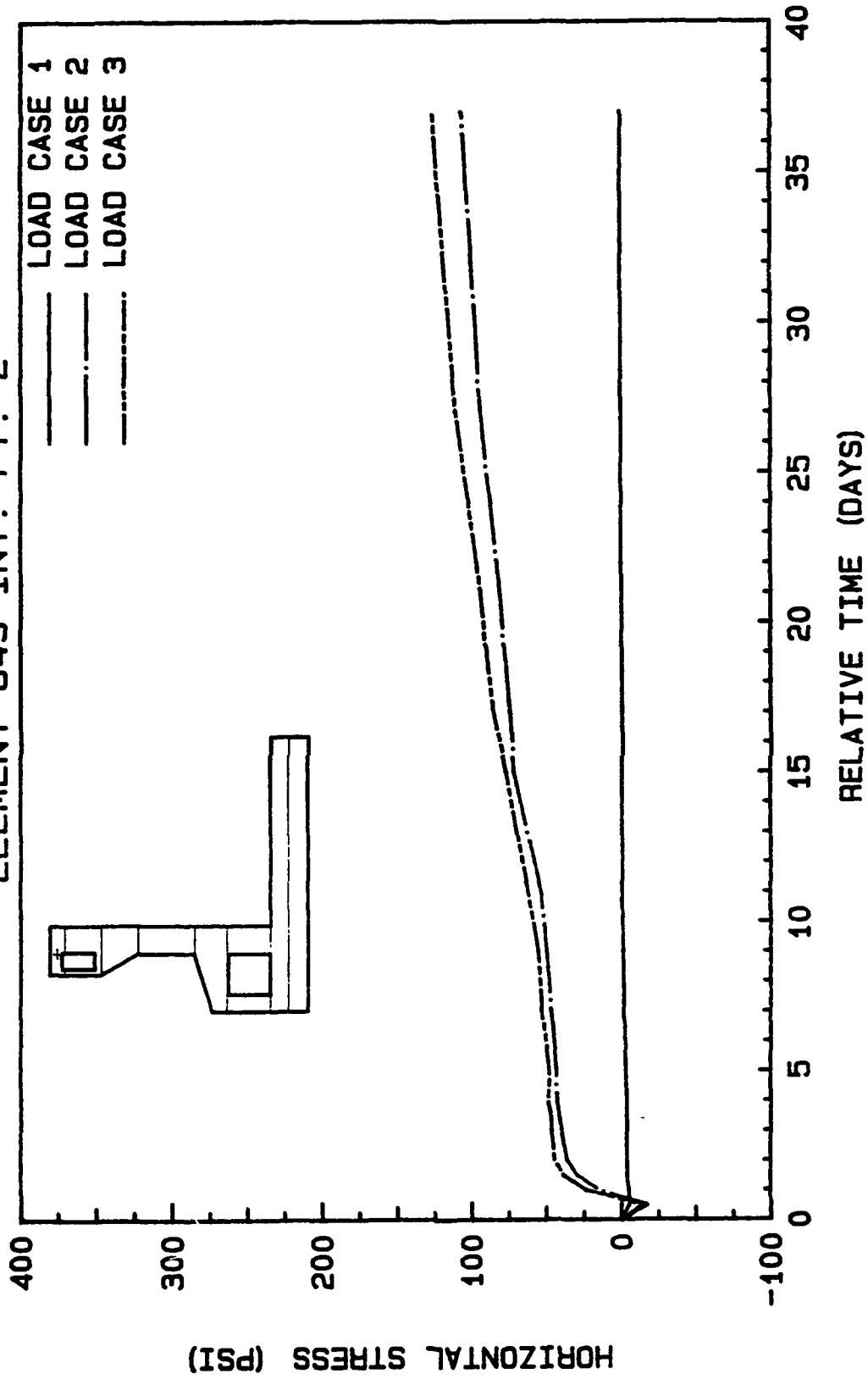


Figure 47. Stress versus time plot varying thermal loading for element 849

# ELEMENT 860 INT. PT. 3

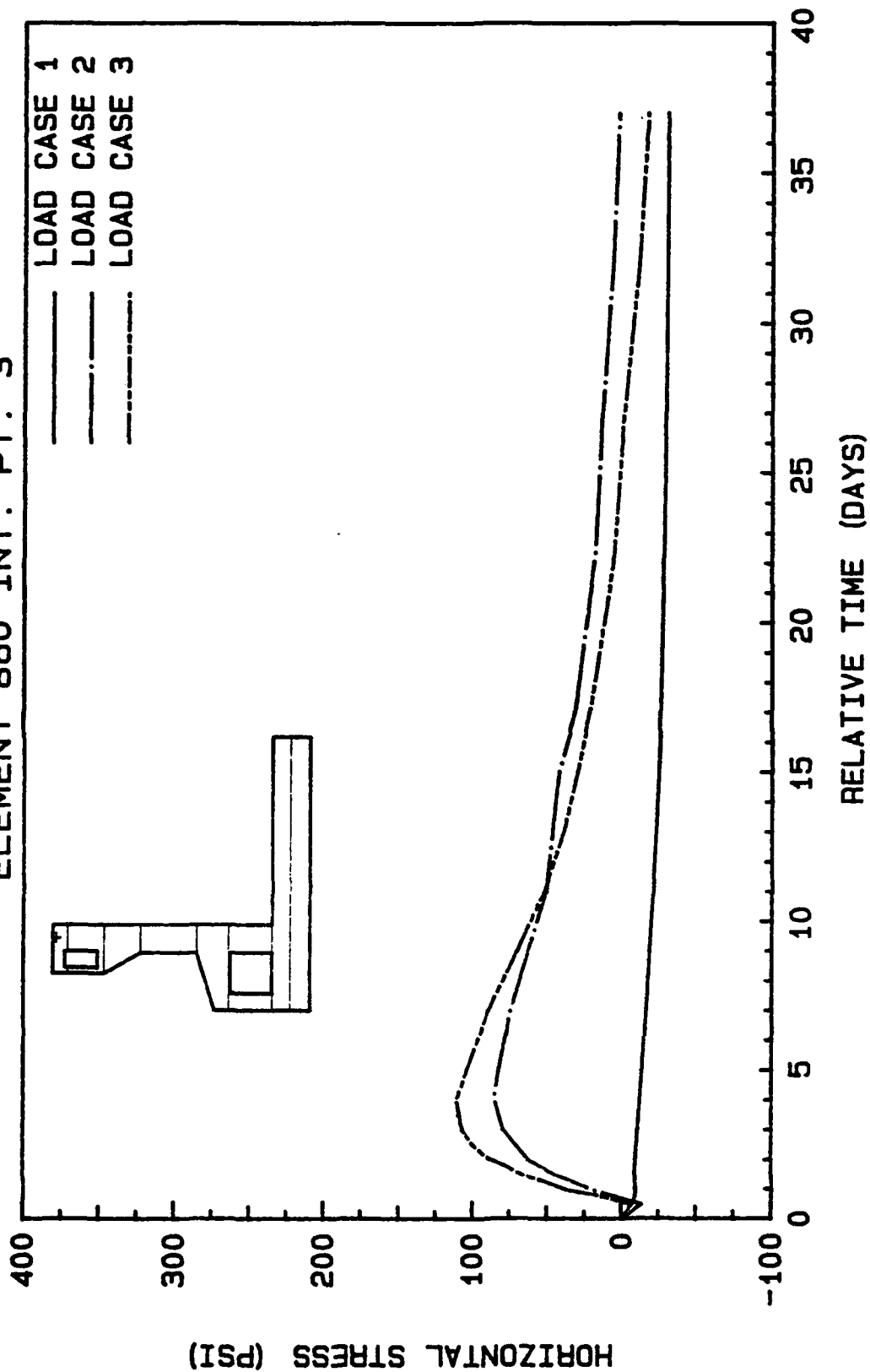


Figure 48. Stress versus time plot varying thermal loading for element 860

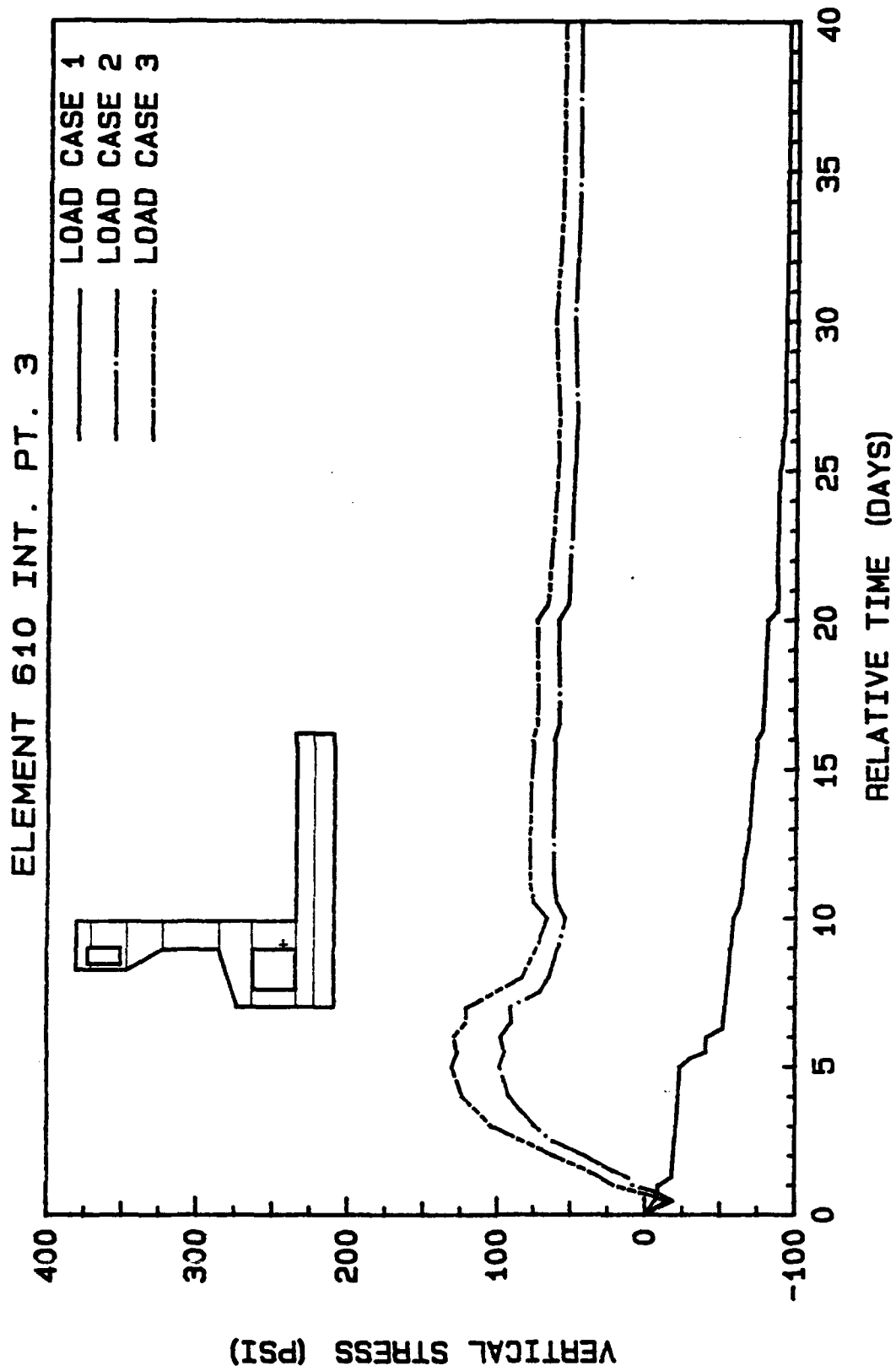


Figure 49. Stress versus time plot varying thermal loading for element 610

# ELEMENT 768 INT. PT. 2

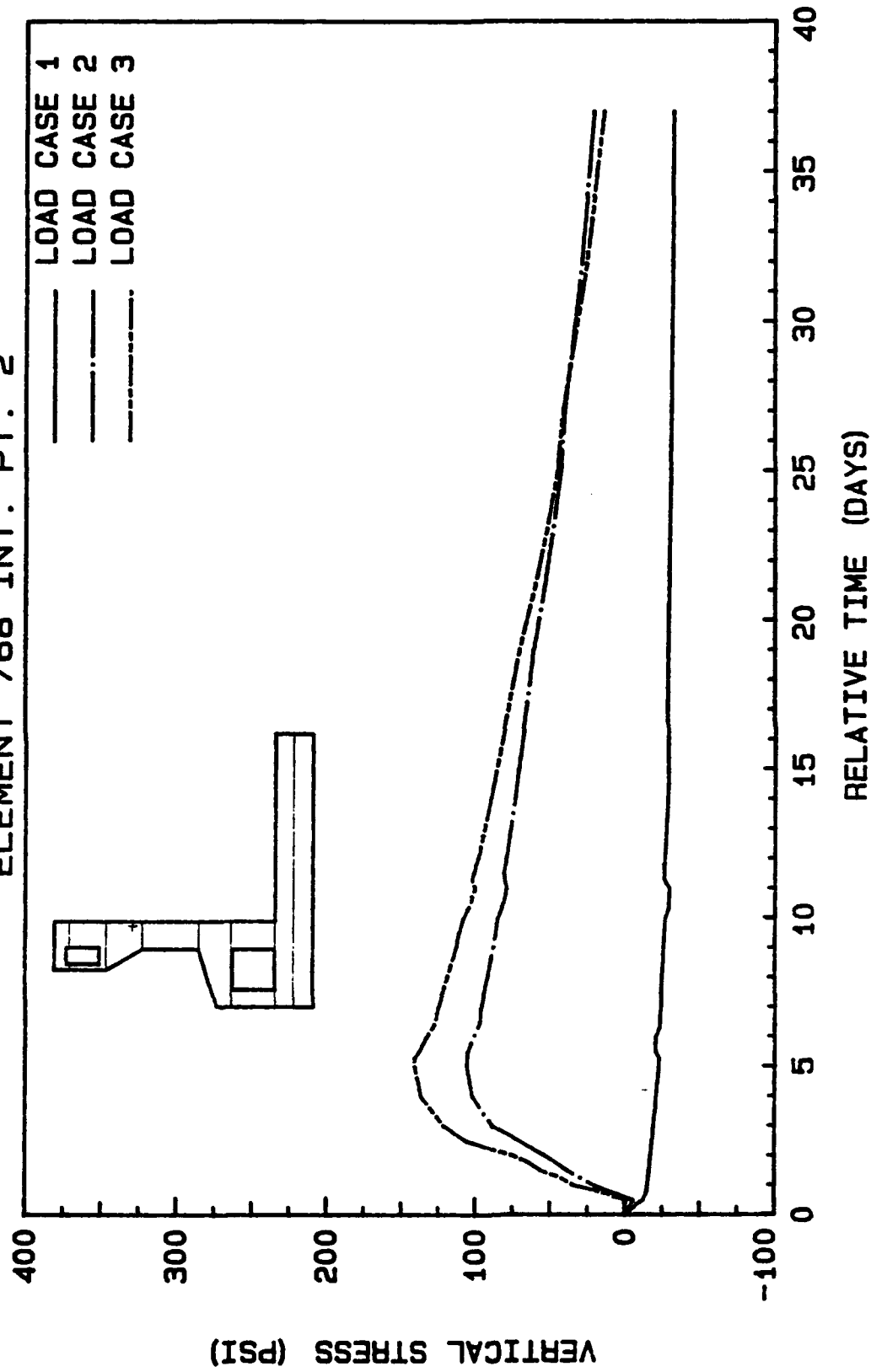


Figure 50. Stress versus time plot varying thermal loading for element 768

# ELEMENT 810 INT. PT. 3

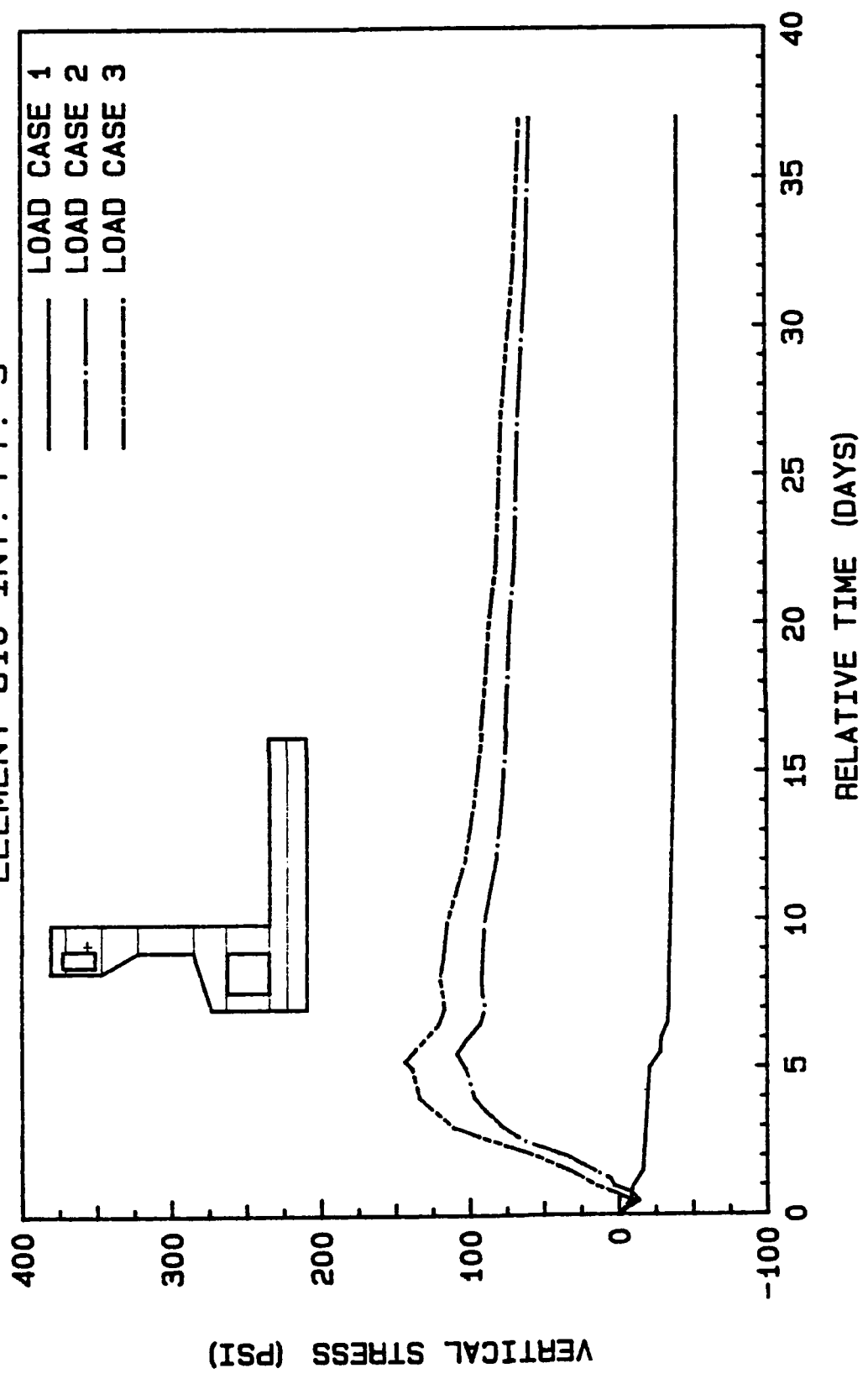


Figure 51. Stress versus time plot varying thermal loading for element 810

which is due to bending. Figure 42 shows similar results as those in Figure 39.

59. Figure 43 is at a location where the multiple point constraint is applied. For all three load cases, the resulting stress is tensile as would be expected since the roof of the culvert is acting as a large beam. It should be noted that no gravity loads are placed on the roof of the culvert until after 1 day when a gravity load is applied to the elements forming the roof. Going back to Figure 40, this is the reason an increase in stress occurs at 11 days. No rational explanation can be given for why load case 2 produces higher stresses than load case 3 after 25 days. However, it may be related to the fact that the Gauss point is near the corner of the culvert, thus producing a point of singularity in the mesh where unusual results may be expected. It may also be related to the numerical method, especially since this is the location where the convergence criteria were not strictly satisfied.

60. Figure 44 shows again a situation that would be compressive but, due to thermal loading, a tensile stress result. Again, compressive stress would be expected at this location for load case 1 since the roof of the culvert is acting like a beam and this would be the top of the beam--thus, there is a downward curvature forcing the element into a compressive mode. The compressive stress is small due to the large size of the member and also since it is supporting only its own weight.

61. Figures 45 and 46 are again similar to Figures 40 and 42 since the locations are near the top of a lift and more lifts are placed above it. Figure 47 is also a location where a multiple point constraint is applied to support the roof until adequate strength is obtained for the concrete to support itself. The magnitude of the stresses is not as high as in Figure 43, but the span of the roof is only 5 ft at this gallery as opposed to 12 ft for the culvert. Also the lift height is not as thick at this location, therefore, less heat "build up" results. For load case 1, the stress is compressive because the elements that form the roof are acting like a fixed-fixed beam. The stress is extremely low but again the weight to span ratio is low.

62. Figure 48 shows the stress at the top of the structure. At this location, the loading is predominantly thermal at early time since gravity loads are nearly nonexistent.

63. Finally, Figures 49-51 shows vertical stresses near the culvert vertical wall, the chamber wall, and the gallery vertical wall. Obviously, without thermal loads, the stress is compressive; with thermal loads, a situation similar to that of an unrestrained slab is found. For load case 3, the stress reaches a value near 150 psi which is significant since this stress is reached at 5 days when the strength of the concrete is low, and because the gravity loads work directly against the thermal loads in the vertical direction. The slight increase in stress at 10 days could be related to the fact that the chamber wall up to lift 5 is bending "in" toward the chamber, producing eccentricity which induces "extra" tension after placement of lift 5. The decreases in stress at 20 days is due to the eccentric load caused by lifts 6 through 8, thus causing the chamber wall to bend now away from the chamber.

64. Based on the above results, the upper bound adiabatic curve will be used in the remaining stress analyses, as was expected.

## PART VI: STRESS ANALYSIS RESULTS SHOWING EFFECT OF CREEP AND SHRINKAGE

### Introduction

65. After the upper bound adiabatic curve was selected, a parametric study of the effect of creep and shrinkage on a mass concrete structure was performed. The results of such a study will now be presented. The various load cases examined are shown in Table 6.1. First, the effect of shrinkage will be assessed by looking at three analyses in which creep was fixed at the lower bound. Shrinkage was given in Figure 15. In the third analysis, shrinkage was neglected. Next, the effect of creep was determined in a similar manner. Then, a series of plots are presented with all the realistic load cases (i.e. load cases 3 through 6 in which both creep and shrinkage are included in the analysis) to determine the load case which consistently produced higher stresses for performing a service load analysis. In addition, the strains for these load cases will also be presented since cracking in concrete is related to both stresses and strains. Finally, locations on the mesh where the horizontal and vertical stresses exceed a specified value at a certain time in the analysis will be presented. There are two reasons for doing this--first, to show areas where cracking may be critical and secondly, to verify that the locations where stress and strain plots were examined are the critical locations in the monolith.

### Effect of Shrinkage on Resulting Stresses

66. Figures 52-65 show stress versus time with creep fixed and shrinkage strains varying, as seen in Table 5, load cases 3, 5, and 7. Consequently, the load cases with shrinkage included tend to produce lower stresses later in time. This is the case in all the figures with the exception of Figures 51, 55, 57, and 61. In these figures, as previously noted, the stresses induced are predominantly due to bending effects and all four locations are near an externally applied support. Figure 55 shows that neglecting shrinkage greatly reduces the stress. This is because shrinkage is a volumetric process occurring in equal amounts in all directions. Therefore, as the element shrinks, the boundary conditions cause the resulting force to be

# ELEMENT 377 INT. PT. 1

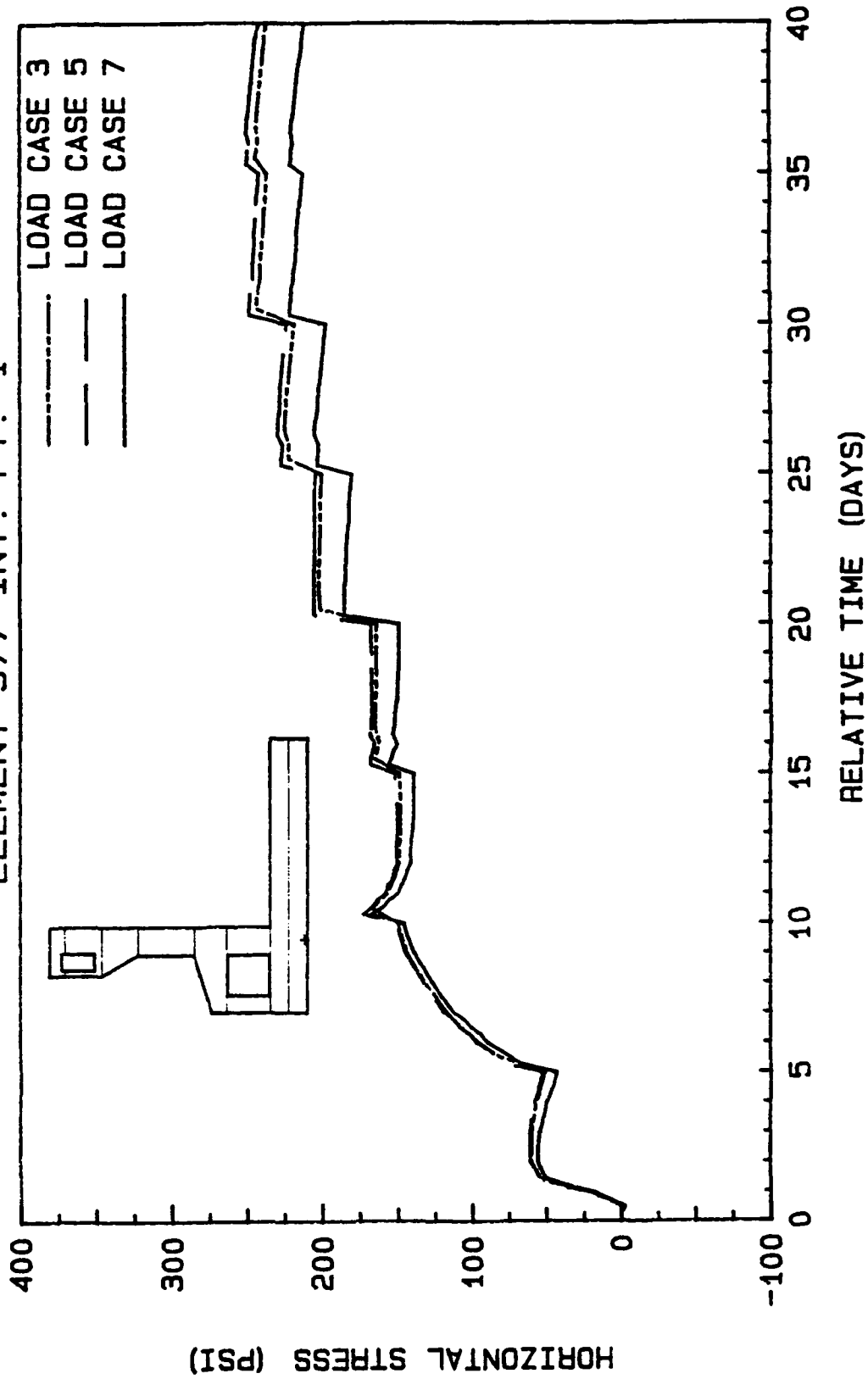


Figure 52. Stress versus time plot varying degree of shrinkage at element 377

# ELEMENT 556 INT. PT. 4

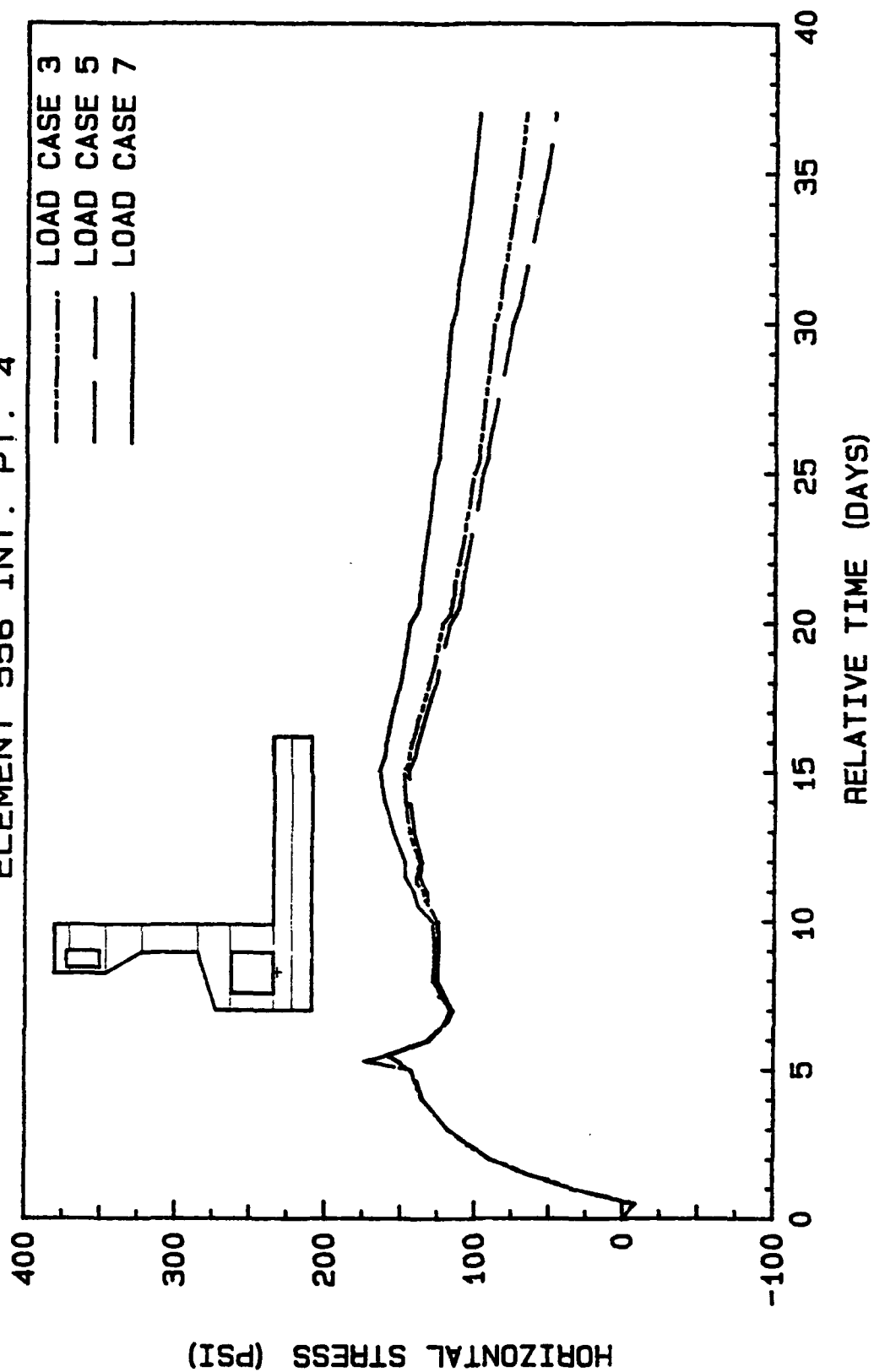


Figure 53. Stress versus time plot varying degree of shrinkage at element 556

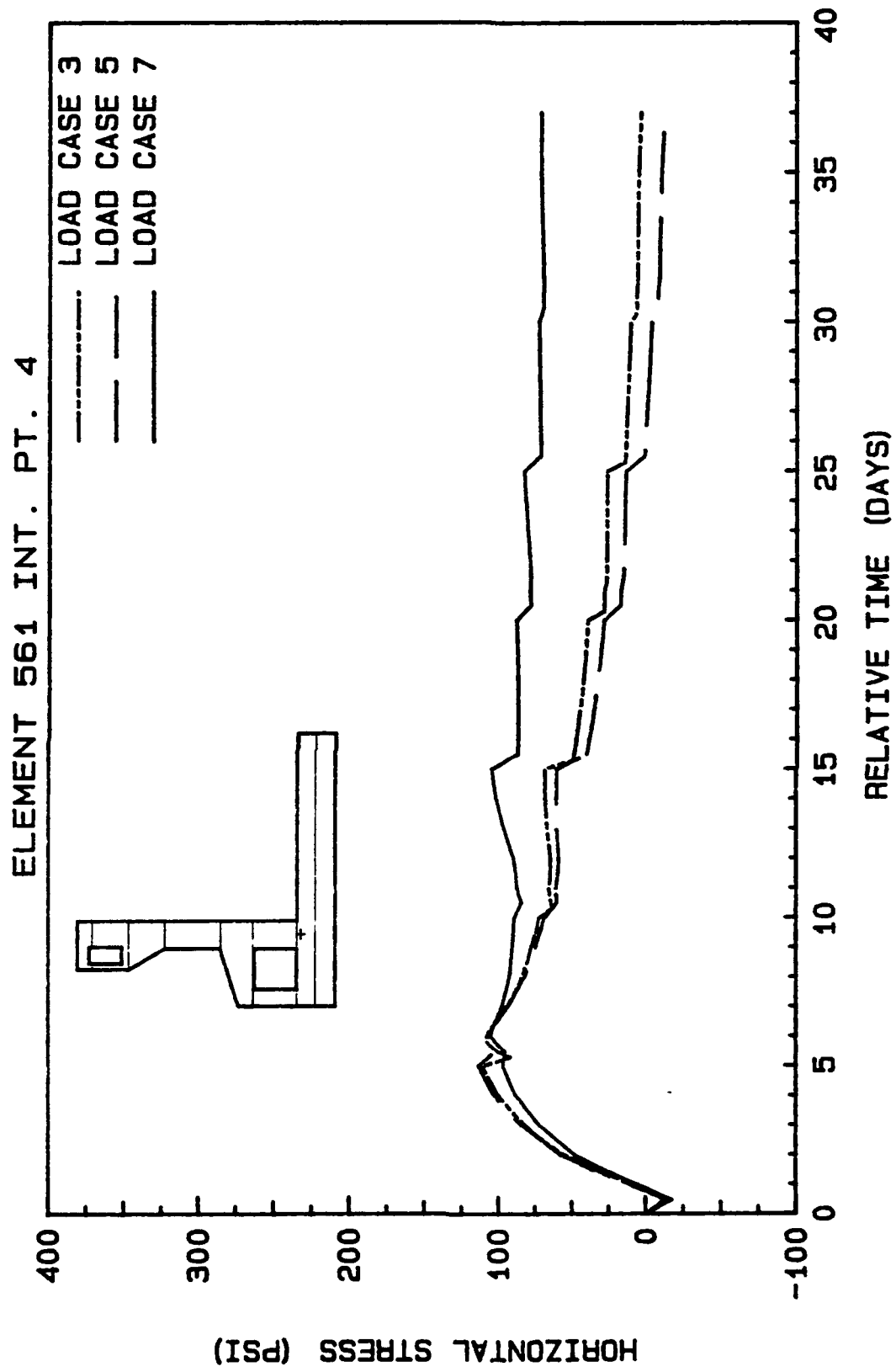


Figure 54. Stress versus time plot varying degree of shrinkage at element 561

# ELEMENT 587 INT. PT. 4

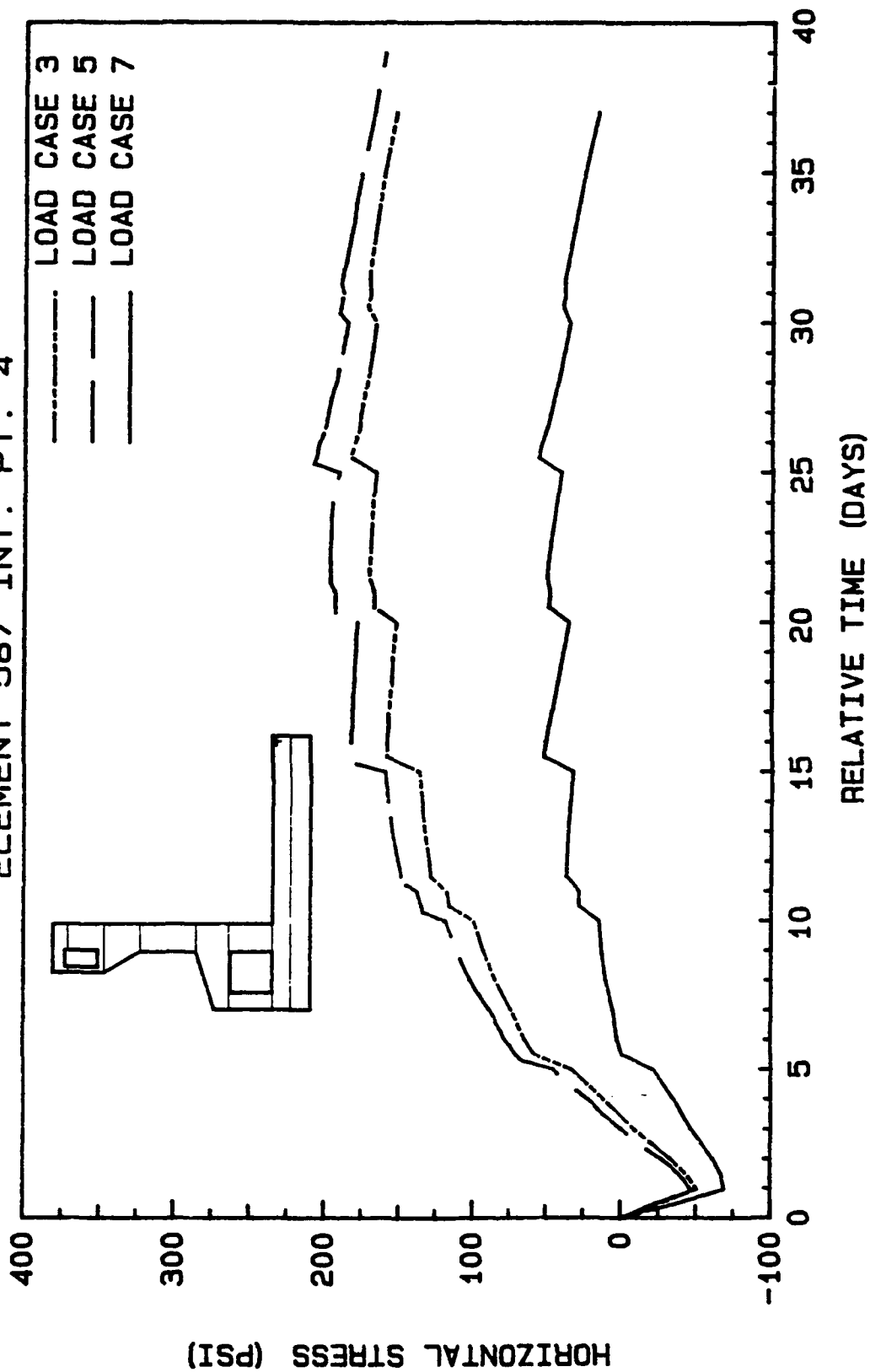


Figure 55. Stress versus time plot varying degree of shrinkage at element 587

# ELEMENT 663 INT. PT. 4

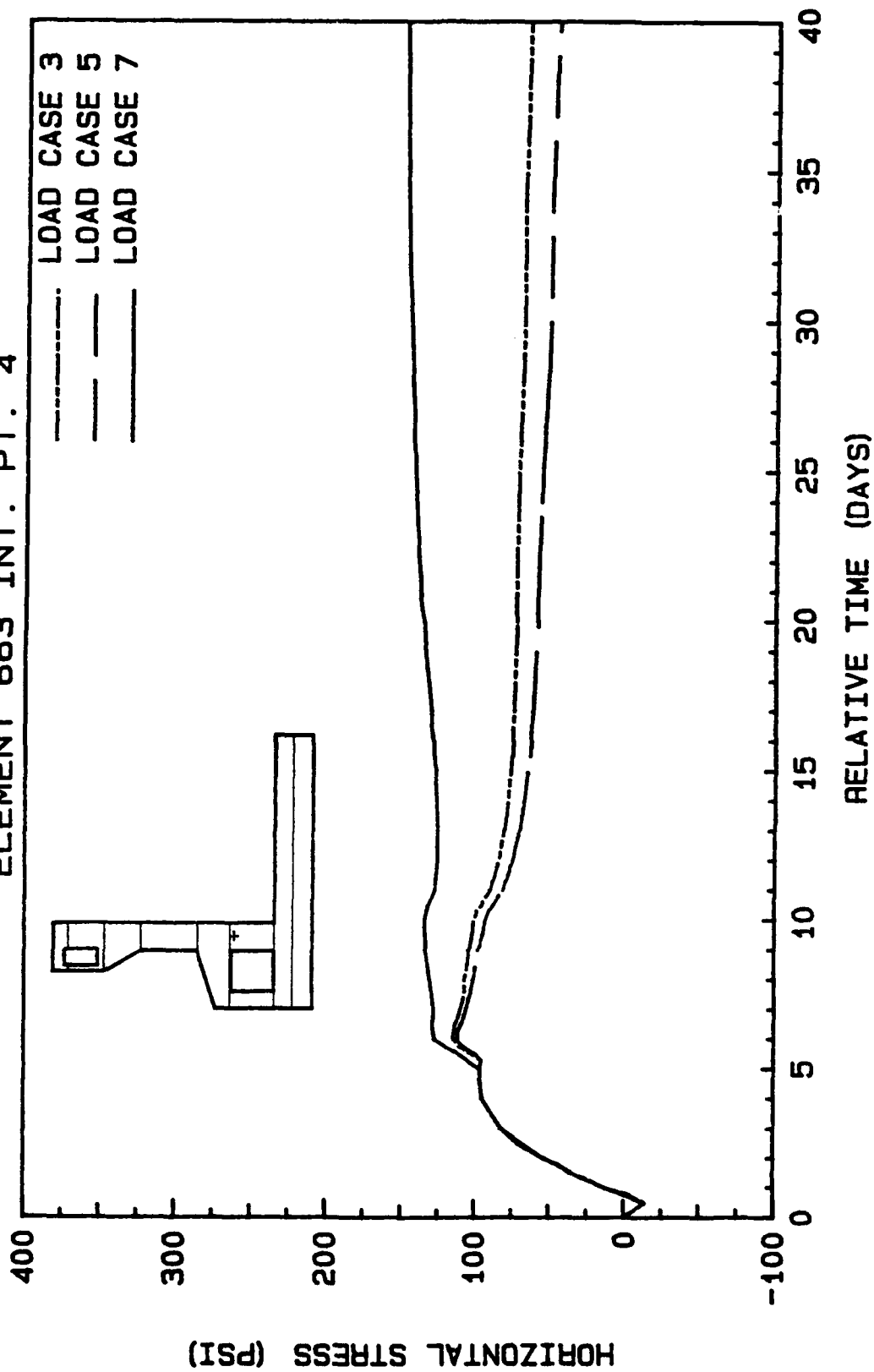


Figure 56. Stress versus time plot varying degree of shrinkage at element 663

# ELEMENT 674 INT. PT. 1

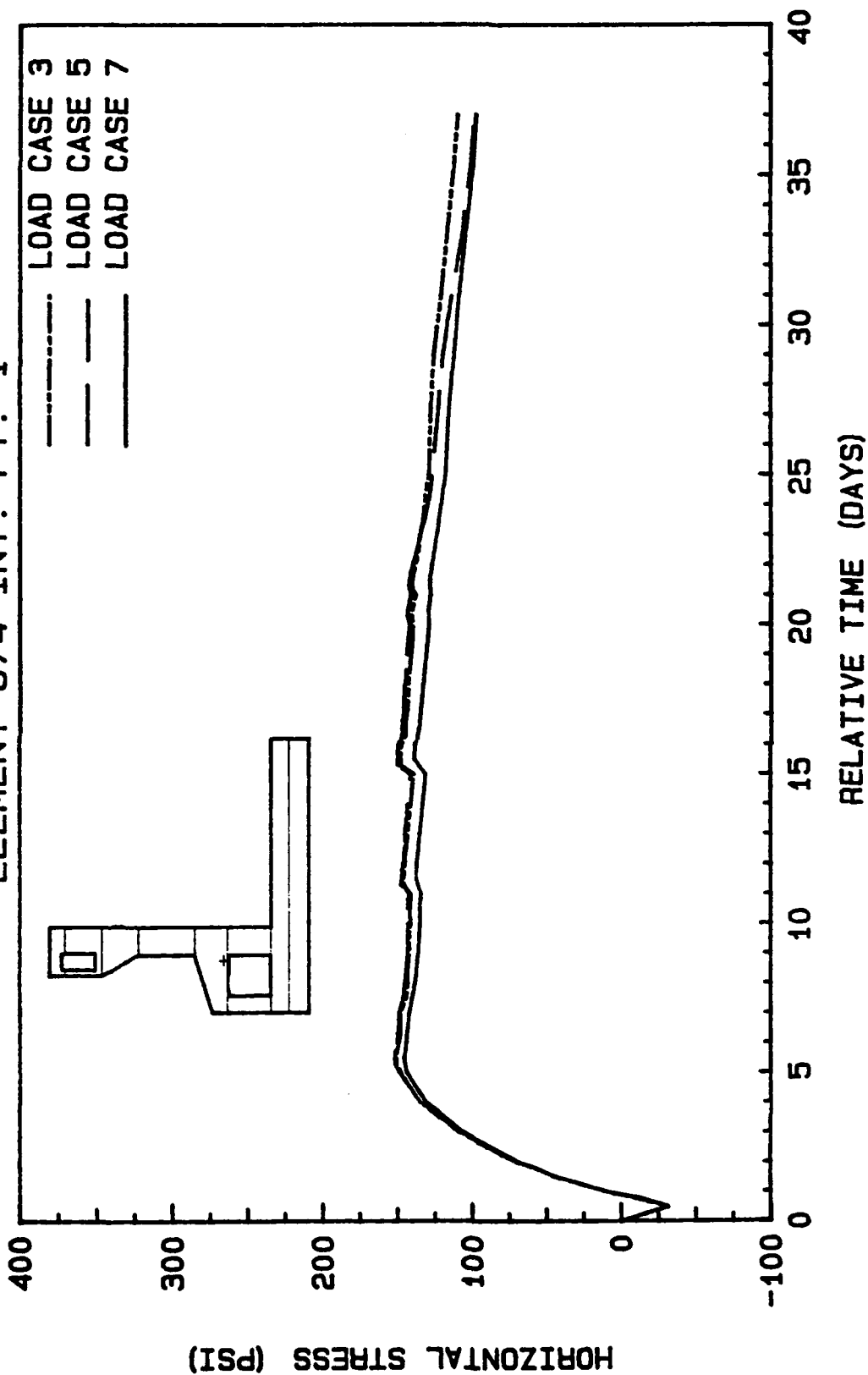


Figure 57. Stress versus time plot varying degree of shrinkage at element 674

# ELEMENT 705 INT. PT. 3

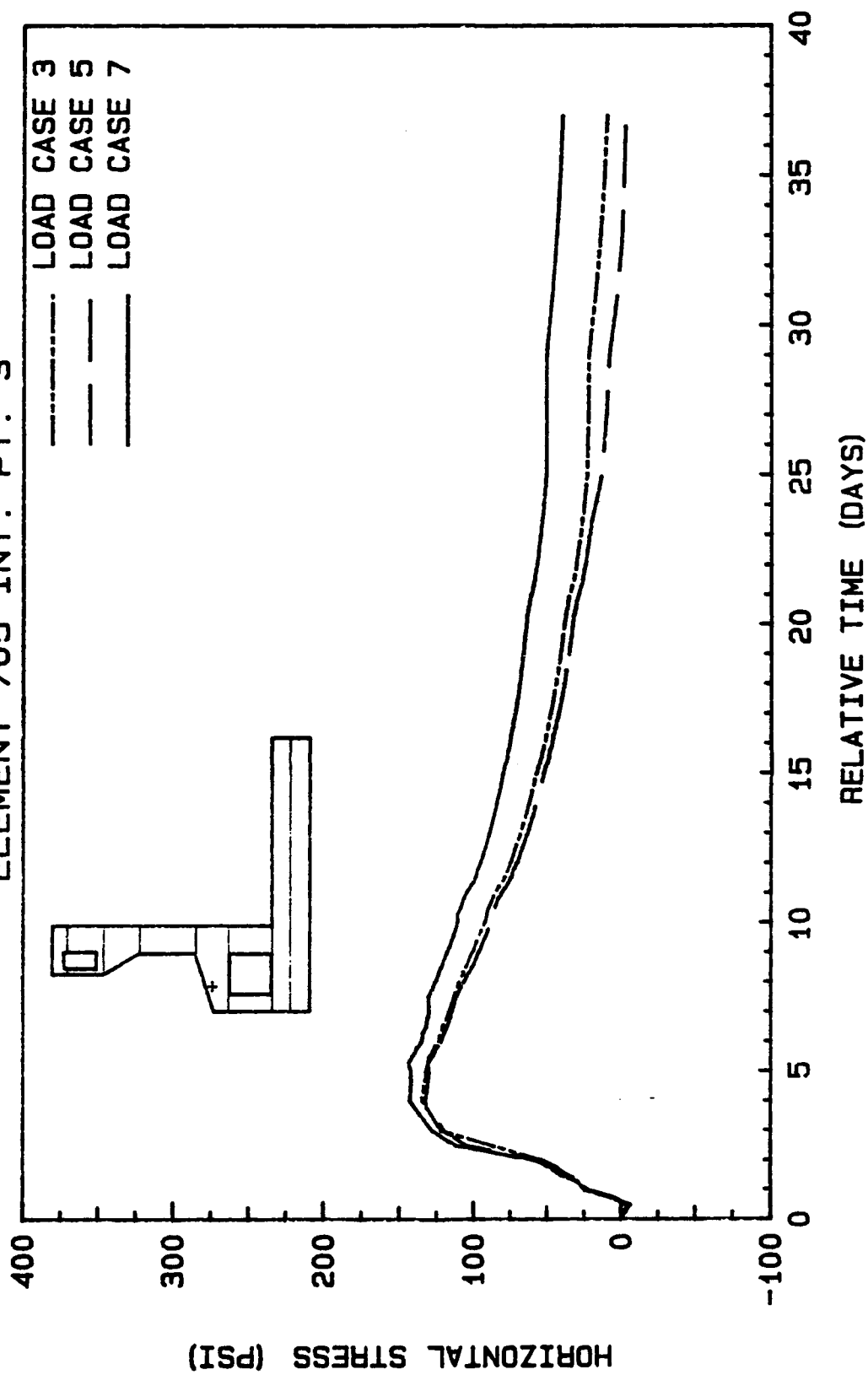


Figure 58. Stress versus time plot varying degree of shrinkage at element 705

# ELEMENT 719 INT. PT. 3

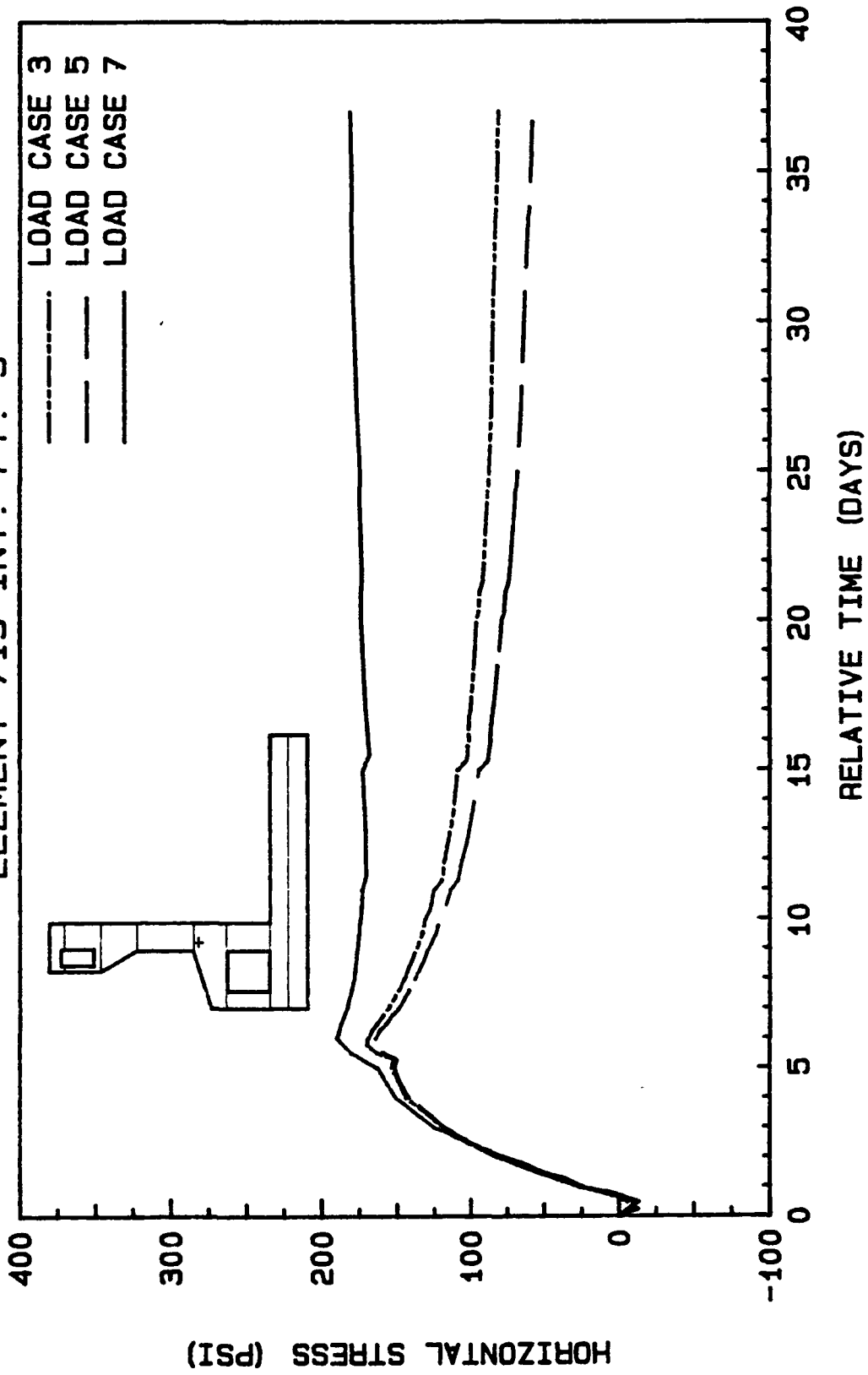


Figure 59. Stress versus time plot varying degree of shrinkage at element 719

# ELEMENT 755 INT. PT. 4

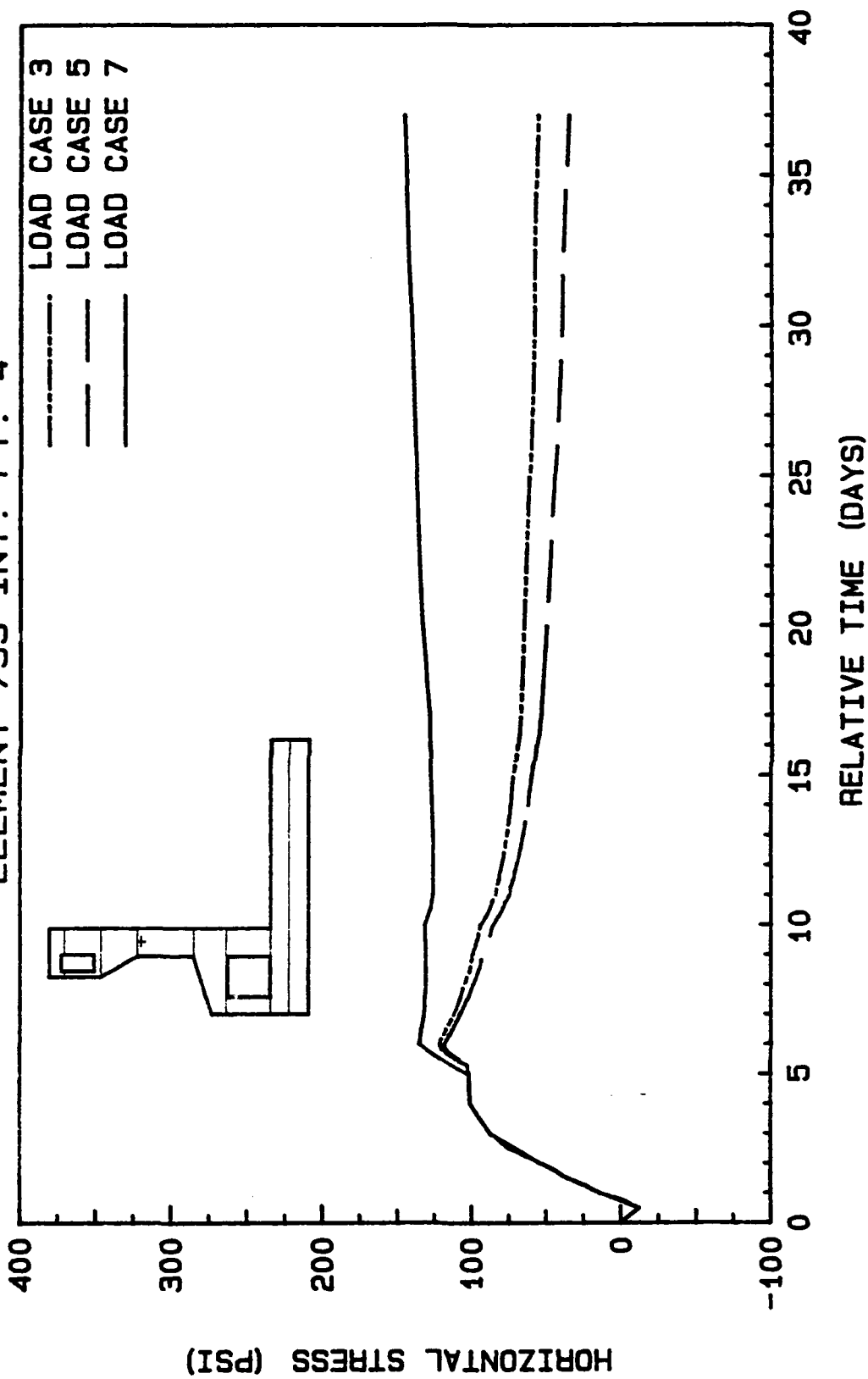


Figure 60. Stress versus time plot varying degree of shrinkage at element 755

# ELEMENT 849 INT. PT. 2

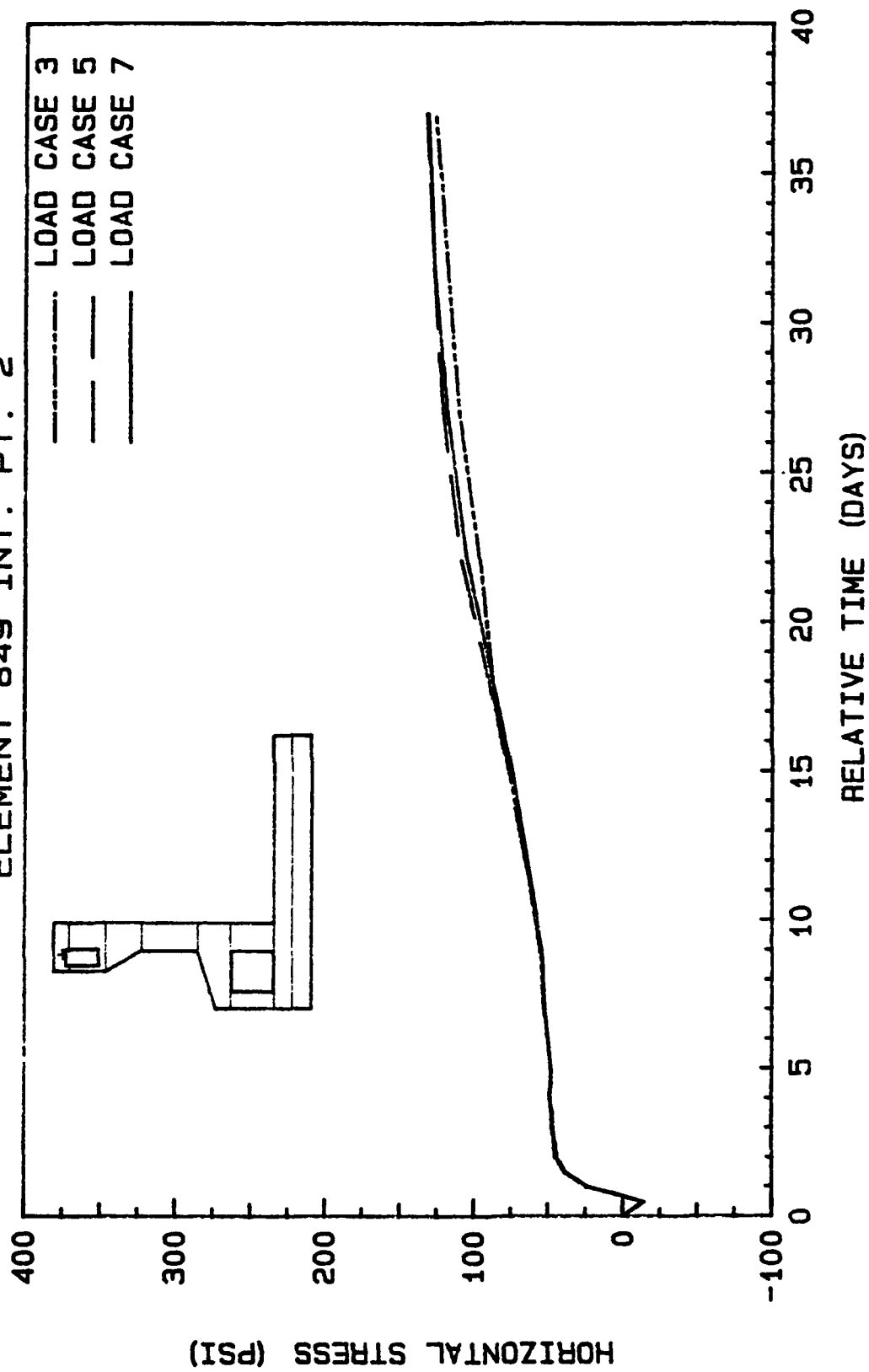


Figure 61. Stress versus time plot varying degree of shrinkage at element 849

# ELEMENT 860 INT. PT. 3

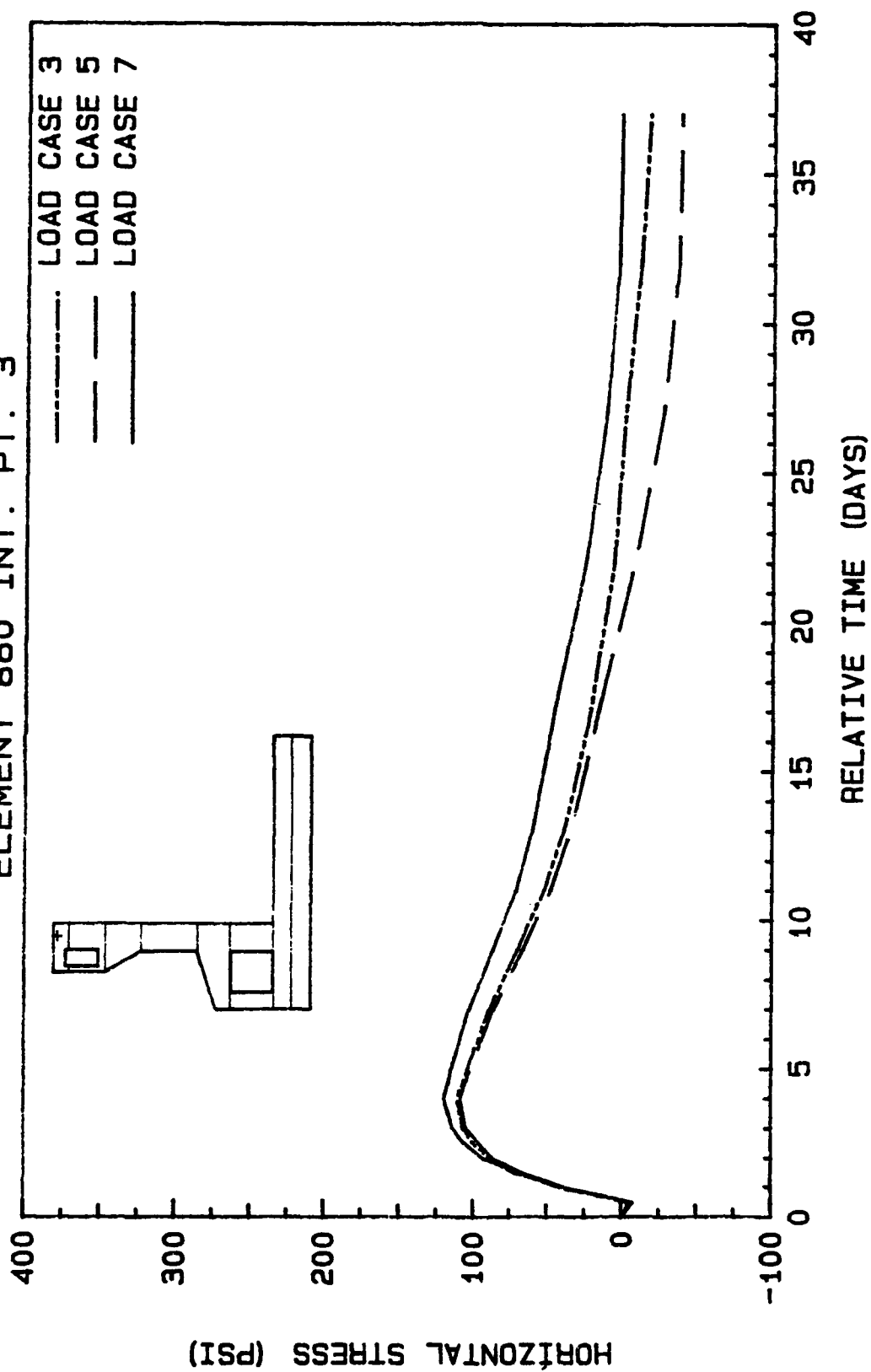


Figure 62. Stress versus time plot varying degree of shrinkage at element 860

# ELEMENT 610 INT. PT. 3

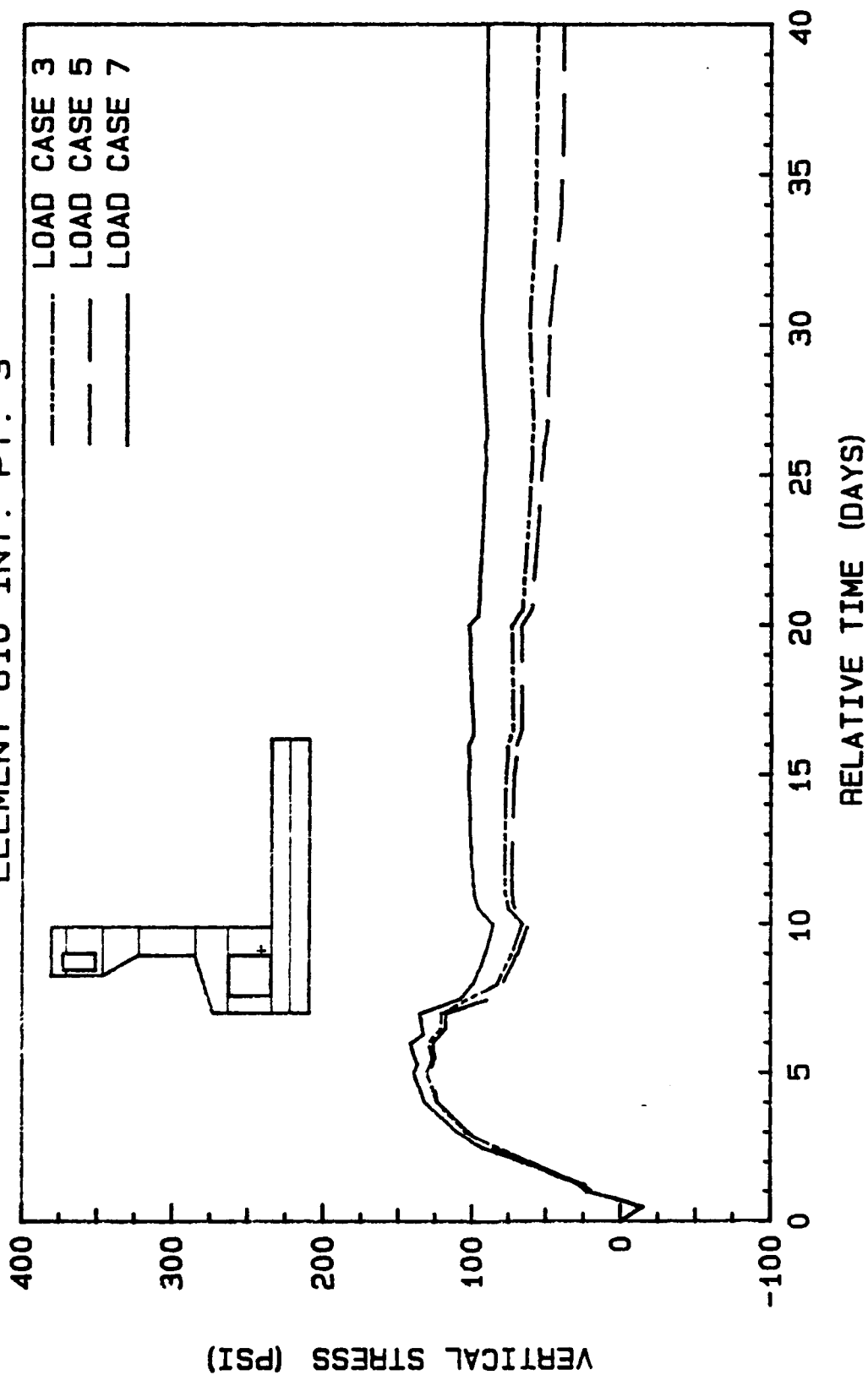


Figure 63. Stress versus time plot varying degree of shrinkage at element 610

# ELEMENT 768 INT. PT. 2

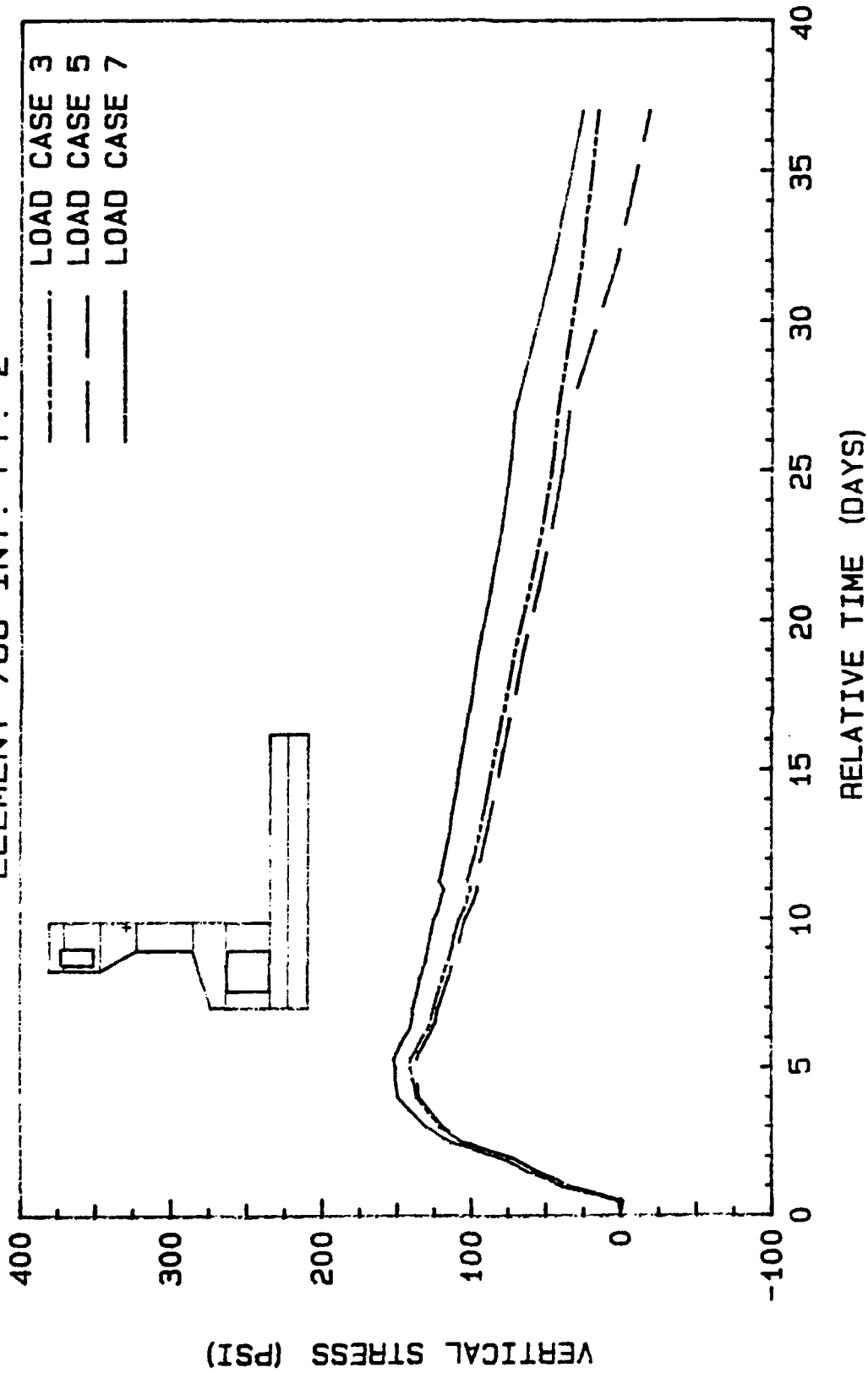


Figure 64. Stress versus time plot varying degree of shrinkage at element 768

# ELEMENT 810 INT. PT. 3

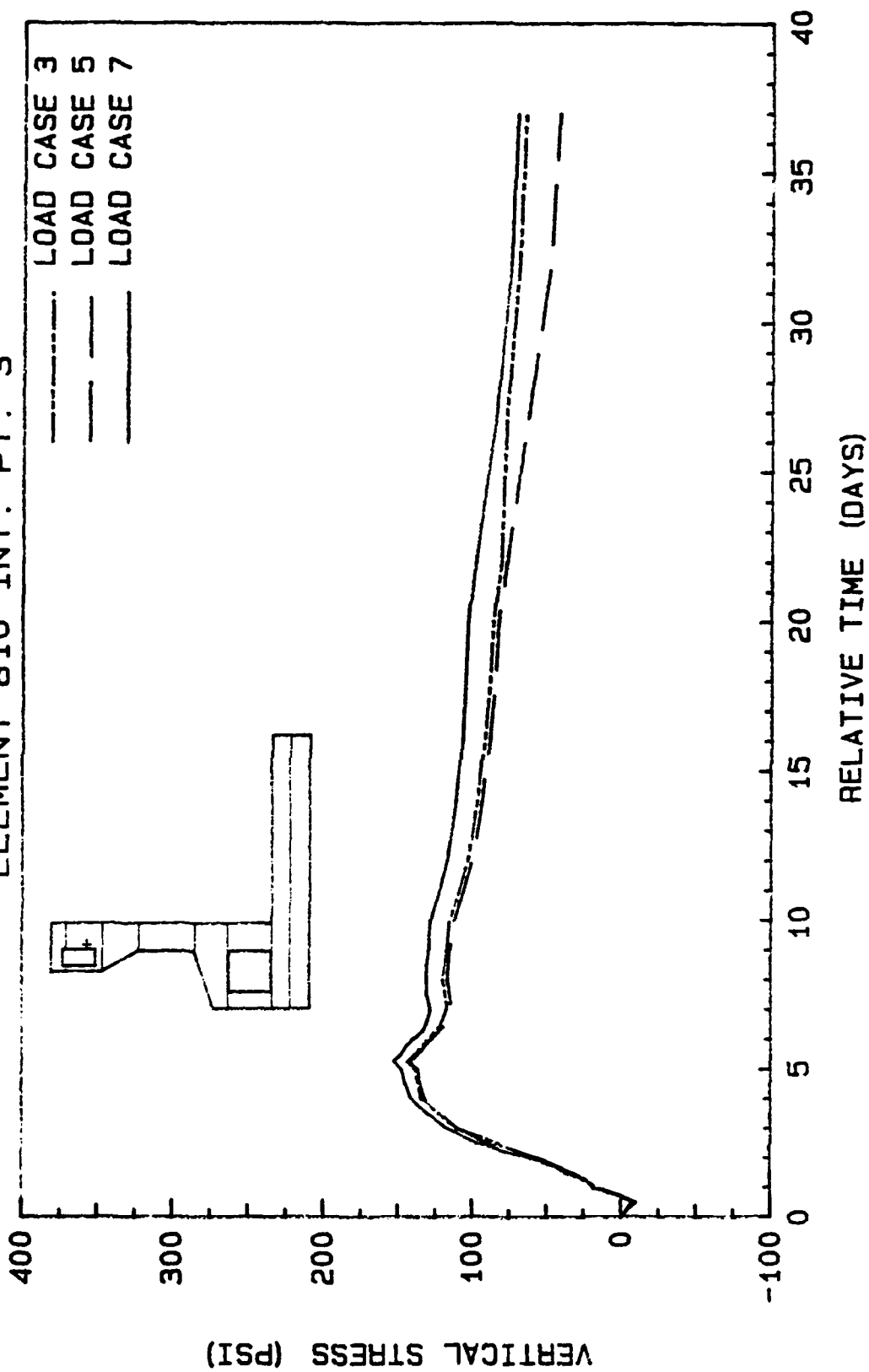


Figure 65. Stress versus time plot varying degree of shrinkage at element 810

tensile. Thus, when more shrinkage occurs, a higher force results. Figures 52, 57 and 61 show that shrinkage has only a minor effect on the stresses.

67. The remaining figures show that with less shrinkage, a higher tensile stress results. It can also be noted that for the first 3-5 days, shrinkage has a lesser effect than at later times. Looking back at Figure 15 it can be seen that although shrinkage strains do increase at a greater rate the first few days, the actual strains are not that high. Consequently, shrinkage starts having an effect on the stresses after 5 days. This is seen in Figures 53, 54, 56, 59, 60 and 63. Notice that the plots with no shrinkage (load case 7) can be produced from the other curves by rotating them counterclockwise at approximately 6 days, resulting in significantly higher stresses after this time. However, for load cases 3 and 5, shrinkage strains prevent this since the element is still shrinking as will be seen when the strain plots are presented.

68. It should be noted that at locations where the element is covered by a new lift--for example, element 719 in Figure 59--the band on the shrinkage plot formed by the different load cases is wider than for the elements that are at an exposed surface--for example, element 705 in Figure 58 (with the exception of Figures 52 and 55).

#### Effect of Creep on Resulting Stresses

69. Figures 66-79 show the results of the analyses with shrinkage fixed at the lower bound value and varying creep. Observing from the figures, creep tends to relax the structure except near the center-line support and at locations where the multipoint constraint is applied (Figure 69 and Figures 71 and 75). These results are expected and justifiable.

70. In small concrete members, creep tends to produce higher stresses since larger deformations will result. Consequently, the stresses also will increase since the stress is proportional to deflection (Fintel 1974). In mass concrete structures, however, large deformations are usually not a major consideration, except for deformations related to settlement. Thus, viscous flow of the material due to creep will work to relieve stresses or place the structure in a more stable state of stress.

# ELEMENT 377 INT. PT. 1

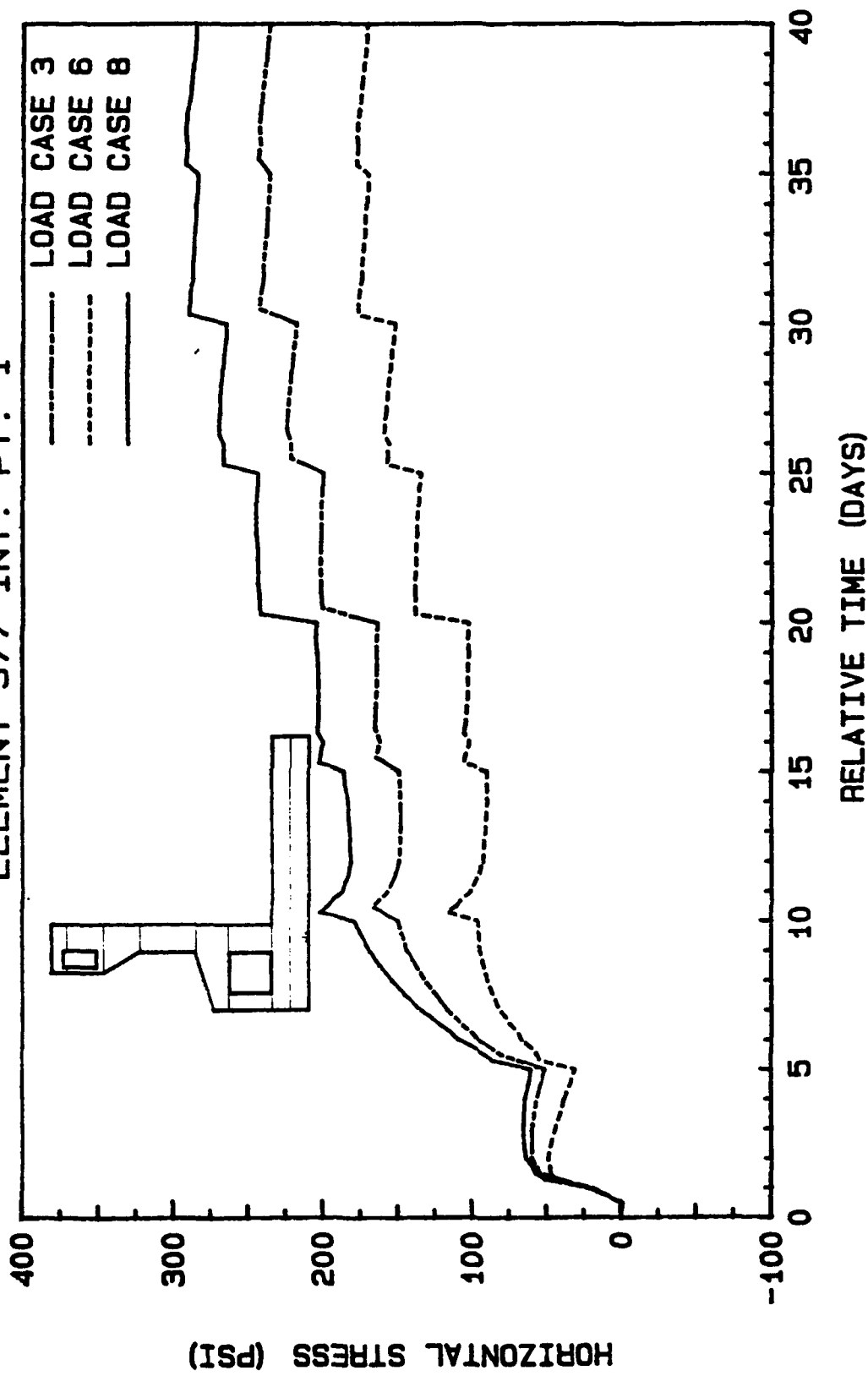


Figure 66. Stress versus time plot varying degree of creep for element 377

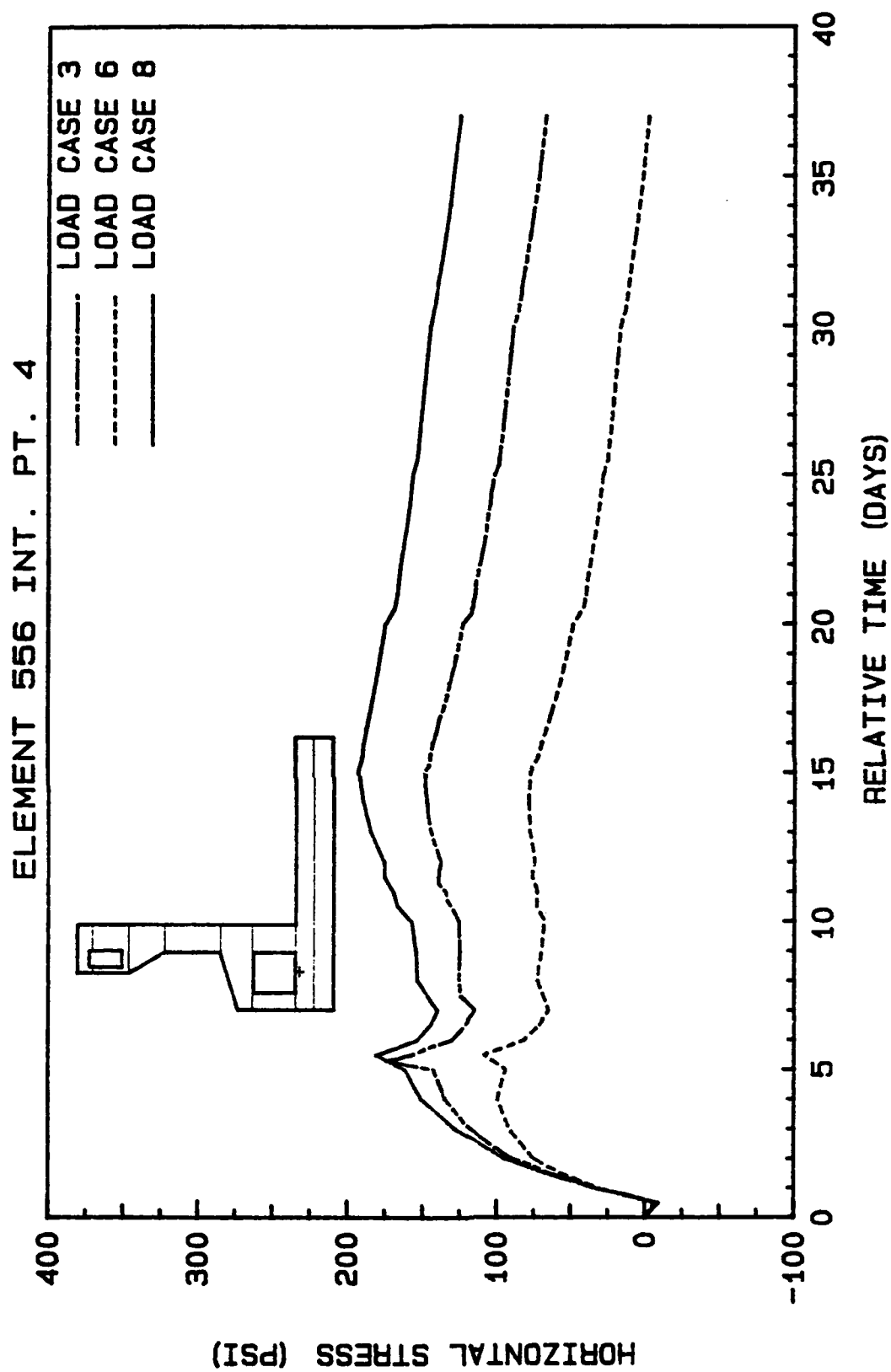


Figure 67. Stress versus time plot varying degree of creep for element 556

# ELEMENT 561 INT. PT. 4

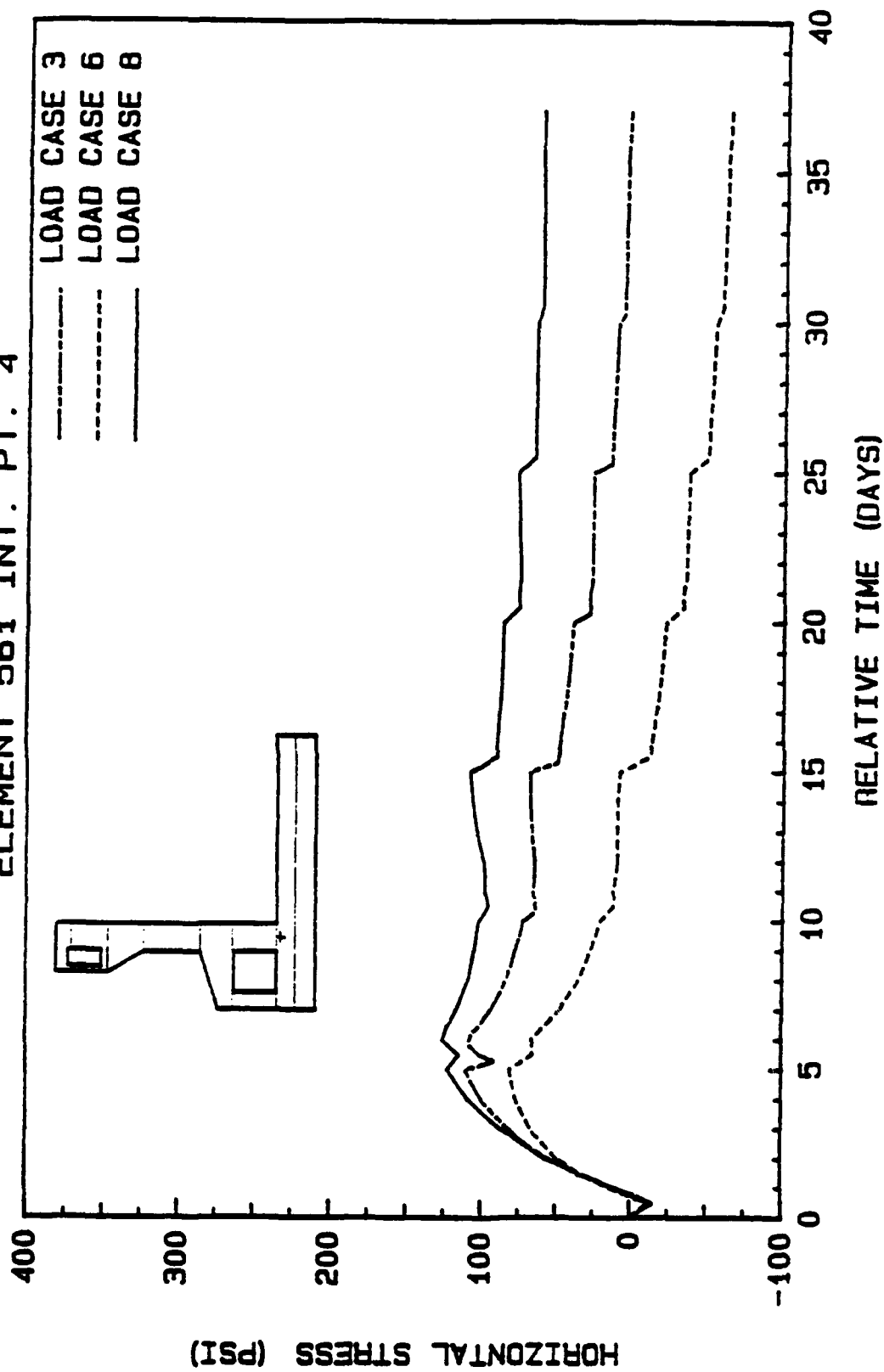


Figure 68. Stress versus time plot varying degree of creep for element 561

# ELEMENT 587 INT. PT. 4

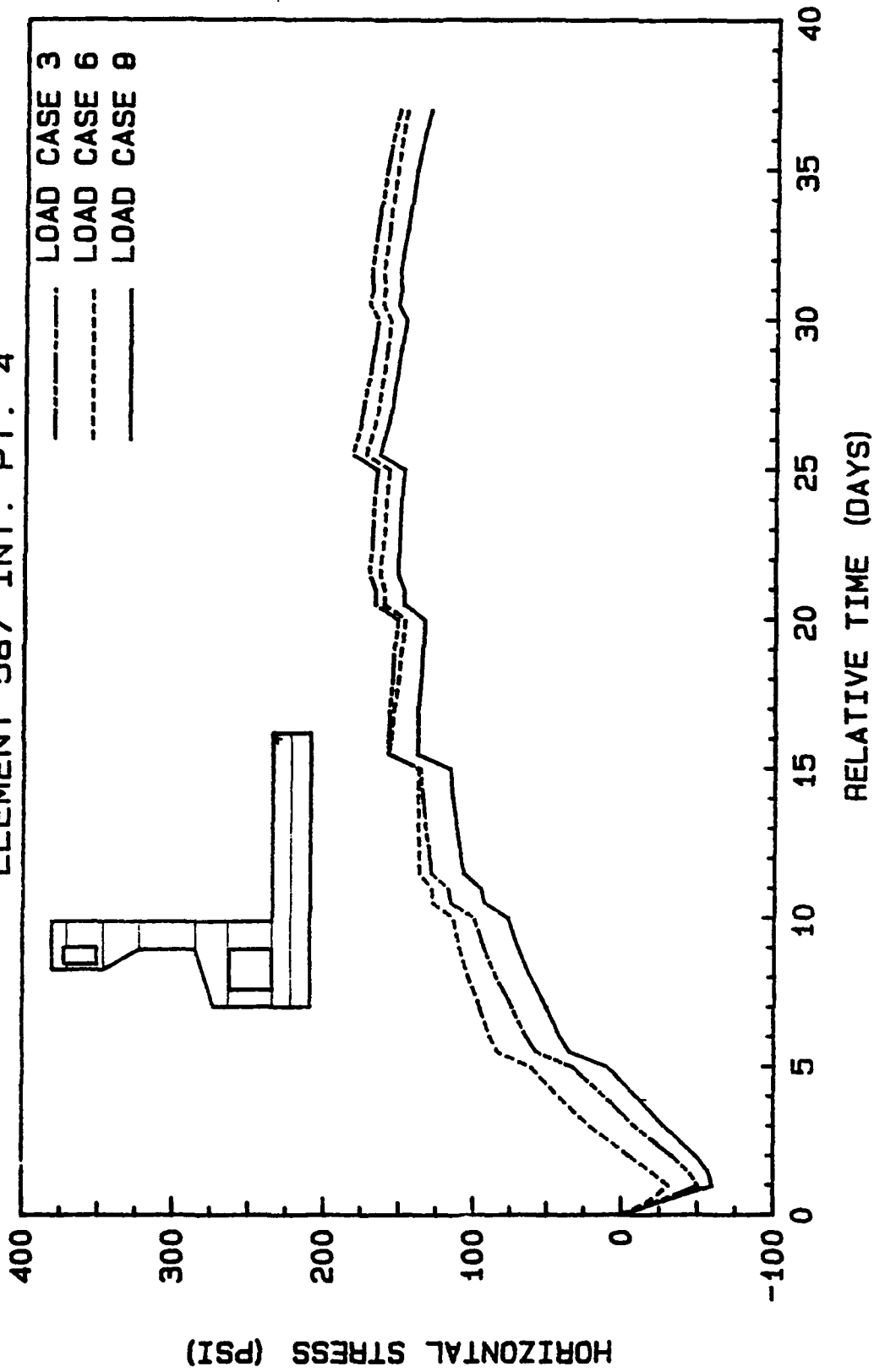


Figure 69. Stress versus time plot varying degree of creep for element 587

# ELEMENT 663 INT. PT. 4

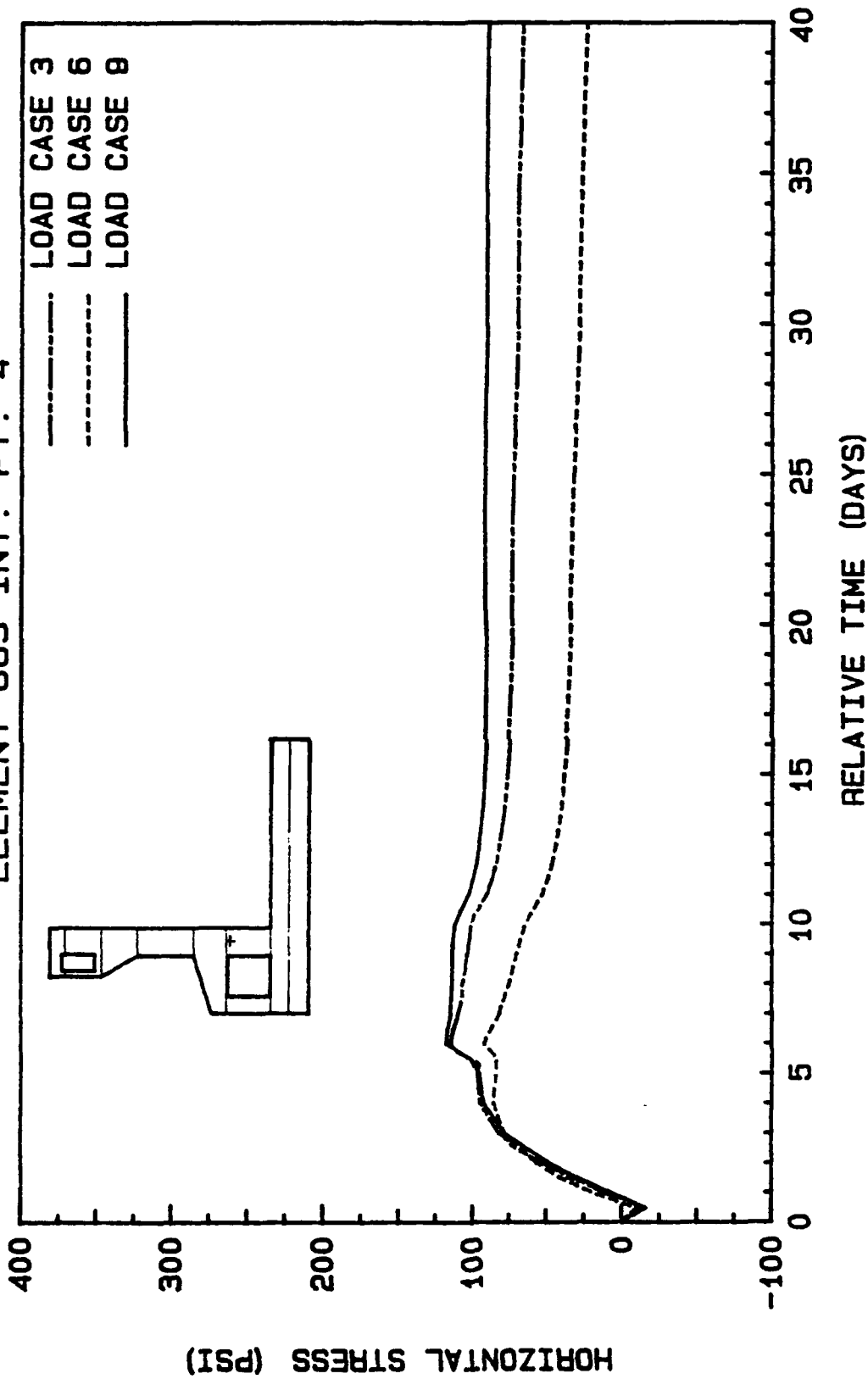


Figure 70. Stress versus time plot varying degree of creep for element 663

# ELEMENT 674 INT. PT. 1

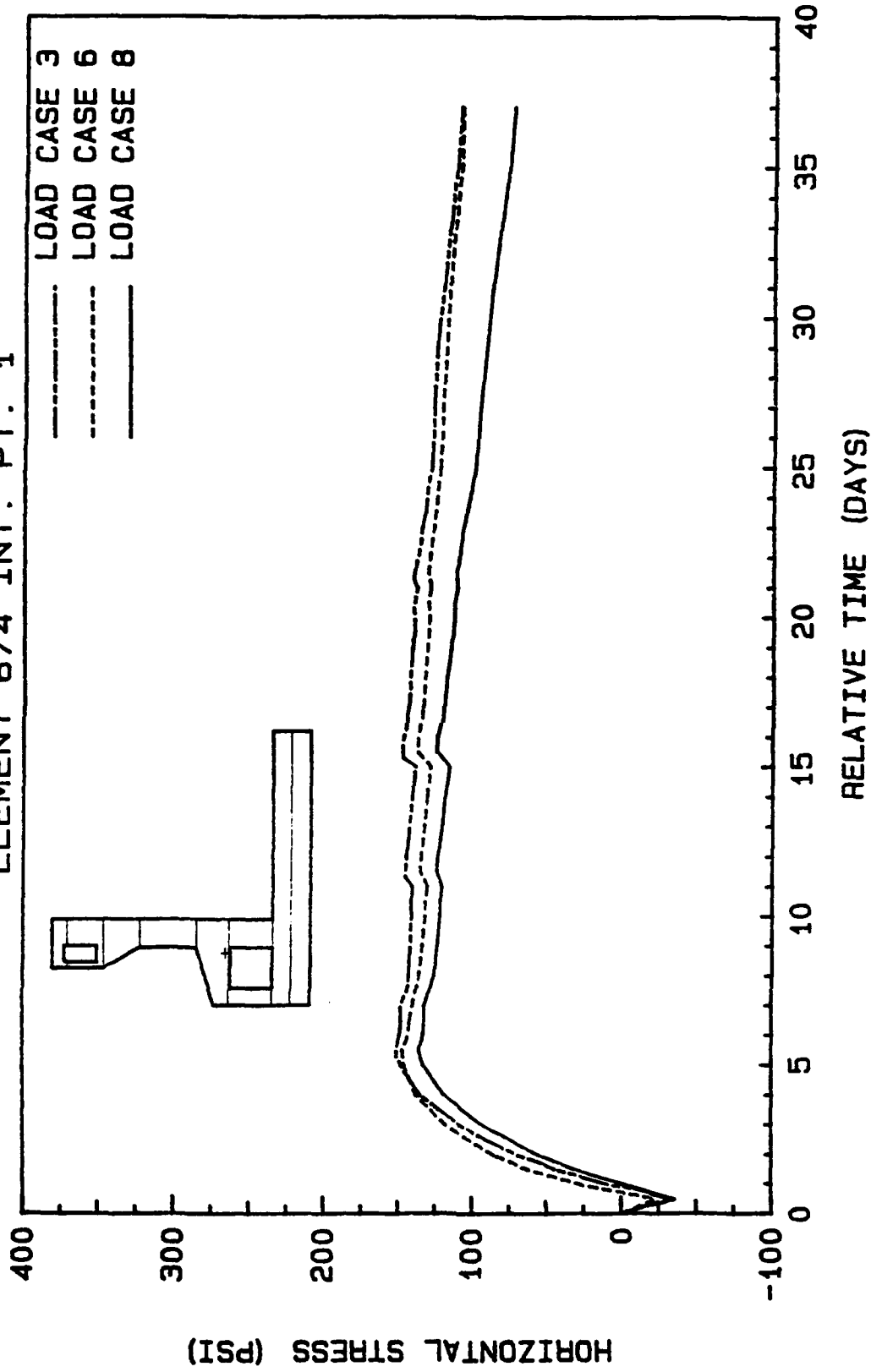


Figure 71. Stress versus time plot varying degree of creep for element 674

# ELEMENT 705 INT. PT. 3

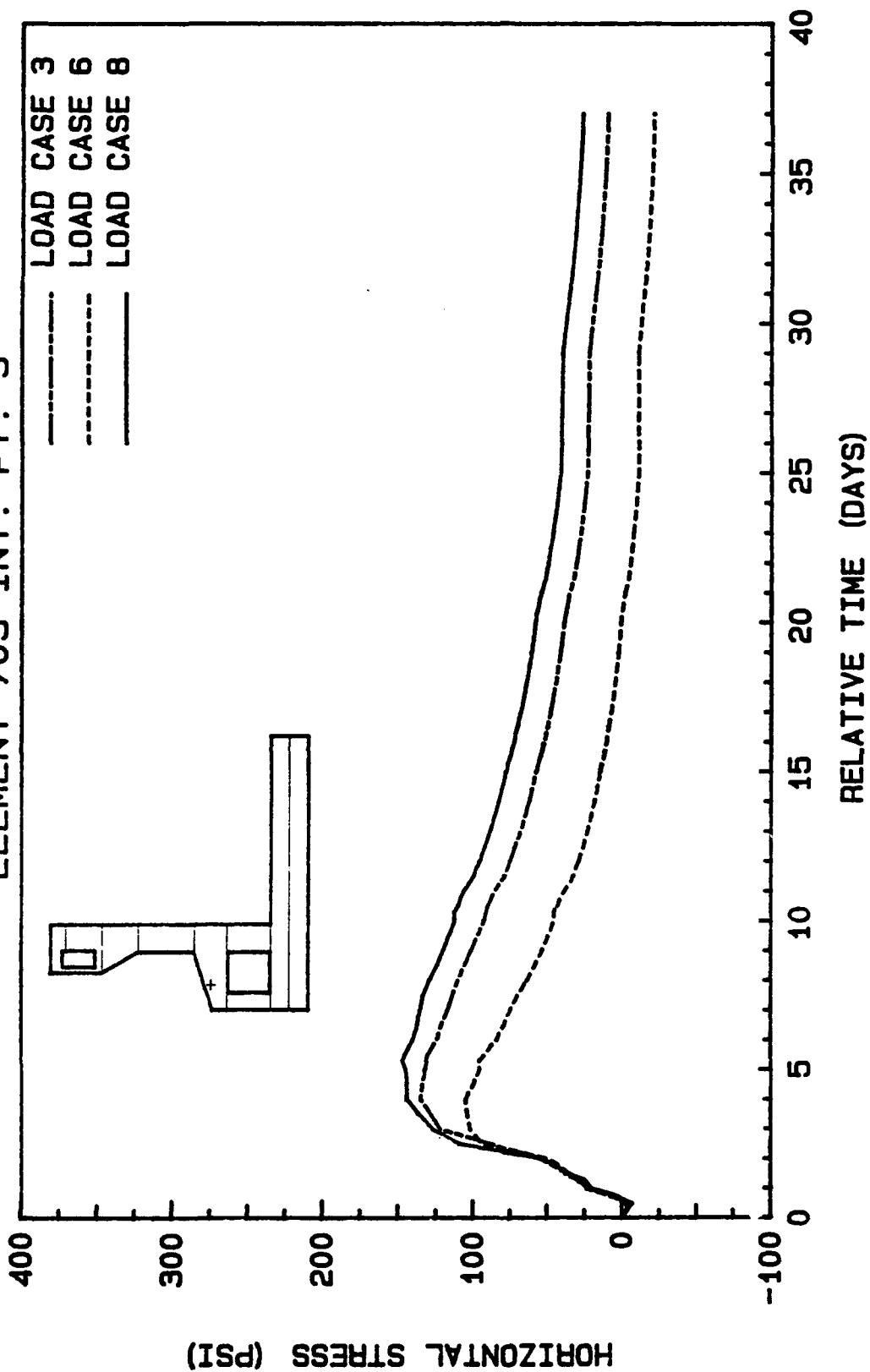


Figure 72. Stress versus time plot varying degree of creep for element 705

# ELEMENT 719 INT. PT. 3

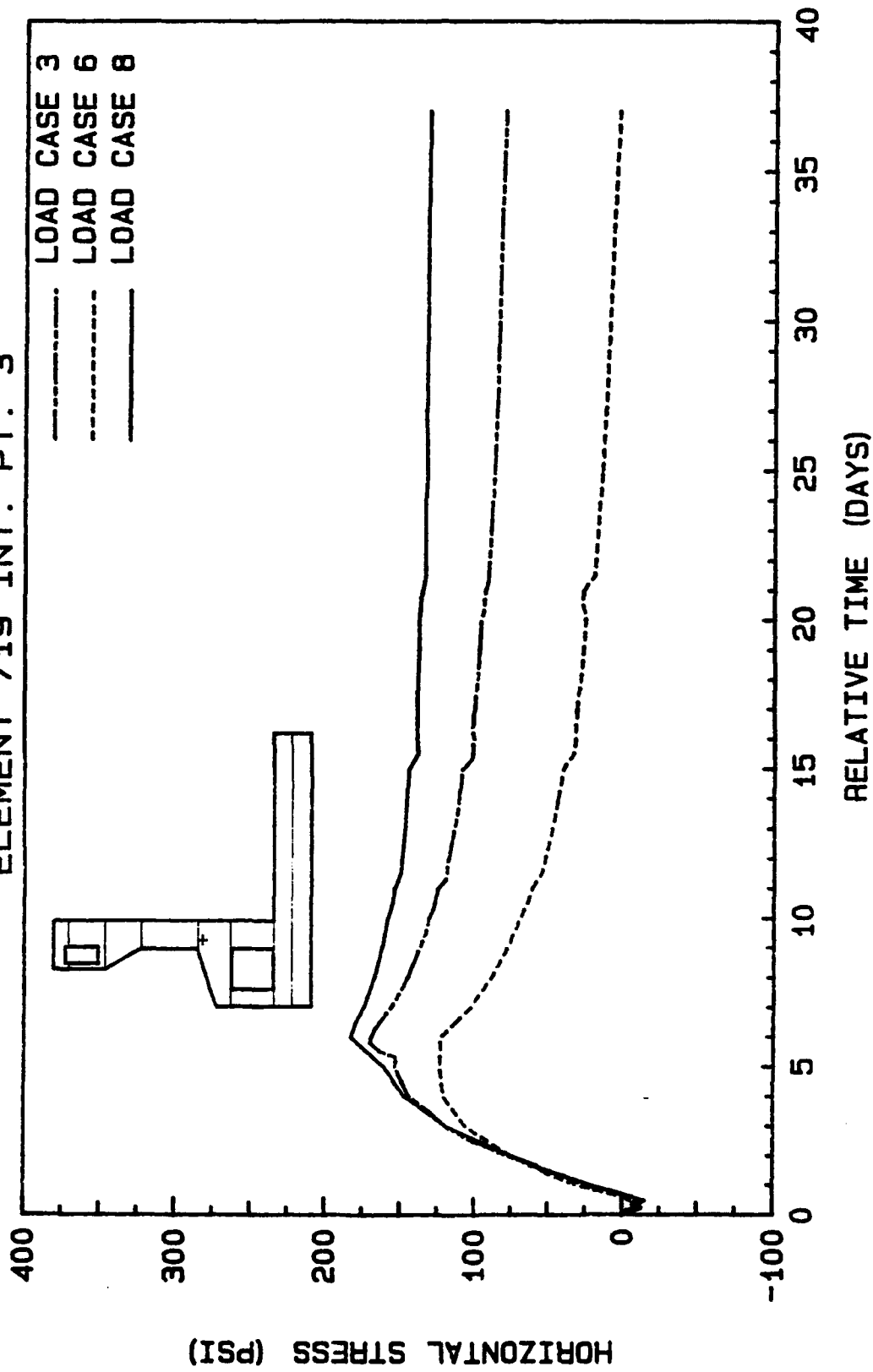


Figure 73. Stress versus time plot varying degree of creep for element 719

# ELEMENT 755 INT. PT. 4

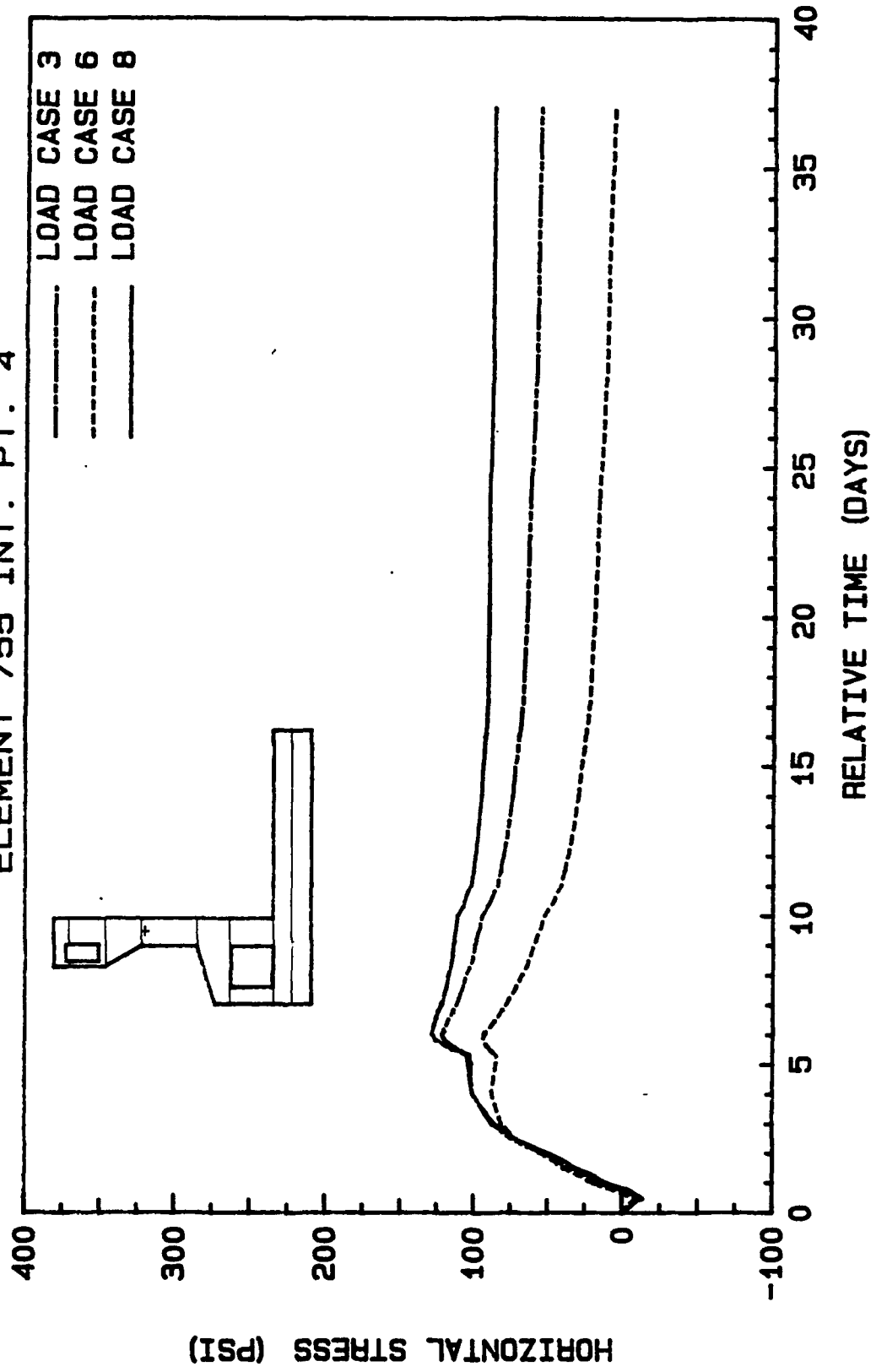


Figure 74. Stress versus time plot varying degree of creep for element 755

# ELEMENT 849 INT. PT. 2

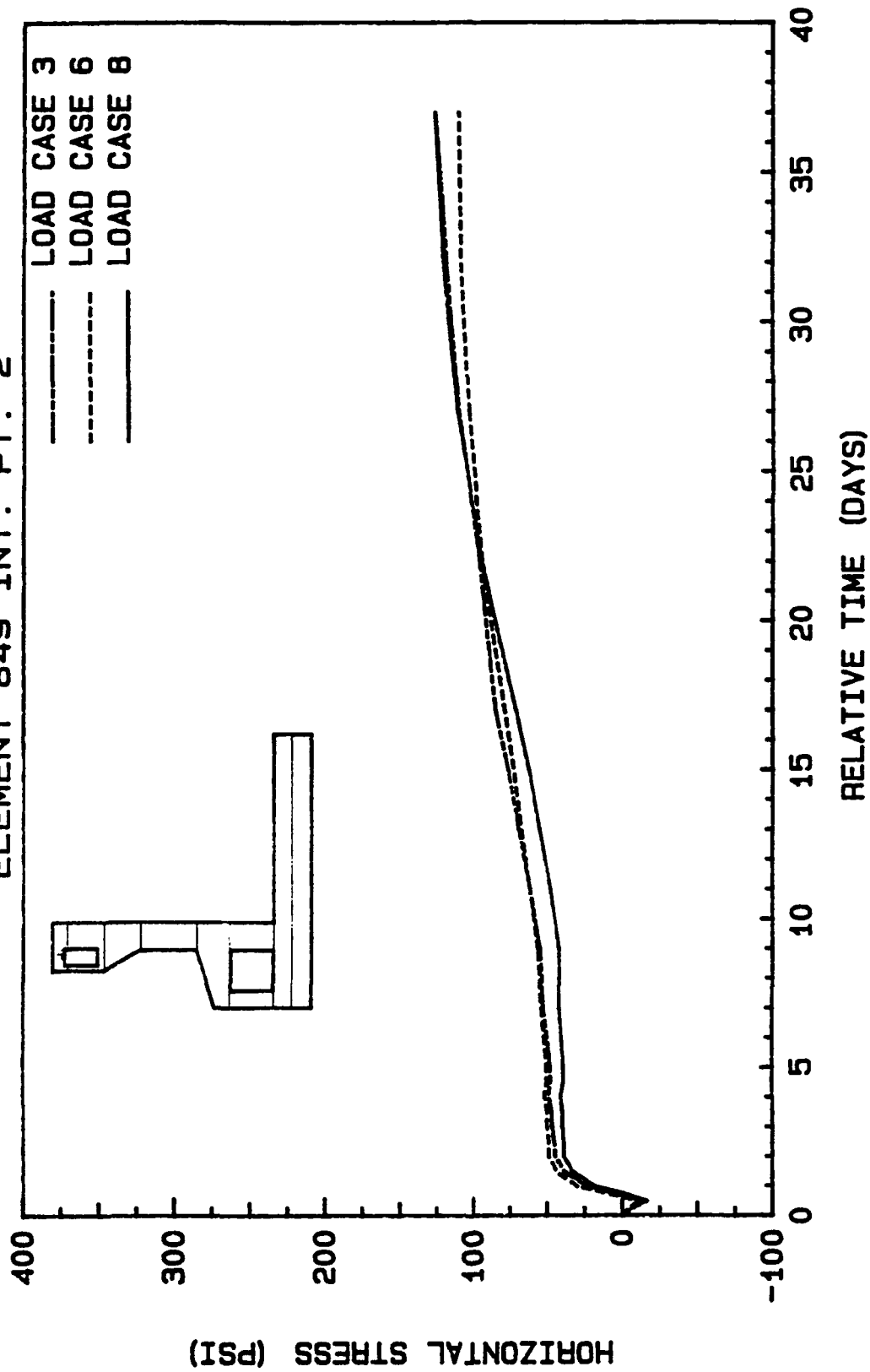


Figure 75. Stress versus time plot varying degree of creep for element 849

# ELEMENT 860 INT. PT. 3

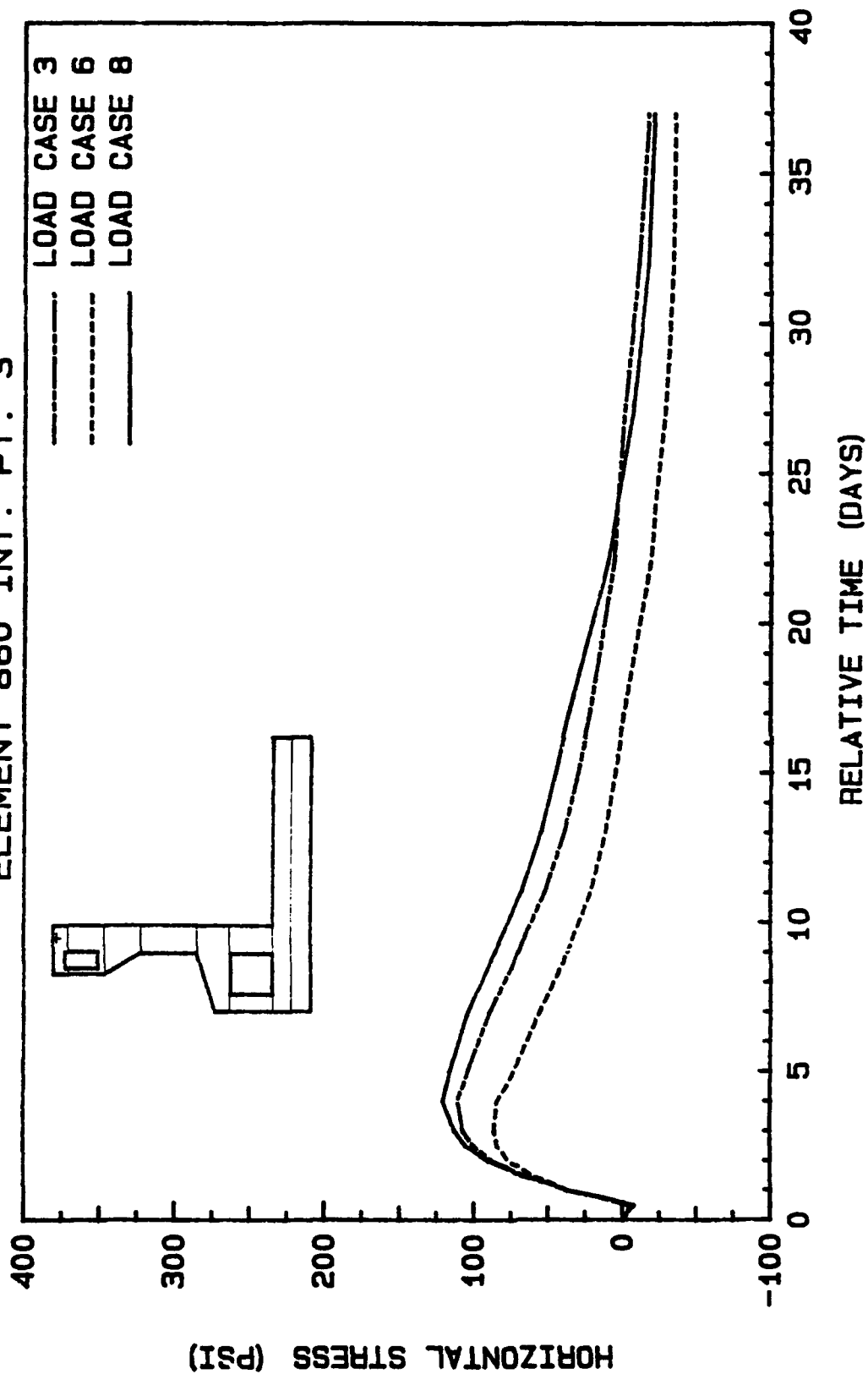


Figure 76. Stress versus time plot varying degree of creep for element 860

# ELEMENT 610 INT. PT. 3

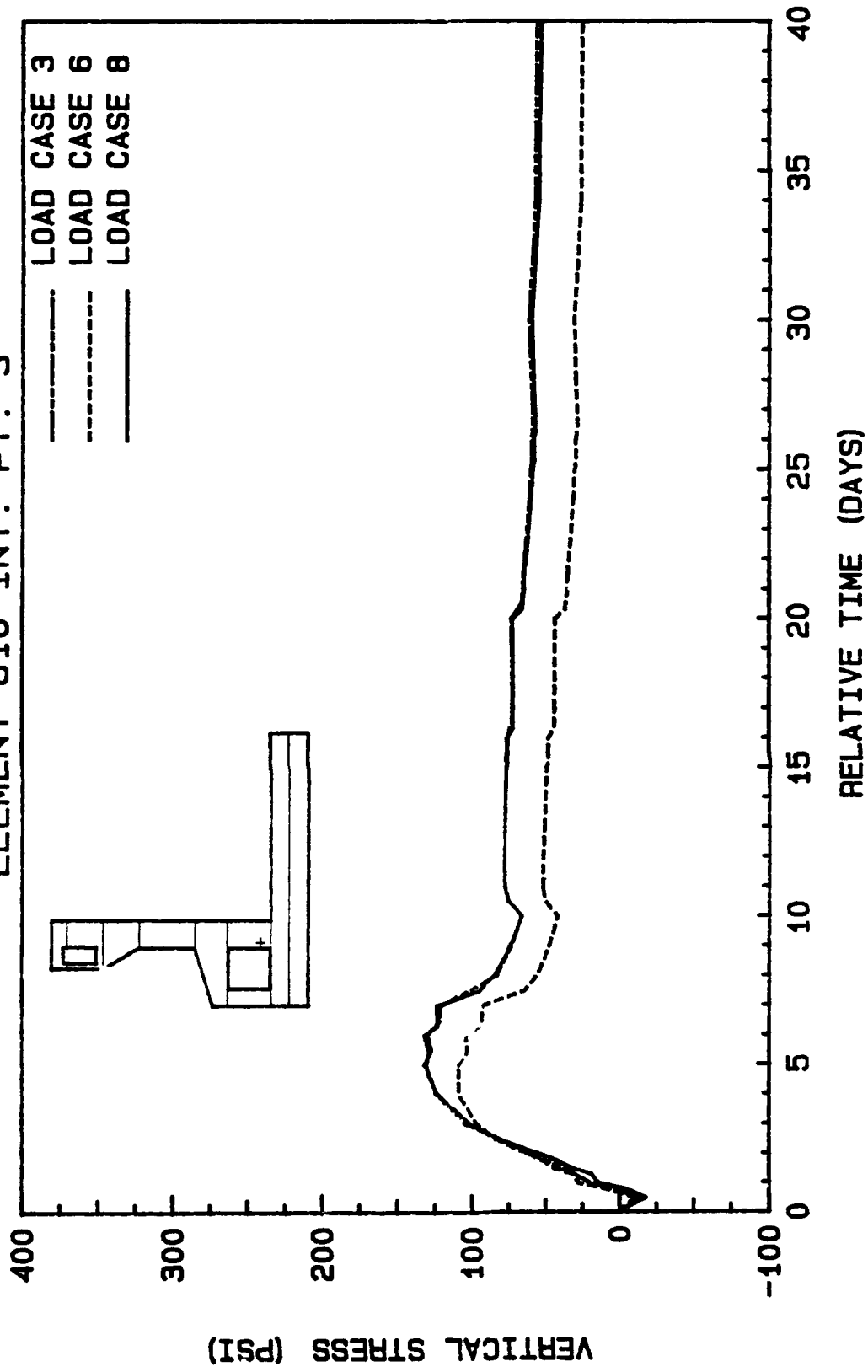


Figure 77. Stress versus time plot varying degree of creep for element 610

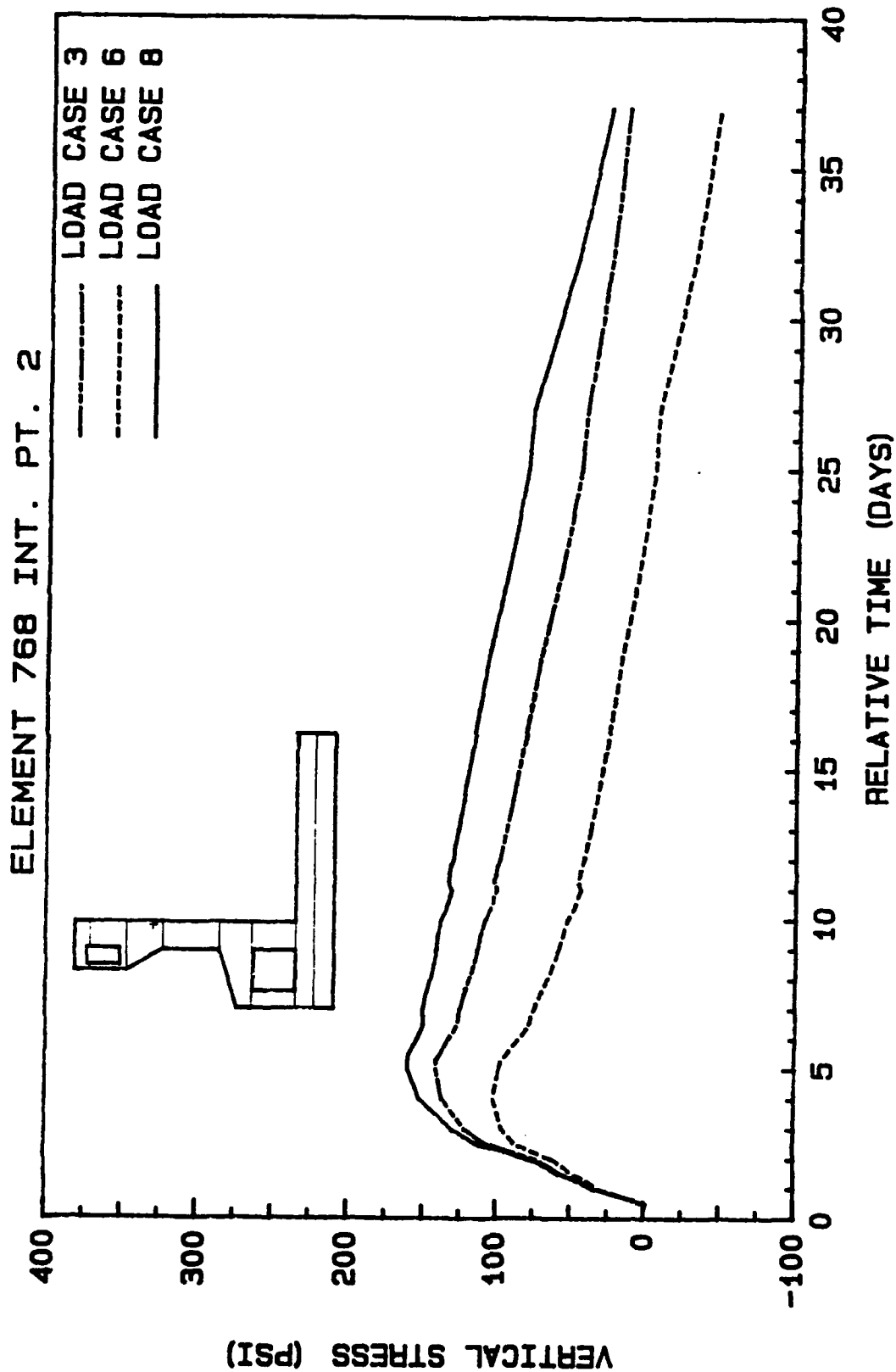


Figure 78. Stress versus time plot varying degree of creep for element 768

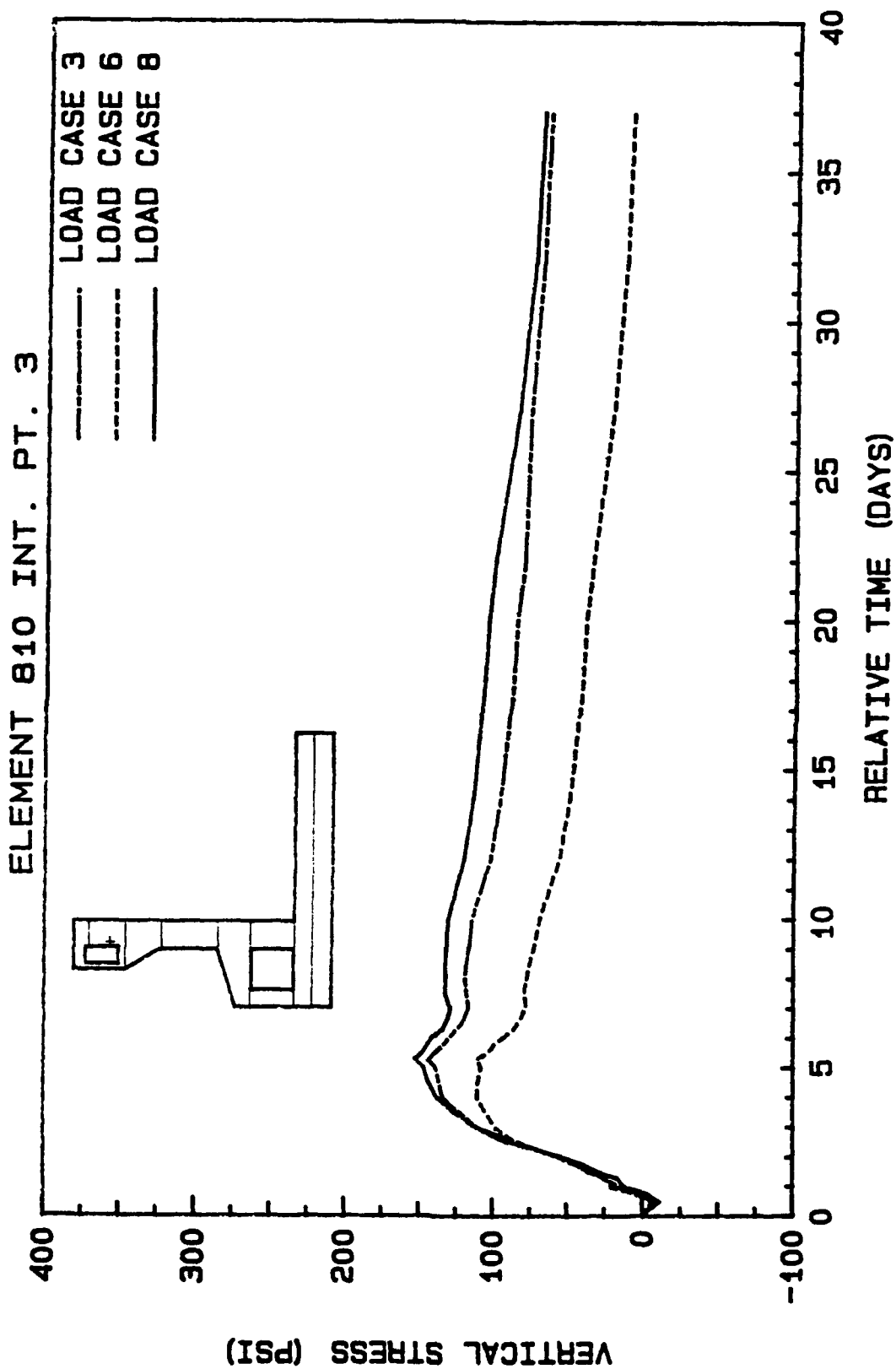


Figure 79. Stress versus time plot varying degree of creep for element 810

71. Looking at the specific creep curve in Figure 16 we can notice that creep will start to effect the stresses in the concrete within 2 days after the material is placed. From the results, it can be observed that the effect of creep is mostly obtained in the first 15 days. Thus, short-term and intermediate-term creep has the greatest effect on the tensile stresses.

72. As was the case with shrinkage, the results shown in Figure 69, 71 and 75 indicate that creep also has an effect of increasing the stresses at these locations. This is related to viscous flow causing the element to move away from the support but the support restrains it, consequently producing higher tensile stresses. After the support is removed (7 days after the lift is placed), the stress pattern for the load cases returns to the same as in the majority of the figures (i.e. load case 8, no creep, produces the highest stresses, followed by load case 3, lower bound creep and finally load case 6, upper bound creep) (Figure 75).

#### Combined Effect of Creep and Shrinkage

73. The results for the four load cases with creep and shrinkage varied among the upper and lower bound parameters and for the load case with creep and shrinkage neglected are shown in Figure 80-93. The results show that load cases 3 and 5 and load cases 4 and 6 are narrowly banded. This indicates that creep has a more pronounced effect on the tensile stresses when the given shrinkage function is used.

74. The results also show that neglecting creep and shrinkage will give conservative results for most of the locations investigated. In addition, elements 561, 719, and 755 show the stresses still increasing after 30 days when creep and shrinkage effects are neglected; whereas, if shrinkage and creep is included, the stresses are fairly stable by this time. Looking back to the previous figures, this is not noticeable. Thus, the increases with time appear to be related to both shrinkage and creep being neglected. However, shrinkage is more of the cause since, as discussed previously, the creep function used does not have much of a long-term effect; whereas, from the shrinkage plot in Figure 15, the shrinkage strains are still increasing after 40 days. Thus, including shrinkage will produce stress relaxation but without shrinkage, a tensile stress increase occurs due to the increasing Young's modulus and thermal cooling which causes the element to shrink.

# ELEMENT 377 INT. PT. 1

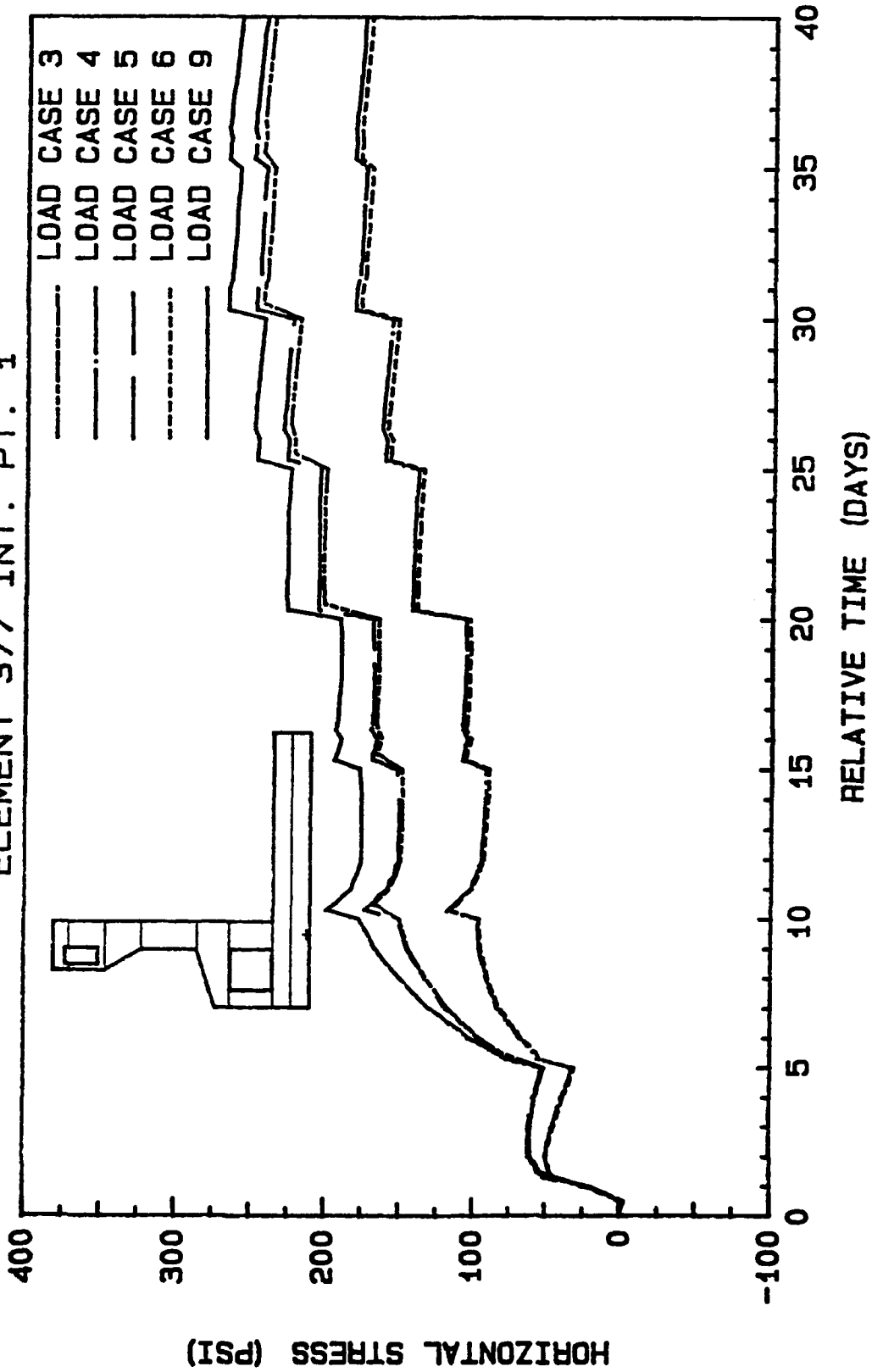


Figure 80. Stress versus time plot for load cases 3-6 and 9 for element 377

# ELEMENT 556 INT. PT. 4

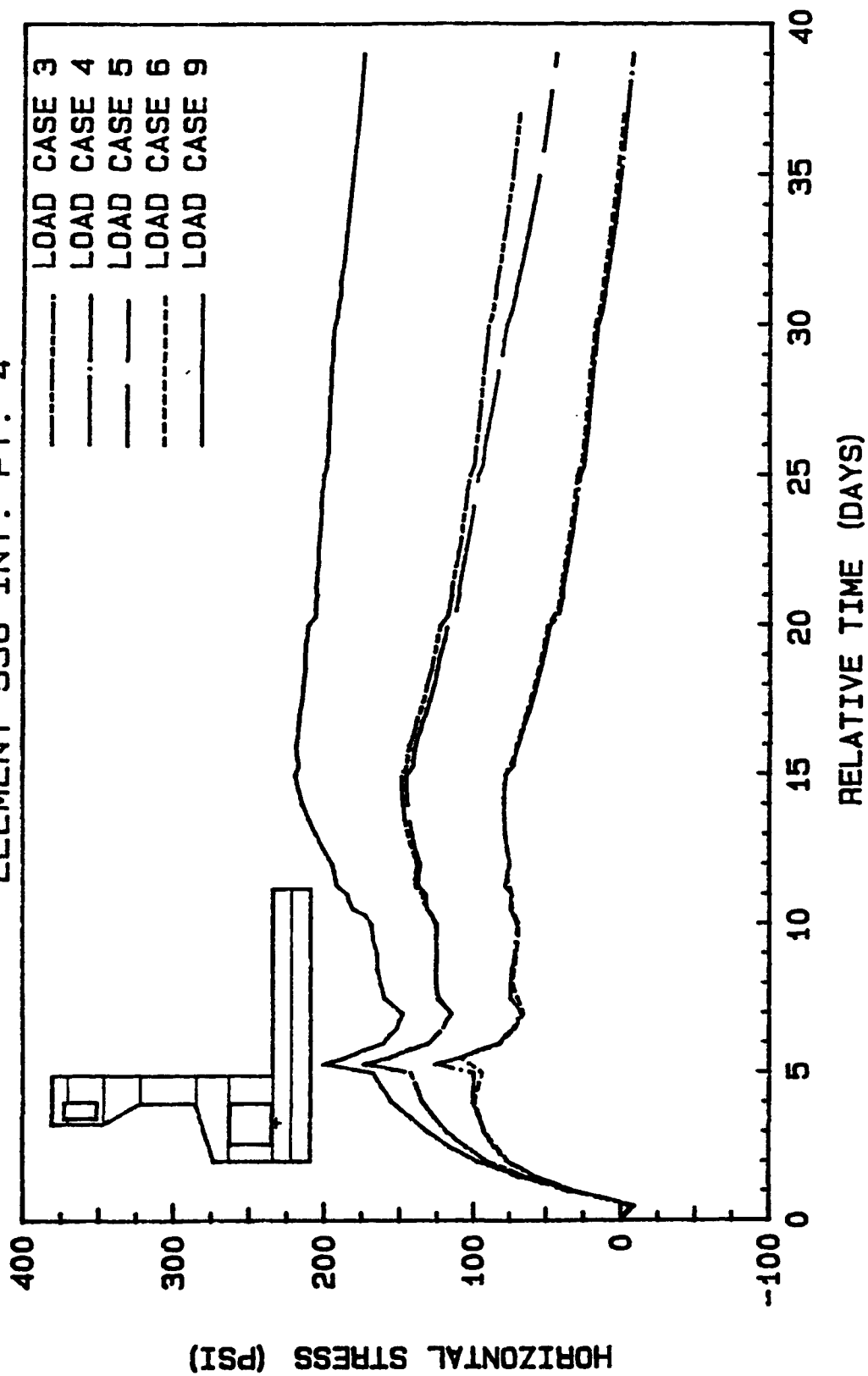


Figure 81. Stress versus time plot for loadcases 3-6 and 9 for element 556

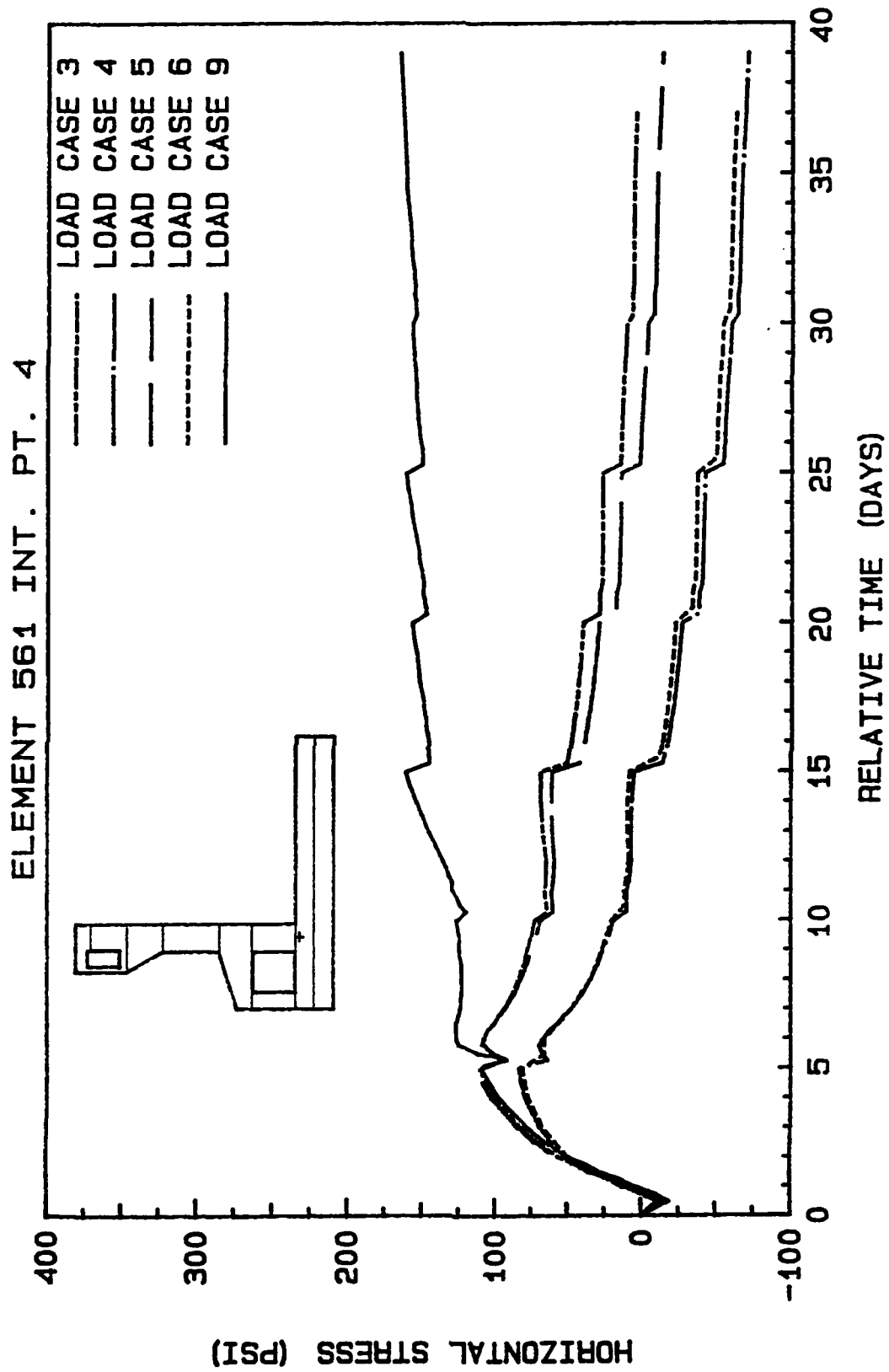


Figure 82. Stress versus time plot for loadcases 3-6 and 9 for element 561

# ELEMENT 587 INT. PT. 4

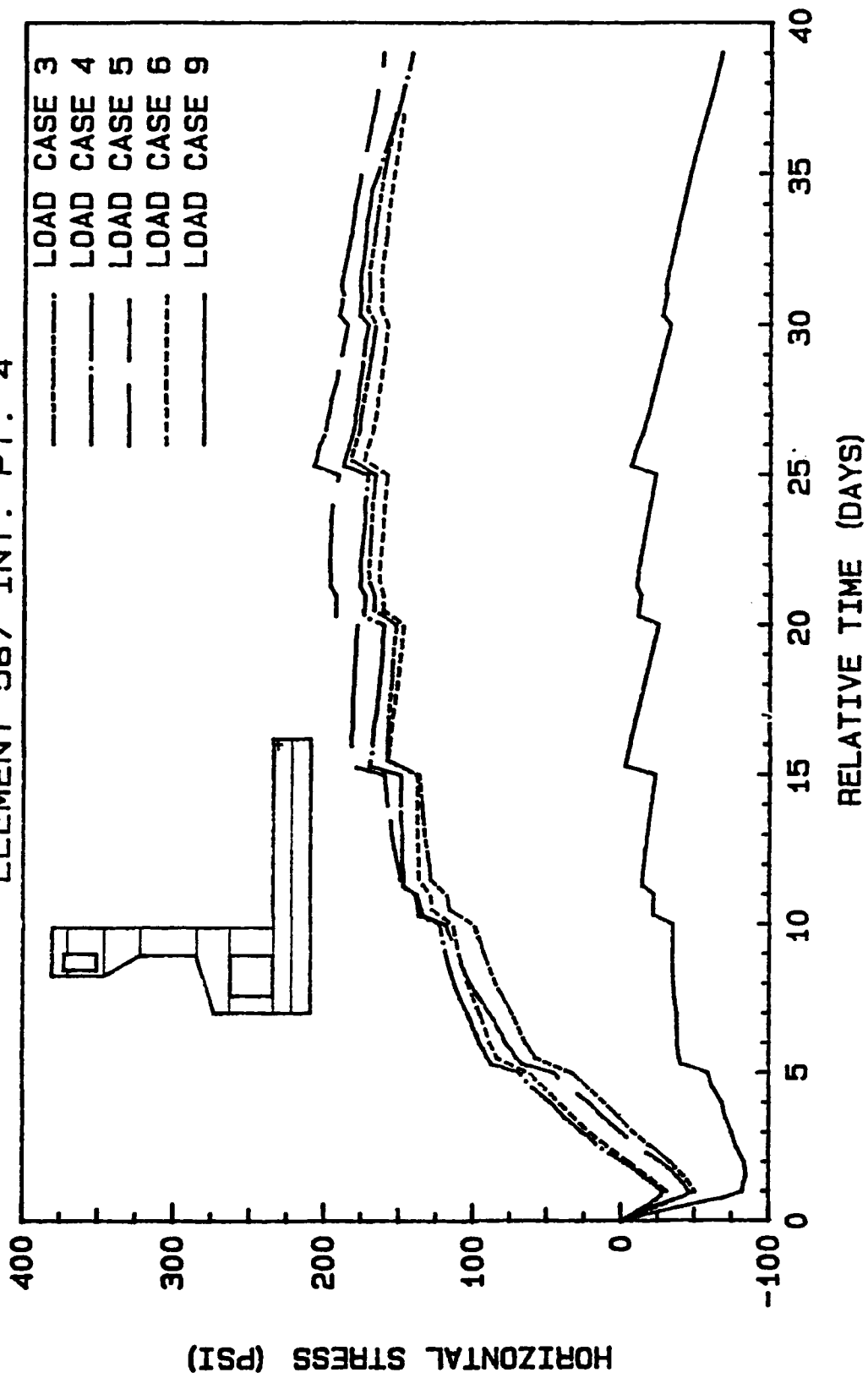


Figure 83. Stress versus time plot for loadcases 3-6 and 9 for element 587

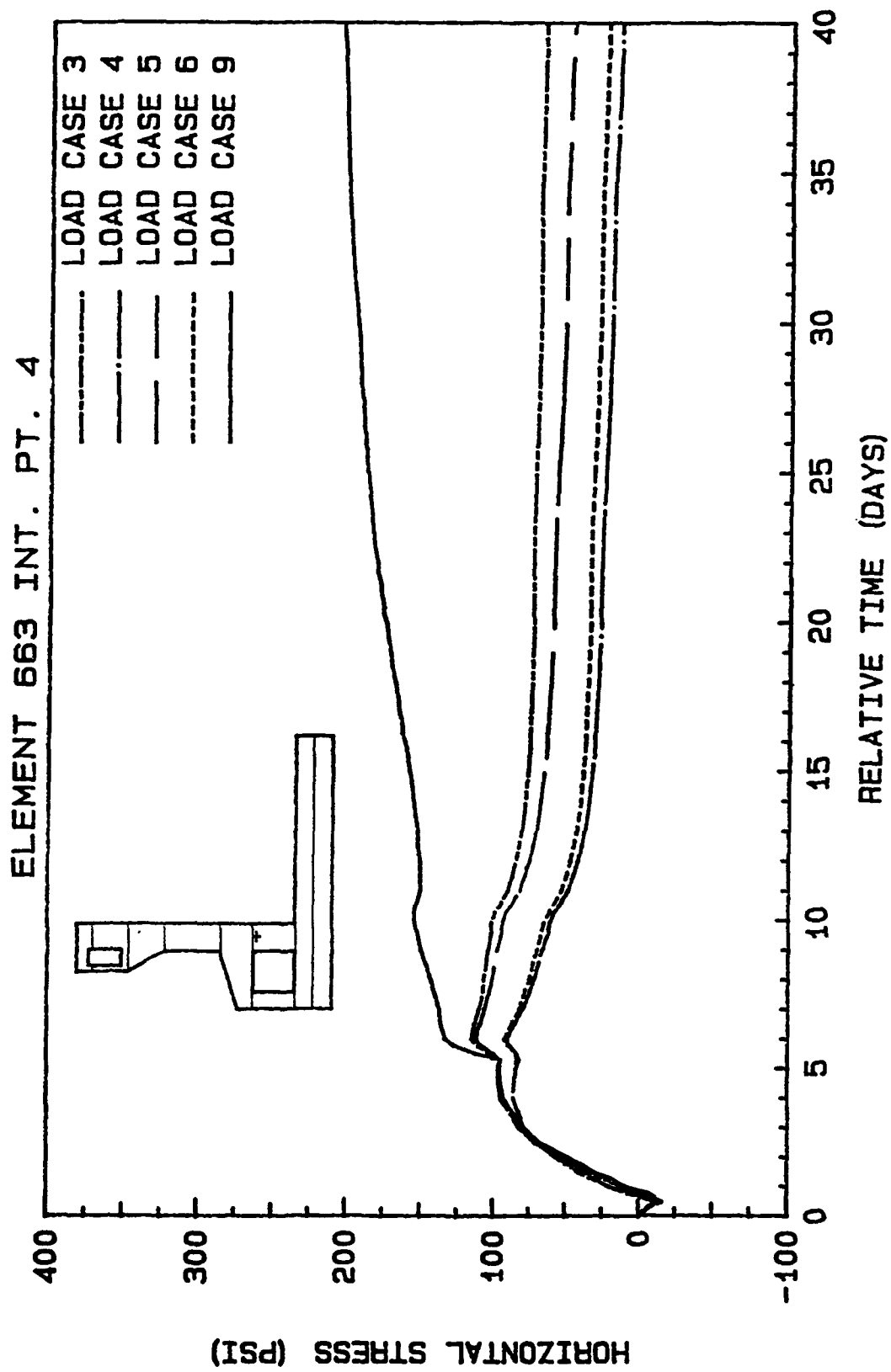


Figure 84. Stress versus time plot for loadcases 3-6 and 9 for element 663

# ELEMENT 674 INT. PT. 1

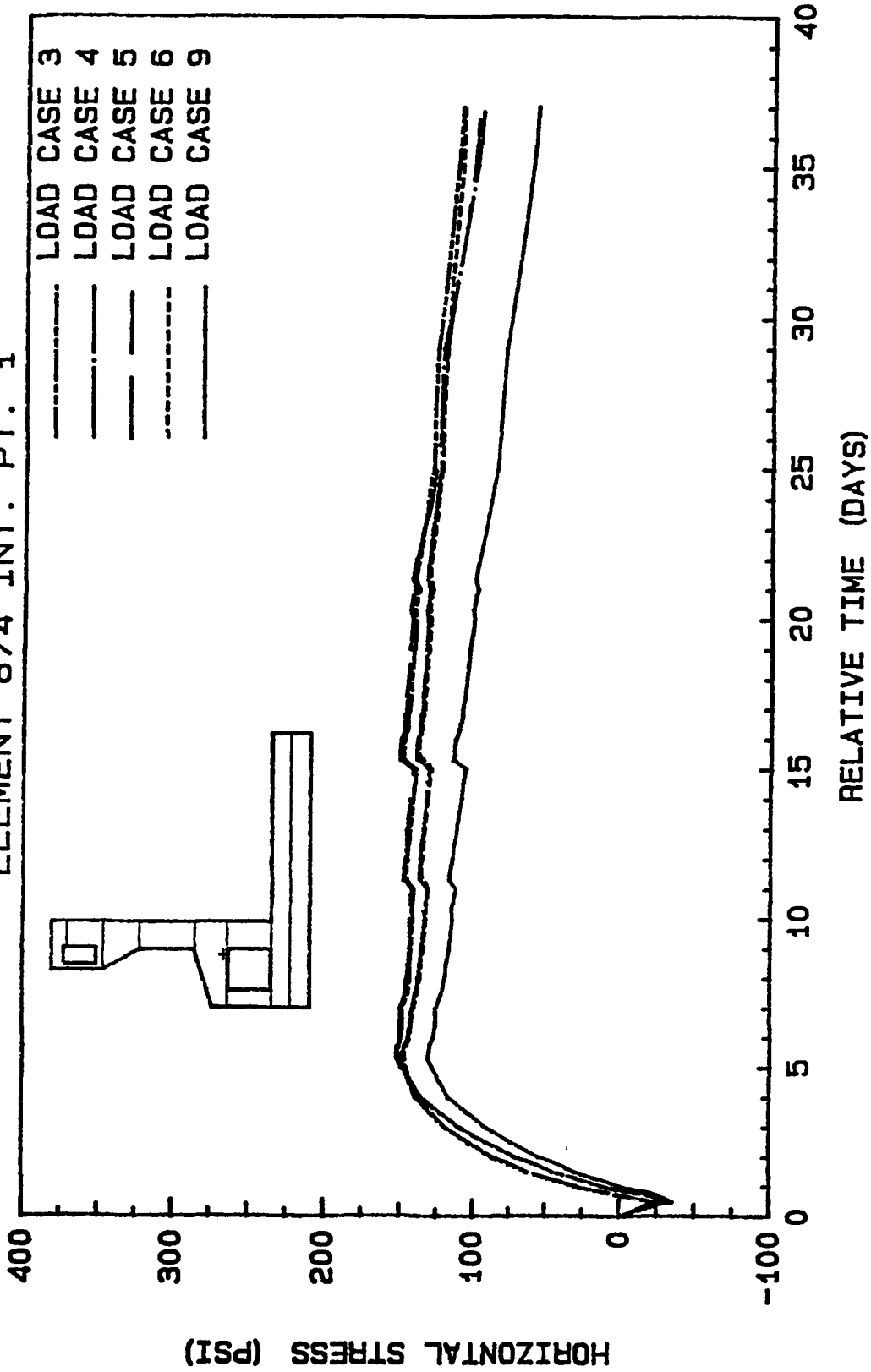


Figure 85. Stress versus time plot for loadcases 3-6 and 9 for element 674

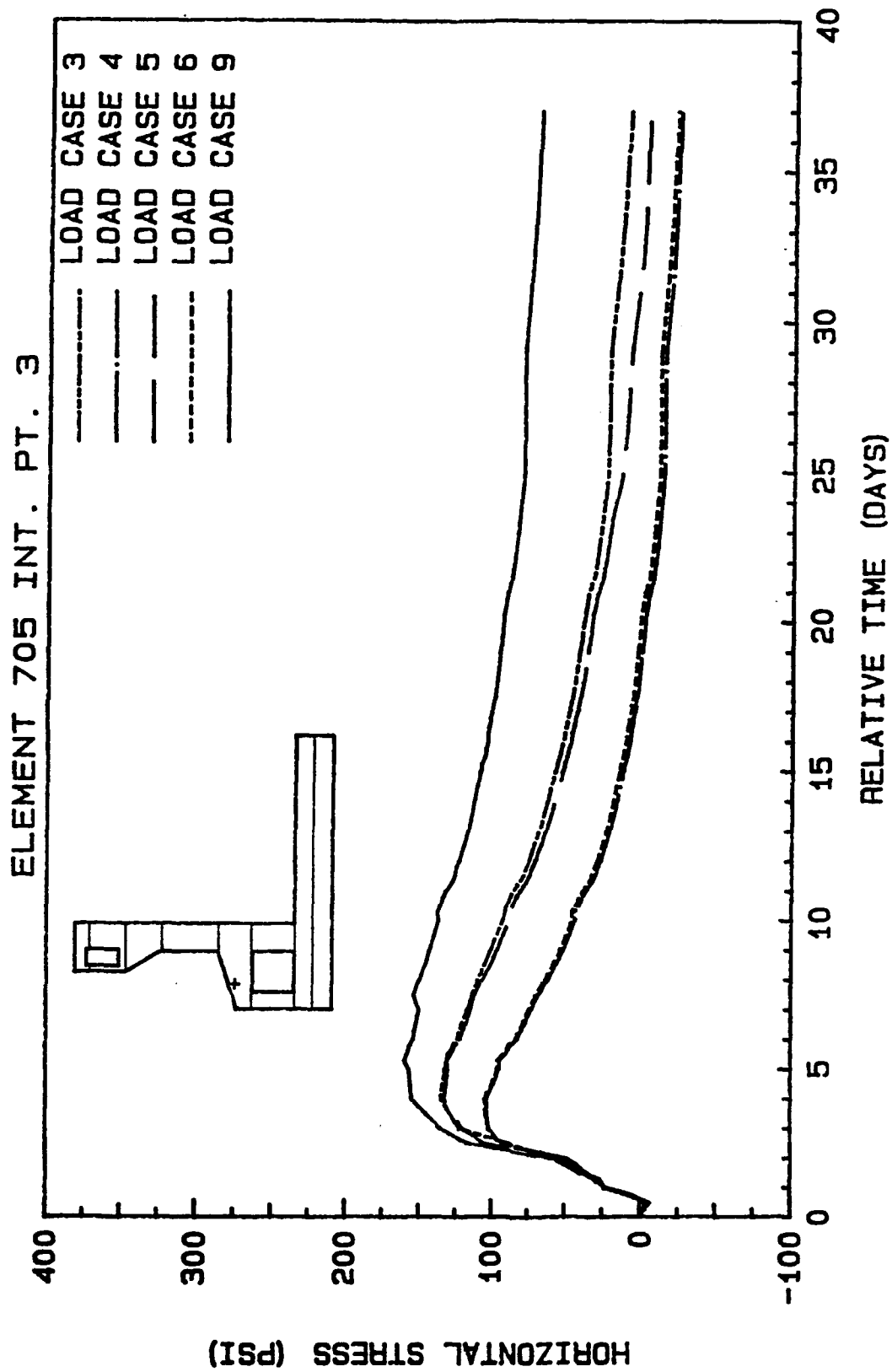


Figure 86. Stress versus time plot for load cases 3-6 and 9 for element 705

# ELEMENT 719 INT. PT. 3

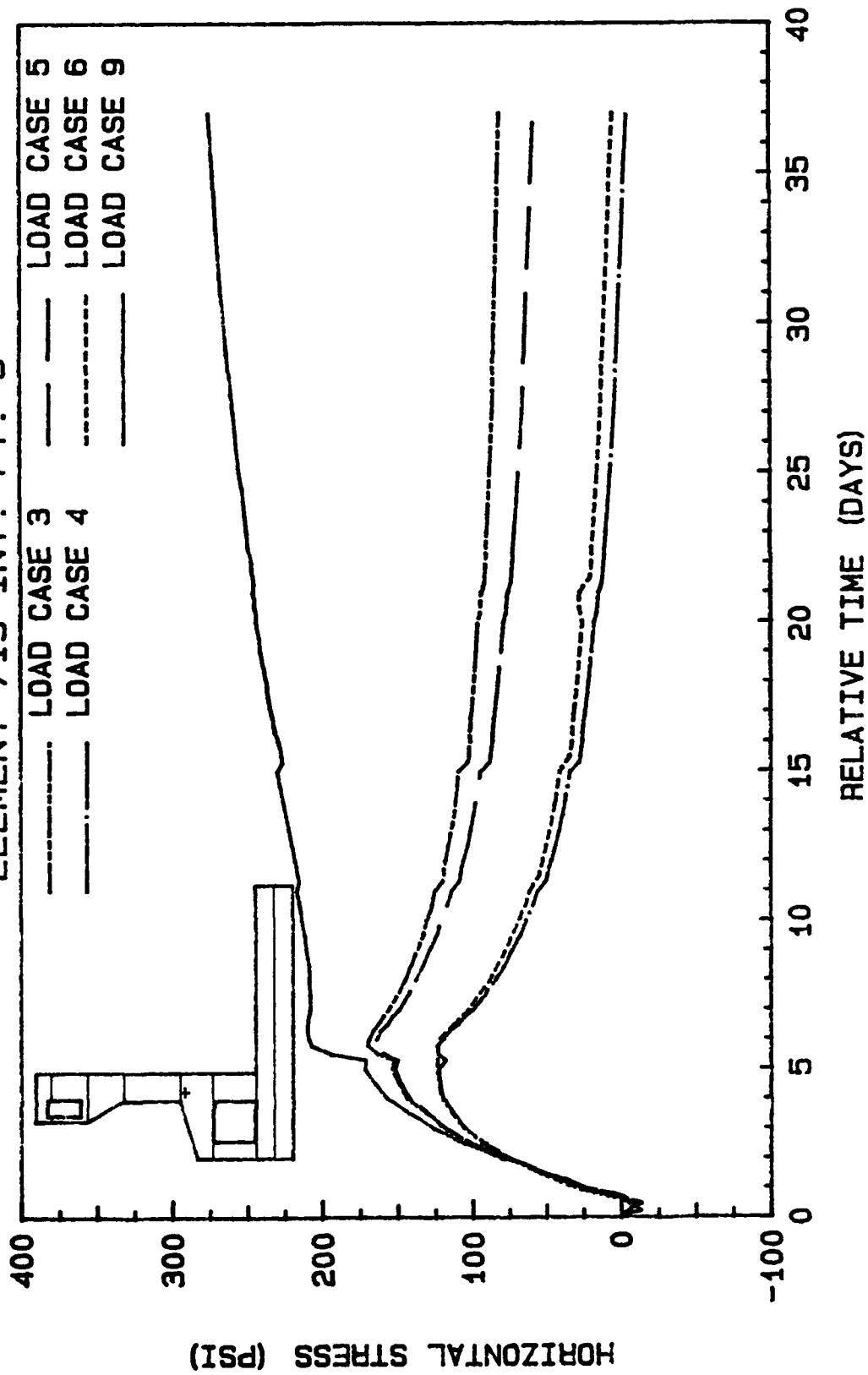


Figure 87. Stress versus time plot for load cases 3-6 and 9 for element 719

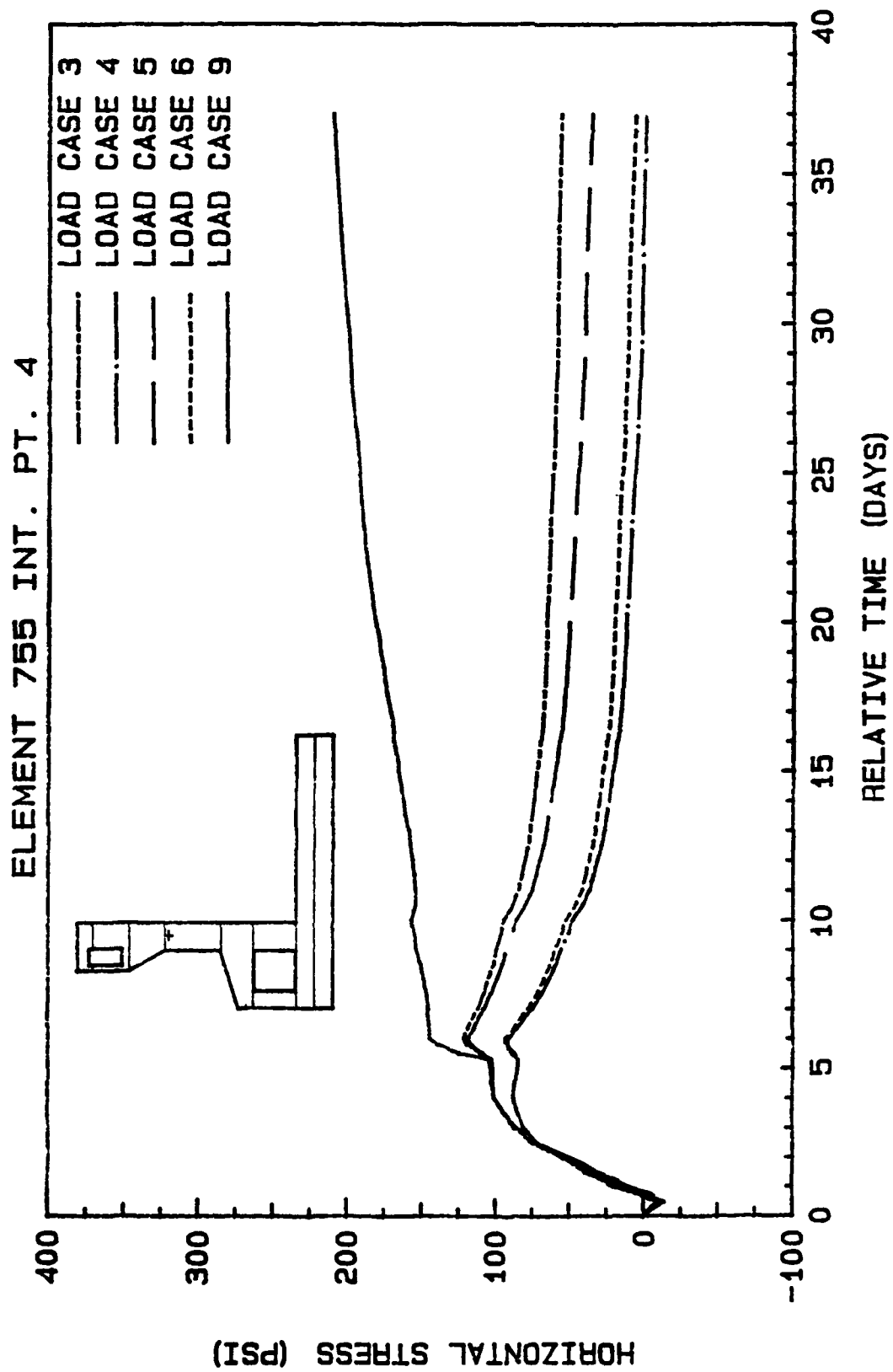


Figure 88. Stress versus time plot for load cases 3-6 and 9 for element 755

# ELEMENT 849 INT. PT. 2

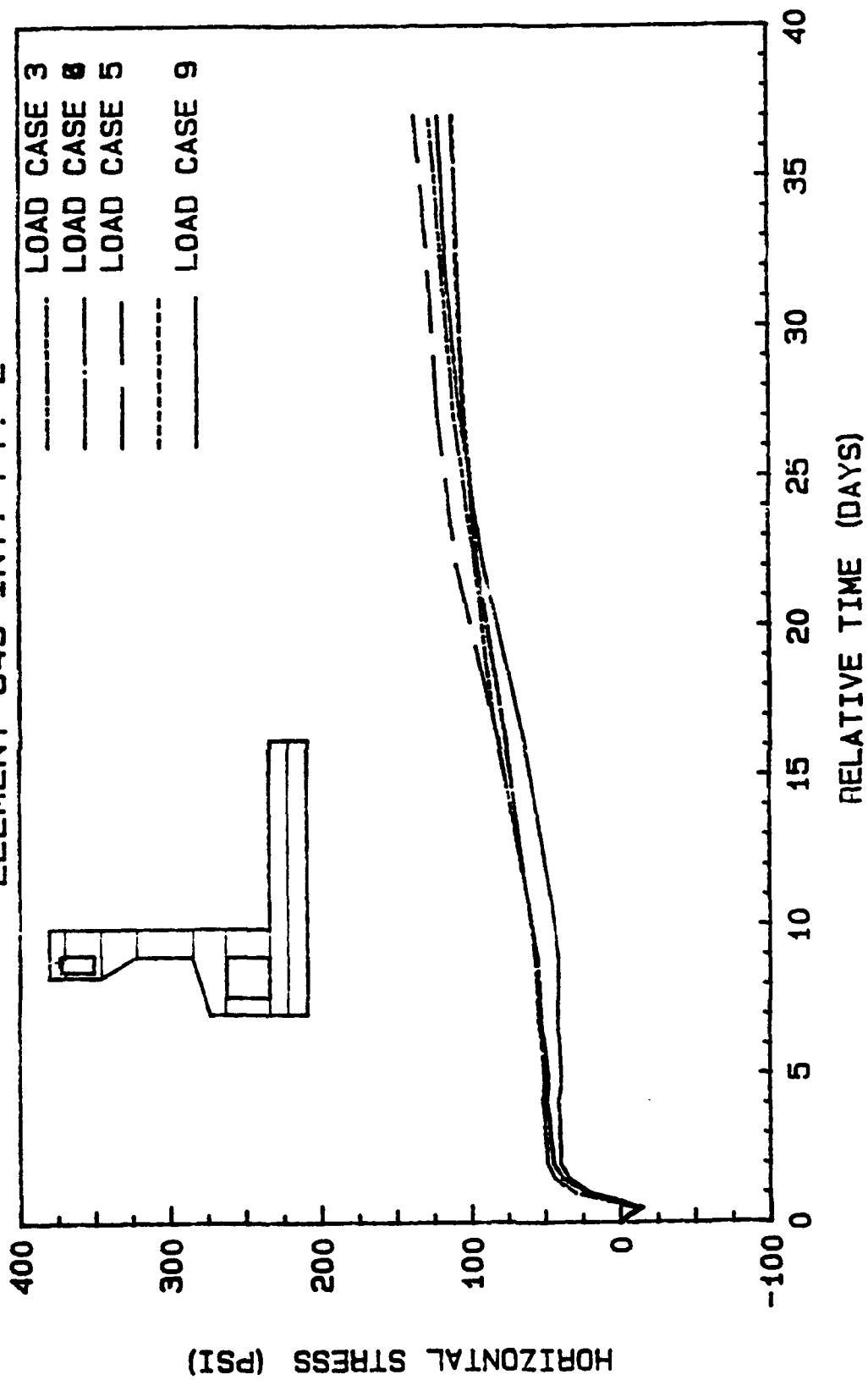


Figure 89. Stress versus time plot for load cases 3-6 and 9 for element 849

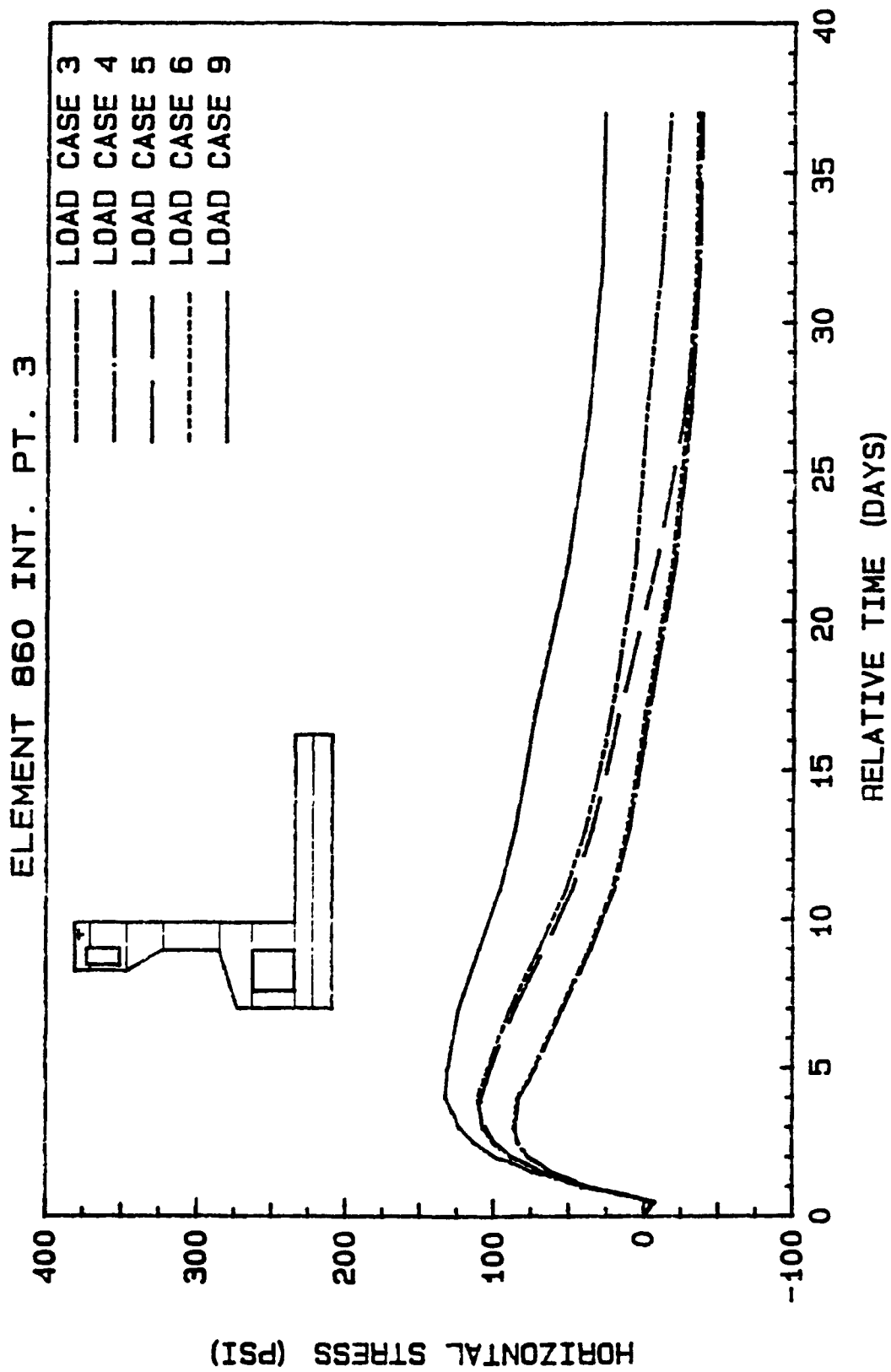


Figure 90. Stress versus time plot for load cases 3-6 and 9 for element 860

# ELEMENT 610 INT. PT. 3

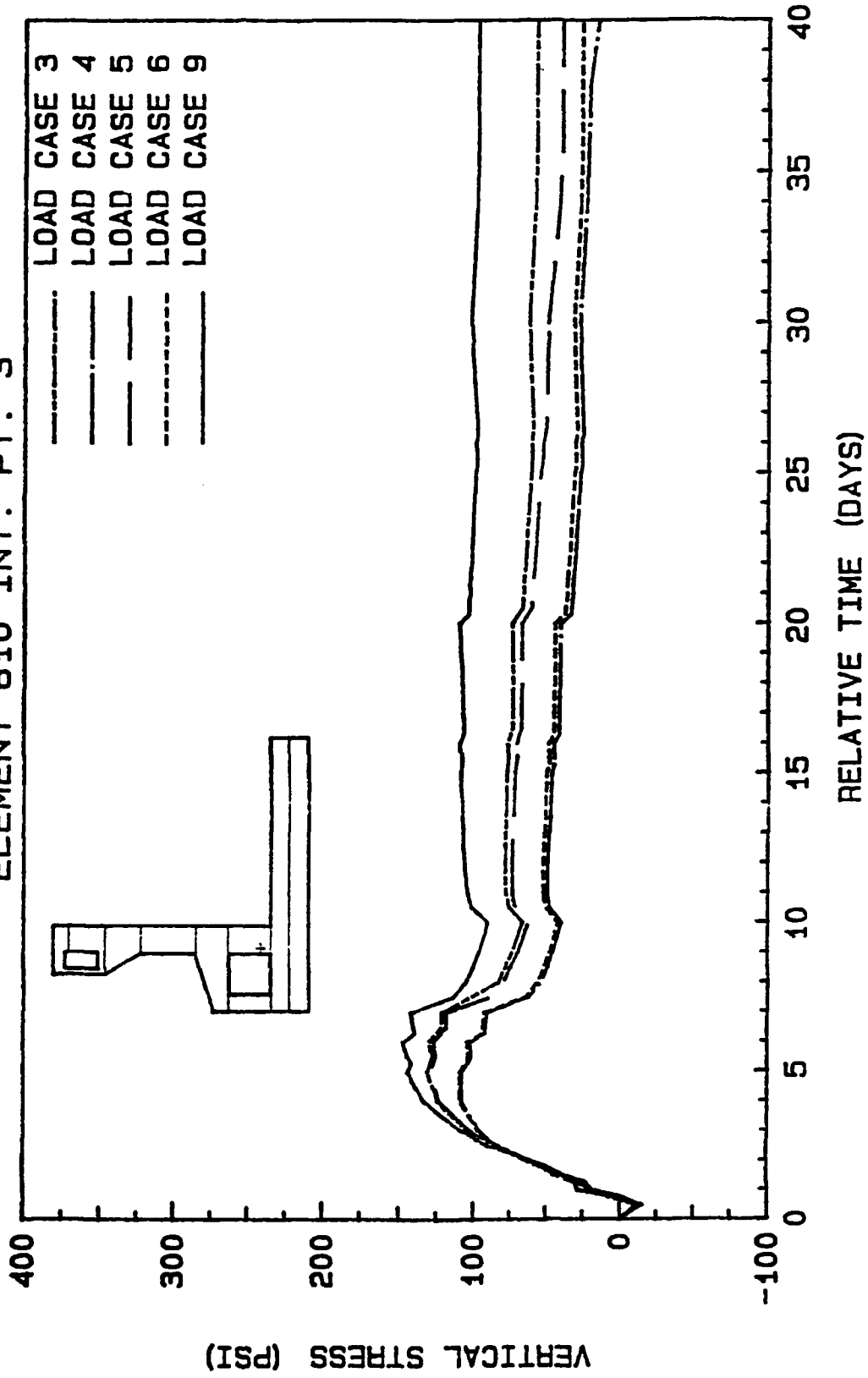


Figure 91. Stress versus time plot for load cases 3-6 and 9 for element 610

# ELEMENT 768 INT. PT. 2

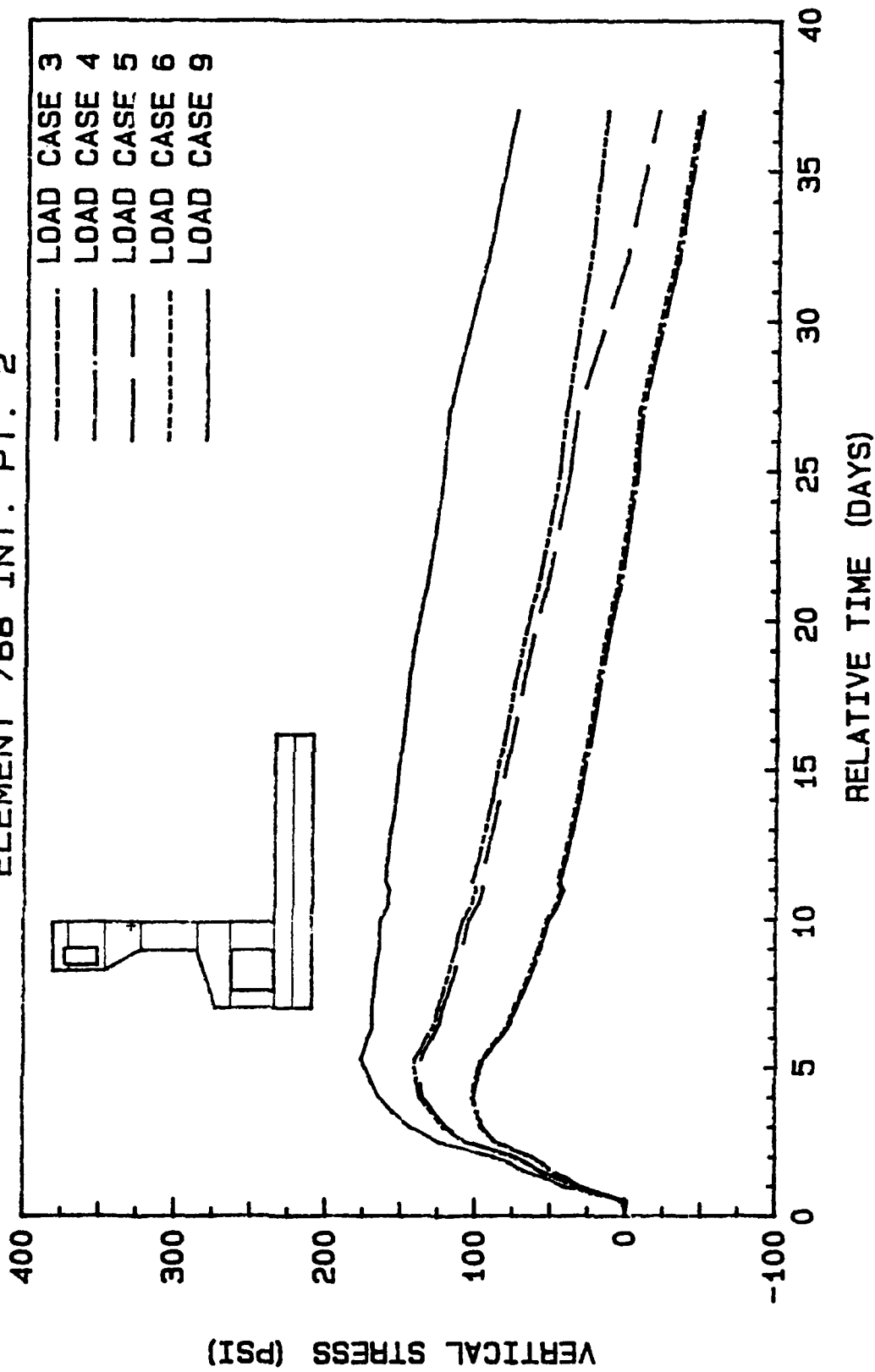


Figure 92. Stress versus time plot for loadcases 3-6 and 9 for element 768

# ELEMENT 810 INT. PT. 3

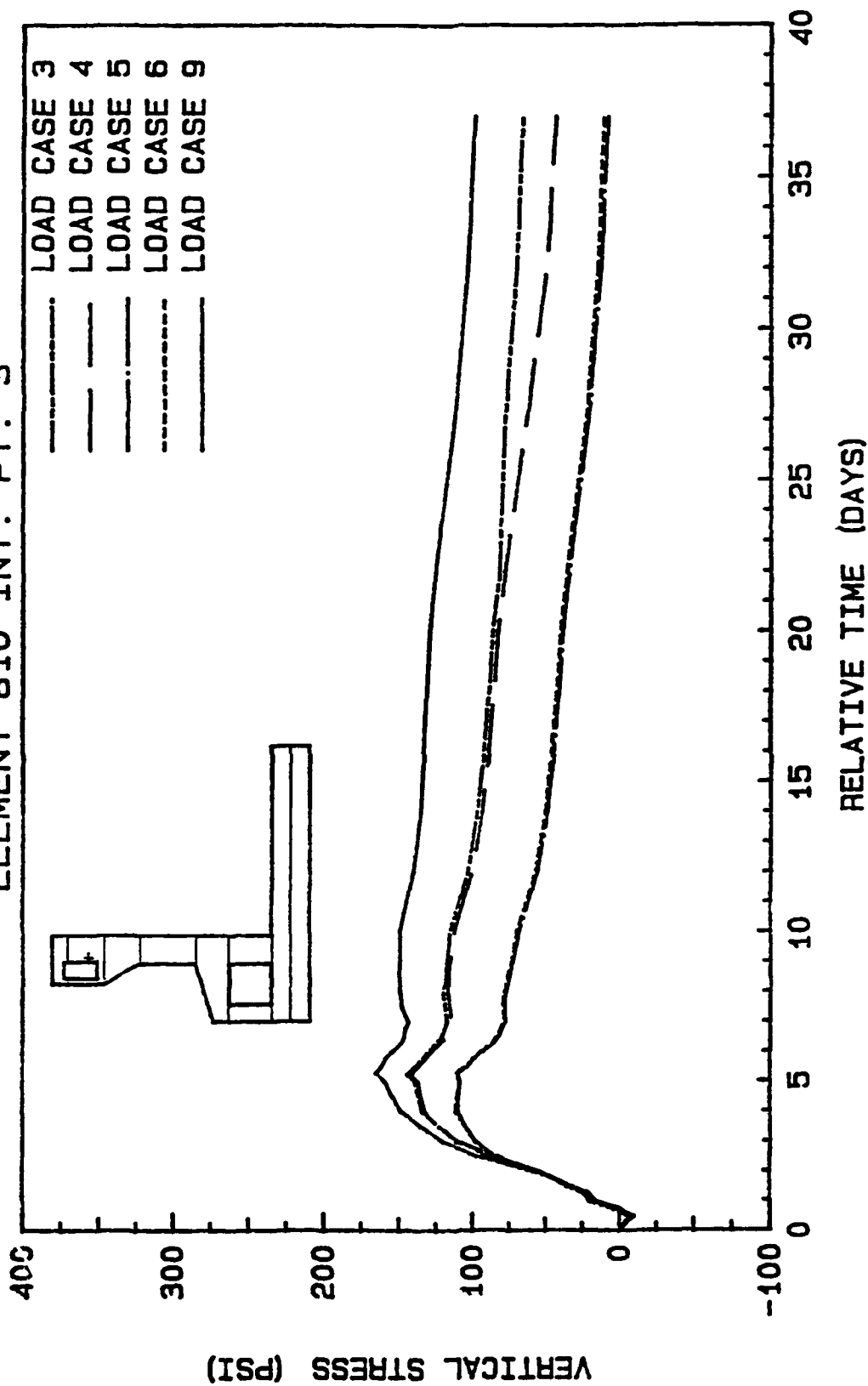


Figure 93. Stress versus time plot for load cases 3-6 and 9 for element 810

### Effect of Creep and Shrinkage on Strains

75. As discussed earlier, looking at stresses alone would not be sufficient in assessing the significance of the response on the structure when performing a parametric thermal analysis of mass concrete. Also, since the cracking criterion used is both stress and strain driven (see Appendix A), the strains as a function of time will also be presented for load case 3 through 6.

76. Figures 94-107 show the strains plotted against time at the same locations as previously examined. A common pattern exists among all of the plots. Initially, after the lift is placed, the strains are positive since the heat added causes the element to expand. At approximately 2 days, the strain starts to decrease due to shrinkage and subsequent cooling. In most cases, the strains become negative since shrinkage and thermal cooling cause the structure to "shrink." For the elements that become embedded under a new lift, (Figures 96, 98, 101 and 102) at 5 days, the strains increase again due to more heat being added to the element.

77. For these realistic load cases, the strains never exceeded 100 micro-strains, a value commonly used by the Corps for predicting when cracking need be considered. However, for element 768, integration point 2, the strains for load case 3 did reach 93.7 micro-strains at 2 days after the lift was placed.

78. A similar pattern is again evident for which load cases produce higher strains consistently. Load case 3 generally produces higher strains from the time period examined. A similar banding also occurs for the strains except, now, load cases 3 and 6 are narrowly banded as are load cases 4 and 5. This type of banding should occur since creep is stress dependent (see Equation 5-3); whereas, shrinkage is strain dependent. Consequently, from a theoretical stand-point, there should not be a difference between load cases 3 and 6 where shrinkage is constant and creep is varied and similarly for load cases 4 and 5. In Figures 99 and 100, this is what does occur.

79. Based on the previous results, load case 3 was selected for further investigation. First, all the locations where the horizontal and vertical stresses exceeded a specified value were found for each time increment. In addition, since load case 3 consistently produced higher tensile stresses, it

# ELEMENT. 377 INT. PT. 1

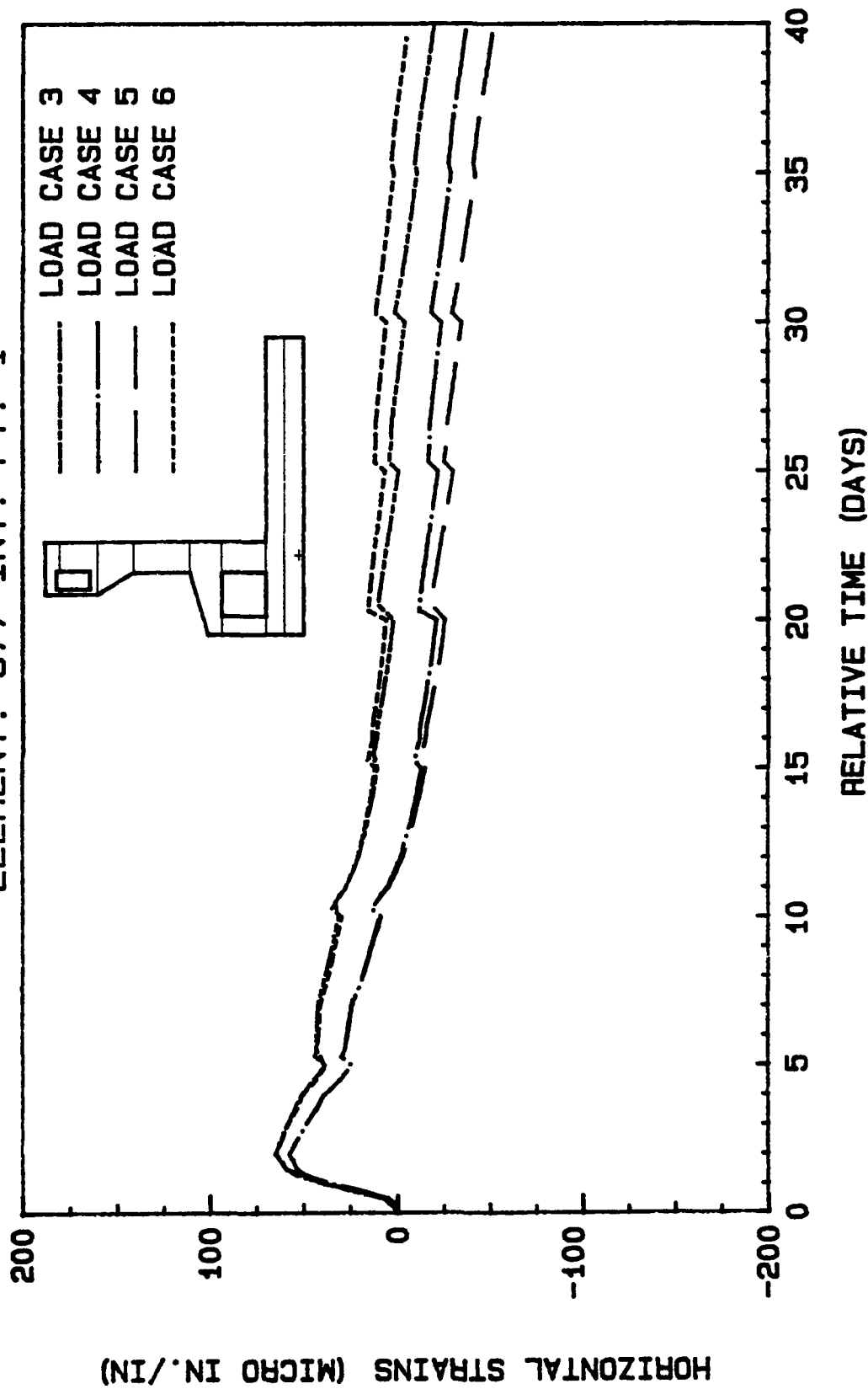


Figure 94. Strain versus time for load cases 3-6 for element 377

# ELEMENT. 556 INT. PT. 4

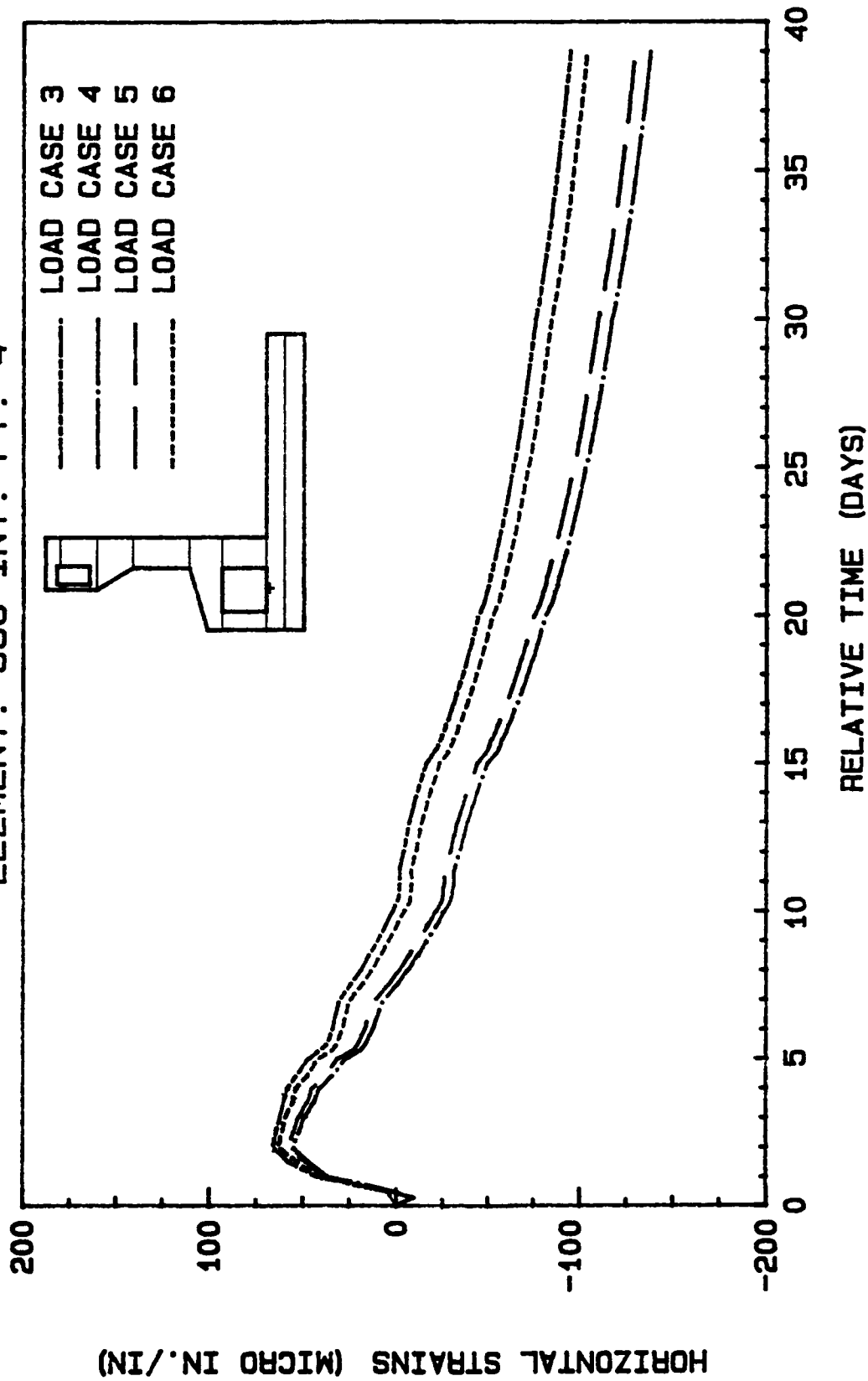


Figure 95. Strain versus time for load cases 3-6 for element 556

# ELEMENT. 561 INT. PT. 4

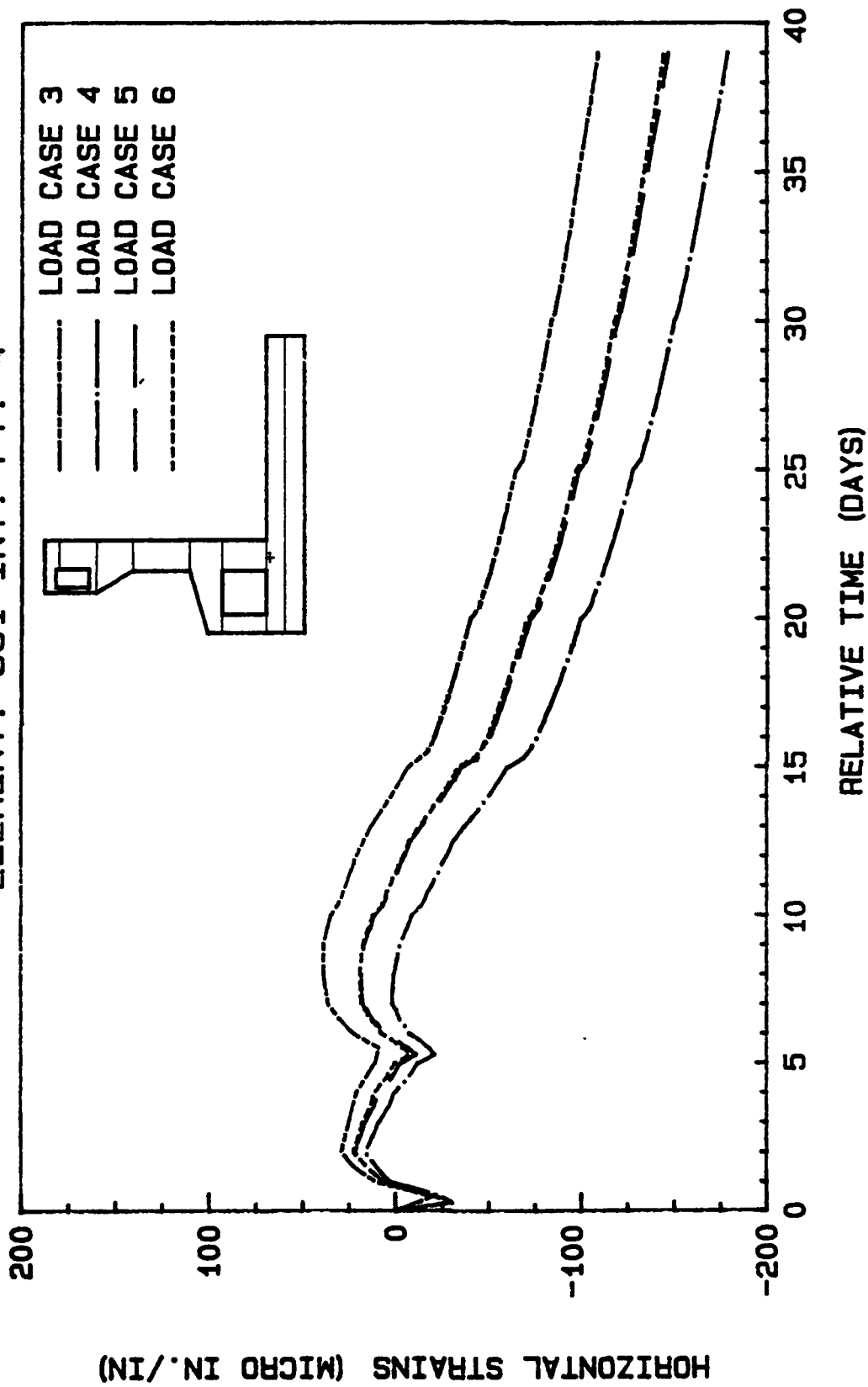


Figure 96. Strain versus time for load cases 3-6 for element 561

# ELEMENT. 587 INT. PT. 4

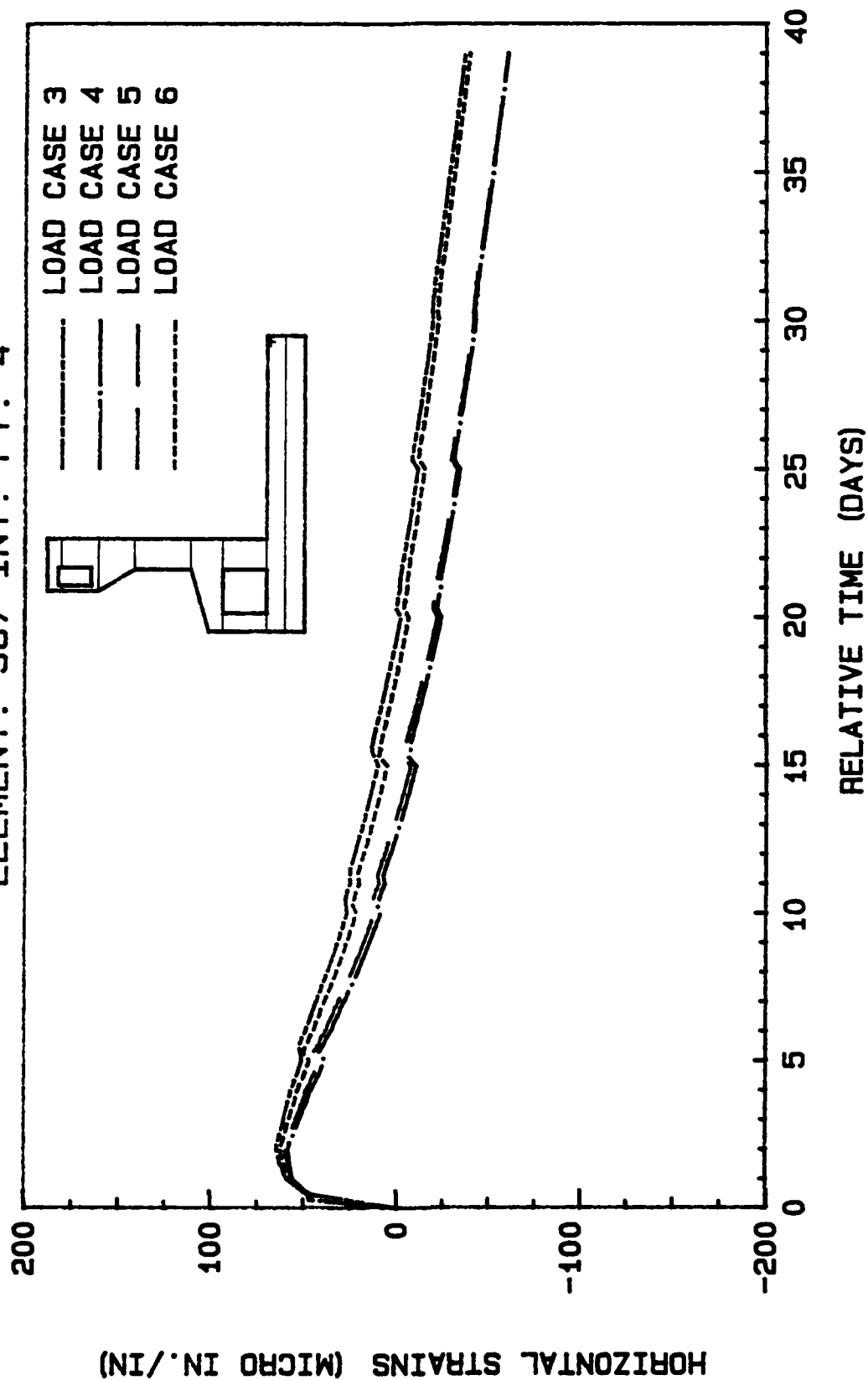


Figure 97. Strain versus time for load cases 3-6 for element 587

# ELEMENT. 663 INT. PT. 4

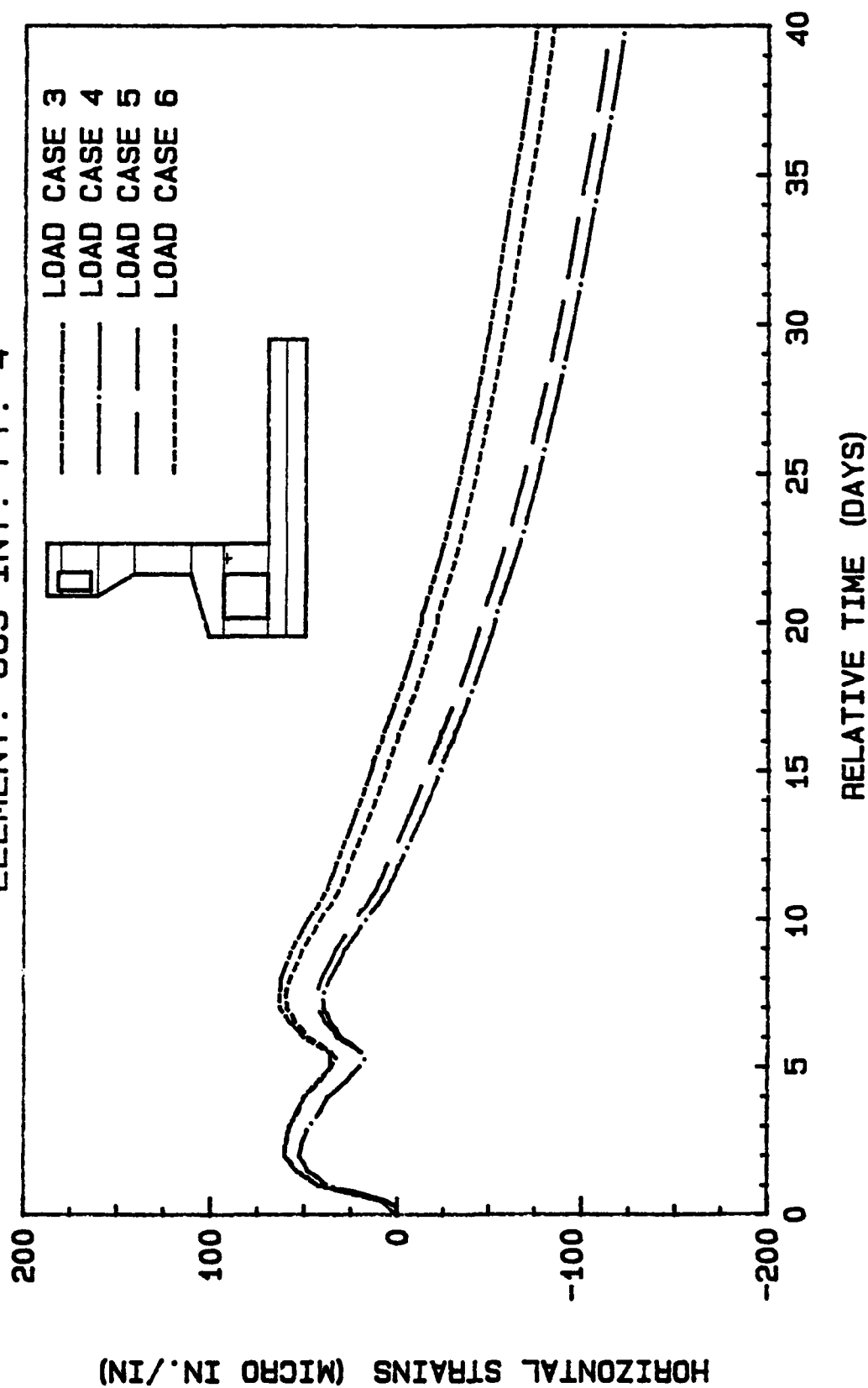


Figure 98. Strain versus time for load cases 3-6 for element 663

# ELEMENT. 674 INT. PT. 1

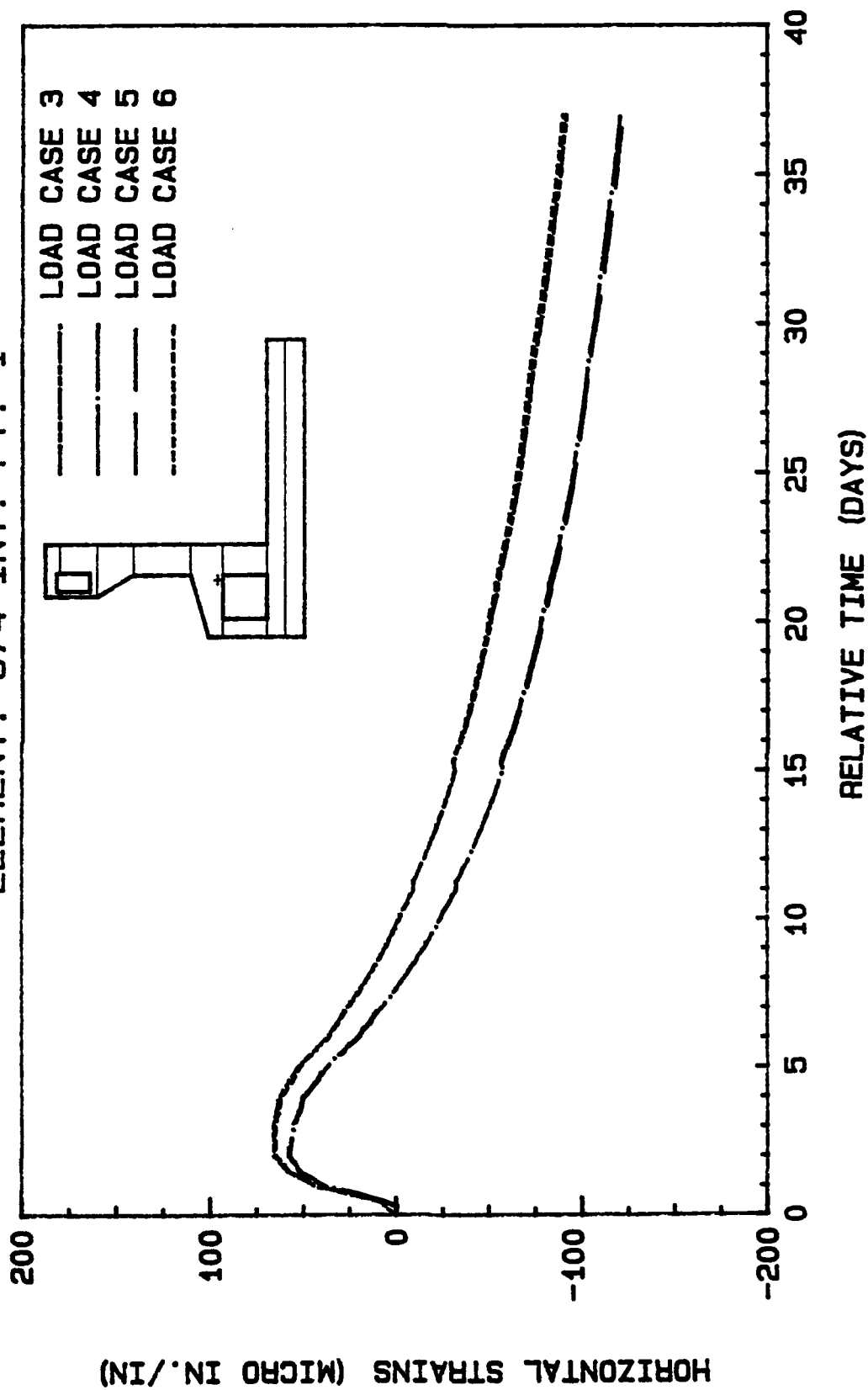


Figure 99. Strain versus time for load cases 3-6 for element 674

# ELEMENT. 705 INT. PT. 3

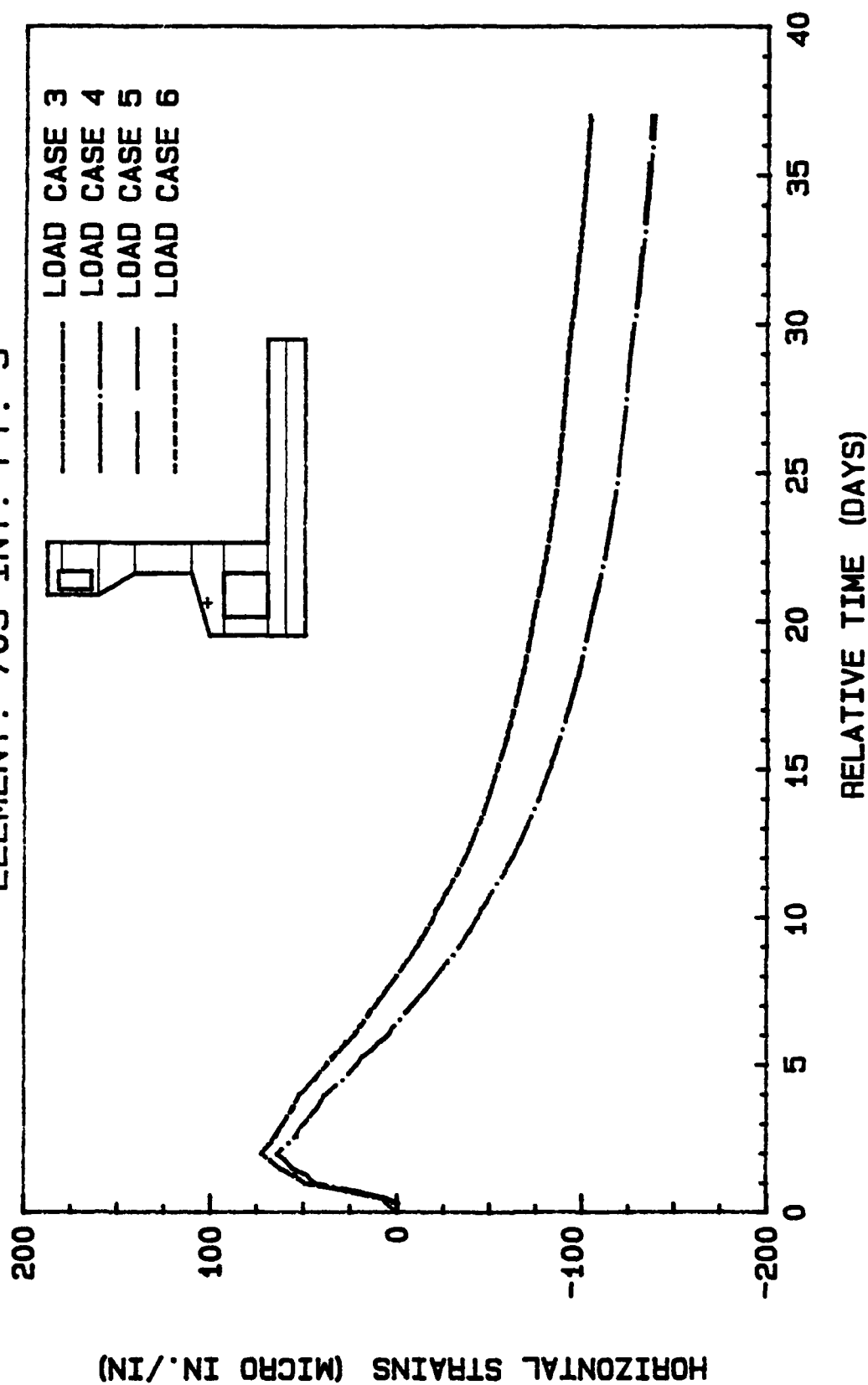


Figure 100. Strain versus time for load cases 3-6 for element 705

# ELEMENT. 719 INT. PT. 3

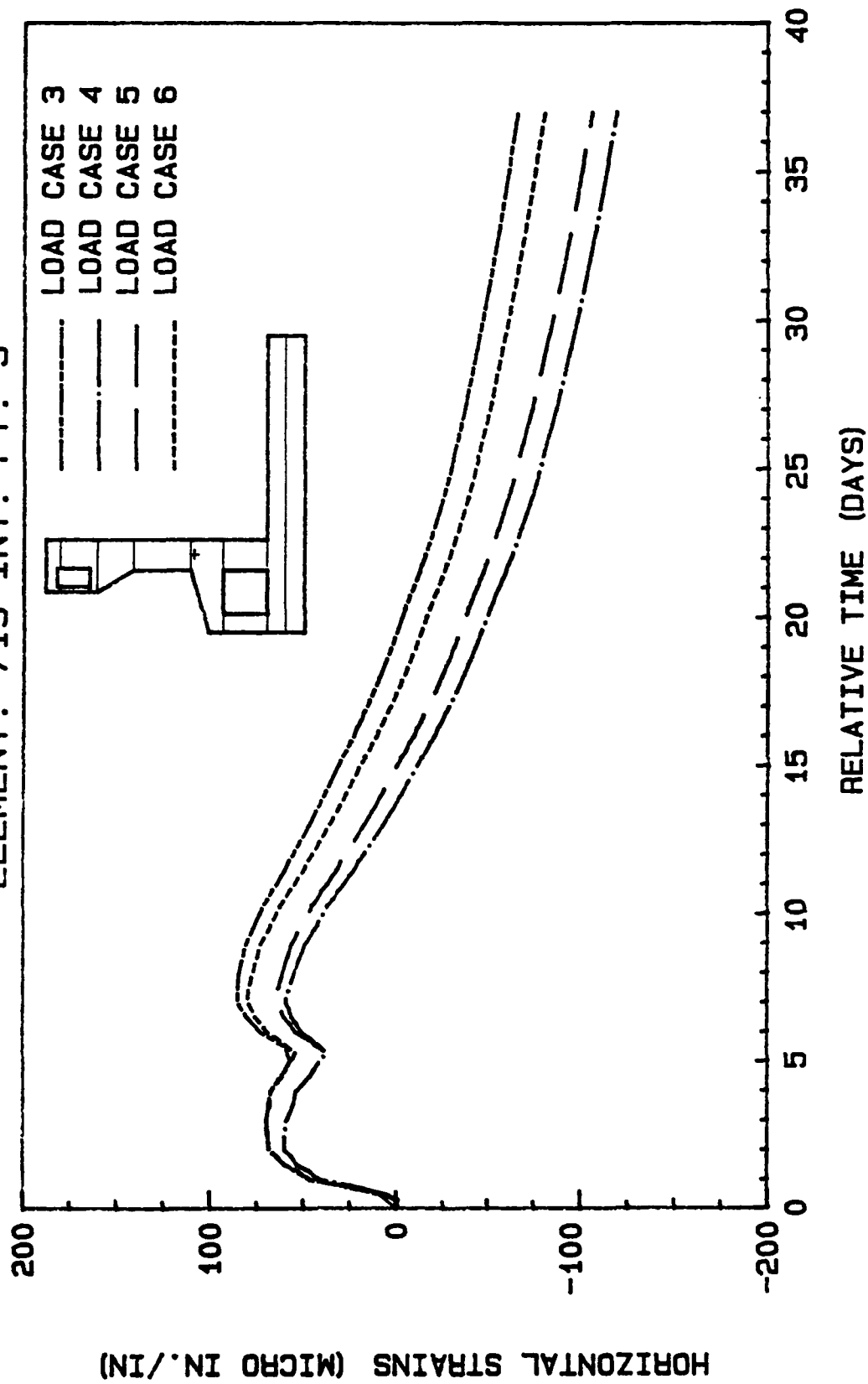


Figure 101. Strain versus time for load cases 3-6 for element 719

# ELEMENT. 755 INT. PT. 4

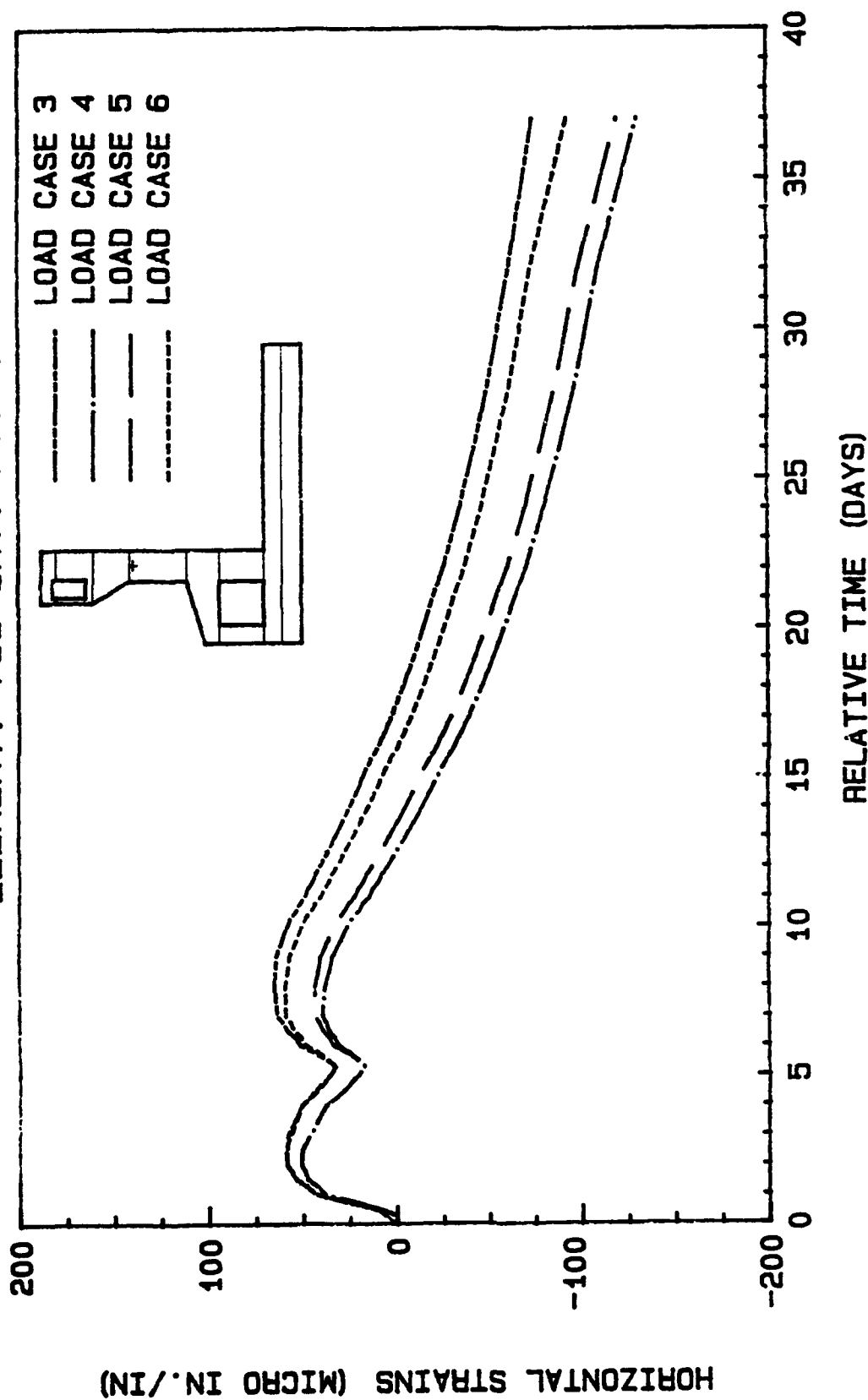


Figure 102. Strain versus time for load cases 3-6 for element 755

# ELEMENT. 849 INT. PT. 2

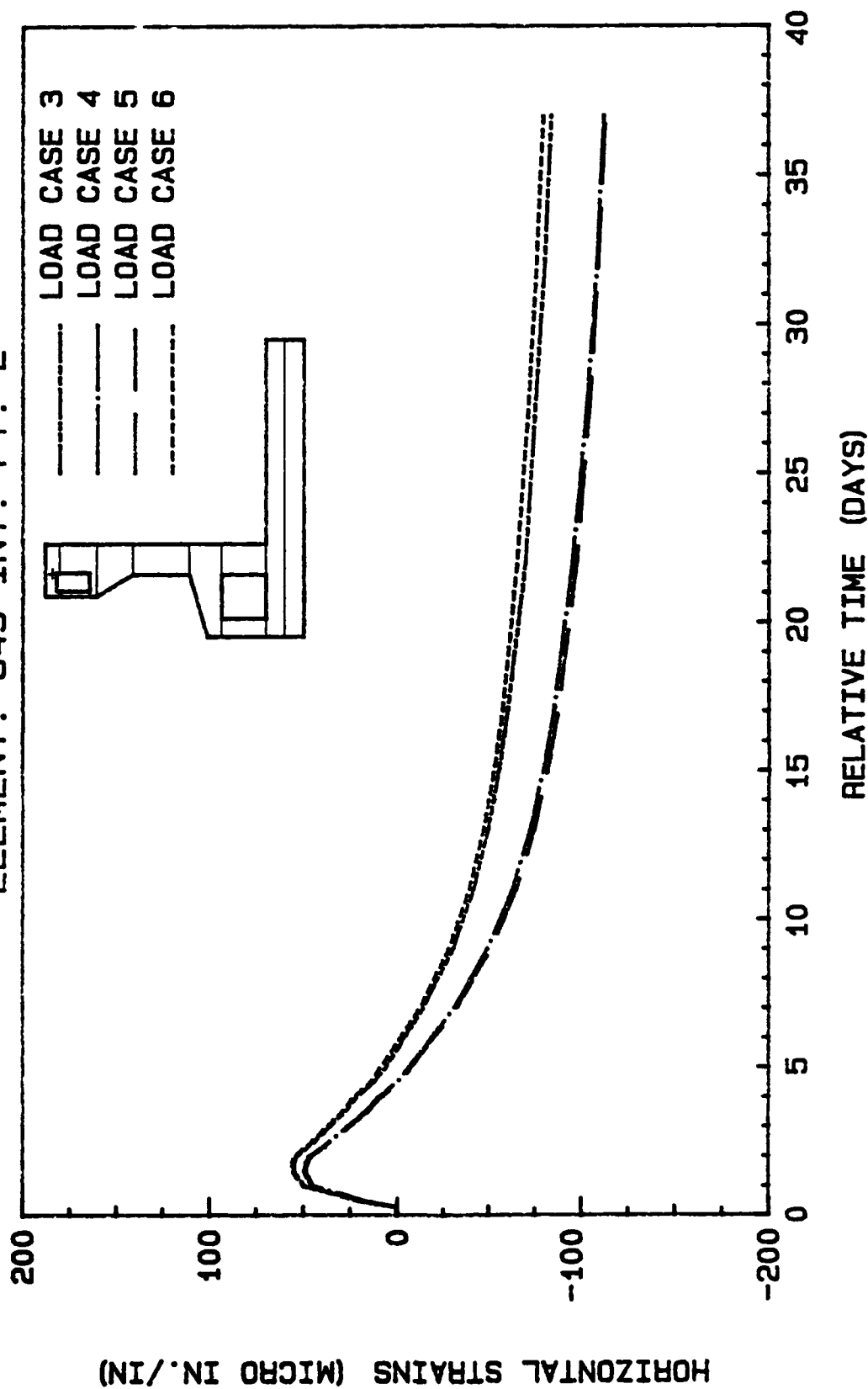


Figure 103. Strain versus time for load cases 3-6 for element 849

# ELEMENT. 860 INT. PT. 3

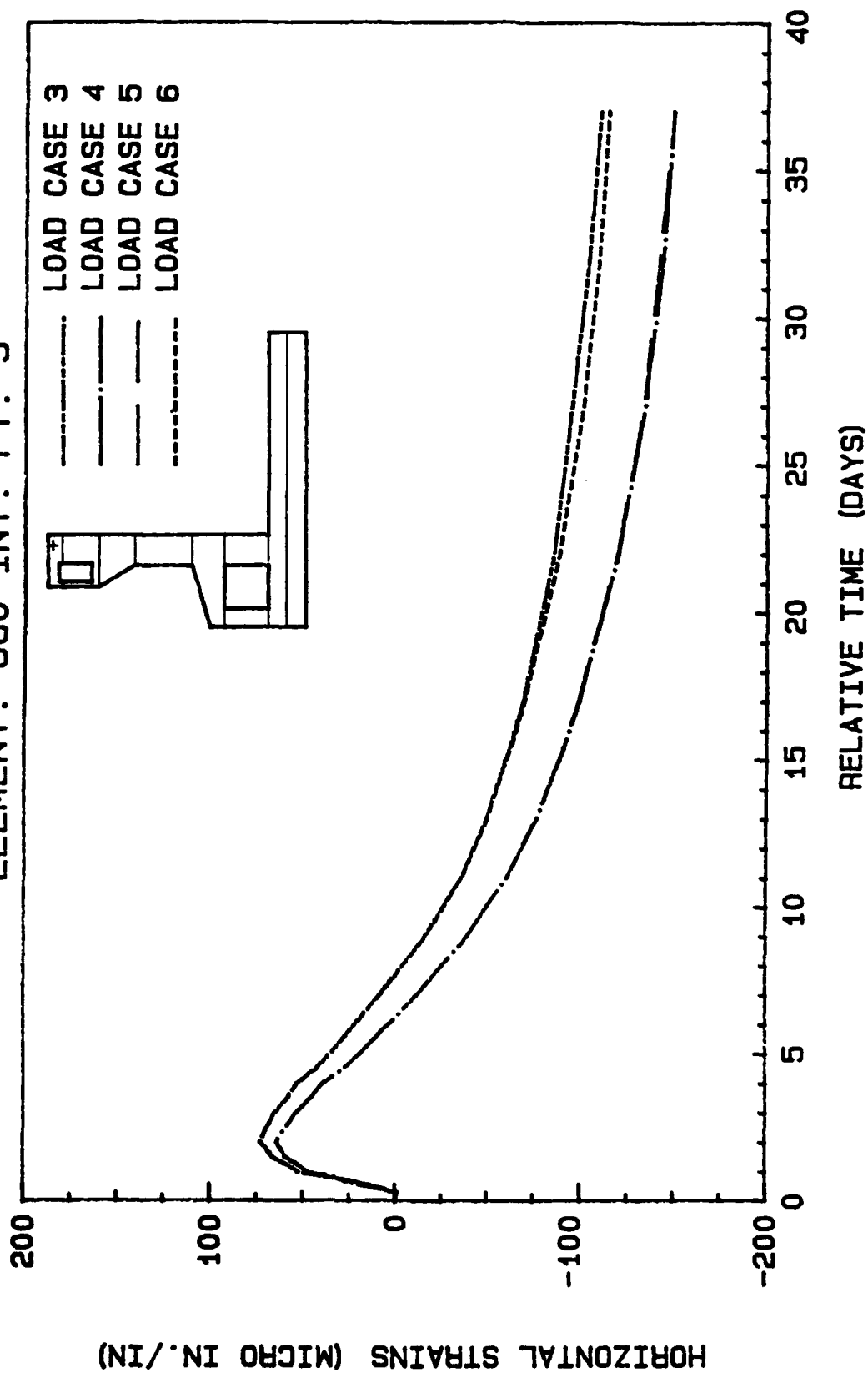


Figure 104. Strain versus time for load cases 3-6 for element 860

# ELEMENT. 610 INT. PT. 3

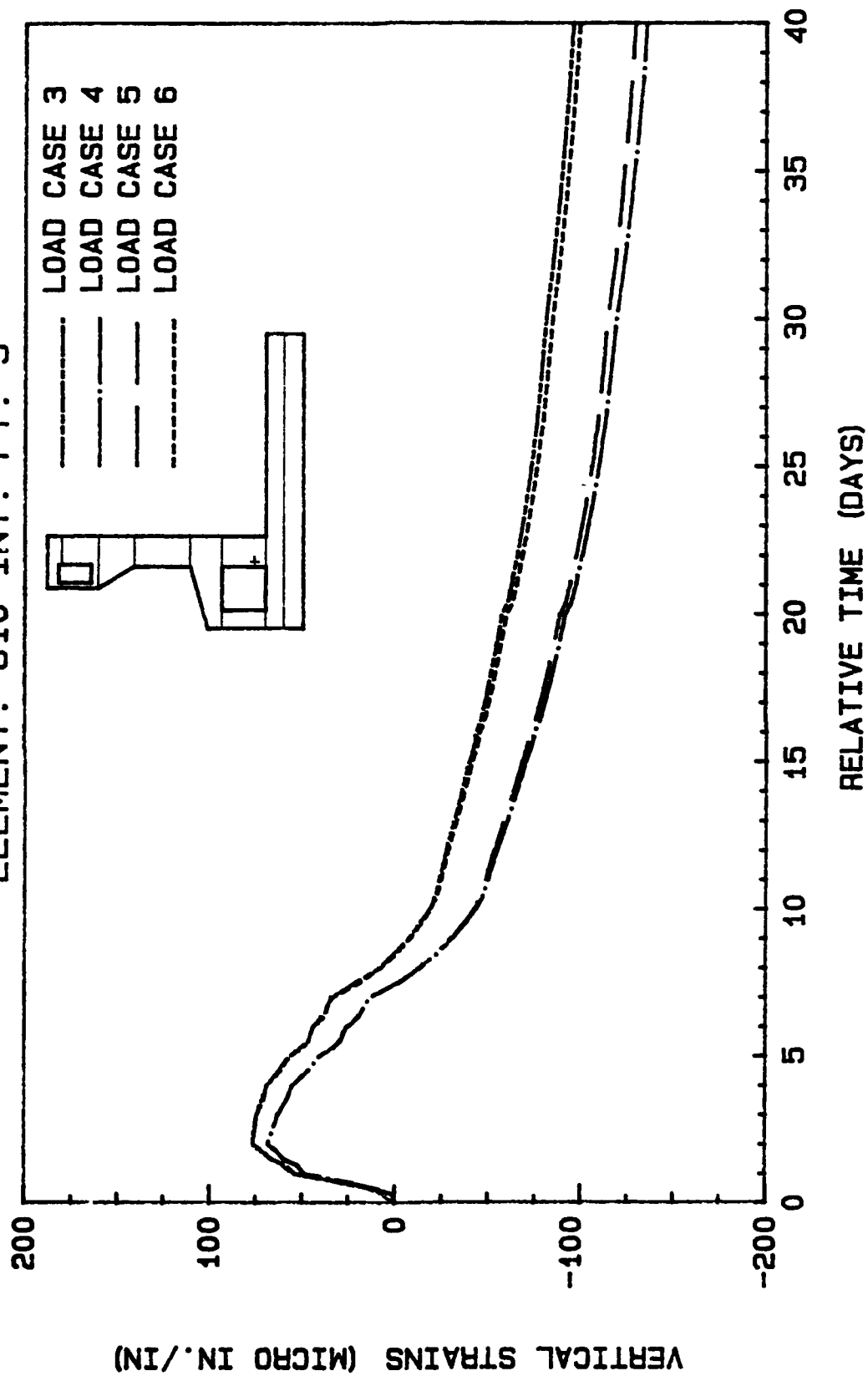


Figure 105. Strain versus time for load cases 3-6 for element 610

# ELEMENT. 768 INT. PT. 2

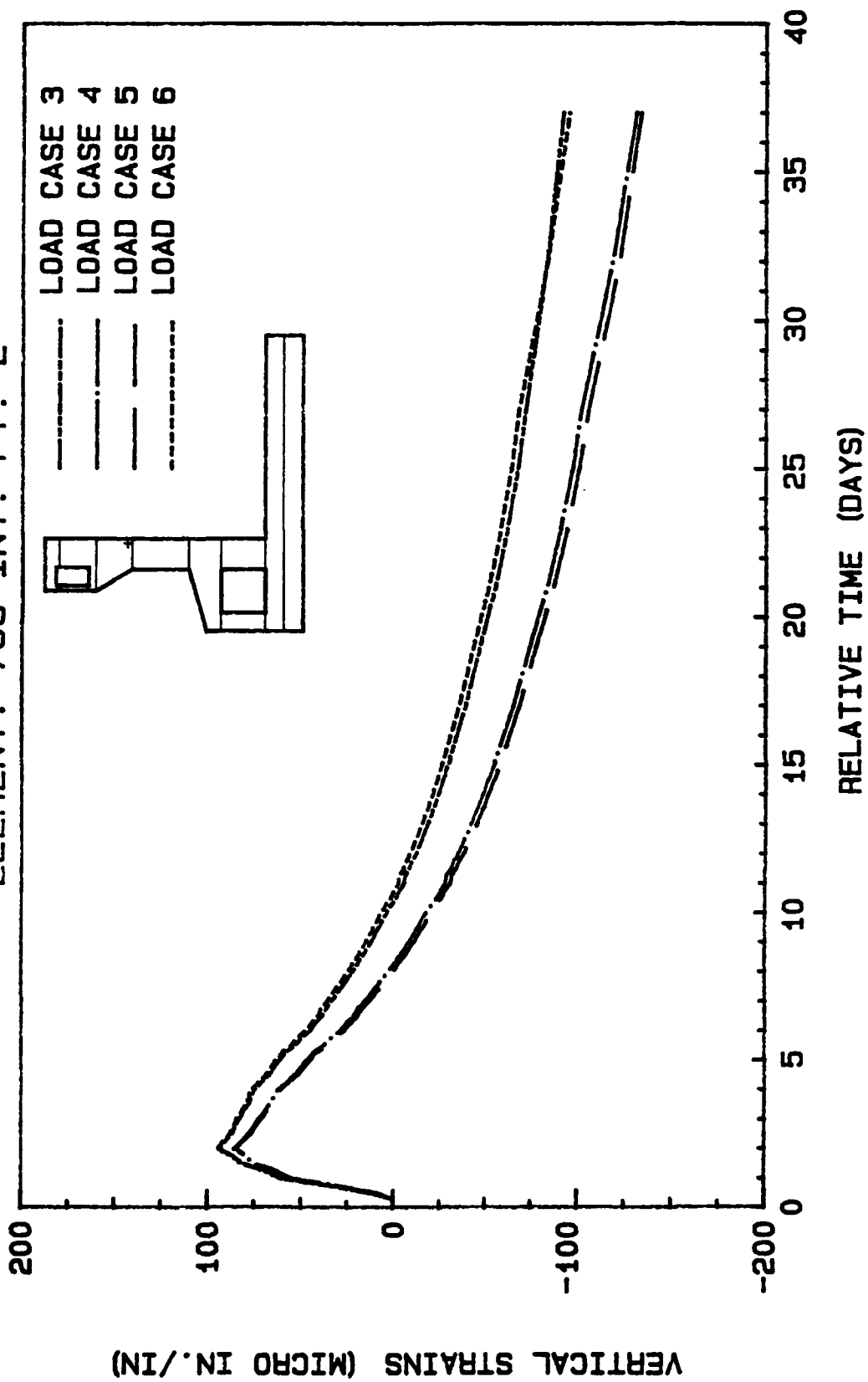


Figure 106. Strain versus time for load cases 3-6 for element 768

# ELEMENT. 810 INT. PT. 2

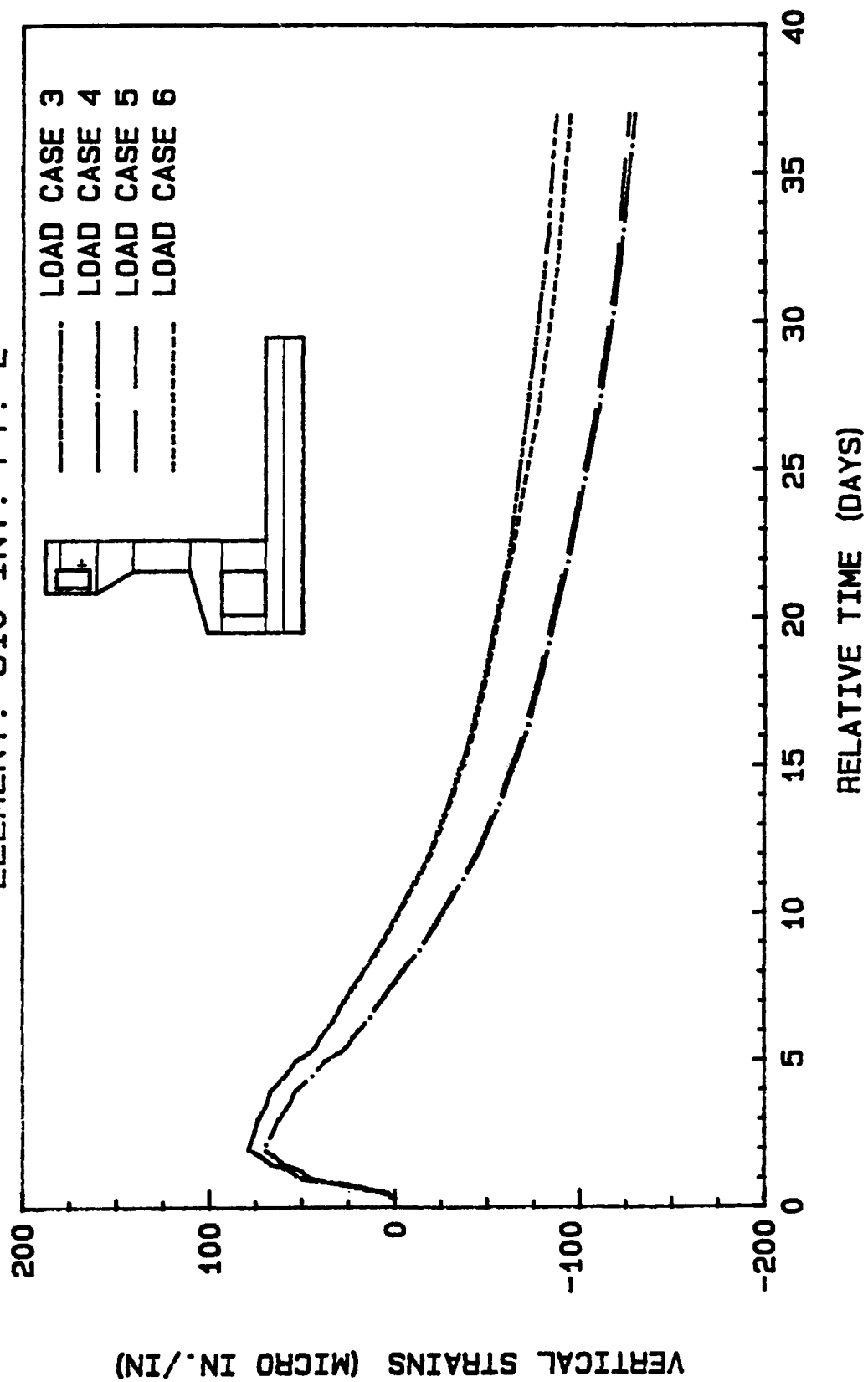


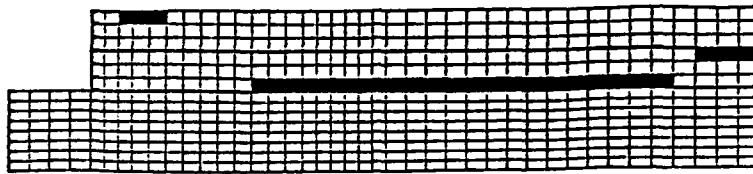
Figure 107. Strain versus time for load cases 3-6 for element 810

was decided that the service load analysis would be preferred for this load case.

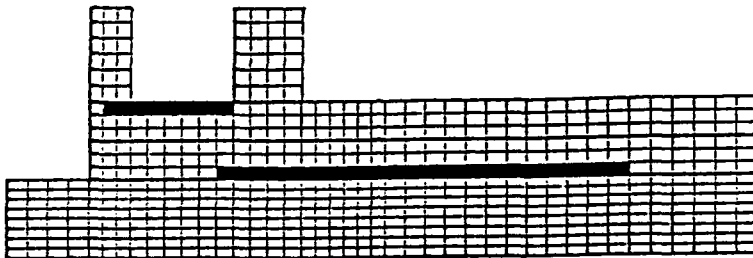
### Locations of High Tensile Stresses

80. A FORTRAN program, made available by personnel at the US Army Engineer District, St. Louis, was used to extract tensile stresses from the ABAQUS data file that exceeded an arbitrary value (Thompson 1987). The value used was 125 psi in the horizontal direction and 100 psi in the vertical. These values were chosen not because these stresses are excessive but to give a clear view of where tension does occur in the structure without over complicating the graphs. The results are shown on the part of the mesh that existed at the time in which these stresses occurred. The element is shaded if the stress value is exceeded. However, all four Gauss points do not necessarily exceed the stress value.

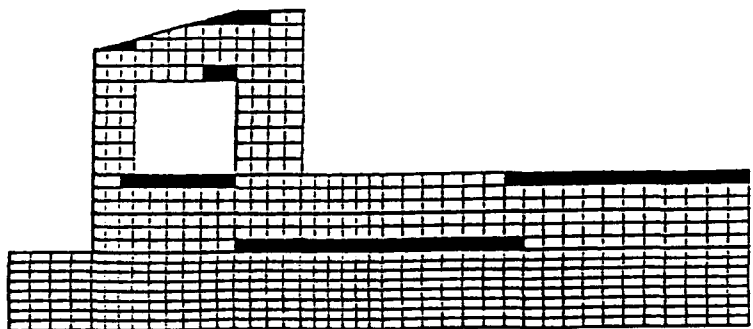
81. Figures 108, 109, and 110 show the locations where the horizontal stress exceeds 125 psi. The large zone of tension at the bottom of the slab in Figure 108 (a) is due to bending effects since the concrete has not yet gained adequate strength for the load to be completely transmitted to the piles. This tension zone is expected since the bottom of the slab does act like a beam on an elastic foundation and the deflection of the slab results in a downward curvature. The small zone at the center line at the top of lift 1 is due to thermal loads and also due to bending since the center line will rotate through a counterclockwise rotation. The top of lift 1 carries most of the force resulting since lift 2 does not yet have adequate strength to do so. The small zone at the right top of lift 2 is due to thermal loads. Figures 108 (b-c), 109 (a-b), and 110 (a-b) show the zone at the concrete-soil interface moving progressively under the rising lockwall. Figure 108(c) shows the high stresses at the top of lift 2 near the center line as the lock wall weight forces a greater deflection under it than at the center line, thus producing flexural stresses. High stresses also appear at the roof of the culvert and at the top of the lift due to thermal effects. As time progresses, the zone at the top right of lift 2 and lift 4 decreases as creep relieves the stresses. When construction is complete (Figure 110 (b)) the only two large zones of tensile stress are at the soil-concrete interface and



(a)

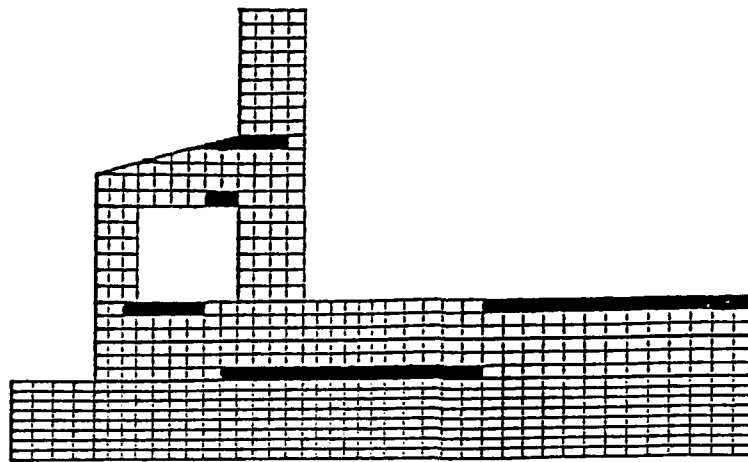


(b)

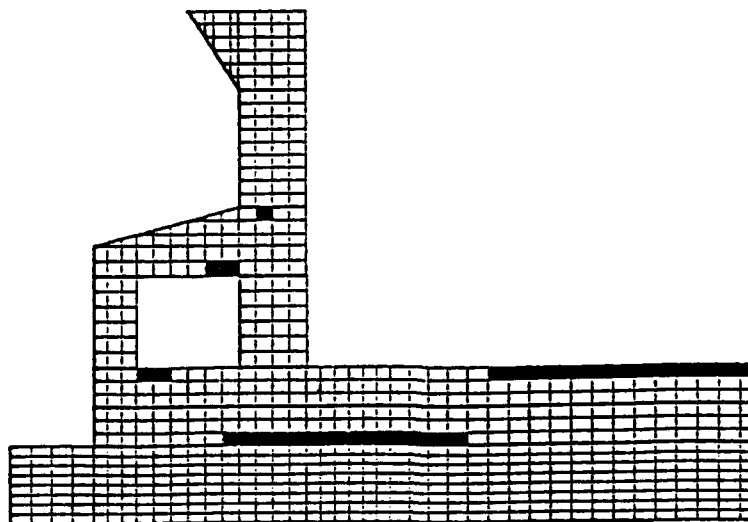


(c)

Figure 108. Locations where horizontal stress exceeds 125 psi at (a) 8 days, (b) 10.5 days, and (c) 19 days

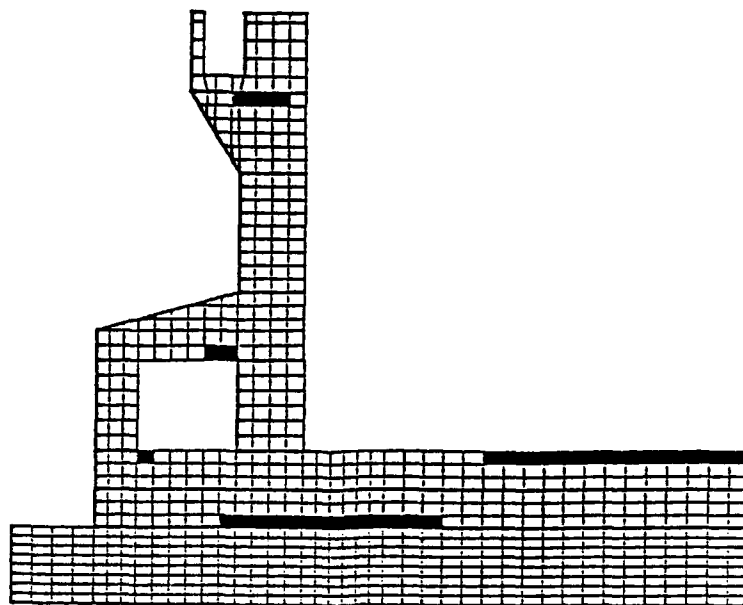


(a)

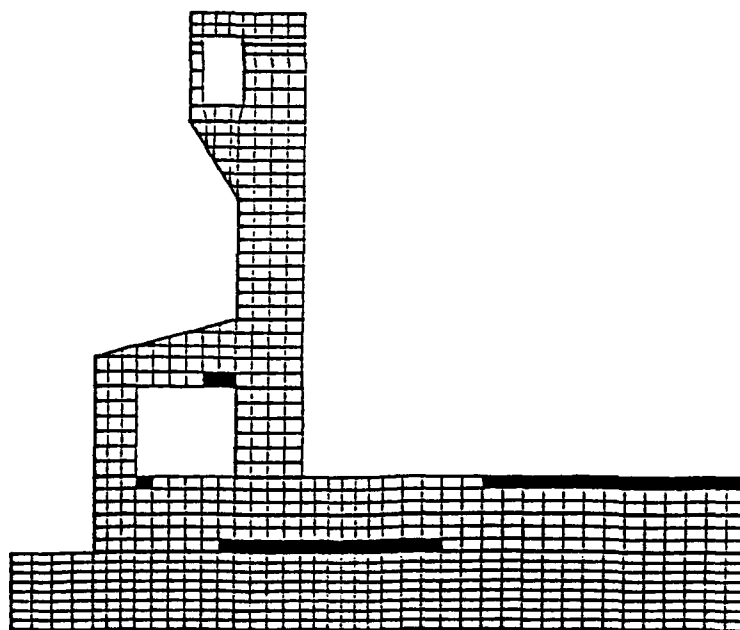


(b)

**Figure 109. Locations where horizontal stress exceeds 125 psi at (a) 21 days and (b) 27 days**



(a)



(b)

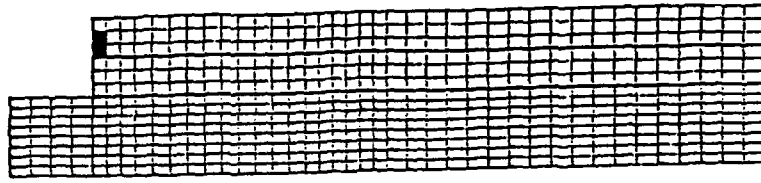
Figure 110. Locations where horizontal stress exceeds 125 psi at (a) 31 days and (b) 35.25 days

at the center line of the top of lift 2 where primarily flexural stresses exist.

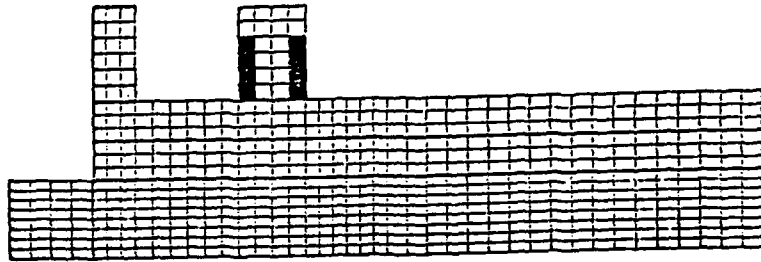
82. Figures 111, 112, and 113 show the location where vertical stresses exceed 100 psi. All of the resulting tensile stresses are obviously thermal induced since, with gravity loads only, the stresses would be compressive. Note in Figure 111 (b), the 8-ft-wide wall has tensile stresses; whereas, 5-ft-thick wall does not since the heat "build-up" is not as great in the smaller member. Also note that, as more weight is placed on the structure, the tensile zones change to compression since the thermal loads cannot continually keep the stresses in tension as the gravity loads increase--the exception being near the top of the structure where the eccentric weight produces bending and tensile stresses on the chamber side of the chamber wall.

#### Summary

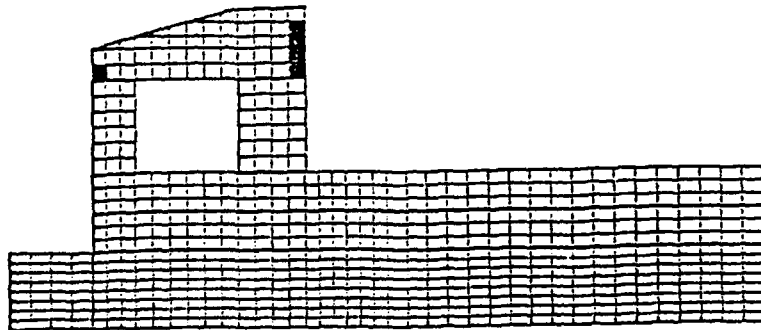
83. The results presented will now be briefly summarized to highlight the significant findings. First, creep and shrinkage relax the stresses when only internal restraint exists. At locations where external restraints are present, creep and shrinkage will produce higher stresses. Most of the strain plots show an increase in strain due to the thermal loads followed by a decrease in a exponential fashion due to creep and shrinkage. The locations where stresses were examined are in zones where stresses were found to be excessive. Finally, load case 3 produces the highest tensile stresses; whereas, load case 4 produces the lowest stresses when the effect of both creep and shrinkage are included in the analysis. The difference in stress in these two load cases is dependent on the location within the structure; however, the difference tends to be anywhere from approximately 25 psi up to 80 psi higher for load case 3 over load case 4.



(a)

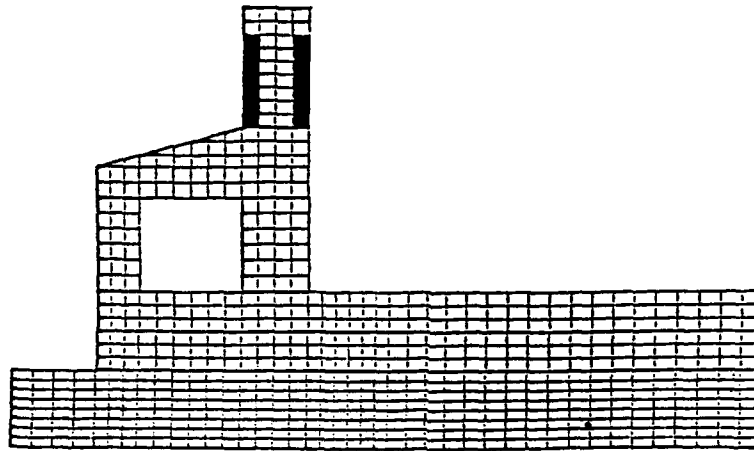


(b)

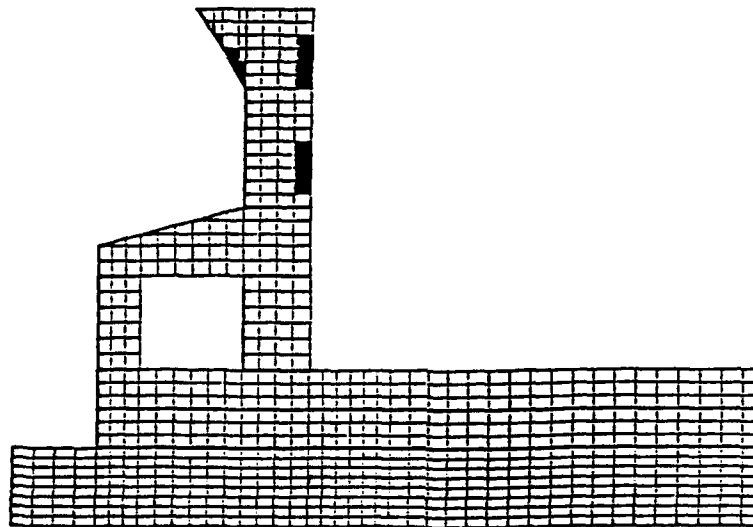


(c)

Figure 111. Locations where vertical stress exceeds 100 psi at (a) 6 days, (b) 14 days, and (c) 19 days

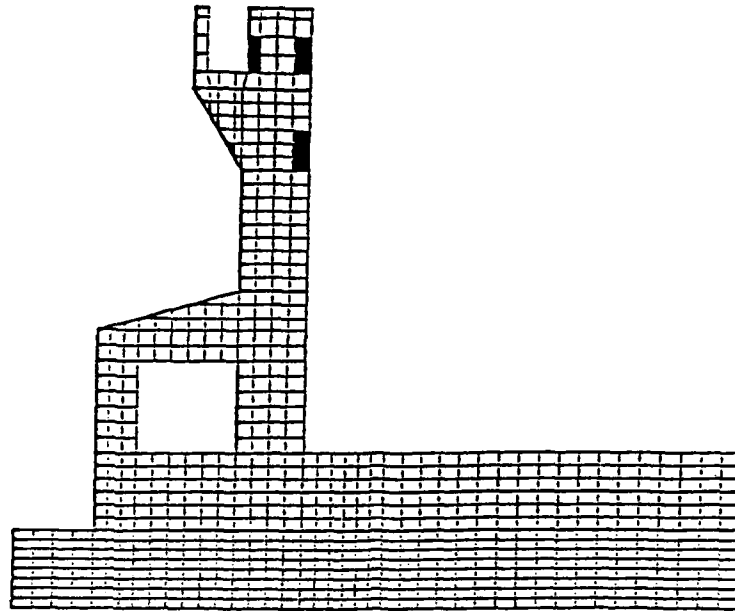


(a)

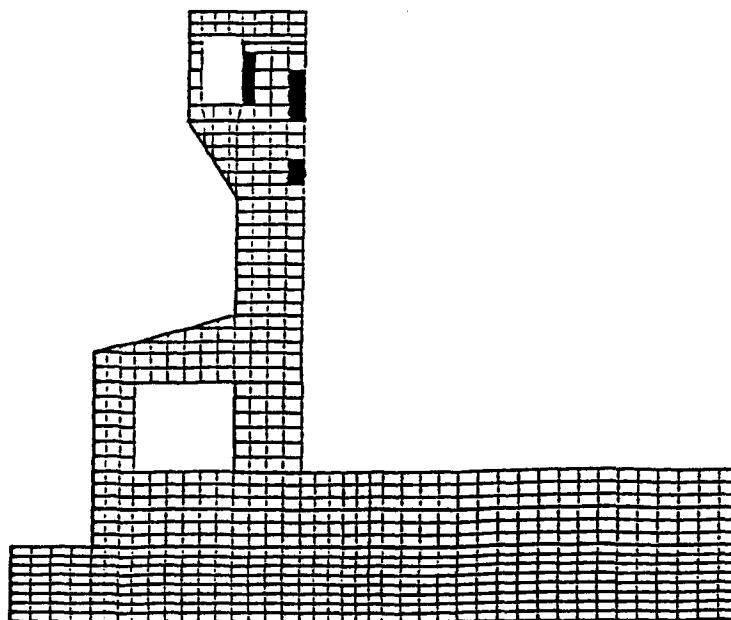


(b)

Figure 112. Locations where vertical stress exceeds 100 psi at (a) 24 days and (b) 29 days



(a)



(b)

Figure 113. Locations where vertical stress exceeds 100 psi at (a) 33.5 days and (b) 35.35 days

## PART VII: STATIC AND PARAMETRIC SERVICE LOAD ANALYSIS

### Introduction

84. Load case 3 was determined from the results in Part VI to be the worst load case when considering both creep and shrinkage and when investigating tensile stresses and the corresponding strains. Therefore, load case 3 was selected to be continued to service load conditions. The analysis was continued for another 72 days after the last lift was placed, allowing the structure to reach thermal equilibrium and to continue to creep and shrink. At 102 days from start of construction (67 days from when the last lift was placed), the service loads shown in Figures 11 and 12 were applied. A static linear elastic analysis was also performed using these same loads plus the dead weight of the structure.

85. In addition, the results will be compared with the results of the parametric analysis of the refined mesh shown in Figure 114. Load case 3 was again used when performing the analysis. The element dimensions are essentially the same in this mesh as in the previous mesh except at the lift interfaces and the exposed surfaces where the element size was set at 1 ft wide in the direction perpendicular to the exposed surface. The reason for using this finer mesh was to obtain stresses closer to the surface since this is the critical location for tensile stresses as shown in Figures 108-113. With this mesh, stresses were obtained as close as 1.75 in. to the surface; whereas, for the mesh in Figure 7, the stresses were obtained on the average of 3.5 in. from the surfaces. The comparison will be made by looking at stress distributions at critical sections in the monolith. In addition, the pile forces as determined from a static, linearly elastic analysis of the entire monolith and the nonlinear incremental construction analysis including thermal loads will be compared.

### Stress Distributions

86. Figures 115-121 show the stress distributions when service loads are also applied to the structure. Figure 115 shows a stress distribution for the slab under the culvert. Figure 116 shows a flexural situation combined with tension resulting from the hydrostatic force on the chamber wall, 0.1 of

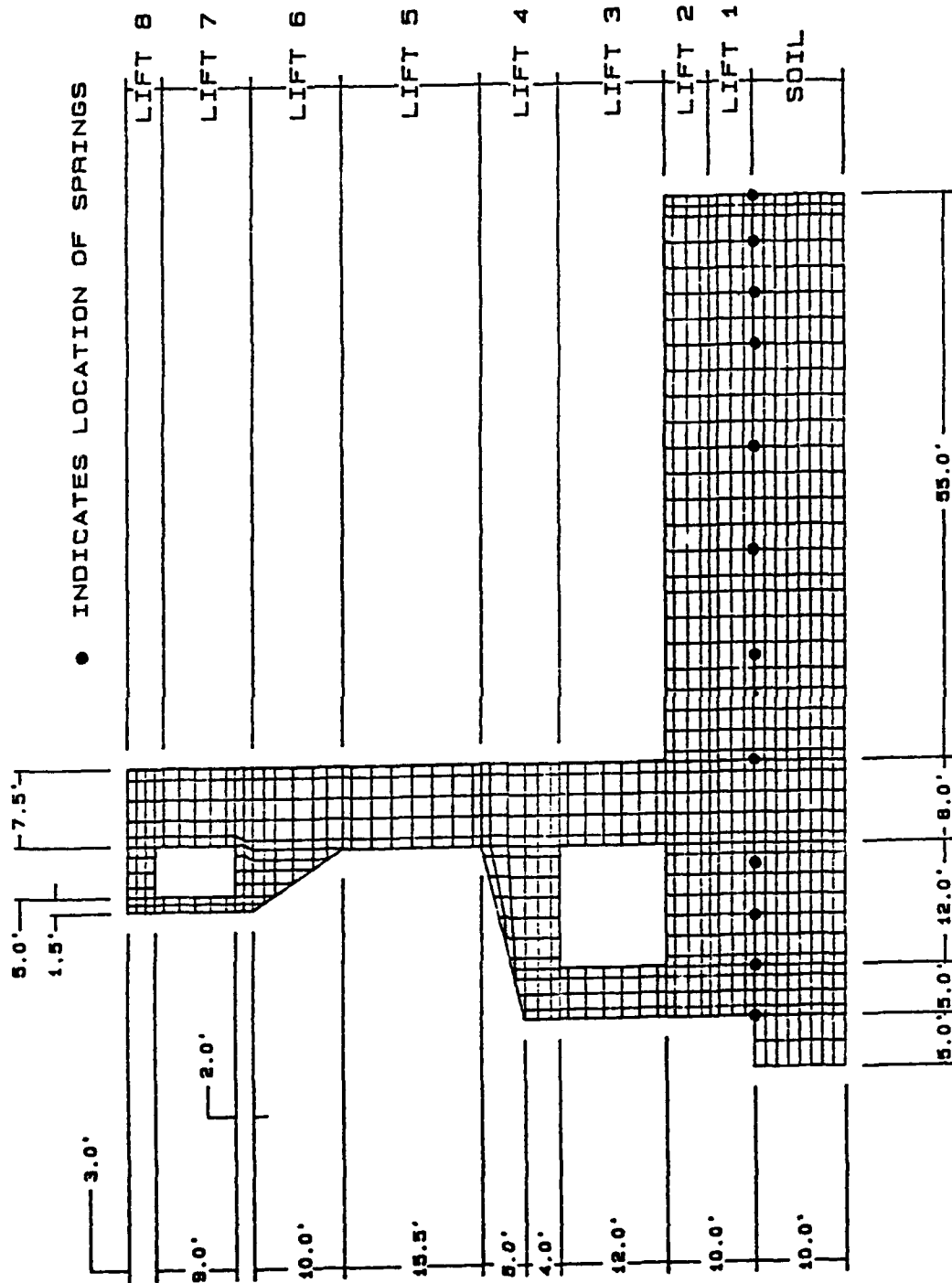


Figure 114. Refined mesh used for chamber monolith

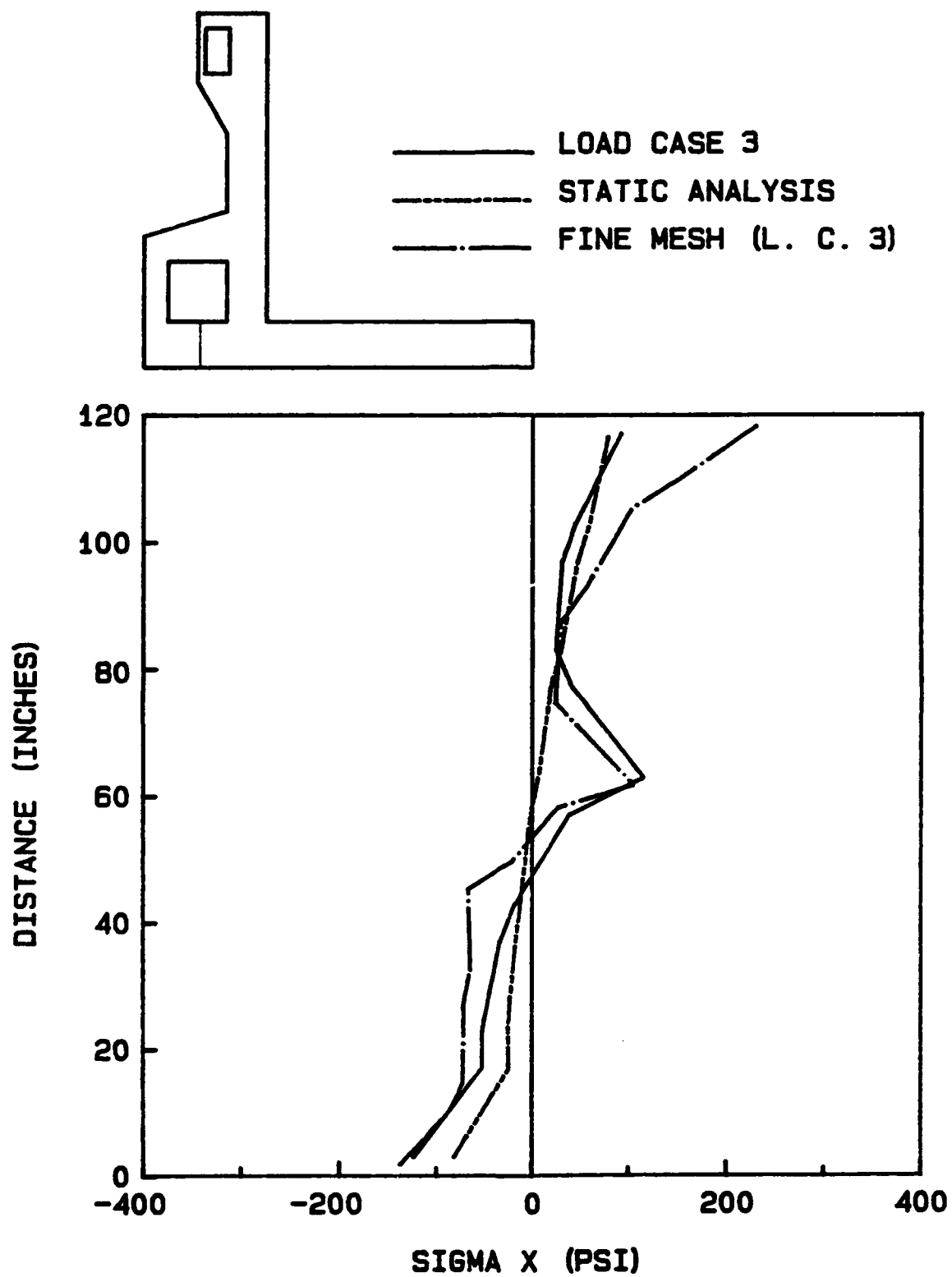


Figure 115. Stress distribution at service loads under culvert

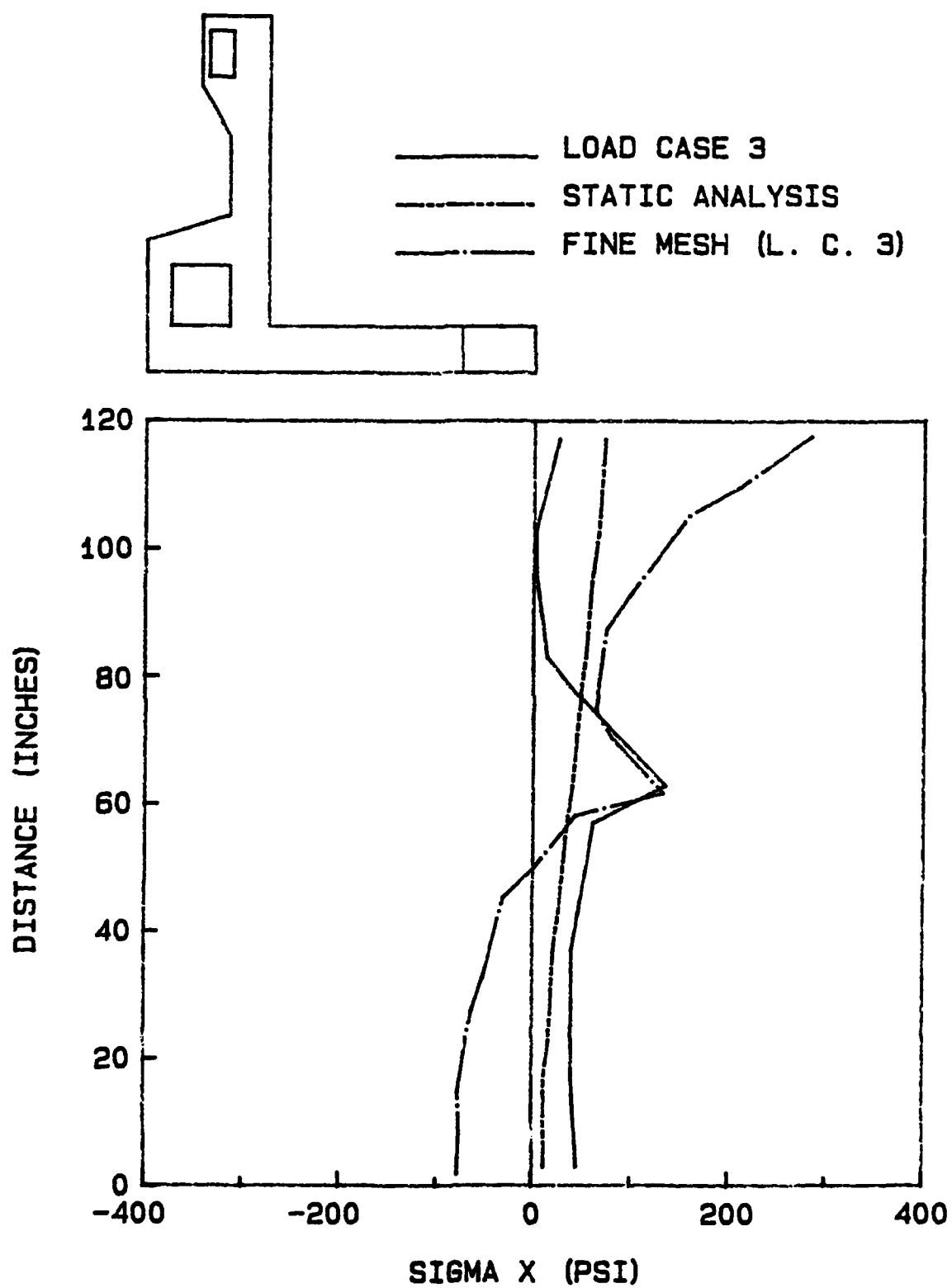


Figure 116. Stress distribution at service loads near center line

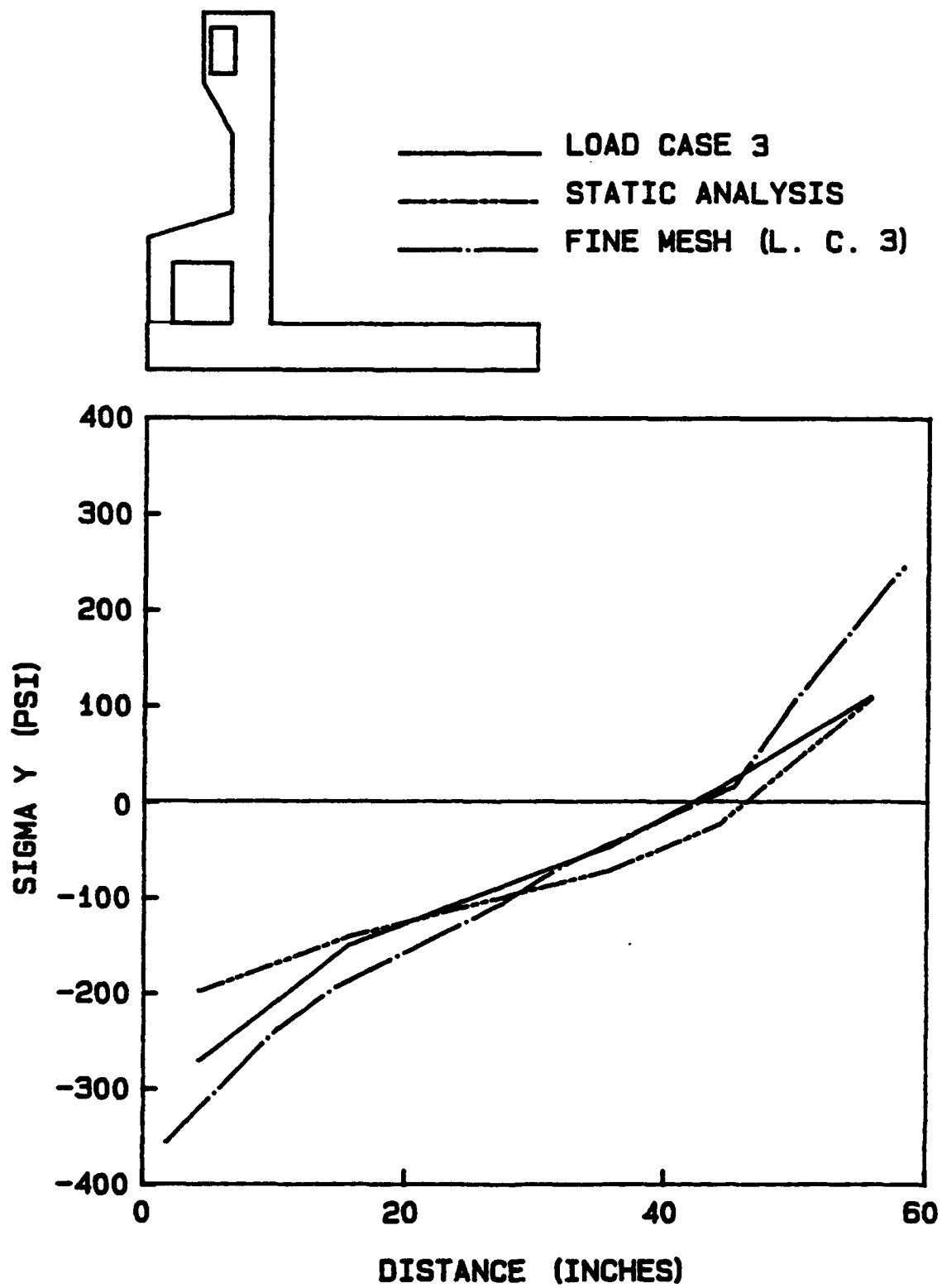


Figure 117. Stress distribution at service loads at left of culvert wall

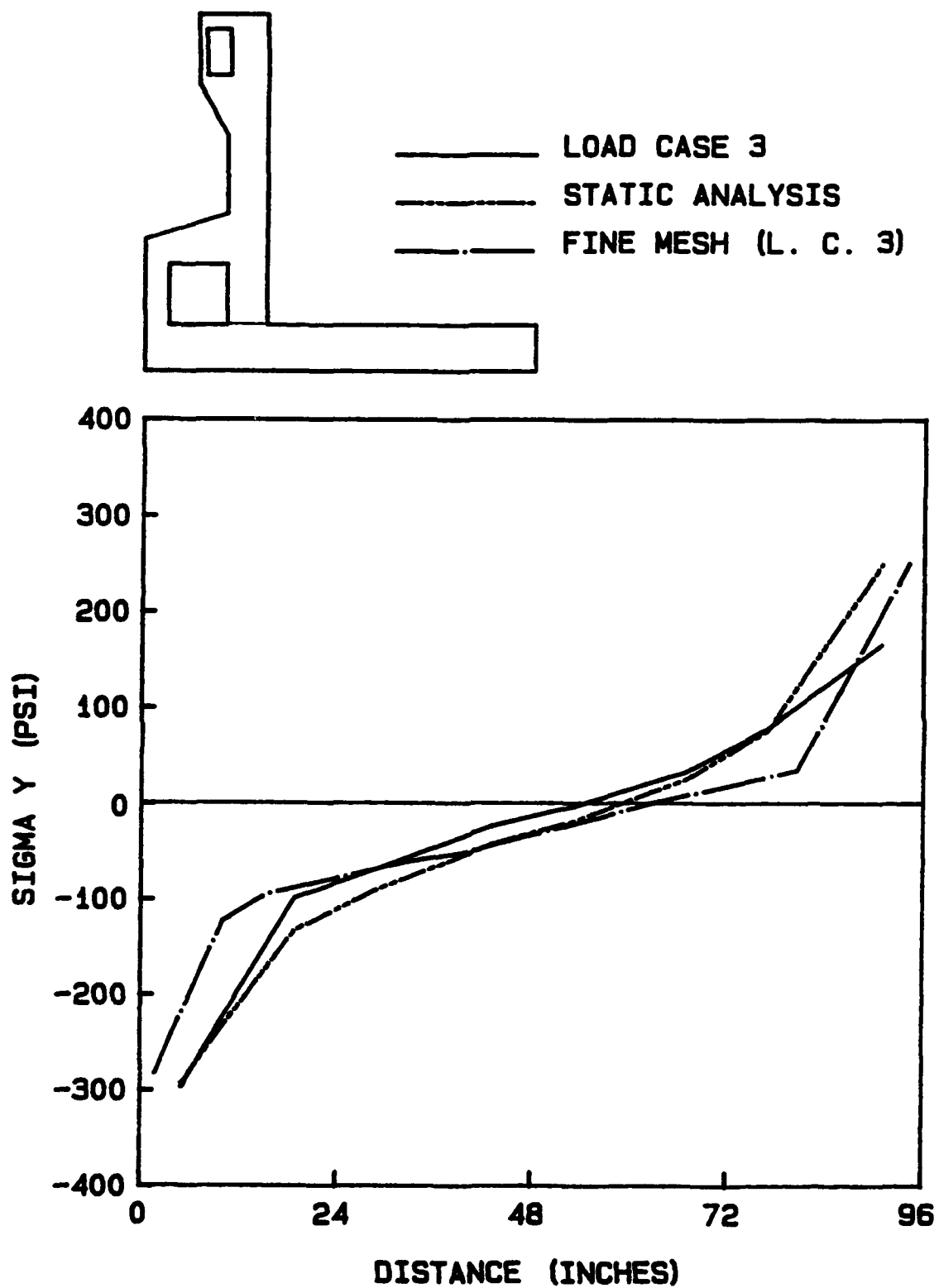


Figure 118. Stress distribution at service loads at right of culvert wall

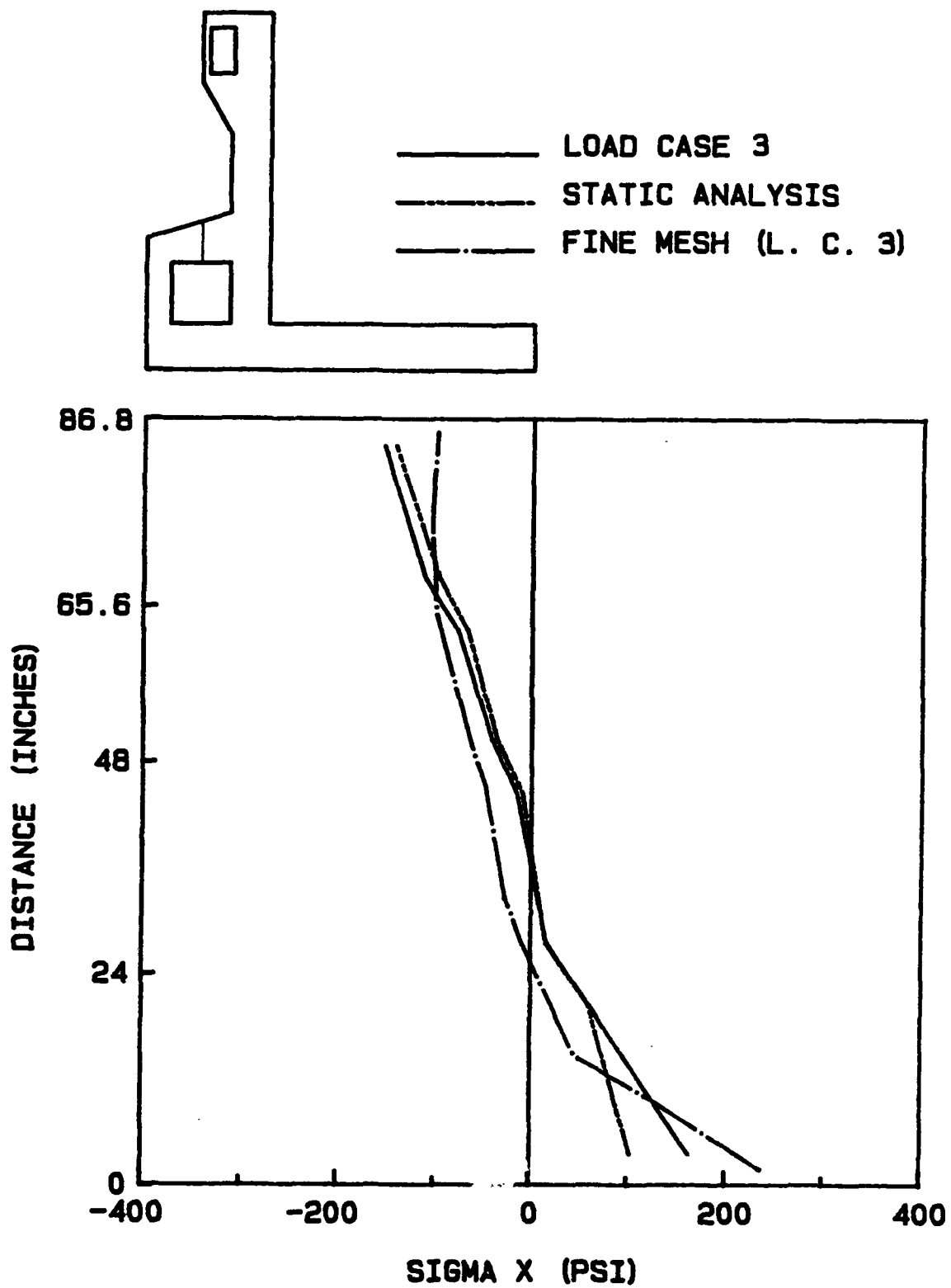


Figure 119. Stress distribution at service loads at roof of culvert

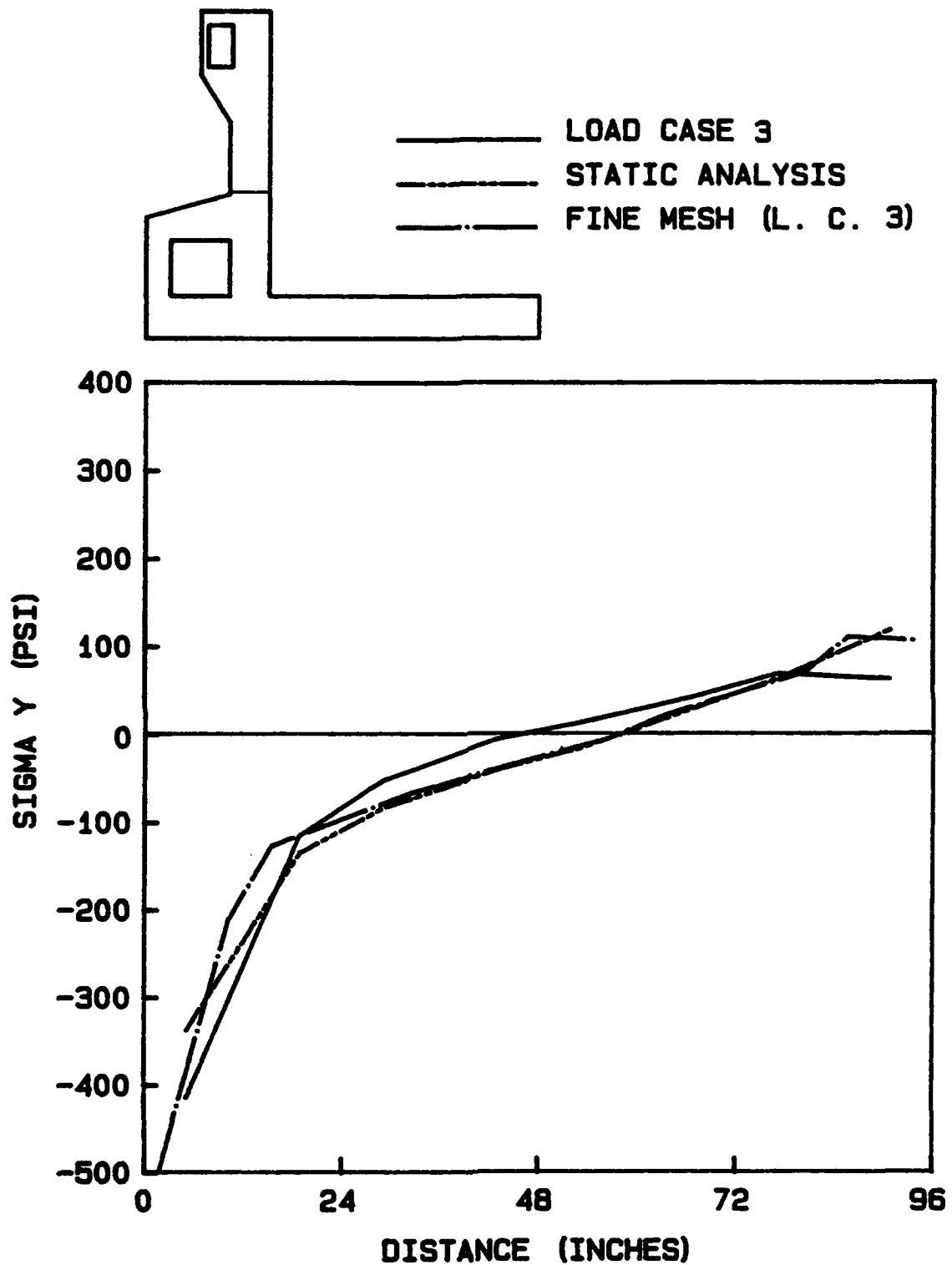


Figure 120. Stress distribution at service loads at bottom of chamber wall stem

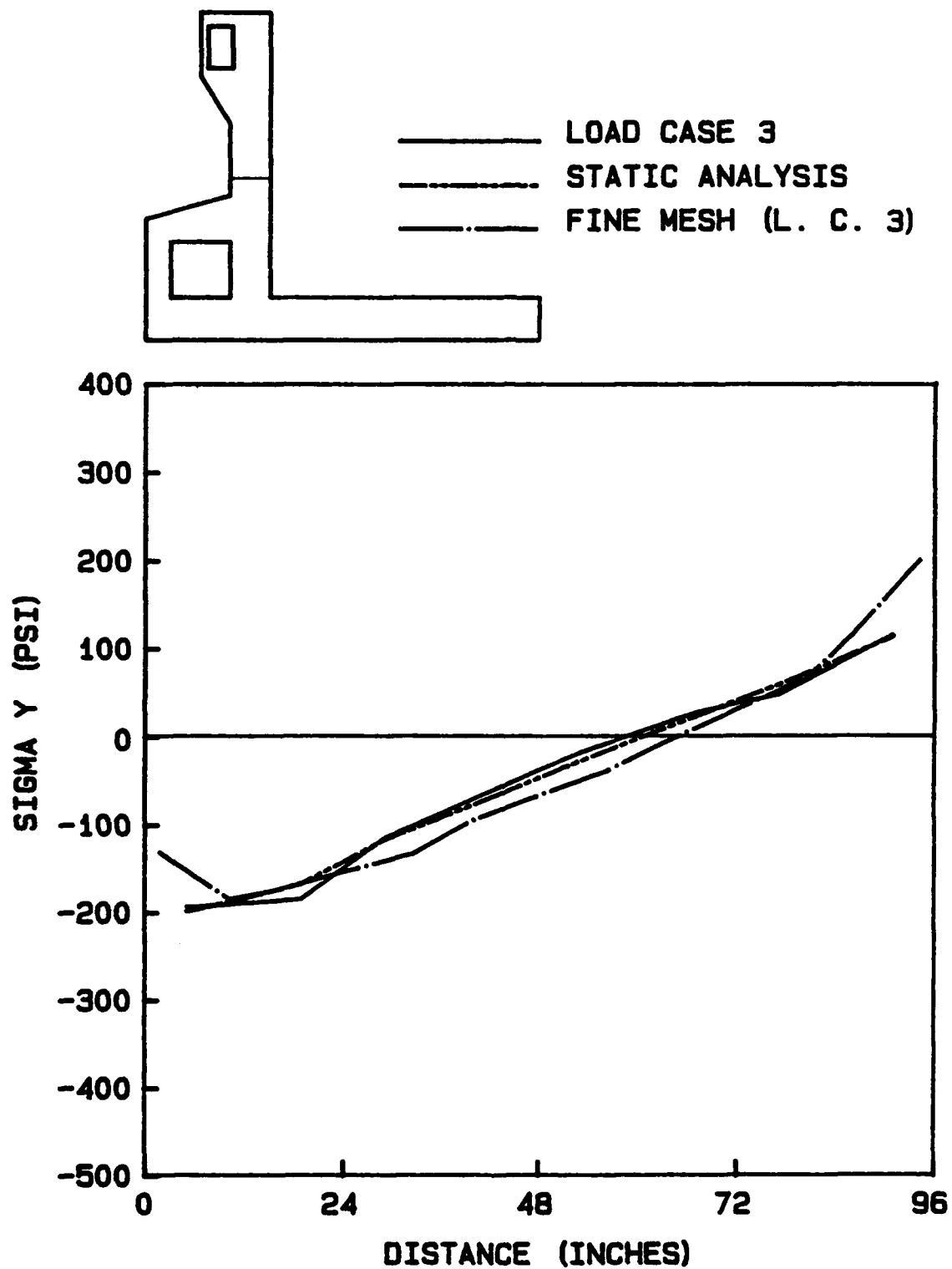


Figure 121. Stress distribution at service loads 2 ft from bottom of chamber wall stem

the dead weight applied as an earthquake load, and the large vertical load associated with the wall. The increase in stress in both Figures 115 and 116 at 60 in. followed by a decrease is related to the lift interface and the residual thermal effects.

87. Figure 117 and 118 show the flexural stresses resulting in the lock wall on both sides of culvert. These stresses are also due primarily to the hydrostatic force on the chamber wall and the earthquake force. The right culvert wall could act like a tension strut while the left culvert wall would act like a compression strut, but, looking at the deflection plot for the parametric analysis in Figure 122, it can be seen that the curvature of both walls indicate the stress distributions are correct. A similar deflection is obtained for the static analysis except that the left side of the lower part of the structure does not have the displacement to the right which is caused by shrinkage.

88. Figure 119 shows the stress distribution for a cut through the roof of the culvert. The tensile stress at the bottom of the culvert roof is due primarily to the dead weight of the concrete above the culvert.

89. Figures 120 and 121 show the stresses in the stem of the chamber wall. Again, a flexural situation is a result of the hydrostatic force and the earthquake force. Figure 121 is included to show that the high stresses at the corner is a result of stress concentrations.

90. All of the figures show that the analyses produce similar results especially in the sense that the resulting moments are in the same direction and of the same relative magnitude. Thus, it is acceptable for a simple static analysis to be performed when dimensioning the structure, saving the engineer valuable time in the preliminary design phase. When the structure is designed for service loads, a thermal analysis should then be performed to check stresses resulting from the construction process especially resulting from the heat "buildup." The results of the refined mesh give further confidence in the results obtained from the original mesh.

#### Pile Forces

91. As was just shown, the engineer can perform a static analysis to design the structure. It will now be shown that the same conclusion can also be made for determining the pile forces for designing the pile layout.

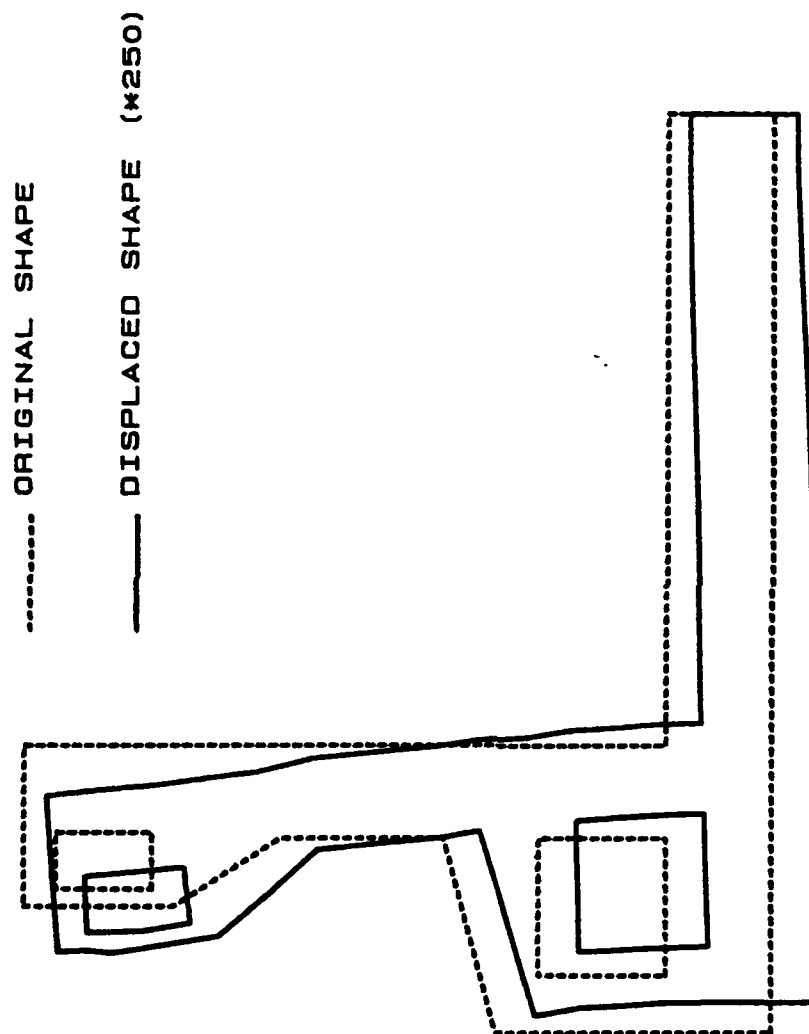


Figure 122. Deflected shape for service loads and load case 3

Table 6 shows the results of the spring forces for the static linearly elastic analysis and the nonlinear, incremental construction analysis including thermal loads. The results for the vertical component are nearly the same especially under the lock wall where the forces are the greatest. The horizontal components are greatly different. This is because of the thermal loads which cause the structure to shrink toward the center line. However, these forces are not as significant since the H-plies, not battered, are selected to support the vertical load and checked for adequacy in the horizontal direction.

PART VIII: OVERVIEW, INTERPRETATION, AND VERIFICATION OF RESULTS  
FOR MONOLITH AL-5

Introduction

92. The significant findings from the results will be further discussed. In addition, assessments will be made on what these results mean to the overall structural response of the chamber monolith. Finally, the results from the finite element program will be verified by checking internal and external equilibrium.

Overview, Significance and Interpretation of Calculated  
Tensile Stress Results

93. The major points of this investigation will now be highlighted. First, it was found that the upper bound adiabatic curve produced higher temperatures in the structure as would be expected. Next, three stress analyses were made with creep and shrinkage fixed, and the adiabatic curve set at the upper and lower bounds and neglected in the third analysis. From this series of analyses, it was concluded that the upper bound adiabatic curve produced higher tensile stresses. Consequently, the upper bound adiabatic curve was used in the remainder of the analyses. In addition, the results of these analyses also showed that thermal loads produced tensile stresses in locations where a gravity turn-on analysis showed consistently compressive stresses. As shown earlier, neglecting thermal loads produces lower stresses. Quite often the nonthermal analysis predicts compressive stress; whereas, the thermal analysis predicts tensile stresses. Thus, performing a thermal analysis is important to locate potential areas for tensile reinforcing.

94. The results from the parametric analysis of creep and shrinkage indicated that both creep and shrinkage tend to have a softening effect on the stresses (i.e. creep and shrinkage reduce thermal induced stresses) when the dominate mode of restraint is internal. Stresses near external restraints show the opposite to be true, but the difference among the various load cases for the stresses is not as significant (Figures 83 and 85). A major conclusion is that the design engineer could generally neglect creep and shrinkage to simplify the analysis without sacrificing any structural integrity.

95. The strain plots show an increase in strain due to thermal expansion, followed by a decrease due to subsequent cooling and shrinkage. This type of behavior is expected. From the stress and strain plots, an assessment was made that load case 3 (lower creep, lower shrinkage) produced the highest tensile stresses/strains consistently out of the possible choices of the realistic load cases. Therefore, it was selected for the service load analysis. Load case 3 was also examined further for locations of high tensile stresses. The result of this investigation showed, among other things, that the stress plots examined were at the locations in the structure where tensile stresses were critical.

96. The parametric and static service load analysis produced similar stress distributions in the structure with the exception of the discontinuities at the lift interfaces. Consequently, the engineer could perform a static analysis to obtain the appropriate dimensions so that the structure could safely resist the worst service load conditions then check the design for localized effects such as cracking and high residual stresses with a thermal stress analysis. The same conclusion is true for determining pile forces.

97. The significance of the calculated stresses depends on the permissible value allowed for tensile stresses in mass concrete. The tensile stress for concrete with a compressive strength of 3,000 psi was predicted to be approximately 370 psi using ACI criteria. The maximum calculated tensile stress was 251 psi for element 378, which approximately is 70 percent of the predicted maximum allowable tensile stress. The Corps of Engineers usually adopts a more stringent criteria for the tensile capacity of concrete. Some districts permit no tension; whereas, others permit a maximum tensile stress of only 30 psi. If these allowable tensile stress values are exceeded, reinforcement is provided to withstand the forces corresponding to the calculated tensile stresses. Since reinforcement needed to resist tensile forces can be of relative large magnitudes, construction material and techniques which minimize thermal-induced tensile stresses should be used whenever practical. Although reinforcement is a costly construction material, it should be used in a prudent manner as grouting of cracks can be a source of high maintenance costs.

98. Cracking was detected within the analysis for load case 7 and 9 near the bottom of lift 6 along the sloped wall (element 758). This cracking, however, may have occurred since no support was provided along the sloped

element face. Nevertheless, tensile stresses are being predicted where cracking is expected to occur.

99. As mentioned earlier, the use of air elements might need to be reconsidered or adjusted. The use of air elements produced rapid changes in the environment inside the culvert and gallery which seem to be unrealistic.

### Verification of Results

100. The maximum stress indicated compares well with studies previously done by the Waterways Experiment Station (WES) and Barry Fehl of the St. Louis District Corps of Engineers (Fehl 1987, Norman, Bombich and Jones 1987). WES analyzed the main lock chamber at Melvin Price Locks and Dam that has the same configuration but slightly different dimensions and lift arrangements. Fehl analyzed a structure of similar shape and dimension (resembles the chamber lock with lifts 6-8 removed). WES used ABAQUS to perform their study and also their own finite element code, WES2DT.

101. Certain quality control procedures were made to verify the performance of ABAQUS. One quality control method was to check element (internal) equilibrium and to check that the sum of the applied forces are equal but opposite to the sum of the reaction forces (external equilibrium). Figures 123 and 124 show the stress distributions at the bottom of the stem (bottom of lift 5) just prior to when the next lift is placed for load case 3. This location was selected because of ease in checking equilibrium since it is statically determinate and also because it shows the effect of thermal loads and eccentrically applied forces. Table 7 shows the results for the equilibrium check. Note that, for determining the actual force resultant across the cut, a linear stress distribution was assumed for ease of calculation.

102. Looking at Figure 123, the stress distribution at 25 days (structure complete up to lift 5) is symmetric, as would be expected, and is the same as that for an unrestrained slab. As lifts are progressively added, the value of the tensile force decreases at the wall surface since more weight is being added. Also, note that the value of the tensile force on the left face drops more quickly since the load is eccentric, thus producing a bending situation. At 62 days, the stresses are redistributed due to creep and shrinkage but the effects of the thermal loads are still apparent.

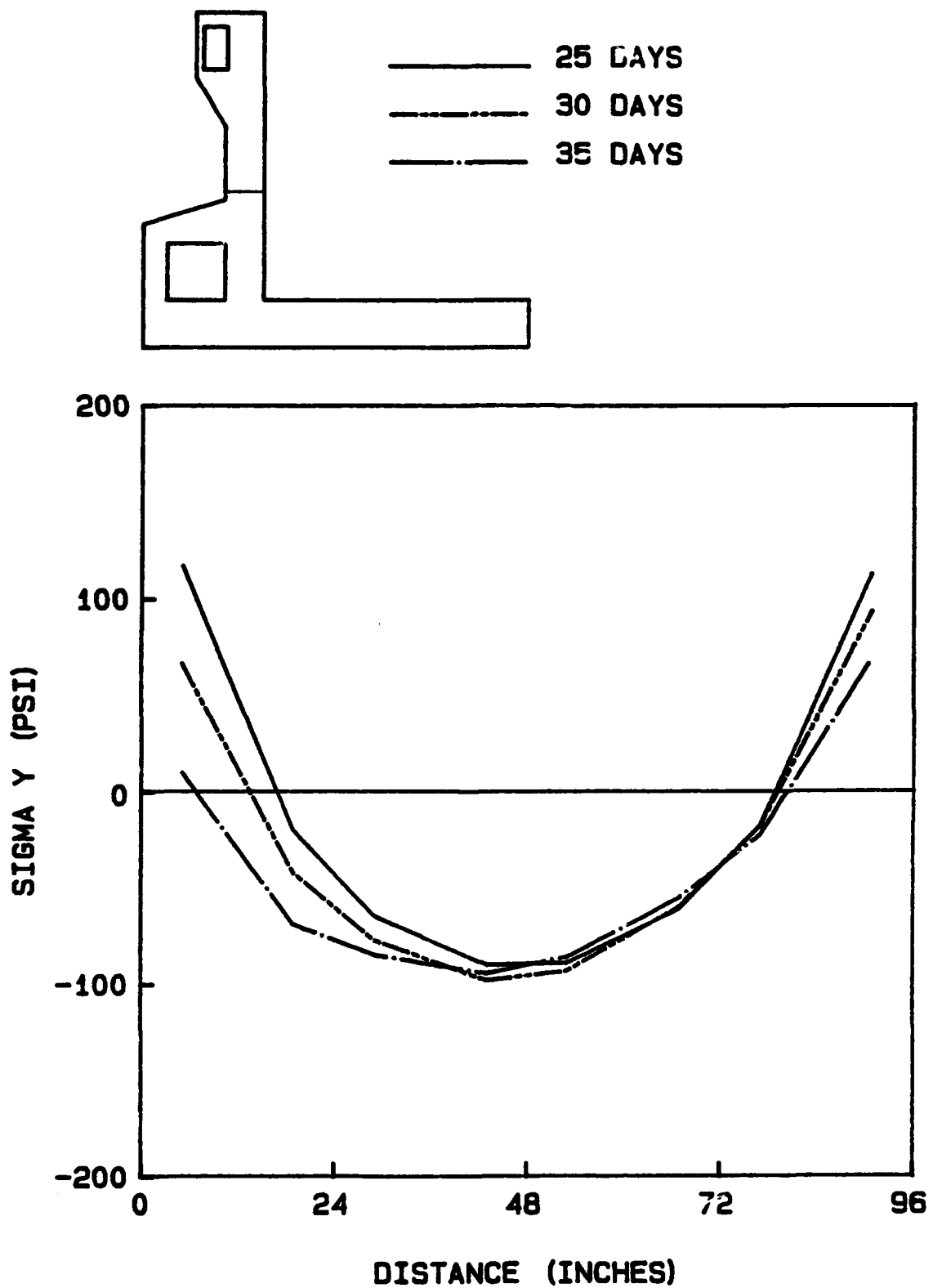


Figure 123. Stress distribution for load case 3

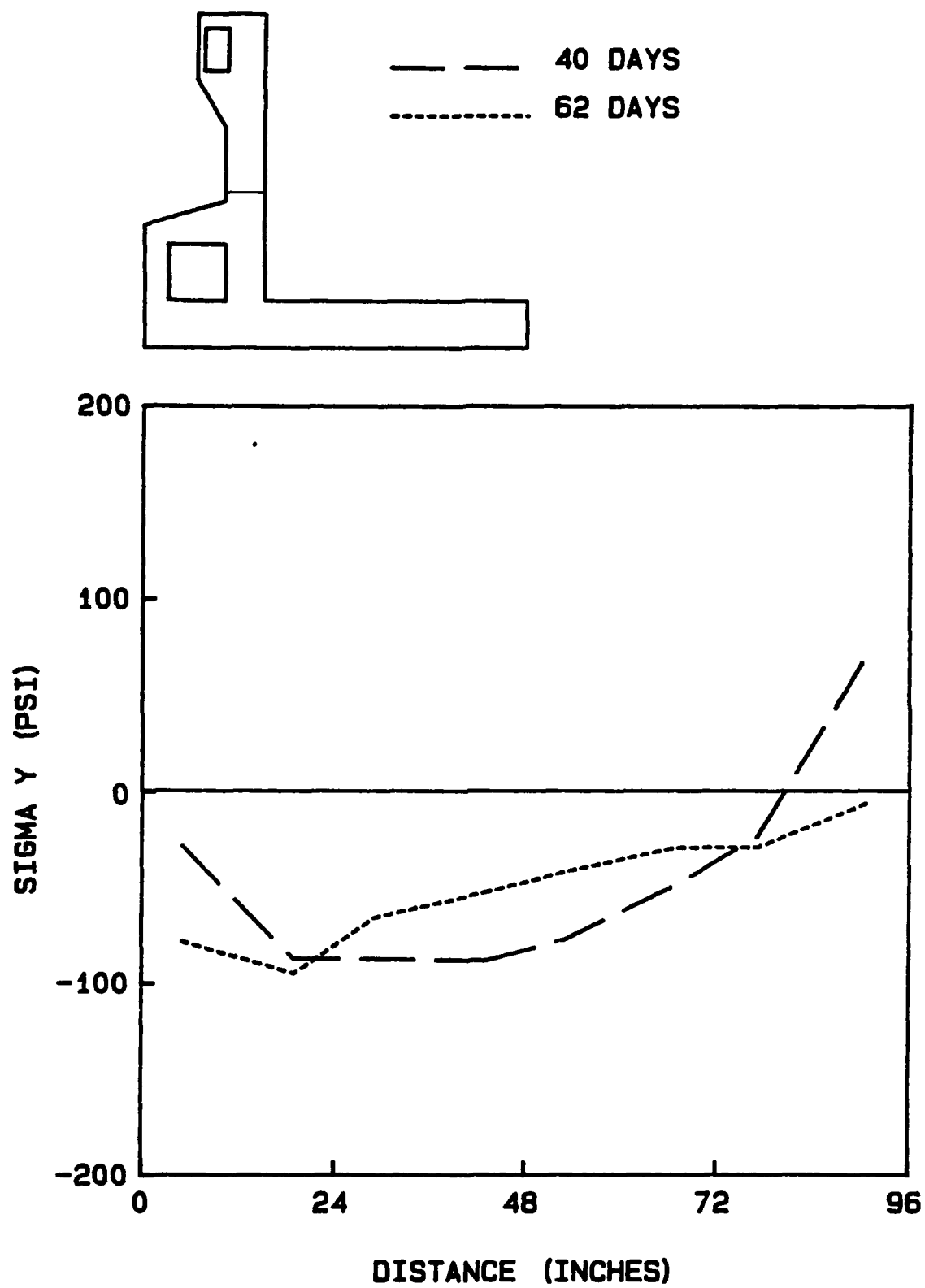


Figure 124. Stress distribution for load case 3

103. The results in Table 7 show that internal equilibrium is satisfied. The largest difference between the internal force and externally applied force is 8.4 percent at 25 days which is below the acceptable 10 percent. The results at later times are within a few percent.

104. External equilibrium was checked for load case 3 at service loads. Because the soil elements are removed, the calculations are simple as only the spring forces and the reaction forces at the center line need to be summed and compared with the sum of the applied forces. The results are shown in Table 8 and indicate external equilibrium is satisfied. Thus, the equilibrium checks are satisfied and the results from the analysis can be accepted with confidence.

## PART IX: MODELING FOR MONOLITH AL-3

### Introduction

105. Most of the modelling parameters for AL-5 are identical for AL-3. The cement type, file coefficients, and finite elements used are the same for both monoliths. Monolith AL-5 was used to fine tune the procedure and parameters for the analysis of AL-3, but several other studies were performed relative to AL-3 such as determining the required soil depth and the use of concrete-soil interface elements.

### Finite Element Mesh

106. The finite element mesh and element used in the heat transfer and stress analyses are shown in Figures 125 and 126. The mesh layout is controlled by (a) the geometry of the structure, (b) the lift heights, and (c) the maximum size of the elements as dictated by Equation 2. For the concrete, the maximum element size was satisfied in both directions. However, for the soil, the maximum was exceeded in the direction perpendicular to the heat flow--that is, the horizontal direction. Stretching the element sizes in the horizontal direction to an aspect ratio of as large as 2:1 was verified, as mentioned earlier.

### Soil Depth

107. For the heat transfer analysis, including a layer of the soil is essential. It was thought that, to save computing time, one could replace the soil with a heat transfer coefficient. However, after the investigation of several values, it was concluded that a conduction coefficient could not reflect the effect of the heat exchange between the soil and the concrete.

108. Having decided to include the soil, the soil depth and its initial temperature were developed. The investigation is based on "how far" below the surface temperature fluctuations occur and on the effects of changing the depth of the soil on the temperature rise at the base of the slab.

109. Norman, Bombich, and Jones (1987) stated that the temperature of the soil is stationary at a depth of 20 ft. However, with the imposed

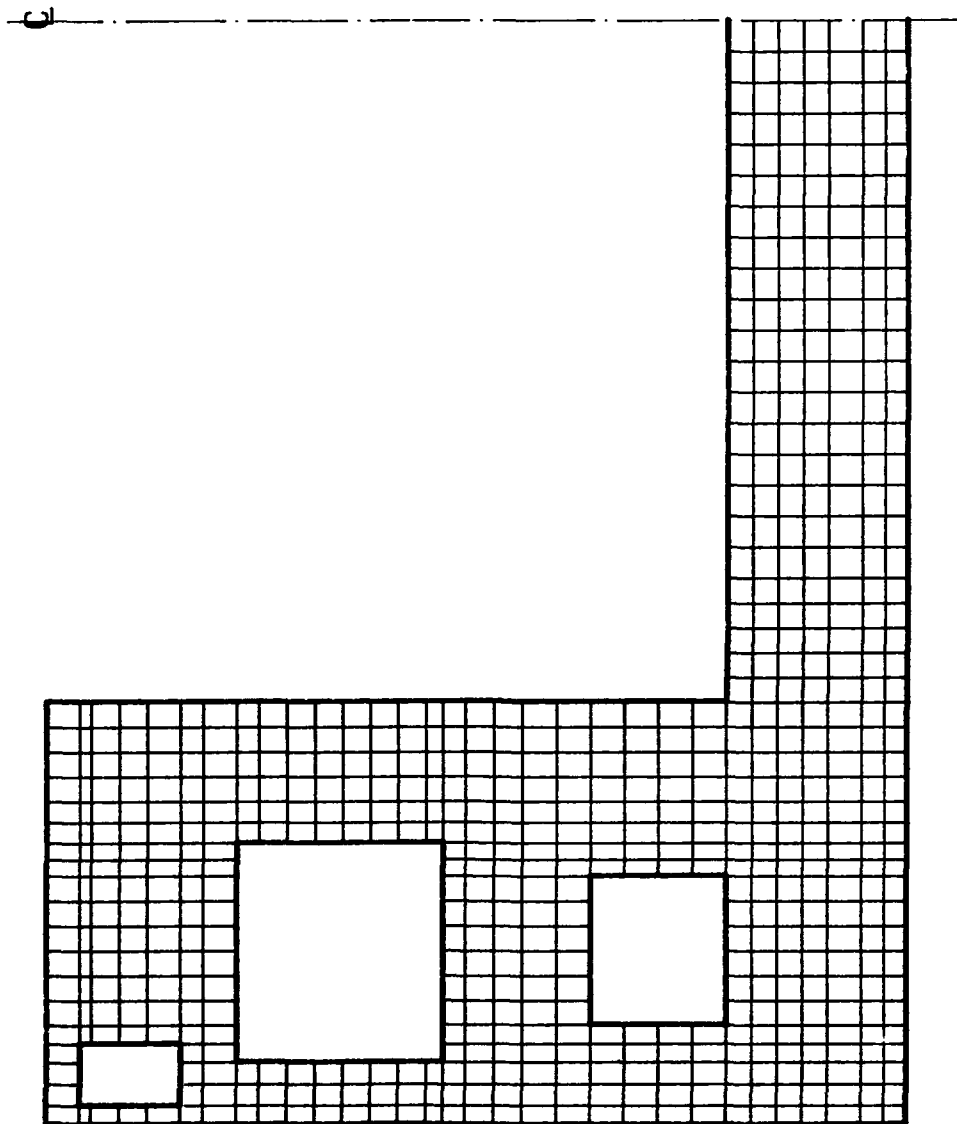
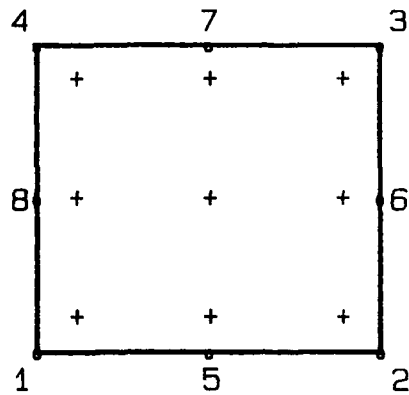
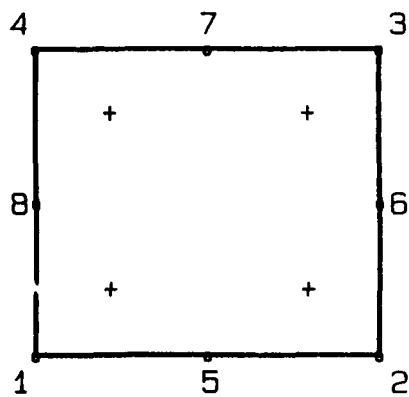


Figure 125. Finite element mesh for monolith AL-3



Element Used For Heat Transfer Analysis  
 (+ is the location of the gauss integration points)



Reduced Integration Point Element Used For Stress Analysis

Figure 126. 8-Node elements used in the heat transfer and stress analysis

restrictions on element size, it is clear that the required number of elements will be too large. With the mesh as shown in Figure 125, reducing the soil depth from 20 ft to 10 ft amounts to about 20 percent savings in the overall number of elements. Two cases were investigated. Case 1 investigates only the temperature distribution within the soil; whereas, case 2 considers the addition of an 18-ft slab.

110. A transient heat transfer analysis was conducted on two models; the first having 10 ft of soil and the other 20 ft. The width in both cases is 20 ft. Each block is exposed to the ambient temperature for a period exceeding 1 year. The boundary conditions used are such that there is heat exchange at the top of the soil and no heat flow on either side of the soil block. The heat exchange between the ambient air and the soil is simulated by a heat transfer coefficient equal to  $0.6792 \text{ (Btu/day.in.}^2\text{°F)}$ . At the bottom of the soil, the temperature of the soil was first fixed at  $55^\circ \text{ F}$  and secondly allowed to vary to provide thermal continuity.

111. The results shown in Figures 127 and 128 provide a good check for the accuracy of the solution. The contours in Figure 127 are all flat proving the continuity of the soil in both directions. On the other hand, the temperature versus time plot shows that the temperature at the top of the soil follows closely the ambient air temperature. As the depth of the soil increases, the curves tend to lag behind, as expected. The curves of Figure 128 show temperature fluctuations within the soil. As the depth increases, the curves tend to flatten out and decrease in amplitude making the differences between the curves almost negligible. For instance, the difference between curve A (top surface) and curve B (5 ft deep) is about 15 deg; whereas, the difference between curve D (15 ft deep) and curve E (20 ft deep) is only about 1 deg. The primary purpose of the above comparison is to have a better understanding of the temperature fluctuations within the soil and to be able to select an acceptable depth.

112. Although the above history plots dealt with the 20-ft layer of soil, the distribution plot shown in Figure 129 compares the temperature distribution within the 20- and the 10-ft soil models. The curves are very close and the difference is considered to be within an acceptable tolerance.

113. Both of the above mentioned observations are preliminary but were not convincing enough to conclude use of 10 ft of soil instead of 20 ft. It

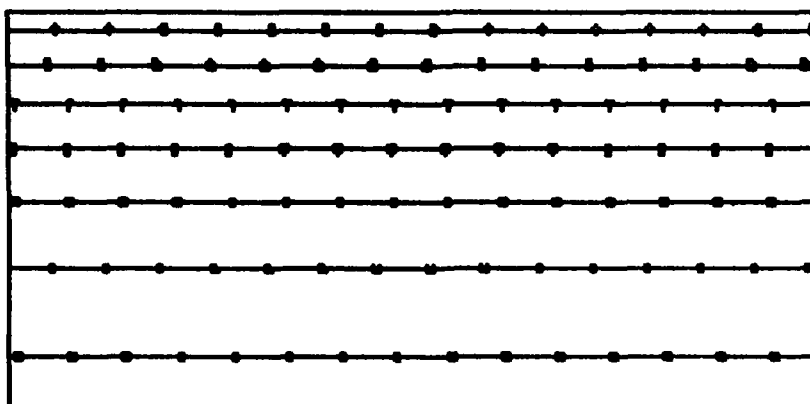


Figure 127. Soil temperature contours, 1 July

is still necessary to investigate the effects that changing the depth of soil has on a concrete slab.

114. To determine the effect of decreasing the soil depth on the lock monolith, an 18-ft slab is added to the previous soil models. The concrete slab consists of two 9-ft lifts. All of the parameters, material properties, and the boundary conditions are the same as the ones used in the transient heat transfer analysis of the lock monolith. Nodal temperatures at some of the typical locations are shown in Figures 130-133 up to an elapsed time of 10 days. The curves lie on top of each other and the difference between using 20 ft and 10 ft of soil is within one-tenth of a degree. The 10-day period covers the critical time, where the maximum temperature and high temperature gradients are found. The lift heights used in the analysis were 9 ft which is considered to be high for a lift close to the foundation. In practice, lift heights near the foundation do not exceed 5 ft. Therefore, the lift heights were cut in half, to 4.5 ft. The results of the analysis are not shown here, but there was no noticeable difference between the two cases.

115. Even though the heat transfer analysis of the soil alone showed a small difference between the use of 10 ft and 20 ft, the addition of the concrete slab showed that the effect of that difference on the concrete is very minor. With this, it was decided that the 10 ft of soil produces nearly identical results as the 20 ft. The conclusion was generalized to the analysis of the monolith, since it has been demonstrated that the difference is minor and only effects the base of the slab.

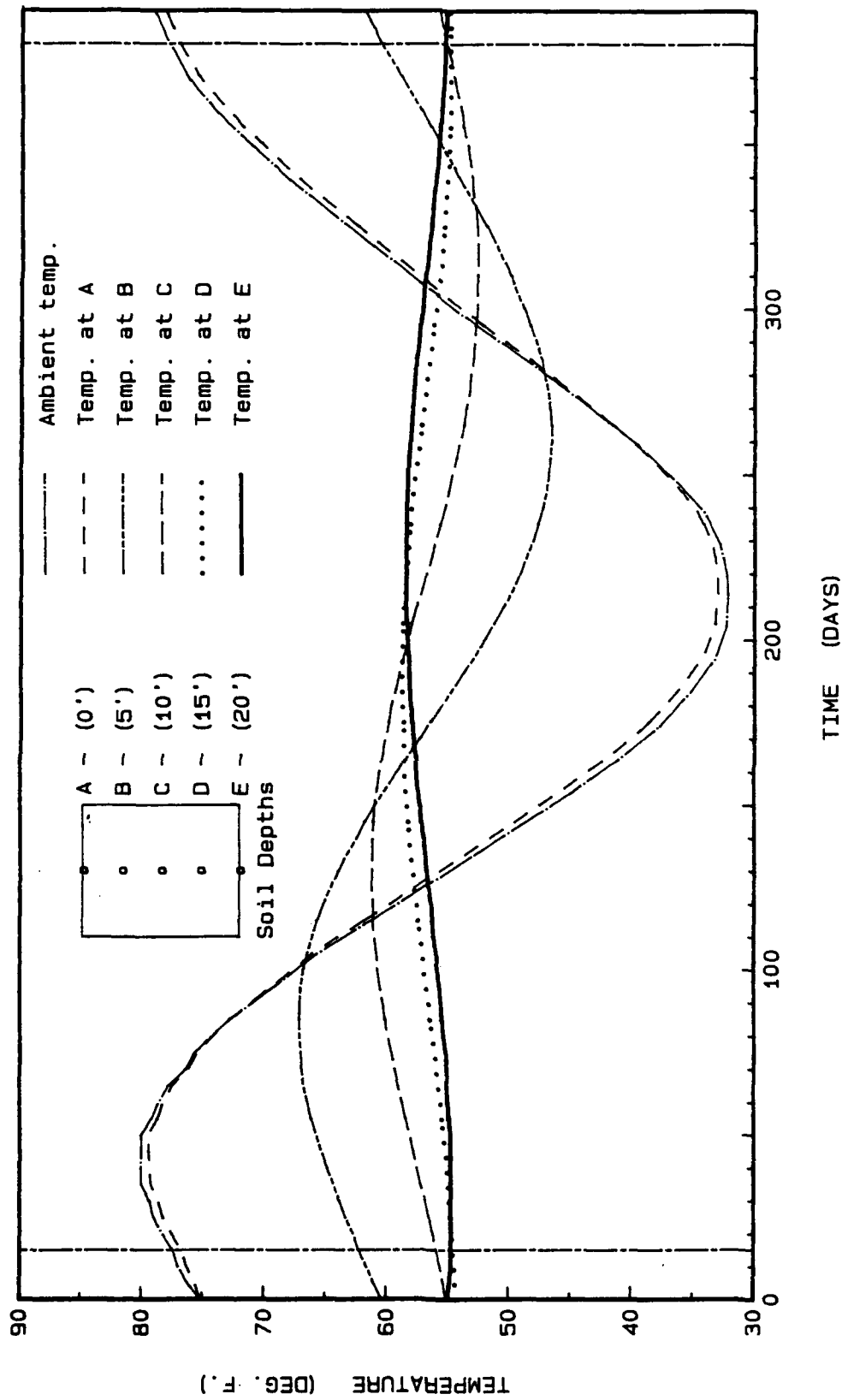


Figure 128. Temperature history at various depths for a 20-ft layer of soil

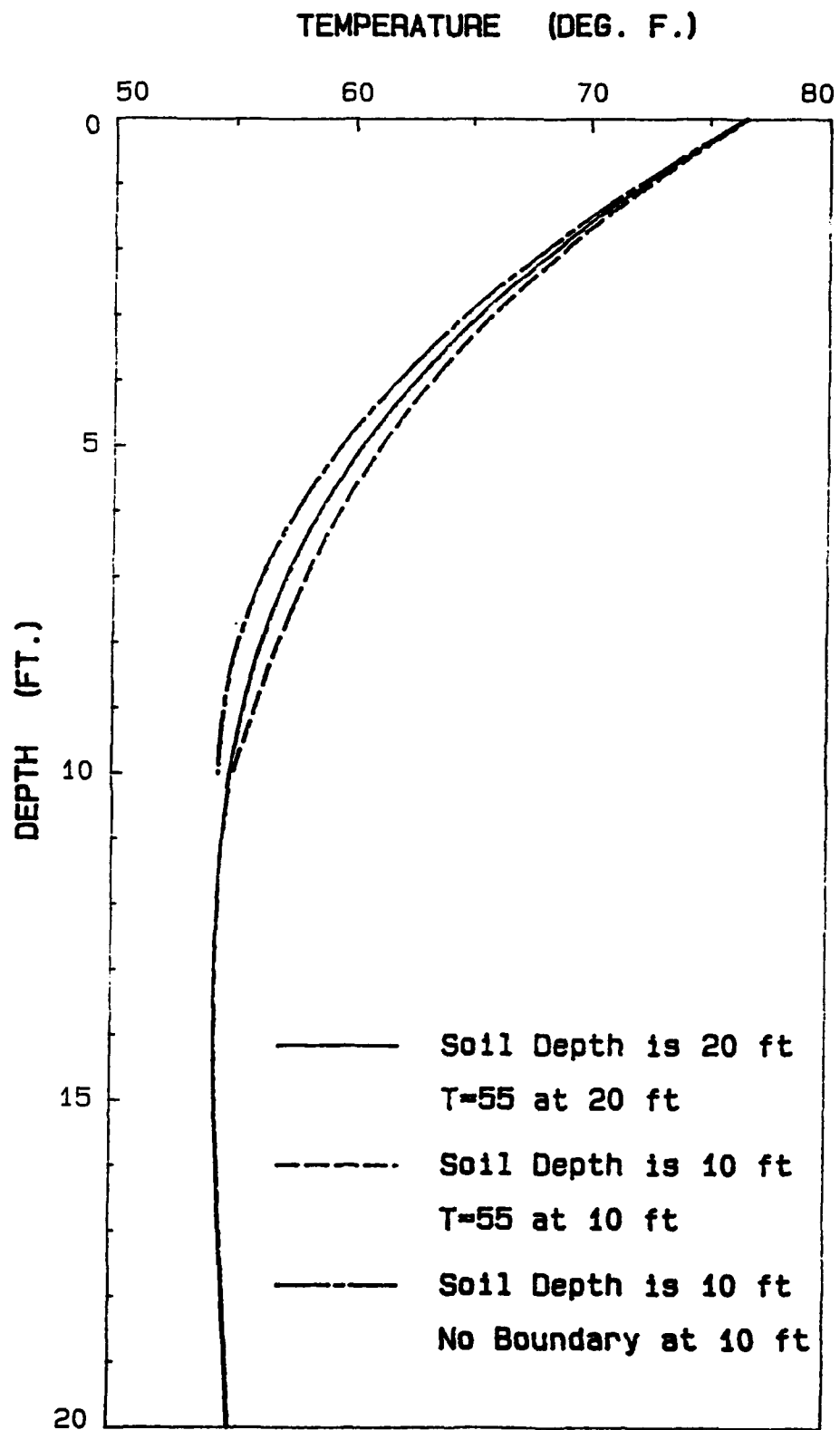


Figure 129. Soil temperature distribution, 1 July

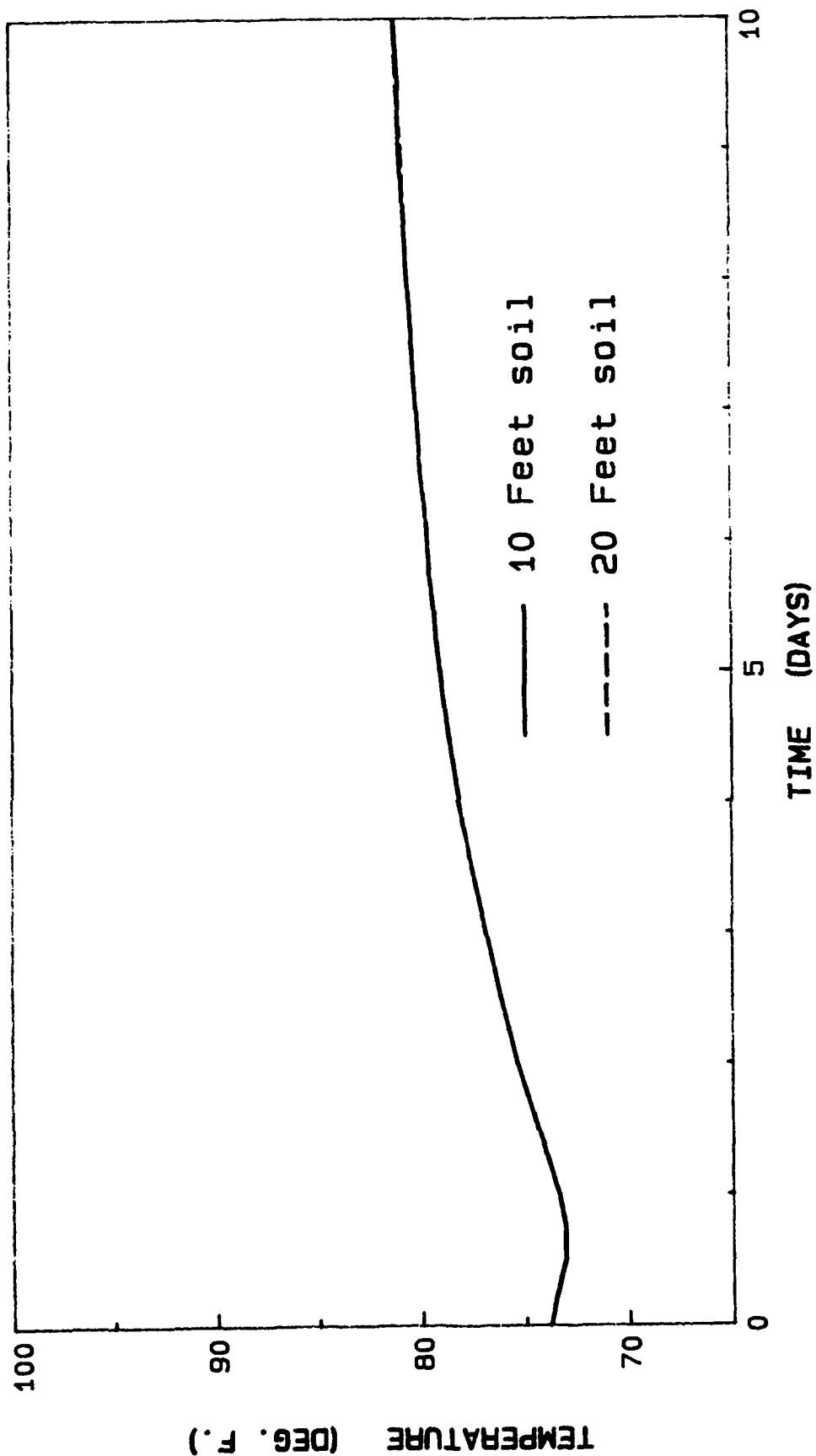


Figure 130. Temperature history 7.5 in. below the bottom of the slab

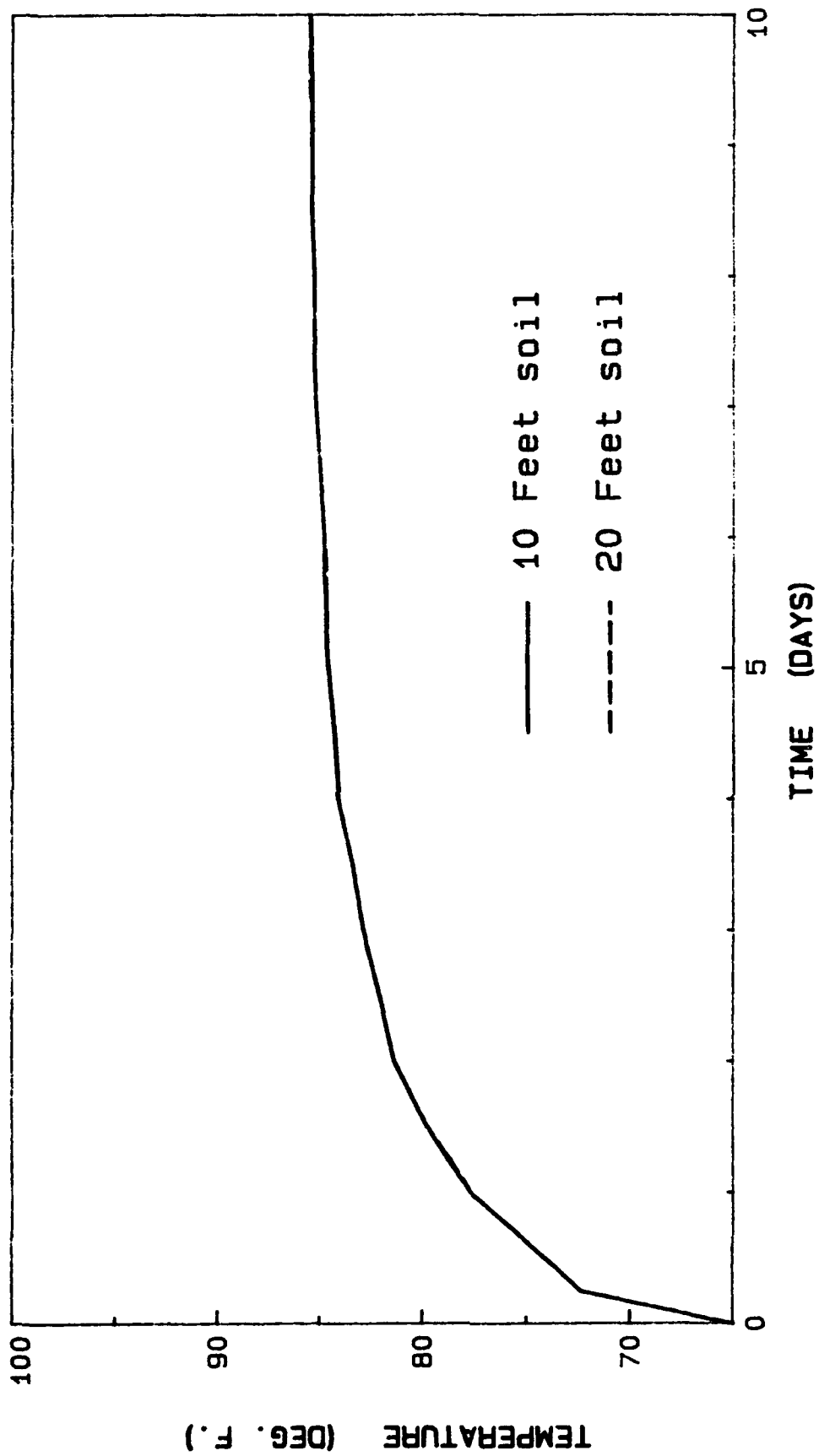


Figure 131. Temperature history at the bottom of the slab

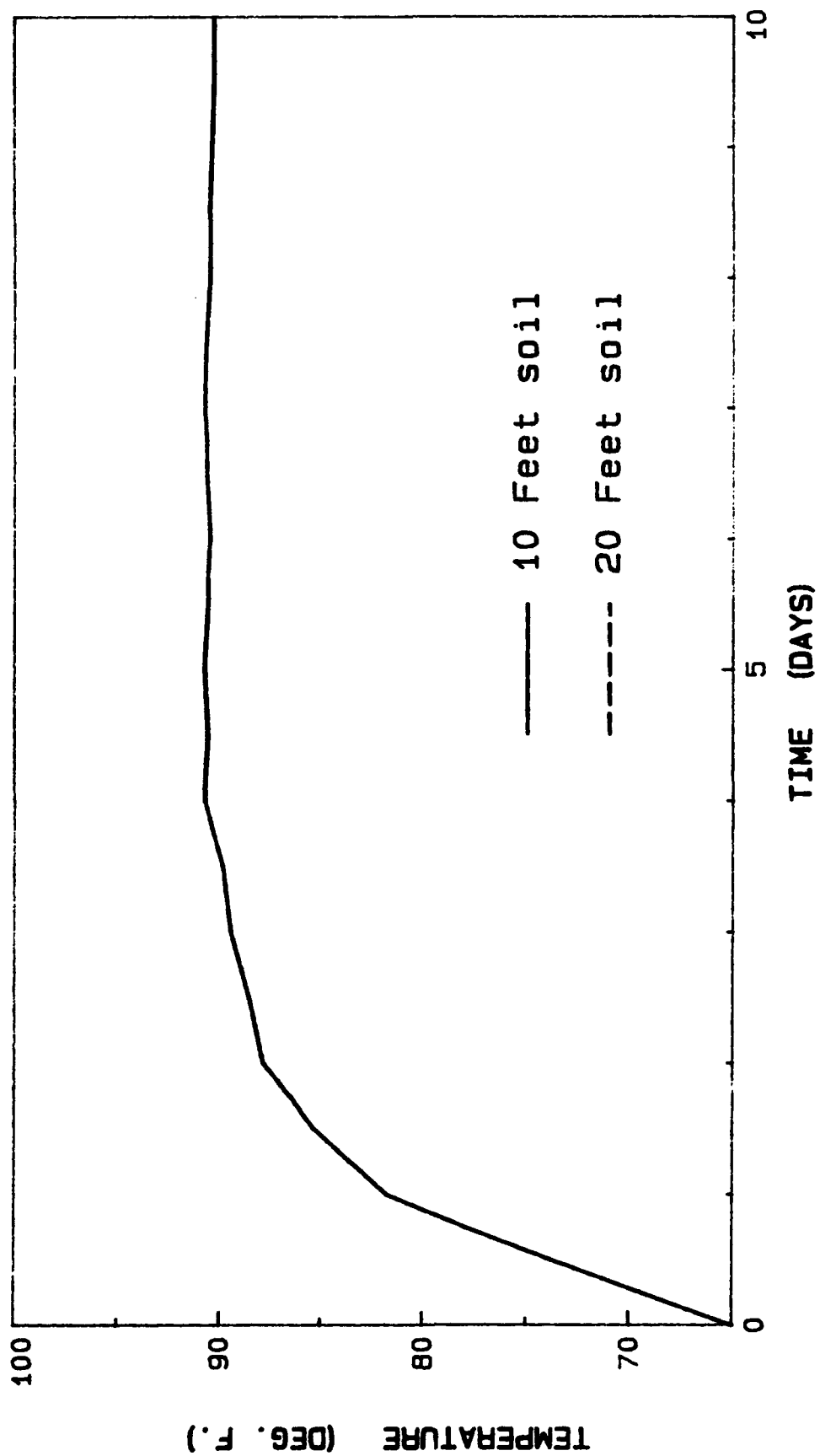


Figure 132. Temperature history 13.5 in. from the bottom of the slab

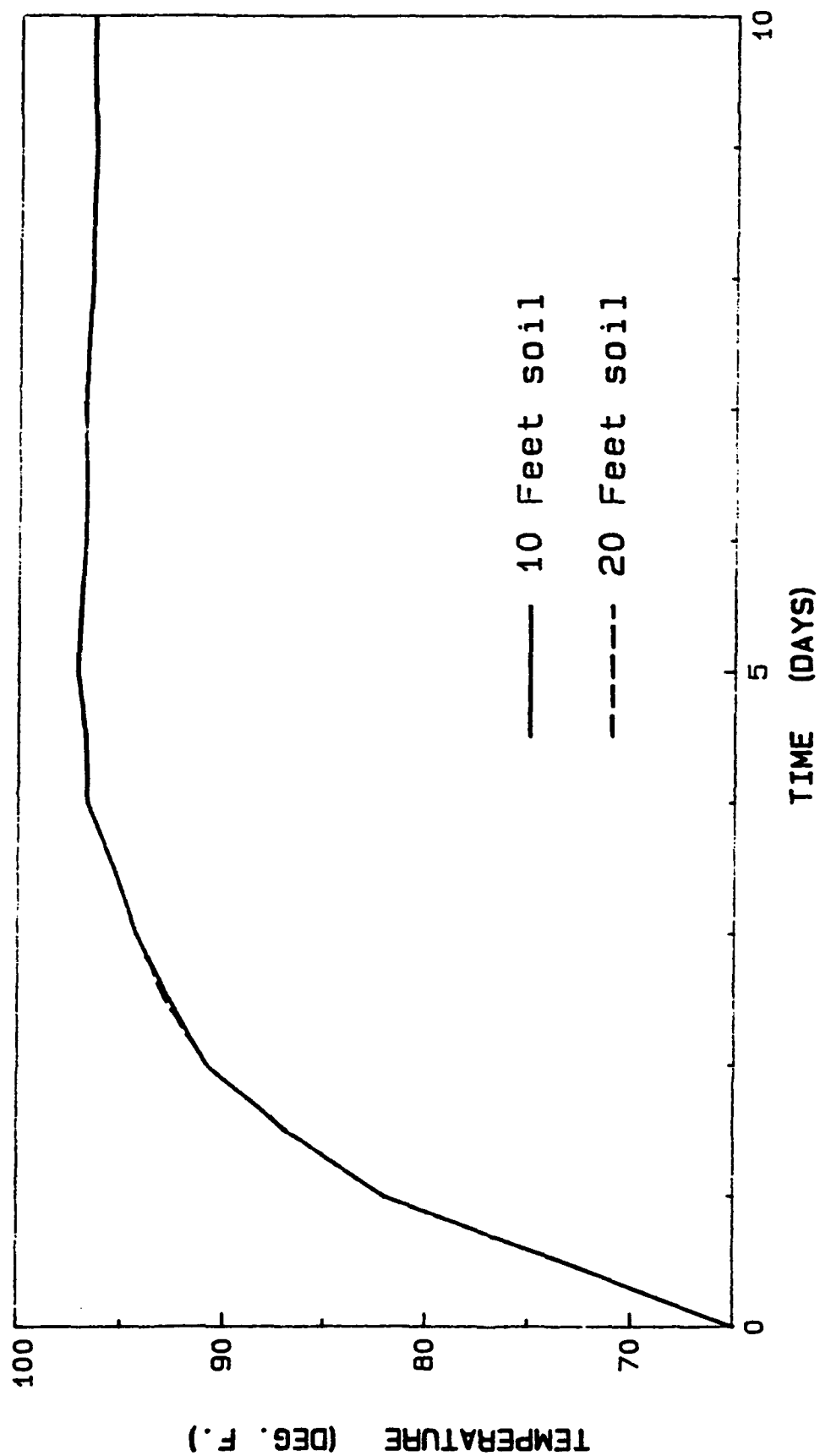


Figure 133. Temperature history at mid-lift 1

### Initial Soil Temperature Distribution

116. To determine the initial temperature distribution of the soil, the previous model used to compare the two soil widths was used. A heat transfer analysis over a year's time was performed to make sure that the temperature stabilizes and the initial offsets vanish. The output temperatures of the transient heat transfer analysis corresponding to 1 July are extracted (Table 9 and Figure 134).

### Concrete - Soil Interface

117. Shown in Figure 135 is the soil-concrete interface. The common nodes a, b, and c can only belong to one of the materials. ABAQUS has available what is called interface or gap elements. They are connecting elements that help the user separate the two surfaces and model the heat exchange between them through the use of a gap conductance. A second variable is the gap closure which is zero for full contact between the two surfaces.

118. To find the proper value of the gap conductance and justify the use of the interface elements, a transient heat transfer analysis was conducted on an 18-ft slab. Three cases were investigated to compare the solutions with and without the interface elements and to determine the effect of changing the gap conductance on the heat exchange between the two surfaces.

119. The model used to determine the range of the values of the gap conductances consists of an 18-ft slab and 10 ft of soil. The finite element mesh is shown in Figure 136. The initial temperature of the soil is equal to the 1 July temperature distribution as given previously. The concrete is placed at 65° F and the temperature of the ambient air is kept constant at 70° F. The material properties are as used in the analysis of the monolith AL-5.

120. The first value of the gap conductance is equal to 0.01 (Btu-in./in.<sup>2</sup> day °F). As expected, this value, being very small, acted as an insulator and did not allow much exchange between the two bodies. The gap conductance is then increased to 200, 1,000, and finally 10,000 (Btu-in./in.<sup>2</sup> day °F). The results were then compared to select a suitable range for the gap conductance. Looking at the nodal temperatures, the difference between the 200 and the 1,000 temperatures was less than 3 percent. On the other

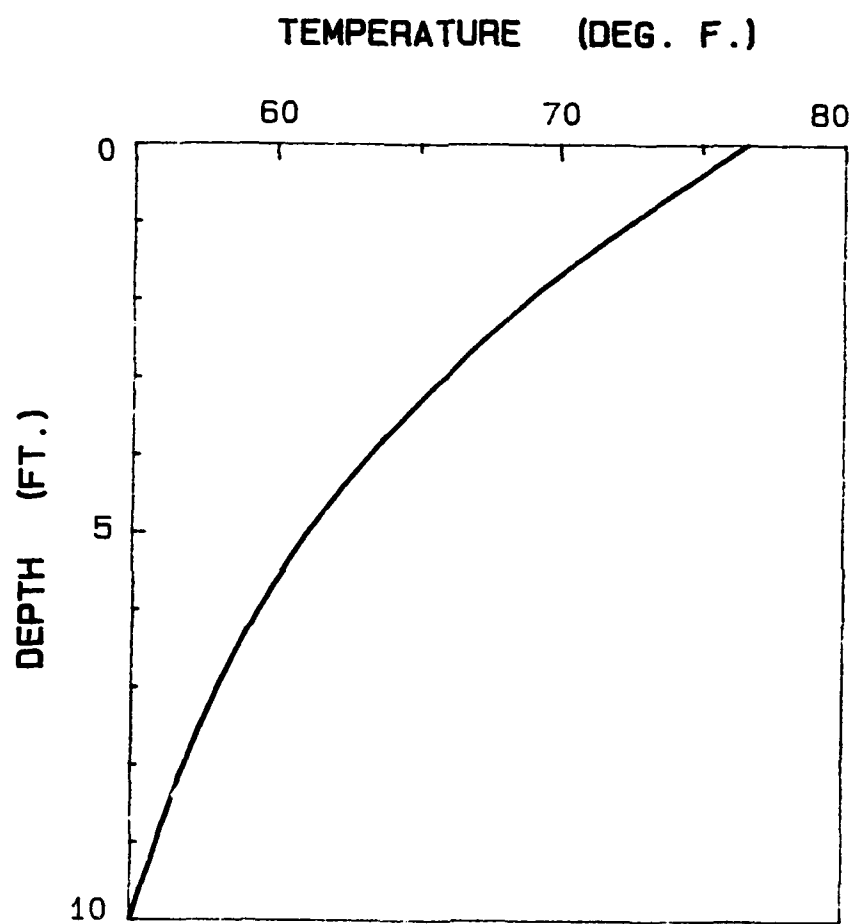
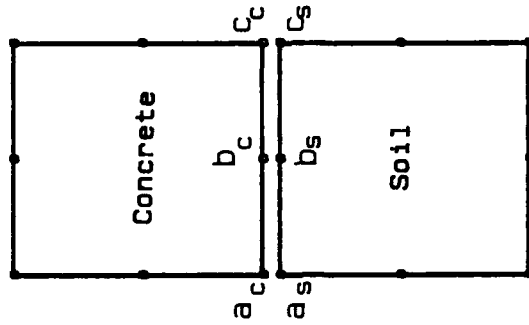
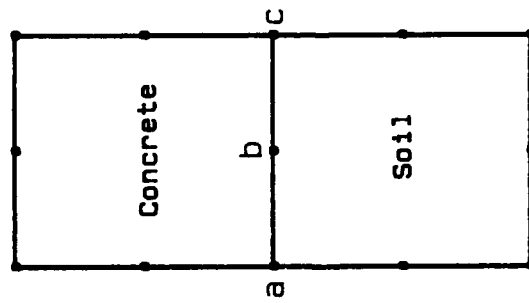


Figure 134. Soil temperature distribution used for the transient heat transfer analysis



(a) Without an interface element, both materials share the nodes a, b and c  
 (b) The materials are separated and the heat exchange is through the interface elements

Figure 135. Soil and concrete elements at interface

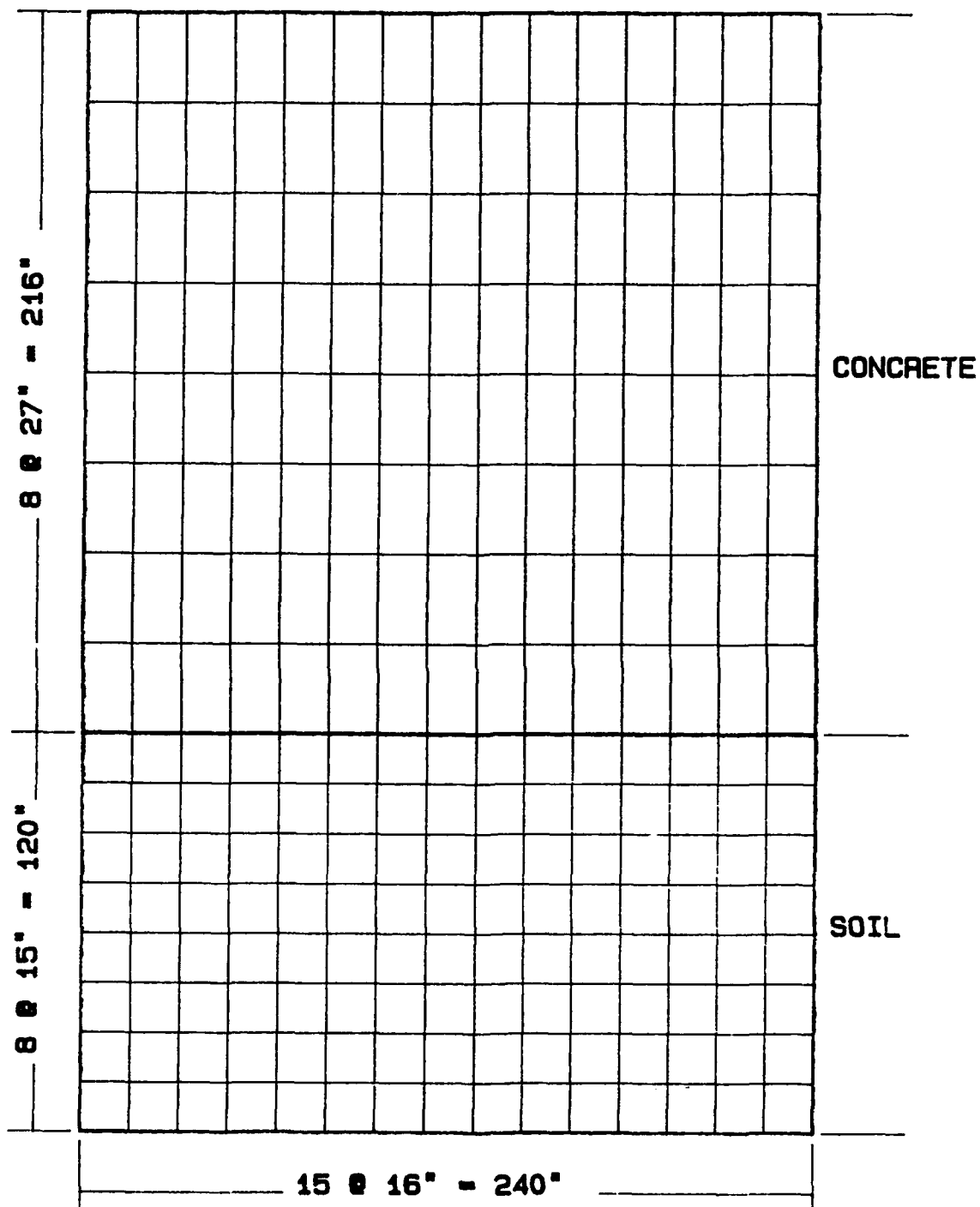


Figure 136. Finite element model used in the interface element study

hand, there was no difference between the 1,000 and the 10,000 values. With the comparisons of the above three cases, one concludes that any gap conductance larger than 200 can be used to simulate a free heat exchange between the concrete and the soil. A value of 1,000 (Btu-in./in.<sup>2</sup> day °F) was used in this study.

121. To determine the effect of the interface elements on the solution, a transient heat transfer was conducted on an 18-ft slab. All of the input parameters are the same as in the soil study. Three cases are presented. The first two cases have the same lift heights but different initial soil temperatures; whereas, the third case has more shallow lift heights.

122. In the first case, the lift heights were 9 ft and the soil initial temperature was that of 1 July. Several of the nodal temperatures around the interface are shown in Figures 137-140. The maximum difference is about 3° F occurring at the bottom of the slab at an elapsed time of 0.5 days. This first jump creates an initial offset between the two curves. The offset is a result of the larger difference between the soil and concrete initial temperatures when the interface elements are used since, with the latter, the user assigns separate nodes to the different materials. For instance, the actual initial temperature at the top of the soil is 76° F which acts as a source of heat to the adjacent concrete producing a sudden rise in the concrete temperature. On the other hand, without the use of the interface elements the user is obliged to assign one initial temperature to the common row of nodes which is 65° F in this case.

123. In case two, the initial temperature of the soil was chosen so that it was about 10° lower than the concrete initial temperature. A 1 May temperature distribution was used. The results are very much like the previous case except, at this time, the heat is driven into the soil since it is cooler than the newly placed concrete.

124. In the third case, the lift heights are changed to 4.5 ft each while the initial temperature was that of 1 July. The results show similar temperature differences as the previous two cases. Like in the previous cases, these differences, which are seen only close to the boundary between the soil and concrete, seem to diminish as time increases.

125. The results showed higher temperature drops when the interface elements were used; however, these temperature drops were localized. They occurred within the first day and close to the interface of the soil and the

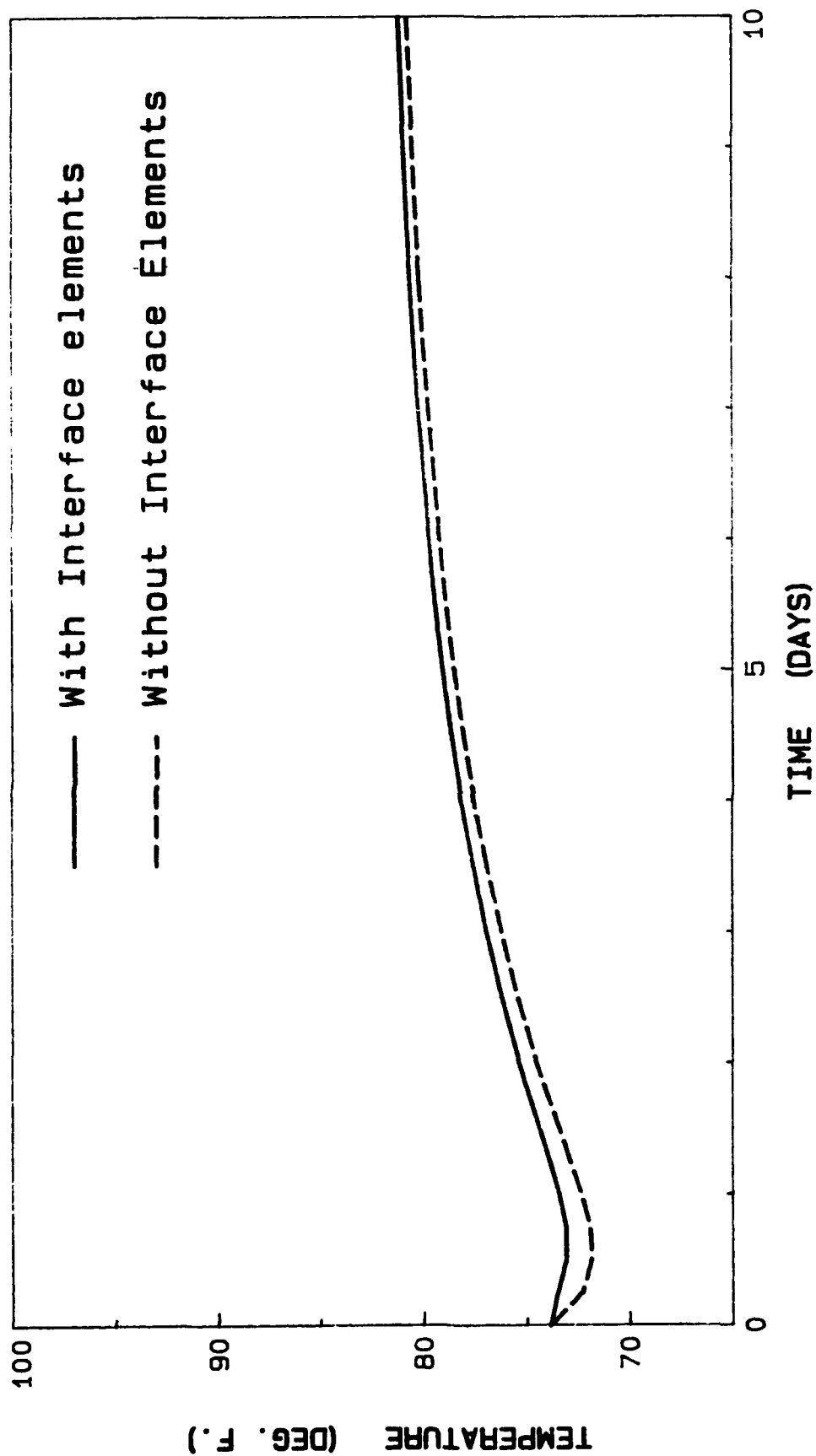


Figure 137. Temperature history at 7.5 in. below slab

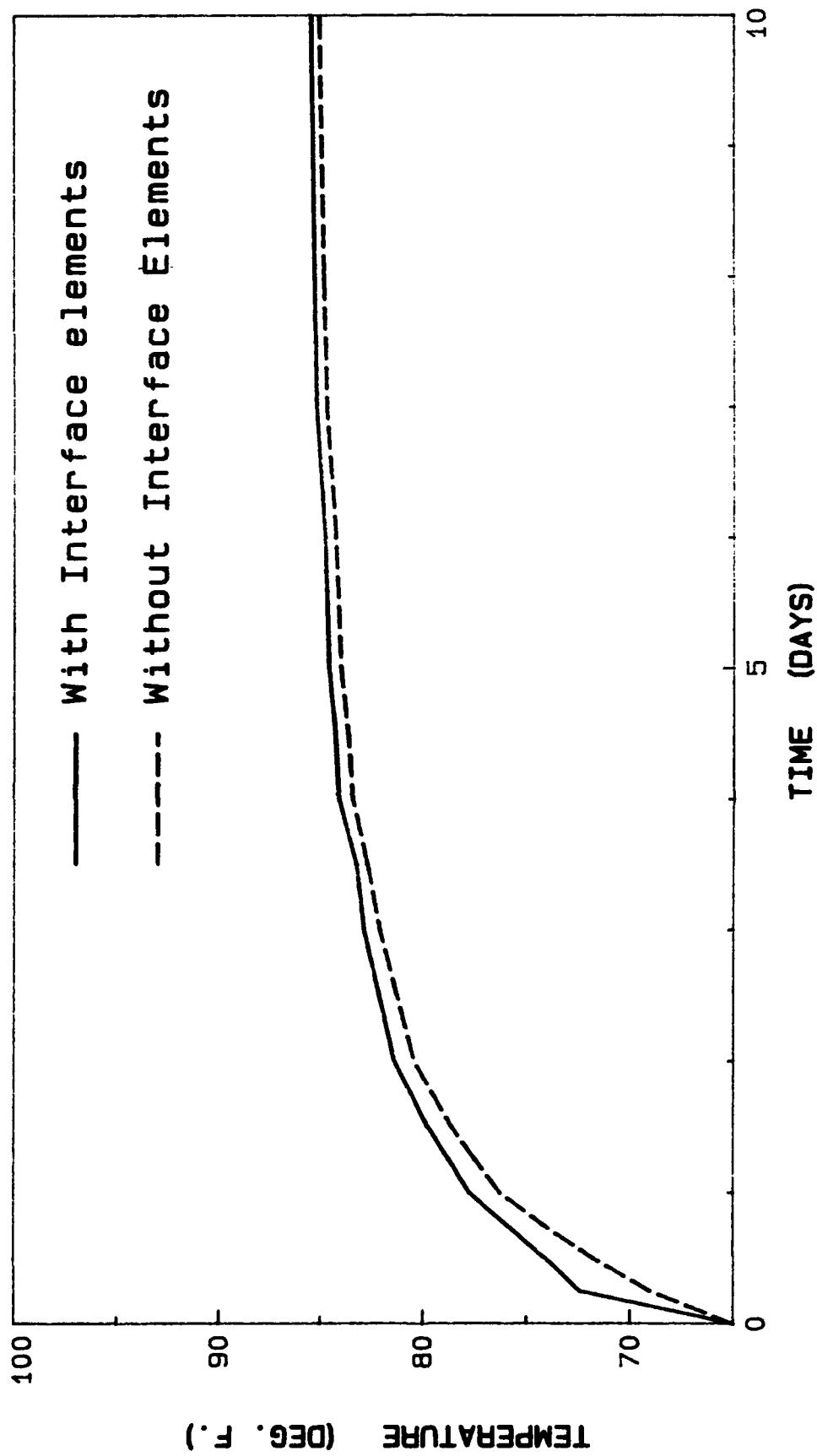


Figure 138. Temperature history at the bottom of the slab

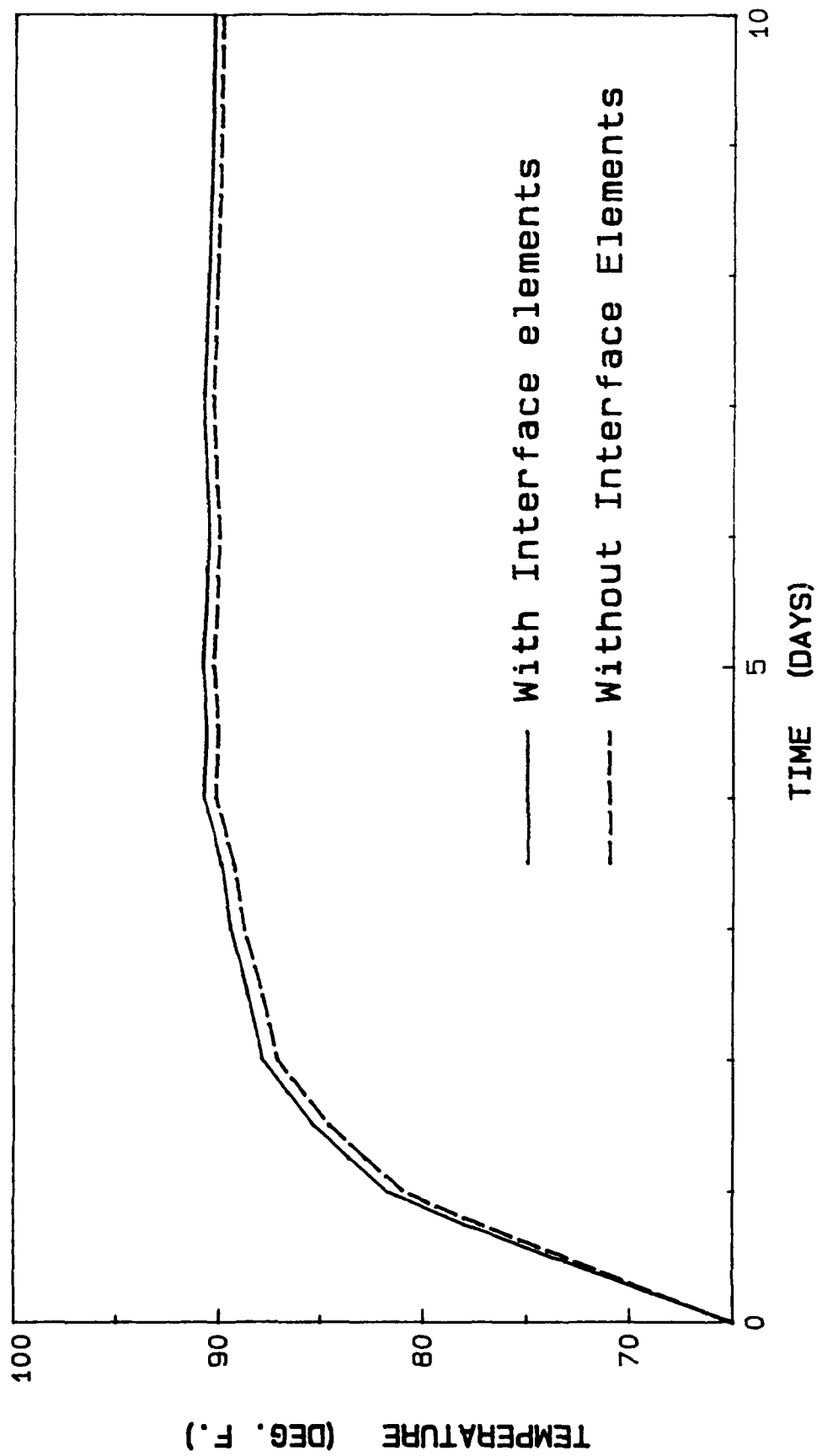


Figure 139. Temperature history at 13.5 in. from the bottom of the slab

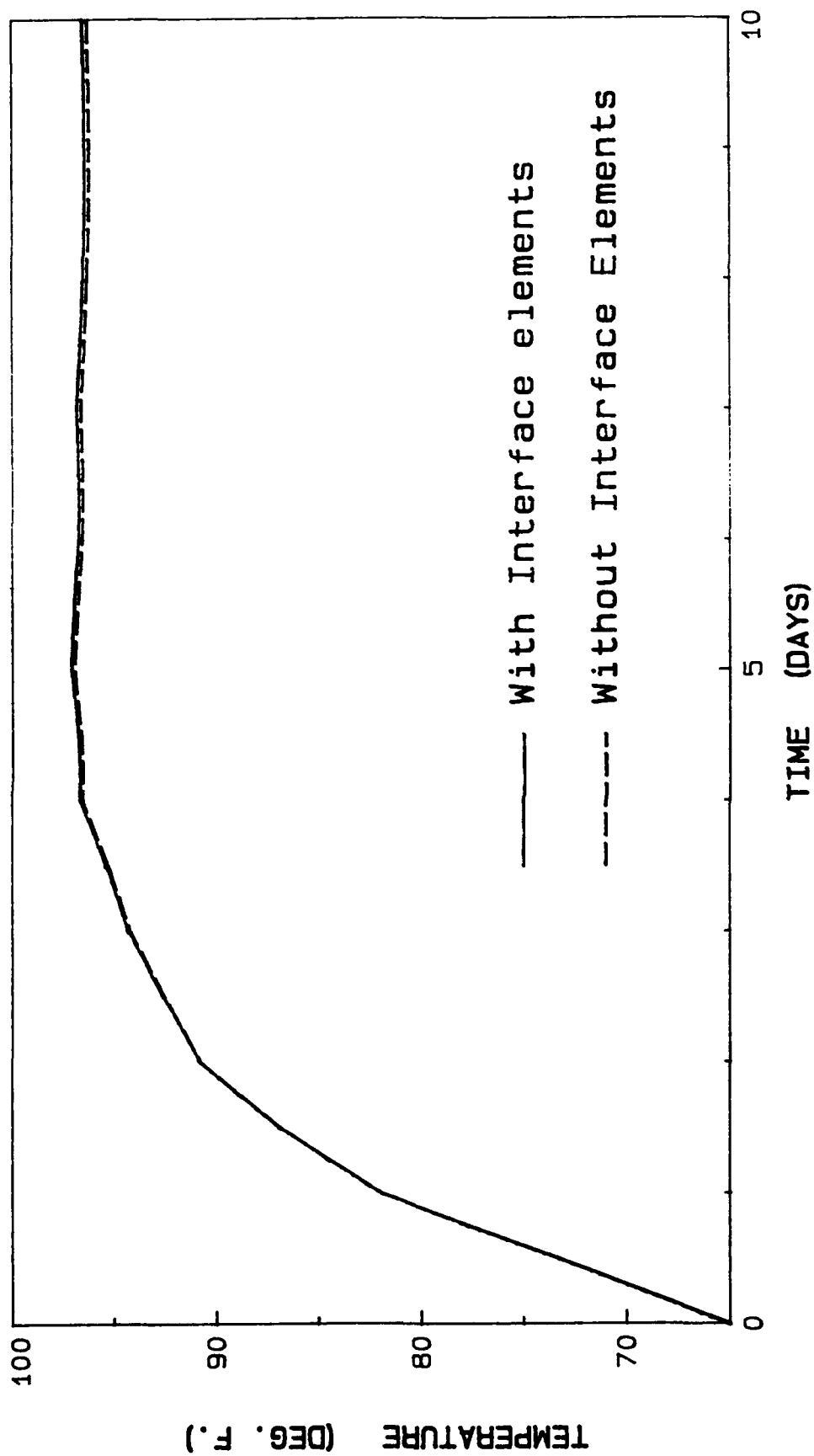


Figure 140. Temperature history at mid-lift 1

concrete. Thus, for very large massive concrete structures, where one is interested in locations away from the support or interface or at a later time, the interface elements are optional and omitting them may save some computing effort.

126. However, in this study, all the transient heat transfer solutions use interface elements between the soil and the concrete. Besides giving the user better control over the input, the interface elements are thought to give a more realistic and better model for the heat exchange between the soil and the concrete.

### Lift Heights

127. For the construction of monolith AL-3, two lift schedules were provided by the US Army Corps of Engineers, St. Louis District. Configuration one, composed of 16 lifts, is shown in Figure 141. It is based on an average lift height of 5 ft. In the slab, the lift heights range from 3 to 4.5 ft; whereas, in the walls, where the sections are relatively thin, the lift heights are as high as 6 ft. The second arrangement has only 11 lifts as shown in Figure 141, which was a means for saving approximately \$700,000 in construction costs (US Army Corps of Engineers, St. Louis District 1988)). This arrangement allows lift heights as large as 12 ft, eliminating construction joints and decreasing construction time.

### Heat Transfer Analysis

128. For the transient heat transfer analysis conducted for this study, the time interval between lifts is kept constant at 5 days. The forms were considered to be removed at 2 days after the lift was placed. These are very optimistic estimates, but were used since these times should produce the highest temperature gradients.

129. Figure 5 shows the mean ambient temperature corresponding to the site location. The daily fluctuations are ignored to simplify the analysis.

130. Table 10 shows the various surface heat transfer coefficients used in this study. The coefficients are based on a 0.75-in. plywood form and a velocity reflecting the air flow through external surfaces and through open and closed voids like the culvert and the gallery, as discussed earlier.

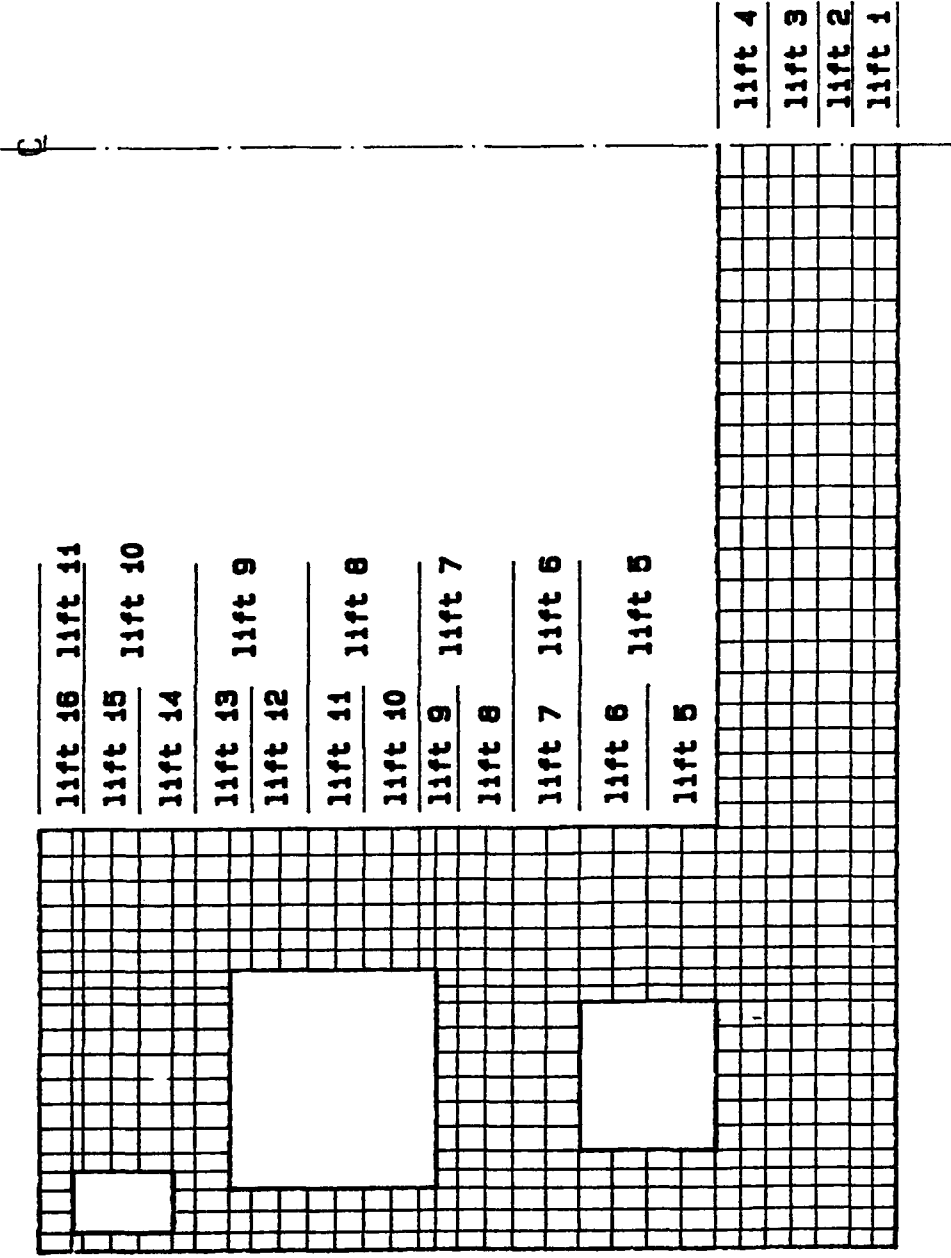


Figure 141. Lift locations for AL-3 (16) and AL-3 (11)

131. Forms are removed after 2 days in all locations except in roof structures like the horizontal top surface of the openings. In these areas, where support is needed, the forms are kept for a period of 7 days through the use of multipoint constraints, MPC's. It should be noted that, in practice, the forms used in most of the openings like the culverts and the galleries are one-piece boxes that are placed at the start of the placement of lifts around the openings and are not removed until 7 days after the opening is closed.

132. The openings are treated like exterior surfaces until they are closed. As shown in Table 10, lower heat transfer coefficients are used after closing because of the low air flow through the openings. Once the lift covering the opening is placed, the opening is then modelled as either closed, where the air elements are activated, or open where heat transfer coefficients are used to define the heat exchange between the concrete and the ambient air. For the monolith under investigation, the machine room, which is referred to as the void, is modelled as being closed with air properties assigned to the enclosed space. On the other hand, the gallery and the culvert are modelled as open since during construction or in service they are assumed to be open with air flowing through them.

133. The properties used in all of the analyses are summarized in Table 11. Lower and upper adiabatic temperature rise curves and heat of hydration curves for two different types of cement, 53 cal/g and 70 cal/g, are shown in Figures 8 and 9. In this study, only the upper adiabatic curve is used for the heat transfer analysis, as discussed in Part IV. The material properties presented here are as provided by the Waterways Experiment Station (Norman, Bombich, and Jones 1987).

### Stress Analysis

134. The stress analysis is dependent upon several of the modelling parameters related to boundary conditions, soil strength, pile stiffness, formwork (MPC), and material properties.

135. The stress related boundary conditions are of two types: (a) symmetry and (b) supports. The symmetry boundary condition is achieved by having rollers along the plane of symmetry. The rollers are free to move vertically but restrained in the horizontal direction. The supports, on the other hand, include the soil, piles, and formwork.

136. At an early age, the freshly placed concrete acts more or less like a liquid. Therefore, full support is needed to control the deflections of the first few lifts. In the case of the first lift, the support is provided through the soil foundation. The piles, on the other hand offer little or no support until the concrete gains strength. Even at later ages, the soil still offers some resistance (approximately 25 percent). Hence, it was decided to include the soil in the two-dimensional model. The soil has a modulus of elasticity equal to 3,000 psi and a Poisson's ratio of 0.35. Along the lower boundary, the soil is supported by hinges placed at every defined node.

137. The location of the piles is shown in Figure 142. For the two-dimensional model, the piles are assumed to be uniformly distributed in the flow direction. Knowing the number of piles, the total stiffness of the piles is converted into a stiffness per inch in the flow direction. In the transverse direction, the piles are moved to the location of the closest node. This is done since ABAQUS only allows piles to be placed at defined nodes.

138. In reference to a technical report published by the US Army Corps of Engineers (Headquarters, US Army Corps of Engineers 1983), the piles can be replaced by springs having lateral and axial stiffnesses as given by the following formulas:

$$\text{Axial Stiffness} = \frac{A E}{L} \quad (7)$$

$$\text{Lateral Stiffness} = C_1 \frac{E I_1}{T_1^3} \quad (8)$$

where  $i$  refers to the local pile axis. For the two-dimensional case, the strong axis is in the direction of flow, hence it is the only axis considered.  $C$  is a pile fixity constant. For a soil with a linearly varying modulus of elasticity and a pile fixity of 100 percent,  $C = 1.075$ .  $E$  is the modulus of elasticity of the steel and equals  $29 \times 10^6$  psi.  $I$  is the moment of inertia of the pile.  $T_1$  is a constant found for this equation:

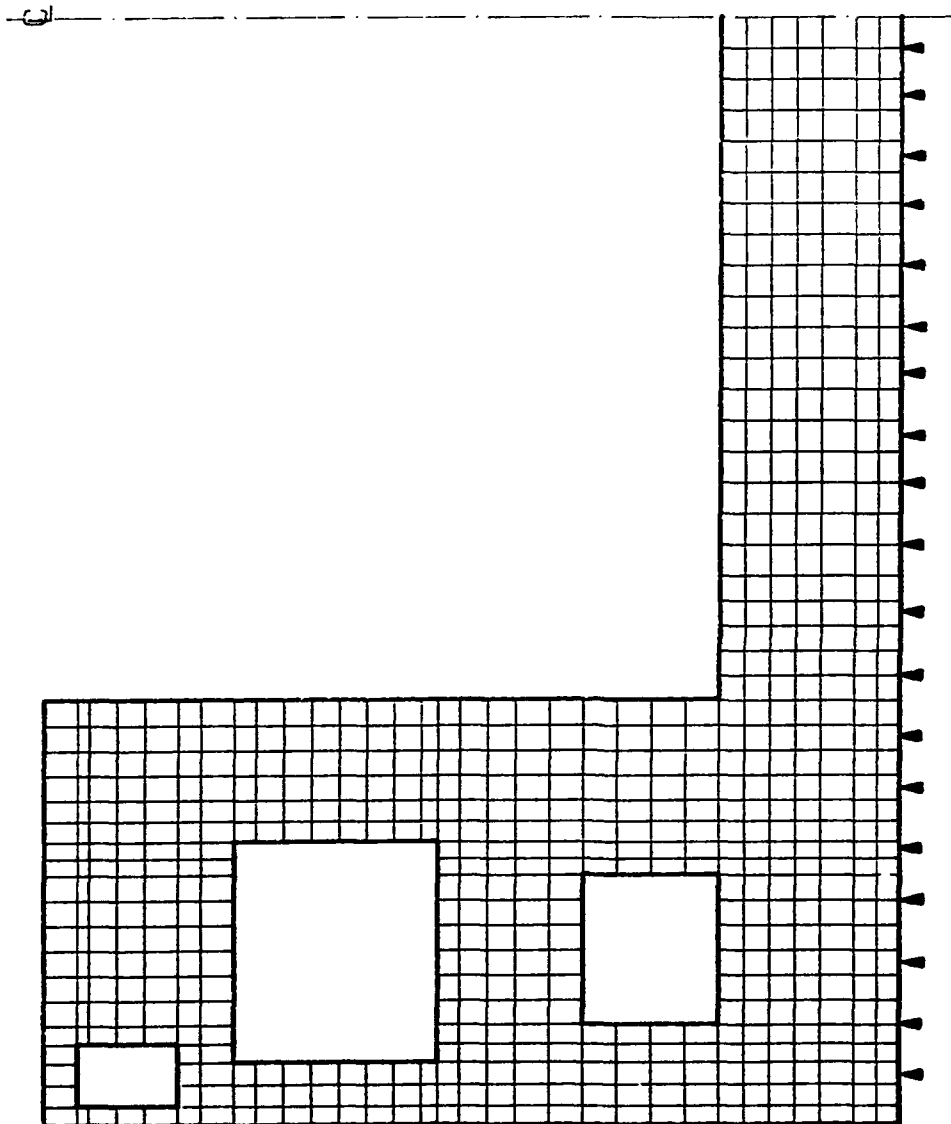


Figure 142. Pile layout for monolith AL-3

$$T_i = \sqrt{\frac{E I_i}{n_h}} \quad (in.) \quad (9)$$

where  $n_h$  is the constant of horizontal subgrade reaction or the change in the soil modulus with depth and was used as  $n_h = 6$  (lb/in.<sup>3</sup>). Given the above numerical values, the spring axial and lateral stiffnesses were computed, then converted into stiffnesses per inch in the direction of flow as axial stiffness of 19,750.8 lb/in. and lateral stiffness of 855.7 lb/in.

139. Due to the large size of the problem, assumptions were made to reduce computing time and simplify the solution. For instance, the forms offer full support along the surfaces. However, to do a finite element model of 3/4-in. thick forms or to replace them with elastic supports was unreasonable at this time. Instead, it is assumed that, at the age of 1 day, the concrete has more or less hardened and is able to support its own weight. Before that, the weight of the freshly placed concrete is applied as a uniform pressure to the previous lift. This assumption was found to work well. On the other hand, for the roofs of the openings where supports are needed for longer periods, the forms are replaced by MPC, as discussed earlier. The idea is to have all the nodes at the roof displace following a prescribed function. In this study, a linear function between the two end nodes of the opening roof is imposed until 7 days after the placement of the lift closing the opening.

#### Material Properties

140. Conducting the proper testing to determine the properties of the materials used is critical for defining the model of a massive concrete structure where creep, shrinkage, and aging modulus are to be considered. All of the material properties used in this study were as provided by the Waterways Experiment Station through the subroutine UMAT (Norman, Bombich, and Jones 1987; Anatech, Inc. 1987) and were discussed in Part III.

### Introduction

141. The temperature results are presented in forms of temperature history plots and temperature distribution plots. The figures will show the temperature variations and their relation to the monolith geometry and modeling techniques. Also, a comparison between the 16-lift and the 11-lift monoliths show the effects of increasing lift heights. The locations considered are outside edge nodes, nodes around the openings, and nodes that are either at the top or the middle of the lifts shown in Figure 143. These locations were chosen based on the results from AL-5. They provide an overall view of typical temperature effects and distributions throughout the monolith AL-3.

### General Trends

142. In general, the history plots for the 16-lift model show a sudden temperature rise at early times, which is most severe for the embedded nodes. This initial temperature rise does not last longer than 2-3 days. For the edge nodes, the rise ranges from about 5° F to 10° F above the ambient air temperatures. Nodes within thick sections and embedded within the lift produce a temperature rise as high as 30° F. Nodes at the top of the lift experience two temperature rises. The first is an initial rise that is 3 to 4 degrees higher than the ambient temperature, the second rise is due to the heat generated from the new lift placed directly above the node. The rise is as high as 20 degrees in several of the cases.

143. For the nodes along the edges, there is a sudden temperature drop following the removal of the forms. This is due to the insulating effect of the 3/4-in.-thick forms. Once the forms are removed, the hot concrete is exposed to relatively cooler temperatures and hence the temperature drops to the ambient temperature (see Figures 144-146). The second small temperature rise shown in Figures 147 and 148 is due to the heat generated from the newly placed lift. The temperature plot shown in Figure 149 is for a node on the floor of the chamber. This resulted in a very small temperature increase above the ambient temperature and a smooth transition instead of a sudden drop.

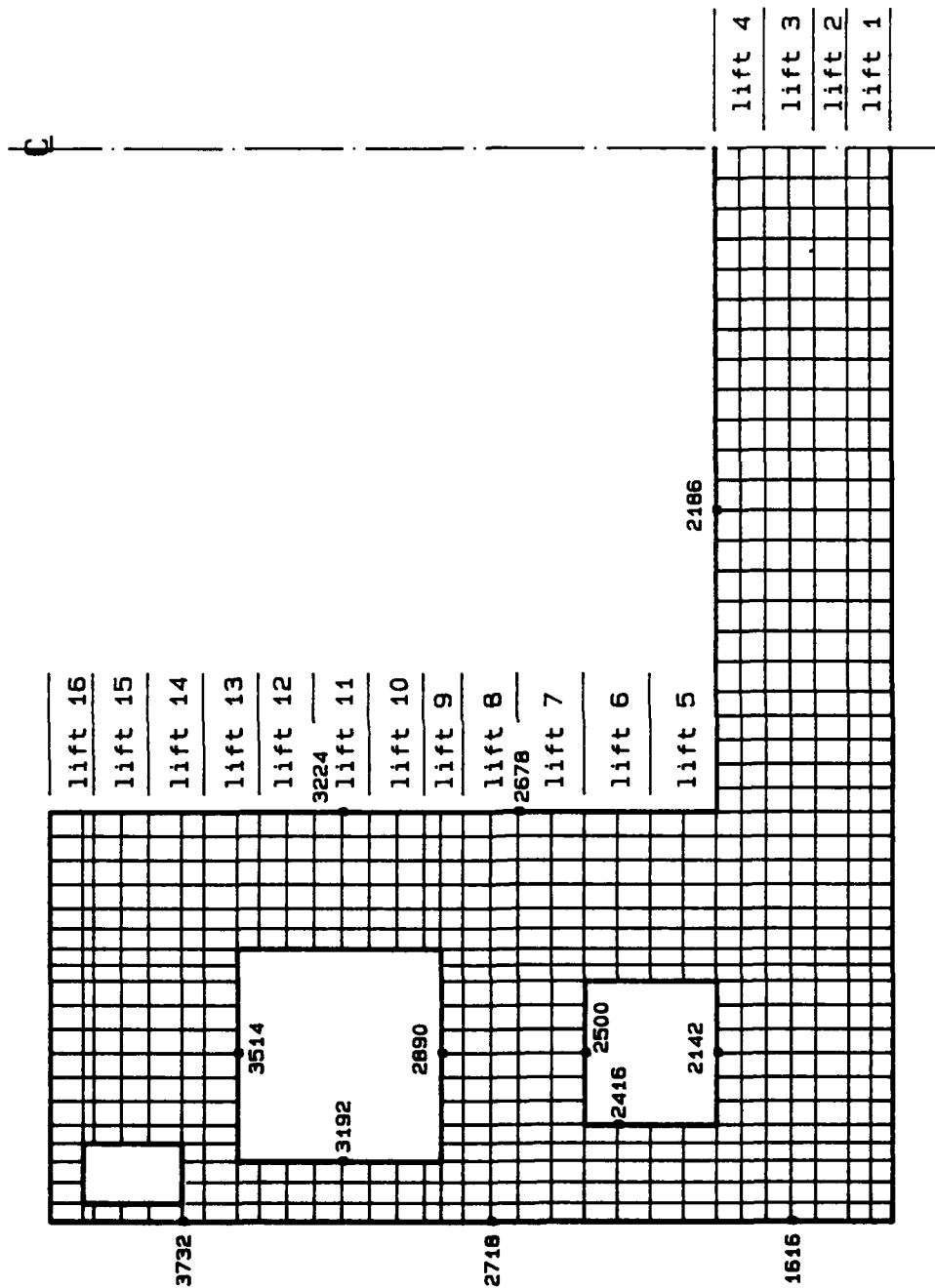


Figure 143. Selected nodes for temperature comparison

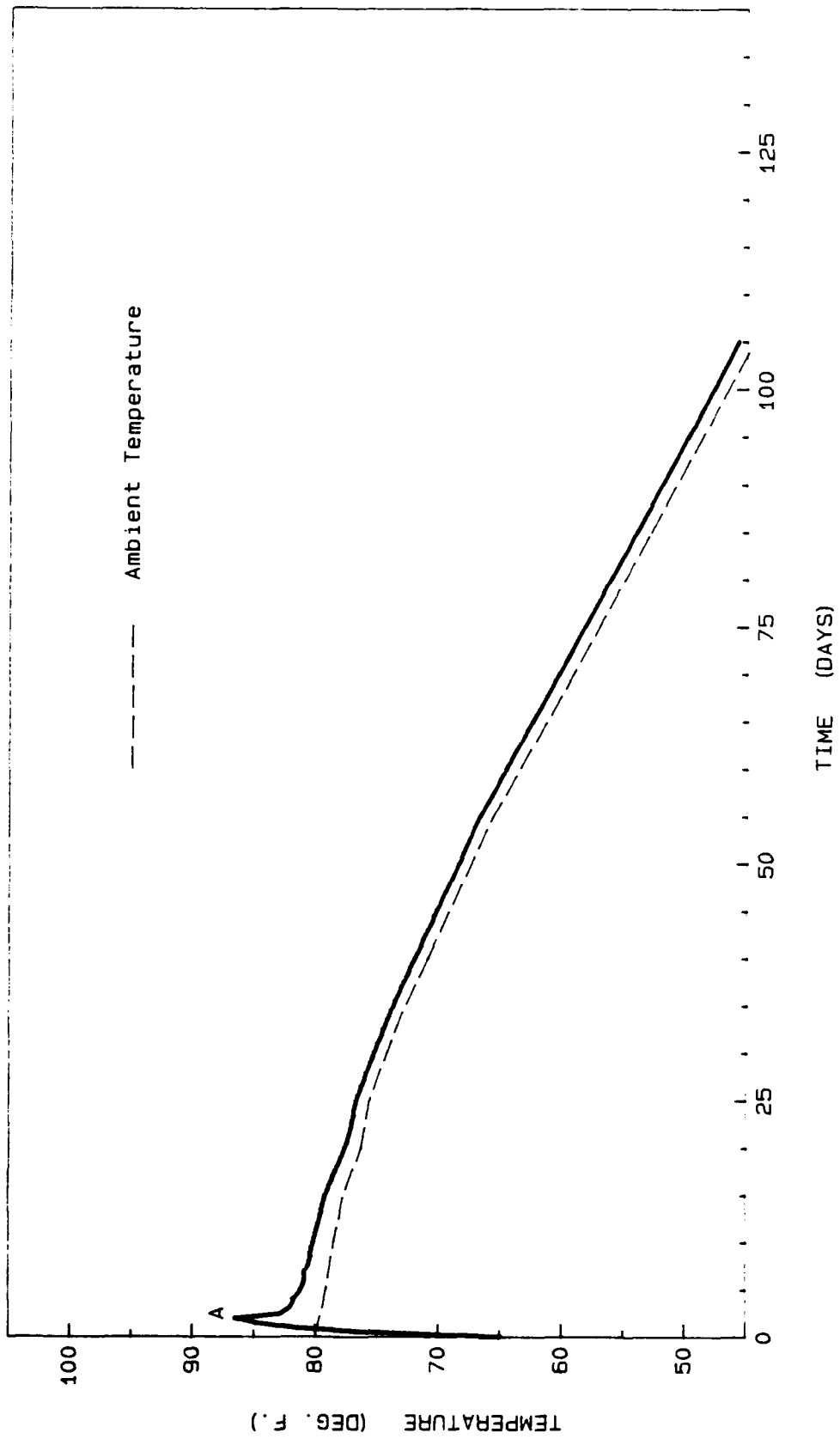


Figure 144. Temperature history at node 2718

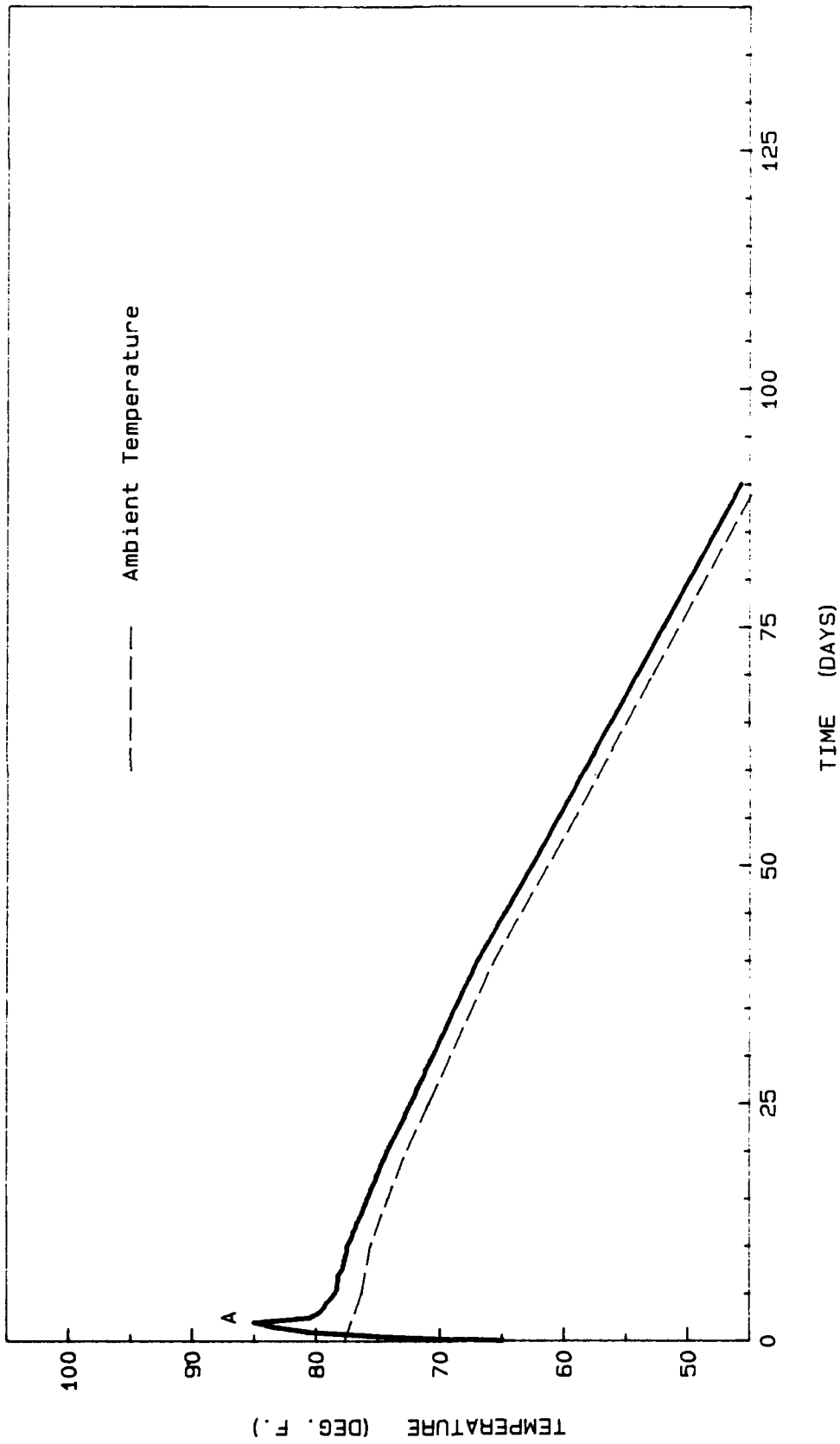


Figure 145. Temperature history at node 3224

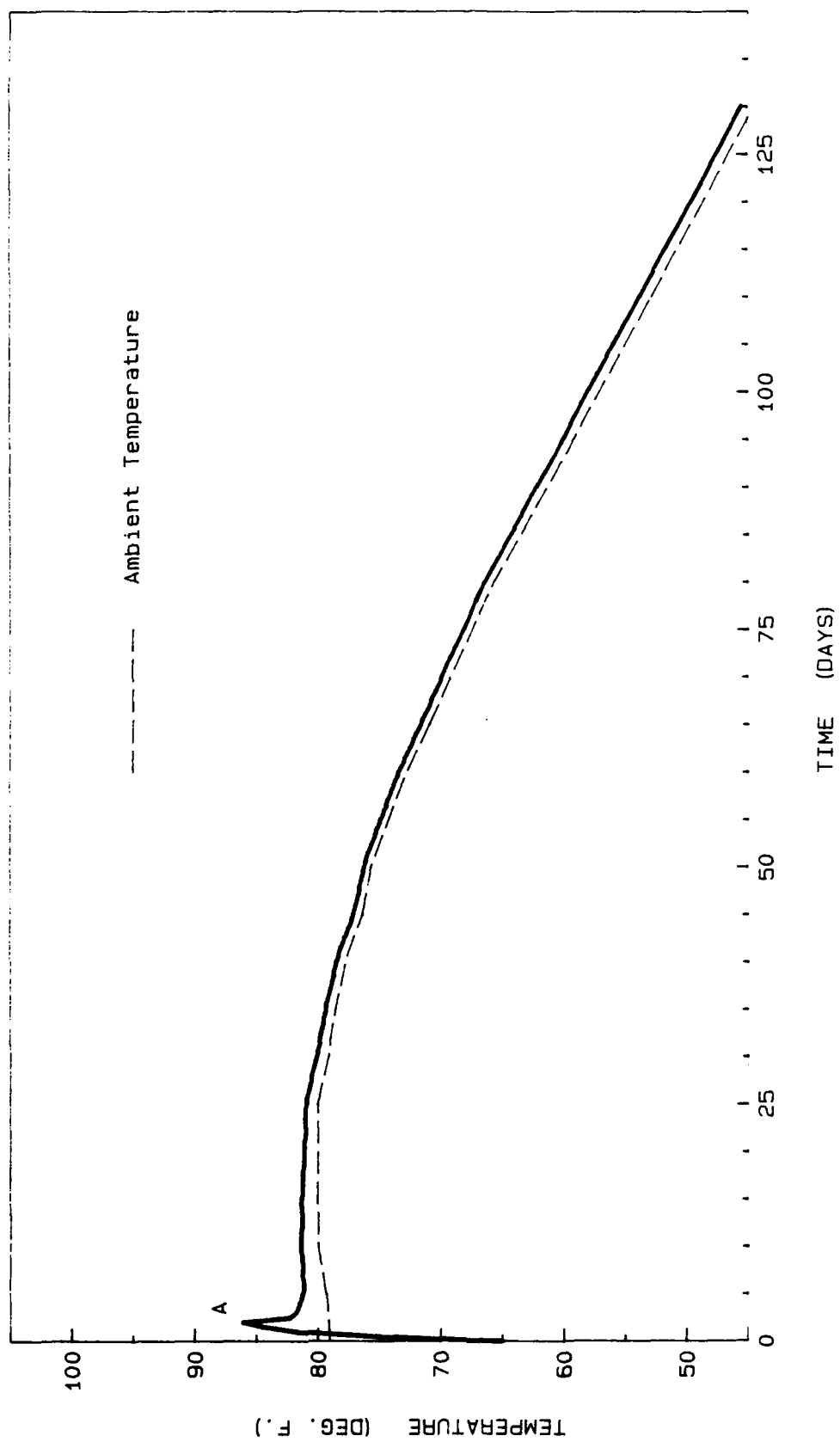


Figure 146. Temperature history at node 1616

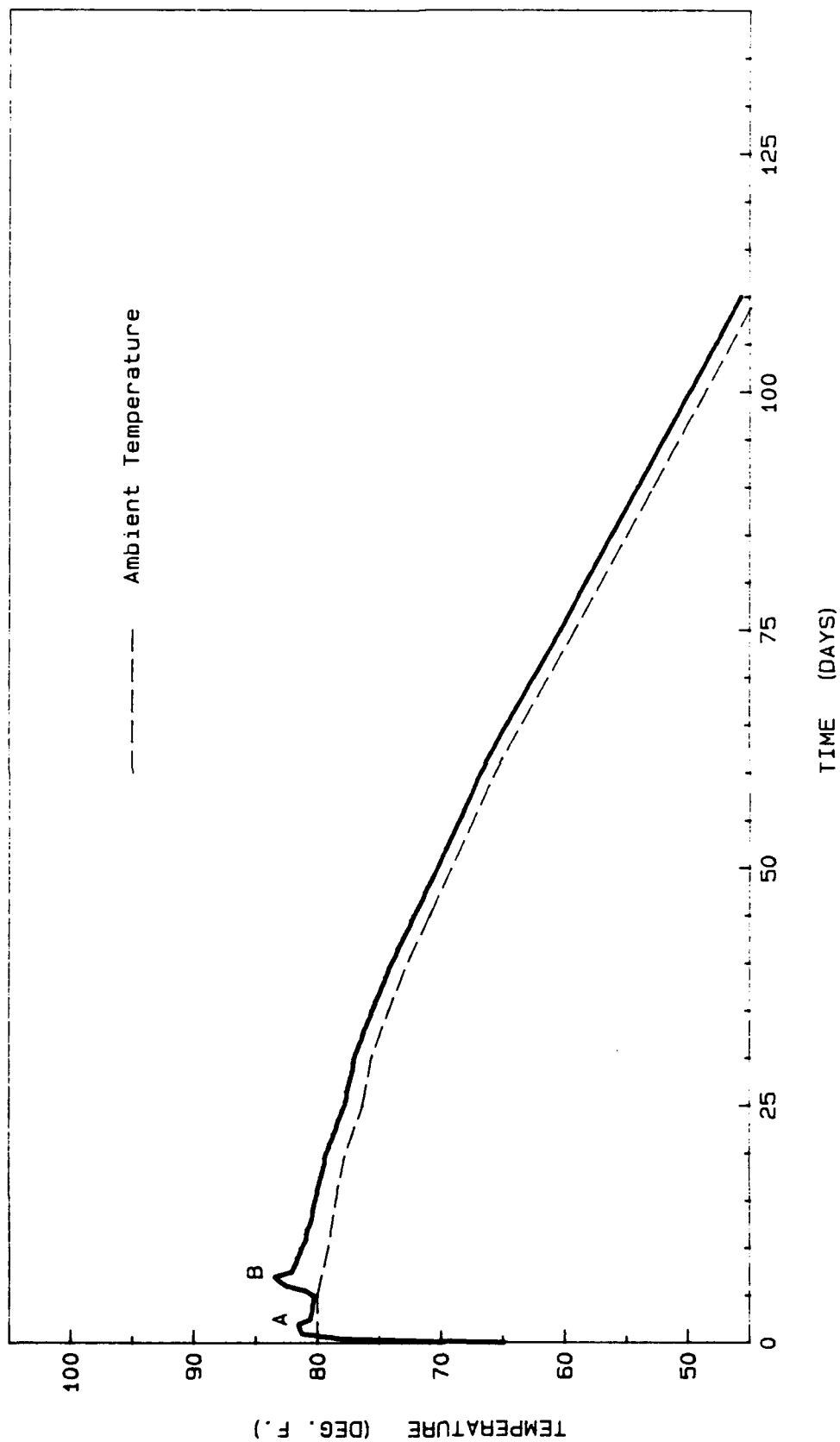


Figure 147. Temperature history at node 2678

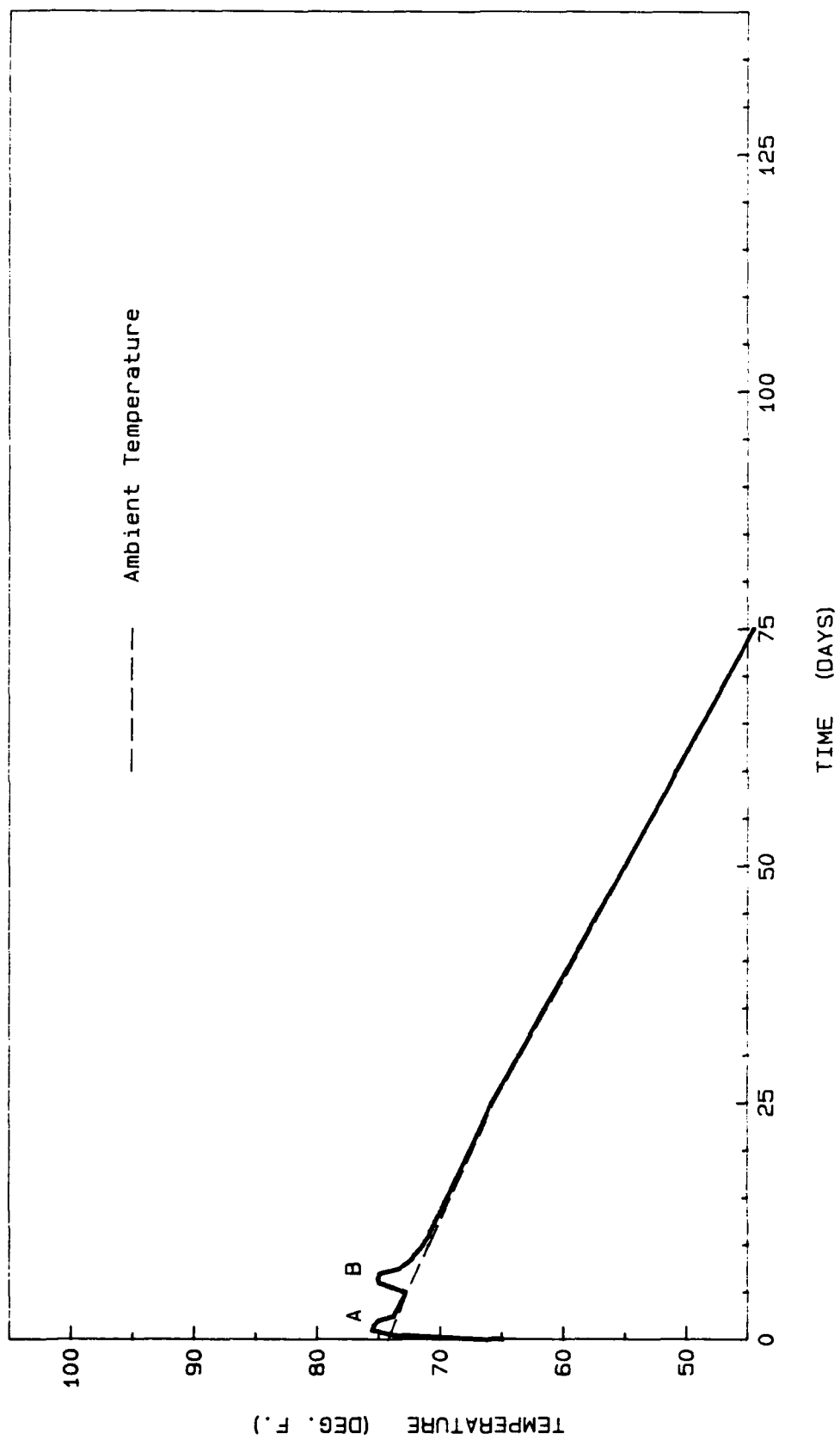


Figure 148. Temperature history at node 3732

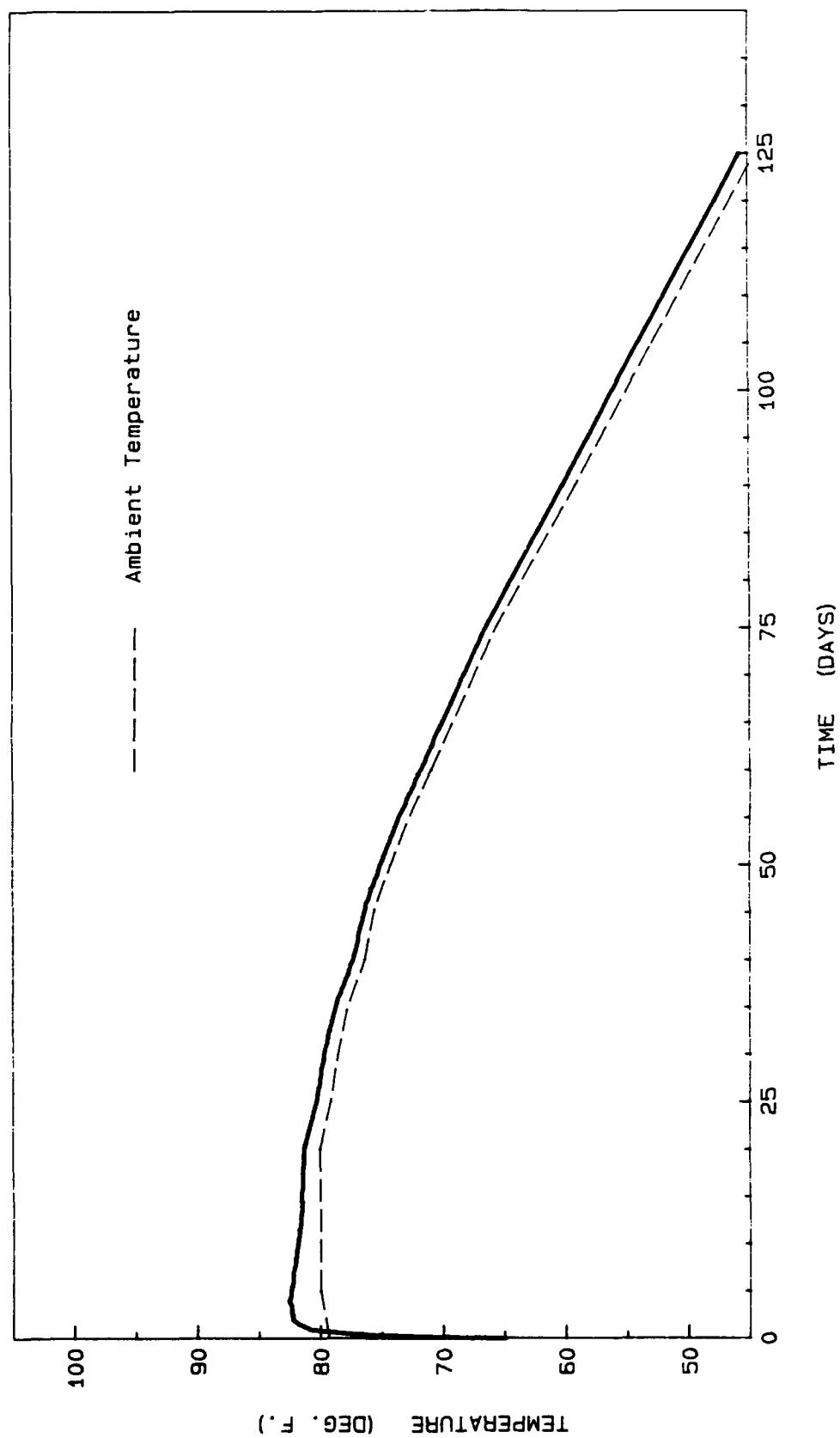


Figure 149. Temperature history at node 2186

144. Several of the curves representing temperature history plots around the openings are presented to show the difference between the two modelling techniques which are: (a) activating the air elements to represent a closed void with no air flow and (b) using reduced heat transfer coefficients to simulate the heat exchange between the open void and the ambient air. The difference between the two models is significant. Activating the air elements creates a connection between the four sides of the opening, allowing heat to flow freely from one side to the other.

145. An investigation of the temperature regime around the void and the culvert was conducted. As expected, the use of the reduced heat transfer coefficients resulted in a small increase in the temperatures of the surrounding concrete. This increase labeled by point C is shown in Figures 150-152. On the other hand, around the void, where air elements are activated, a jump in temperatures of 15° F is seen. This is shown in Figures 153-154 at points labeled D.

146. Figure 155 shows locations where different distribution plots were made. A temperature distribution plot representing temperature at 5 days after the placement of lift 9, just before the void is closed, and 15 days after the void is closed is shown in Figure 156. The first two plots are similar in shape but the second is lower since heat is lost during the 15-day period. Figure 157 shows two curves. The dashed curve corresponds to a time just before the closing of the void, and the solid curve corresponds to a time 15 days after closing the void. For each section on either side of the void, the temperature distribution has a parabolic shape with the temperature being low at the sides and increasing as the center of the section is approached, similar to an unrestrained slab. On the other hand, the second curve, which corresponds to 15 days after the void has been closed, shows higher temperatures corresponding to the edges of the void. The same curve is plotted in Figure 158 where the void is eliminated and the two edges are connected. The curve has a parabolic shape showing that the two sections act more like a single member with the combined dimensions once the void is closed.

147. Another way of interpreting the temperature results and checking the heat transfer solution is to look at the temperature distribution plots along sections as shown in Figure 155. Two sections are presented here. The first is "cut through" the bed of the chamber, the second is through the member between the culvert and the void. The plots are shown at 1/2 day and

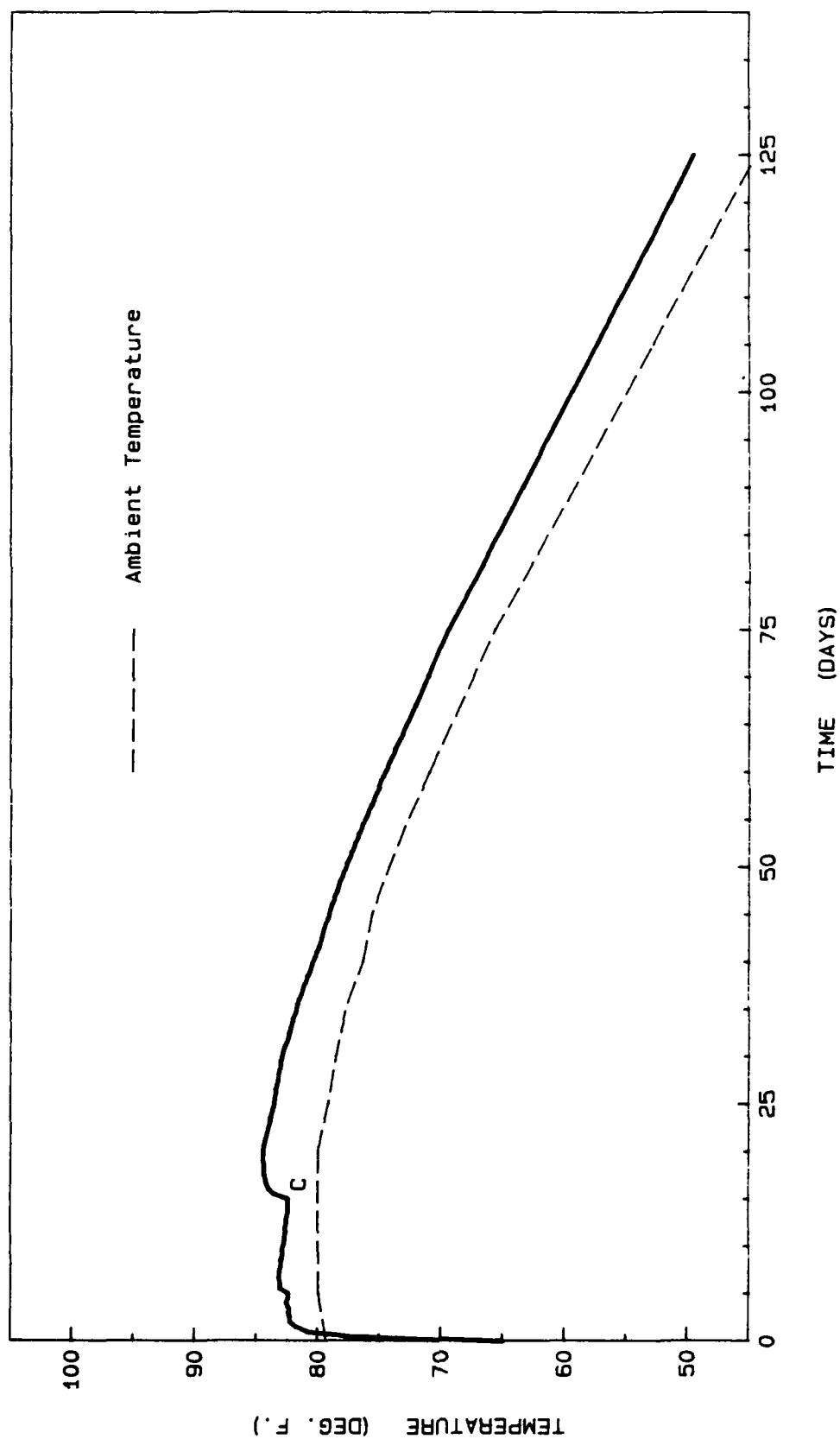


Figure 150. Temperature history at node 2142

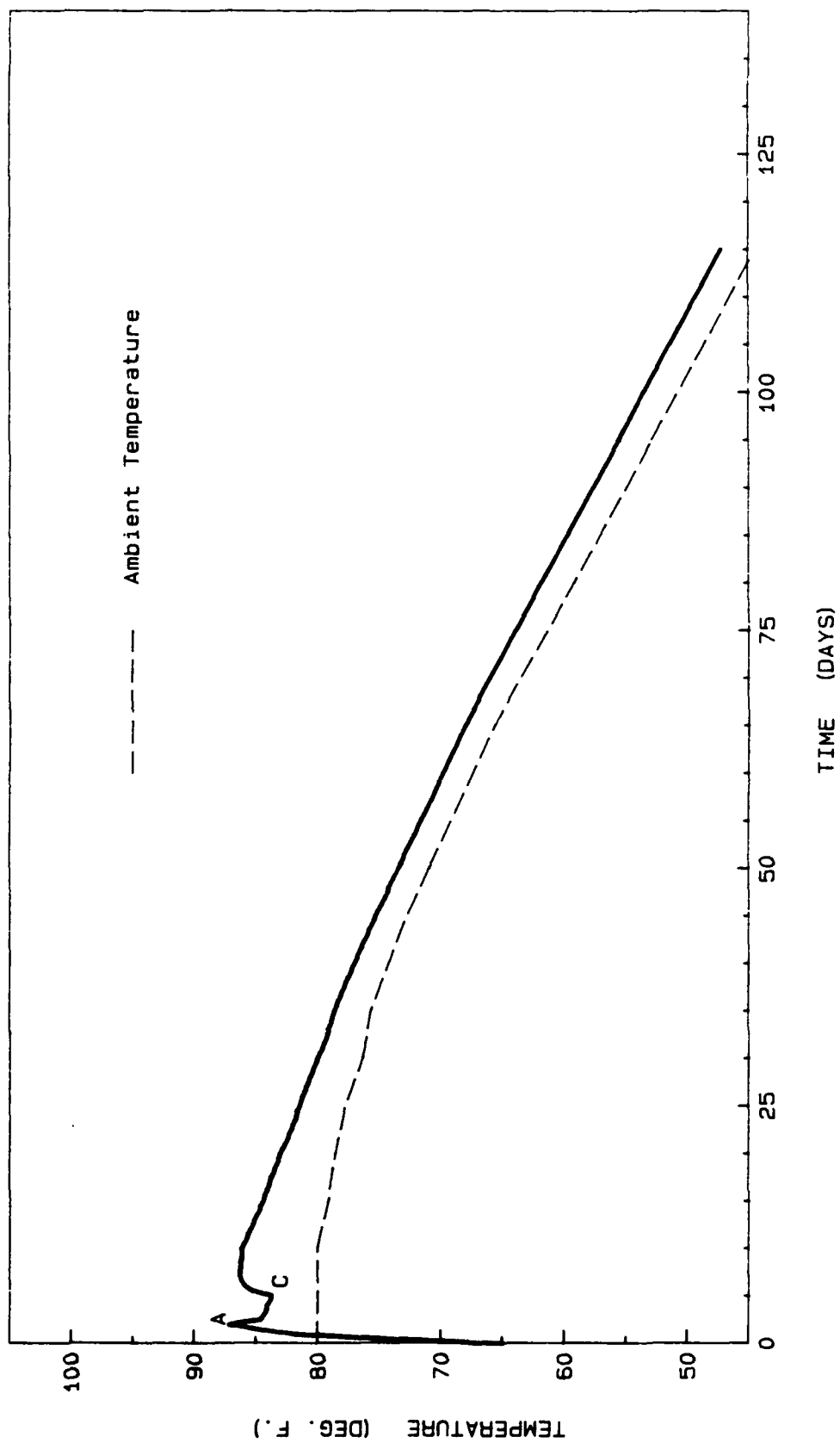


Figure 151. Temperature history at node 2416

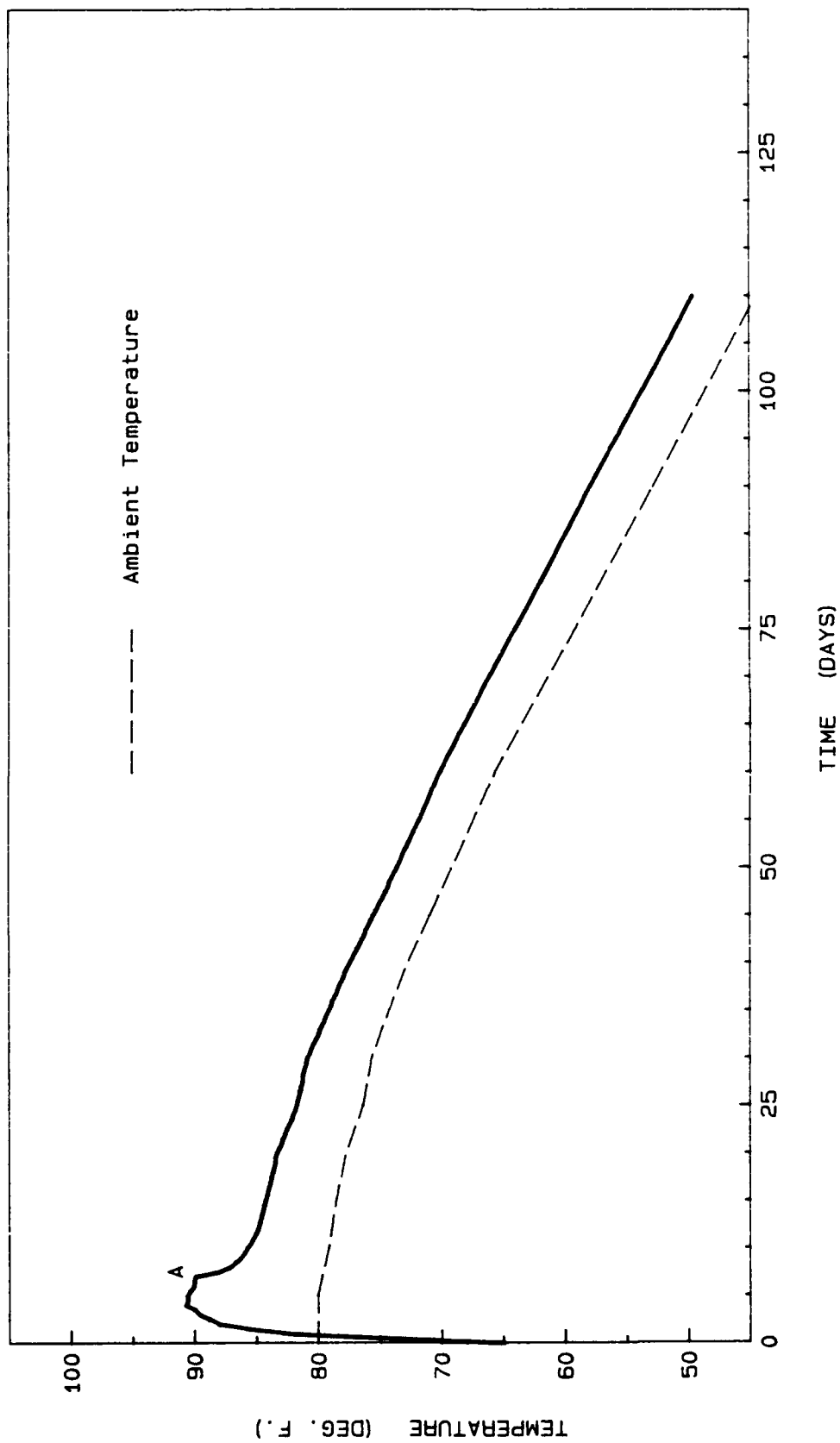


Figure 152. Temperature history at node 2500

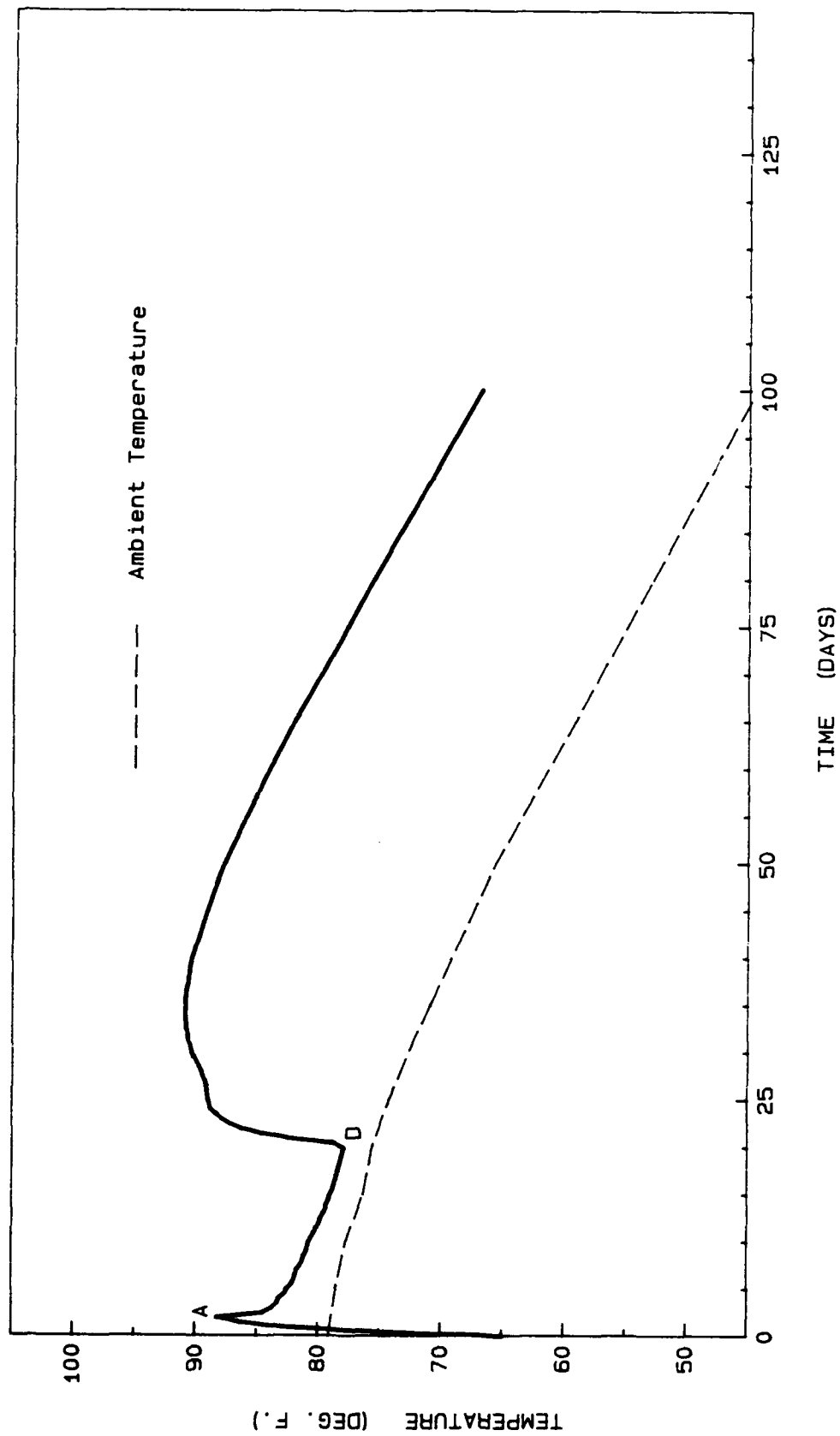


Figure 153. Temperature history at node 2890

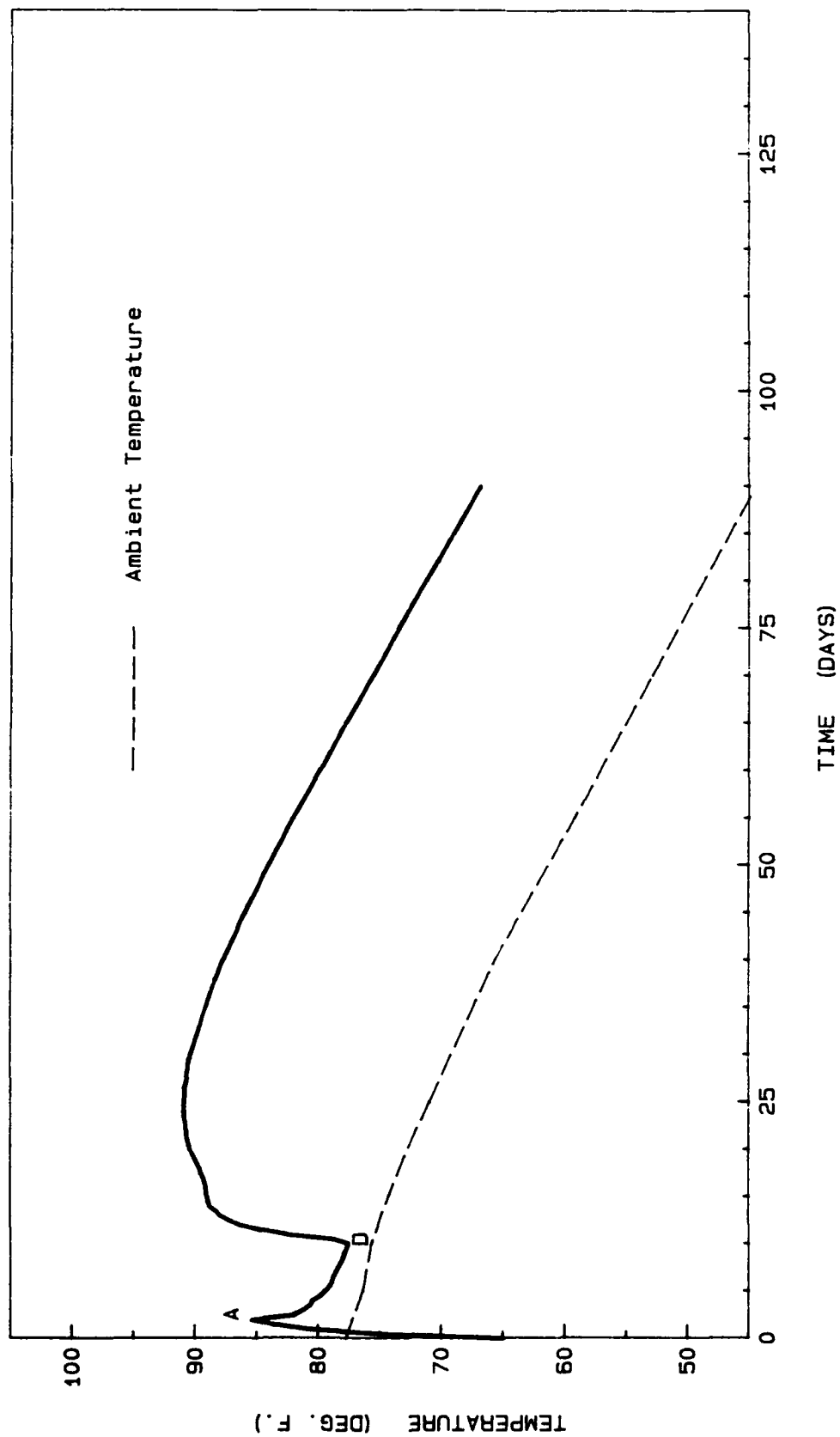


Figure 154. Temperature history at node 3192

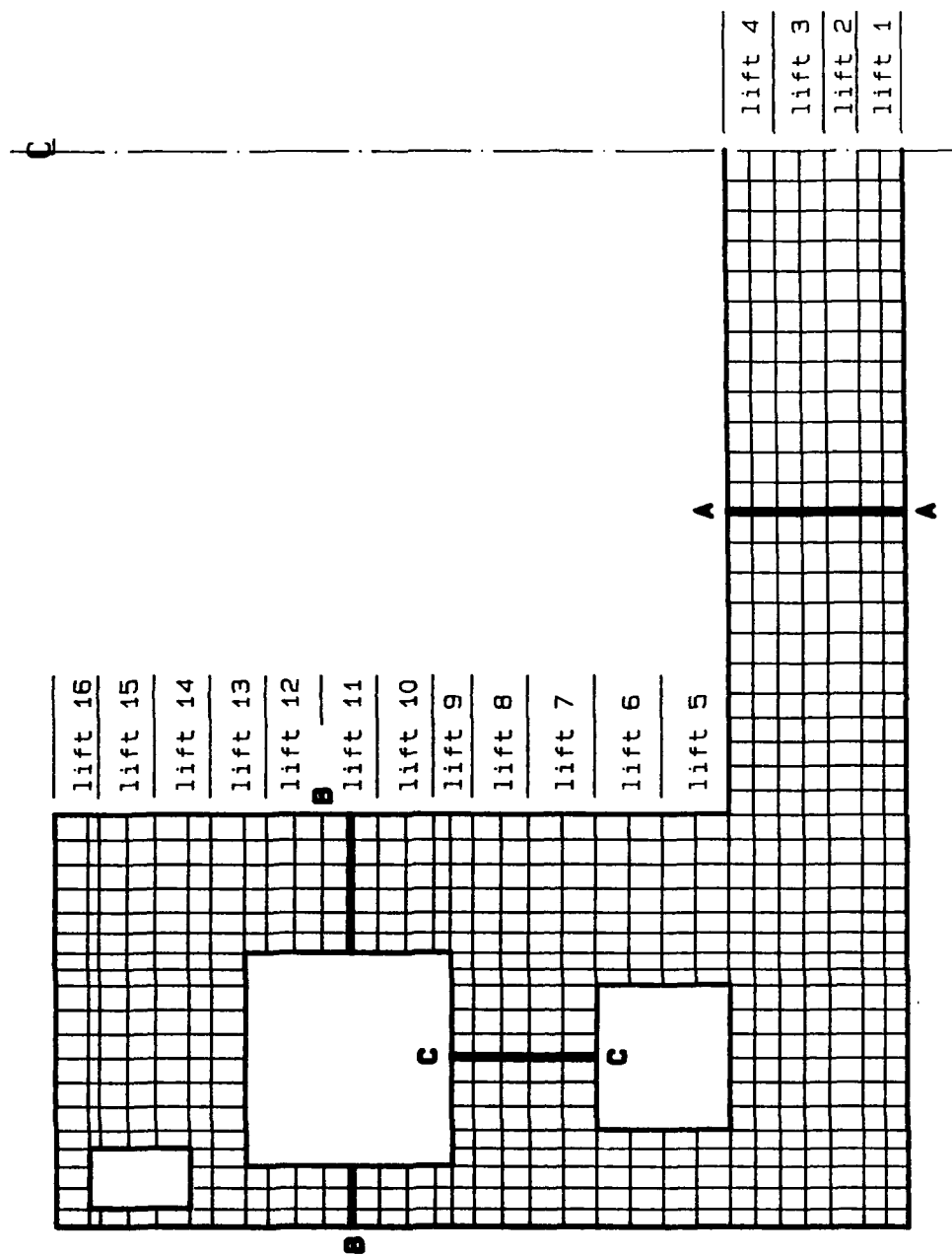


Figure 155. Selected cross-section for temperature distributions

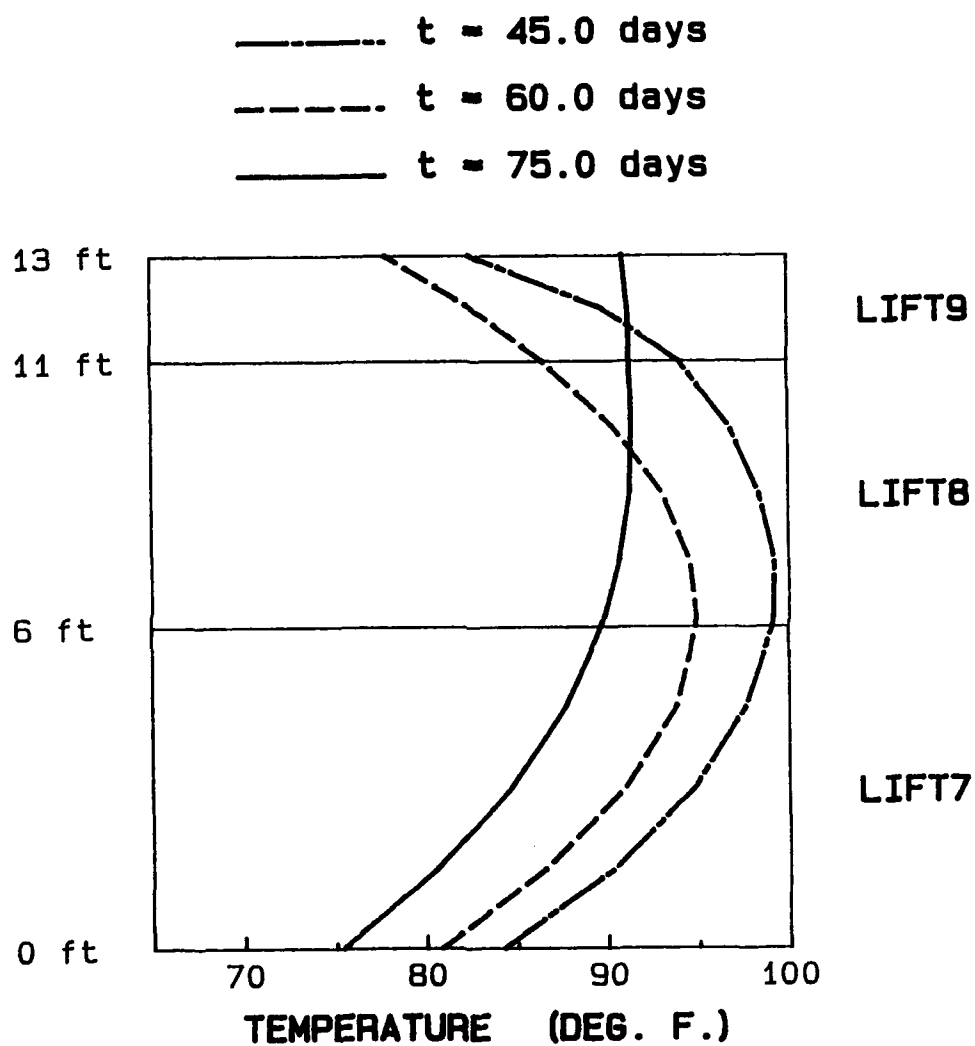


Figure 156. Temperature distribution along section C-C before and after closing the void

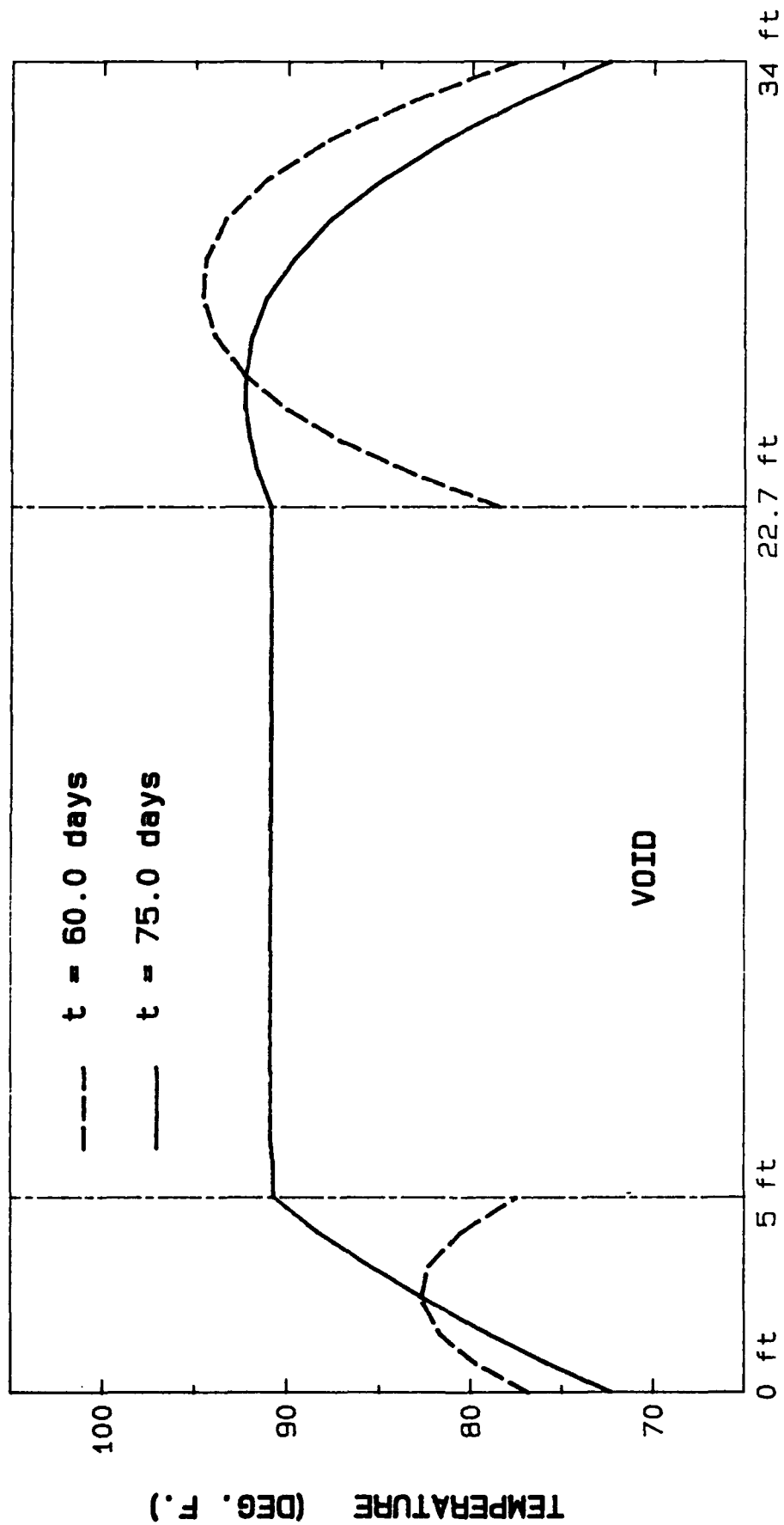


Figure 157. Temperature distribution along section B-B before and after closing the void

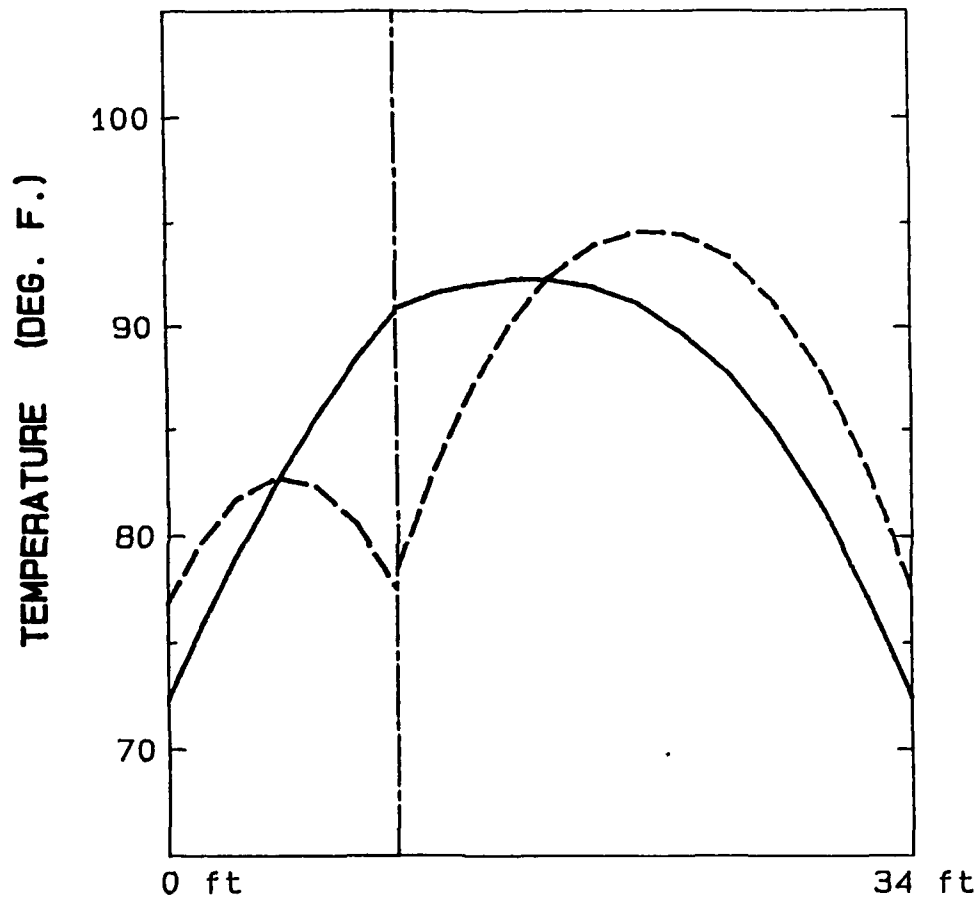


Figure 158. Temperature distribution along section B-B with the void eliminated

5 days after the placement of each lift. In all of the Figures 159-163, the 1/2-day distributions show high temperatures at the top and the bottom of the lift since they are exposed to heat generated from the bottom lift and to the warmer ambient air at the top. At the middle of the lift, the temperature quickly increases to a maximum temperature. The curves also show smooth transitions across lift joints which is expected, because after a period of time all the lifts should act as one block with temperature gradually varying from one end to the other.

148. Figure 164 shows the temperature distribution through the wall sections on either side of the void. Initially, the temperature distribution is flat, with relatively high values at the end due to the ambient temperature. After 2 days, the temperature at the middle has almost reached its maximum. At the edges, the temperature is controlled by the ambient temperature and the formwork. The sudden drop in temperature is due to the removal of the forms. After 5 days, the temperature tends to be a parabolic distribution similar to that of an unconfined slab.

#### Temperature Comparison Between the 11-Lift and 16-Lift Procedures

149. Figure 165 shows all of the pertinent node locations. Figures 166-174 show the temperature history plots at several typical lift interfaces. The time frame used is relative for both lift plans, meaning that time zero corresponds to the placement of the lift containing the node. All but two of the curves have the same trend. Two temperature rises are seen. The first due to the ambient temperature and heat of hydration; whereas, the second is due to the heat generated by the new lift. Figures 166 and 172 are different from the others because they are edge or boundary nodes. They are affected only by ambient air temperature and the film coefficients used to model the forms.

150. The difference in temperature between the 11-lift and the 16-lift plans is almost negligible for the nodes close to the culvert and relatively small at nodes around the void. The maximum difference is only about 7° F and occurs at the top of the void. The 11-lift plan shows higher temperature near the void since the void is closed at an earlier time due to a slightly higher ambient air temperature and less heat dissipation before closing the void.

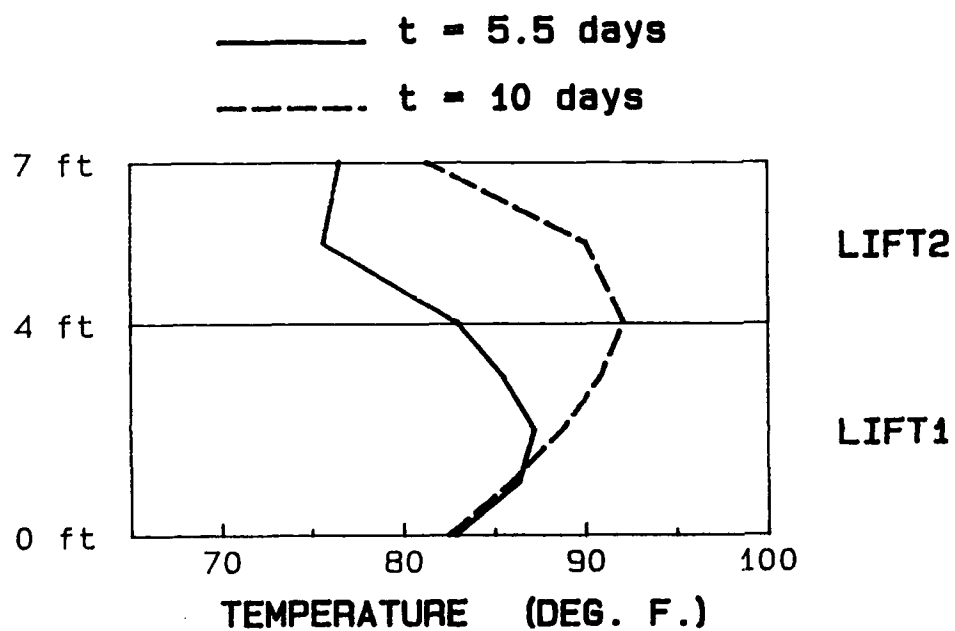


Figure 159. Temperature distribution along section A-A  
0.5 and 5 days after placing lift 2

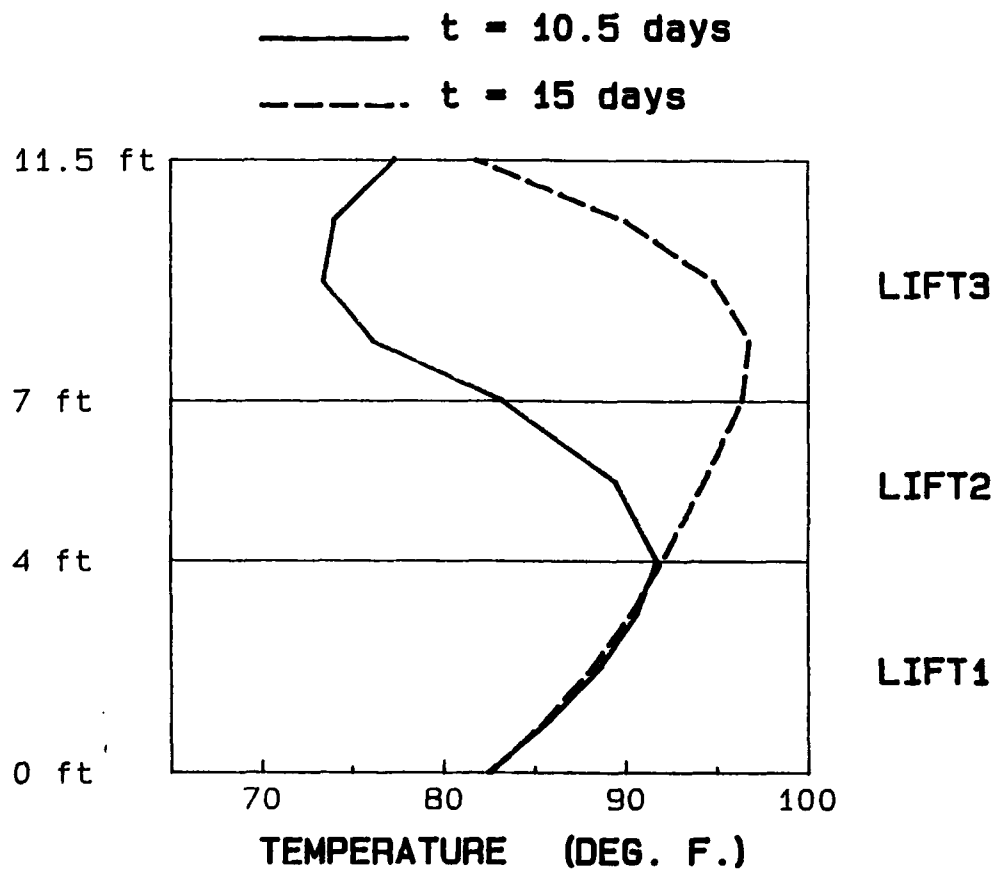


Figure 160. Temperature distribution along section A-A  
0.5 and 5 days after placing lift 3

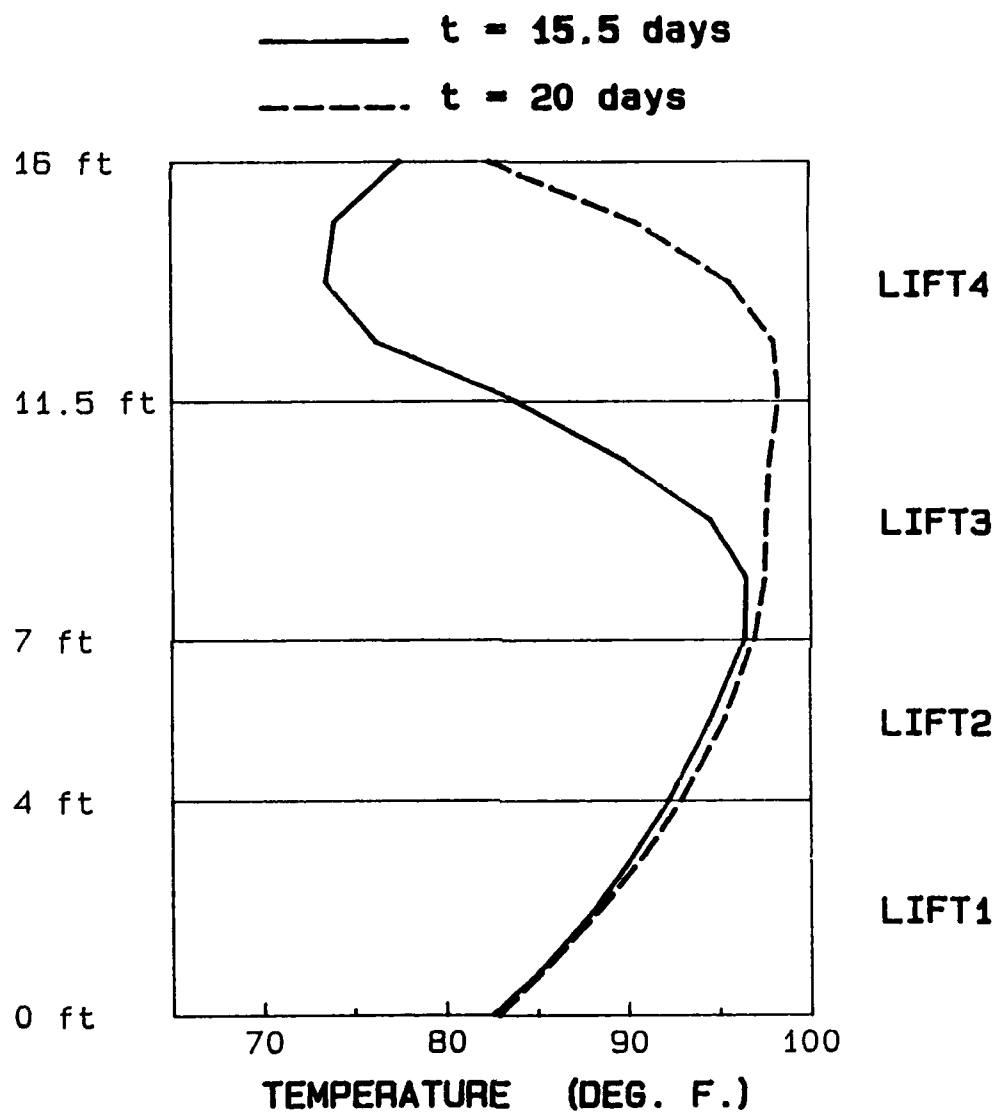


Figure 161. Temperature distribution along section A-A  
 0.5 and 5 days after placing lift 4

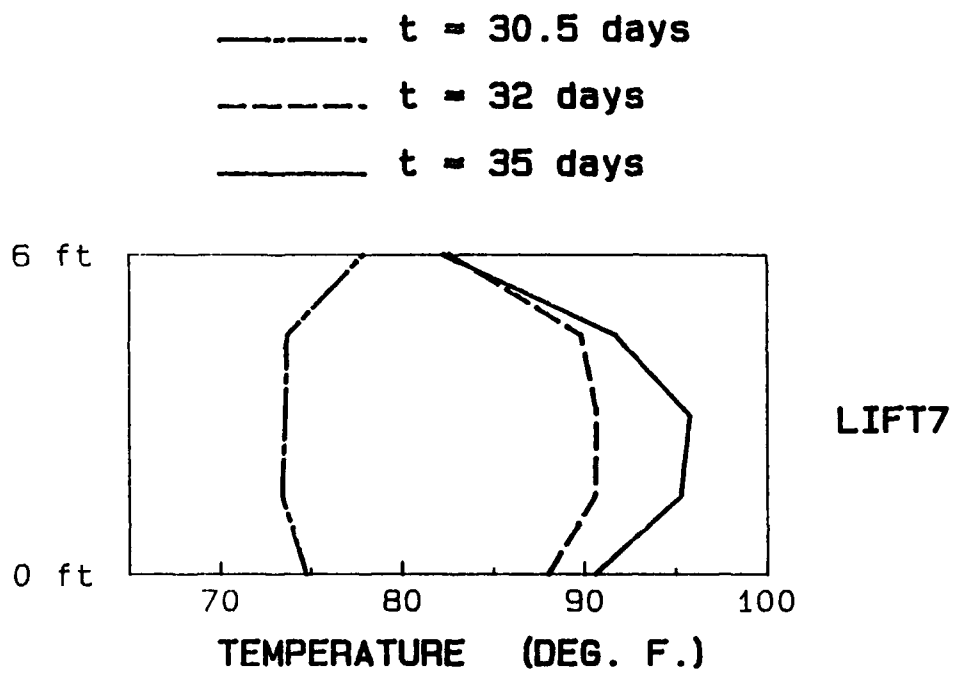


Figure 162. Temperature distribution along section C-C  
0.5, 2, and 5 days after placing lift 7

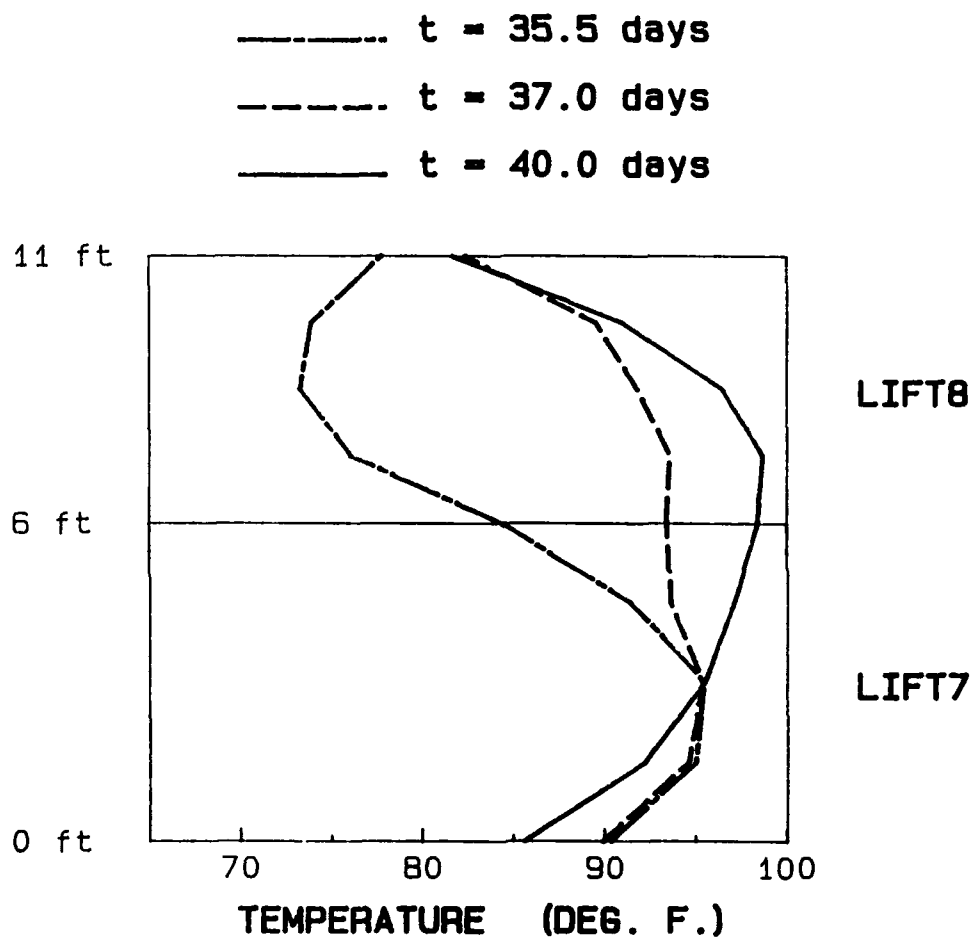


Figure 163. Temperature distribution along section C-C  
 0.5, 2, and 5 days after placing lift 8

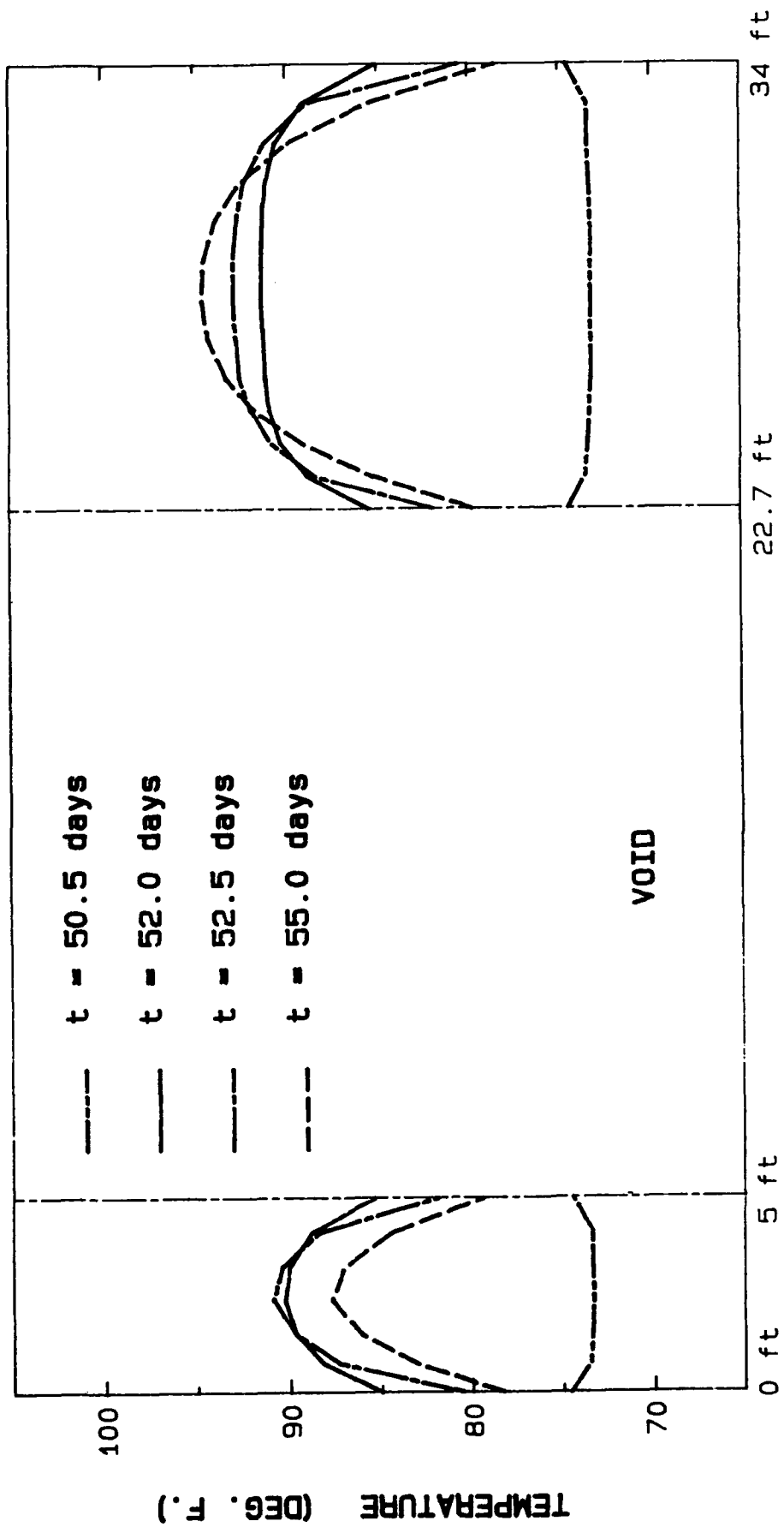


Figure 164. Temperature distribution along section B-B

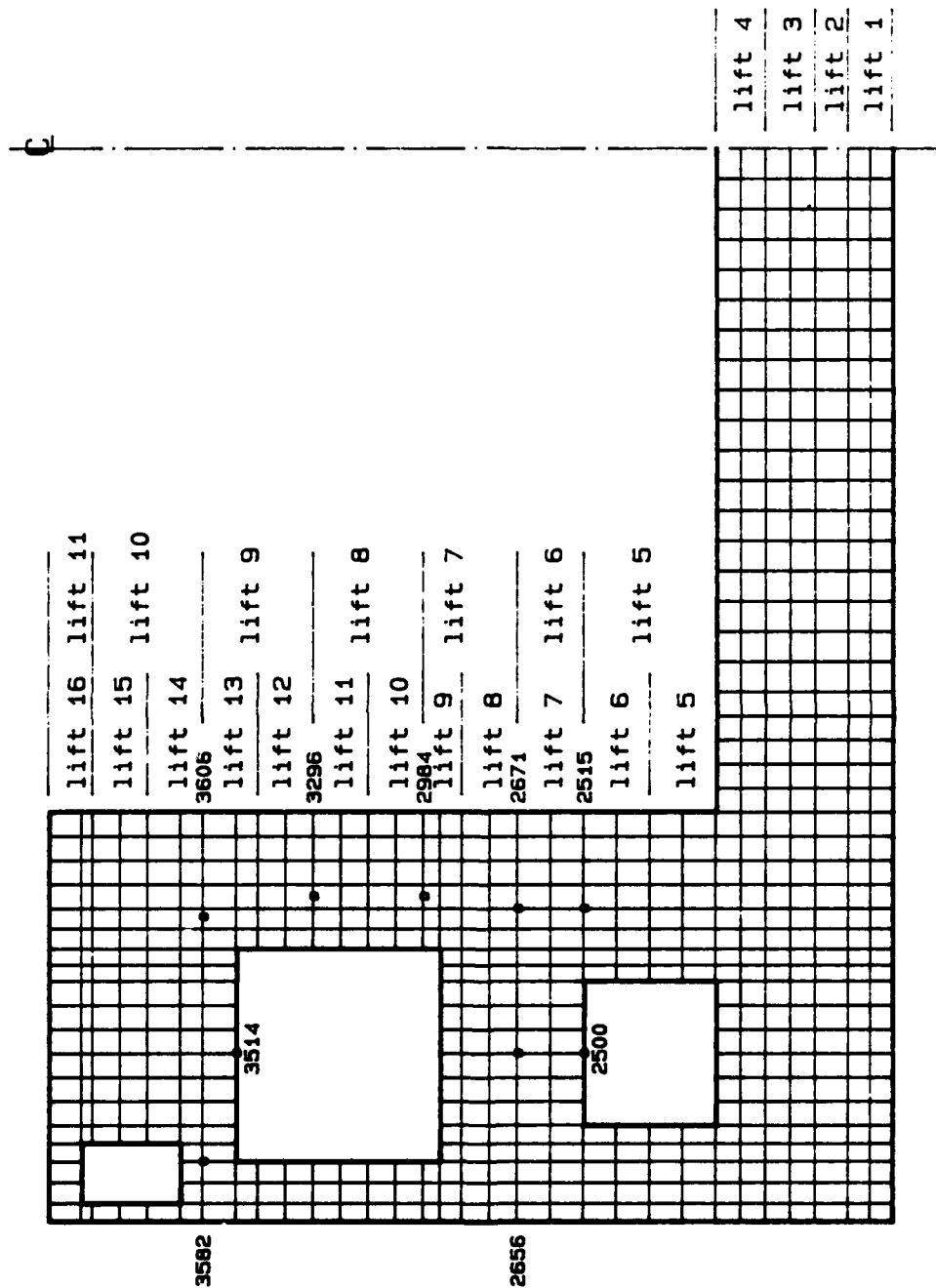


Figure 165. Node locations used for comparing 11 and 16 lift plans

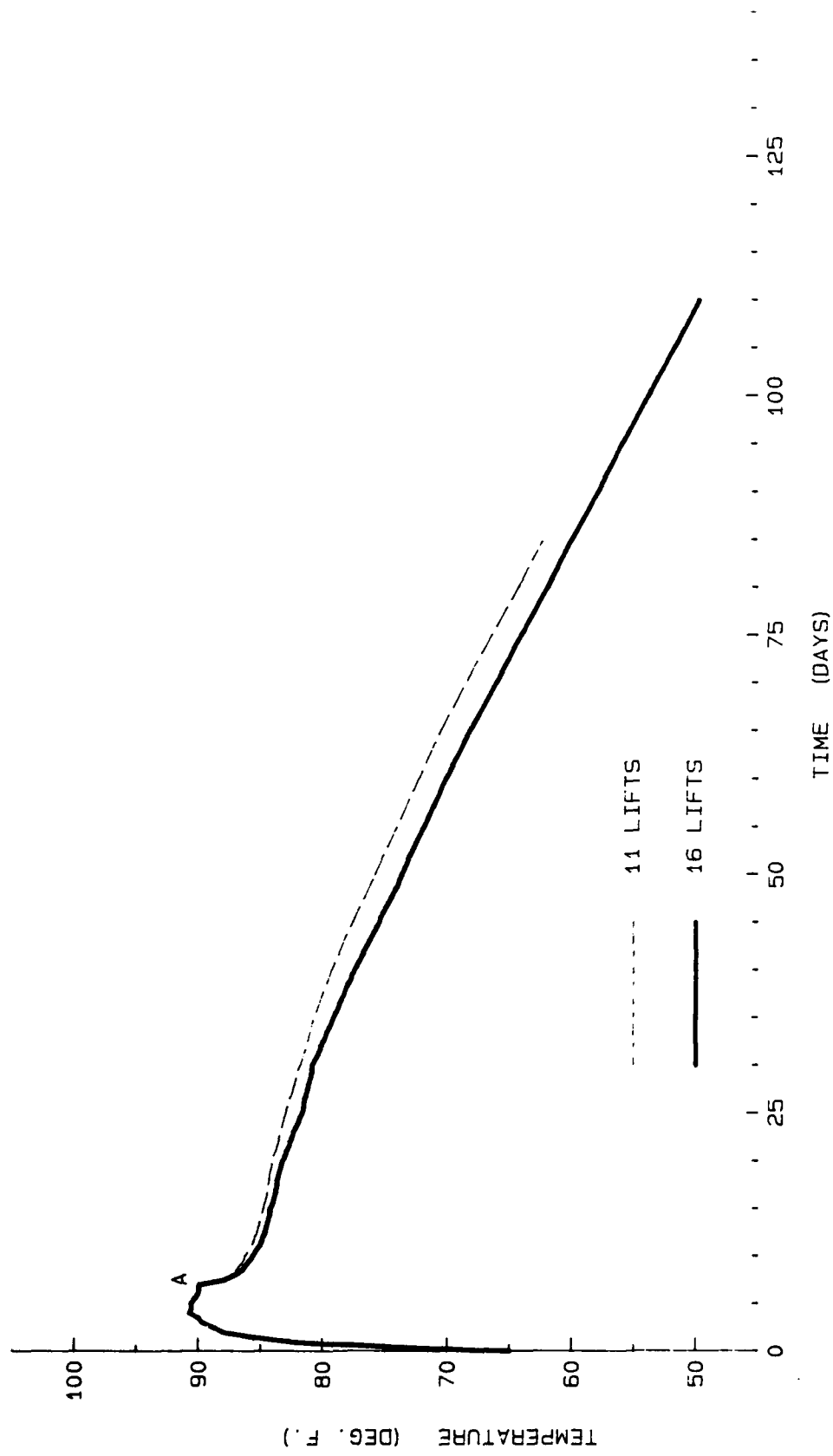


Figure 166. Temperature history at node 2500

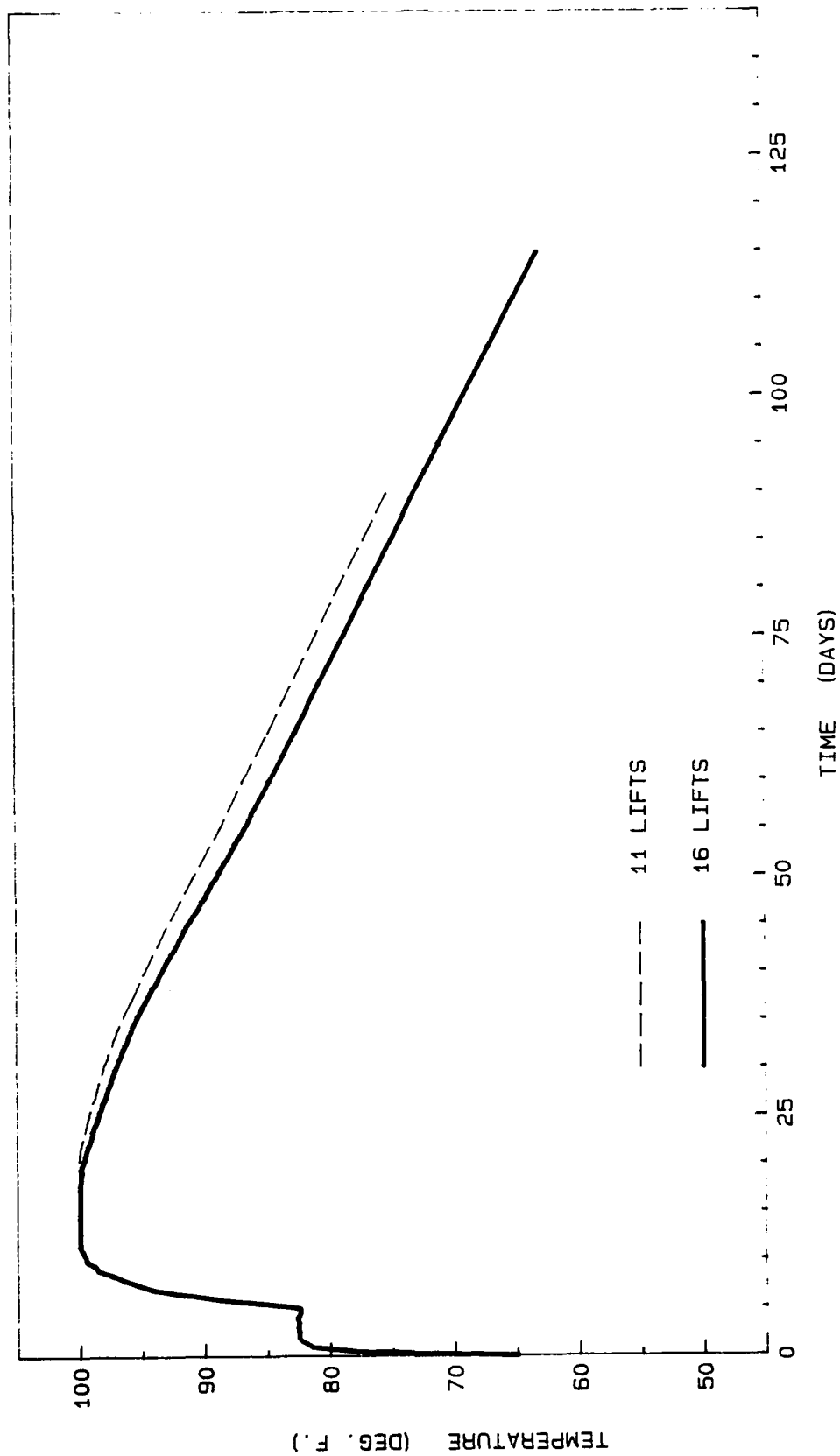


Figure 167. Temperature history at node 2515

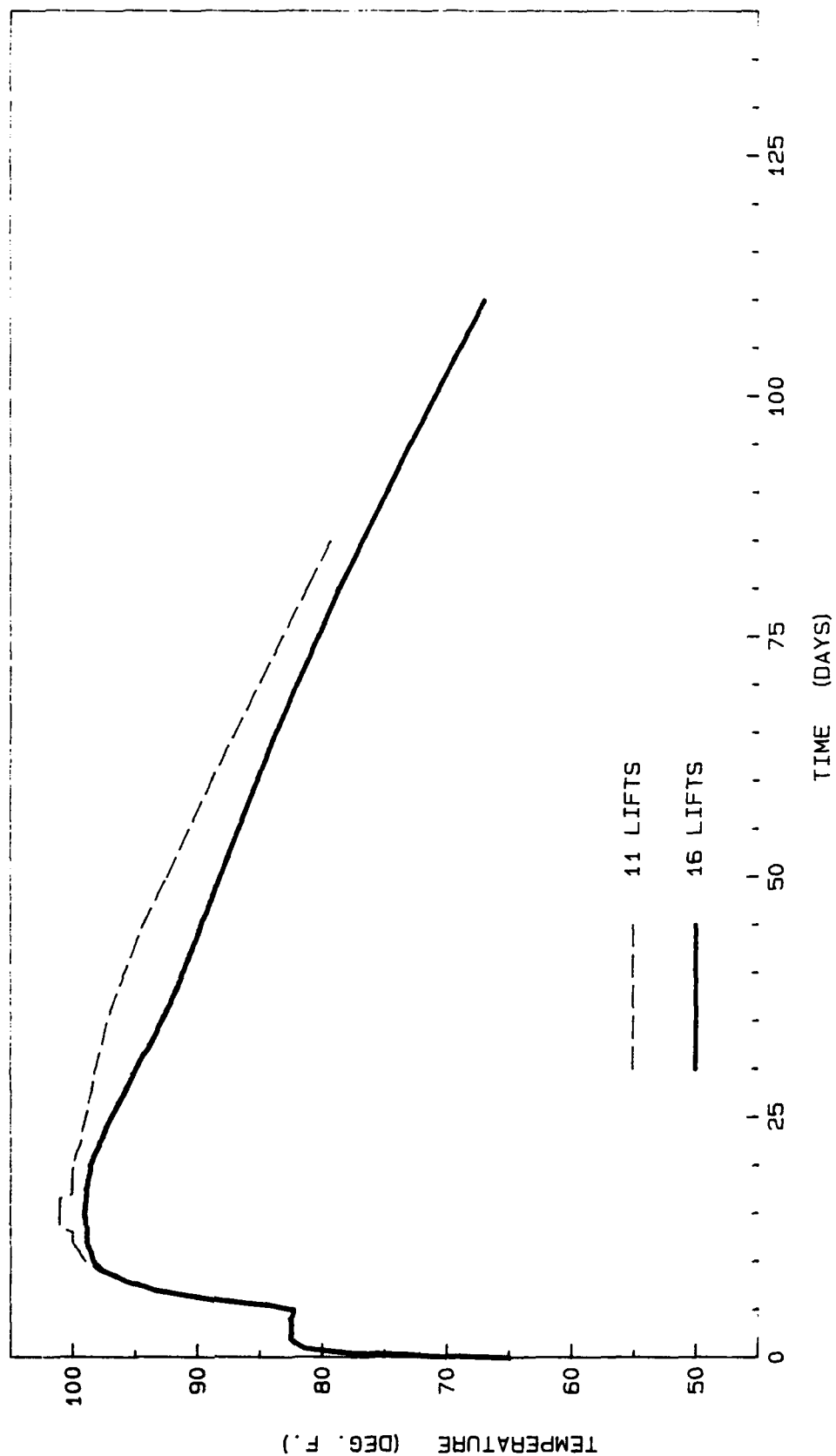


Figure 168. Temperature history at node 2656

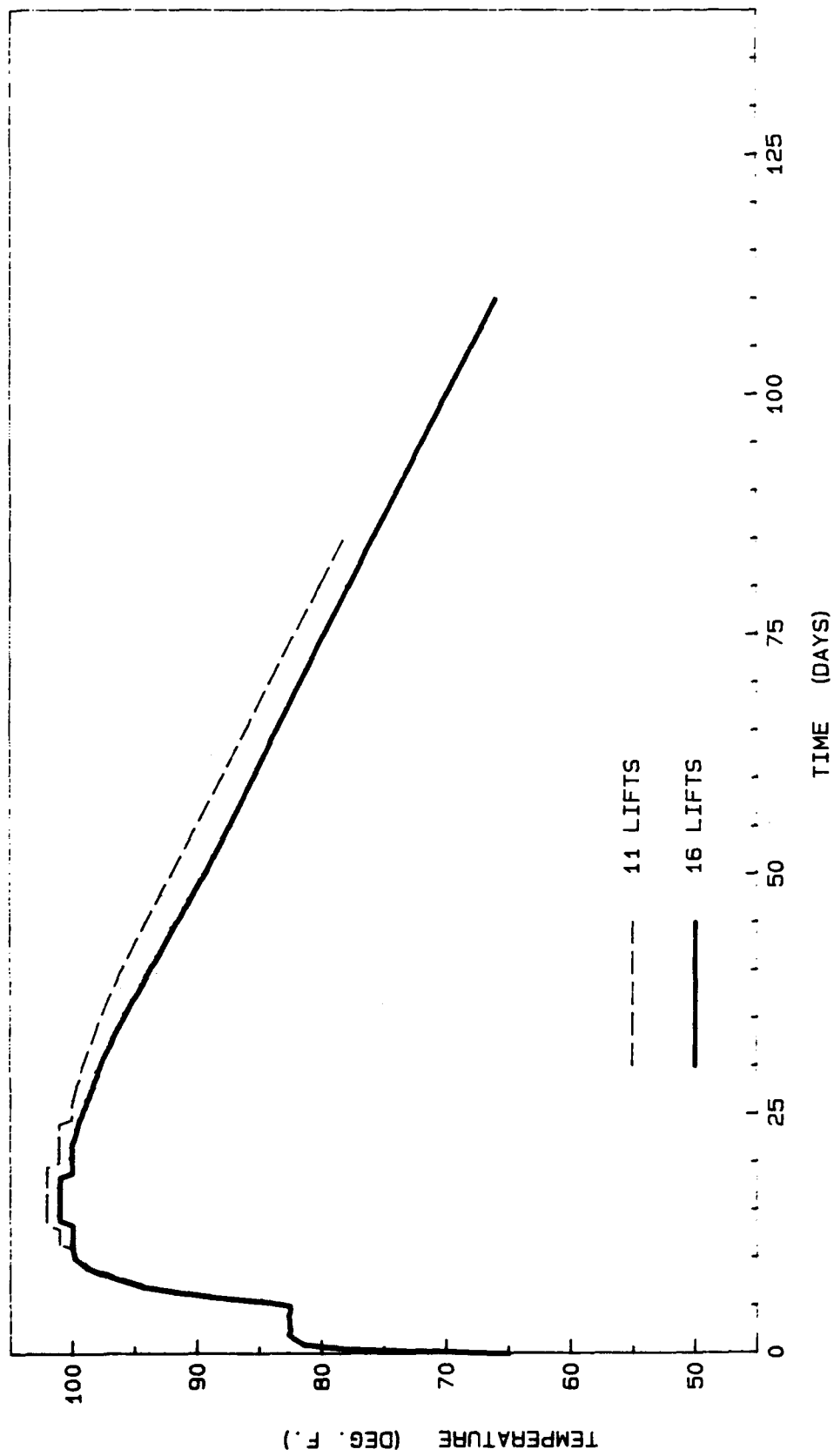


Figure 169. Temperature history at node 2671

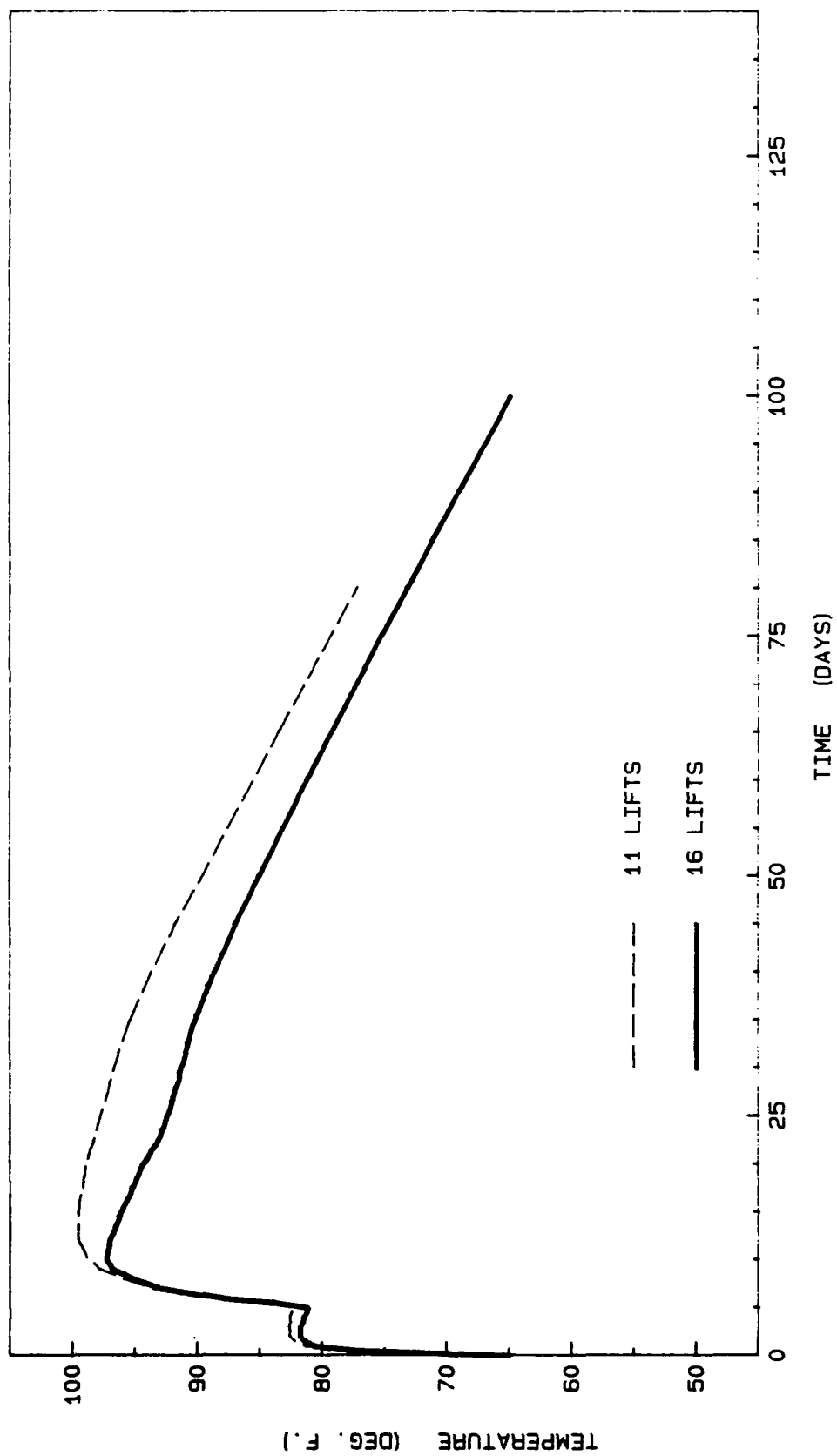


Figure 170. Temperature history at node 2984

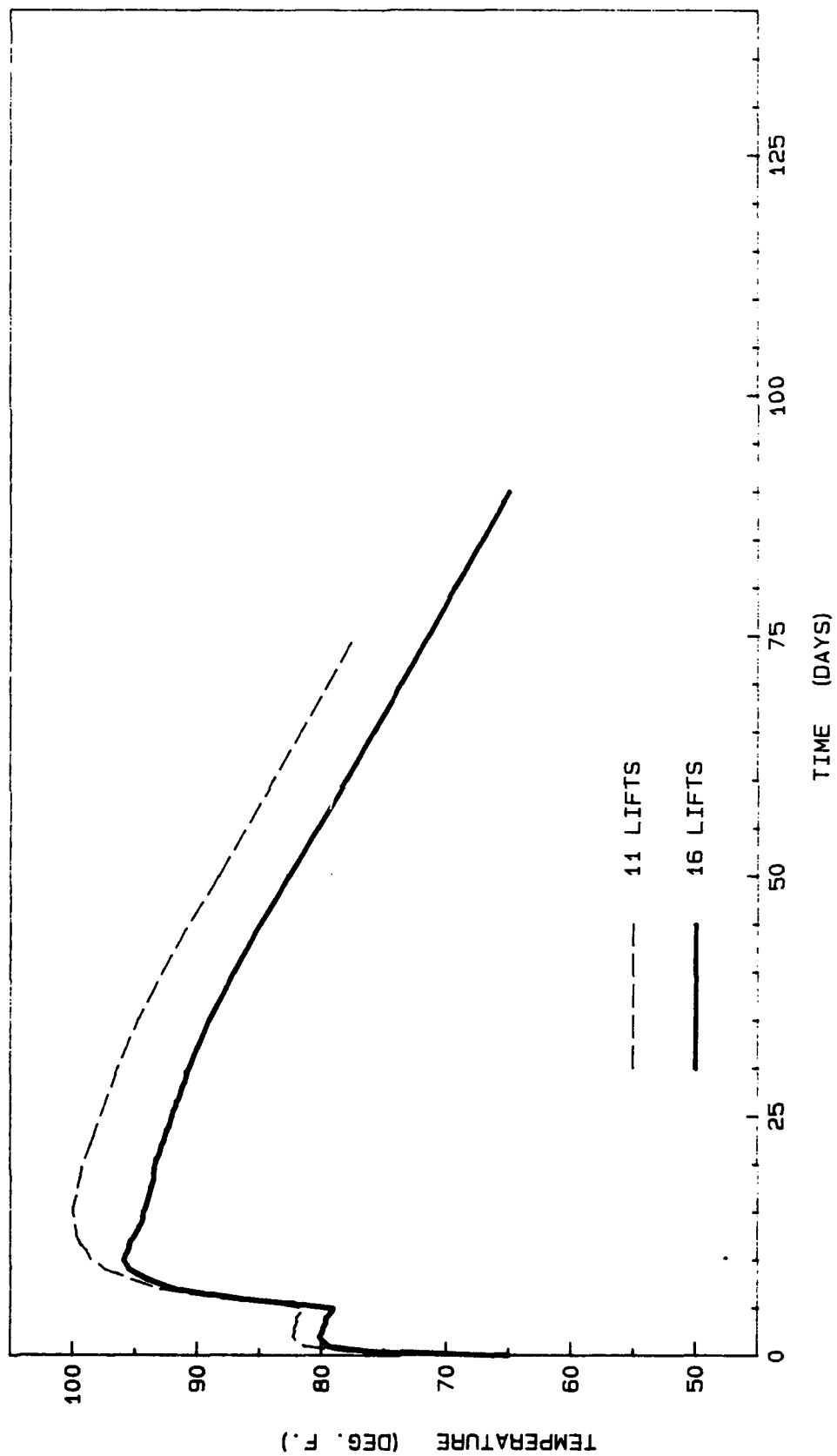


Figure 171. Temperature history at node 3296

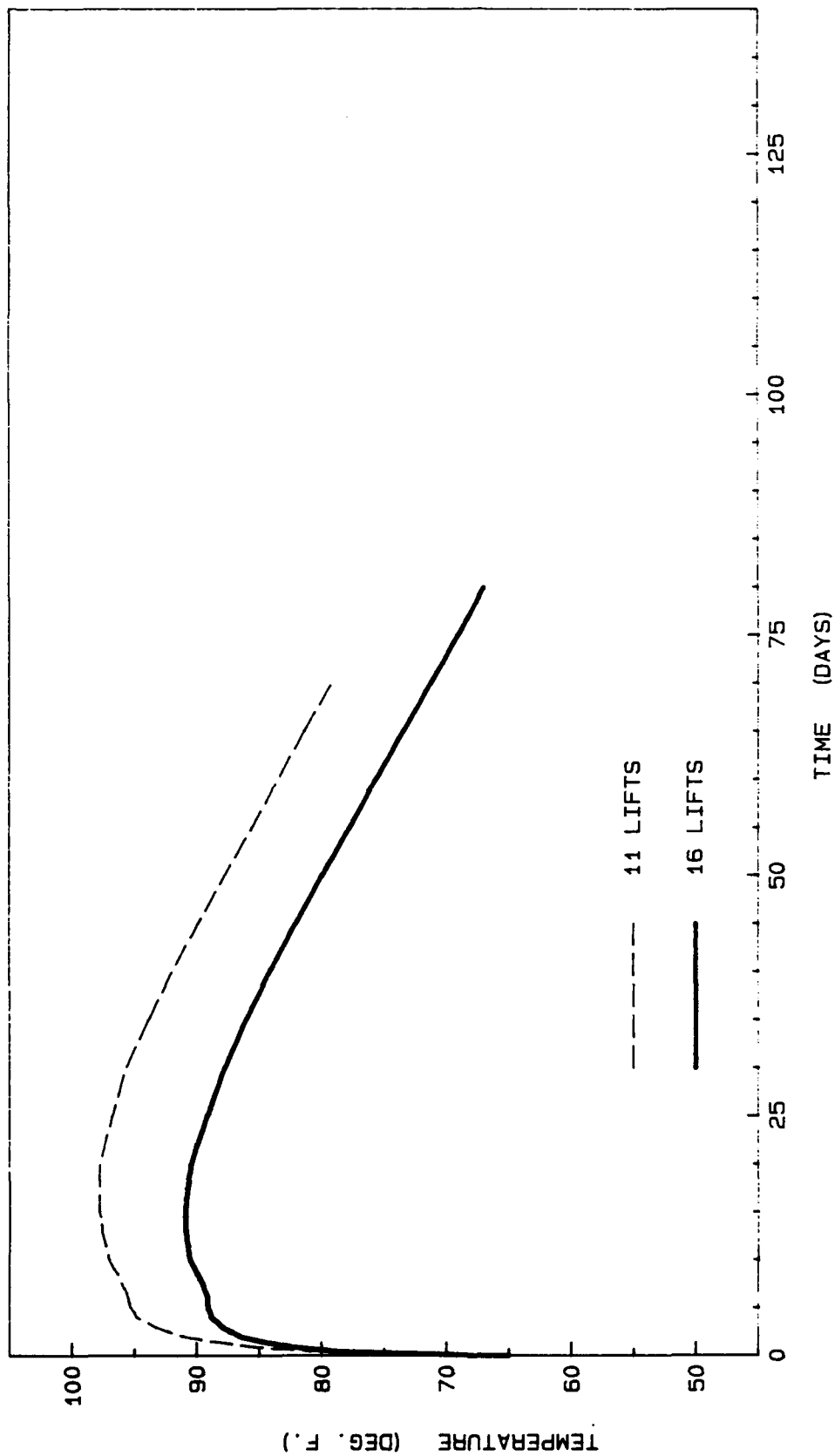


Figure 172. Temperature history at node 3514

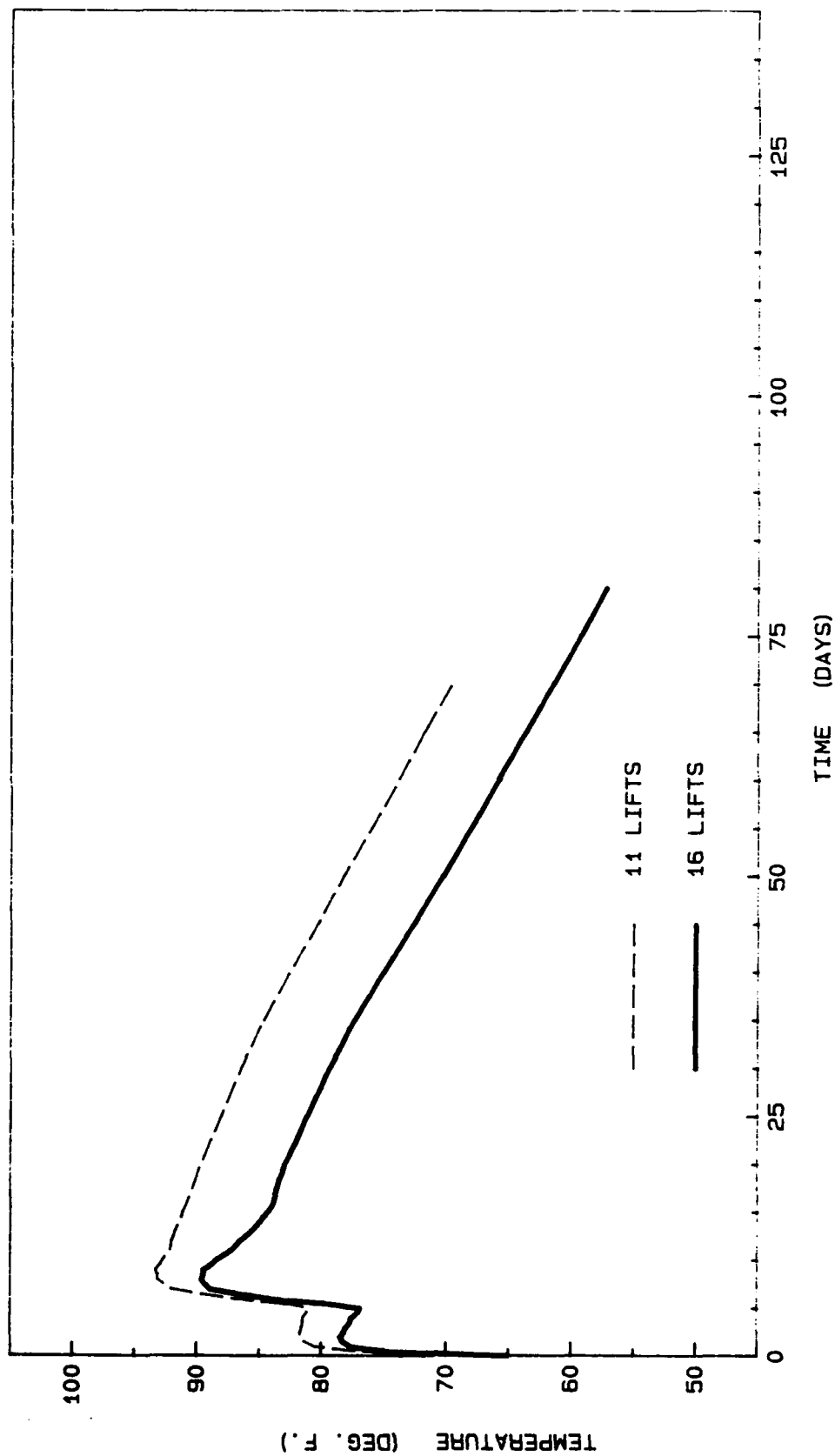


Figure 173. Temperature history at node 3582

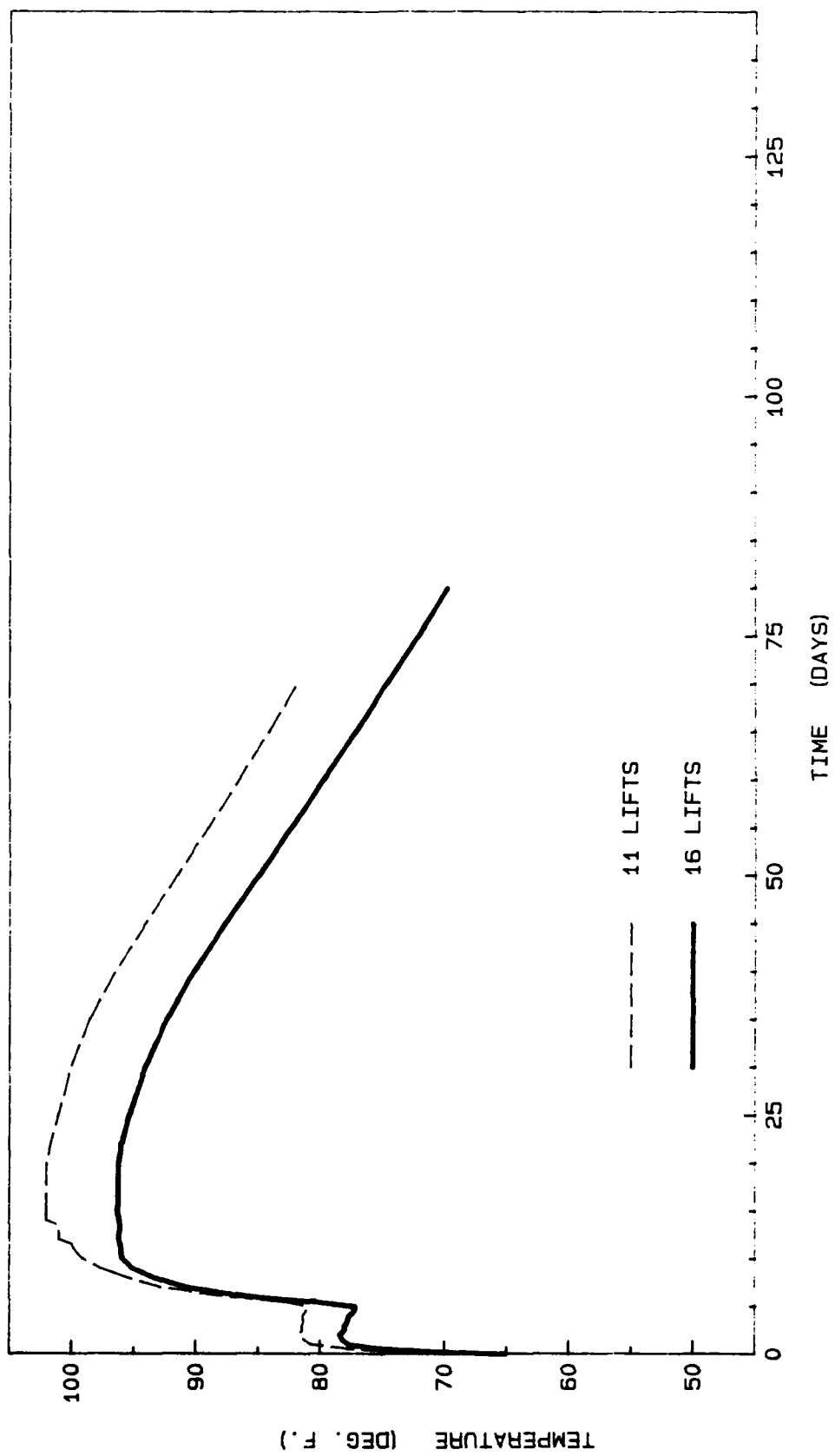


Figure 174. Temperature history at node 3606

151. Figure 175 shows the appropriate nodes and their locations. Figures 176-180 show the time history plots (real time) of some of the mid-lift nodes. Since every proposed lift for the 11-lift schedule is a combination of two of lifts used in the 16-lift schedule, every figure consists of three curves. One is for the 11-lift plan labeled B plus the node number and the other curves which are labeled A plus the node number are for the 16-lift plan. This was done in order to have a good comparison of embedded nodal temperatures. The difference is relatively small but it seems to increase for the upper sections. The maximum difference is only about 5° F to 6° F occurring above the void. Even though this section is relatively thick, the entire difference in temperature should not be attributed to increasing the lift height. The ambient temperature, which seen earlier to effect the temperature rise, is not the same for the corresponding compared sections. For example the ambient temperature is 79.1° F at the time the void is closed in the 11-lift plan and it is only 75.6° F in the case of the 16-lift plan. The earlier closing of the void in the 11-lift plan is believed to be the largest contributor to the difference in temperature between the two lift plans.



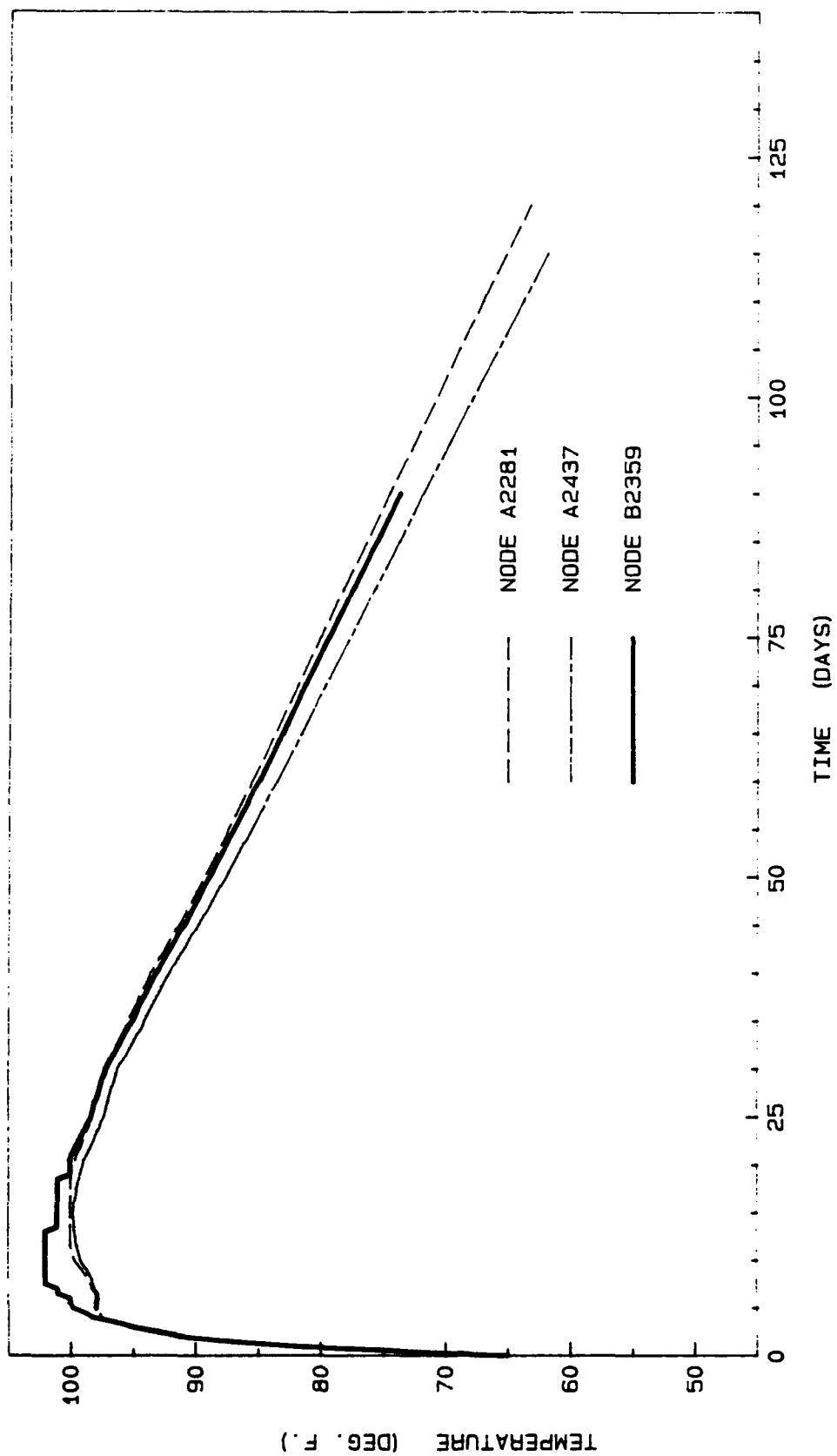


Figure 176. Temperature comparison between the 11-lift and the 16-lift plans

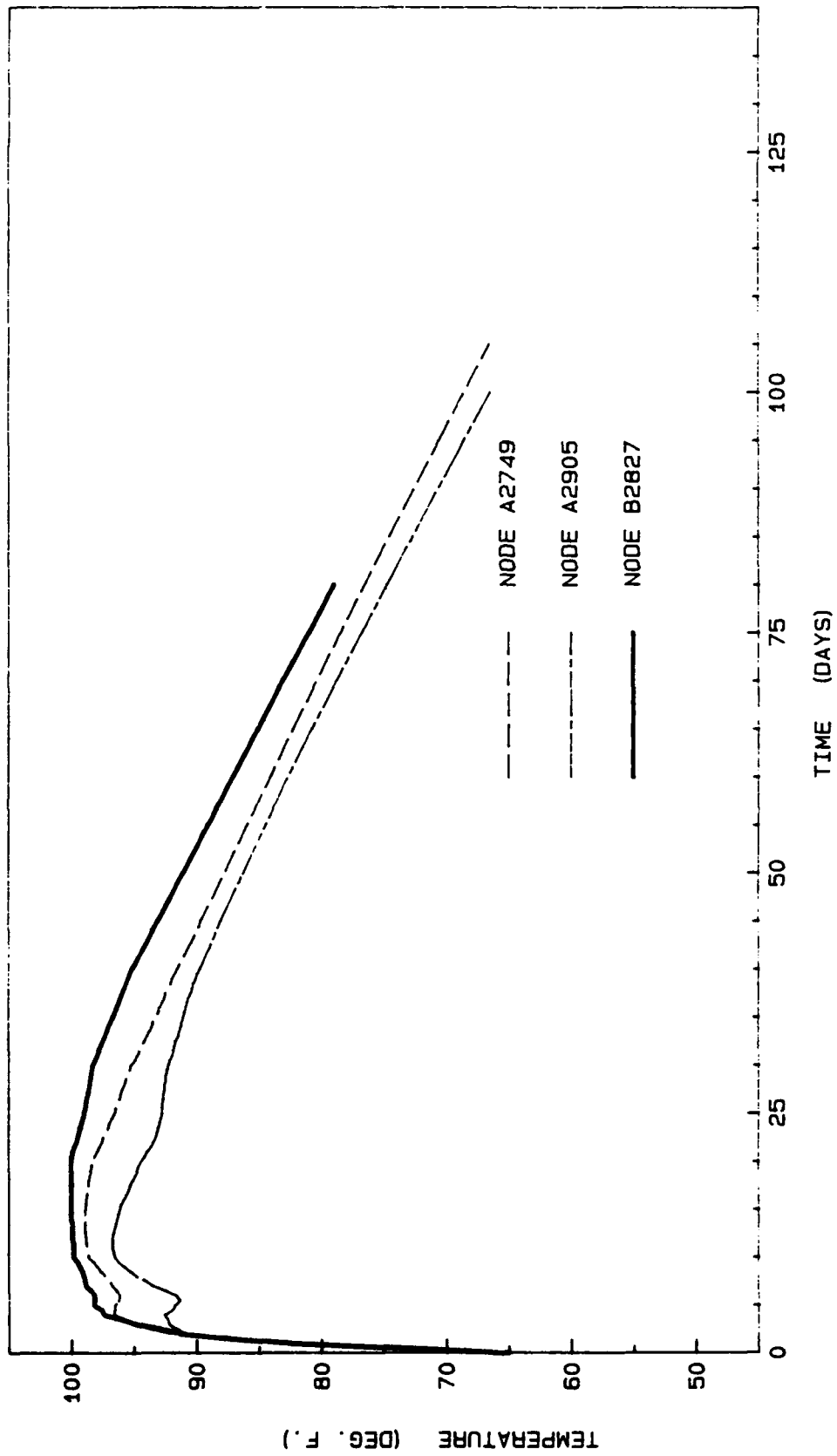


Figure 177. Temperature comparison between the 11-lift and the 16-lift plans

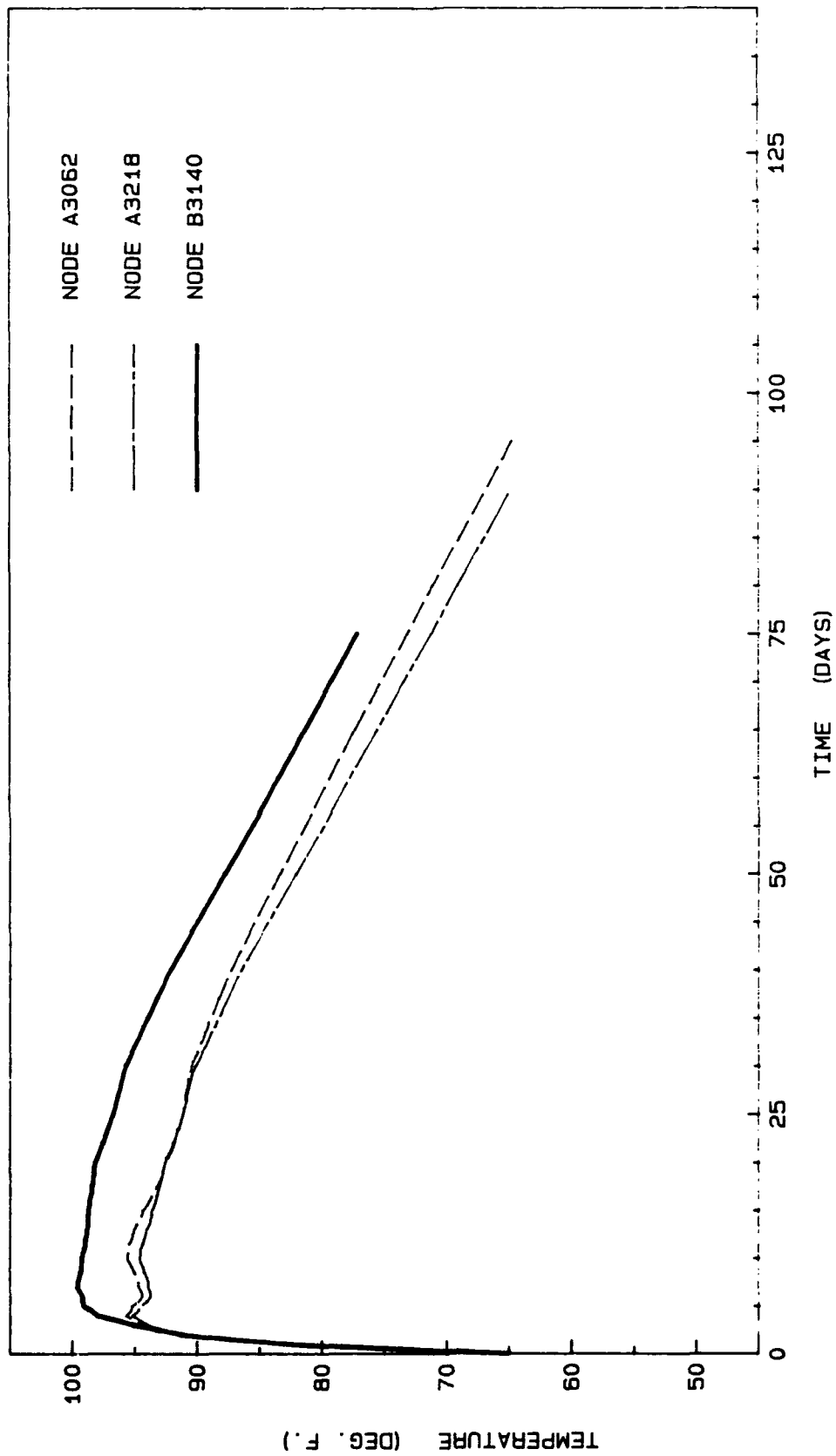


Figure 178. Temperature comparison between the 11-lift and the 16-lift plans

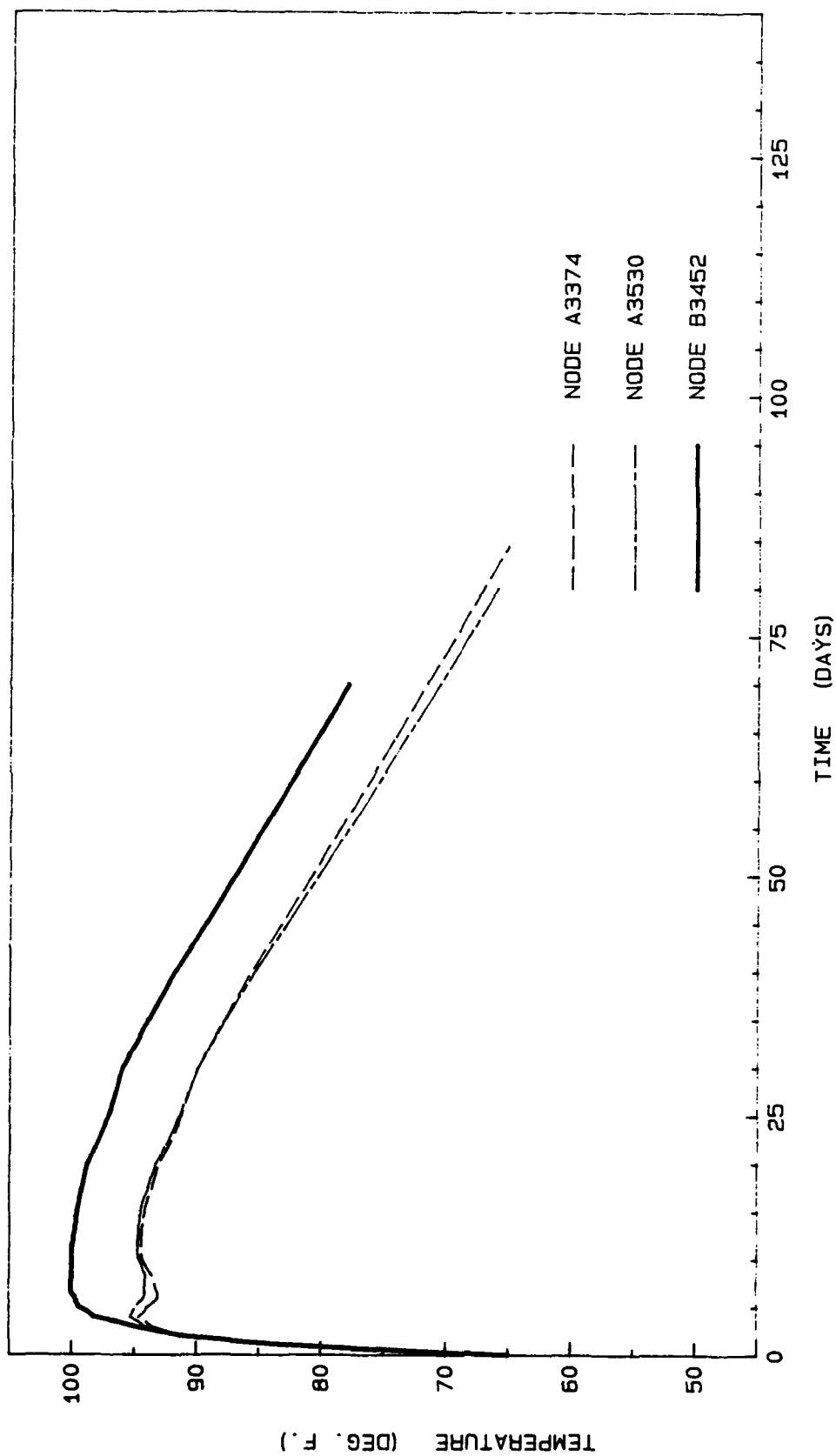


Figure 179. Temperature comparison between the 11-lift and the 16-lift plans

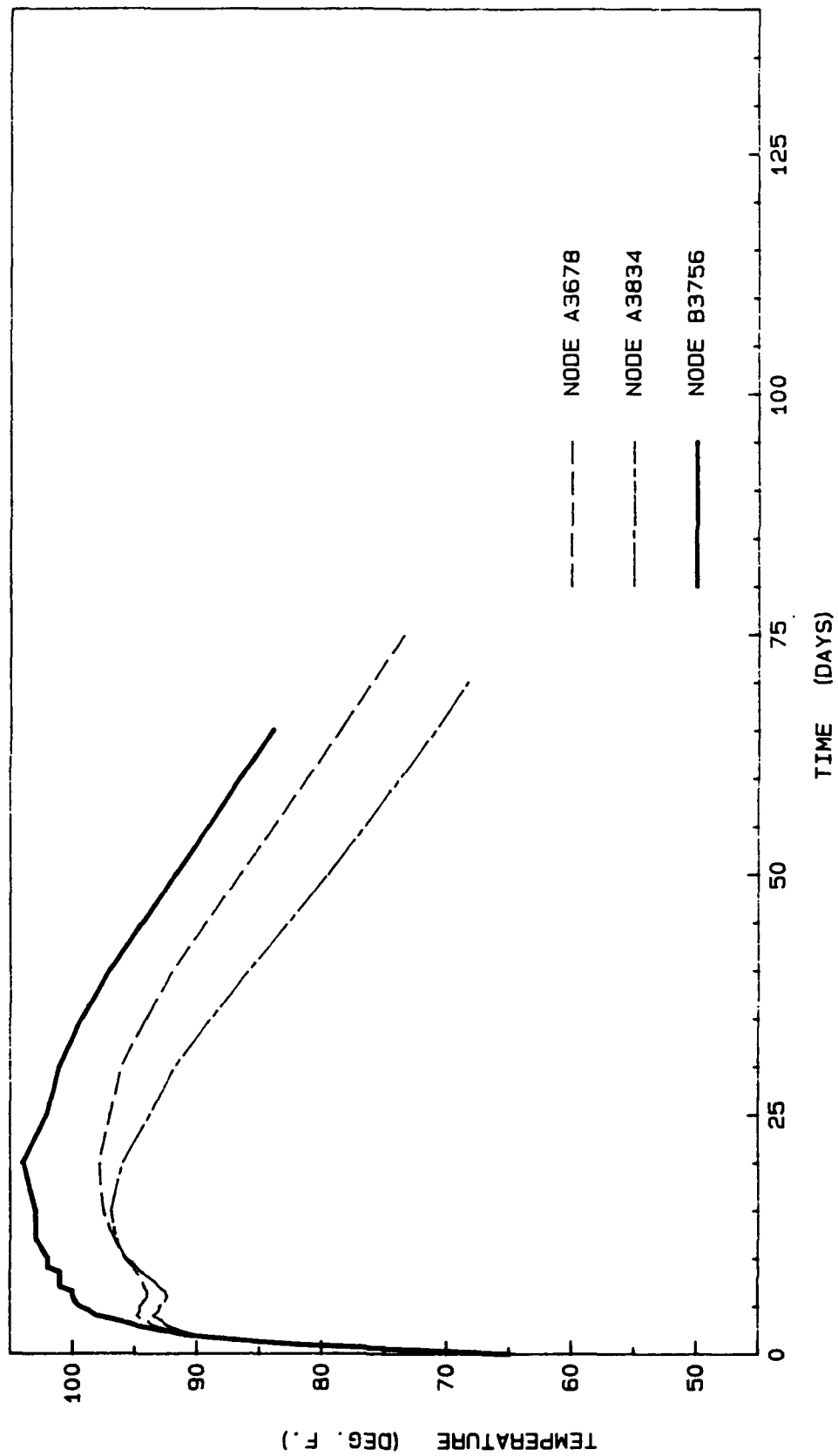


Figure 180. Temperature comparison between the 11-lift and the 16-lift plans

## PART XI: RESULTS FROM THE STRESS ANALYSIS FOR MONOLITH AL-3

### Introduction

152. The results of the stress analysis are presented in forms of history plots of the horizontal and vertical stresses in forms of stress and strain distribution plots at some typical sections. The latter are to check the modelling techniques while the former are mostly used to compare the two lift schedules.

### Incremental Construction

153. As a check to the incremental construction model used, horizontal stress distributions across the slab were investigated for the 16-lift model. Even though the stress variations seem to be well behaved within a lift, there is a discontinuity at the lift interfaces.

154. Two sections are chosen, as shown in Figure 181, to illustrate this discontinuity. Also, the two extreme load cases of lower creep-lower shrinkage, LC, LS, UA, and the upper creep-upper shrinkage, UC, US, UA were used. Section A-A is located about 23 ft to the left of the center line while section B-B is underneath the culvert 13.6 ft from the left side of the monolith. Both distributions, as shown in Figures 182 and 183, initially have a parabolic shape which is typical for the newly placed lifts. Both the top and the bottom of the lift are in tension while the middle is in compression. This phenomenon is mainly due to the expansion of the slab with increasing temperature.

155. Temperature rise, as shown in Part X, is not the only parameter that needs to be considered to interpret the results shown in Figures 182-200. The slab is supported by piles and by the soil which forms an elastic foundation, coupled with the gravity loads produce bending along with the thermal effect. This flexure phenomenon is seen clearly in the stress distribution for section A-A in Figures 184-189. The bottom increases in tension as more lifts are poured while the top becomes compressive. However, for later times, as shown in Figure 190, the situation is reversed. Because of the added weight on either side of the monolith, the slab stresses are reversing with tension at the top and compression at the bottom. The stress distributions

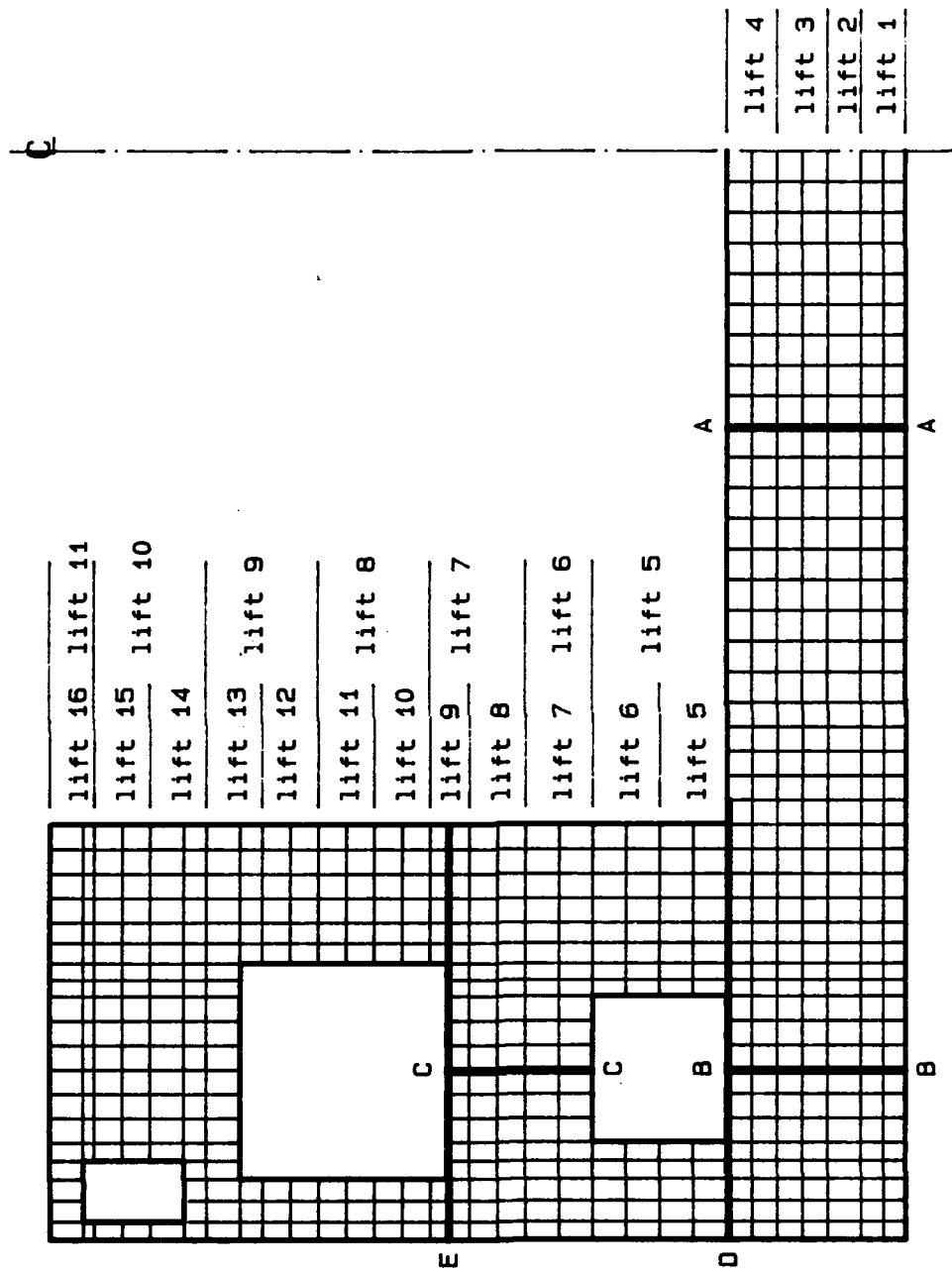


Figure 181. Selected cross-sections used for stress distribution plots

**t = 2.0 days**

— LC, LS, UA

----- UC, US, UA

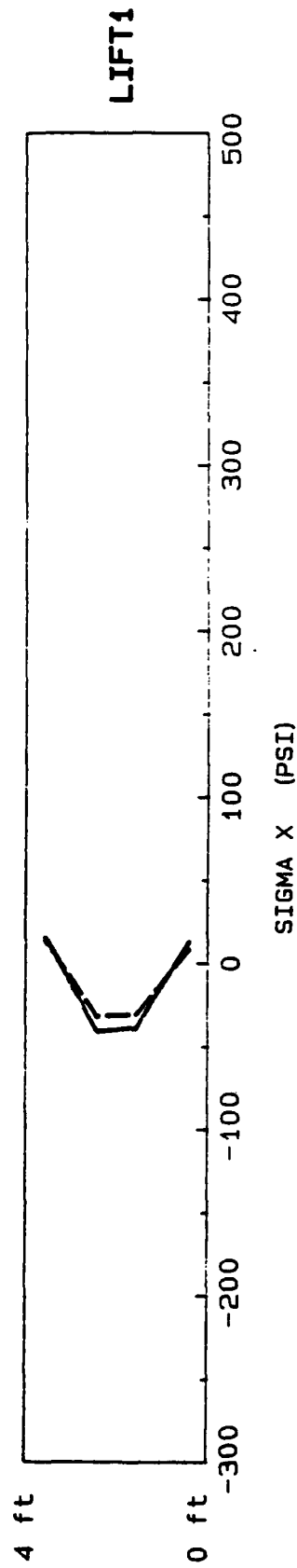


Figure 182. Horizontal stress distribution along section A-A  
2 days after the placement of lift 1

**t = 5.0 days**

— LC, LS, UA

- - - UC, US, UA

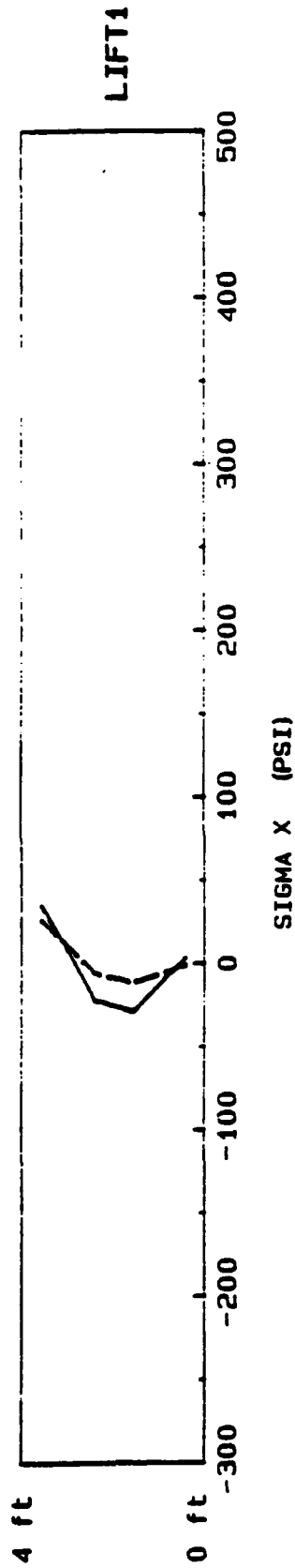


Figure 183. Horizontal stress distribution along section A-A 5 days after the placement of lift 1

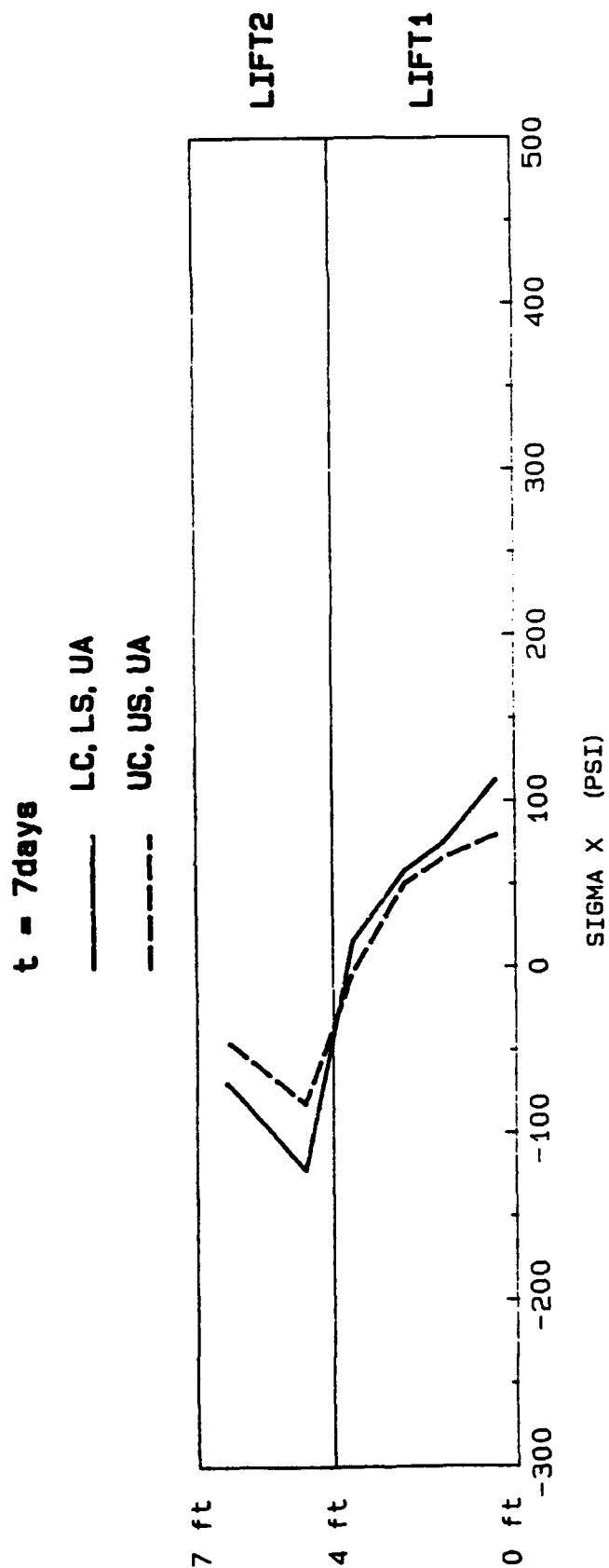


Figure 184. Horizontal stress distribution along section A-A  
2 days after the placement of lift 2

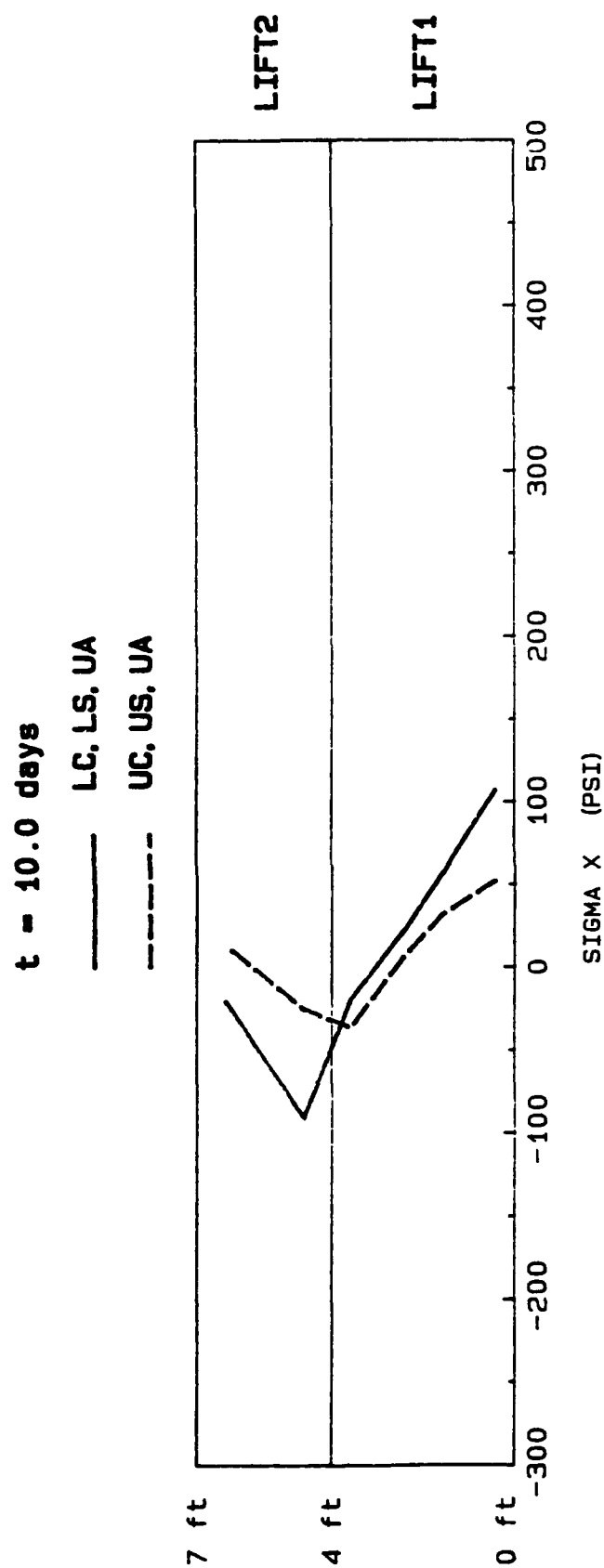


Figure 185. Horizontal stress distribution along section A-A  
5 days after the placement of lift 2

**t = 12.0 days**

— LC, LS, UA

- - - UC, US, UA

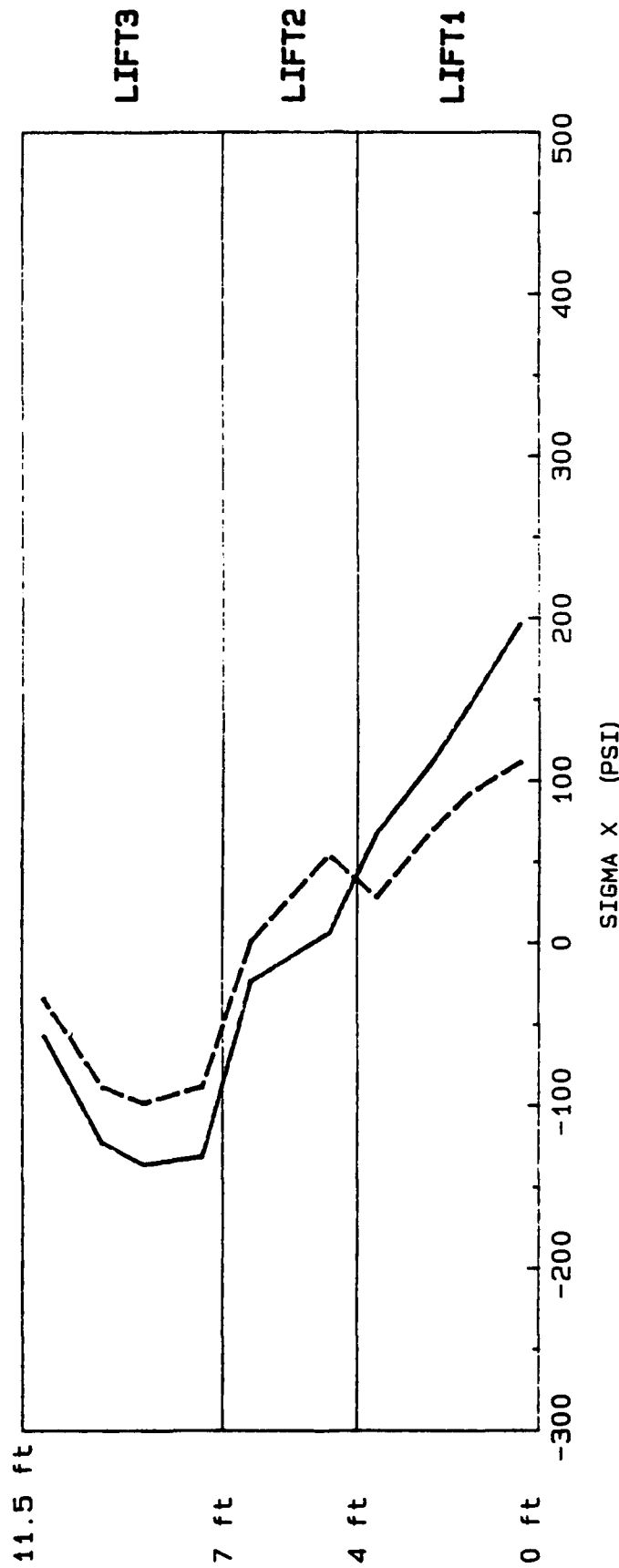


Figure 186. Horizontal stress distribution along section A-A  
2 days after the placement of lift 3

**t = 15.0 days**

— LC, LS, UA  
 ---- UC, US, UA

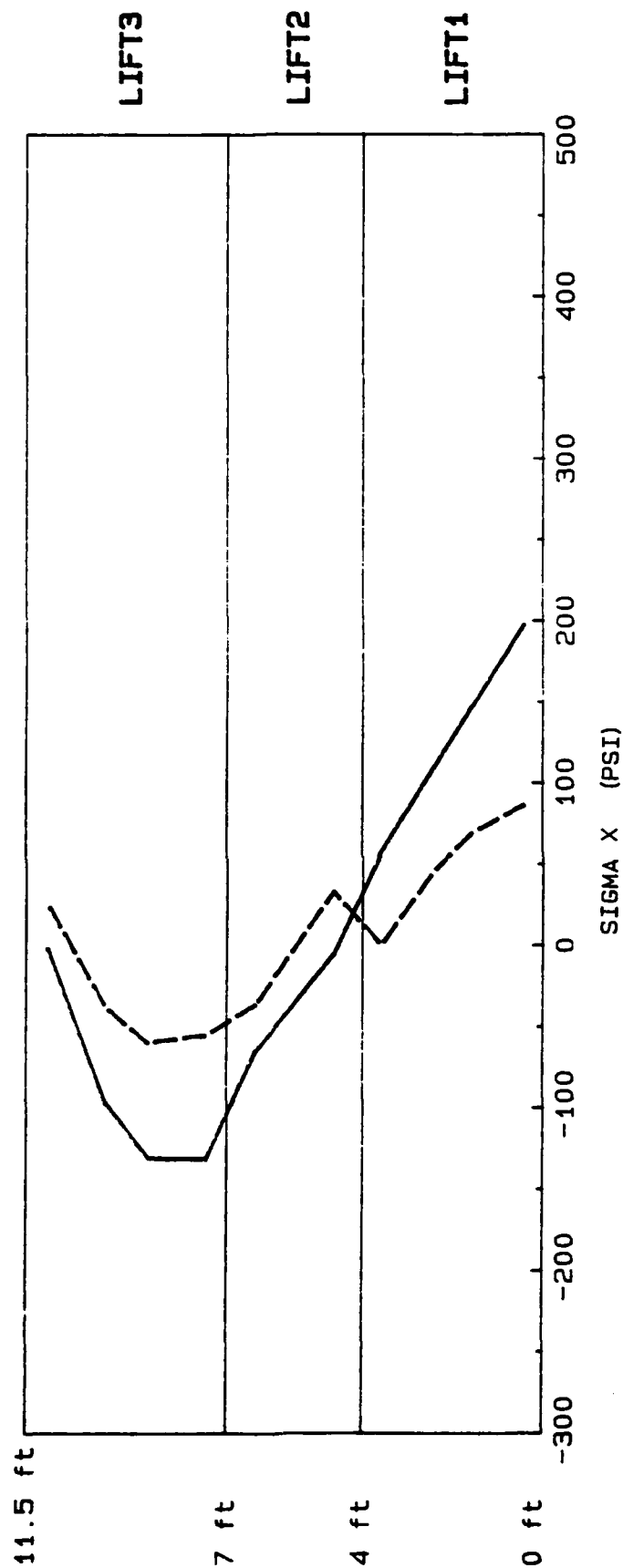


Figure 187. Horizontal stress distribution along section A-A  
 5 days after the placement of lift 3

$t = 17.0$  days

— LC, LS, UA

- - - UC, US, UA

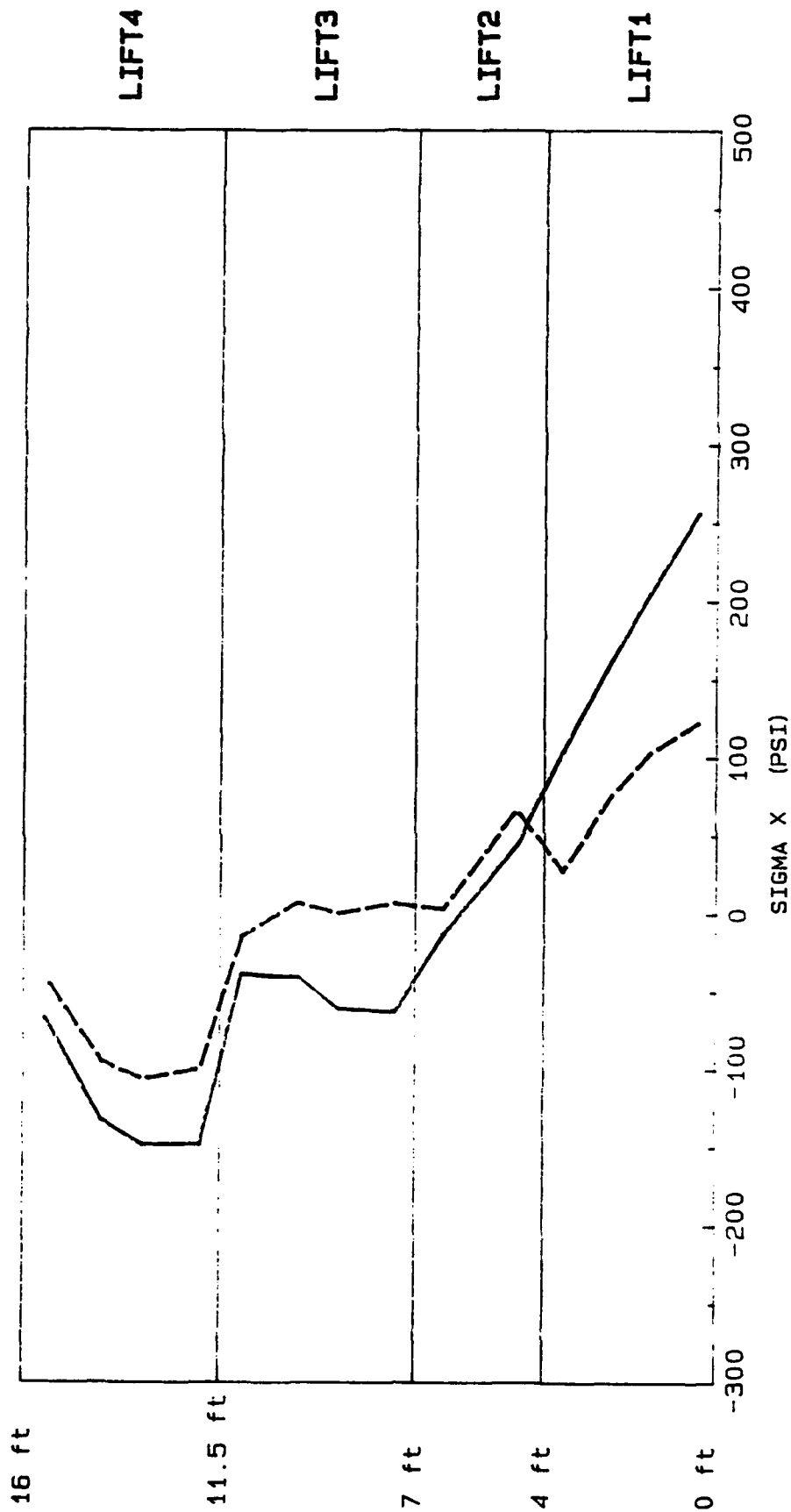


Figure 188. Horizontal stress distribution along section A-A  
2 days after the placement of lift 4

t = 20.0 days

— LC, LS, UA

- - - UC, US, UA

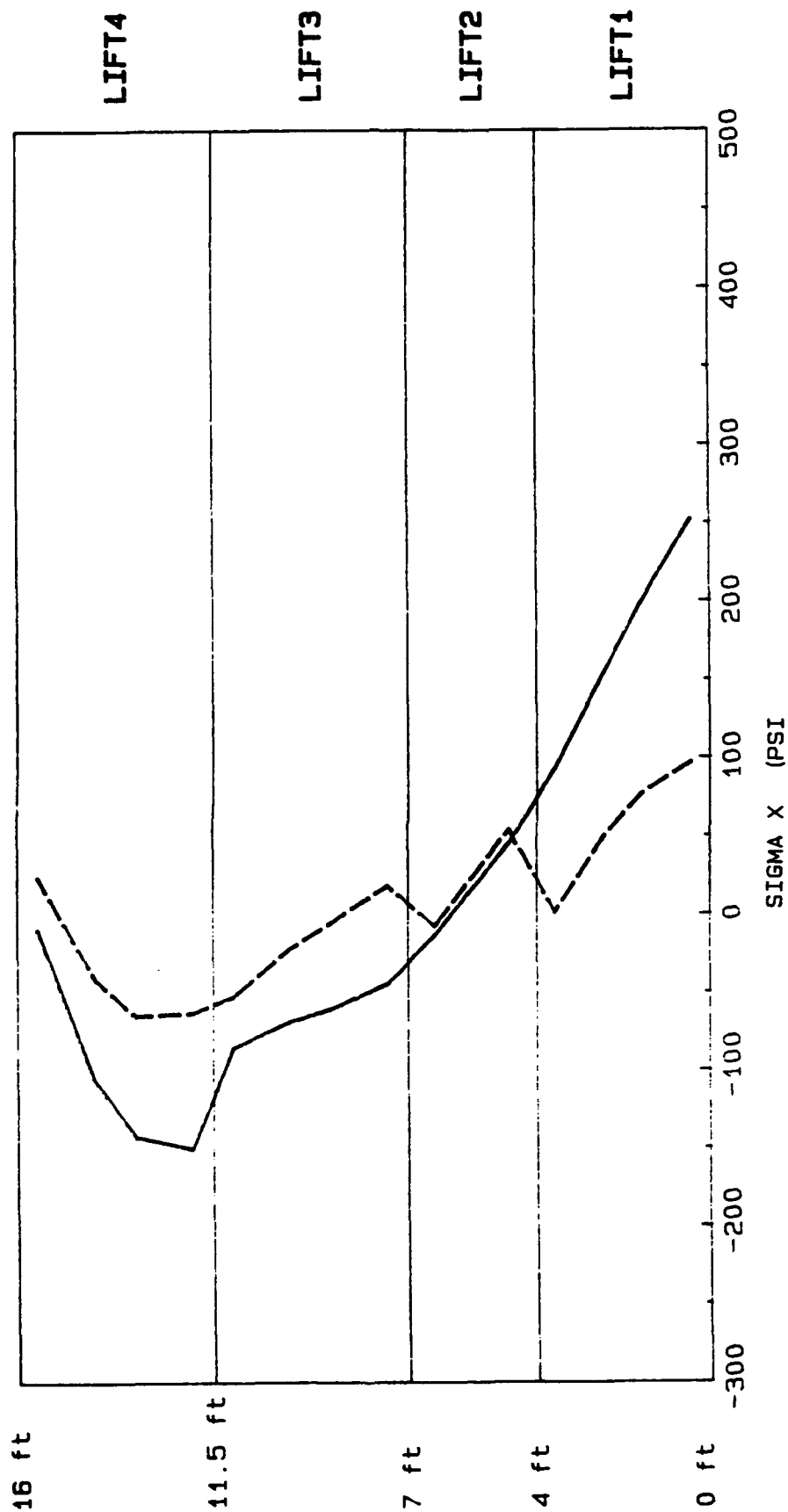
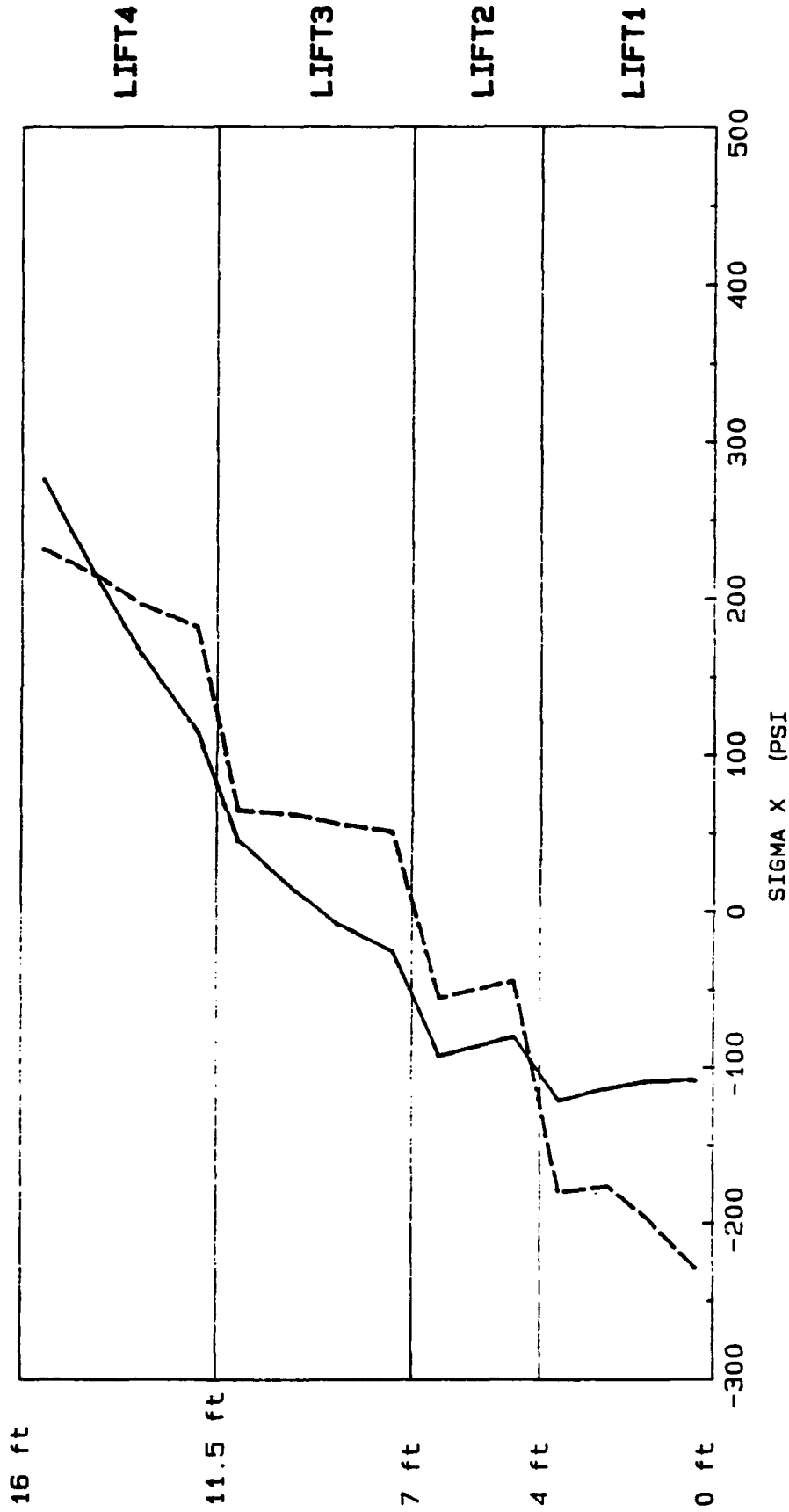


Figure 189. Horizontal stress distribution along section A-A  
5 days after the placement of lift 4

**t = 80.0 days**

—— LC, LS, UA

----- UC, US, UA



**Figure 190. Horizontal stress distribution along section A-A at the end of construction -- 16 lifts**

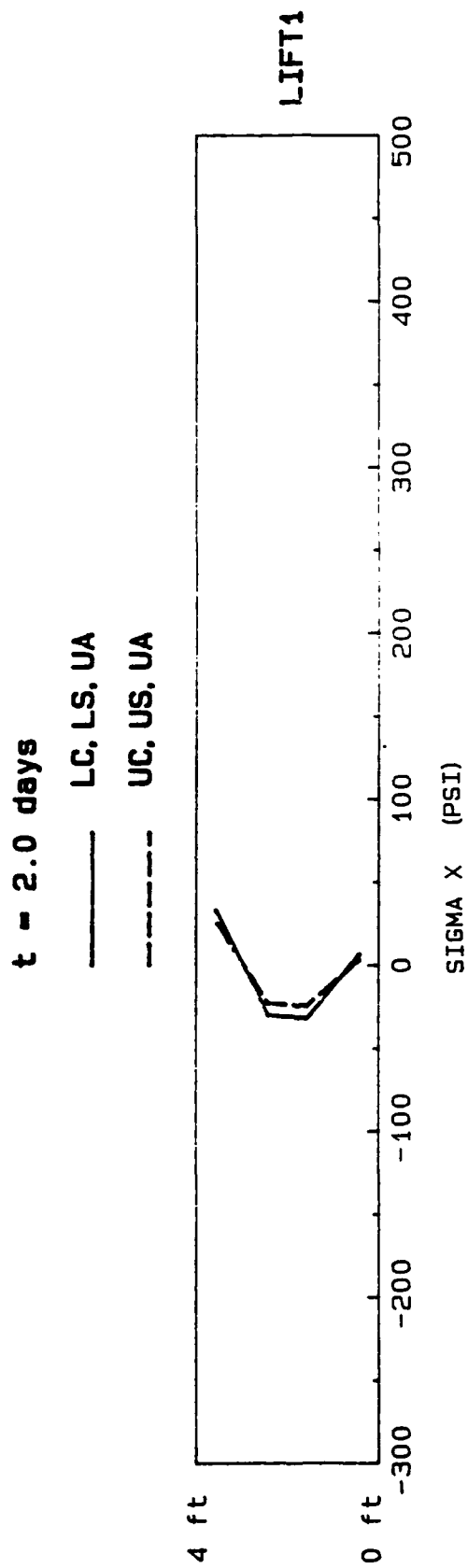


Figure 191. Horizontal stress distribution along section B-B  
2 days after the placement of lift 1

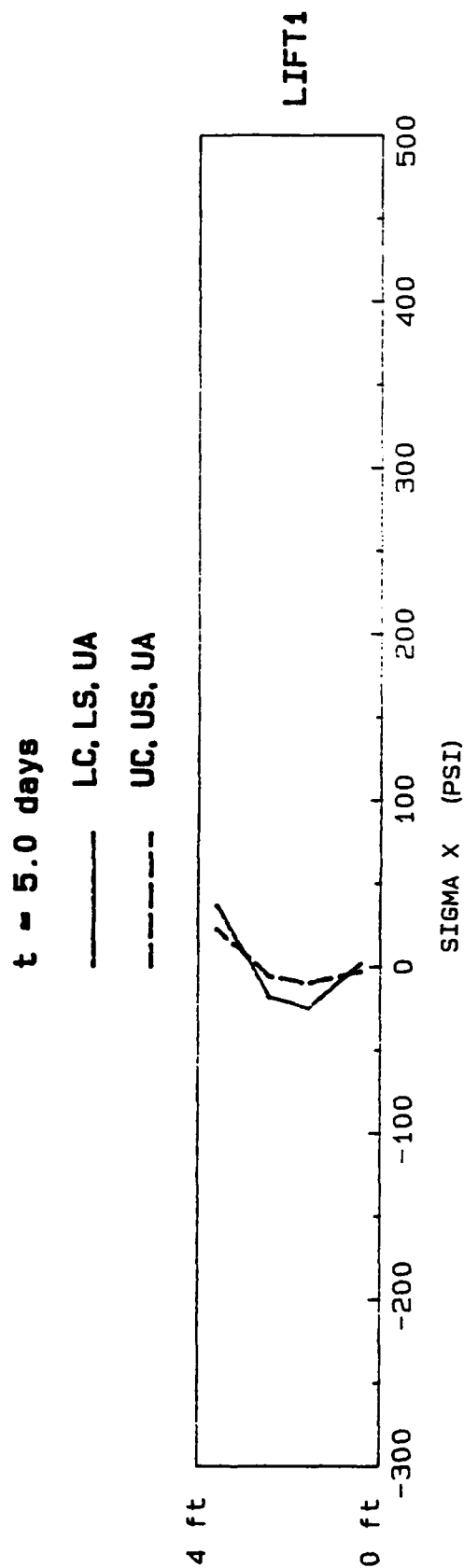


Figure 192. Horizontal stress distribution along section B-B  
5 days after the placement of lift 1

$t = 7.0$  days

— LC, LS, UA

- - - UC, US, UA

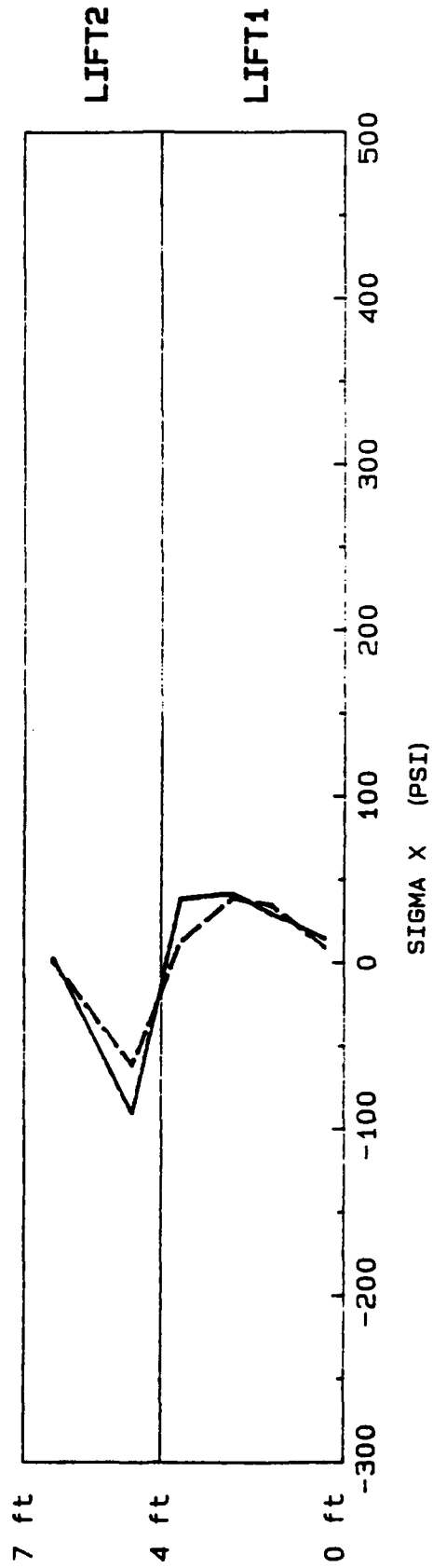


Figure 193. Horizontal stress distribution along section B-B  
2 days after the placement of lift 2

t = 10.0 days

— LC, LS, UA

- - - UC, US, UA

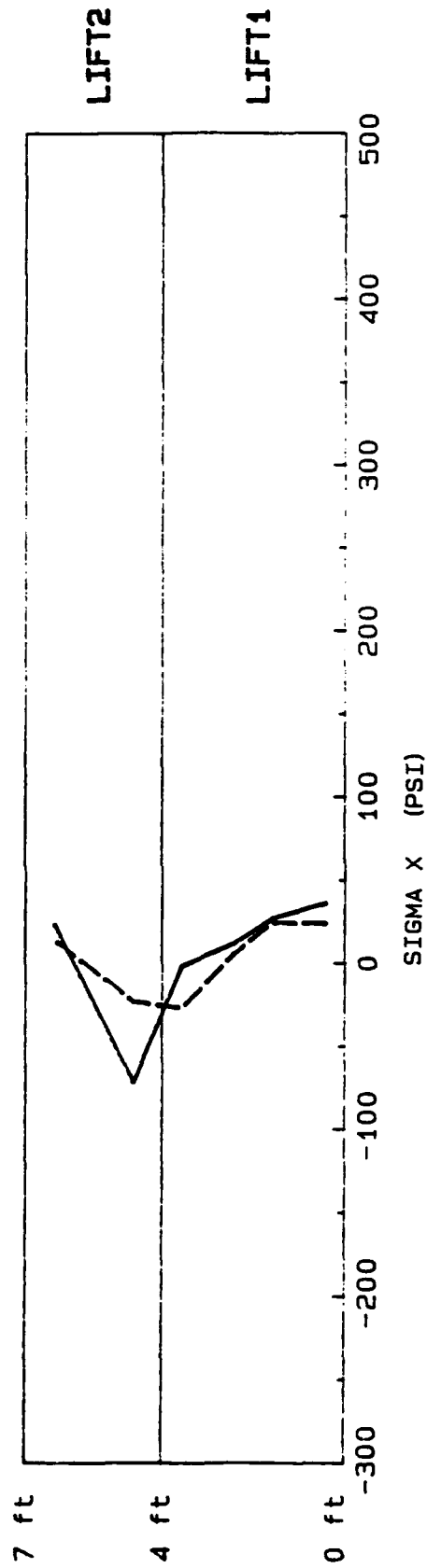


Figure 194. Horizontal stress distribution along section B-B  
5 days after the placement of lift 2

t = 12.0 days

— LC, LS, UA  
 - - - UC, US, UA

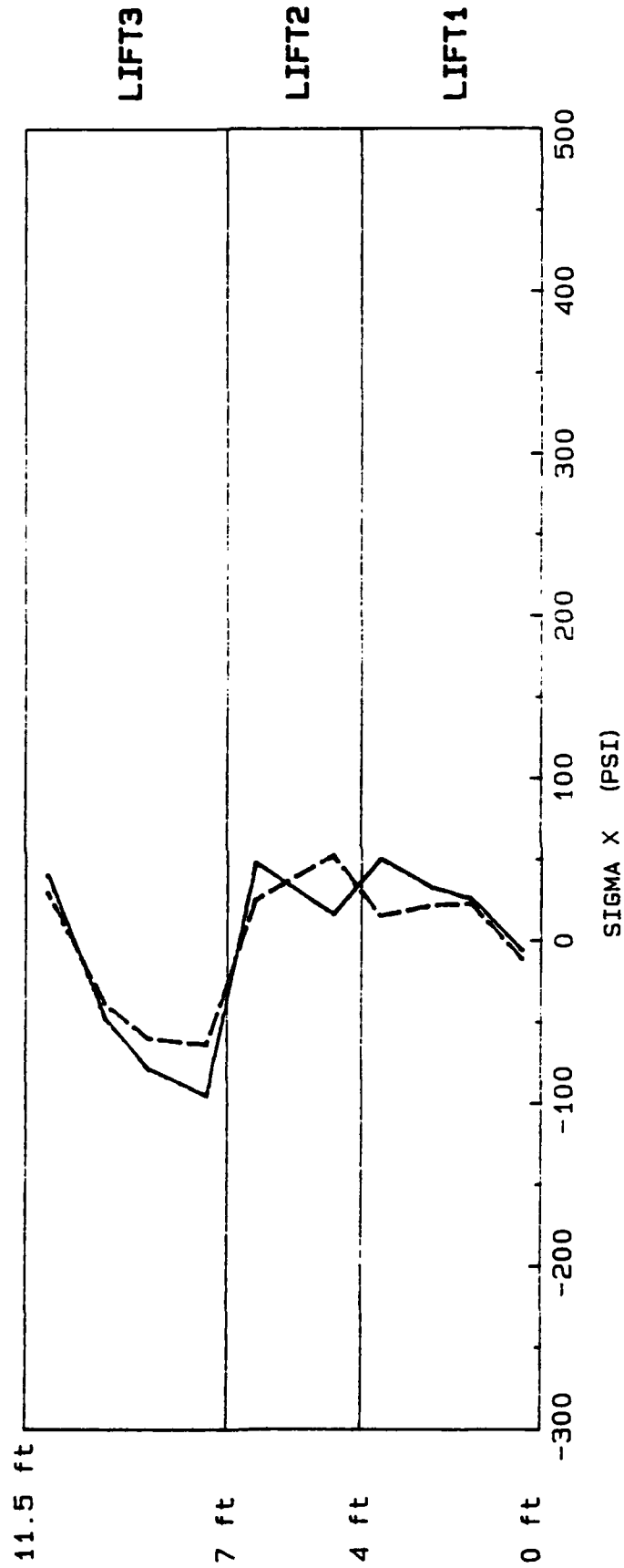


Figure 195. Horizontal stress distribution along section B-B  
 2 days after the placement of lift 3

$t = 15.0$  days

— LC, LS, UA

- - - UC, US, UA

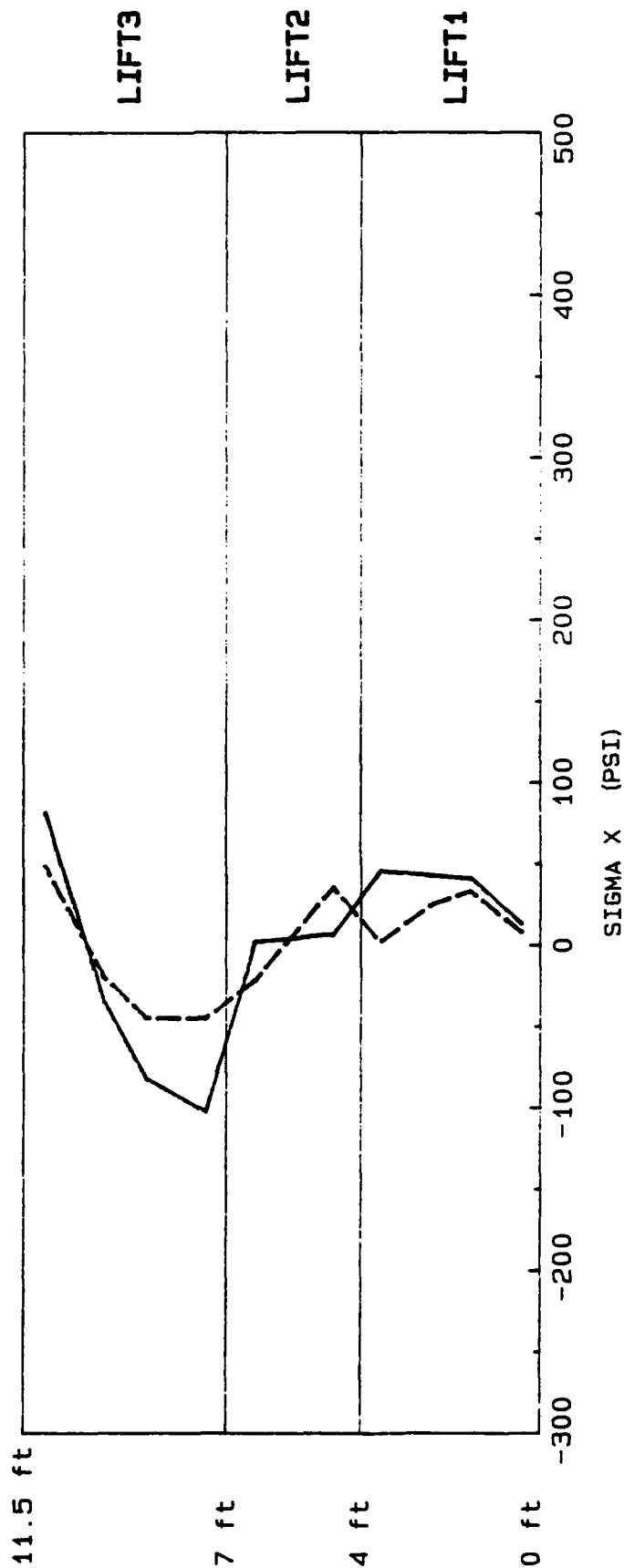


Figure 196. Horizontal stress distribution along section B-B  
5 days after the placement of lift 3

$t = 17.0$  days

— LC, LS, UA

- - - UC, US, UA

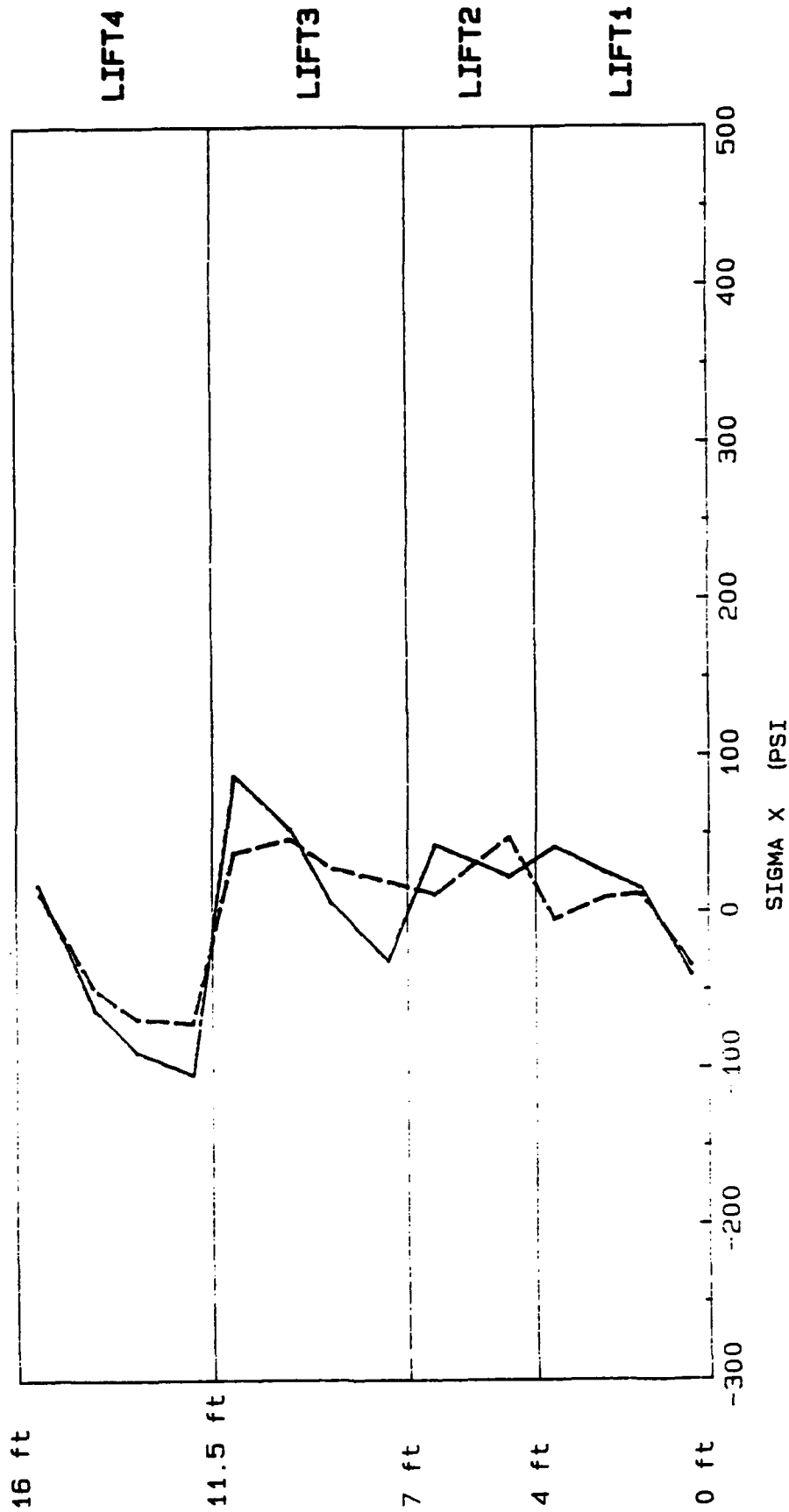


Figure 197. Horizontal stress distribution along section B-B  
2 days after the placement of lift 4

t = 20.0 days

— LC, LS, UA

- - - UC, US, UA

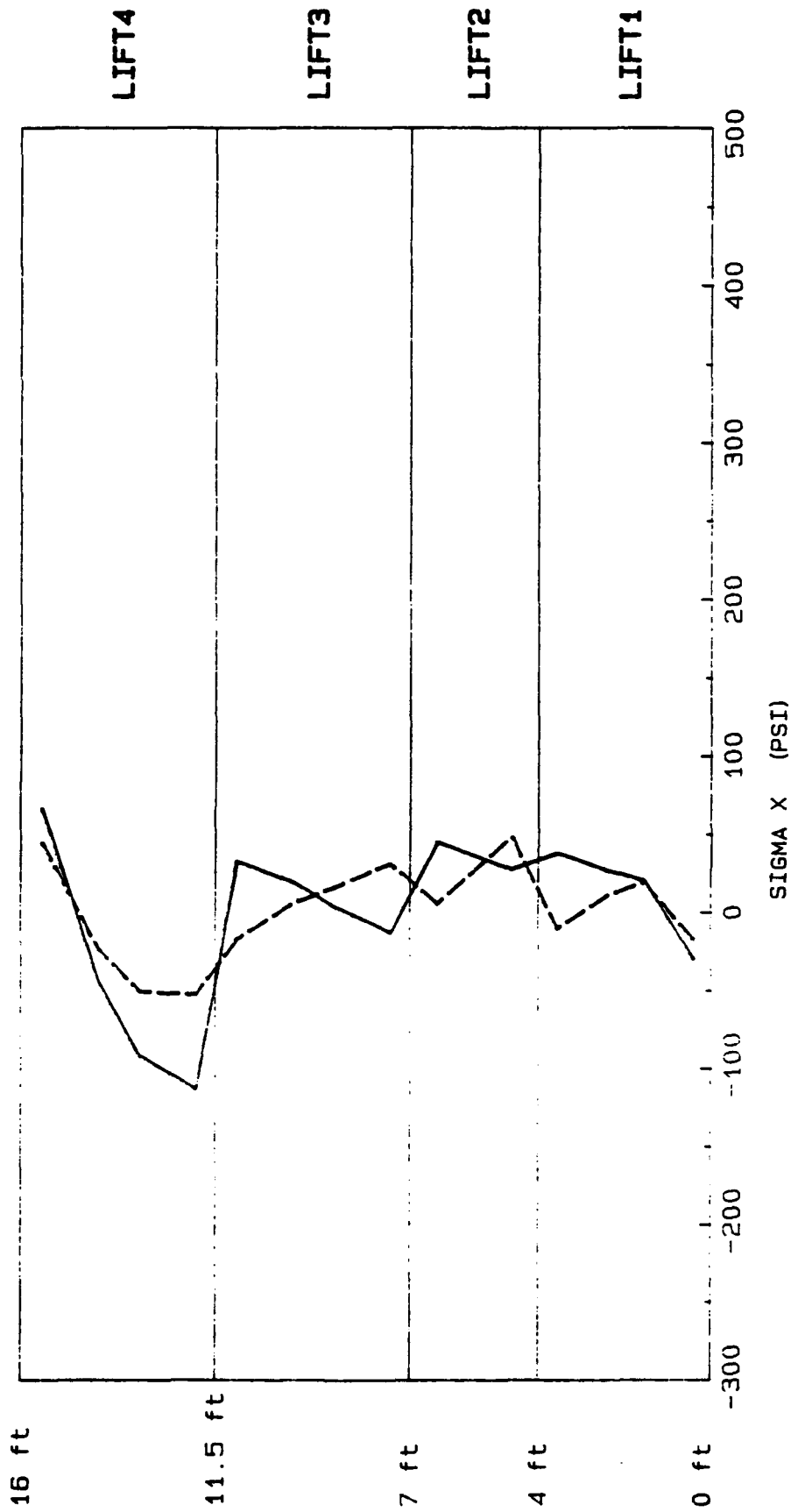


Figure 198. Horizontal stress distribution along section B-B  
5 days after the placement of lift 4

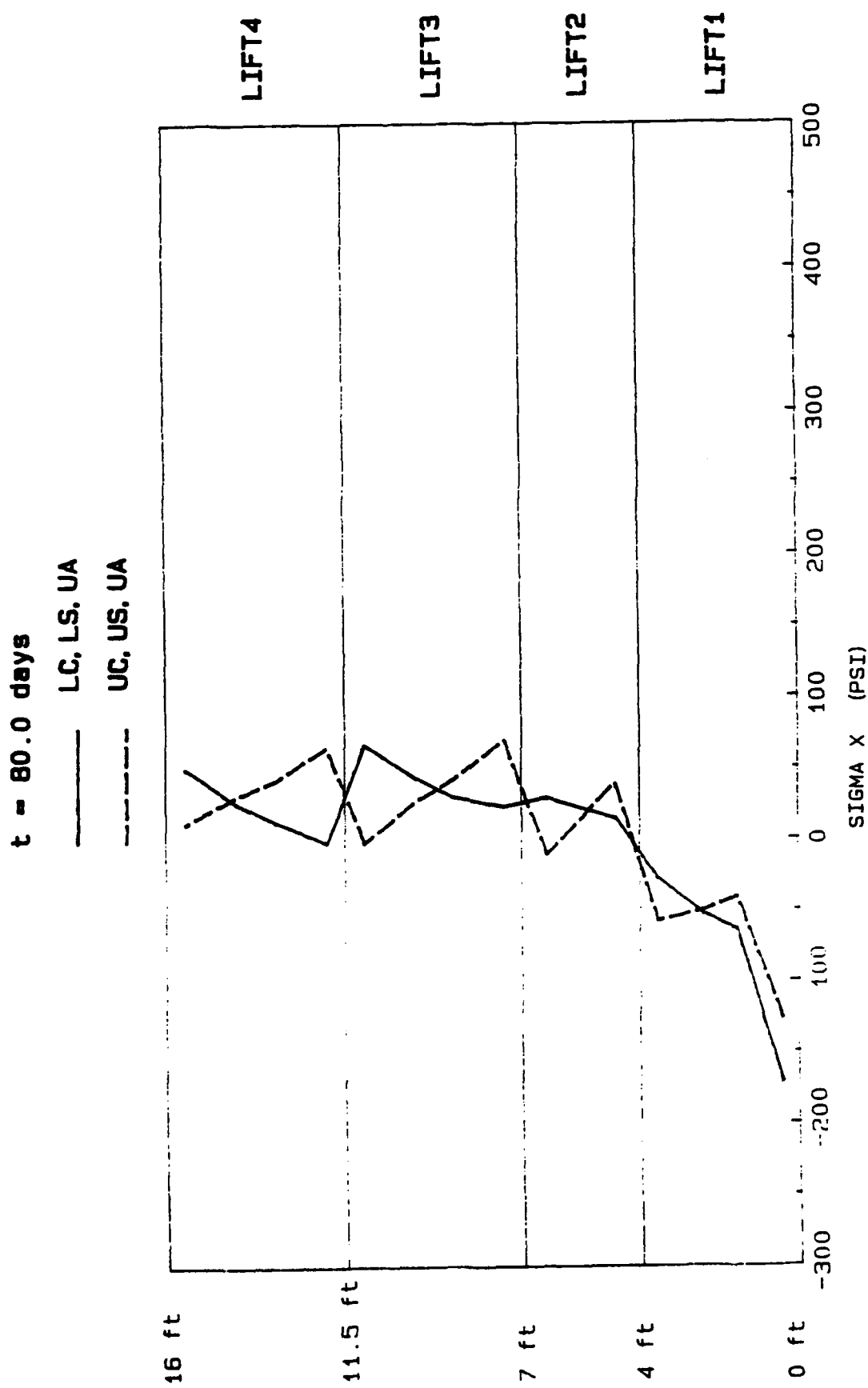


Figure 199. Horizontal stress distribution along section B-B at the end of construction -- 16 lifts

$t = 130.0$  days

— LC, LS, UA

- - UC, US, UA

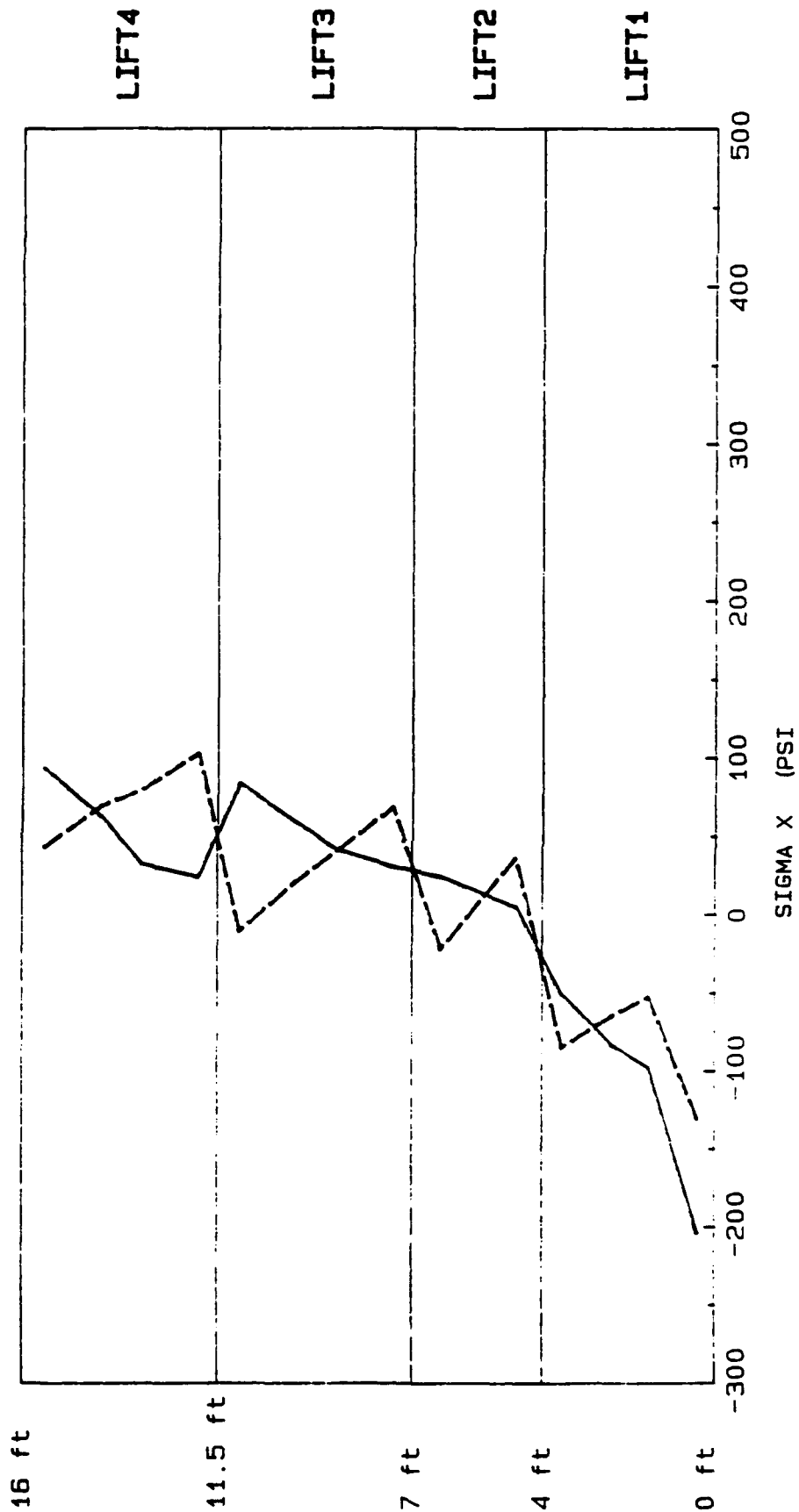


Figure 200. Horizontal stress distribution along section B-B  
50 days after the end of construction -- 16 lifts

are smooth within each lift. However, at many lift interfaces there is a discontinuity in the horizontal stress that is more severe at later times. The strain plots shown in Figures 201-209 clearly show that there is a strain differential at the lift interfaces. Due to the difference in material properties and the nonhomogeneity of the lifts, residual stresses and strain incompatibility might be expected. However, one would like to see these diminish with time. At later times this seems to be most evident when the upper creep and upper shrinkage material properties are used. Current investigations are being performed to try and interpret this phenomenon more clearly.

156. As mentioned in the section on modelling, the top of the openings are temporarily supported by multipoint constraints (MPC). The following is a presentation and a discussion of the results related to the MPC and the model used for the openings.

157. Figures 210 and 211 show horizontal stress and strain histories at the bottom of the culvert. The sudden jump corresponds to the placement of the lift closing the void. Through the investigation of the distributions, shown in Figures 212-215 of the horizontal (Section B-B, Figure 181) and vertical stresses (Section D-D, Figure 181) just below the bottom of the culvert and also through the investigation of some displaced shape plots, (Figures 216 and 217), it is observed that once the lift closing the void is placed, 30 days--real time, the section to the left and below the culvert bends outward. This mechanical action gives rise to the horizontal stresses at the bottom of the culvert and mainly at the left corner. Both Figures 212 and 213 which are stress distribution through a vertical section below the culvert (B-B) show the distribution as pivoting as if being bent. The distributions are rotating about a point near the point of zero stress with increasing tension at the top and increasing compression at the bottom.

158. Figures 214 and 215 which represent stress distributions at a horizontal section just below the culvert show an increase in the horizontal stress following the placement of the lift closing the void. The vertical stress distribution, on the other hand, shows that both sections on either sides of the culvert tend to bend outward. The above phenomenon seems to be related mainly to the incremental construction.

159. Initially, the two wall sections are nothing more than cantilevers attached to the base slab, which are loaded by only gravity and thermal

t = 2.0 days - 11 LIFTS

—— LC, LS, UA

----- UC, US, UA

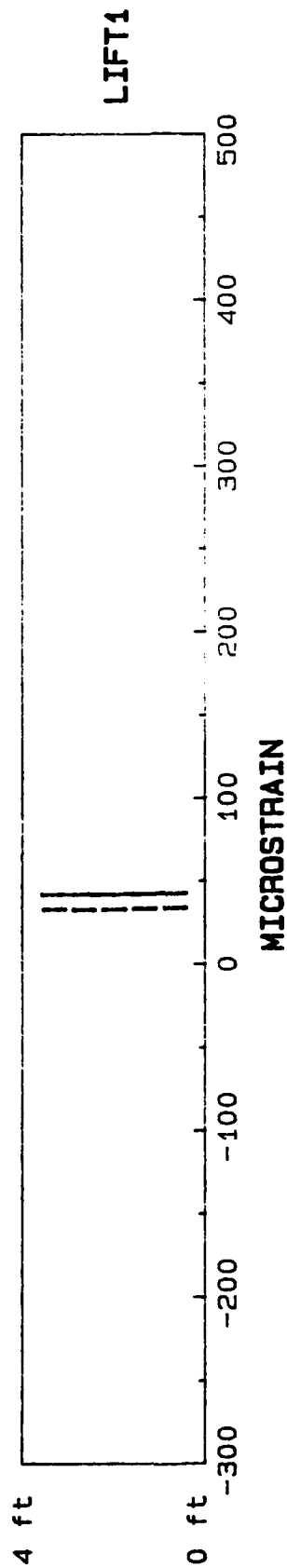


Figure 201. Horizontal strain distribution along section A-A  
2 days after the placement of lift 1

t = 5.0 days - 11 LIFTS

—— LC, LS, UA

----- UC, US, UA

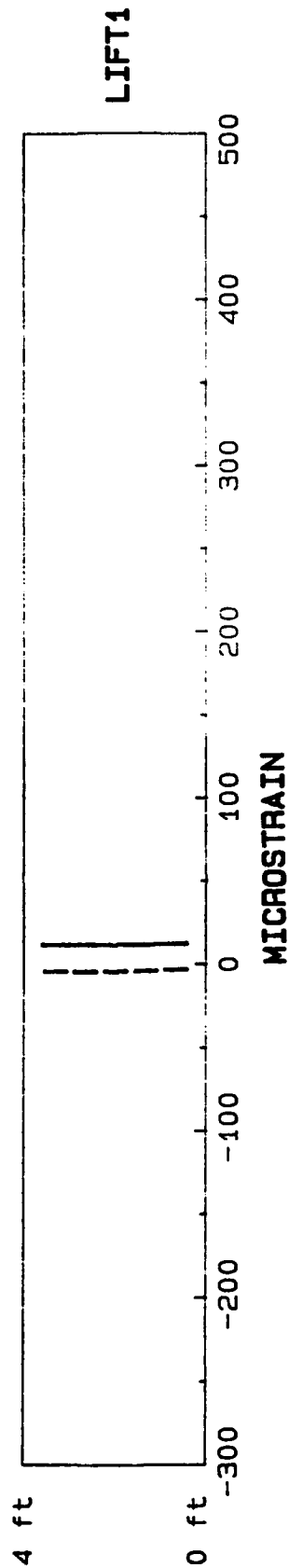


Figure 202. Horizontal strain distribution along section A-A  
5 days after placing lift 1

t = 7days - 11 LIFTS

—— LC, LS, UA

----- UC, US, UA

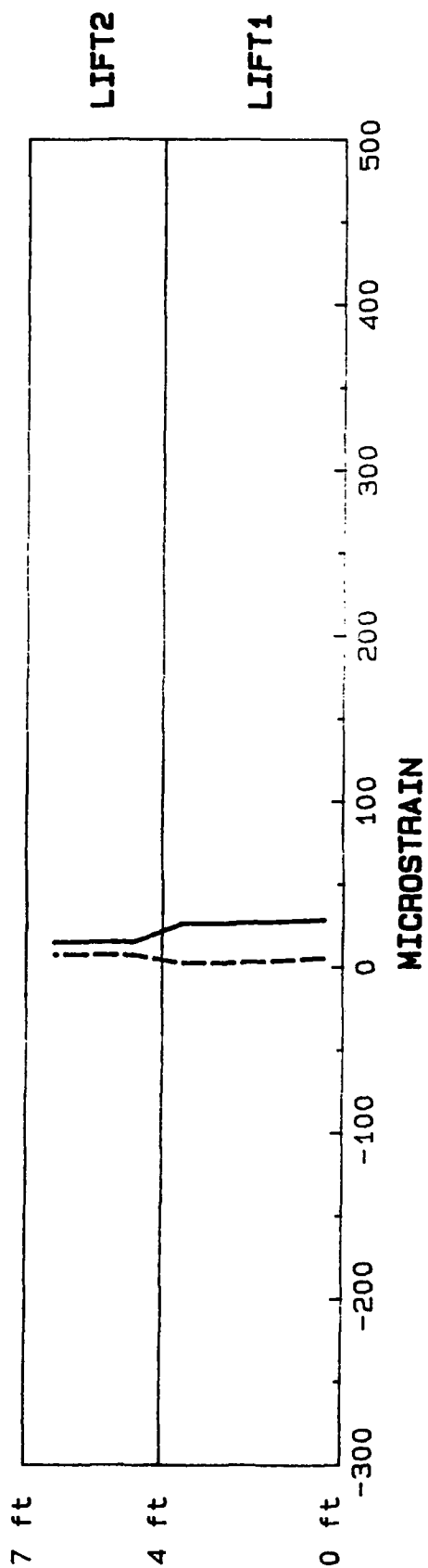


Figure 203. Horizontal strain distribution along section A-A  
2 days after the placement of lift 2

t = 10.0 days - 11 LIFTS

— LC, LS, UA

- - - UC, US, UA

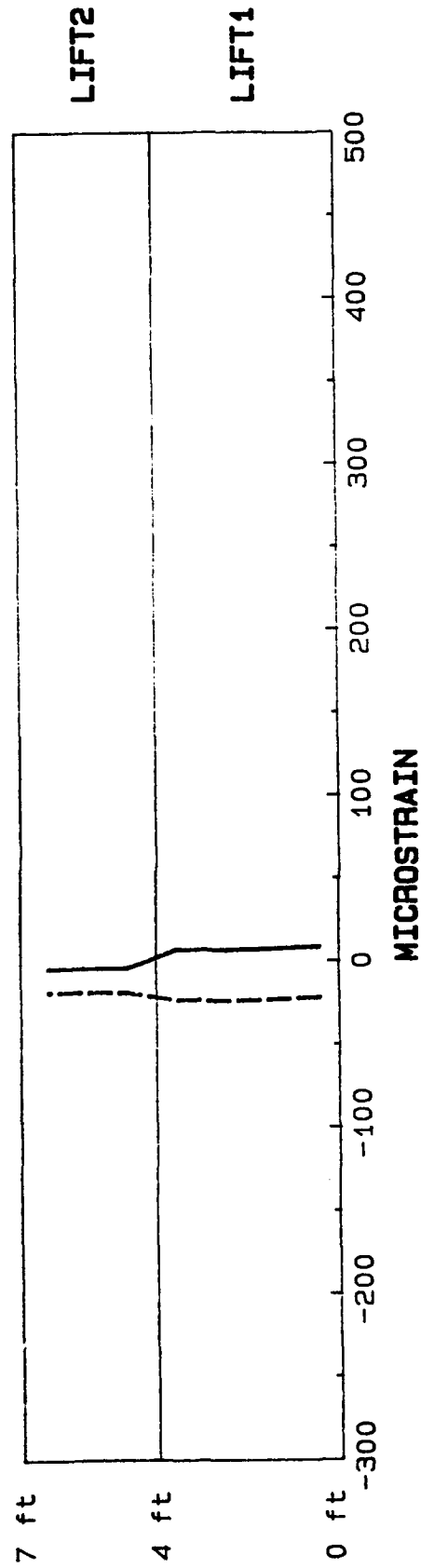


Figure 204. Horizontal strain distribution along section A-A  
5 days after the placement of lift 2

t = 12.0 days - 11 LIFTS

—— LC, LS, UA

----- UC, US, UA

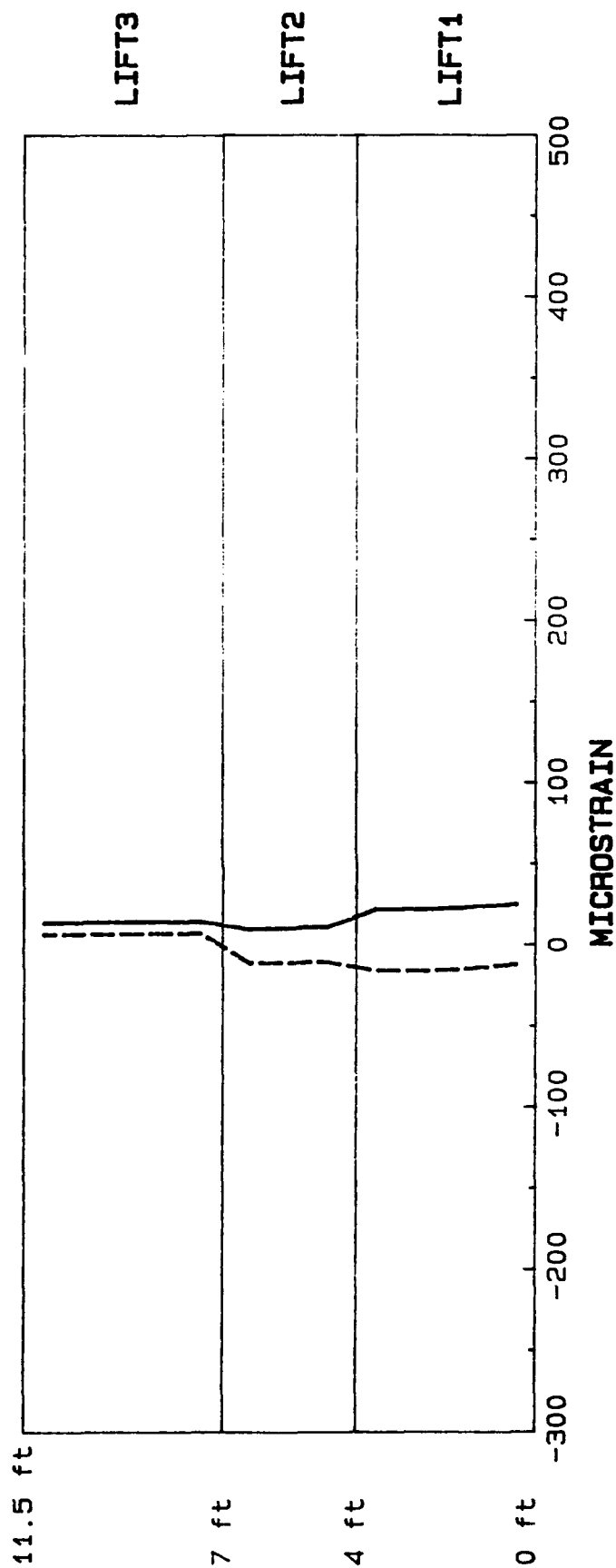


Figure 205. Horizontal strain distribution along section A-A  
2 days after the placement of lift 3

t = 15.0 days - 11 LIFTS

—— LC, LS, UA

---- UC, US, UA

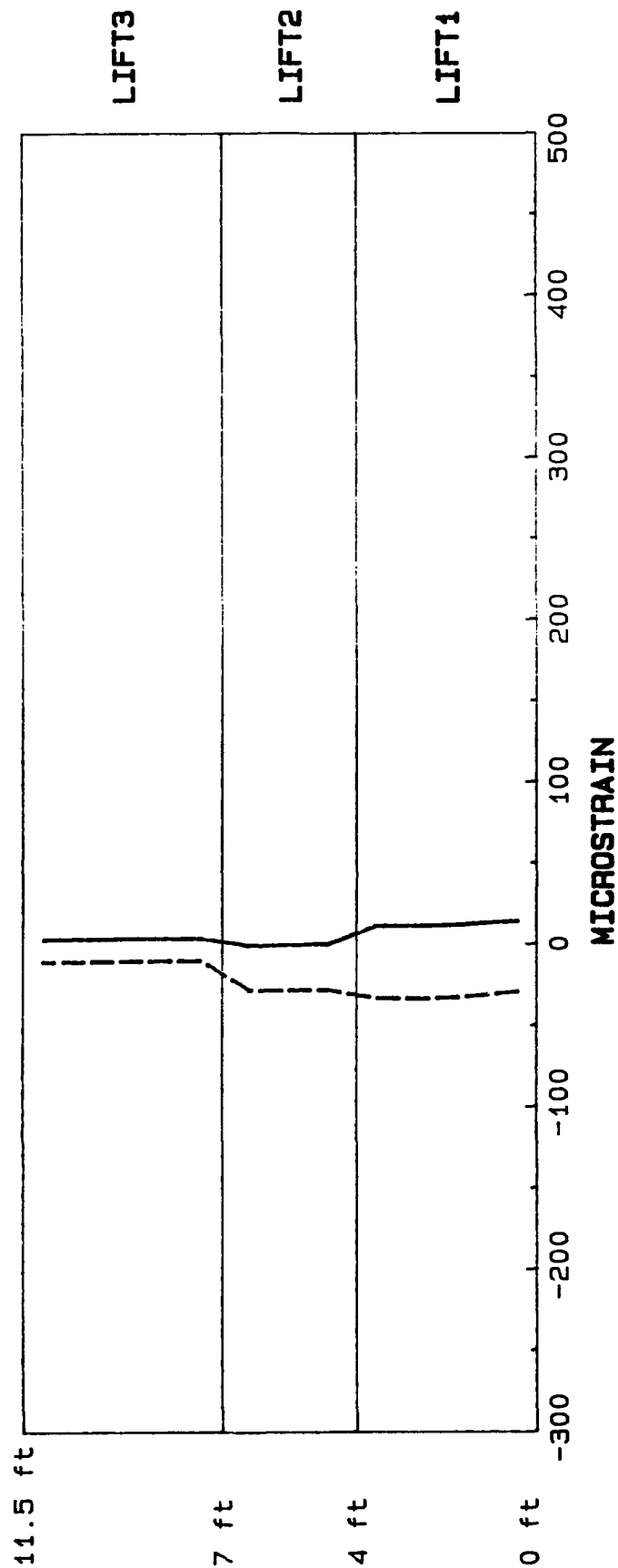


Figure 206. Horizontal strain distribution along section A-A  
5 days after the placement of lift 3

t = 20.0 days - 11 LIFTS

—— LC, LS, UA

----- UC, US, UA

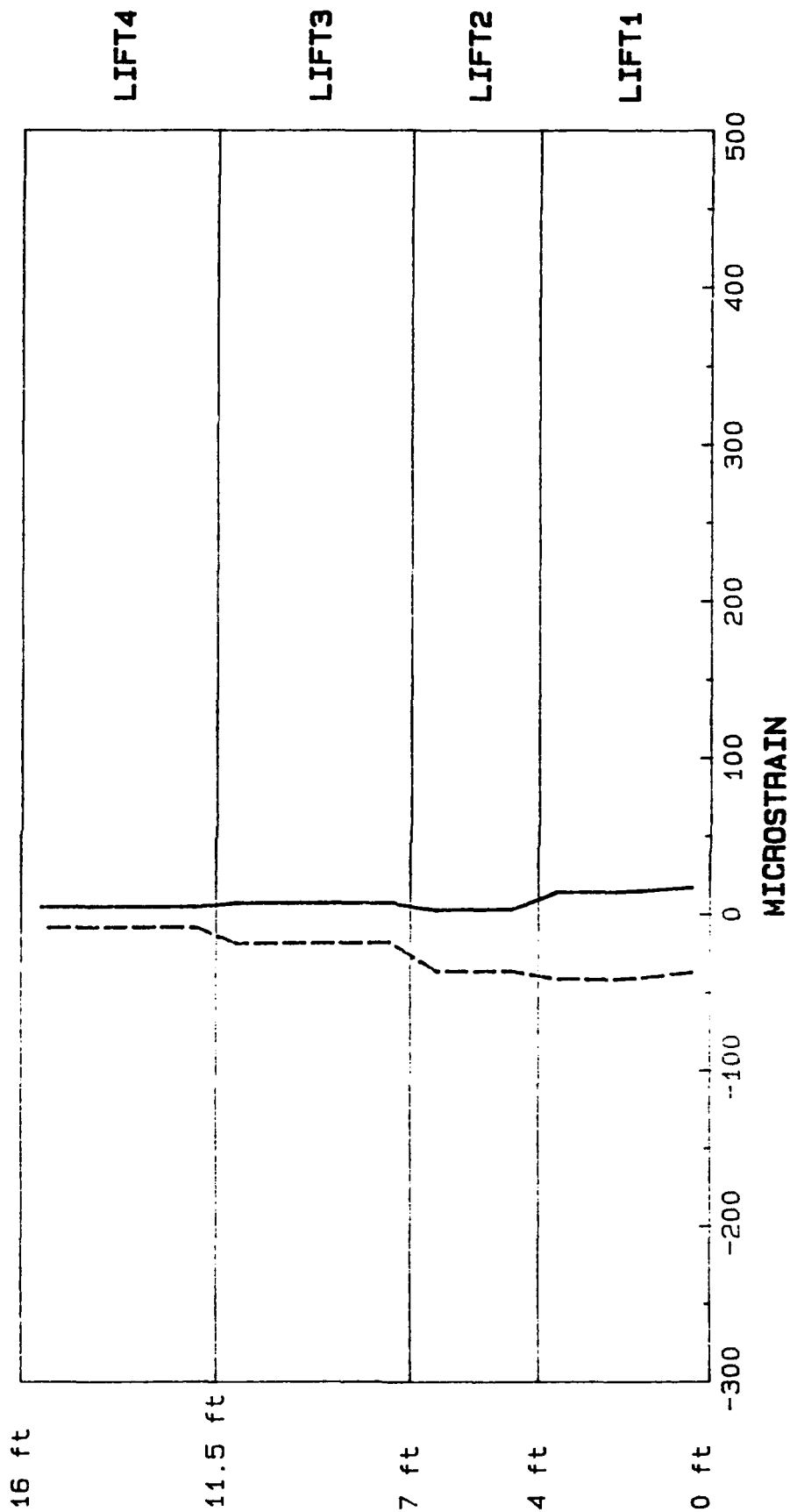


Figure 207. Horizontal strain distribution along section A-A  
5 days after the placement of lift 4

t = 55.0 days - 11 LIFTS

—— LC, LS, UA

----- UC, US, UA

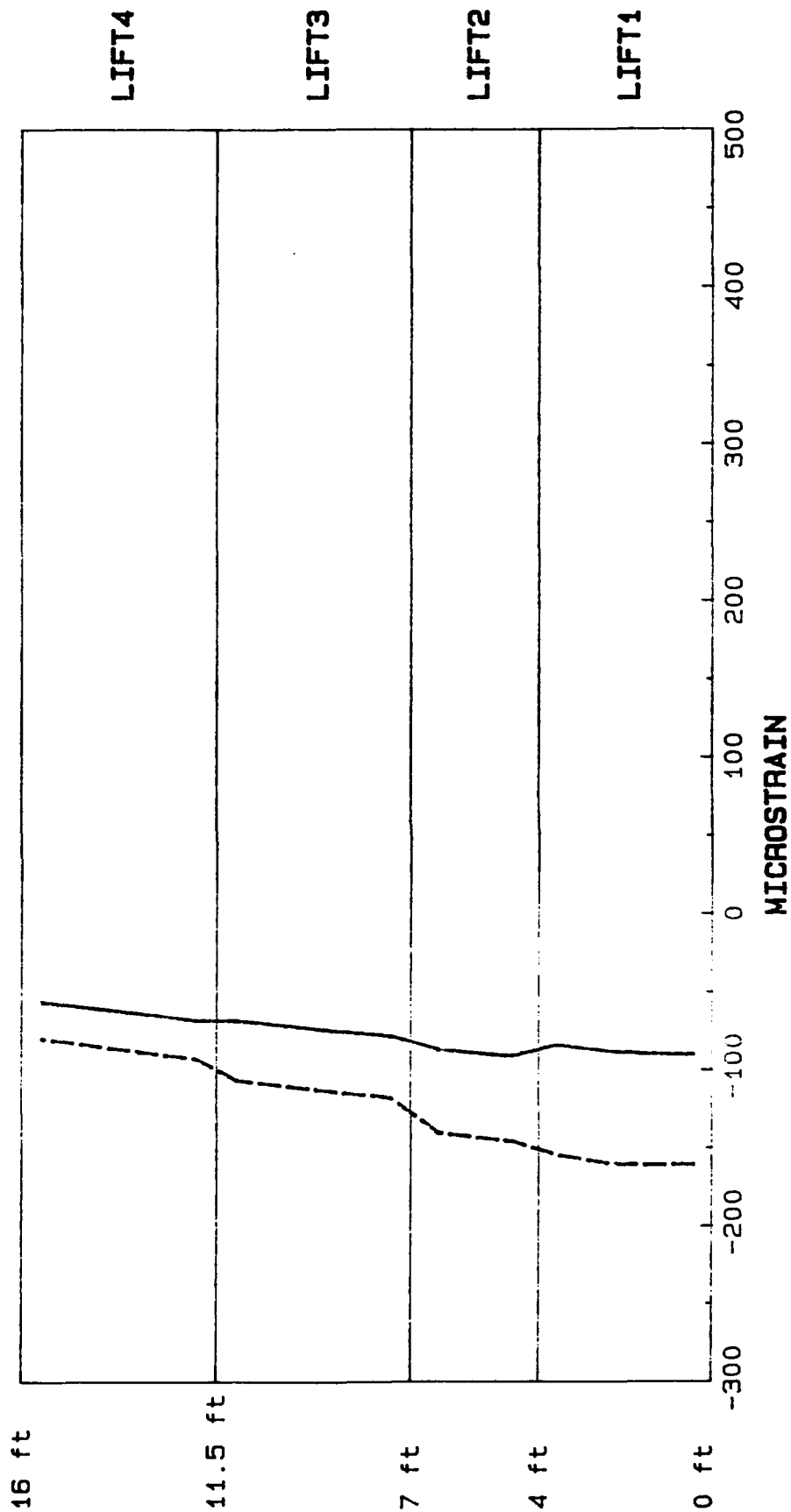


Figure 208. Horizontal strain distribution along section A-A at end of construction

t = 105.0 days - 11 LIFTS

—— LC, LS, UA

----- UC, US, UA

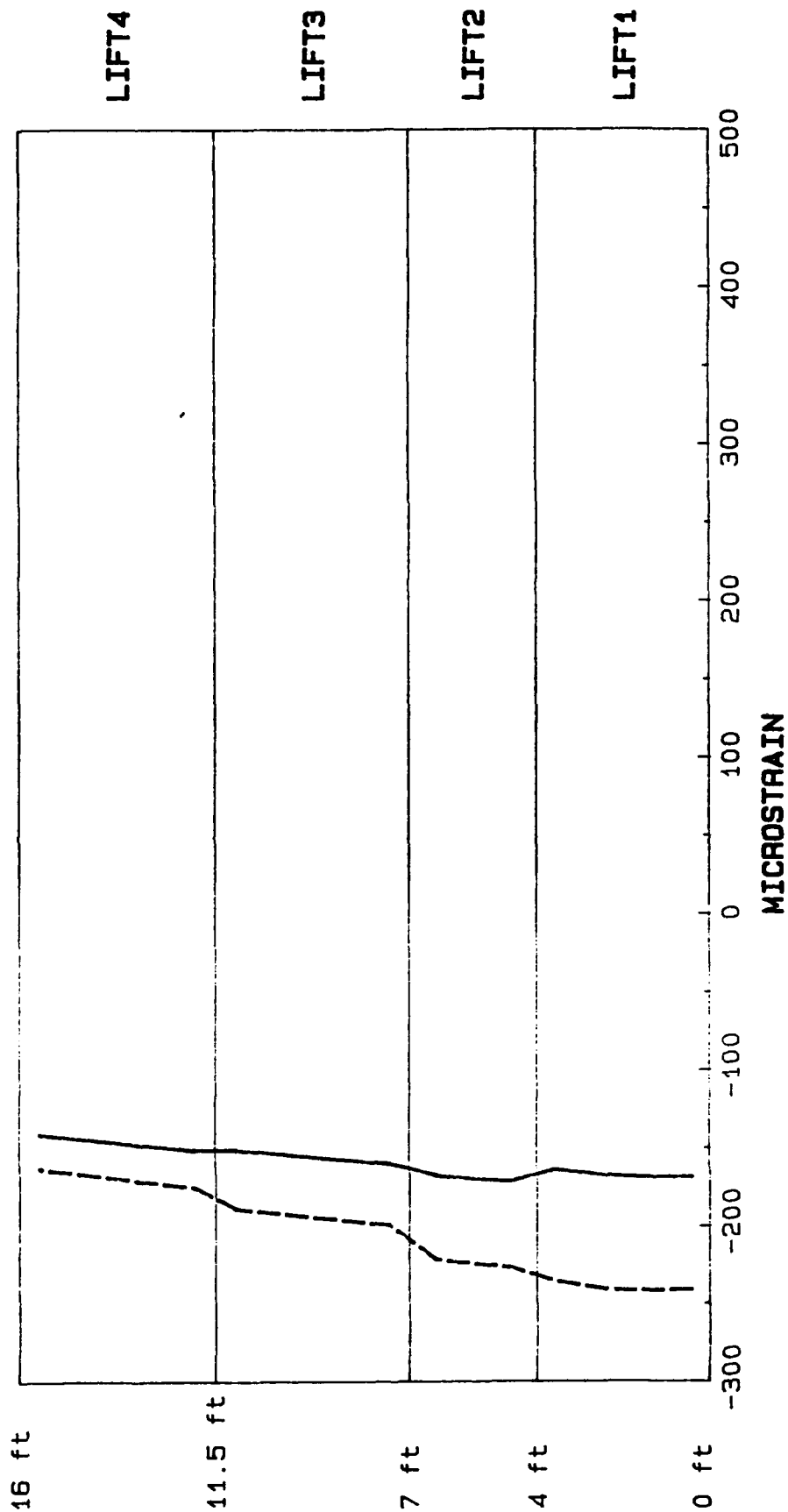


Figure 209. Horizontal strain distribution along section A-A  
50 days after the end of construction

ELEM. 513 INT. PT. 3 - 16 LIFTS

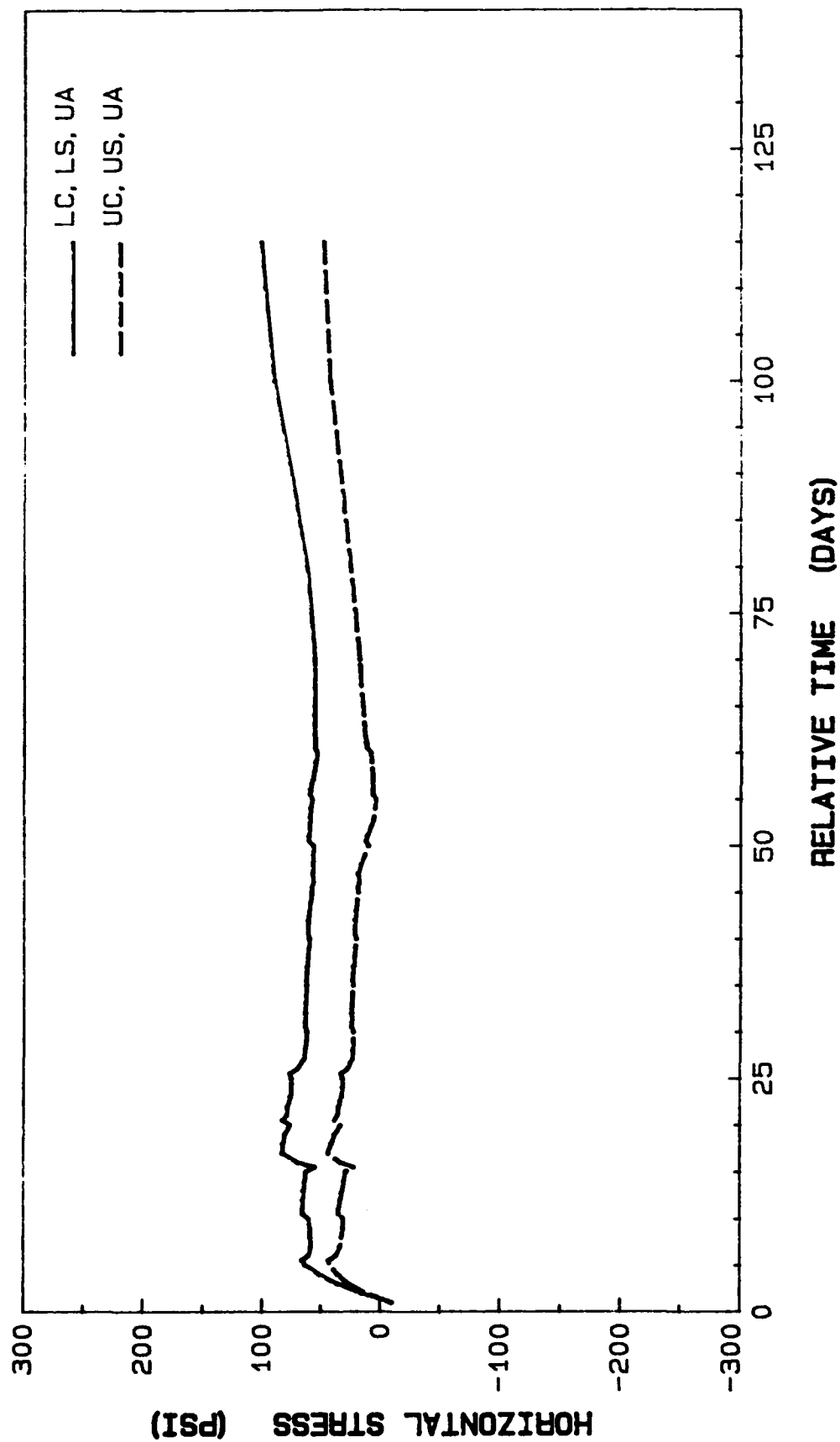


Figure 210. Horizontal stress history at element 513, integration point 3

ELEM. 513 INT. PT. 3 - 16 LIFTS

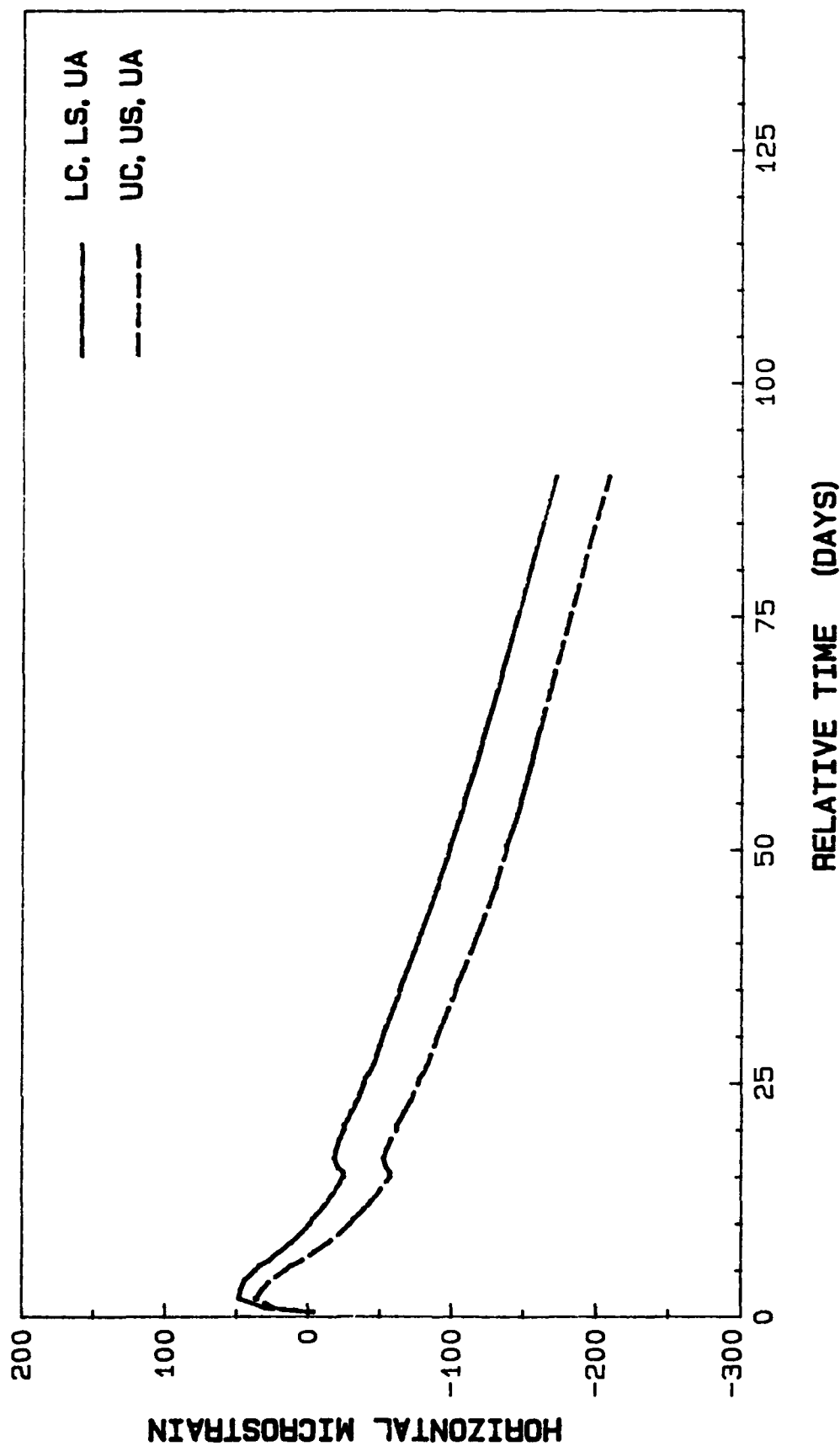


Figure 211. Horizontal strain history at element 513, integration point 3 (16 lifts)

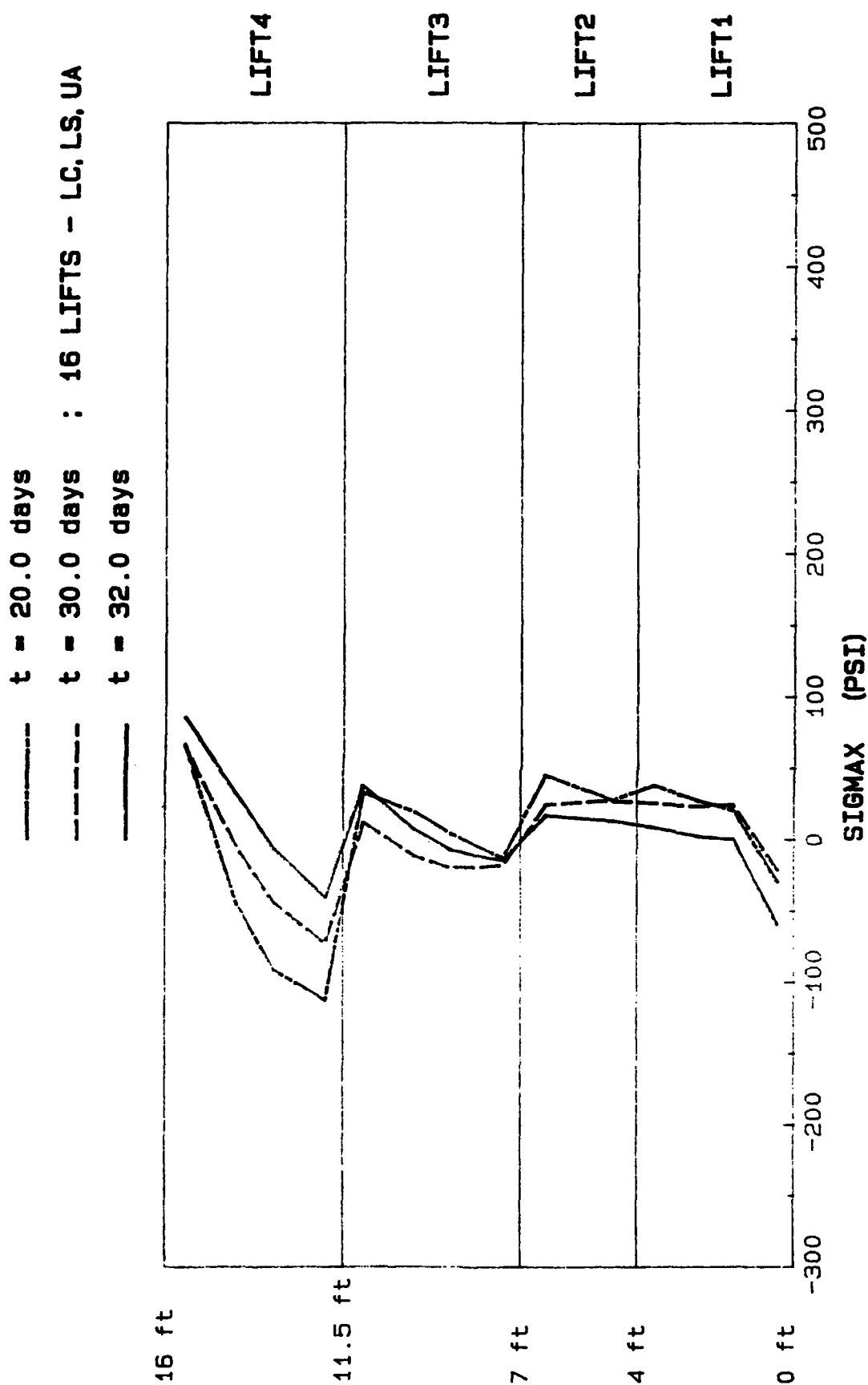


Figure 212. Horizontal stress distribution along section B-B (16 lifts) - upper adiabatic, lower creep, lower shrinkage)

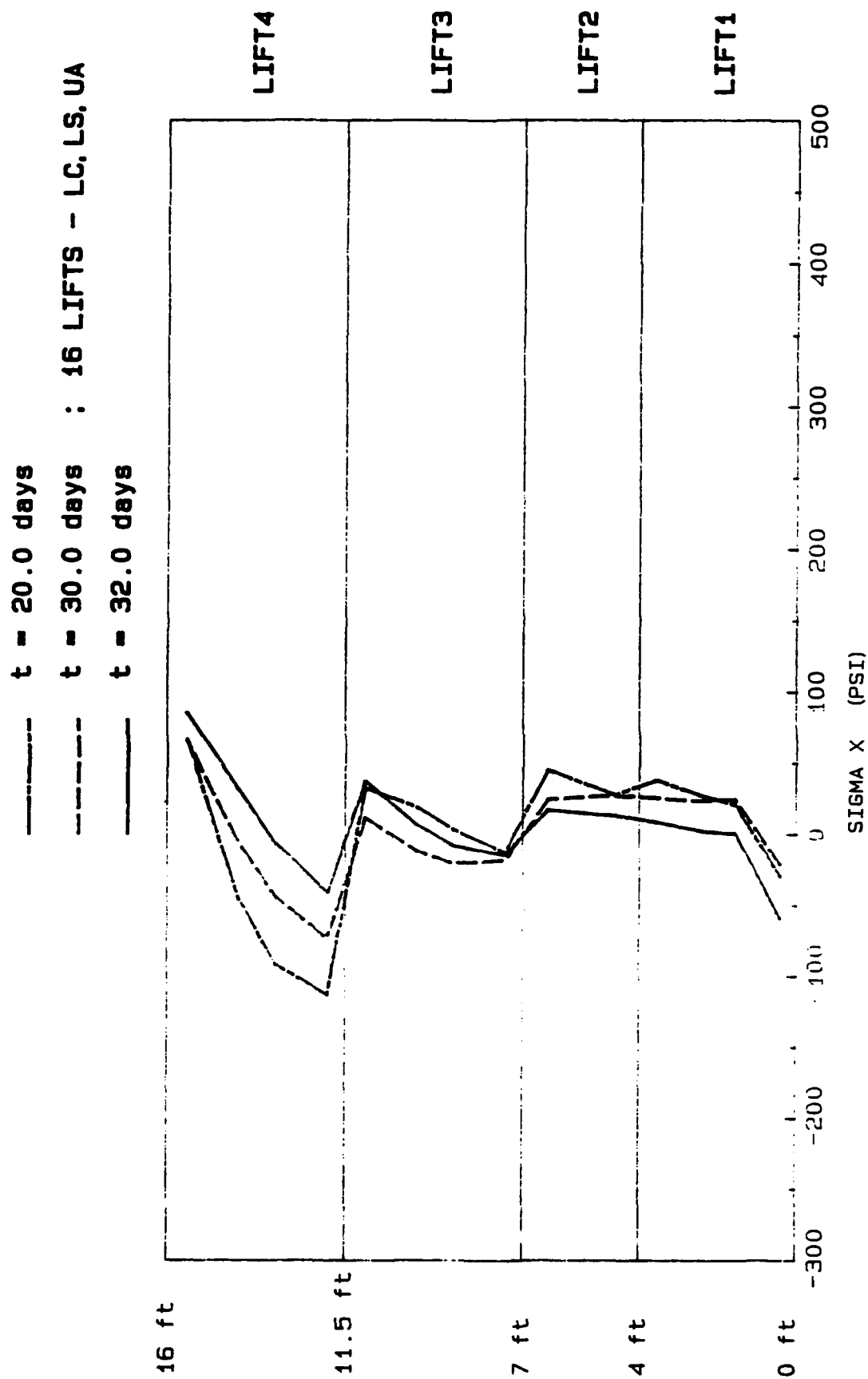


Figure 213. Horizontal stress distribution along section B-B (16 lifts - upper adiabatic, lower creep, lower shrinkage)

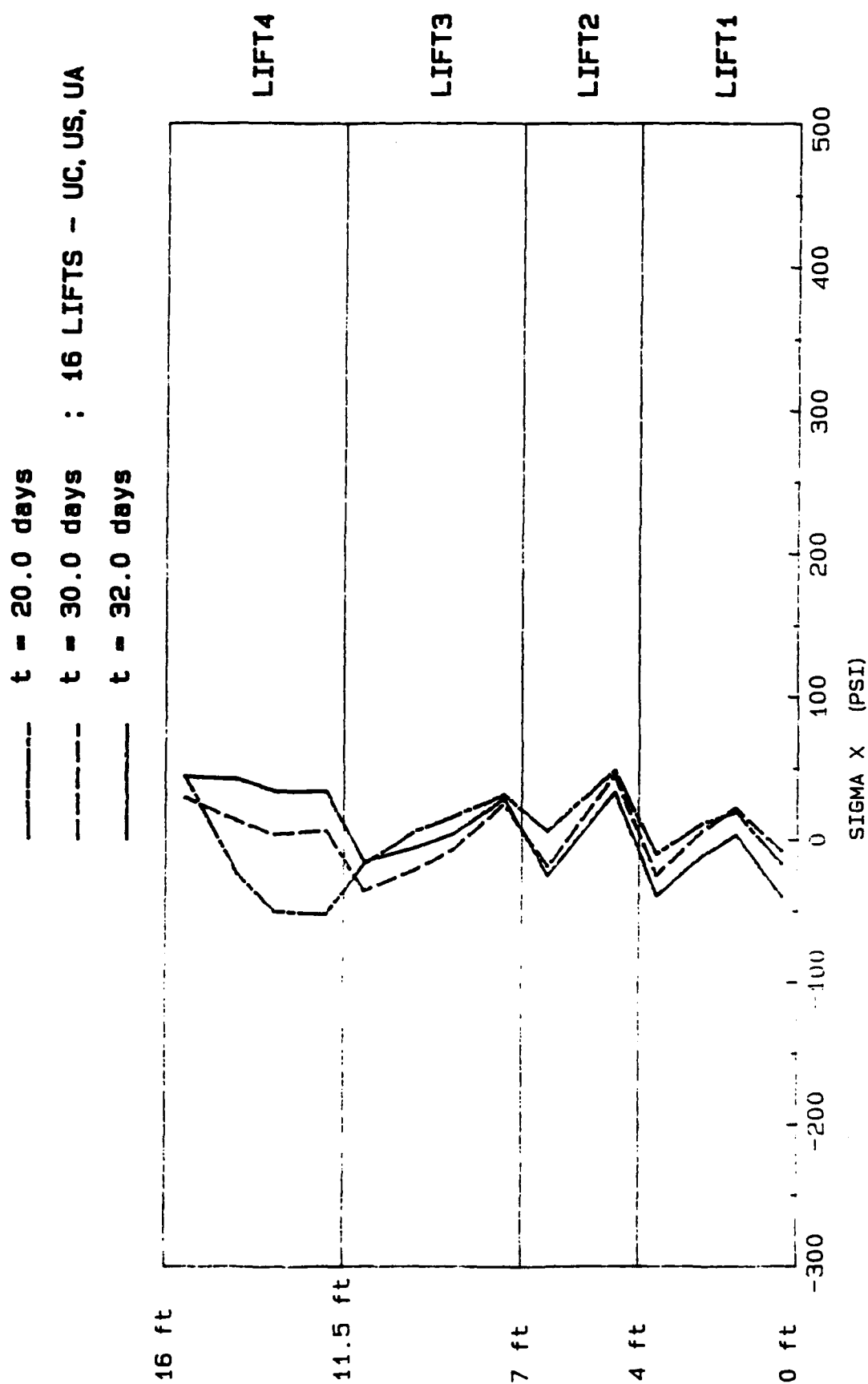


Figure 214. Horizontal stress distribution along section B-B (16 Lifts - upper adiabatic, upper creep, upper shrinkage)

# 16 LIFTS - LC, LS, UA

--- t = 30.0 days

— t = 32.0 days

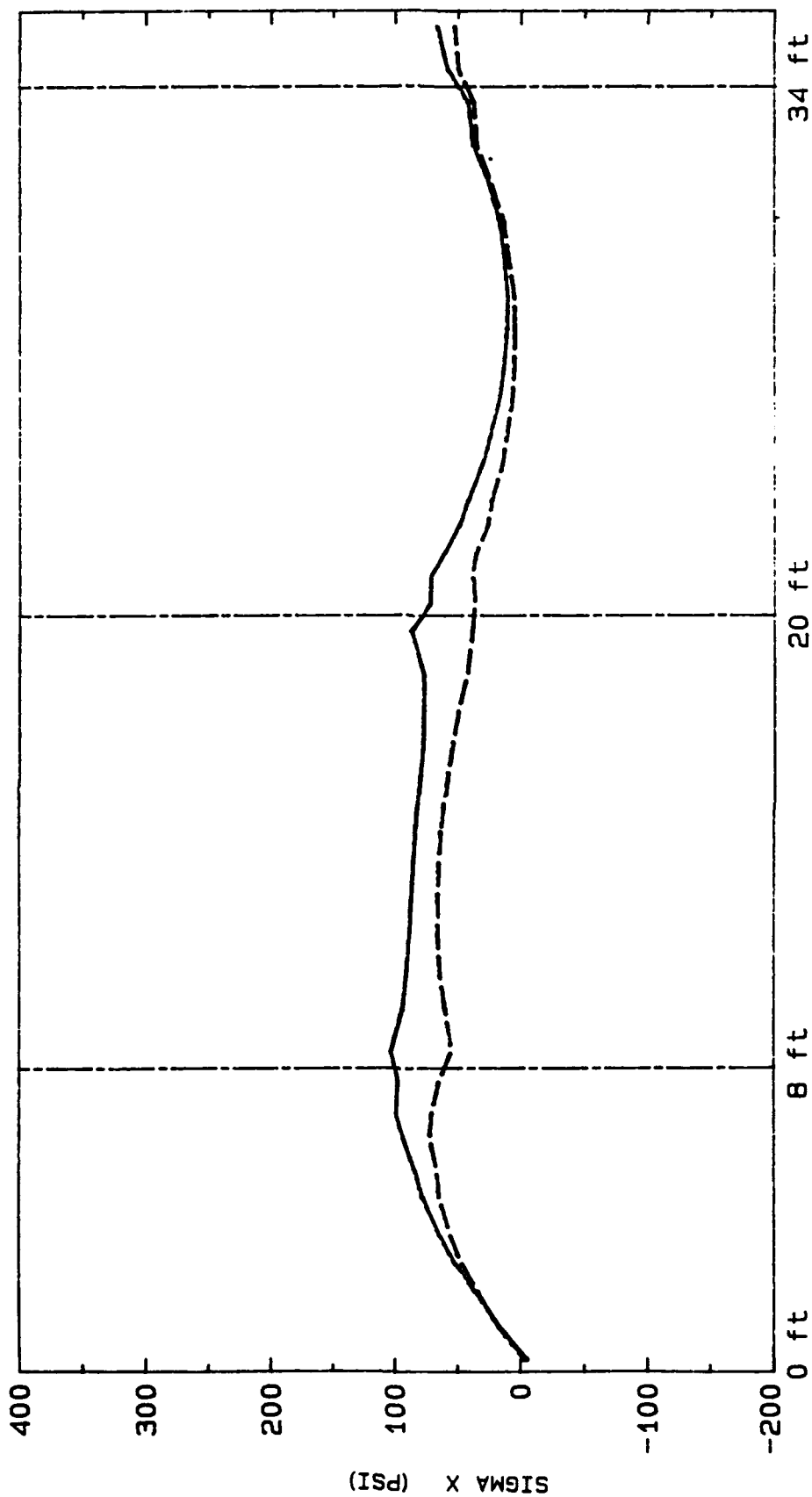


Figure 215. Horizontal stress distribution along section D-D (16 lifts - upper adiabatic, lower creep, lower shrinkage)

# 16 LIFTS - LC, LS, UA

----- t = 30.0 days

\_\_\_\_\_ t = 32.0 days

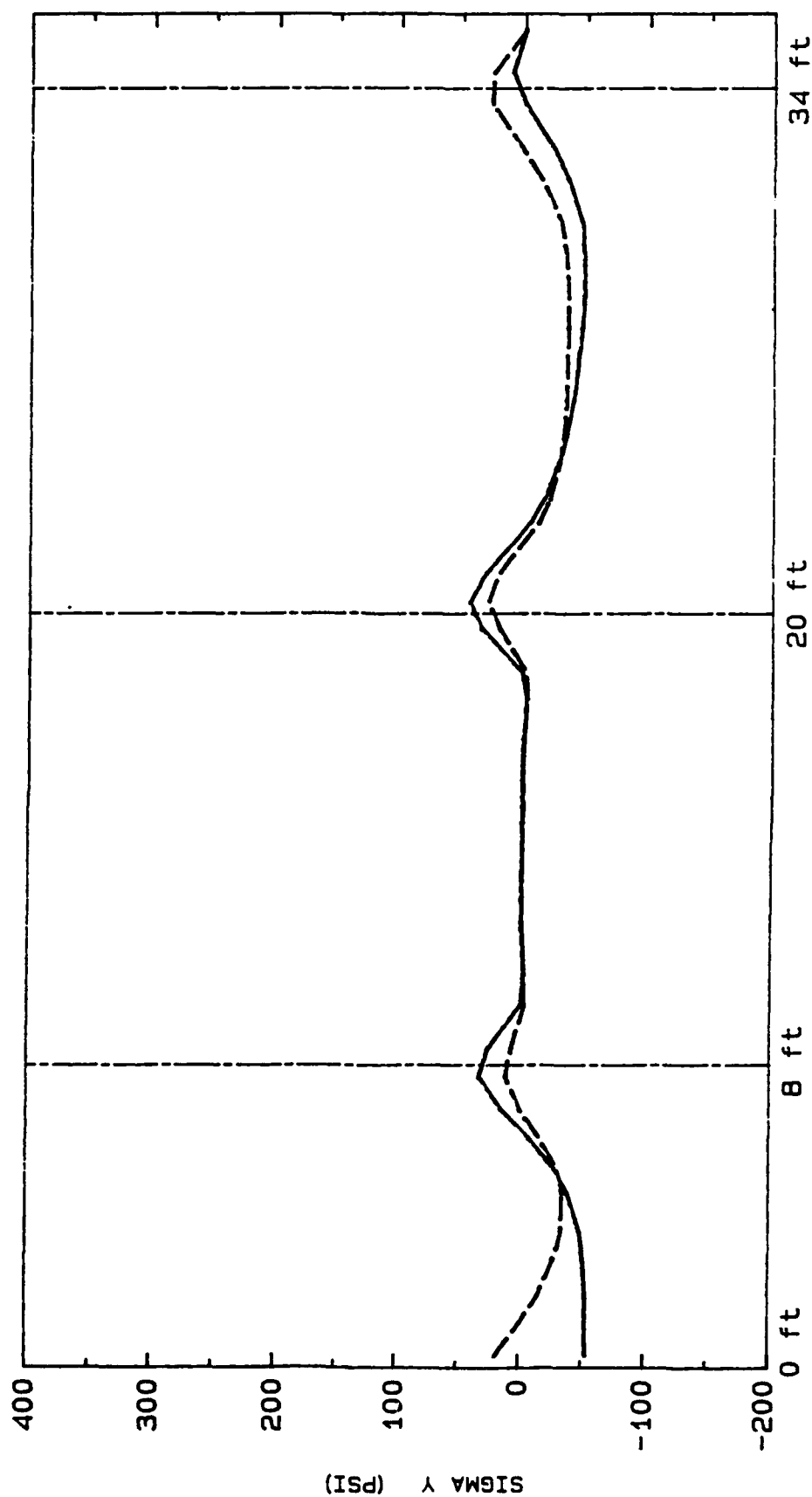


Figure 216. Vertical stress distribution along section D-D (16 lifts - upper adiabatic, lower creep, lower shrinkage)

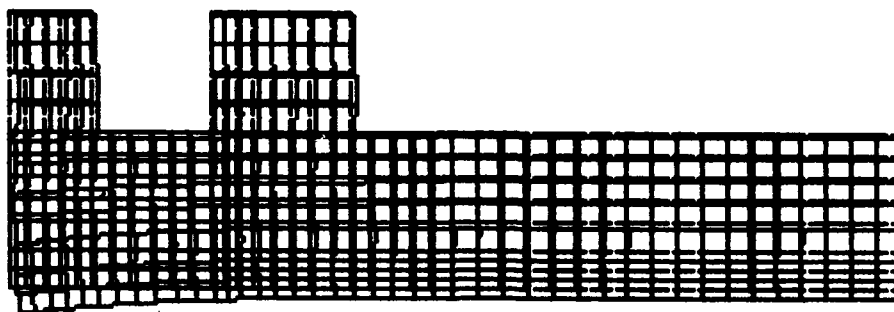


Figure 217. Displaced shape just before  
the culvert is closed

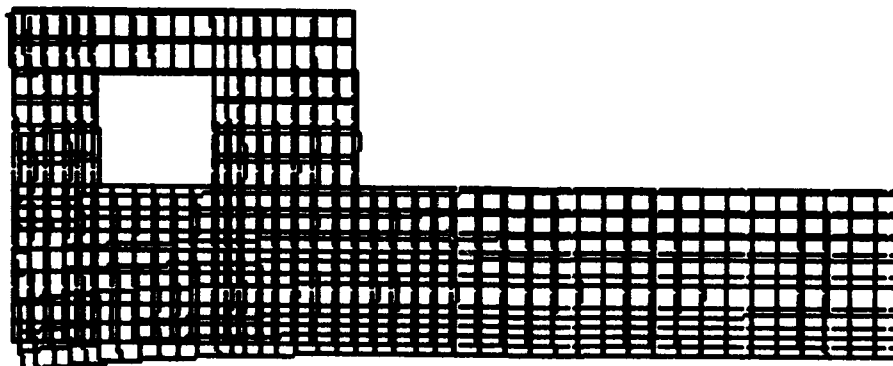


Figure 218. Displaced shape 2 days after closing  
the culvert (upper adiabatic, lower creek, lower  
shrinkage - 16 lifts)

effects. After the enclosing lift for the culvert is placed, the left and right walls are bent outward due to the expansion of the new concrete. The inner regions of the culvert increase in tension for the vertical stress while the outer portions become more compressive, as shown in Figure 215. The left wall is affected more since the right wall is thicker and stiffer. The displaced shapes are shown in Figures 216 and 217. The use of the MPC's also help reduce the vertical stress at the lower corners since the load of the enclosing lift is carried into the first set of nodes on either side of the culvert roof and is then transferred to the nodes at the bottom of the culvert. Therefore, the bending effects could be larger than those shown in Figure 215, but are reduced due to the large vertical loads. This should be studied carefully if small enclosing lifts and side walls are used.

160. From the investigation of the stress distribution around the culvert due its closing, one expects a similar situation for the void. Unlike the culvert, the void has more slender and taller walls, a wider span, and thinner floor. Even though most of the stress is dissipated at the base of the void walls, one still expects some propagation of the load to affect the junction between the culvert walls and the bottom slab.

161. Figures 218-220 show the stress history at two integration points and the strain history for the latter integration point between the void and the culvert. The first is located just at the bottom center of the void. The stress plot shows a sudden drop in the stress from around 25-psi tension to 100-psi compression due to the additional load from the placement of the enclosing lift. The second node, which is located halfway between the top of the culvert and the bottom of the void, shows an increase in the stress. The comparison of the above two points suggests that the section below the void is placed in a bending state with compression at the top and tension at the bottom.

162. Figures 221 and 222 show the stress distribution at Section C-C in Figure 181 just before and after the void is closed. Looking at the member between the culvert and the void, composed of lift 7, 8 and 9, one sees that the top of lift 9 is suddenly compressed with a jump in stress of about 100 psi after closing which is due to several reasons. First, as soon as the void is closed, it has a dramatic rise in temperature. Therefore, it tries to expand, but is heavily restrained by the other lifts. Secondly, the enclosing lift is placed which causes the culvert walls to spread due to expansion of

ELEM. 703 INT. PT. 3 - 16 LIFTS

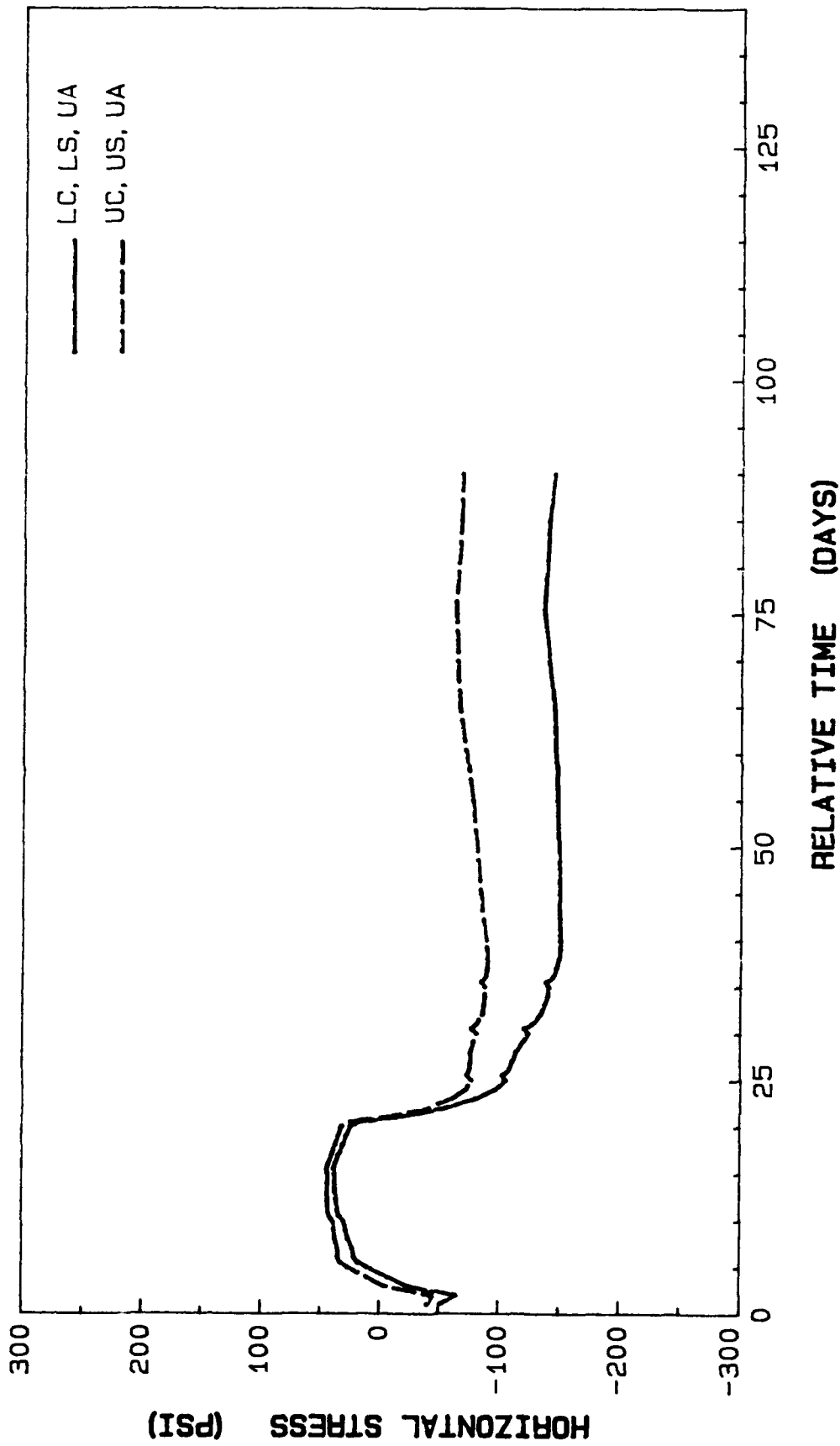


Figure 219. Horizontal stress at element 703, integration point 3

# ELEM. 668 INT. PT. 2 - 16 LIFTS

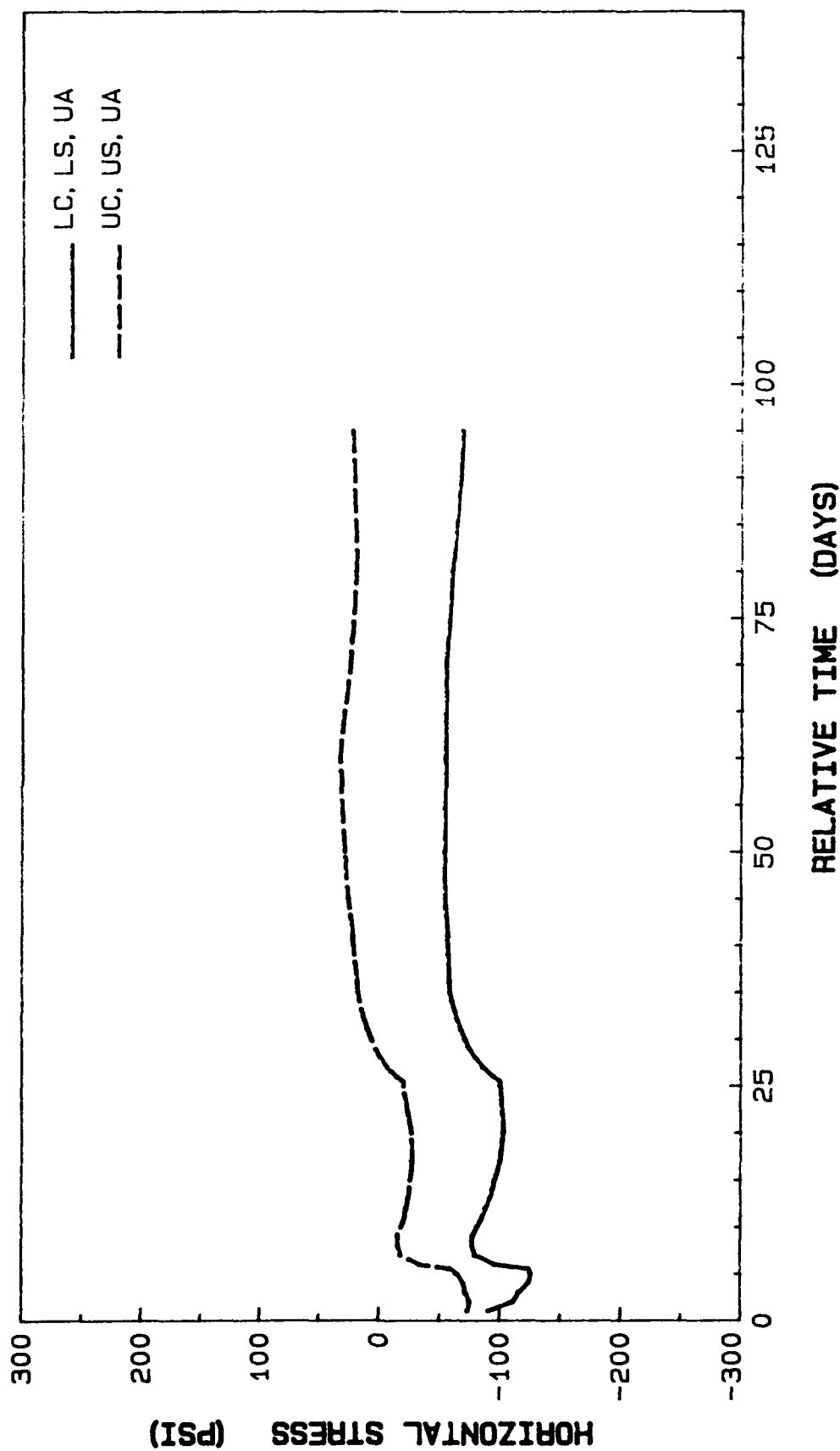


Figure 220. Horizontal stress at element 668, integration point 2

ELEM. 668 INT. PT. 2 - 16 LIFTS

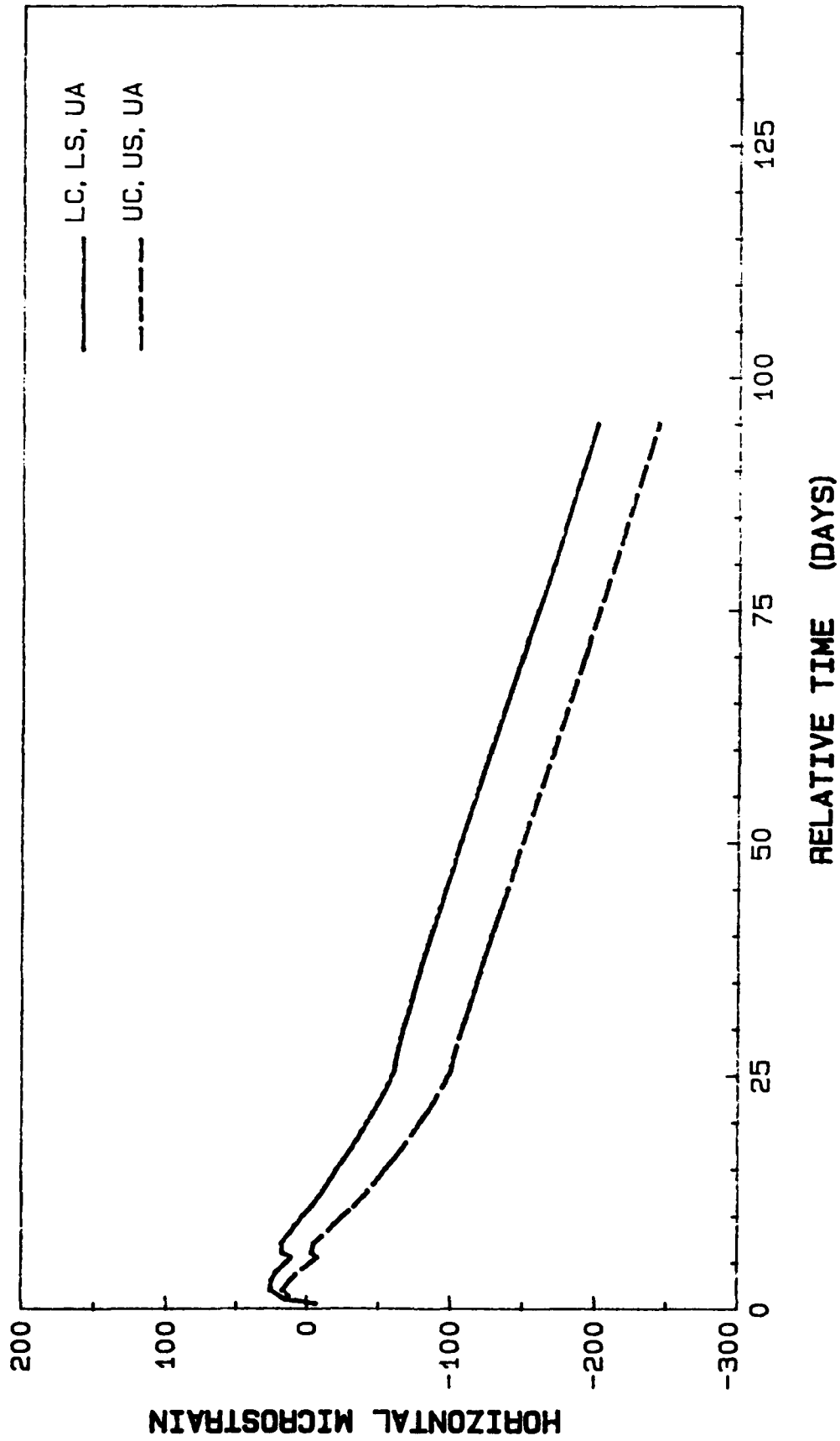


Figure 221. Horizontal strain history at element 668, integration point 2

# 16 LIFTS - LC, LS, UA

--- t = 45.0 days

— t = 60.0 days

--- t = 62.0 days

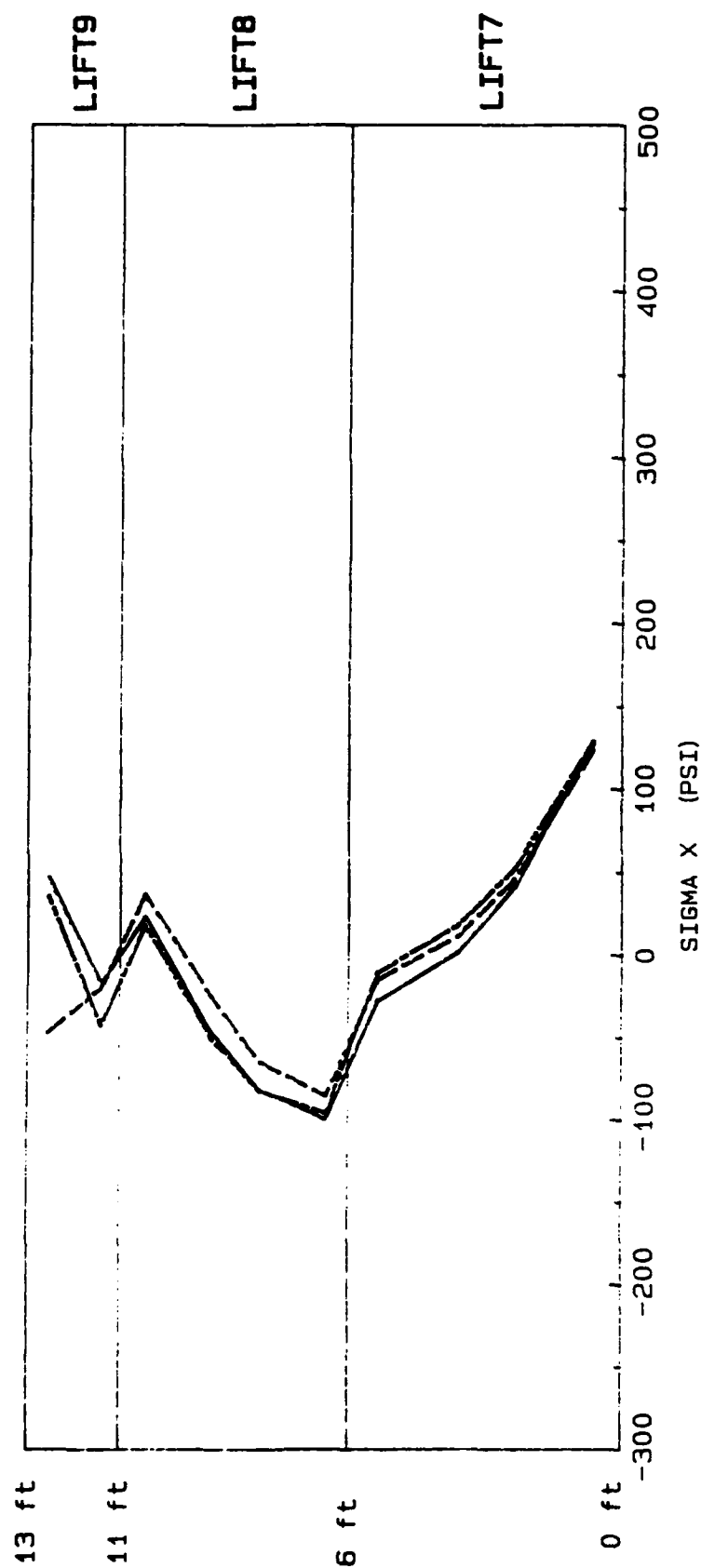


Figure 222. Horizontal stress distribution along section C-C before and after closing the void (16 lifts - upper adiabatic, lower creep, lower shrinkage)

the lift, placing the intermediate member between the culvert and the void in a slight bending situation.

163. Figures 223-226 show the horizontal and vertical stress distributions at a horizontal section just below the void, and the displaced shapes before and after the closing of the void. The displaced shapes show that the left side of the void is displaced to the outside and as expected downward while the right side has hardly moved. The vertical section to the right of the openings is much stiffer than the left. Figures 227 and 228 show the effect that closing the void has on the stresses below the culvert. Closing the void affects the left corner the most since the left wall is the weaker section as far as lateral restraint is concerned.

#### Comparison Between the 16- and 11-Lift Schedules

164. To compare the two lift schedules, the results are grouped as (a) horizontal stress history plots of nodes in the slab, (b) horizontal stress history plots at the lift interfaces, (c) horizontal stress history plots at mid-lift locations, and (d) vertical stress history plots at outside edge nodes.

165. Figure 229 shows the locations for which the stresses are presented while Figures 230-238 shows the stress histories. Within the slab (see Figures 230 and 234), the difference between the two lift arrangements is small with the exception of points close to the center line. It was explained earlier that the chamber floor arches as more loads are added to the wall sections which results in high tension at the top of the slab and higher compression at the bottom as seen in Figures 230 and 234 during the 11-lift construction. The latter two figures show that the higher stress is only due to the heavier lifts and earlier time of application. At later times the stresses coincide. For every additional lift, the 11-lift curve shows a higher jump or increase, due to the larger lift heights.

166. At several of the boundaries, the difference between the two lift plans is noticeable (see Figures 233, 235, and 236). The highest difference occurs at the bottom of the void and is shown in Figure 236. The maximum horizontal stress for the 11-lift is about 180 psi; whereas, for the 16-lift, it is only about 50 psi. This difference is primarily attributed to the large thickness of the lift just below the void (lift 7). To explain this idea one

# 16 LIFTS - UC, US, UA

- t = 45.0 days
- t = 60.0 days
- t = 62.0 days

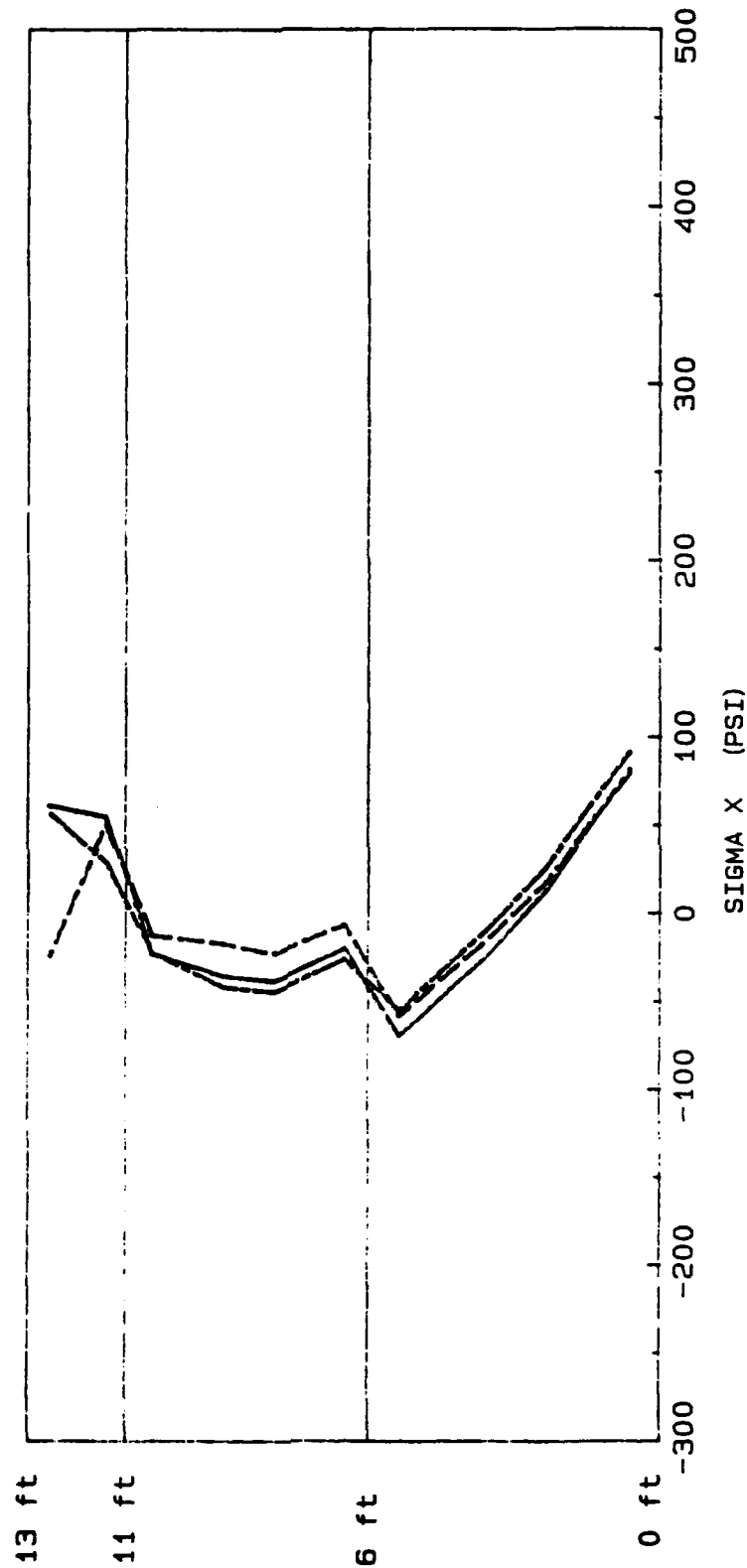


Figure 223. Horizontal stress distribution along section C-C before and after closing the void (16 lifts - upper adiabatic, upper creep, upper shrinkage)

# 16 LIFTS - LC, LS, UA

--- t = 60.0 days

— t = 62.0 days

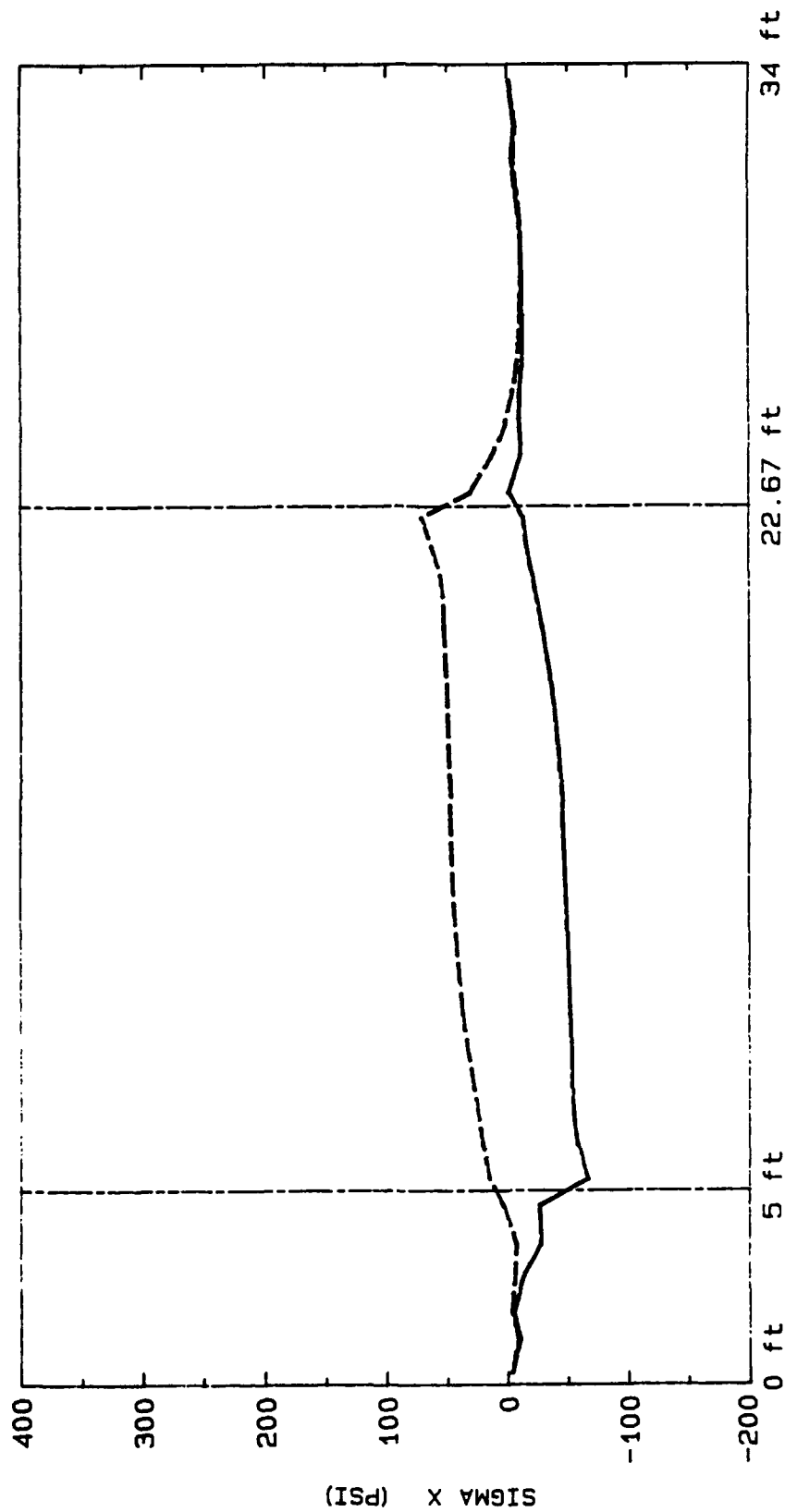


Figure 224. Horizontal stress distribution along section E-E before and after closing the void (upper adiabatic, lower creep, lower shrinkage - 16 lifts)

# 16 LIFTS - LC, LS, UA

--- t = 60.0 days

— t = 62.0 days

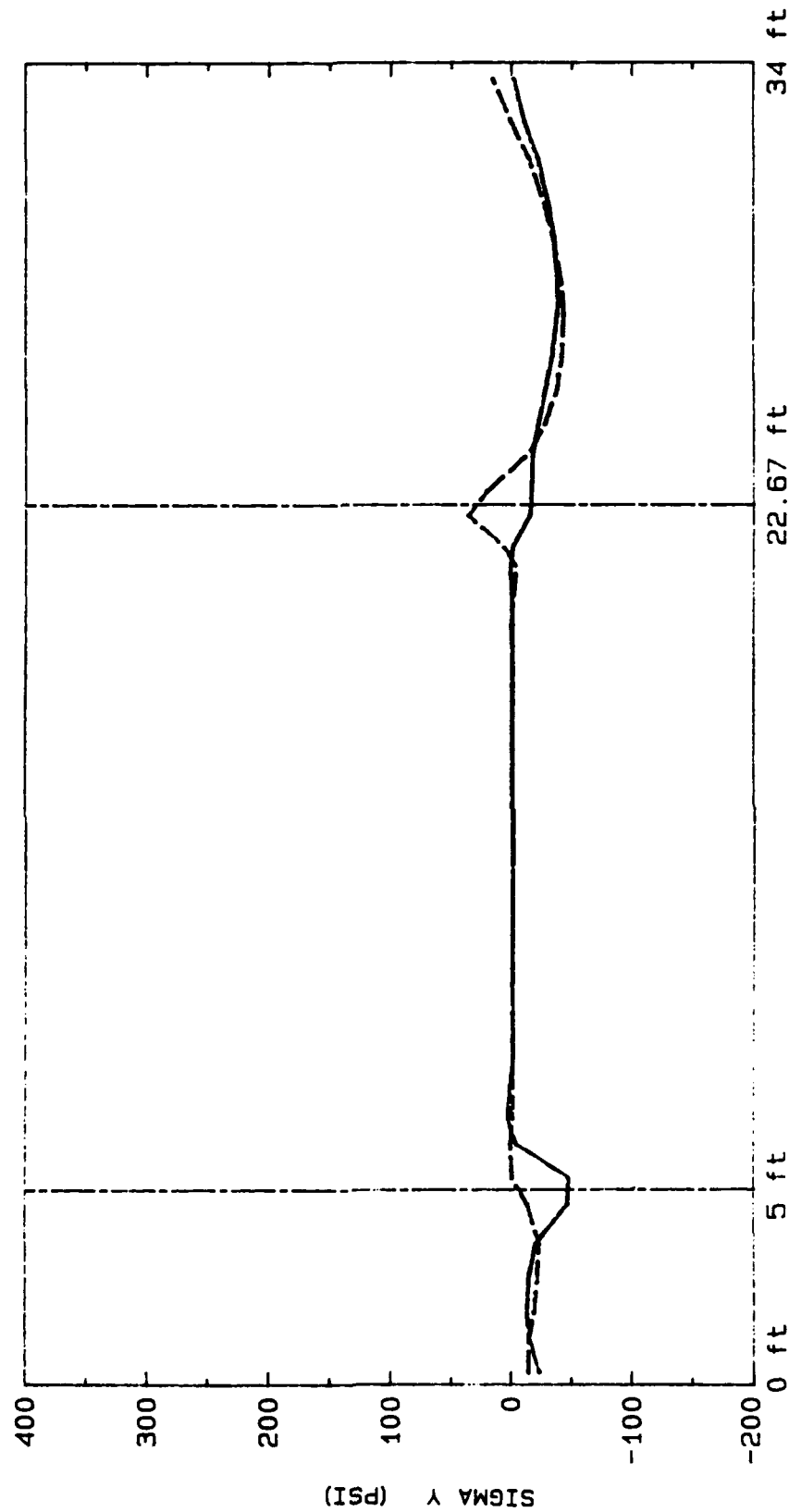


Figure 225. Vertical stress distribution along section E-E before and after closing the void (upper adiabatic, lower creep, lower shrinkage - 16 lifts)

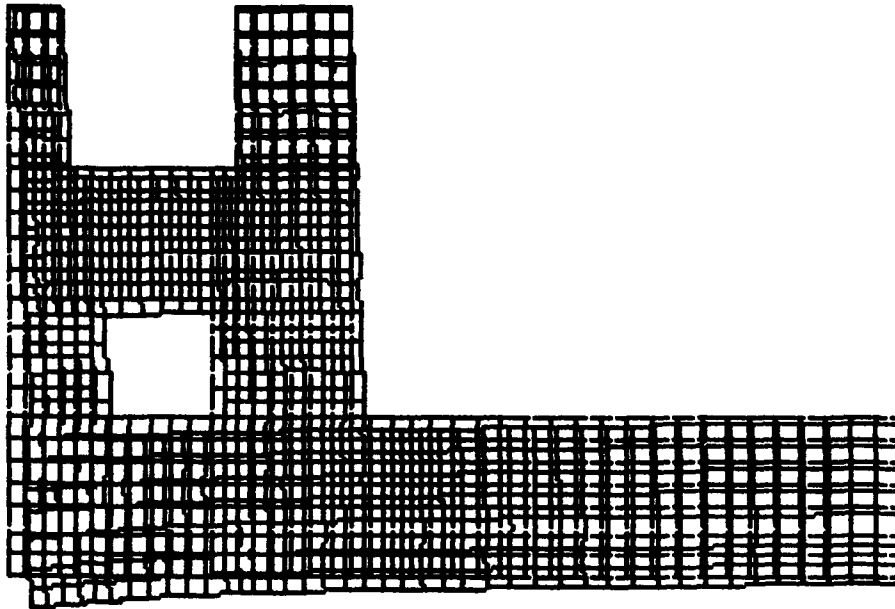


Figure 226. Displaced shape just before closing the void

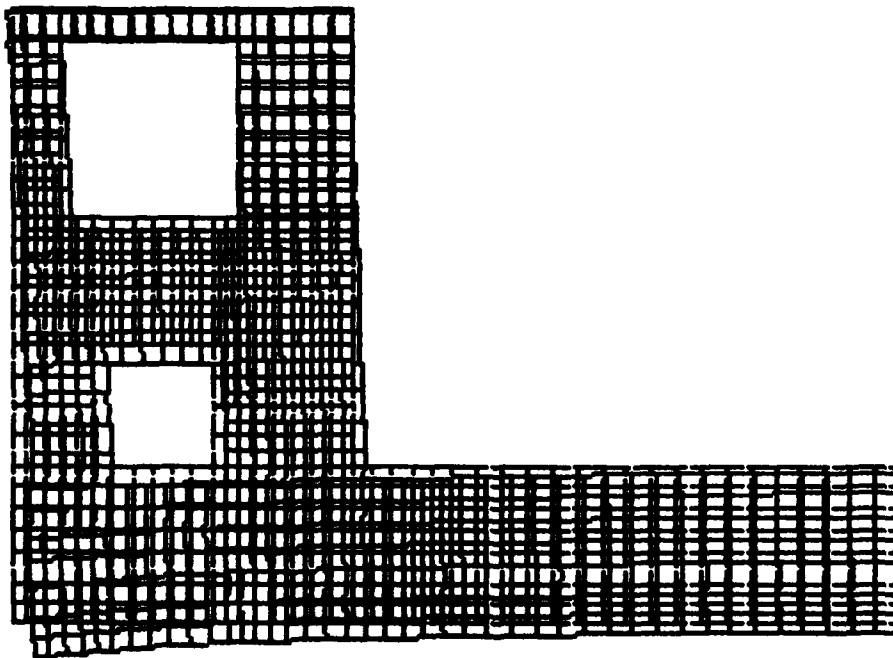


Figure 227. Displaced shape 2 days after closing the void (upper adiabatic, lower creep, lower shrinkage - 16 lifts)

# 16 LIFTS - LC, LS, UA

----- t = 60.0 days

\_\_\_\_\_ t = 62.0 days

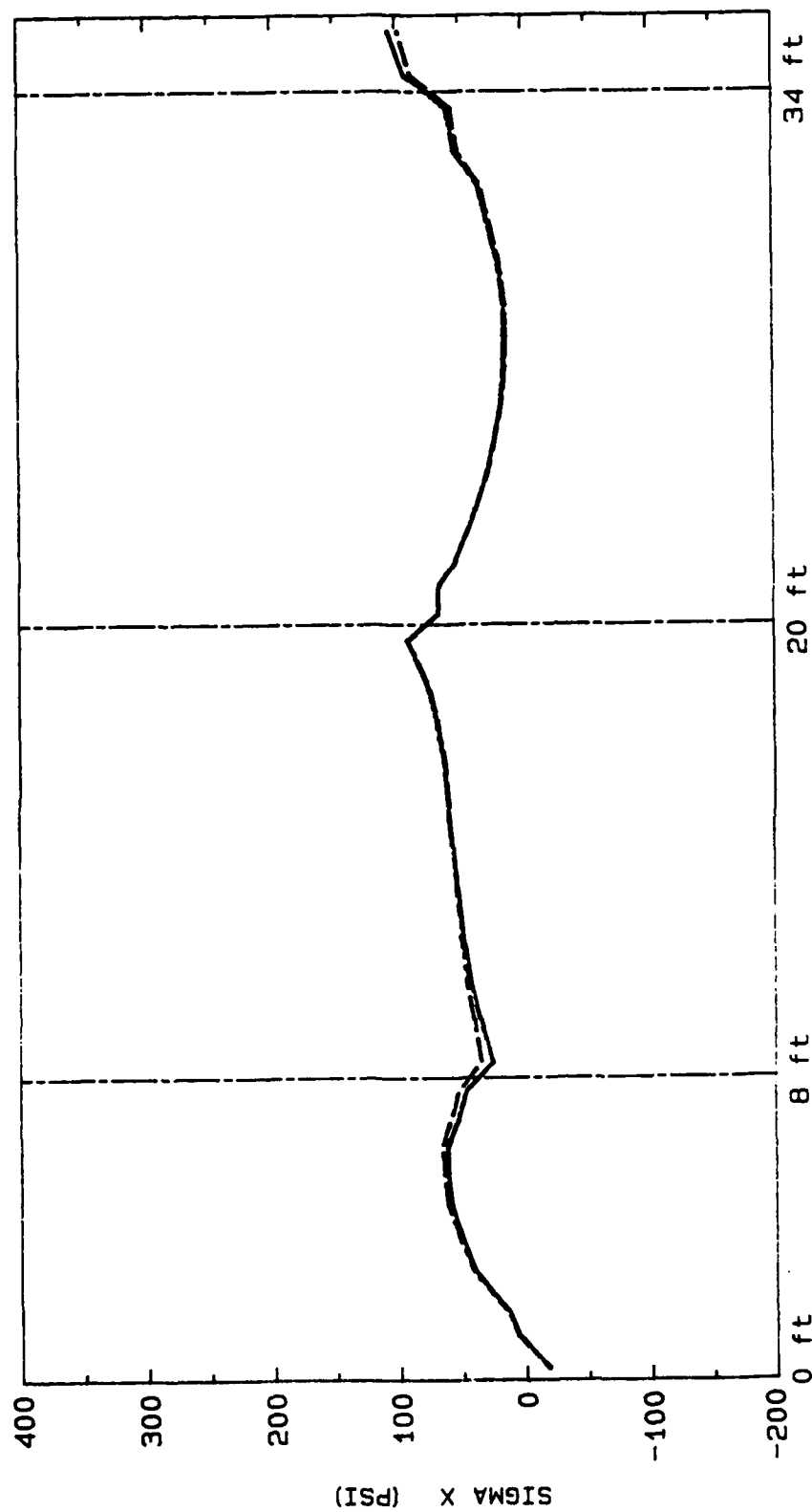


Figure 228. Horizontal stress distribution at section D-D before and after closing the void  
(upper adiabatic, lower creep, lower shrinkage - 16 lifts)

# 16 LIFTS - LC, LS, UA

----- t = 60.0 days

\_\_\_\_\_ t = 62.0 days

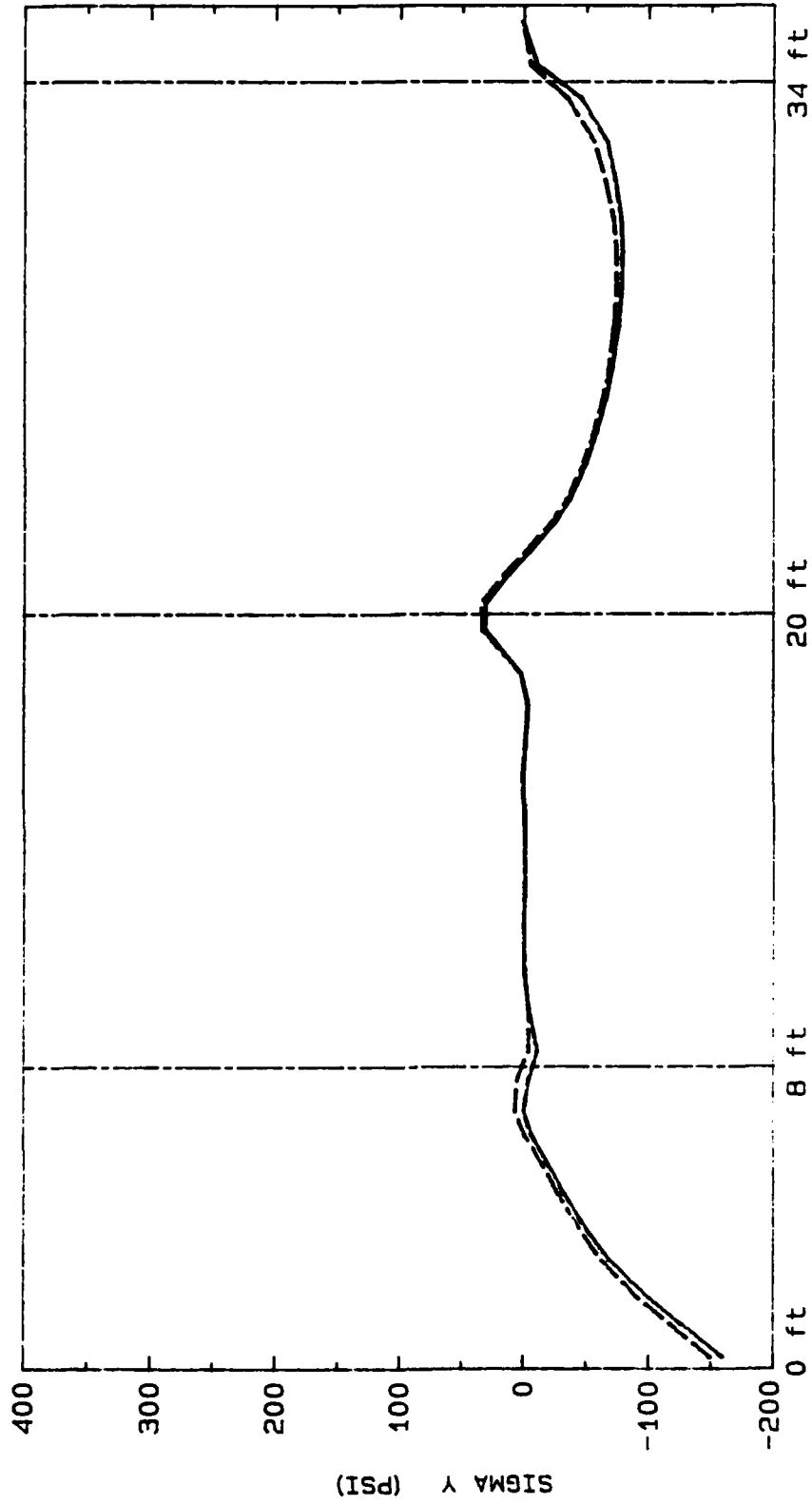


Figure 229. Vertical stress distribution at section D-D before and after closing the void  
(upper adiabatic, lower creep, lower shrinkage - 16 lifts)

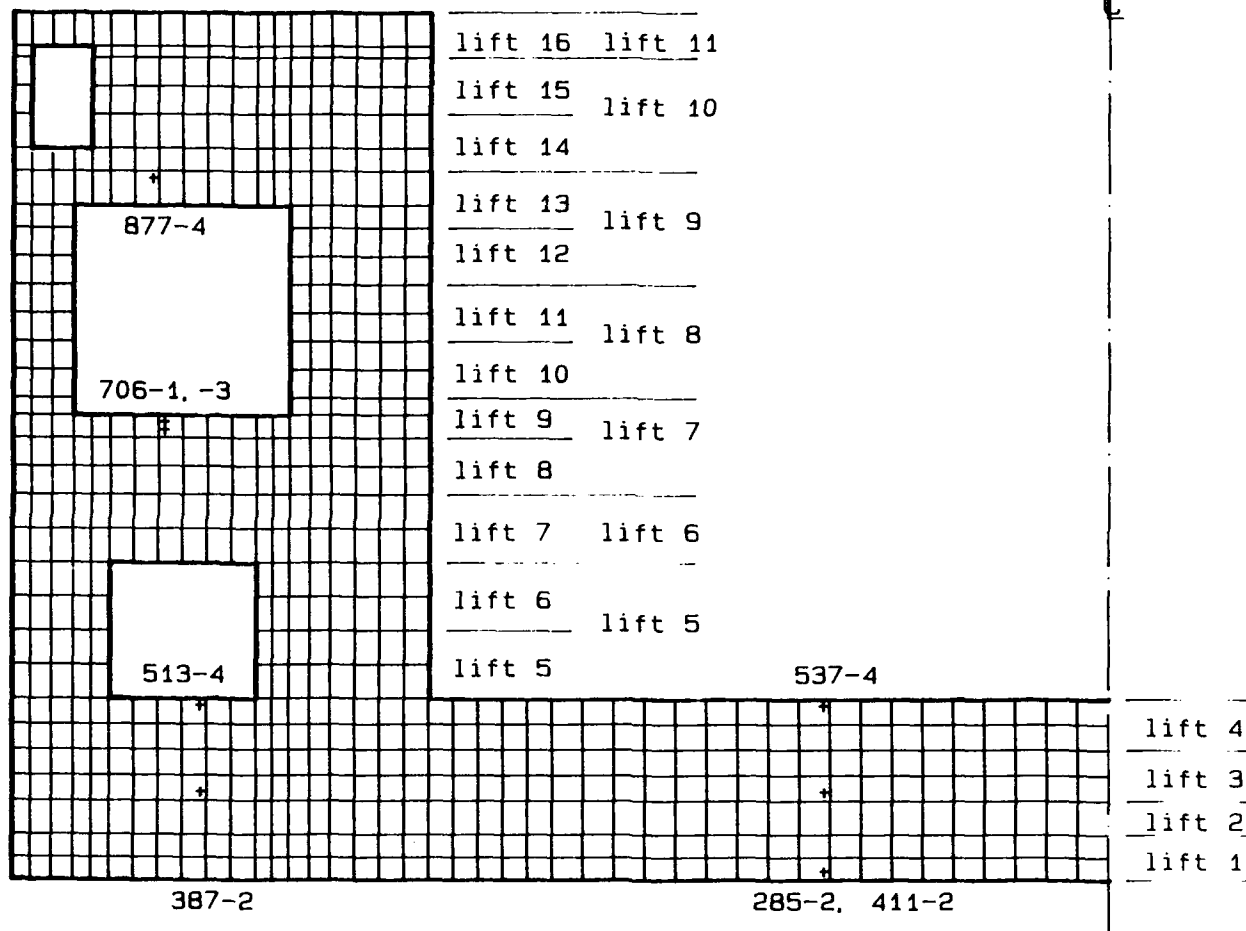


Figure 230. Selected elements for horizontal stress comparisons

ELEM. 285 INT. PT. 2 - UA, LC, LS

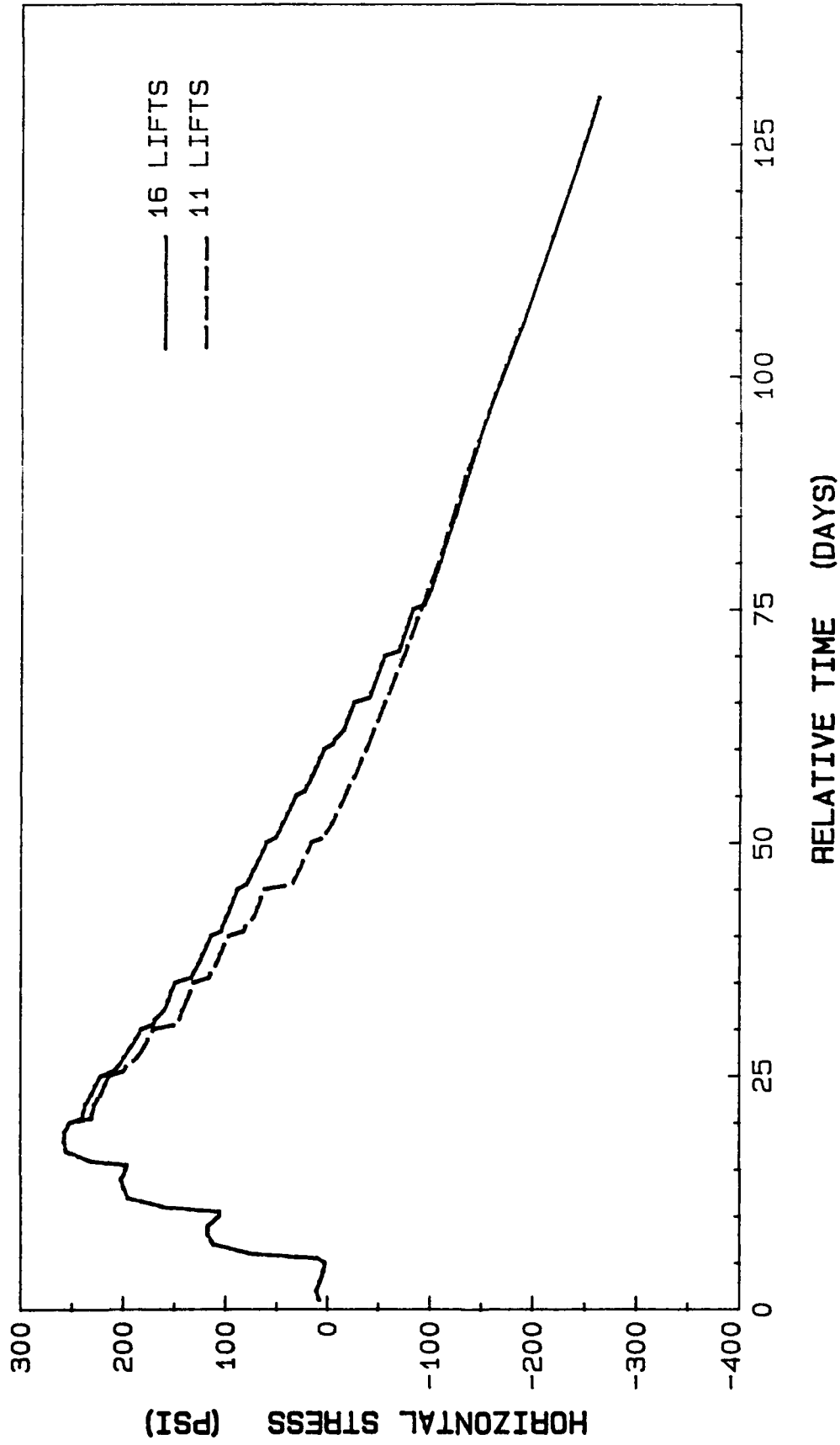


Figure 231. Horizontal stress history at element 285 integration point 2

ELEM. 387 INT. PT. 2 - UA, LC, LS

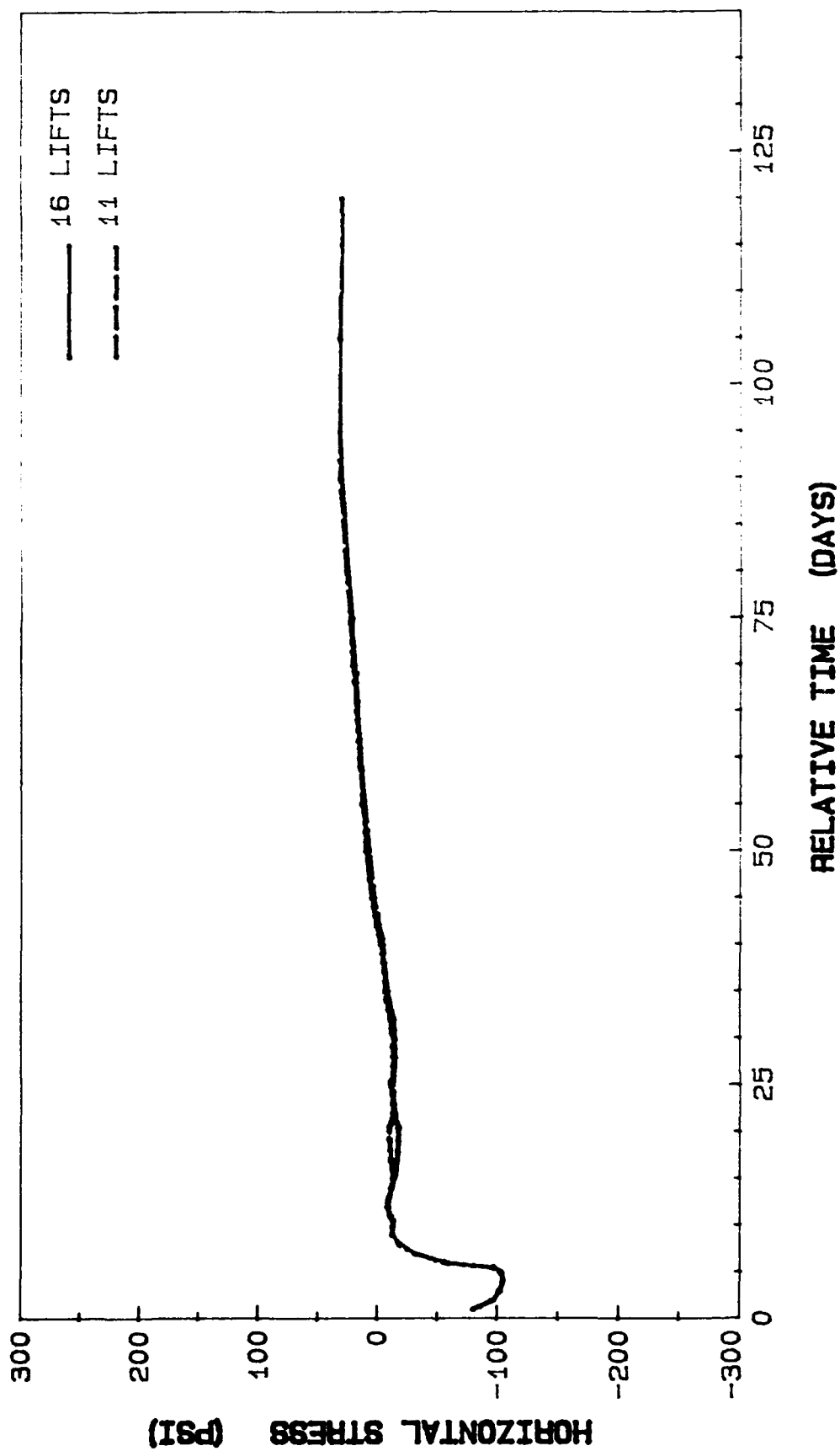


Figure 232. Horizontal stress history at element 387 integration point 2

ELEM. 411 INT. PT. 2 - UA, LC, LS

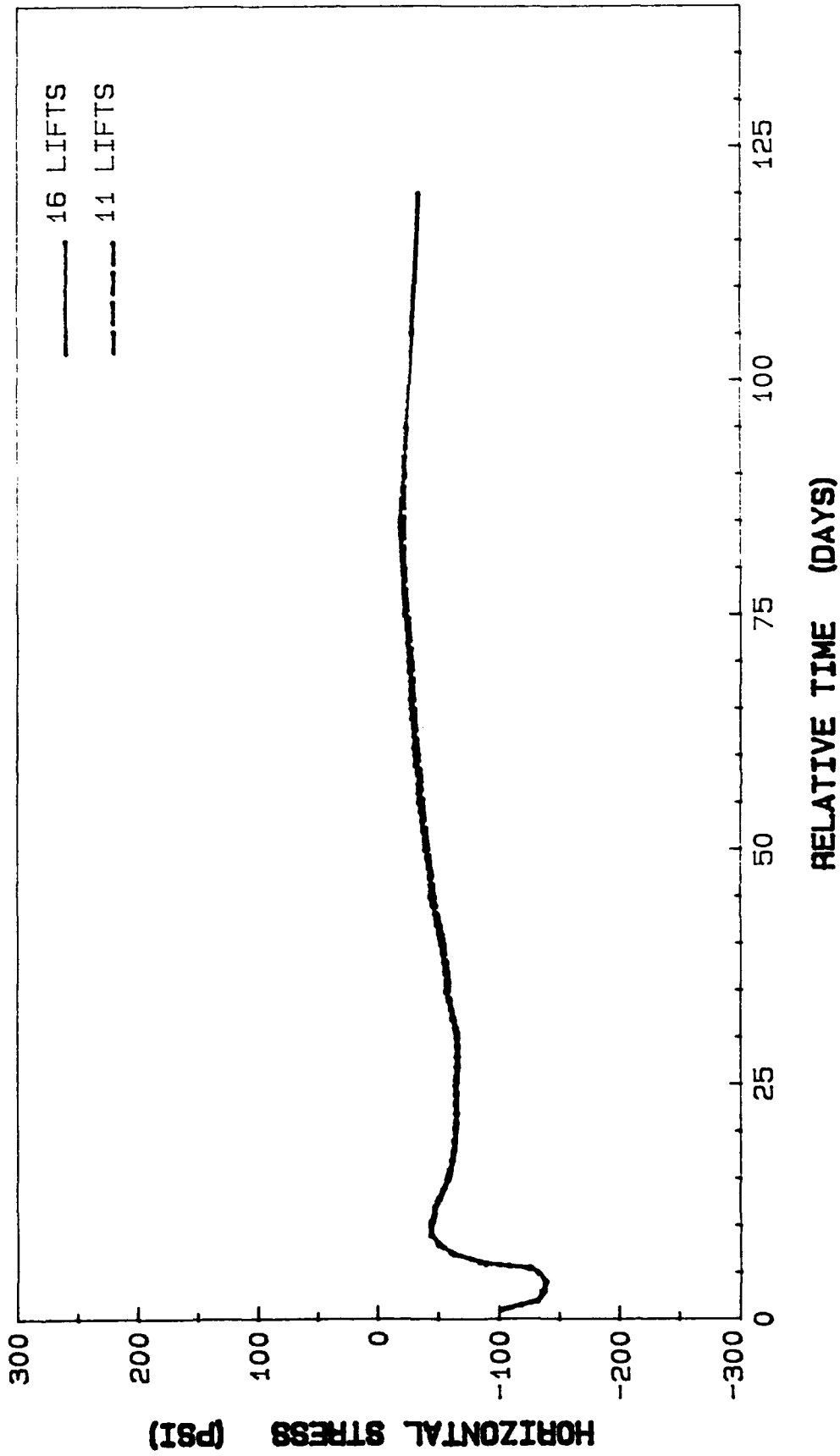


Figure 233. Horizontal stress history at element 411 integration point 2

ELEM. 513 INT. PT. 4 - UA, LC, LS

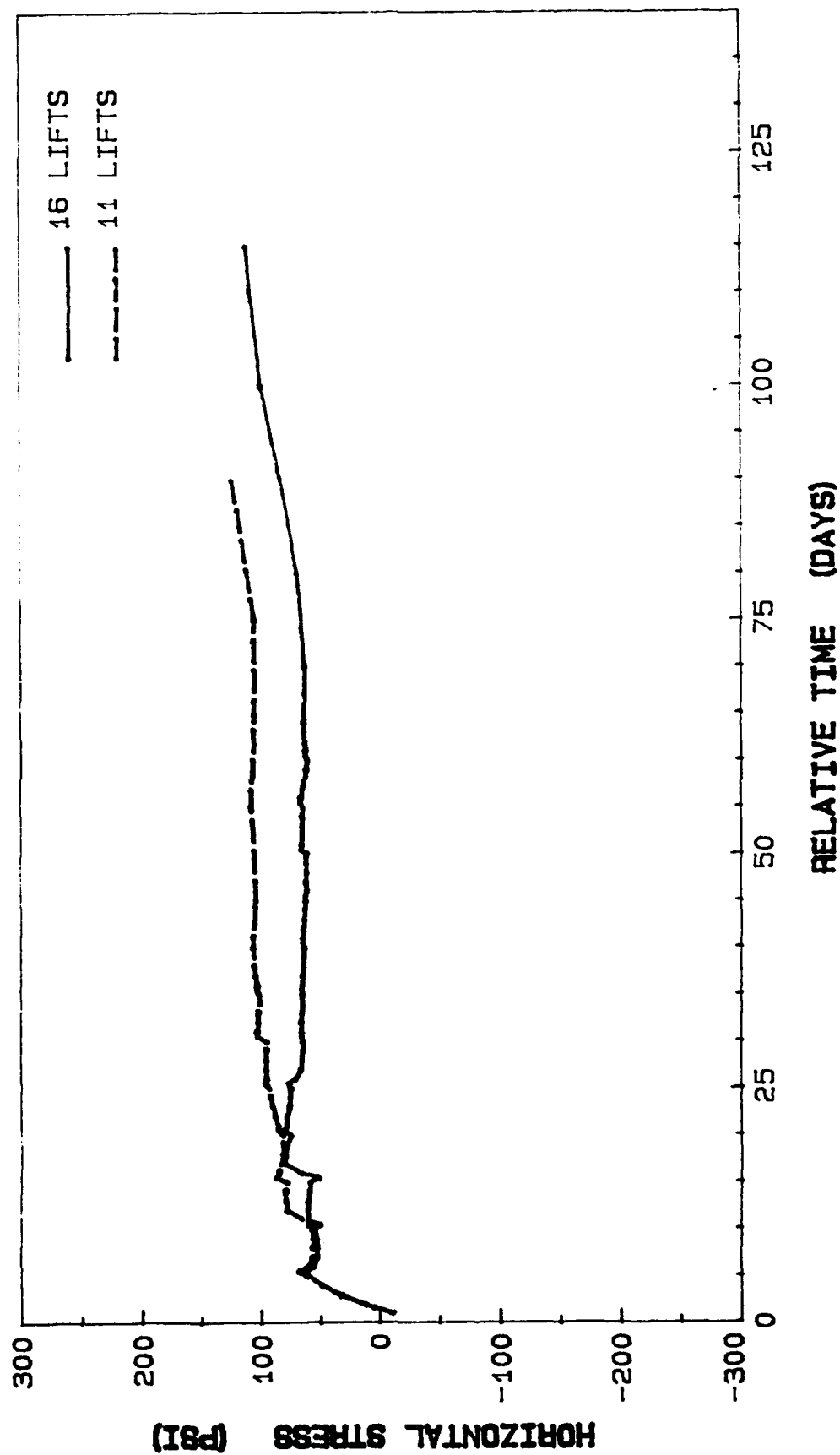


Figure 234. Horizontal stress history at element 513 integration point 4

ELEM. 537 INT. PT. 4 - UA, LC, LS

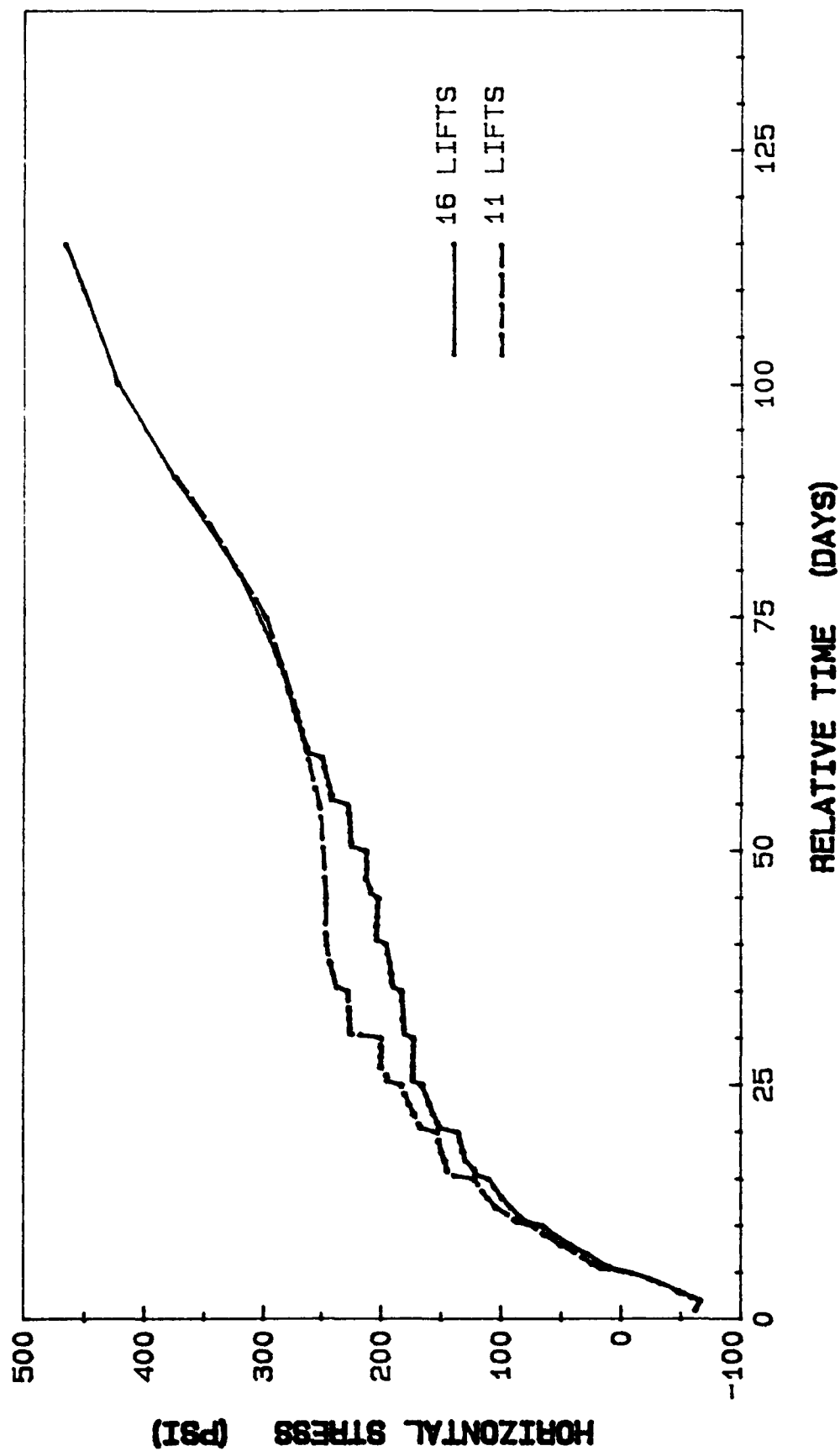


Figure 235. Horizontal stress history at element 537 integration point 4

ELEM. 706 INT. PT. 1 - UA, LC, LS

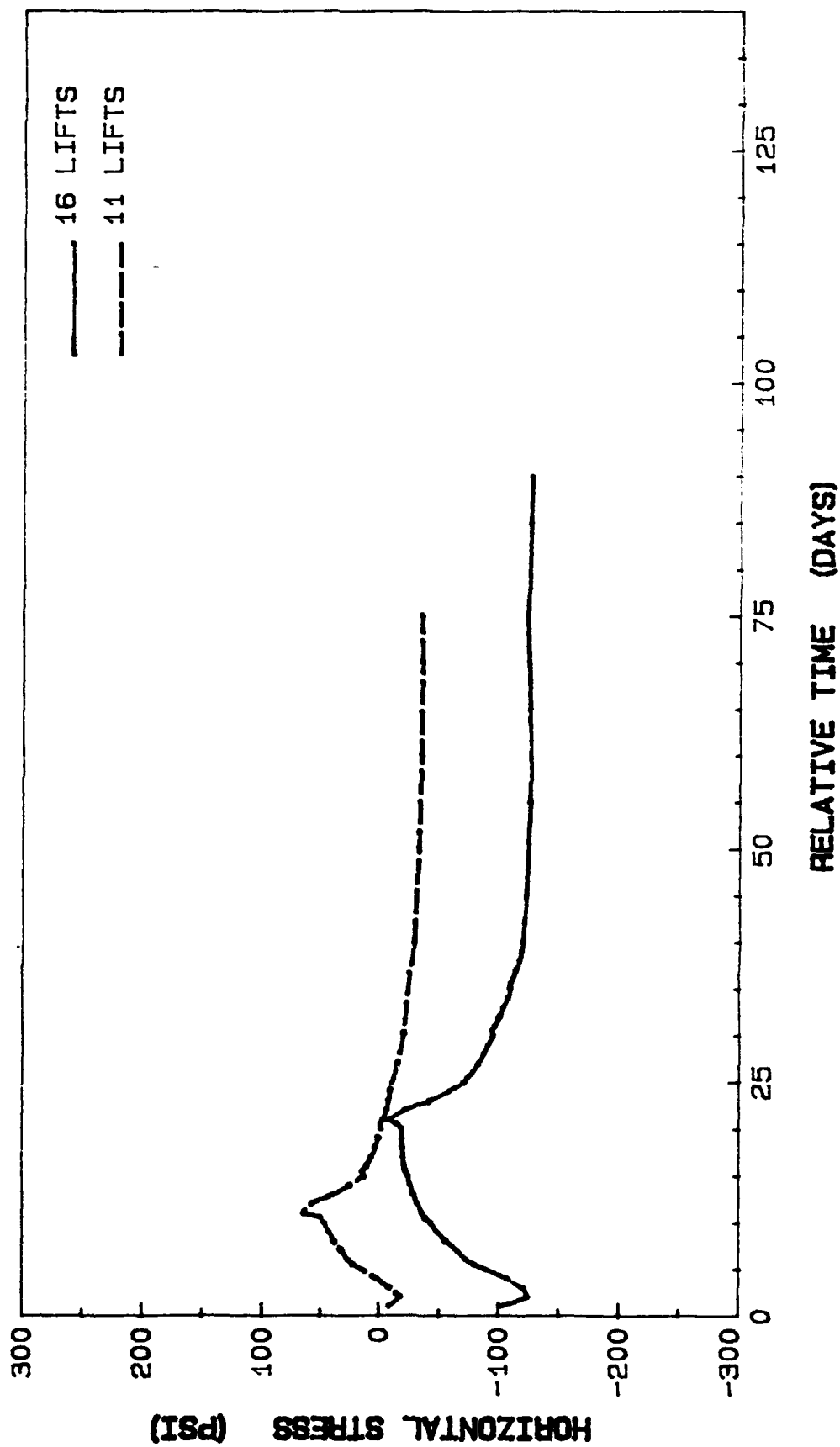


Figure 236. Horizontal stress history at element 706 integration point 1

ELEM. 706 INT. PT. 3 - UA, LC, LS

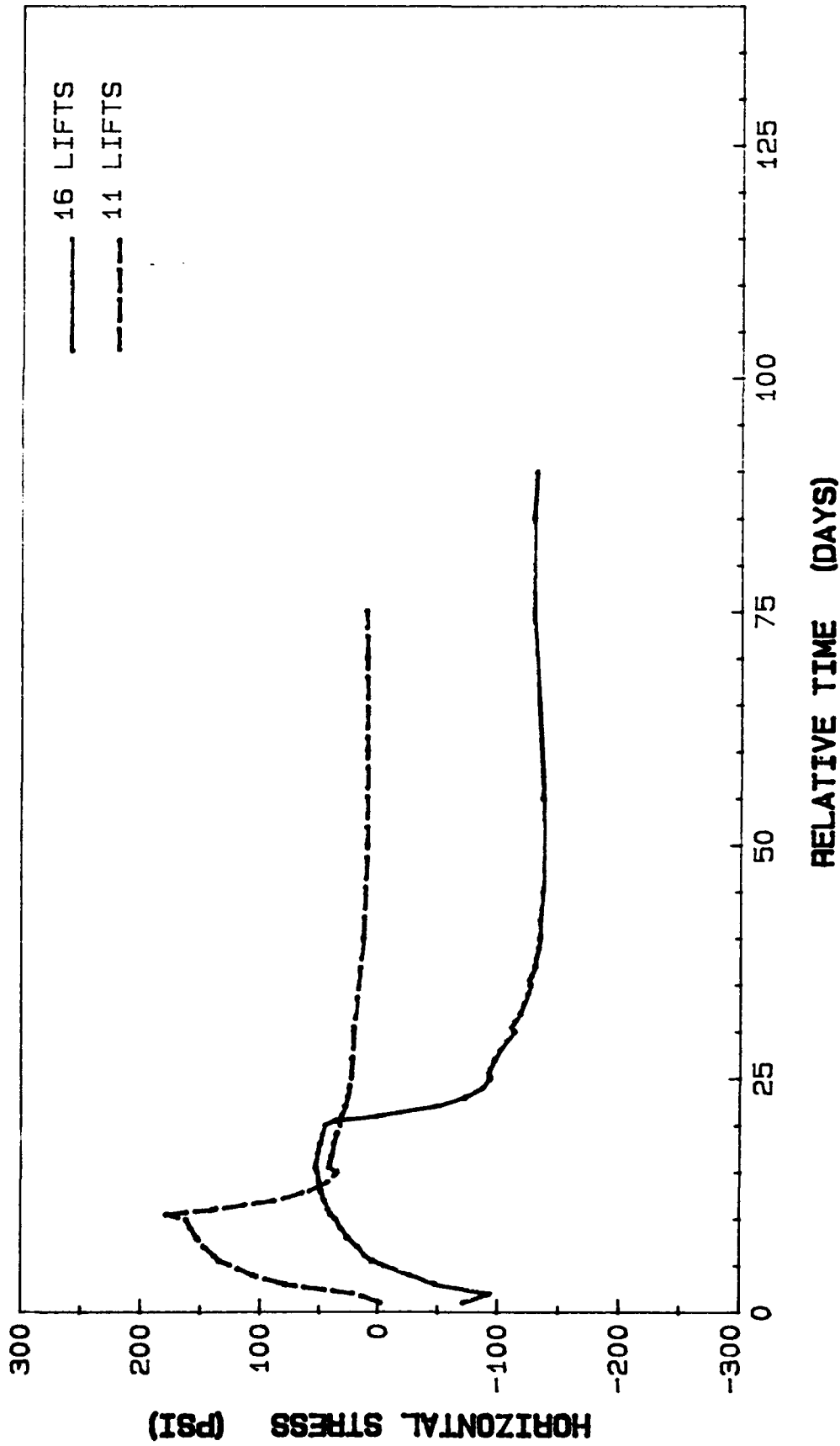


Figure 237. Horizontal stress history at element 706 integration point 3

ELEM. 877 INT. PT. 4 - UA, LC, LS

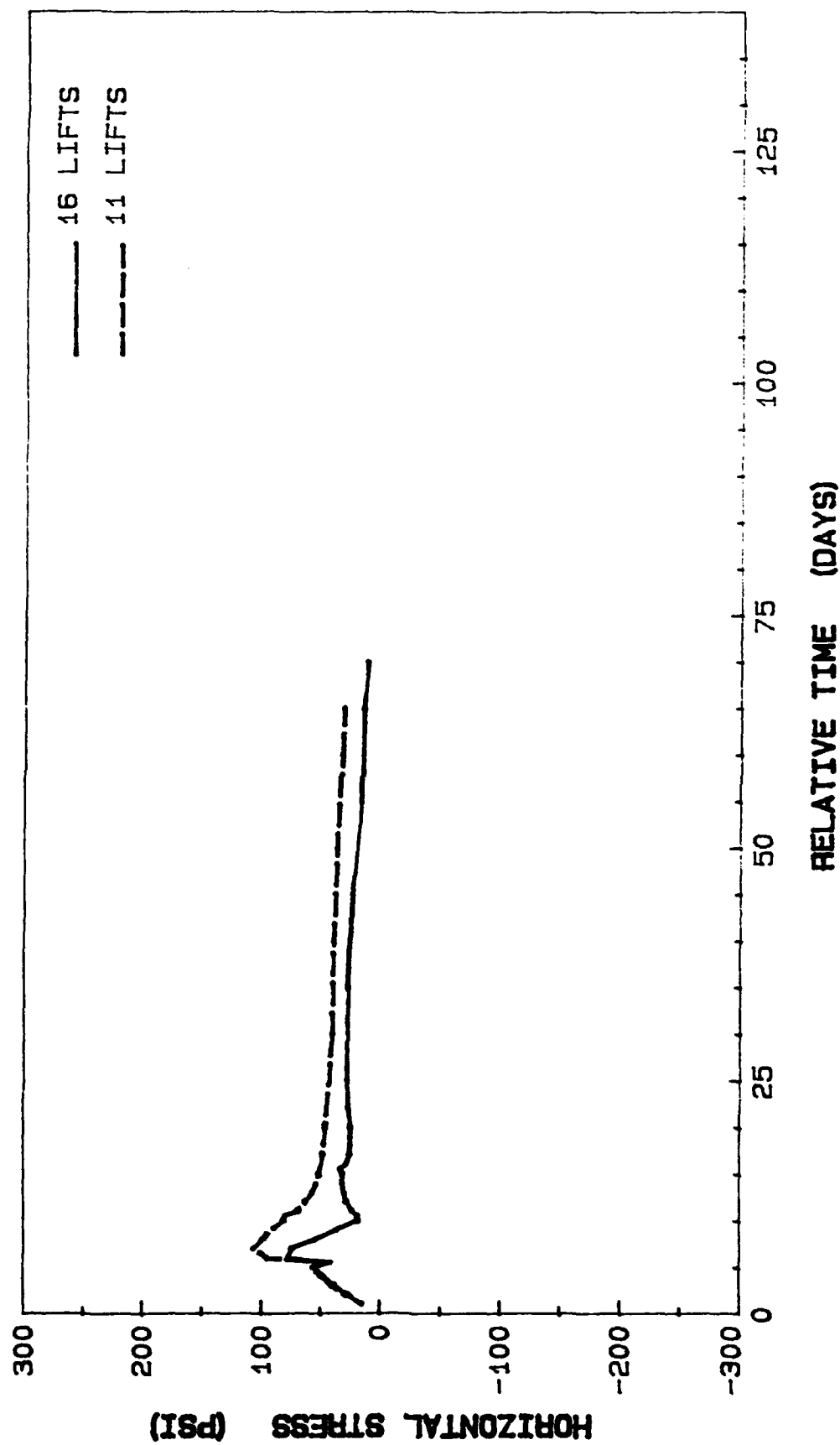


Figure 238. Horizontal stress history at element 877 integration point 4

needs to consider the lift itself and the surrounding lifts as well. In general, every new lift is considered to be more or less restrained at the bottom and free at the top. This results in tension at the top and compression at the bottom depending on how much restraint exists and how thick the lift is.

167. To summarize, for the points investigated in this region, the only significant difference between the 11- and 16-lift sequence occurs at the bottom of the void. This is primarily related to the larger thickness of lift 7. Although the stresses are greatly different, the maximum stress of 180 psi is not large in terms of design nor did it cause any cracking to occur.

168. Figures 238-245 are plots of the stress histories for the same locations previously discussed but using the upper creep and the upper shrinkage load case. The results produce smaller differences especially at the bottom of the void which substantiates that the lower creep with lower shrinkage is the controlling load case. Figures 243 and 244 are presented to show the effect creep and shrinkage have on the stresses below the void. The stress history for the lower creep shrinkage case shows a peak of about 180 psi for the 11-lift schedule; whereas, the upper creep and shrinkage produce a stress of 50 psi.

169. At the lift interfaces, the 11-lift and the 16-lift plans give similar results with the exception of the interface between lift 7 and 8 and the one between lifts 9 and 10 with reference to the 11-lift case. Stress history plots for the lower creep, lower shrinkage load case for all of the locations shown in Figure 246 are given in Figures 247-256. A stress history plot corresponding to a point just below the interface of lifts 7 and 8 is shown in Figure 252. The difference is about 70 psi between the two peaks. For the lift interface between lifts 9 and 10, a stress history plot at a point just below it is shown in Figure 255 and has a difference of about 50 psi. These two lift joints give the highest differences between the two lift plans.

170. For the upper creep and upper shrinkage load case, the results are shown in Figures 257-266. Again, this load case shows a much smaller difference than in the lower creep and lower shrinkage results. For instance, the maximum difference in the lower creep and lower shrinkage case was about 70 psi; whereas, in this case, it is only about 35 psi.

ELEM. 285 INT. PT. 2 - UA, UC, US

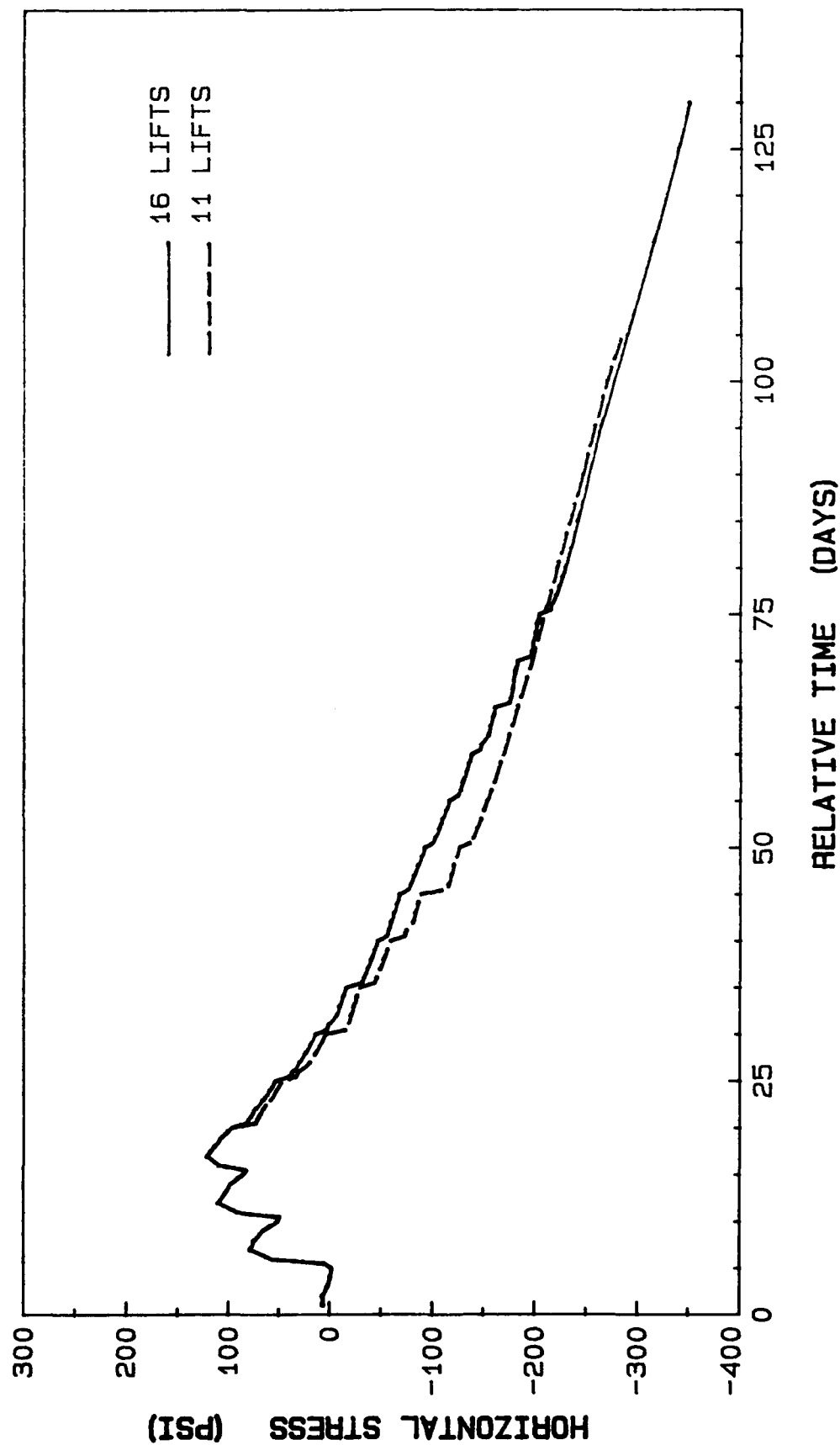


Figure 239. Horizontal stress history at element 285 integration point 2

ELEM. 387 INT. PT. 2 - UA, UC, US

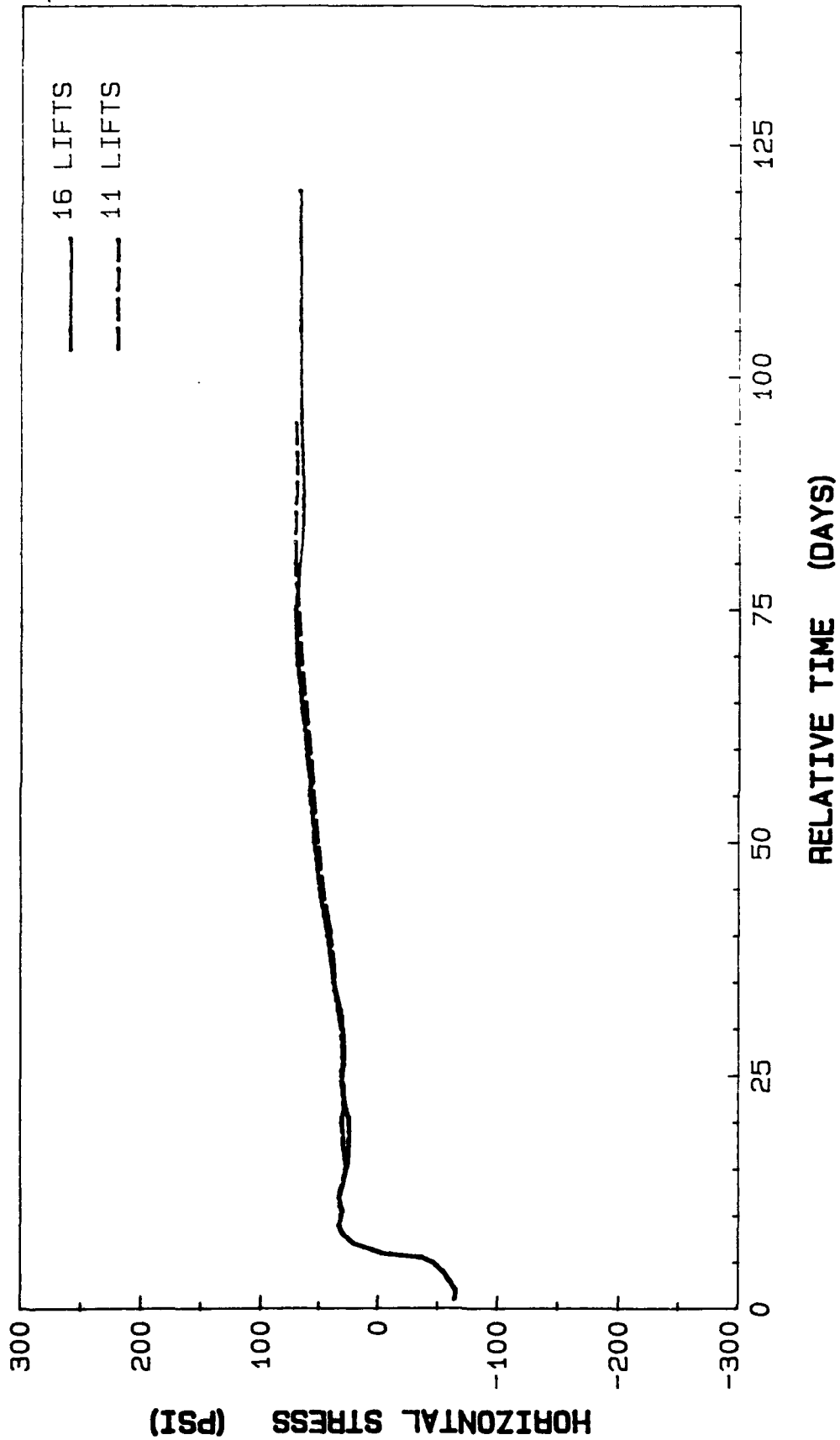


Figure 240. Horizontal stress history at element 387 integration point 2

ELEM. 411 INT. PT. 2 - UA, UC, US

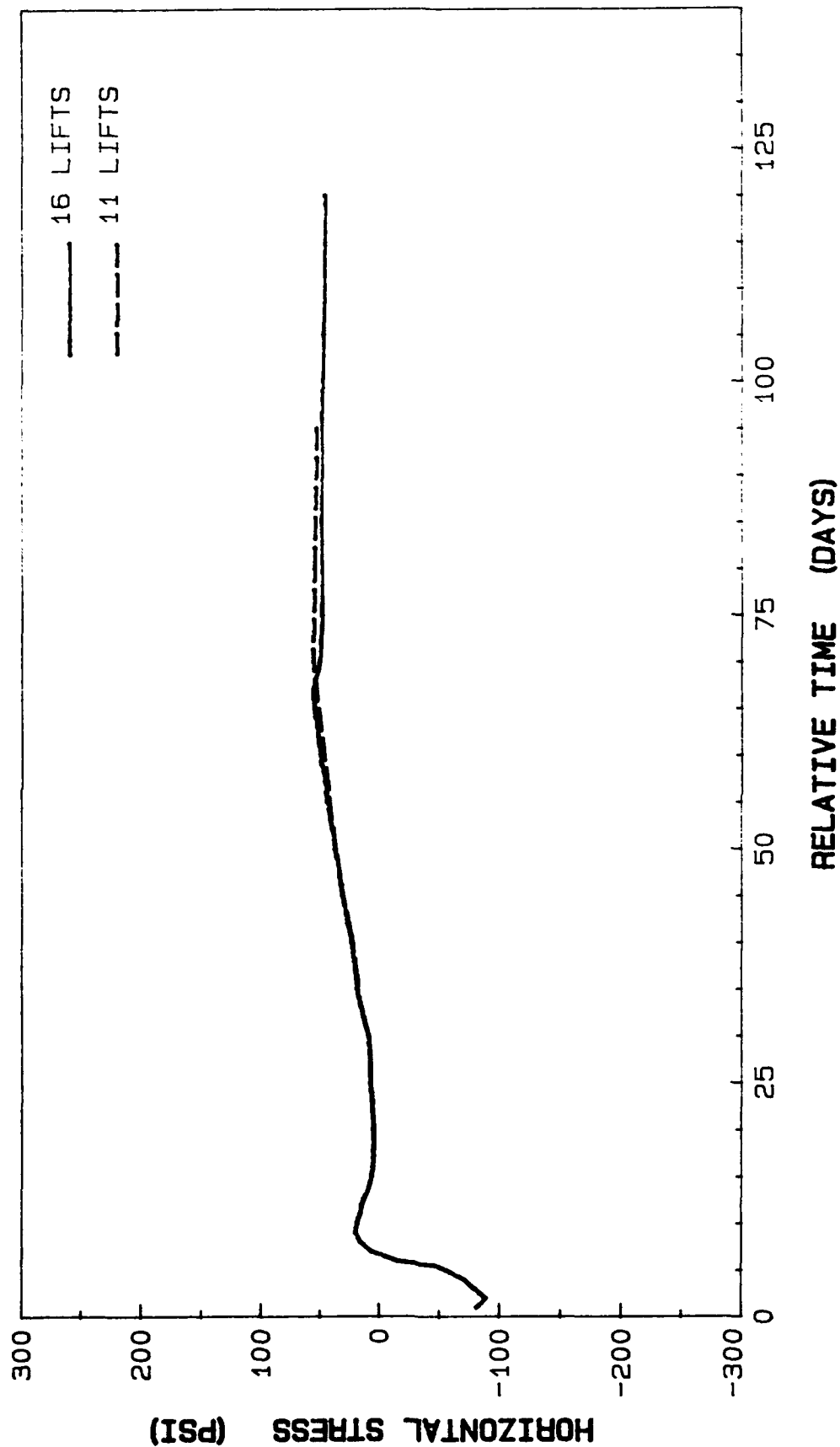


Figure 241. Horizontal stress history at element 411 integration point 2

ELEM. 513 INT. PT. 4 - UA, UC, US

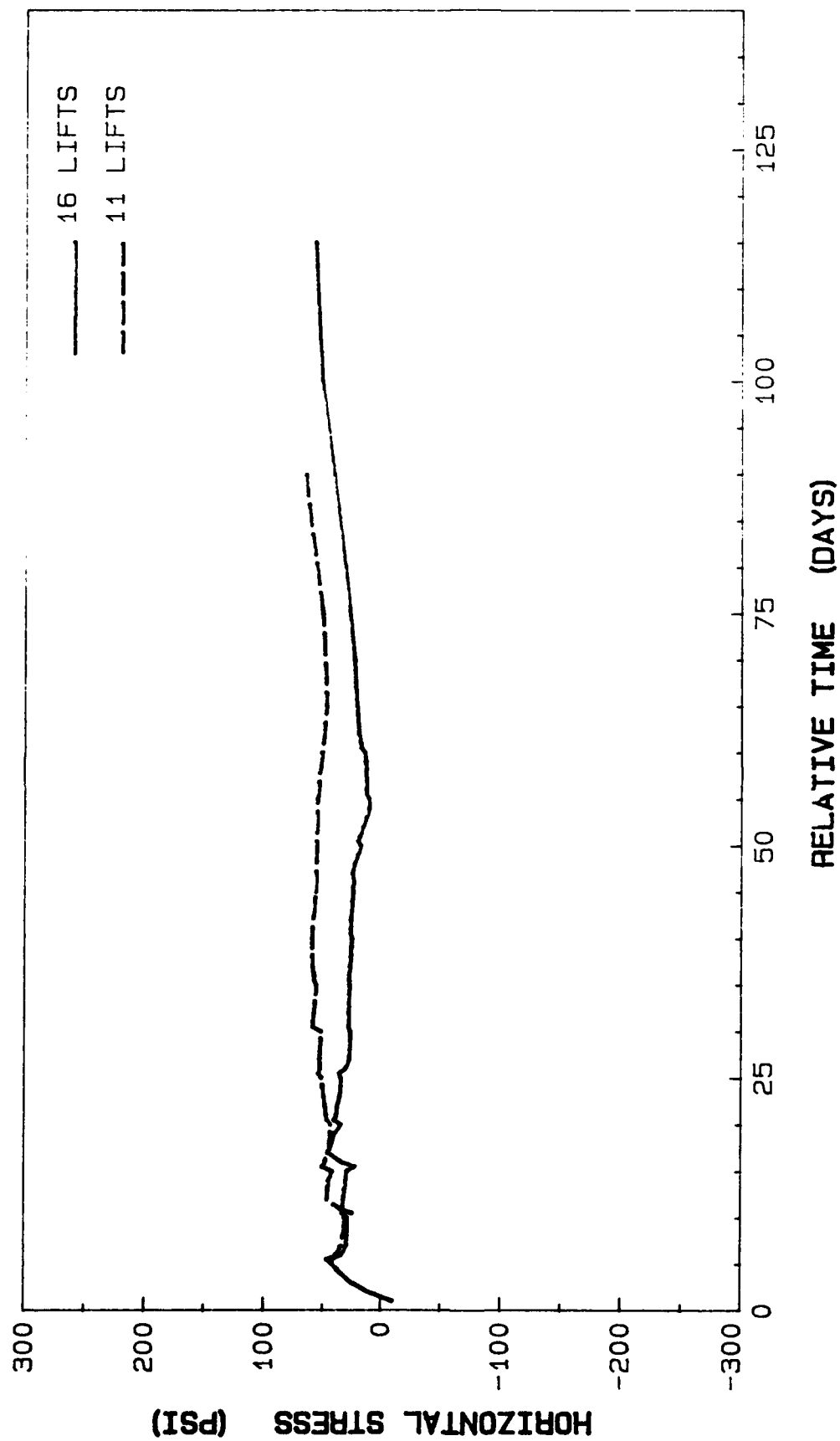


Figure 242. Horizontal stress history at element 513 integration point 4

ELEM. 537 INT. PT. 4 - UA, UC, US

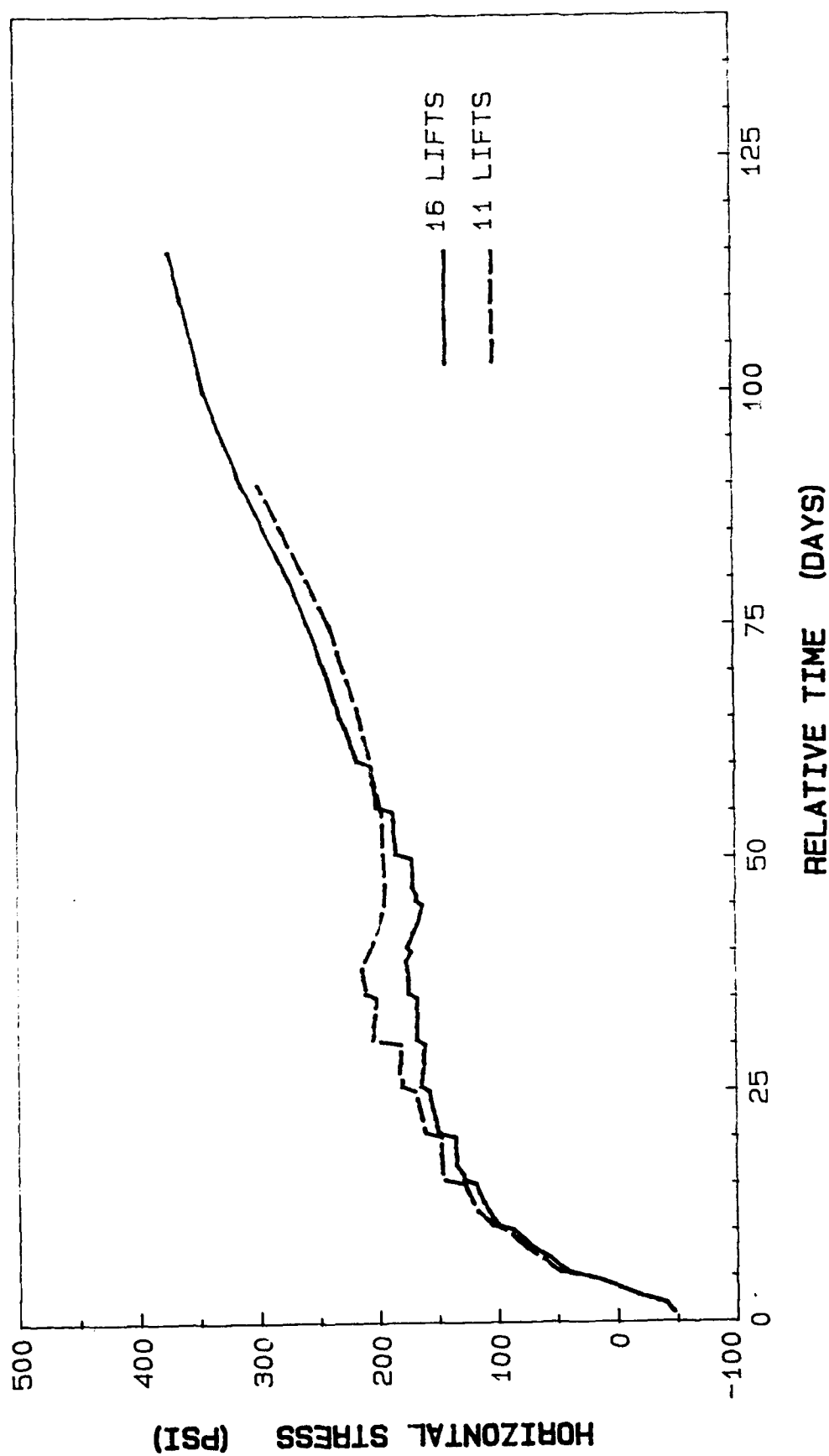


Figure 243. Horizontal stress history at element 537 integration point 4

ELEM. 706 INT. PT. 1 - UA, UC, US

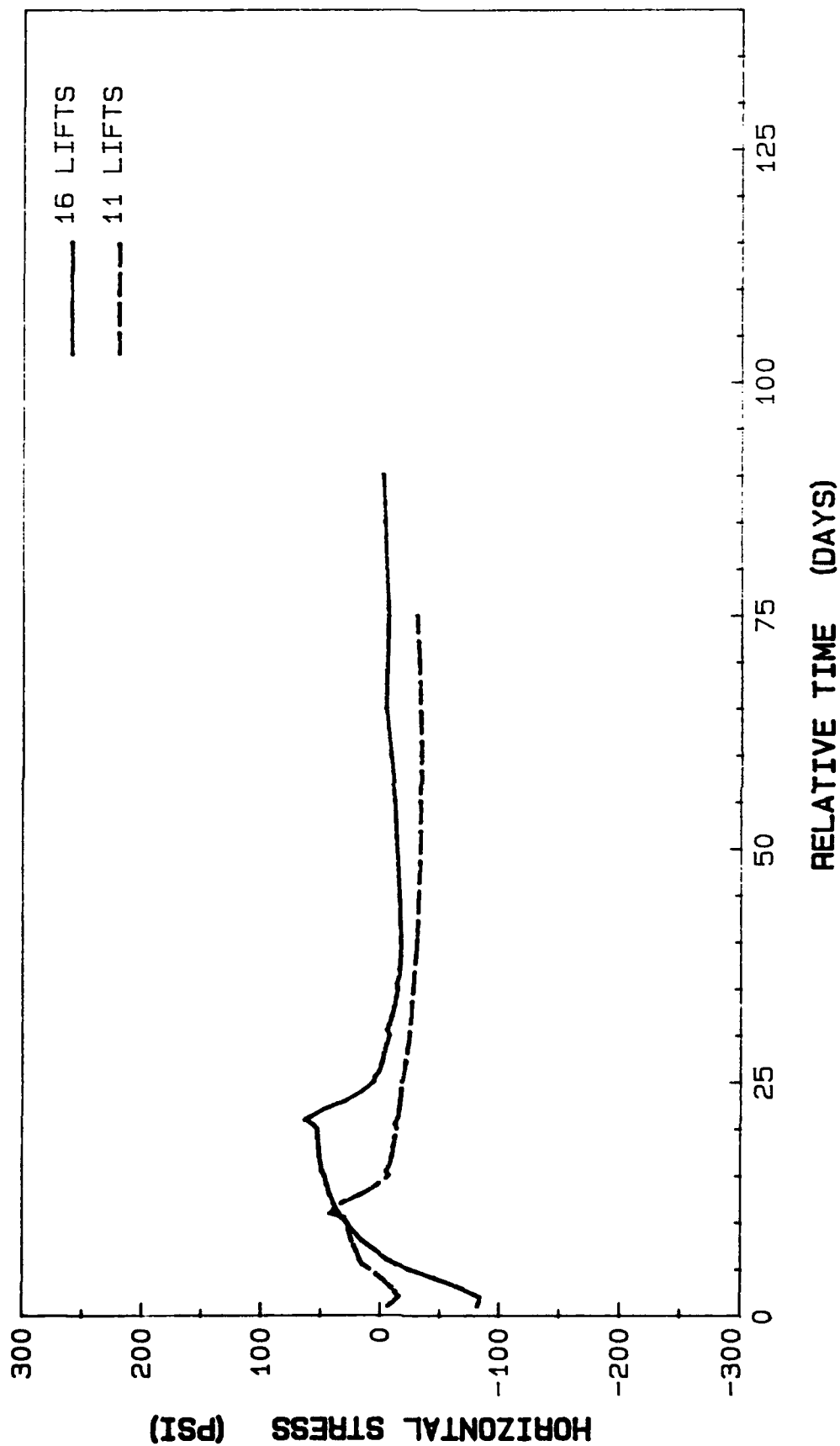


Figure 244. Horizontal stress history at element 706 integration point 1

ELEM. 706 INT. PT. 3 - UA, UC, US

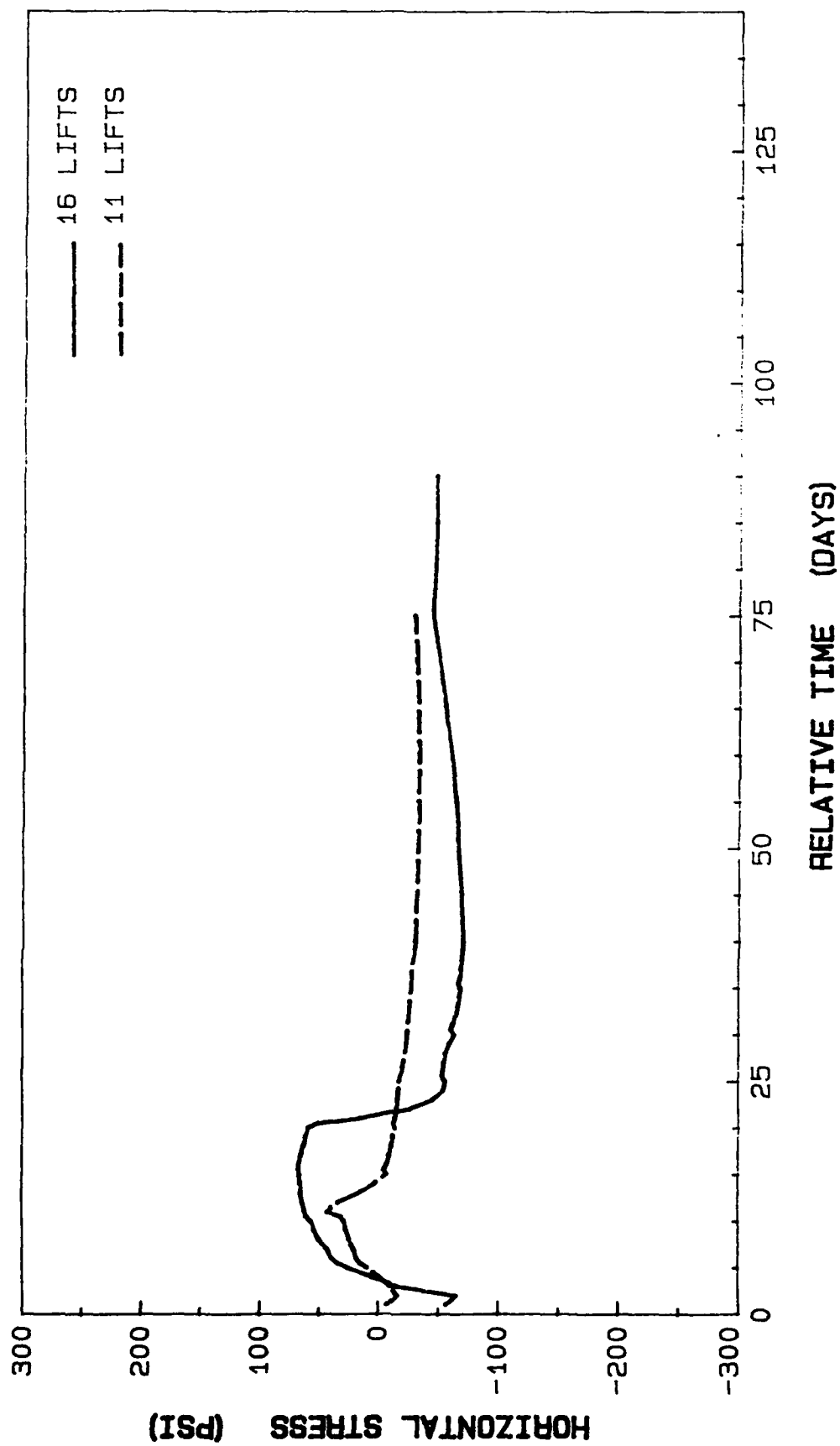


Figure 245. Horizontal stress history at element 706 integration point 3

ELEM. 877 INT. PT. 4 - UA, UC, US

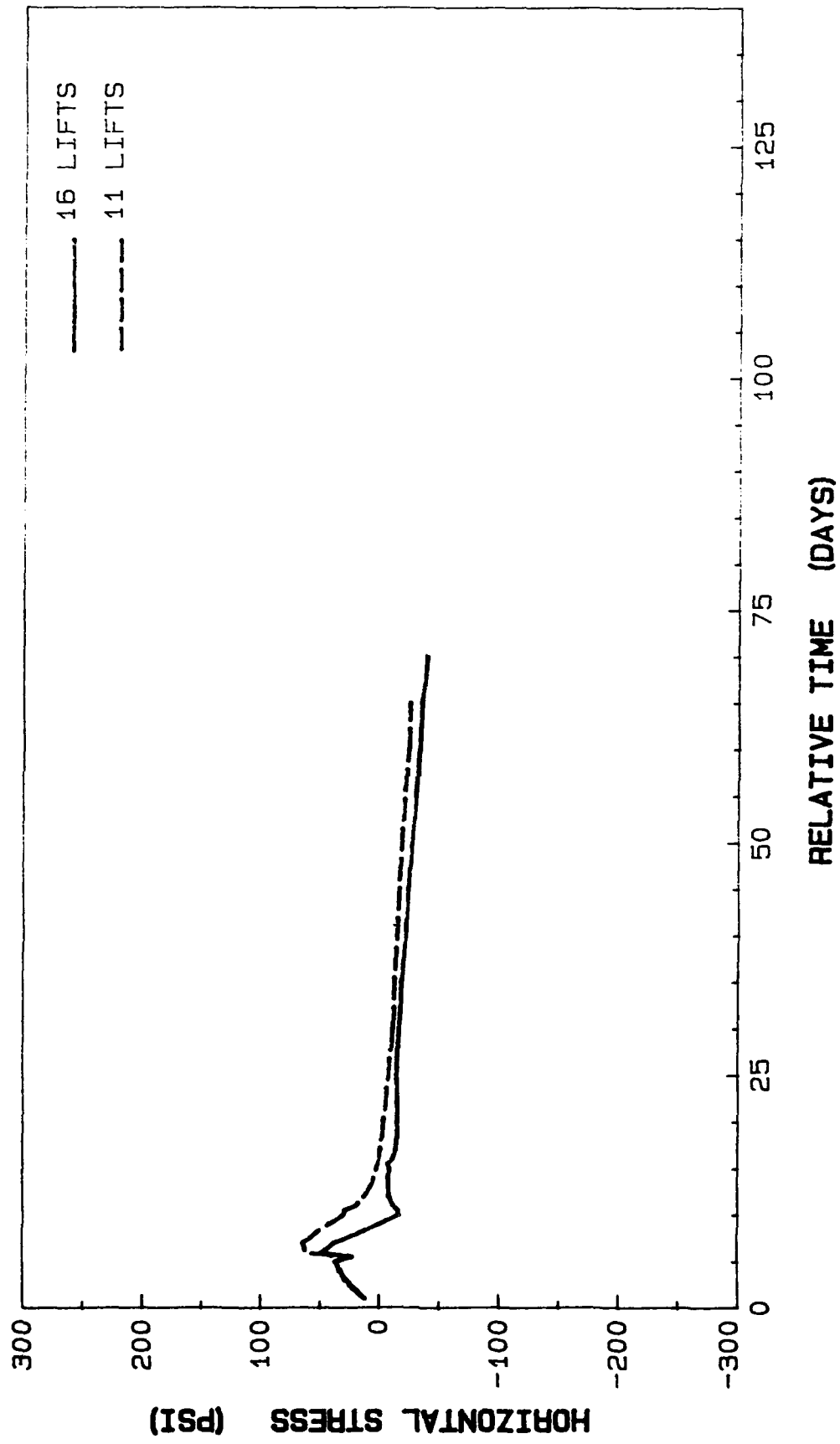


Figure 246. Horizontal stress history at element 877 integration point 4

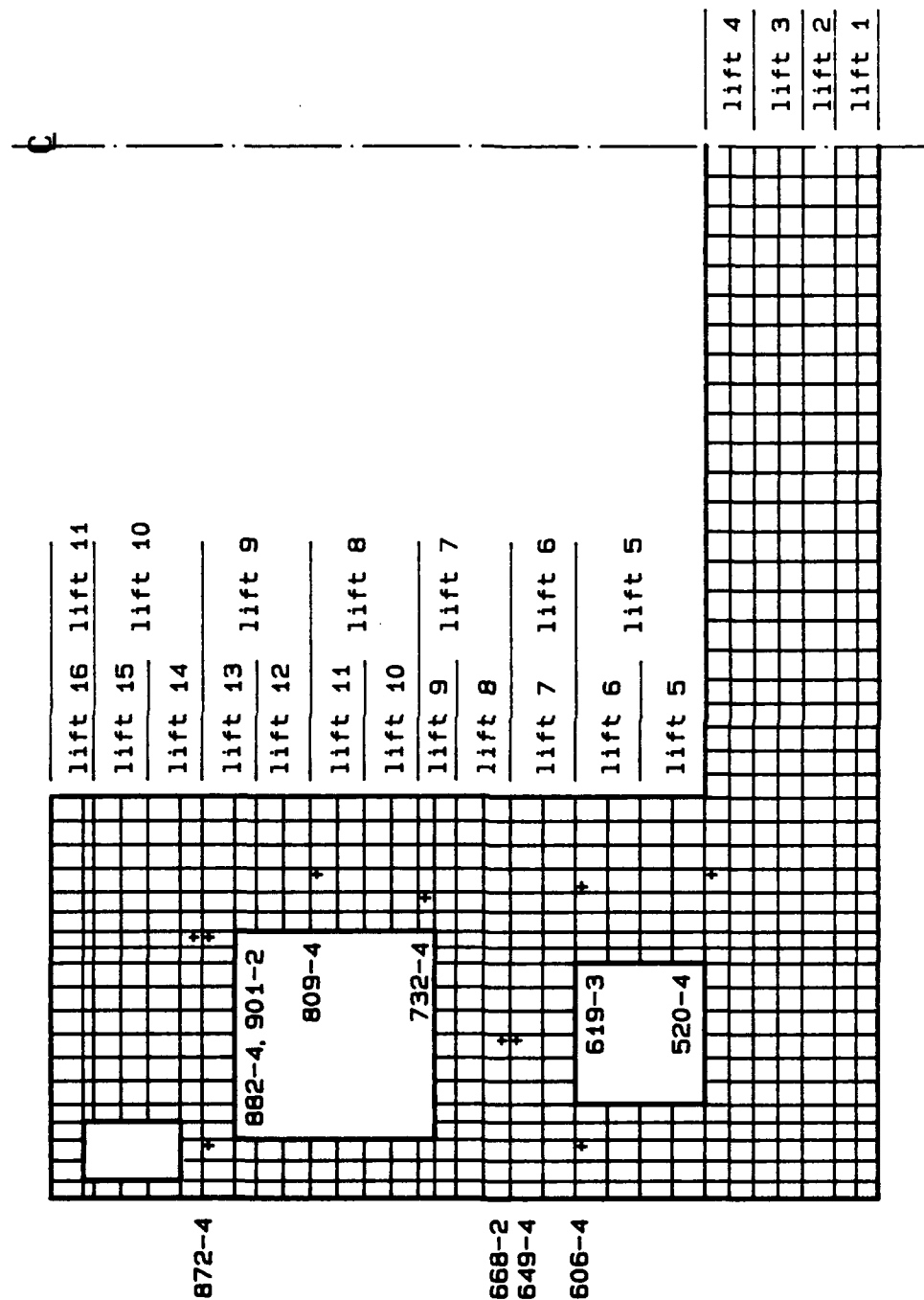


Figure 247. Selected elements for horizontal stress comparison at lift interfaces

ELEM. 520 INT. PT. 4 - UA, LC, LS

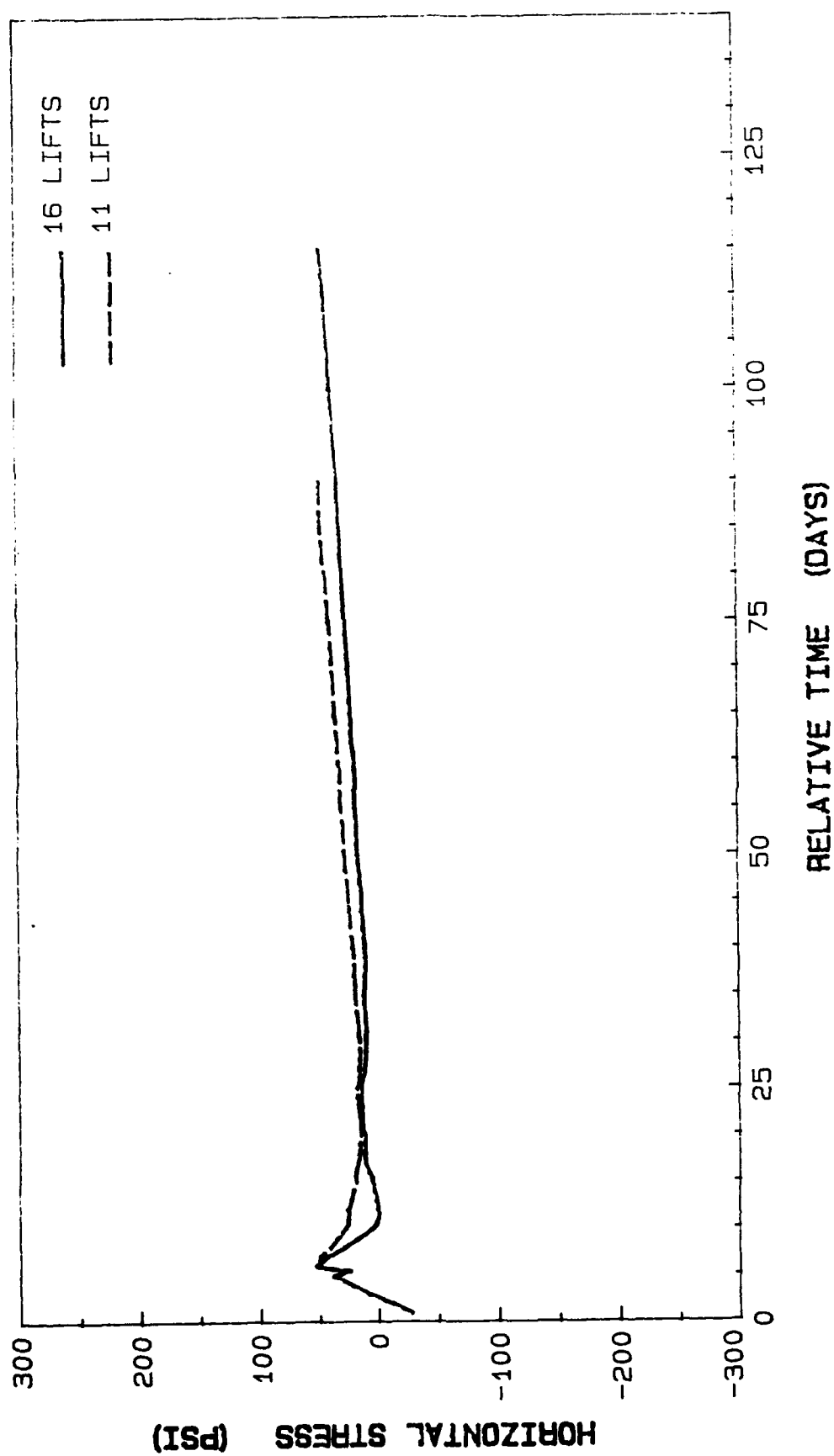


Figure 248. Horizontal stress history at element 520 integration point 4

ELEM. 606 INT. PT. 4 - UA, LC, LS

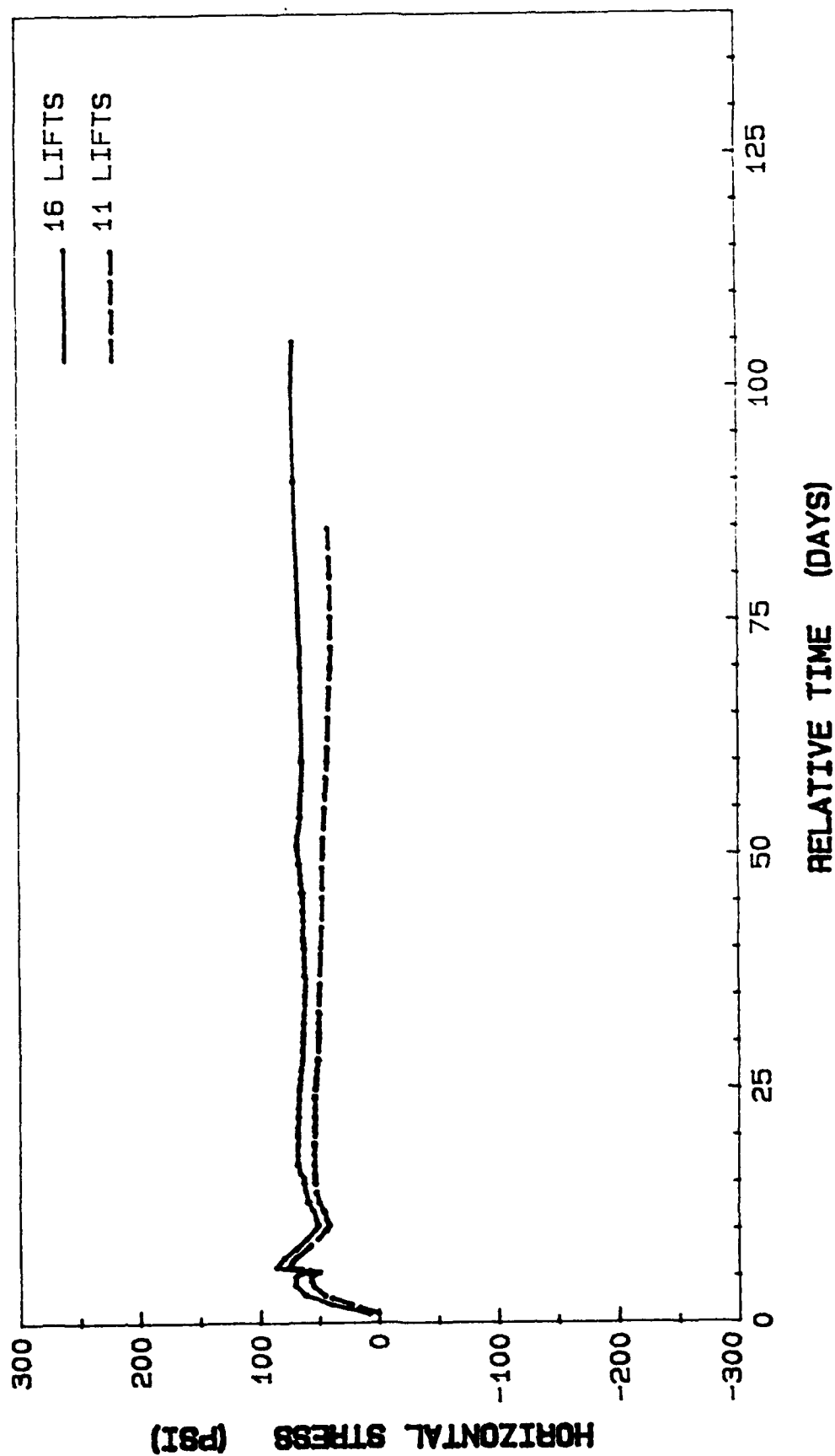


Figure 249. Horizontal stress history at element 606 integration point 4

ELEM. 619 INT. PT. 3 - UA, LC, LS

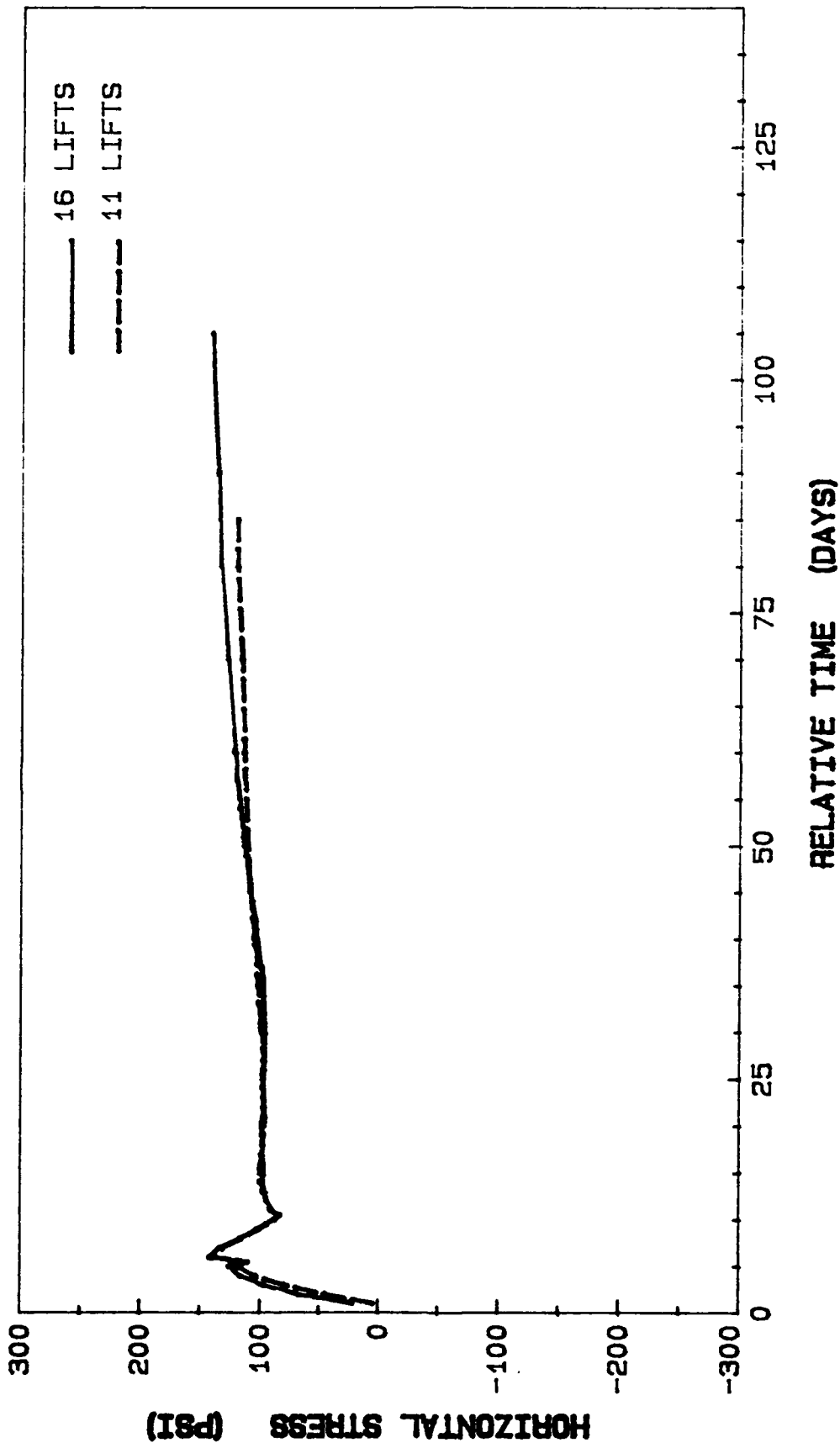


Figure 250. Horizontal stress history at element 619 integration point 3

ELEM. 649 INT. PT. 4 - UA, LC, LS

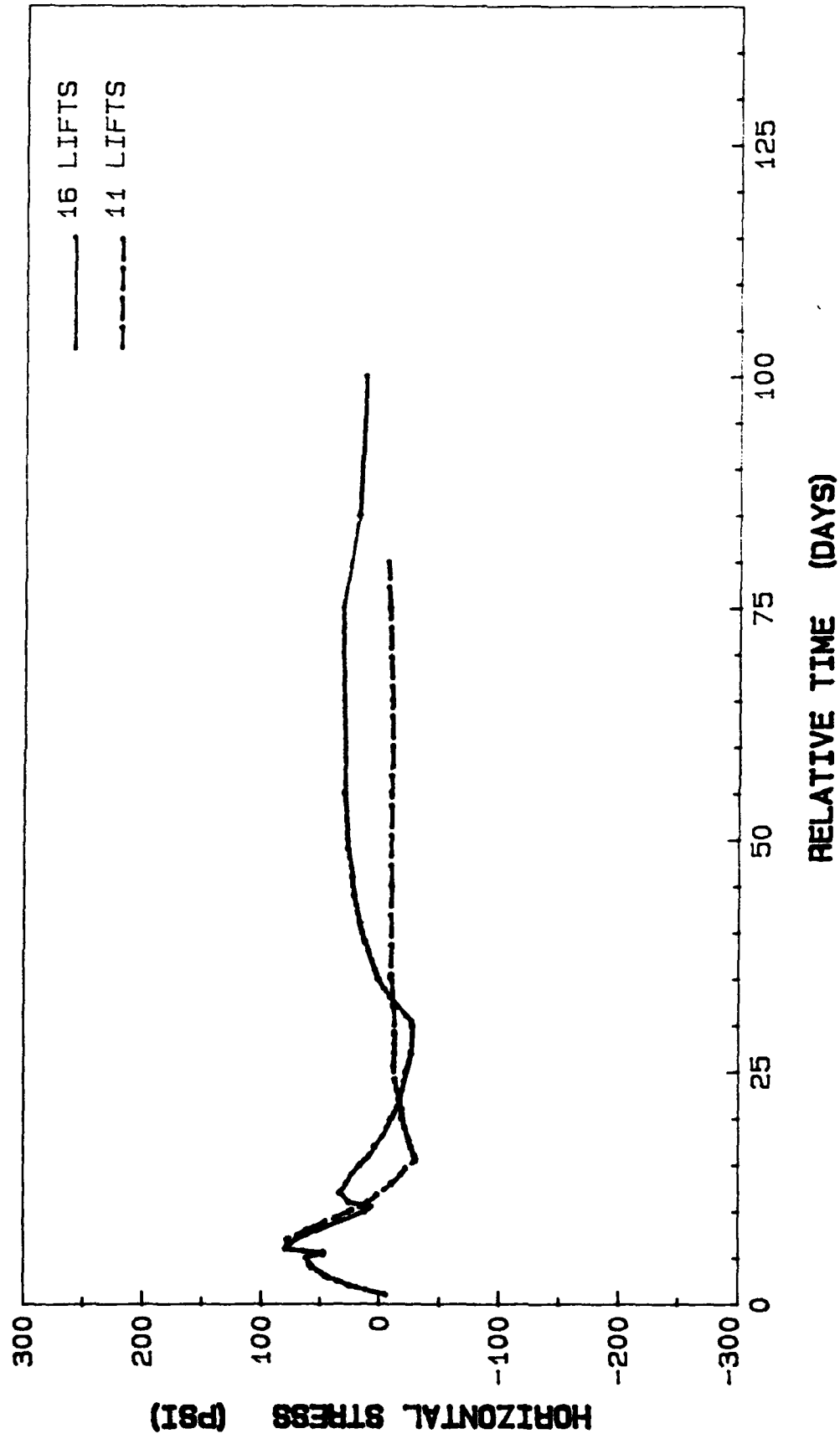


Figure 251. Horizontal stress history at element 649 integration point 4

ELEM. 668 INT. PT. 2 - UA, LC, LS

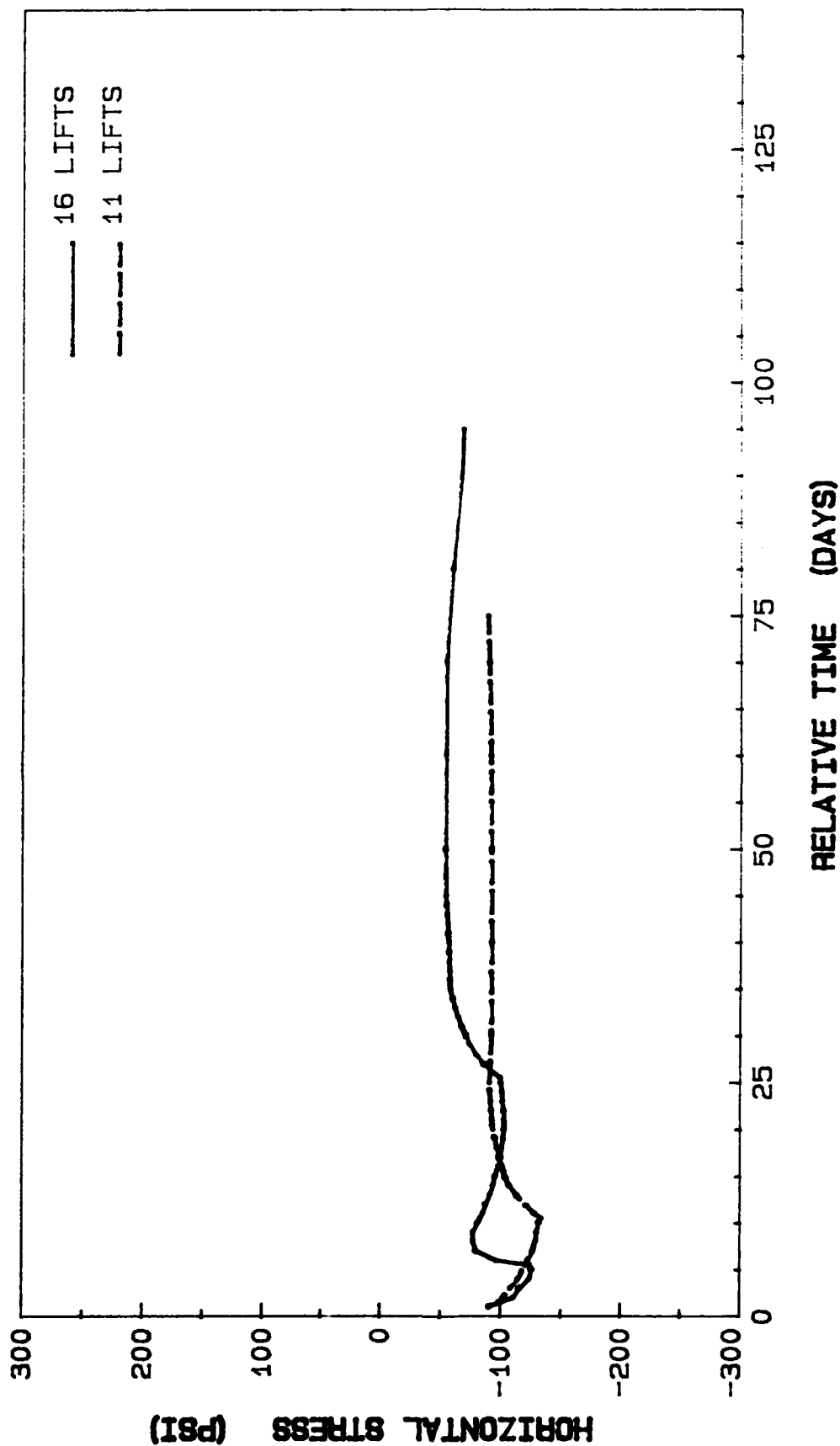


Figure 252. Horizontal stress history at element 668 integration point 2

ELEM. 732 INT. PT. 4 - UA.LC.LS

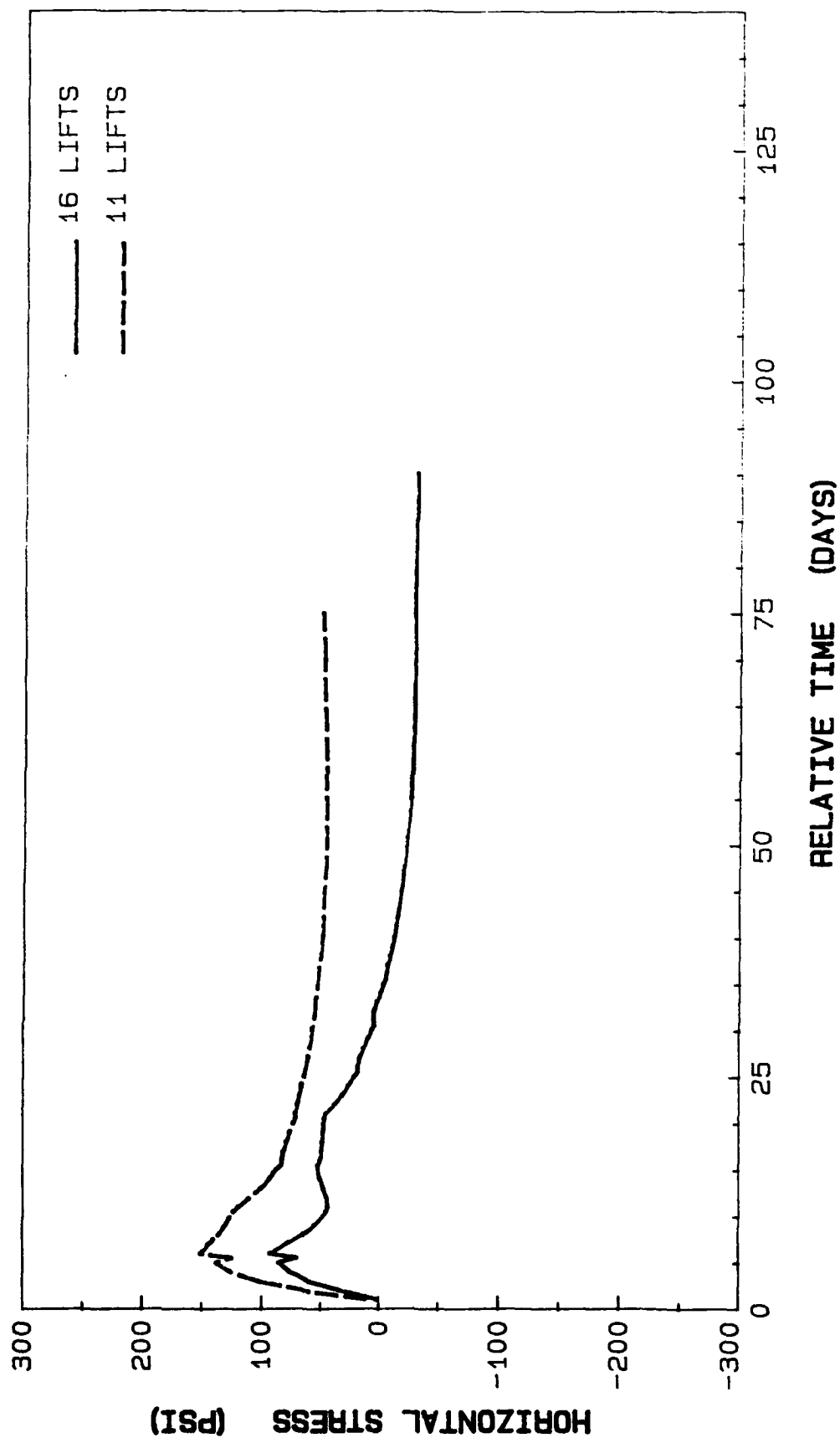


Figure 253. Horizontal stress history at element 732 integration point 4

ELEM. 809 INT. PT. 4 - UA, LC, LS

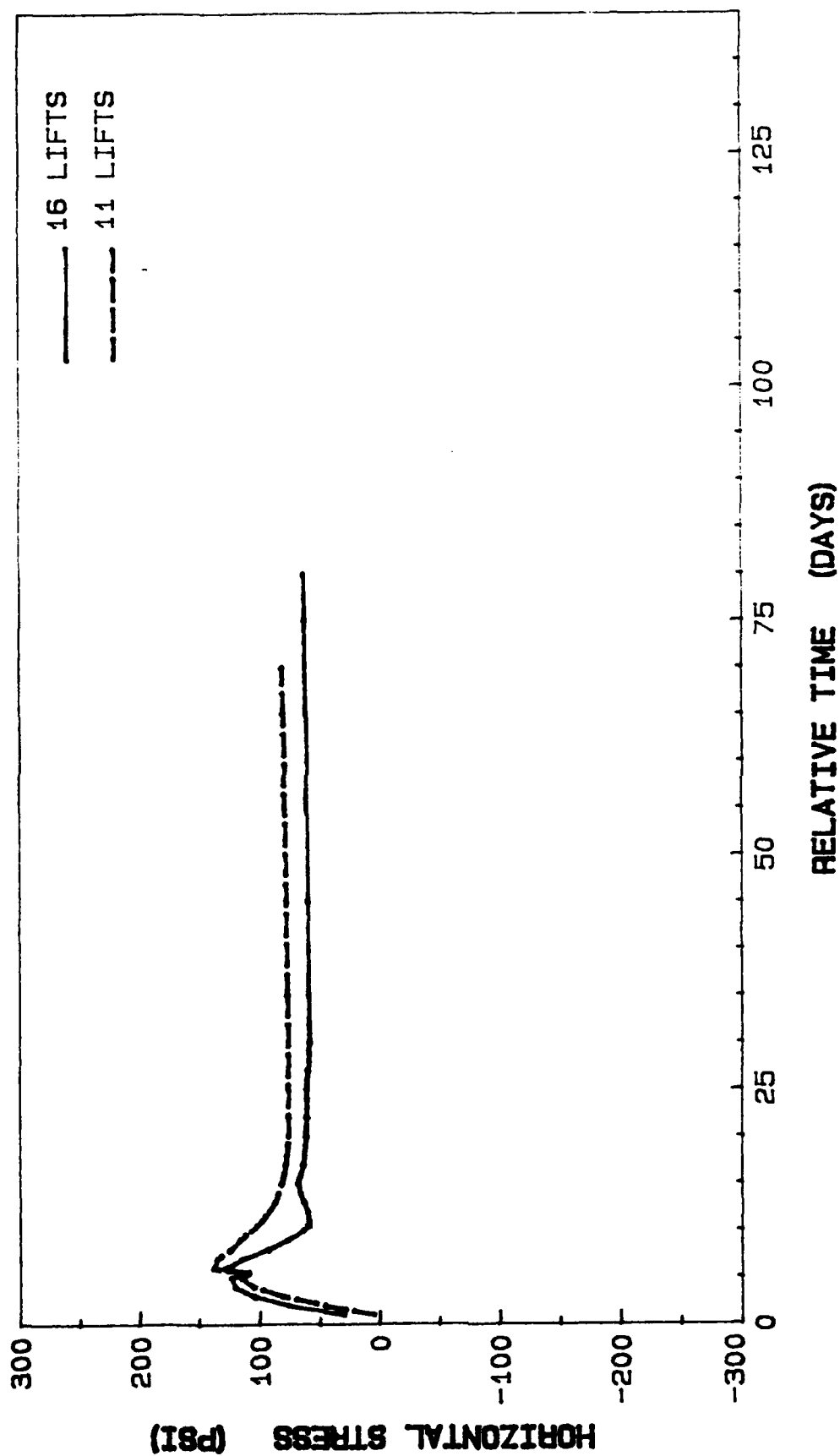


Figure 254. Horizontal stress history at element 809 integration point 4

ELEM. 872 INT. PT. 4 - UA, LC, LS

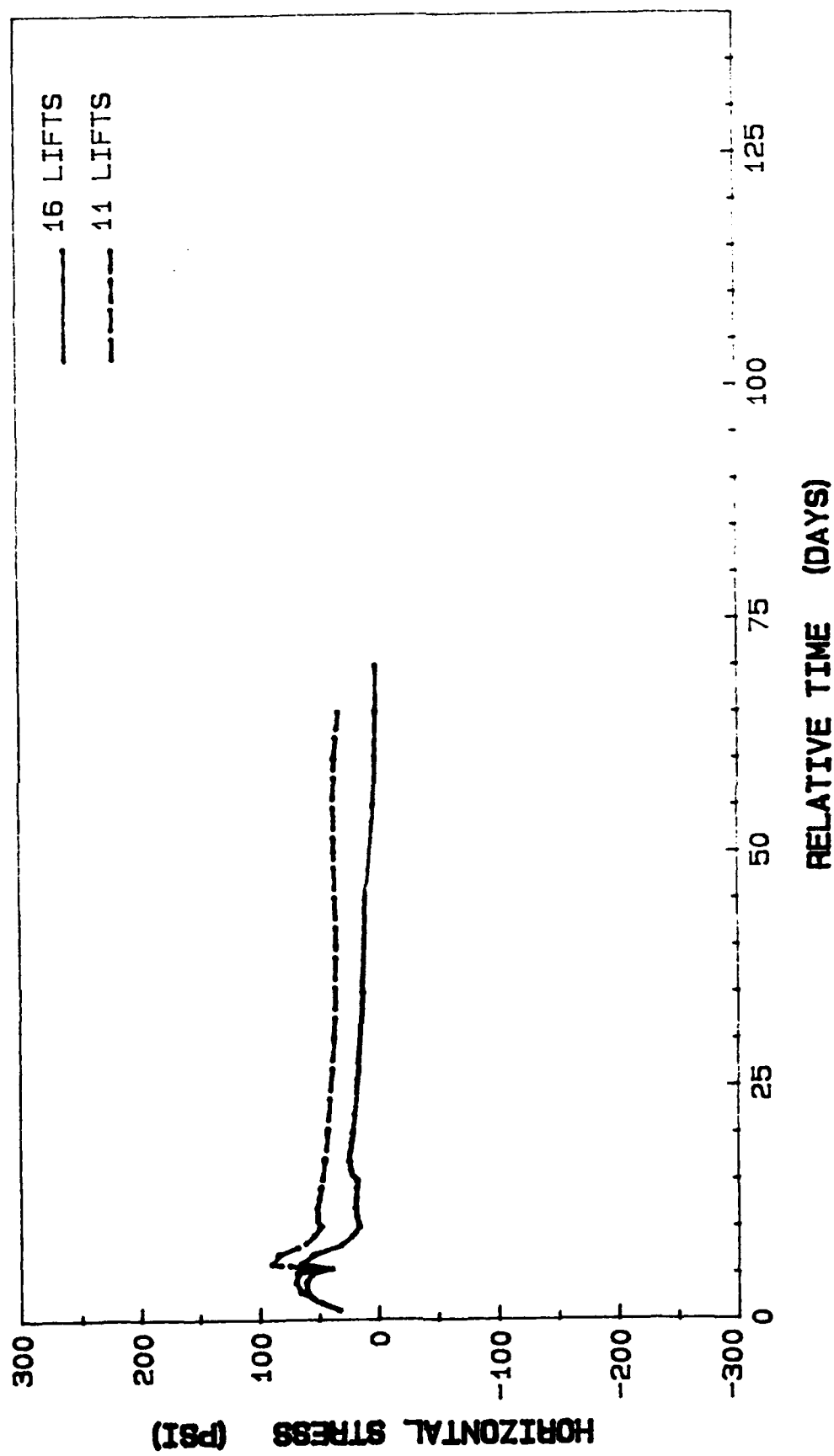


Figure 255. Horizontal stress history at element 872 integration point 4

ELEM. 882 INT. PT. 4 - UA, LC, LS

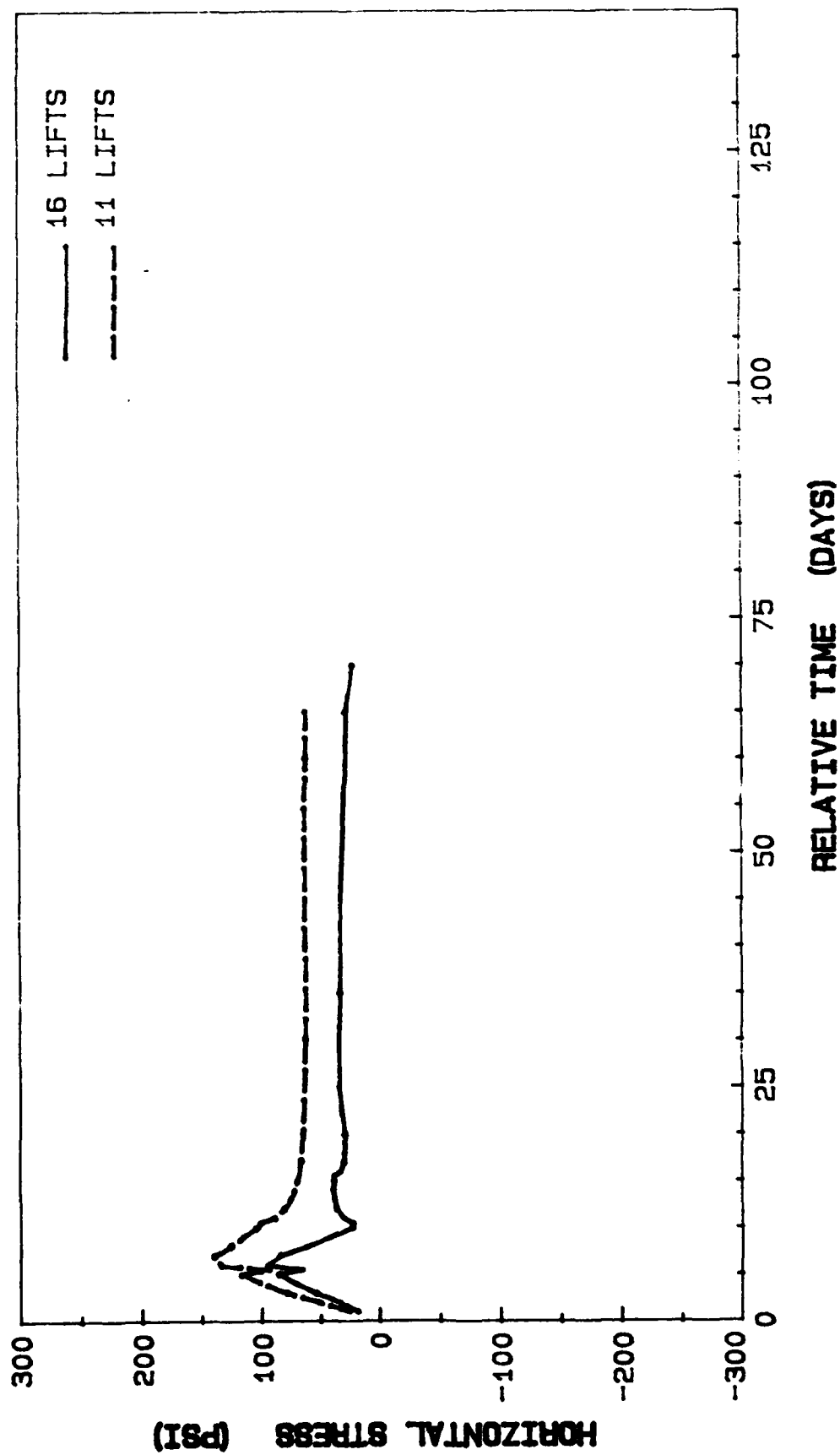


Figure 256. Horizontal stress history at element 882 integration point 4

ELEM. 901 INT. PT. 2 - UA, LC, LS

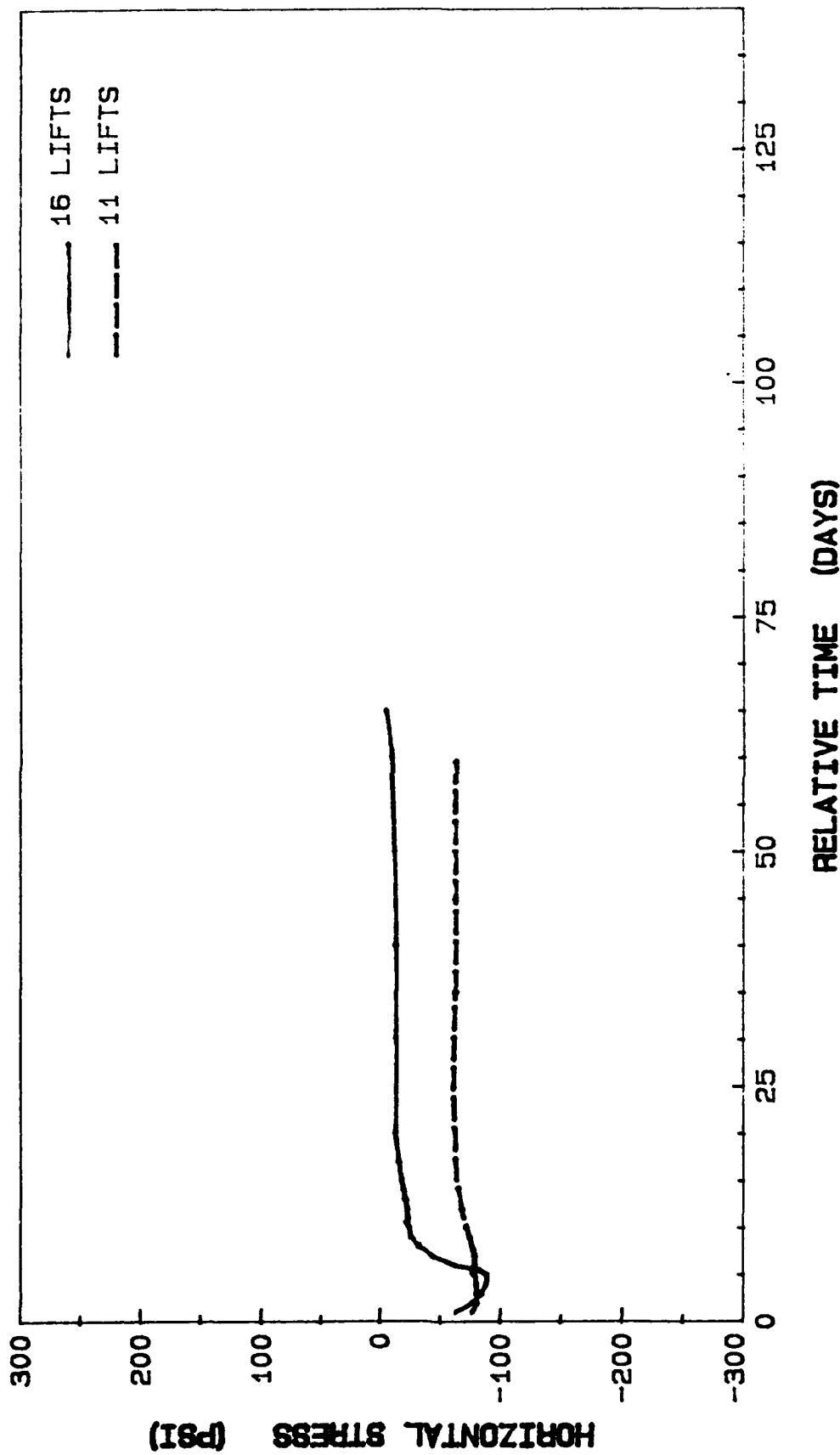


Figure 257. Horizontal stress history at element 901, integration point 2

ELEM. 520 INT. PT. 4 - UA, UC, US

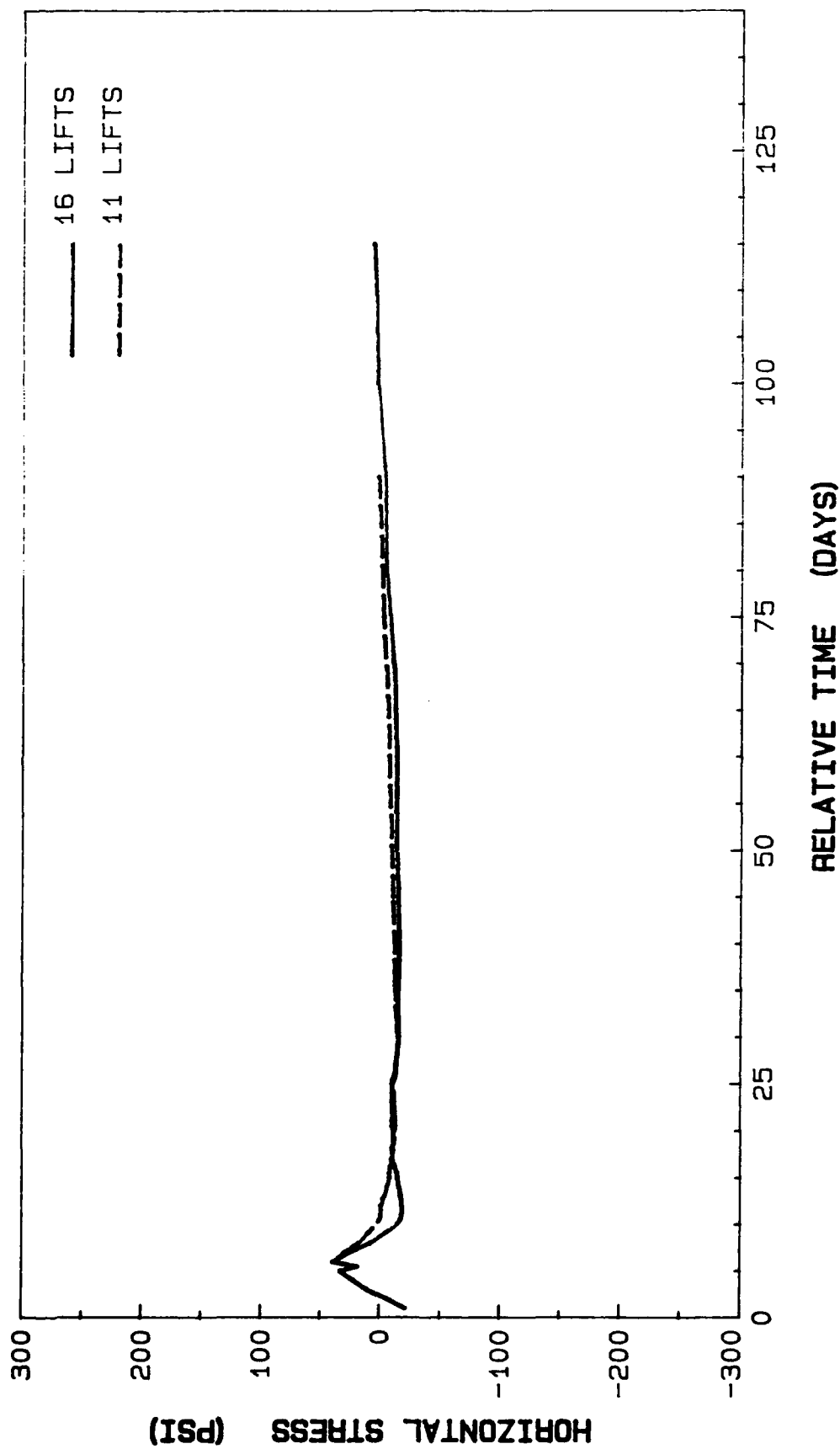


Figure 258. Horizontal stress history at element 520, integration point 4

ELEM. 606 INT. PT. 4 - UA, UC, US

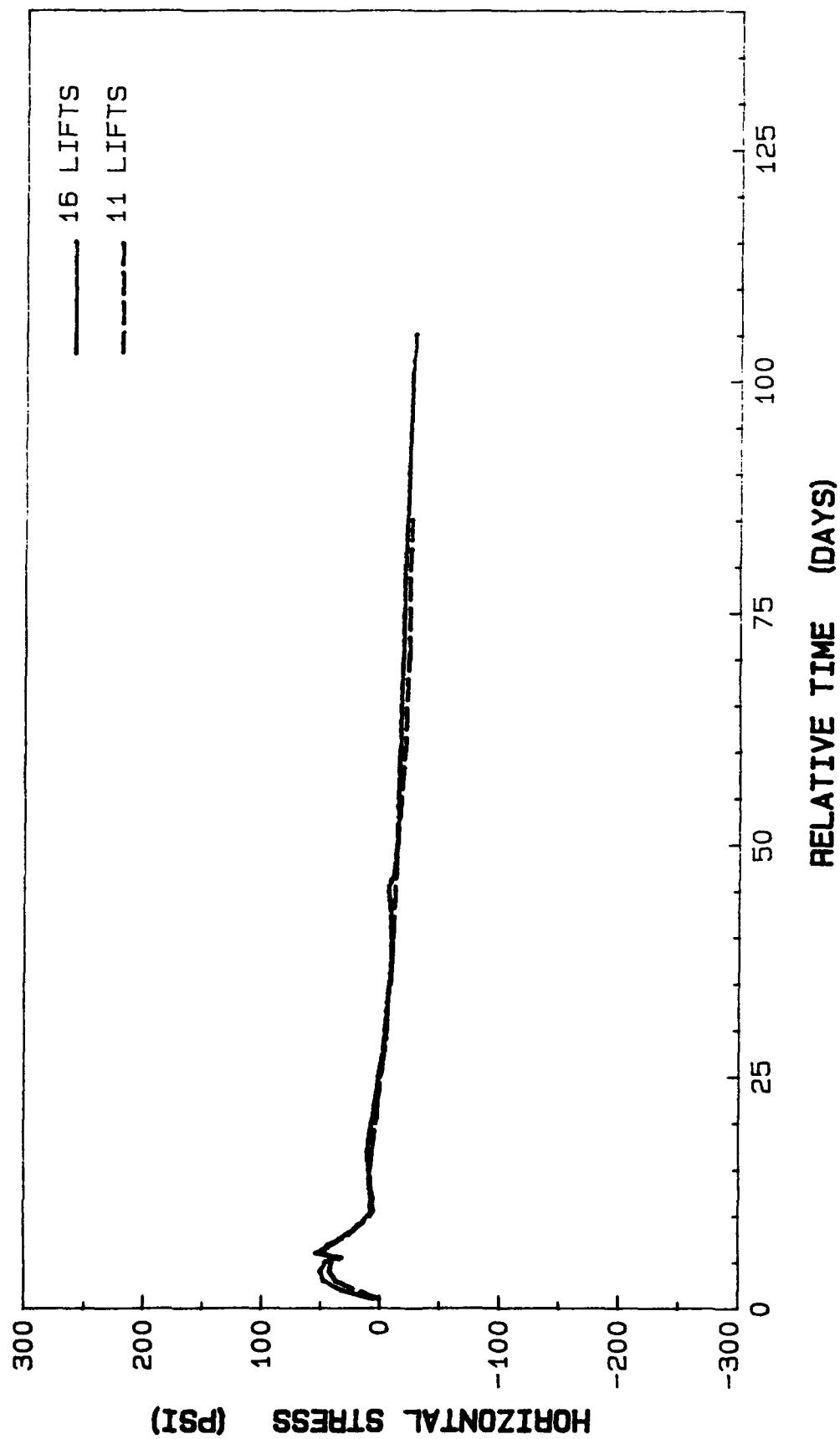


Figure 259. Horizontal stress history at element 606, integration point 4

ELEM. 619 INT. PT. 3 - UA, UC, US

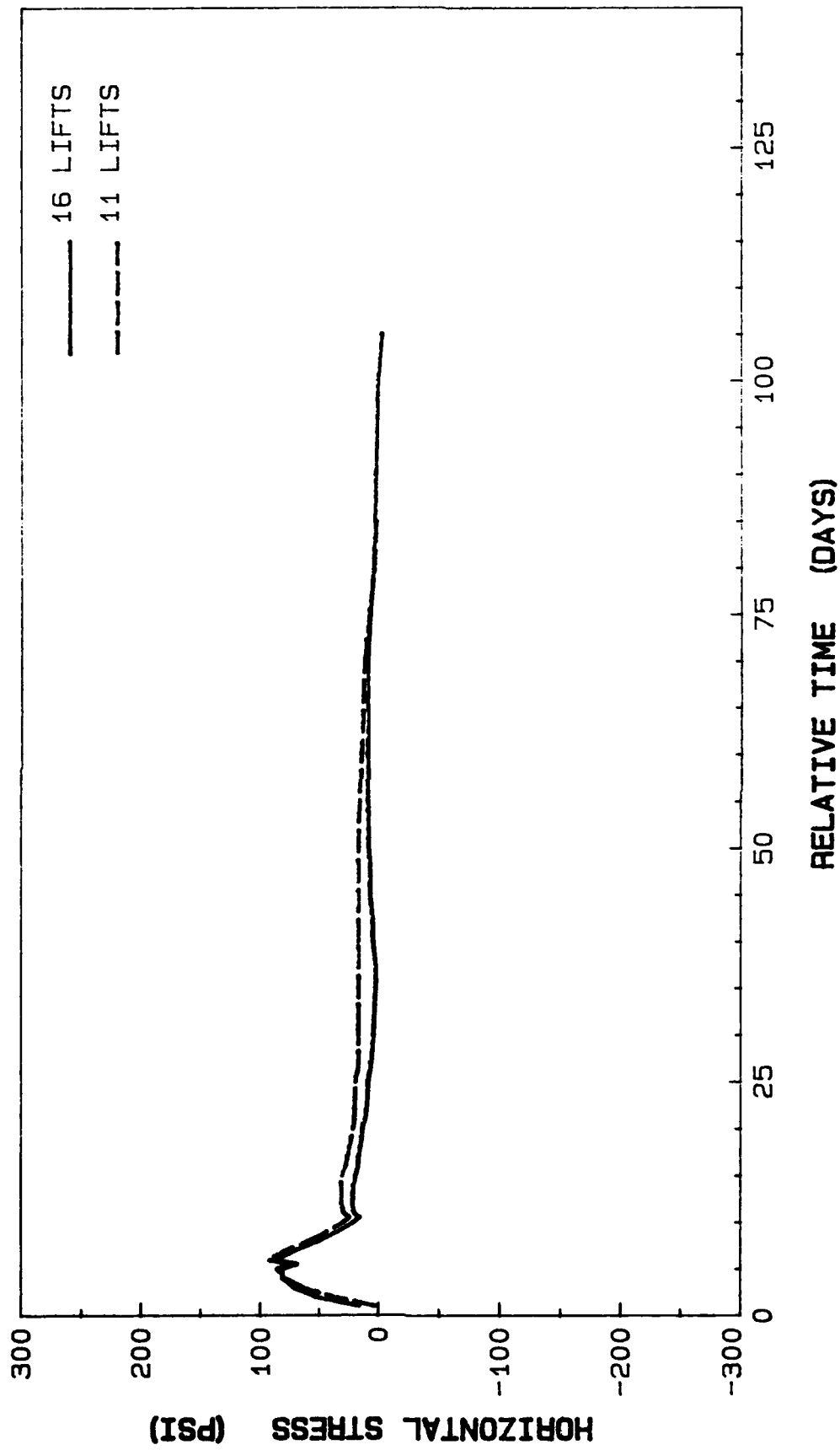


Figure 260. Horizontal stress history at element 619, integration point 3

ELEM. 649 INT. PT. 4 - UA, UC, US

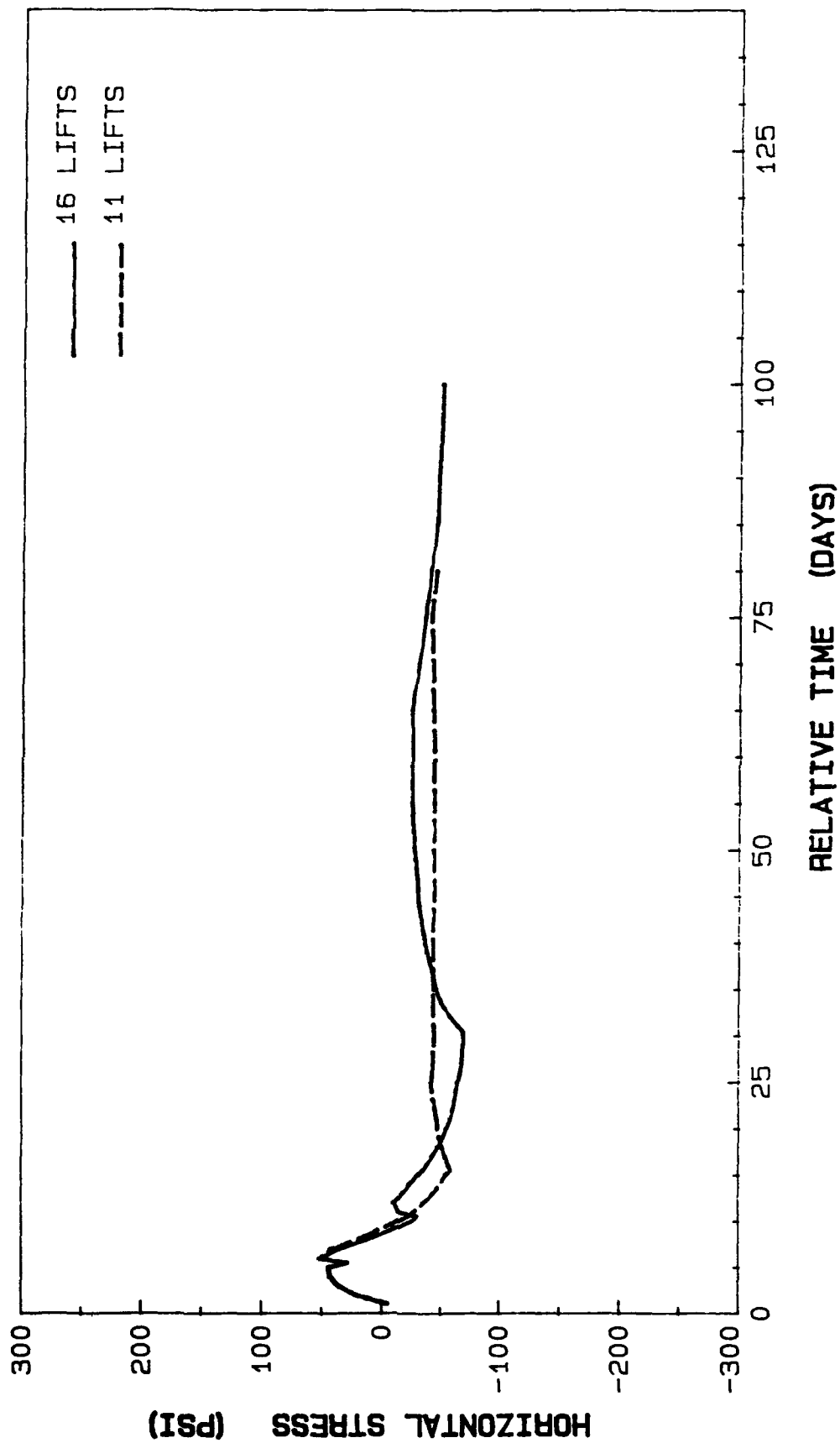


Figure 261. Horizontal stress history at element 649, integration point 4

ELEM. 668 INT. PT. 2 - UA, UC, US

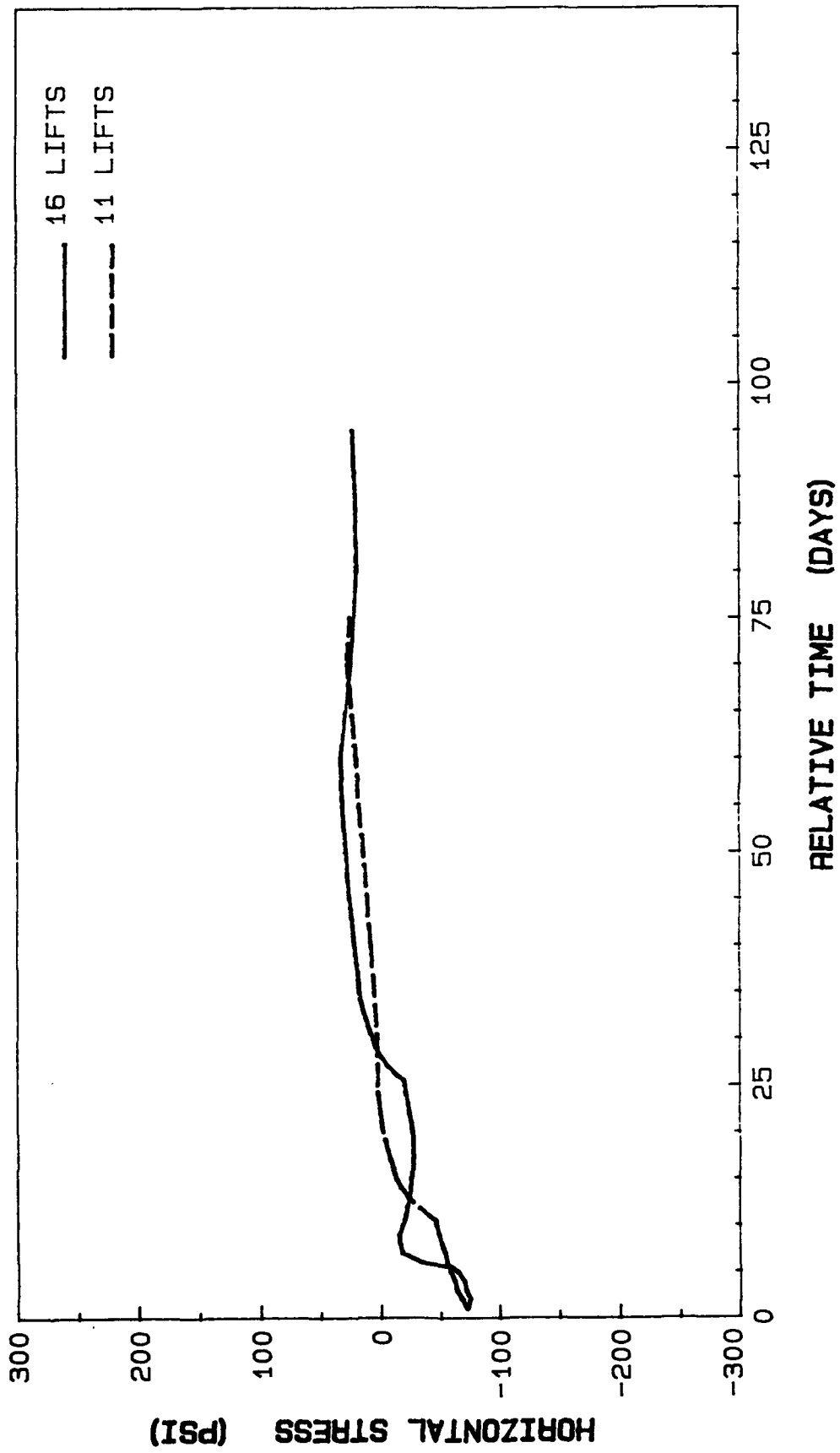


Figure 262. Horizontal stress history at element 668, integration point 2

ELEM. 732 INT. PT. 4 - UA, UC, US

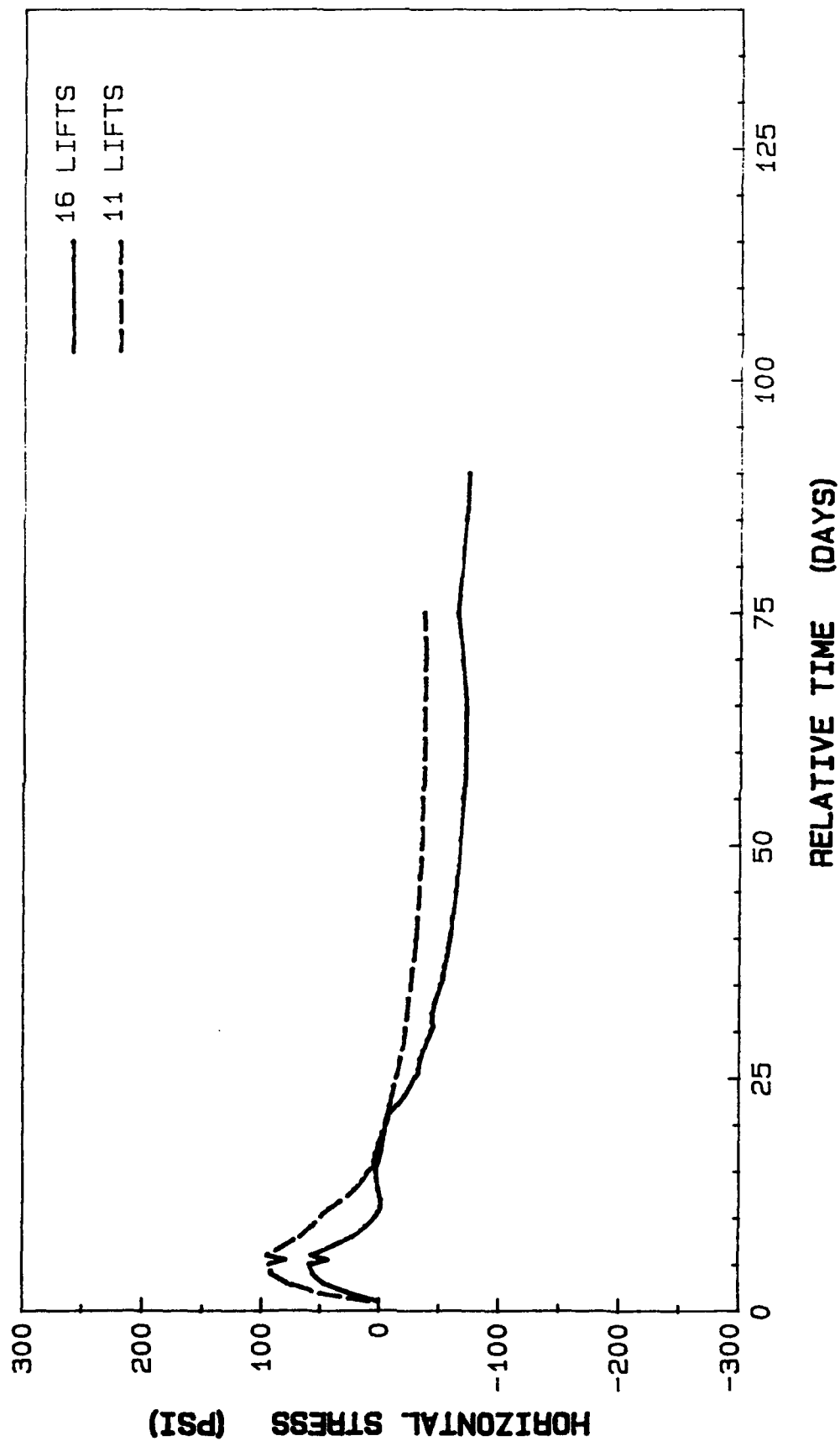


Figure 263. Horizontal stress history at element 732, integration point 4

ELEM. 809 INT. PT. 4 - UA, UC, US

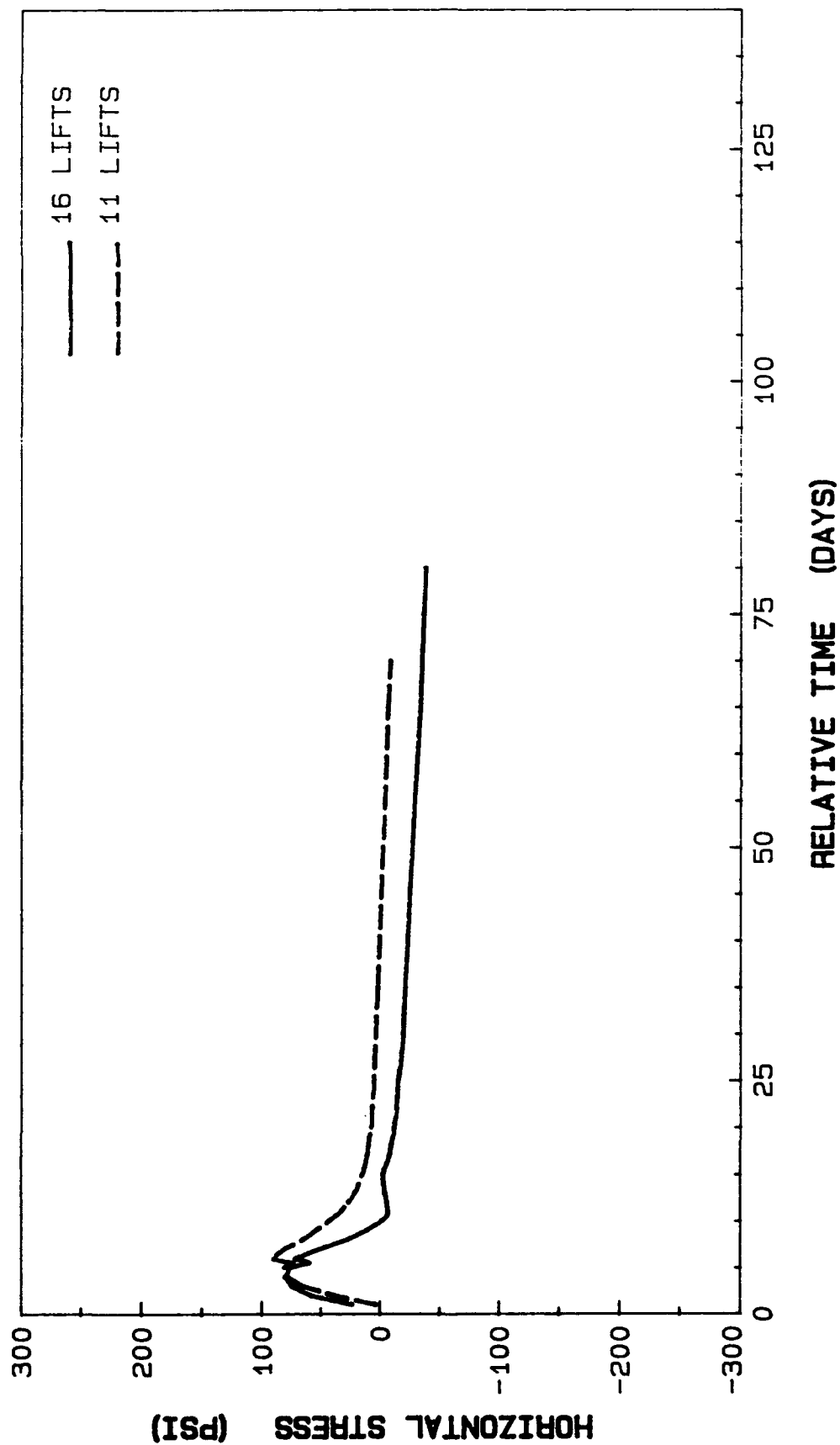


Figure 264. Horizontal stress history at element 809, integration point 4

ELEM. 872 INT. PT. 4 - UA, UC, US

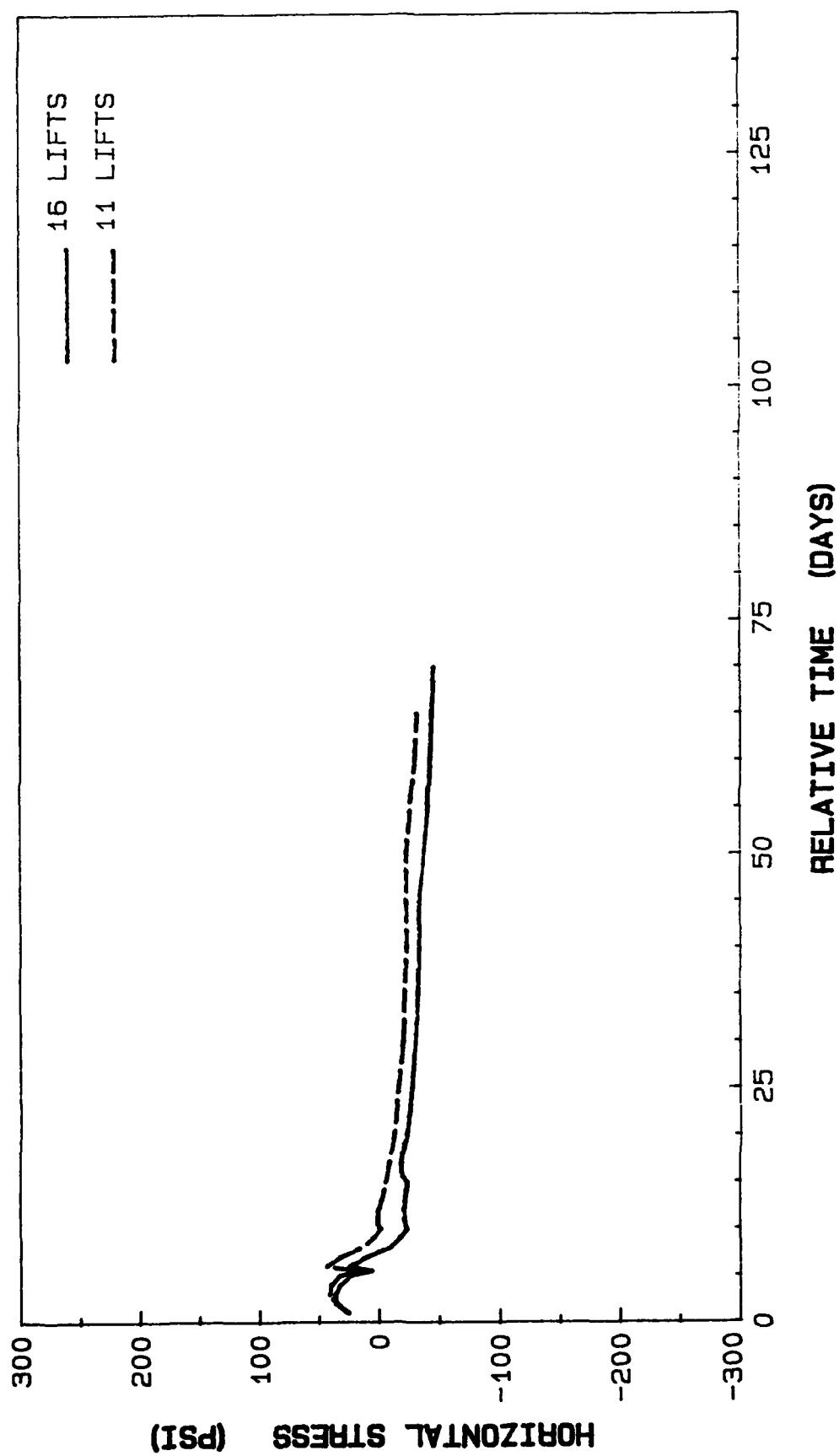


Figure 265. Horizontal stress history at element 872, integration point 4

ELEM. 882 INT. PT. 4 - UA, UC, US

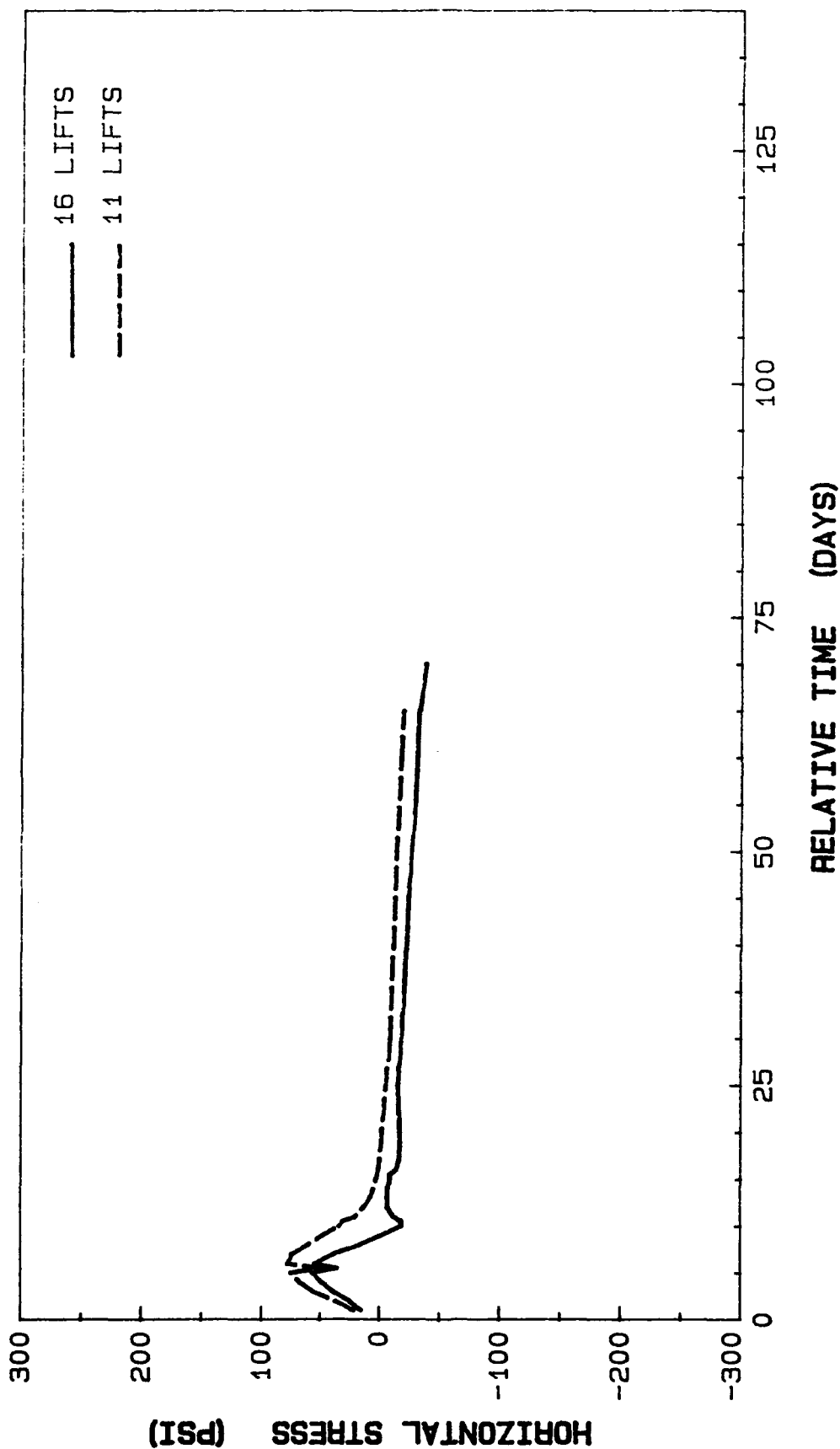


Figure 266. Horizontal stress history at element 882, integration point 4

171. Figure 267 shows the elements for which the horizontal stress histories for embedded nodes are plotted. The results for the lower creep lower shrinkage load case show a small difference in the horizontal stresses. Figures 268-275 present some of the results. Each figure contains three curves. One is for the 11-lift and the other two are for the 16-lift. The locations are picked in order to compare the stress history at the middle of the thick lift (11 lift node) to the middle of the two thin lifts (16 lift) which form the thick lift. In all of the compared cases, the difference is considered to be within the computational tolerance of 10 lb. The 11- and 16-lift schedules have little or no effect in the interior portions of the lifts.

172. Figure 276 shows the elements for which the vertical stress histories are plotted in Figures 277-295. The difference in tensile stresses is significant for the elements 558, 565, 660, 661, 736, 812, and 945. These high tensile stresses are caused by the thermal and mechanical effects. Once the vertical members are placed, the thermal effects which are typical of a free slab produce tension on the surface and compression in the center. These effects can be reduced or magnified due to bending and displacement as well. The large tensile stresses at element 558 which is located just above the right corner are due primarily to thermal effects while element 565 has high tension because of the bending of the whole wall section. Elements 945, 736, and 812 which are located next to the chamber wall have high tension at later times due to the body as well. The left side of the wall section undergoes higher downward displacement making the whole section bend towards the outside. None of the tensile stresses surpass 185 psi which is low enough to be of little concern.

ELEM. 901 INT. PT. 2 - UA, UC, US

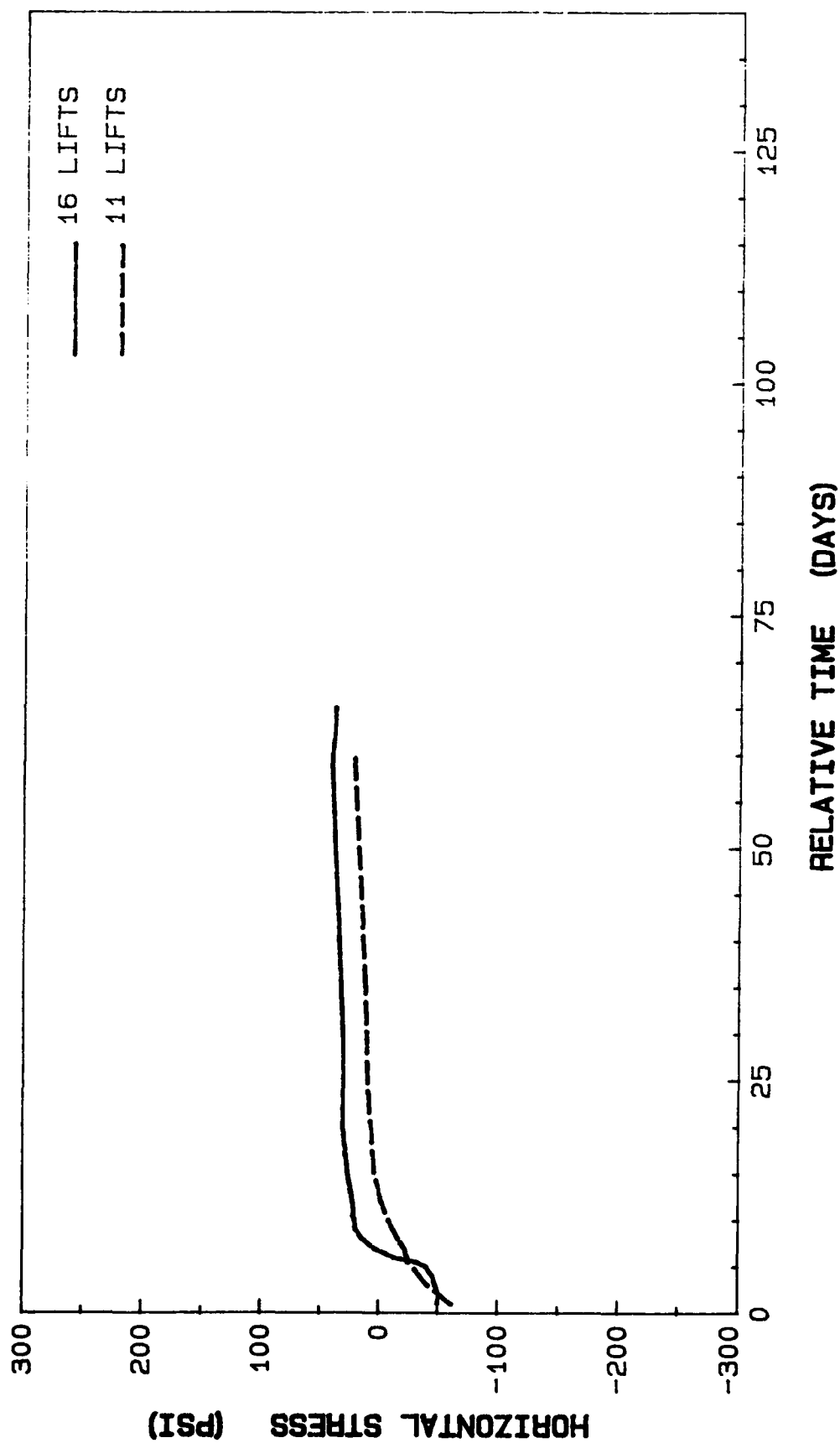


Figure 267. Horizontal stress history at element 901, integration point 2

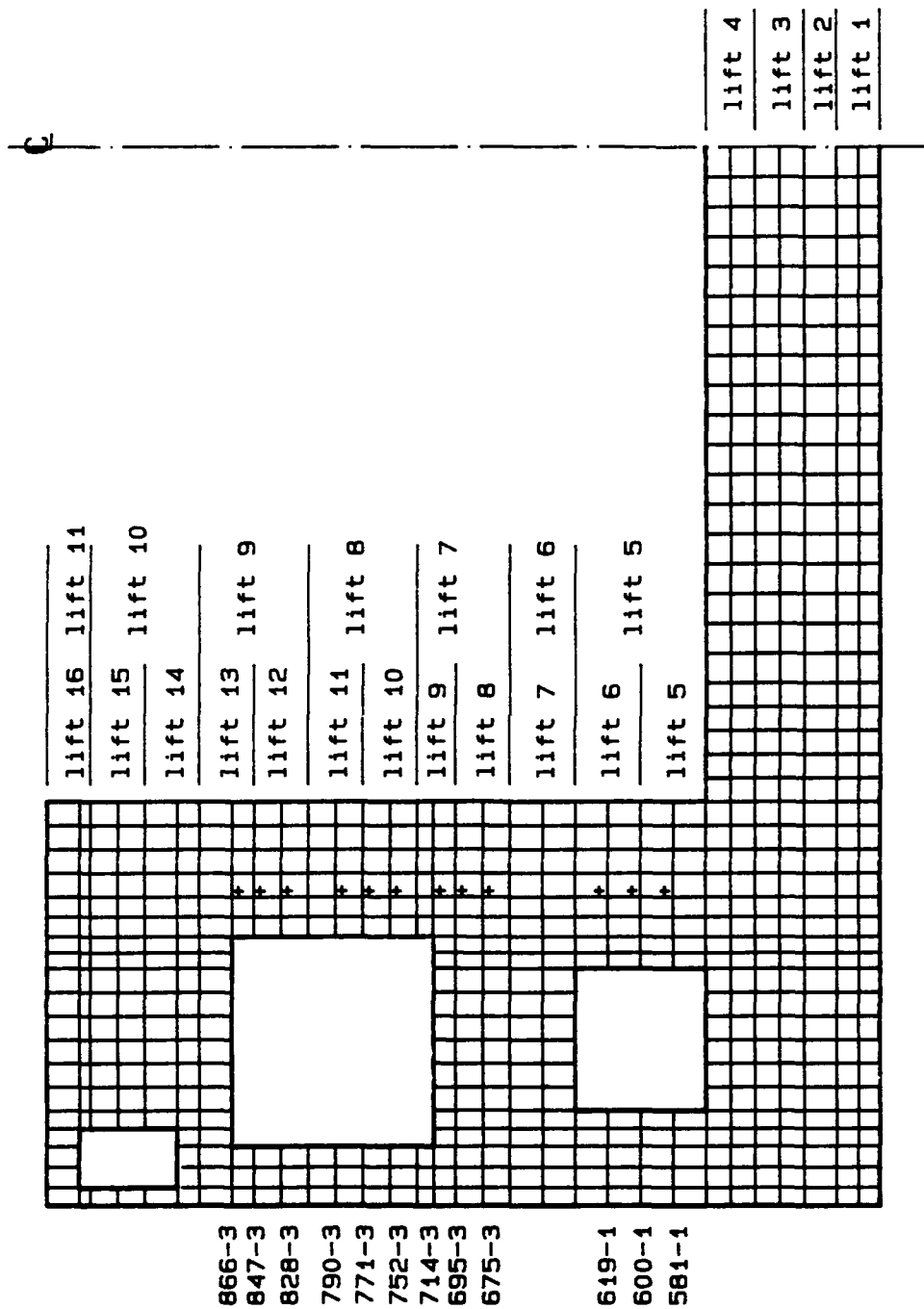


Figure 268. Selected elements for mid-lift horizontal stress comparison

# UA, LC, LS

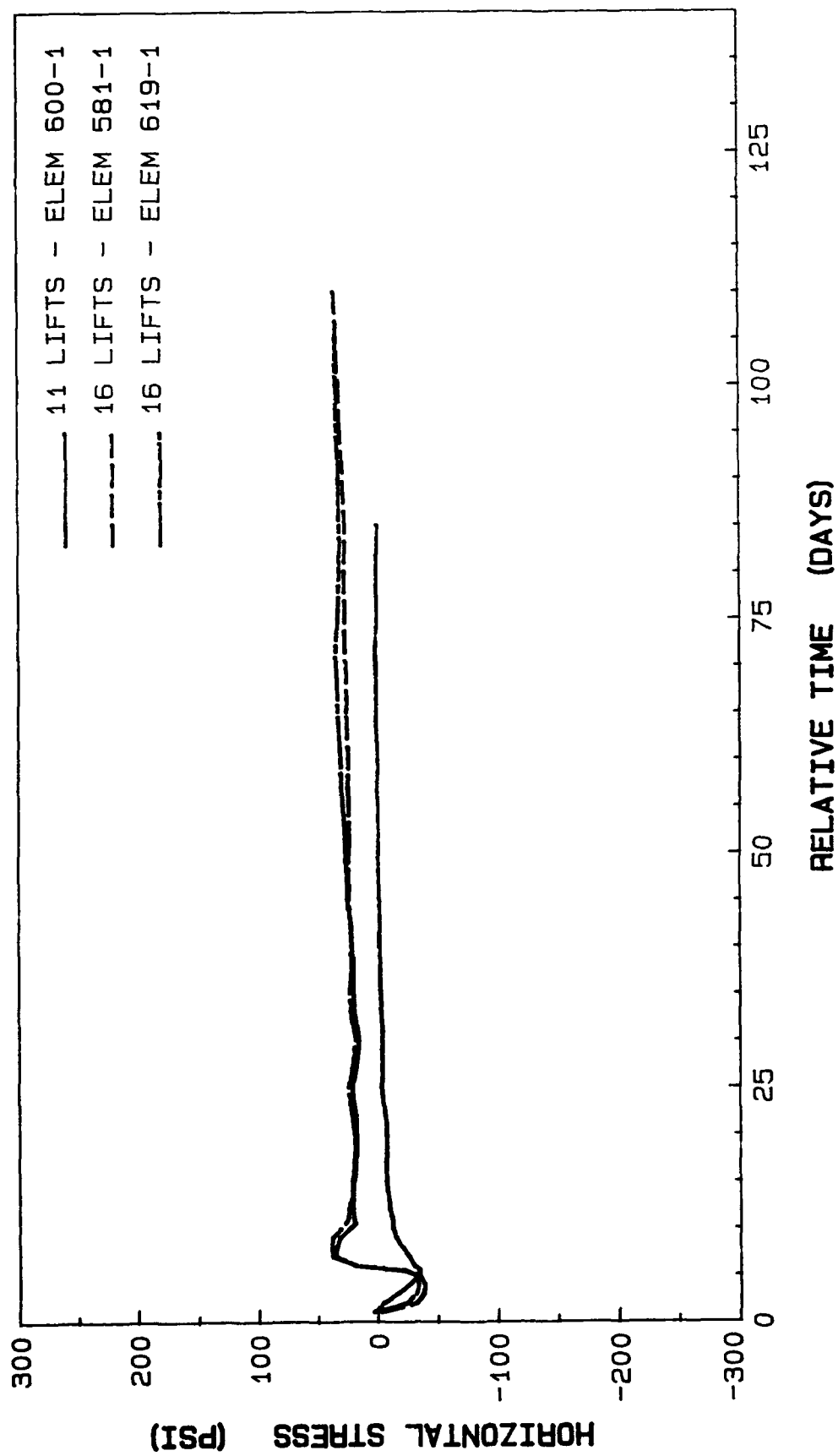


Figure 269. Horizontal stress comparison at mid-lifts in culvert wall (UA, LC, LS)

# UA, LC, LS

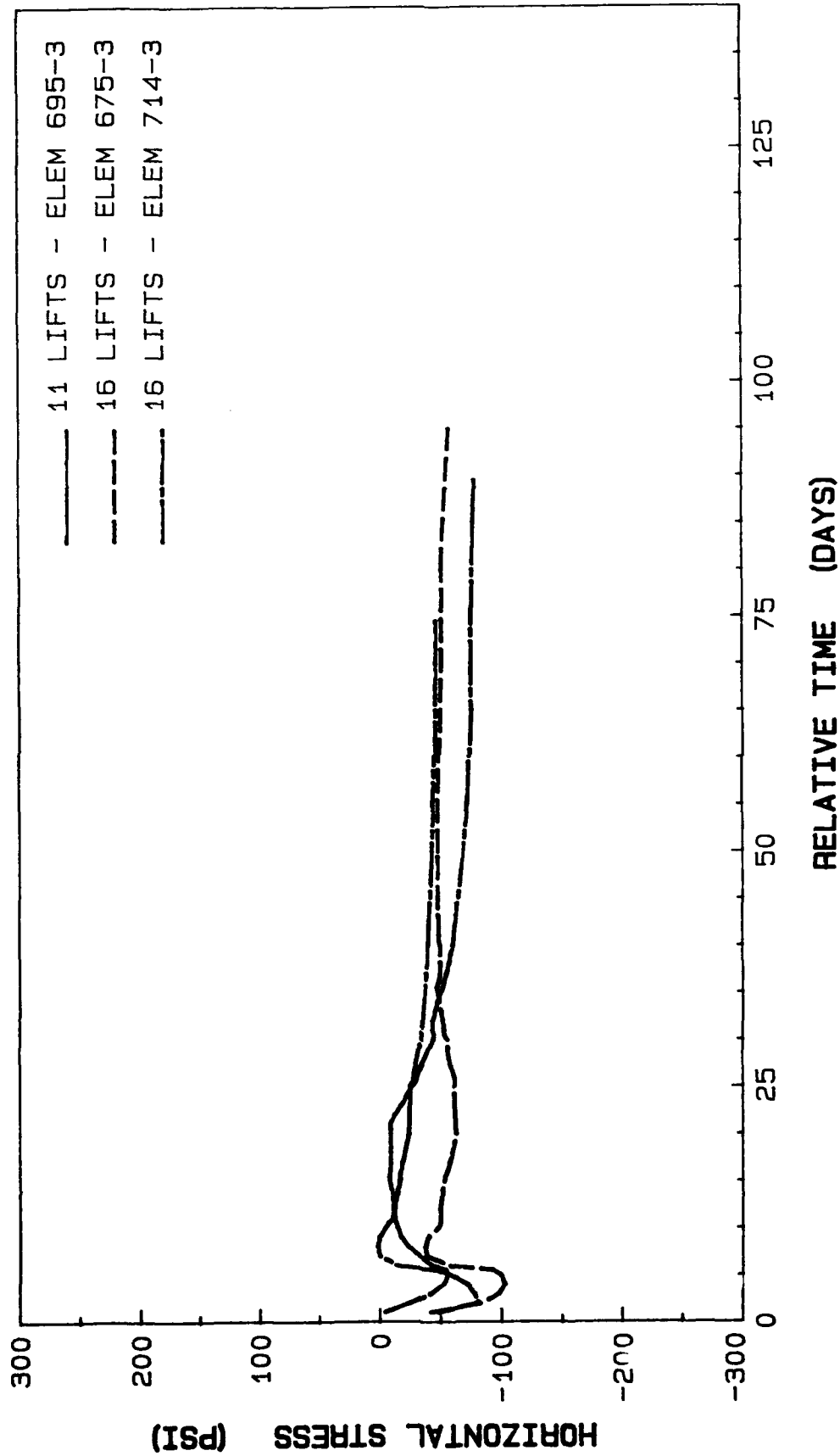


Figure 270. Horizontal stress comparison at mid-lifts below machinery room (UA, LC, LS)

# UA, LC, LS

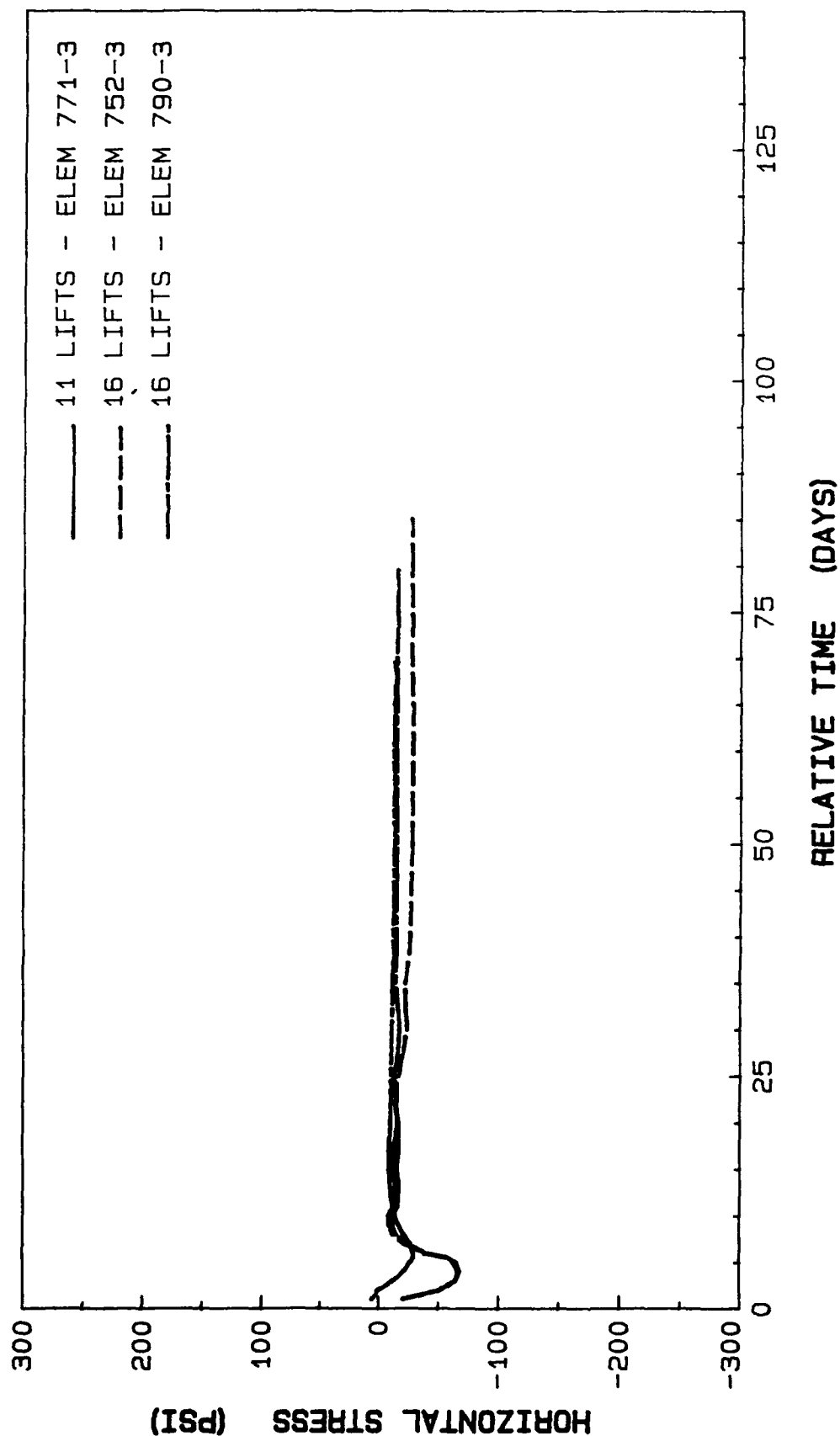


Figure 271. Horizontal stress comparison at mid-lifts at bottom of outside machinery room wall (UA, LC, LS)

# UA, LC, LS

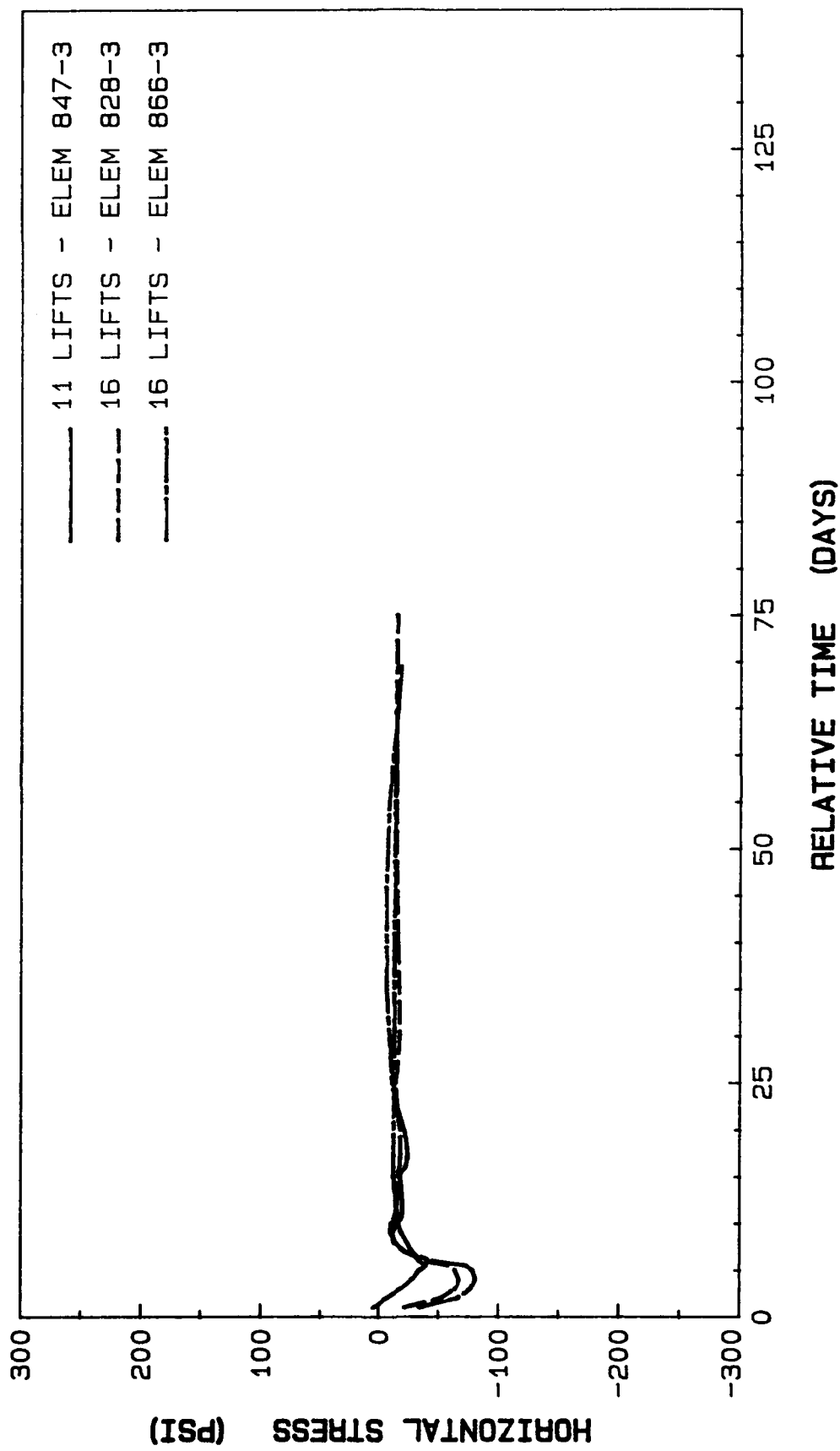


Figure 272. Horizontal stress comparison at mid-lifts at top of outside machinery room wall (UA, LC, LS)

UA, UC, US

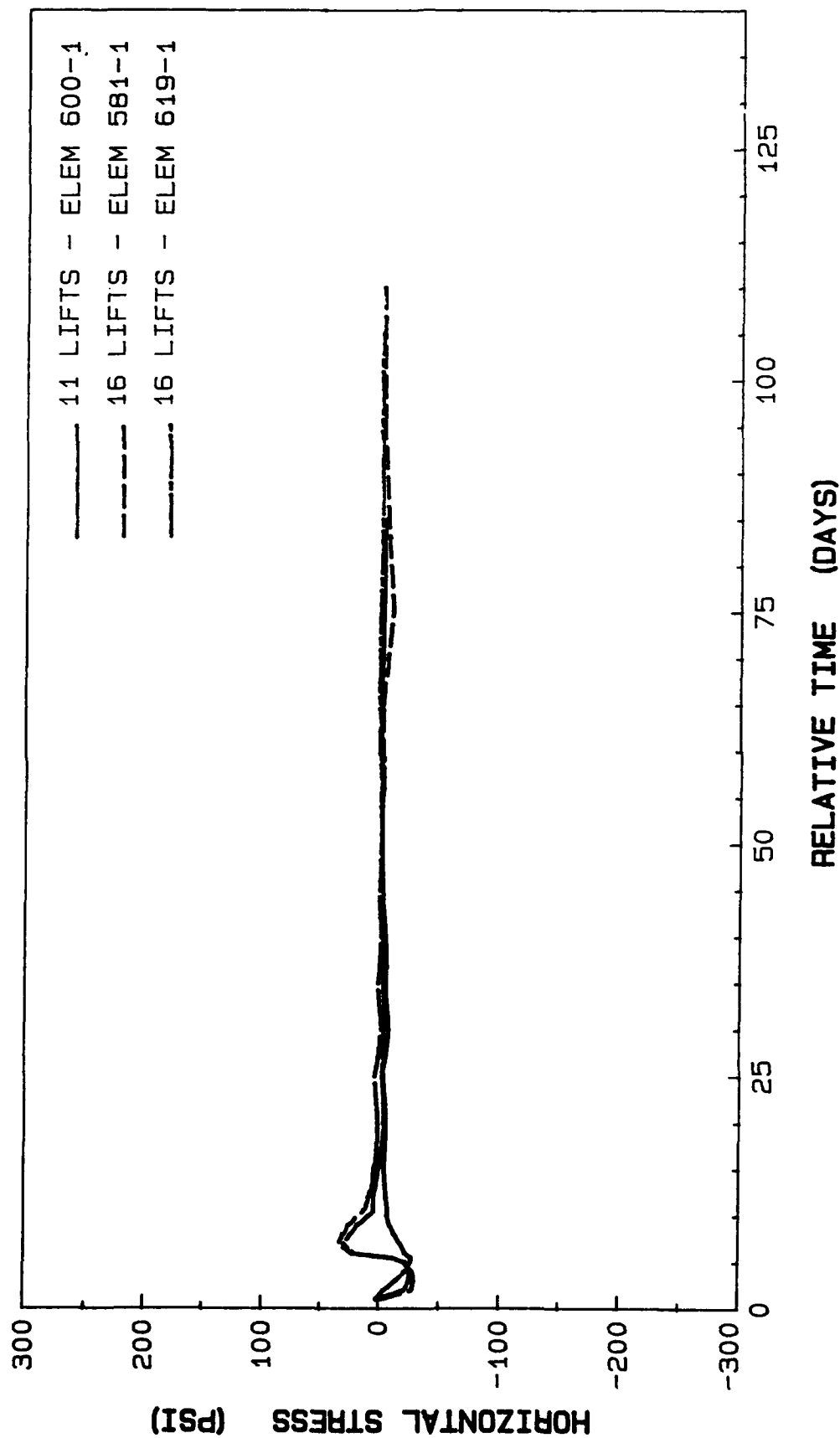


Figure 273. Horizontal stress comparison at mid-lifts in culvert wall (UA, UC, US)

# UA, UC, US

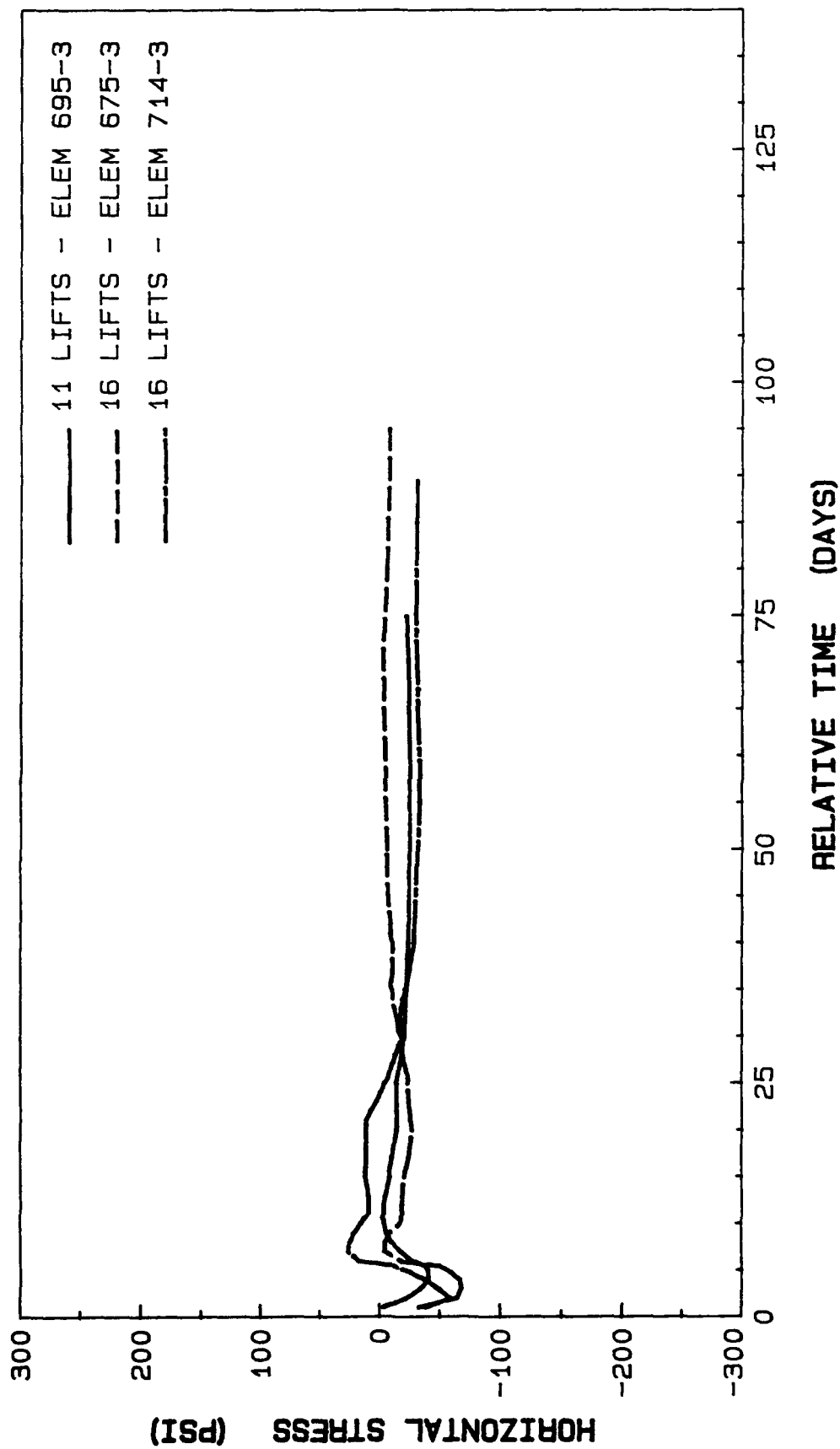


Figure 274. Horizontal stress comparison at mid-lifts below machinery room (UA, UC, US)

UA, UC, US

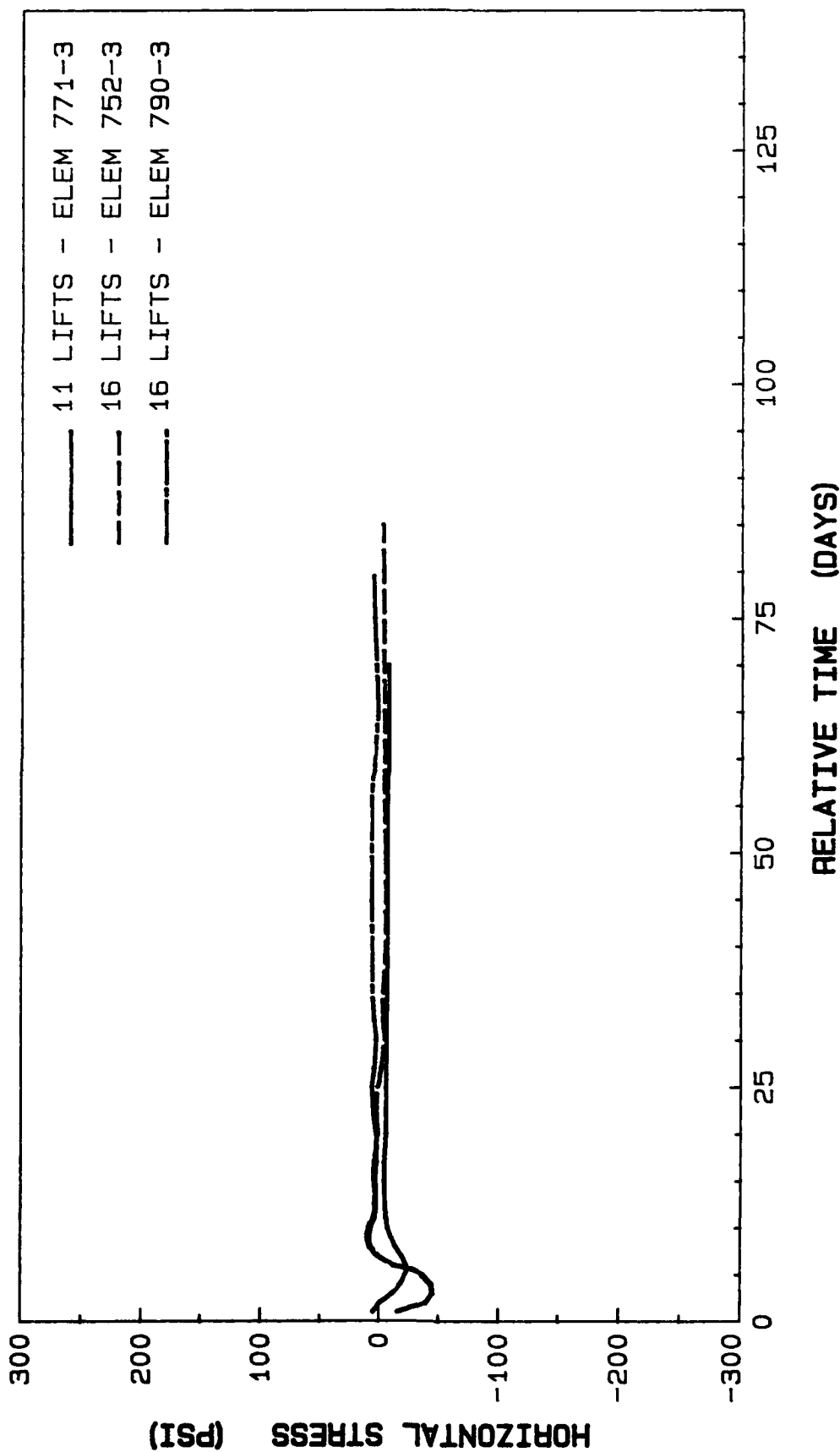


Figure 275. Horizontal stress comparison at mid-lifts at bottom of outside machinery room wall (UA, UC, US)

UA, UC, US

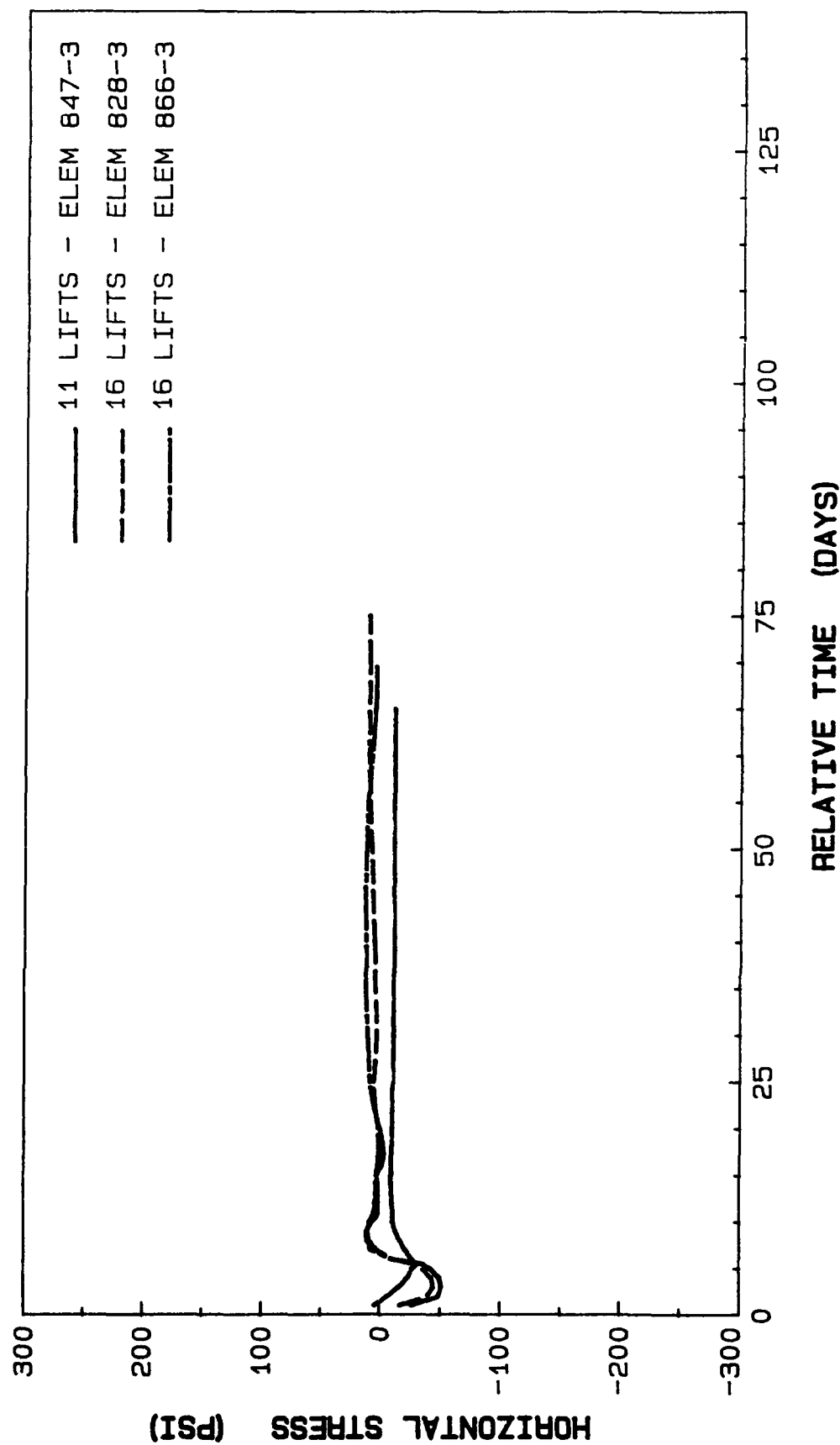


Figure 276. Horizontal stress comparison at mid-lifts at top of outside machinery room wall (UA, UC, US)

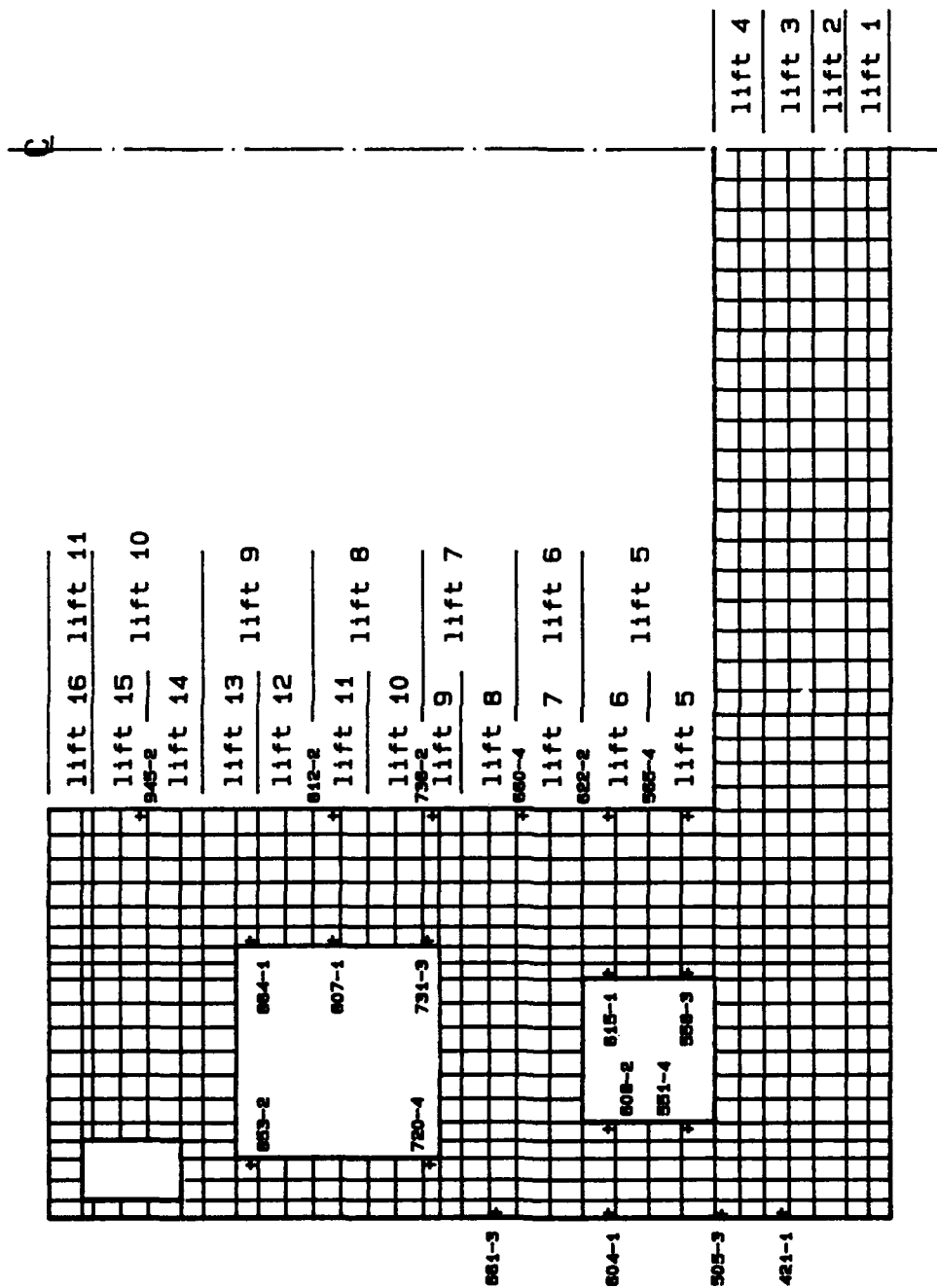


Figure 277. Selected elements for vertical stress comparisons

ELEM. 421 INT. PT. 1 - UA, LC, LS

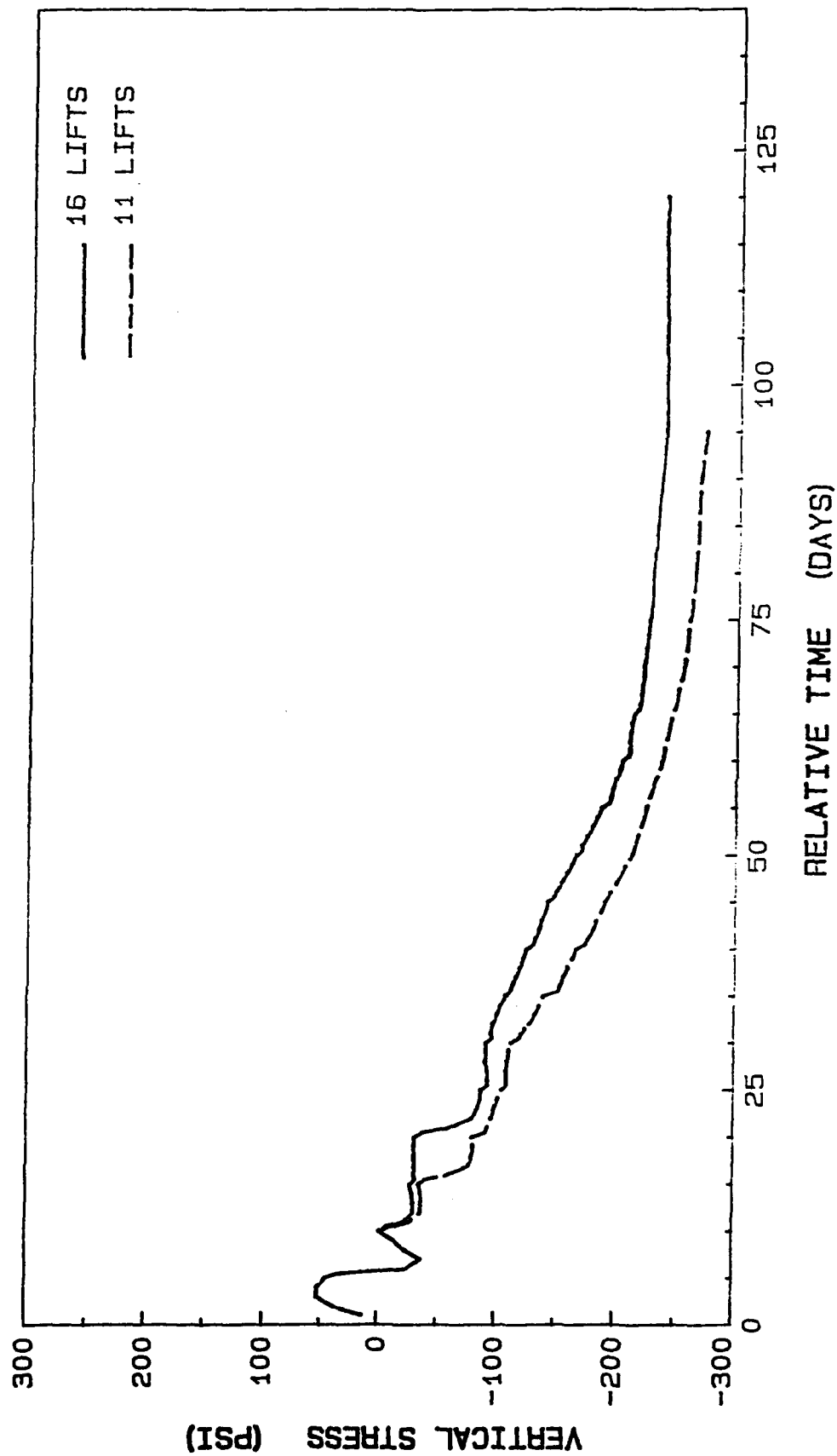


Figure 278. Vertical stress history at element 421, integration point 1

ELEM. 505 INT. PT. 3 - UA, LC, LS

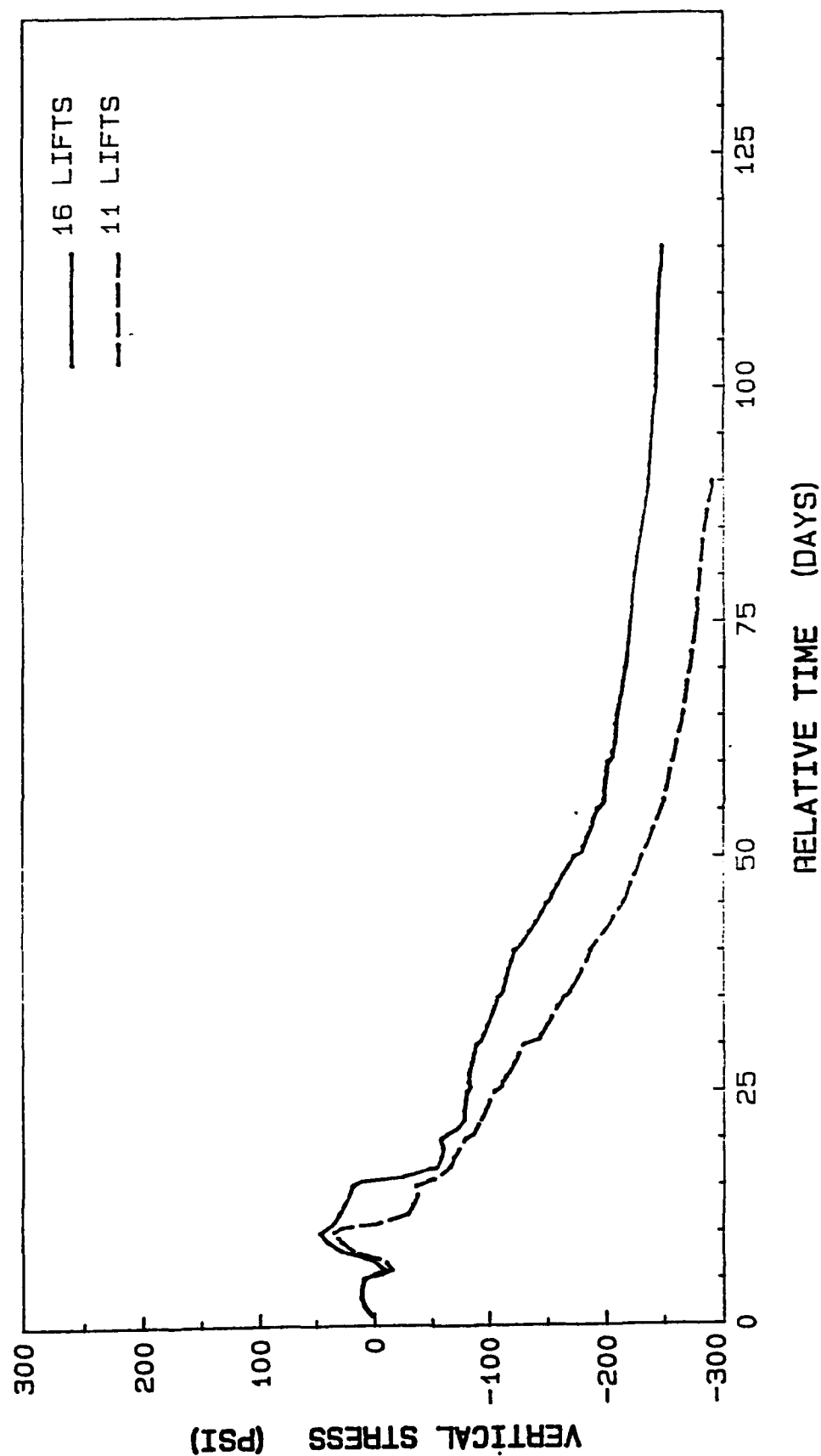


Figure 279. Vertical stress history at element 505, integration point 3

ELEM. 551 INT. PT. 4 - UA, LC, LS

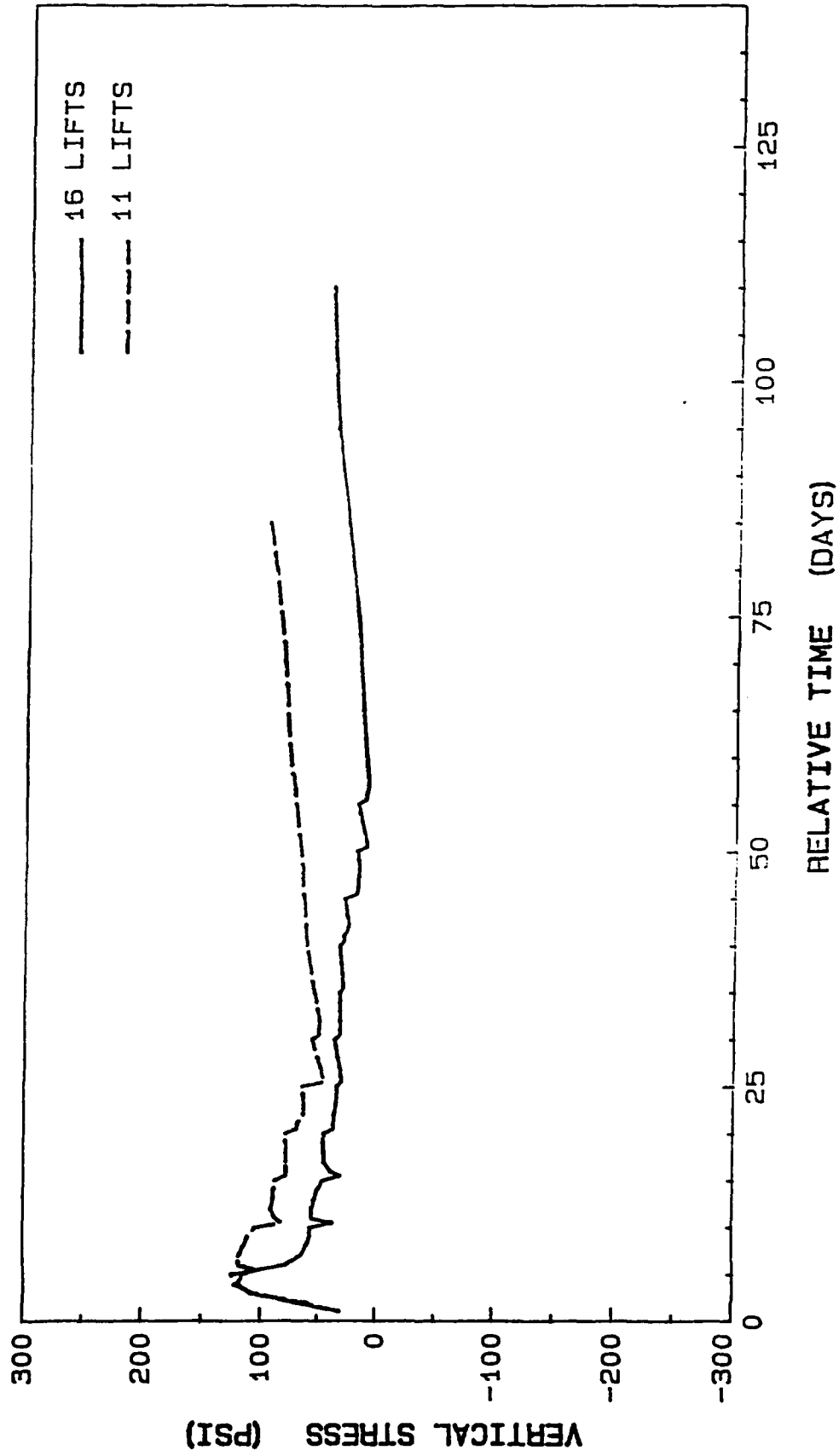


Figure 280. Vertical stress history at element 551, integration point 4

ELEM. 558 INT. PT. 3 - UA, LC, LS

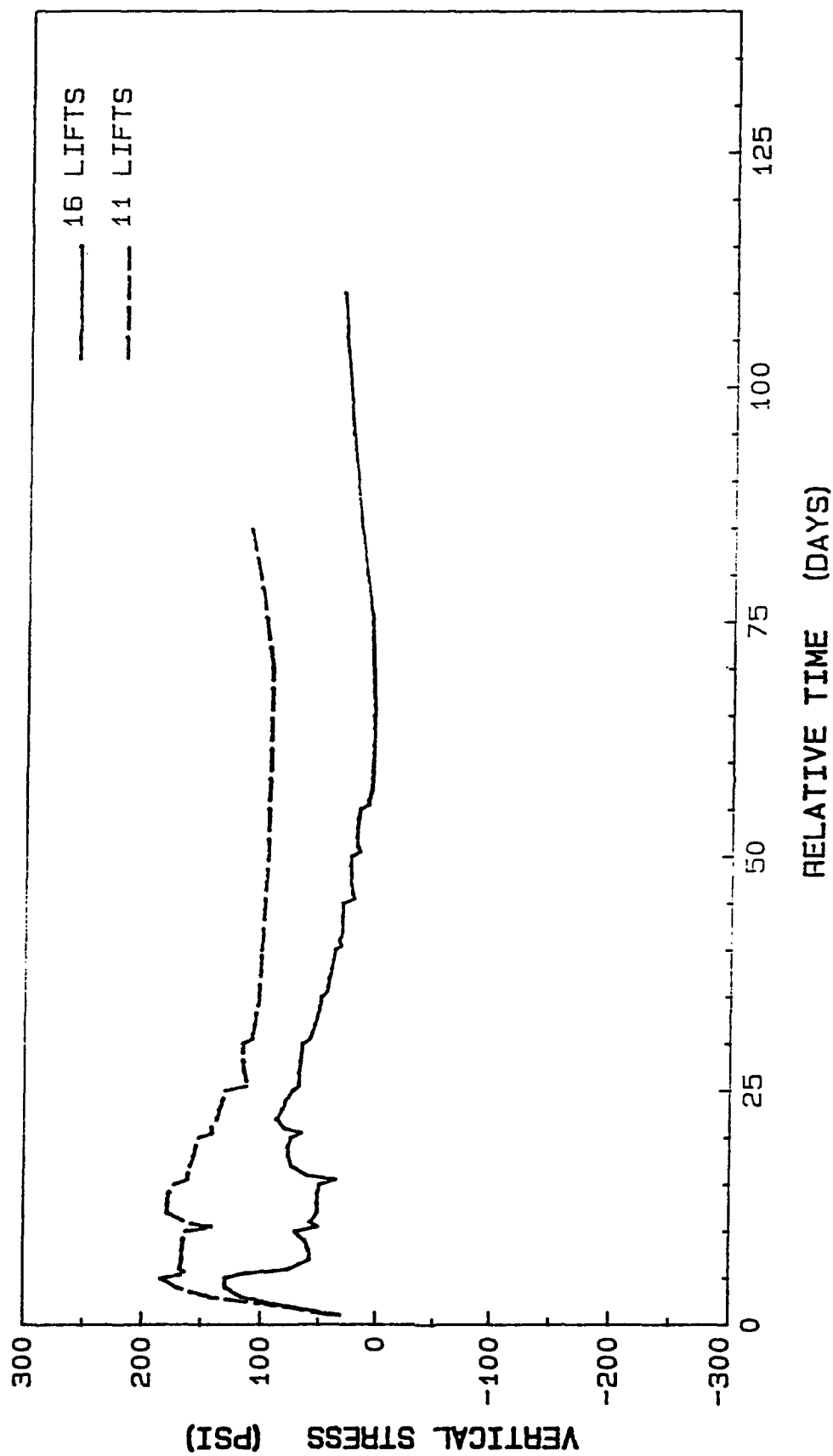


Figure 281. Vertical stress history at element 558, integration point 3

ELEM. 565 INT. PT. 4 - UA, LC, LS

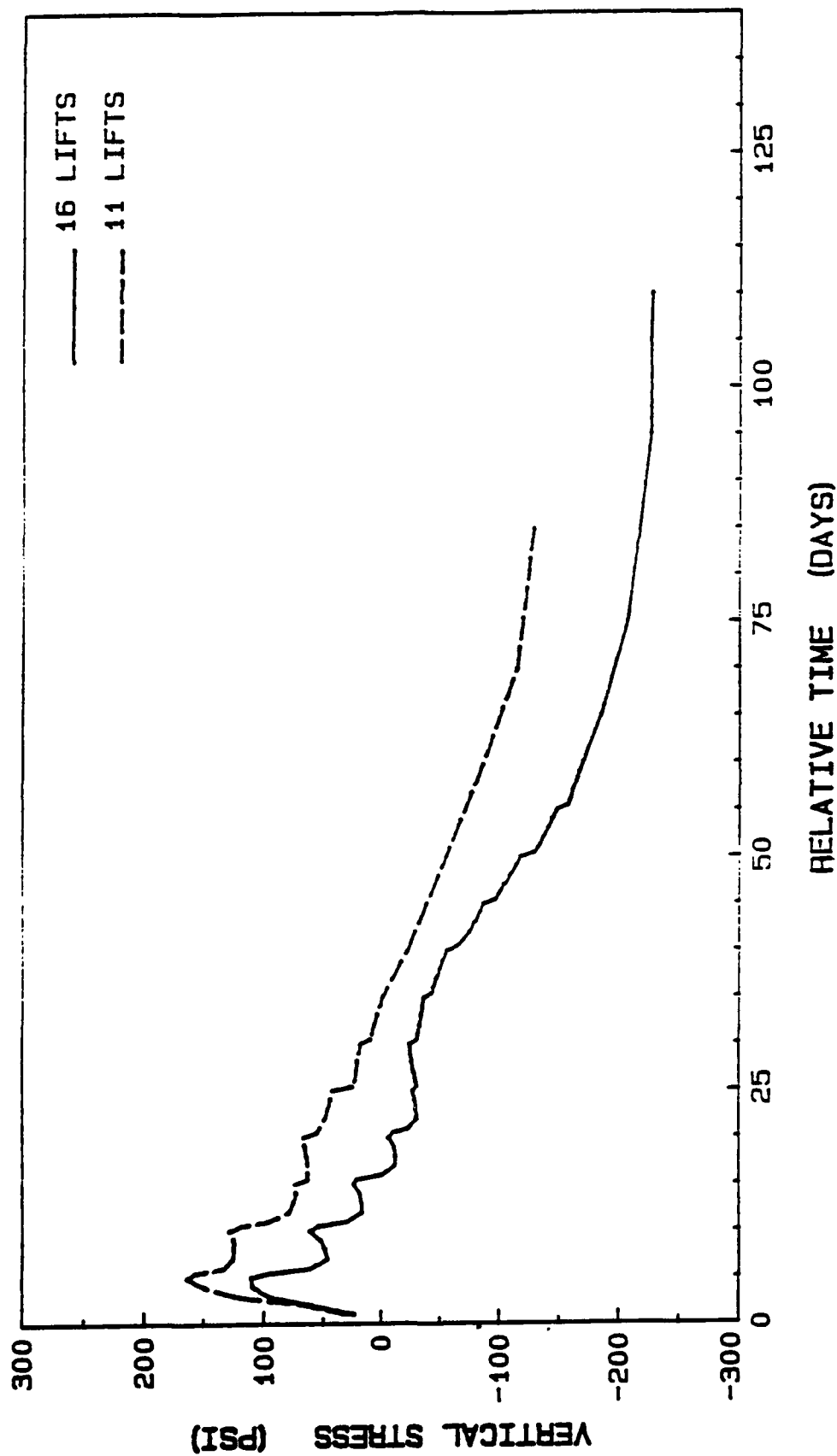


Figure 282. Vertical stress history at element 565, integration point 4

ELEM. 604 INT. PT. 1 - UA, LC, LS

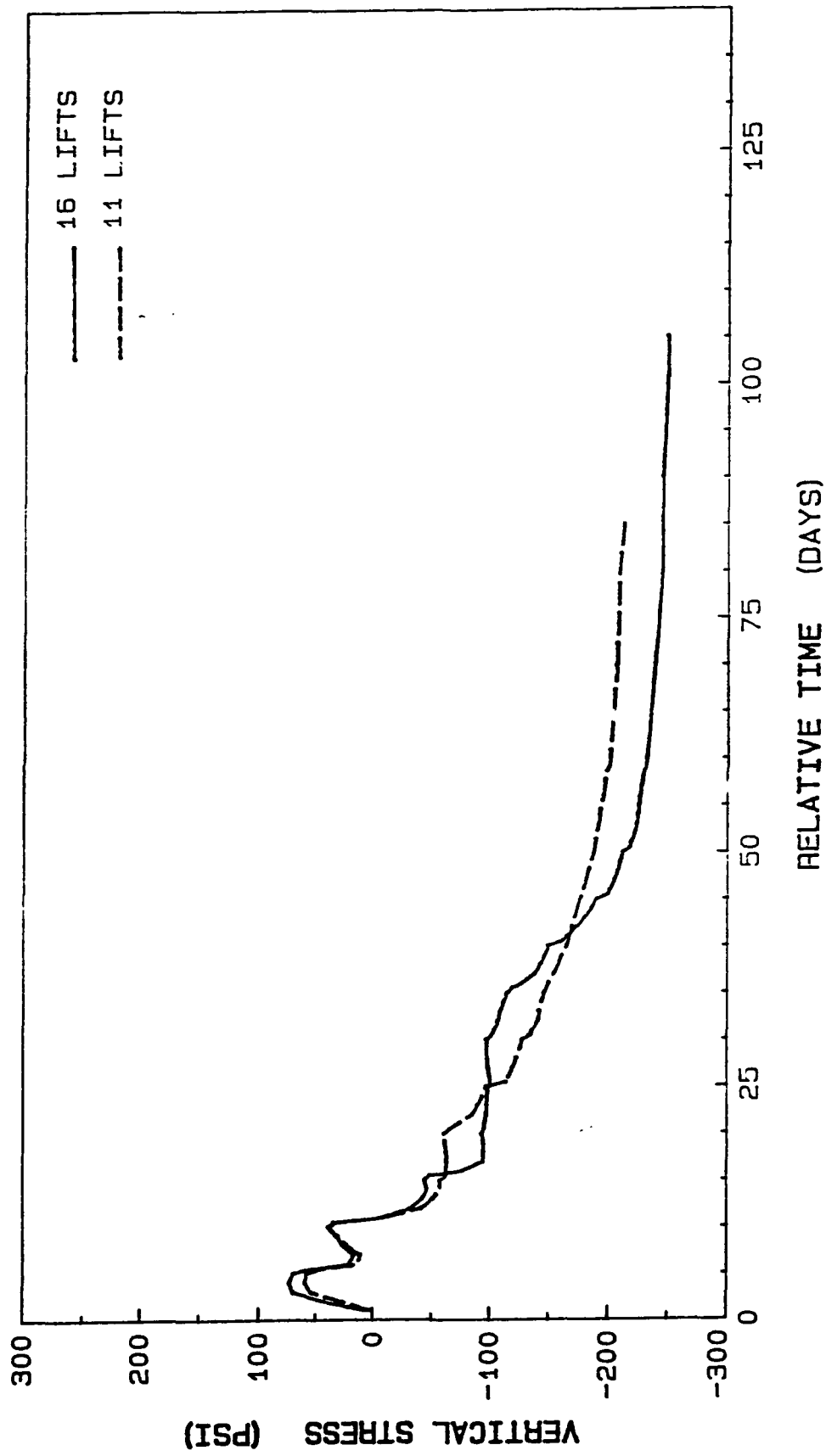


Figure 283. Vertical stress history at element 604, integration point 1

ELEM. 608 INT. PT. 2 - UA, LC, LS

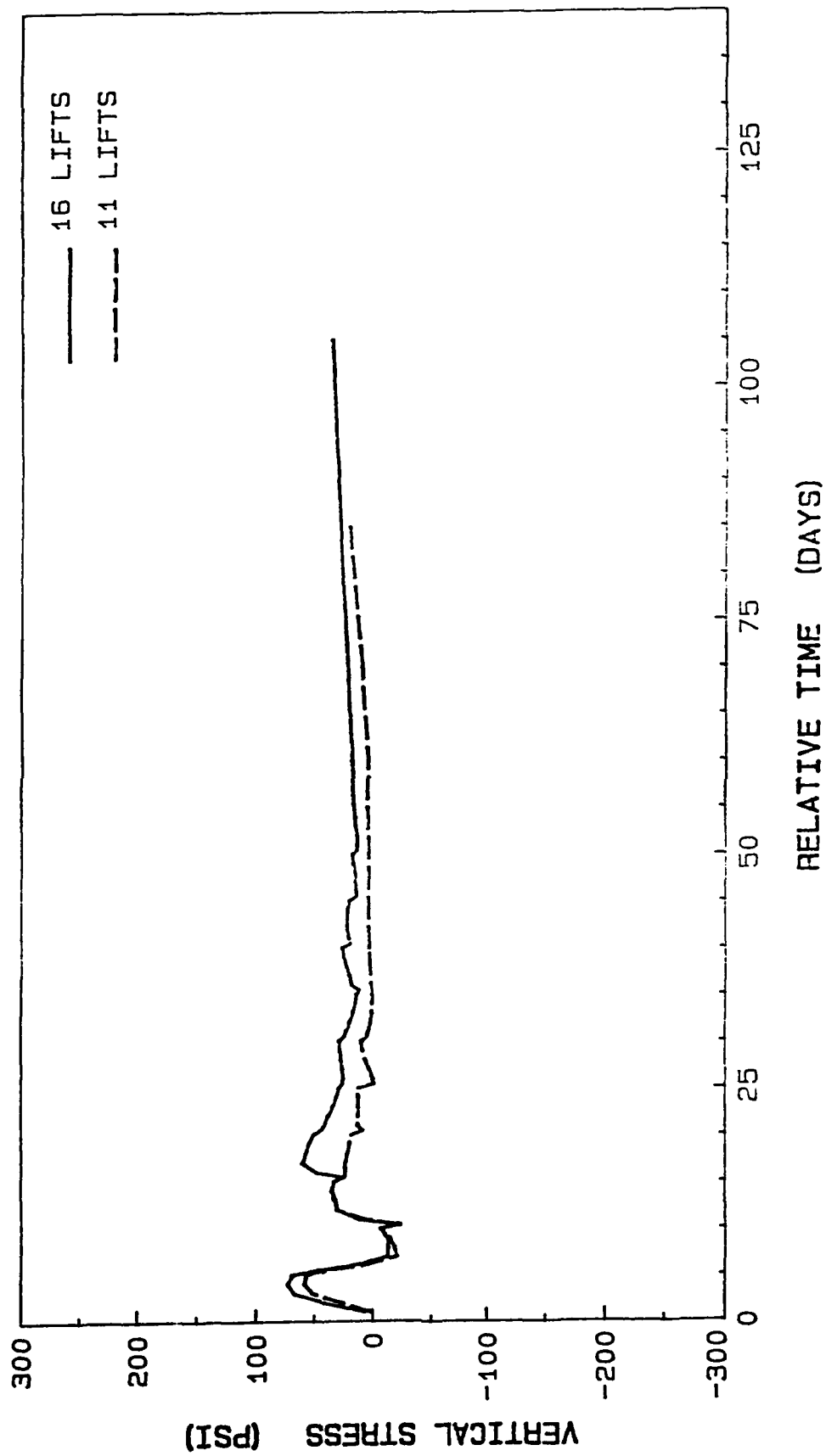


Figure 284. Vertical stress history at element 608, integration point 2

ELEM. 615 INT. PT. 1 - UA, LC, LS

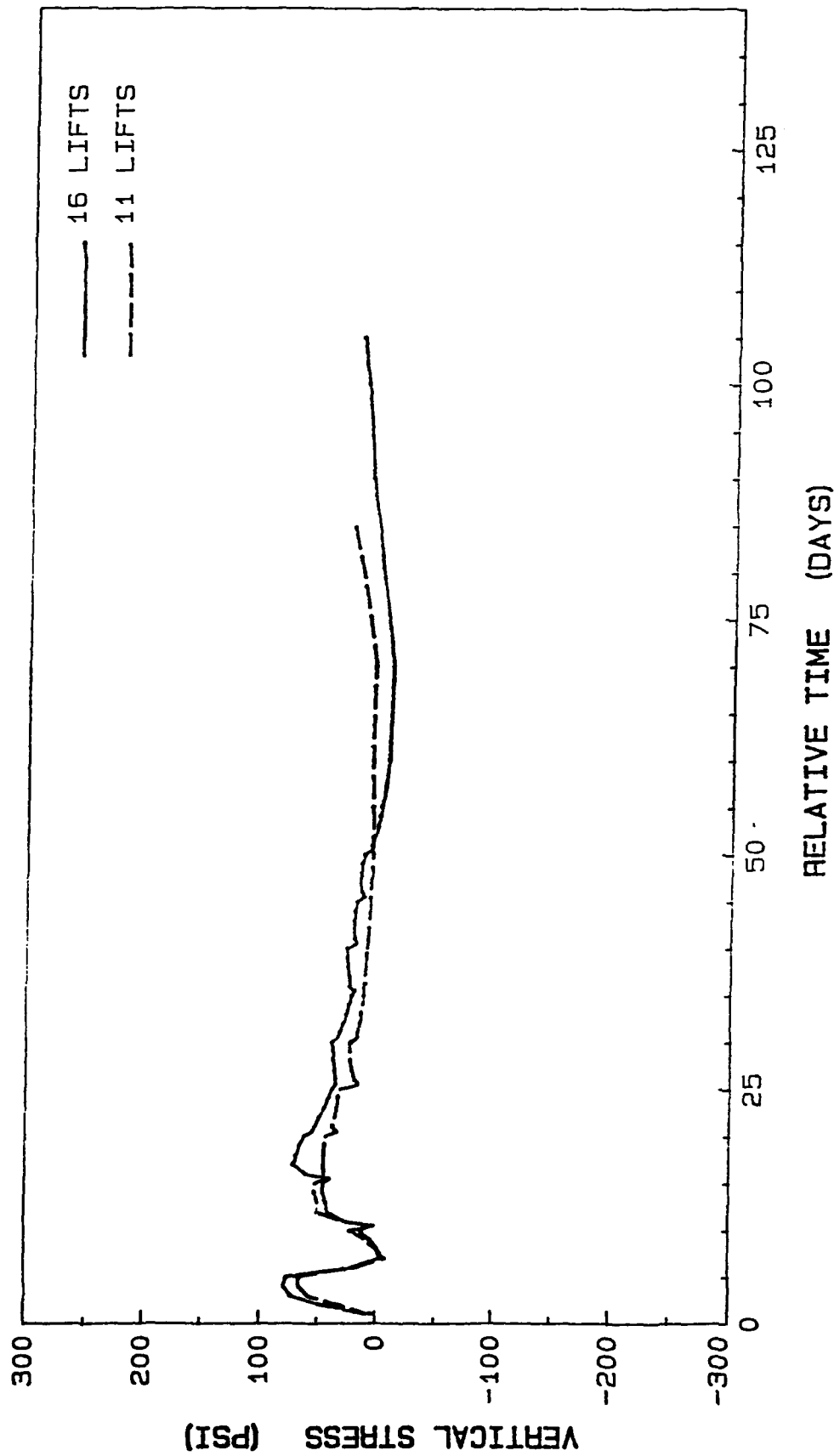


Figure 285. Vertical stress history at element 615, integration point 1

ELEM. 622 INT. PT. 2 - UA, LC, LS

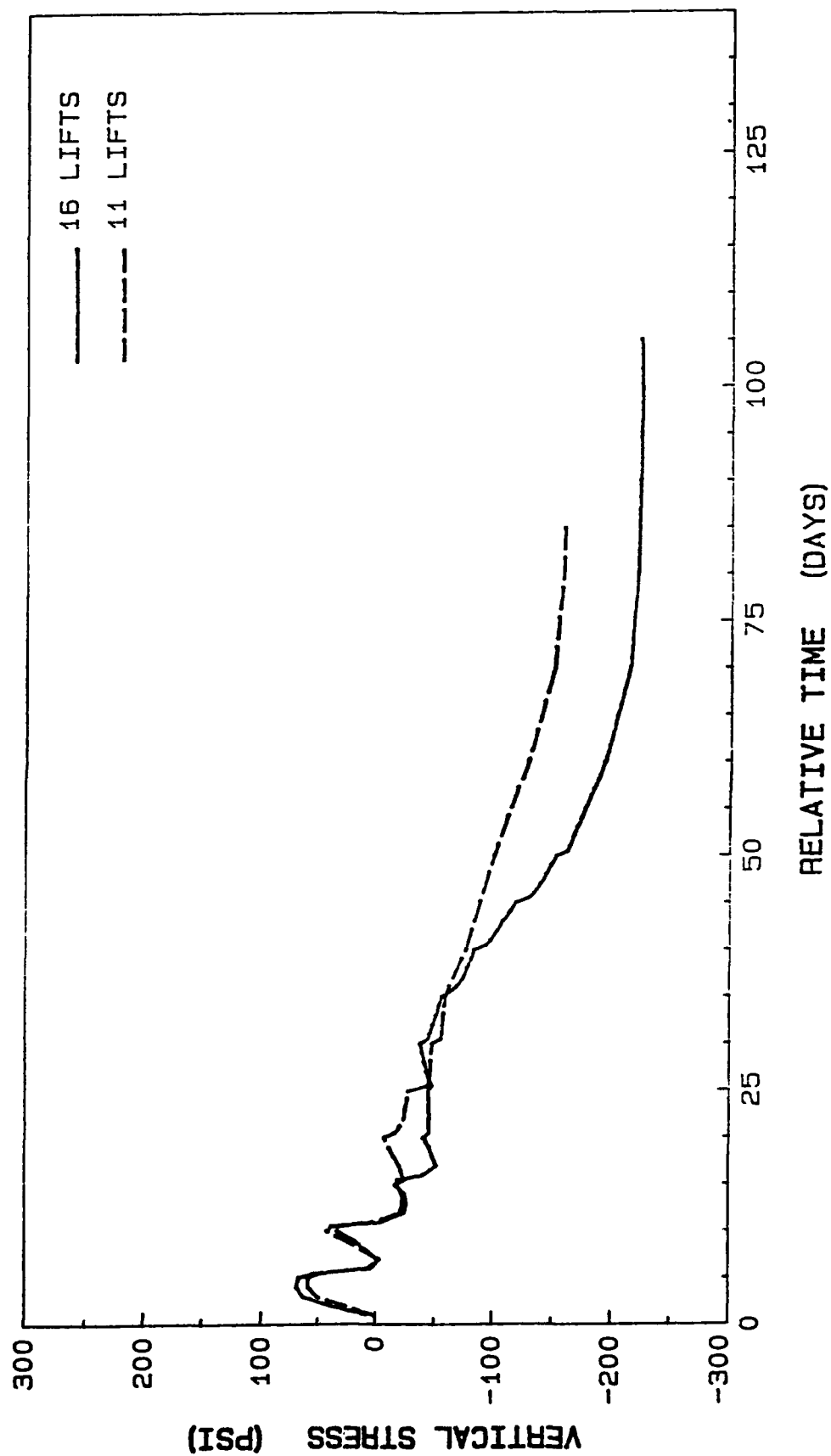


Figure 286. Vertical stress history at element 622, integration point 2

ELEM. 660 INT. PT. 4 - UA, LC, LS

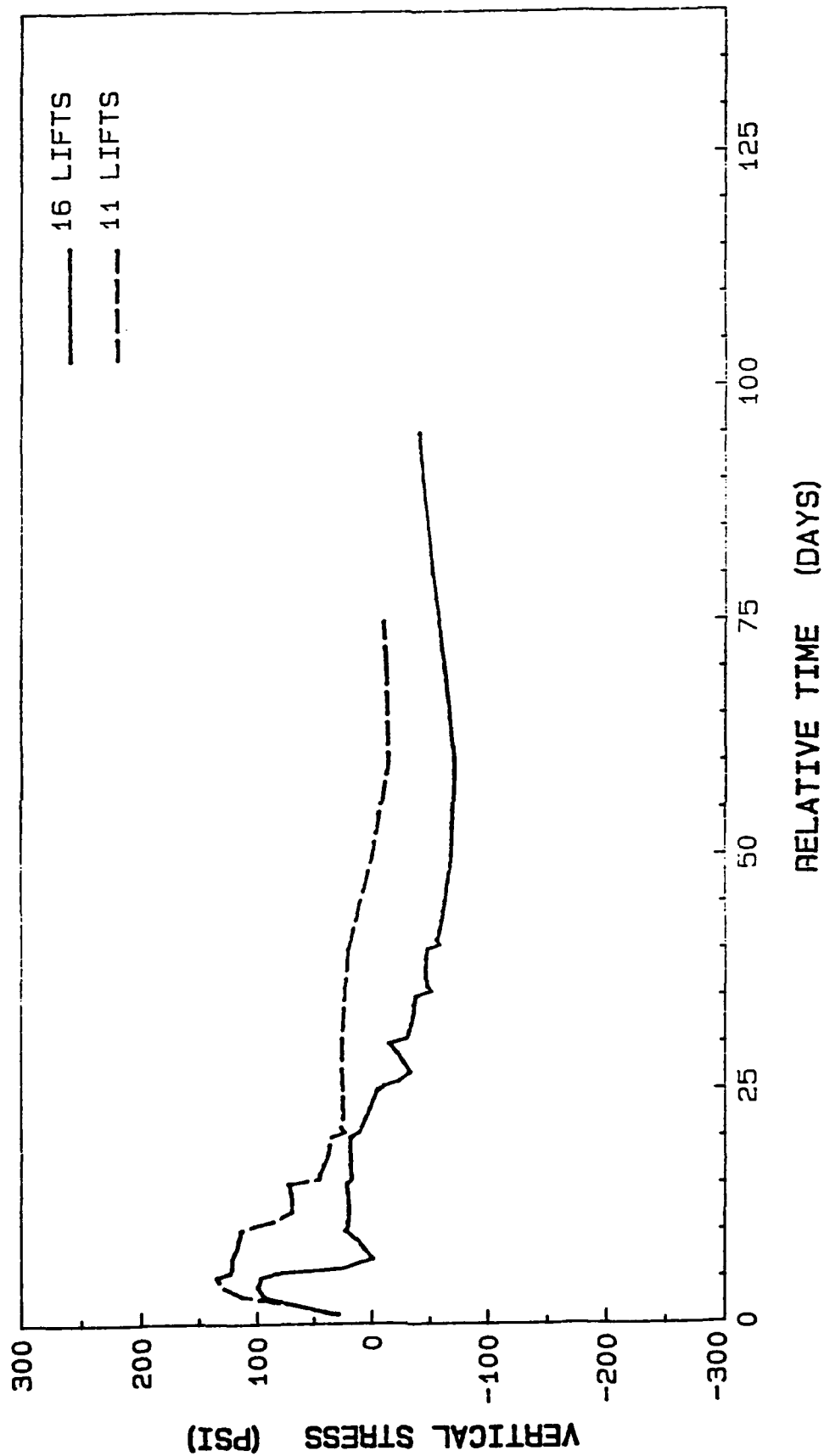


Figure 287. Vertical stress history at element 660, integration point 4

ELEM. 661 INT. PT. 3 - UA, LC, LS

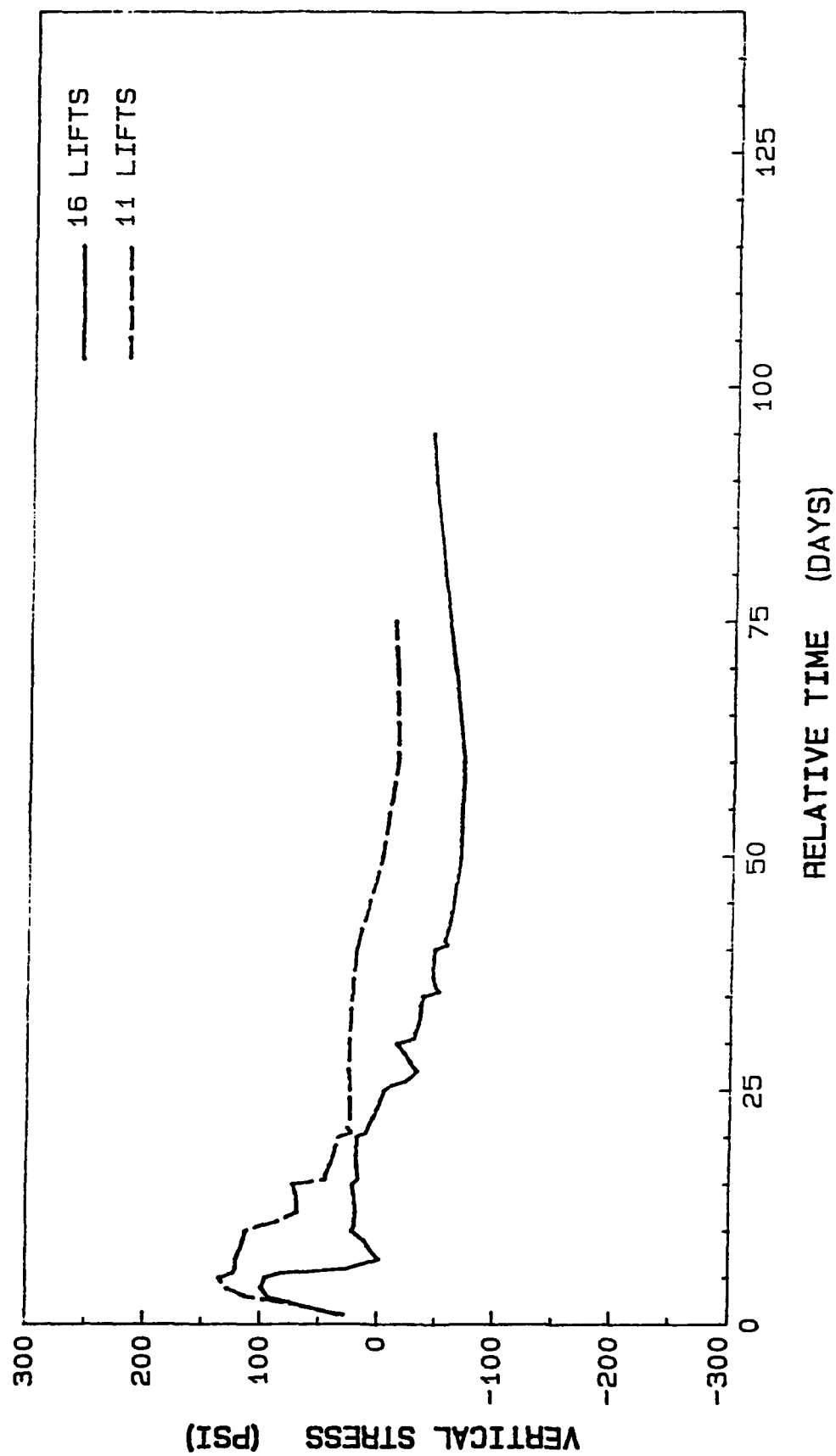


Figure 288. Vertical stress history at element 661, integration point 3

ELEM. 720 INT. PT. 4 - UA, LC, LS

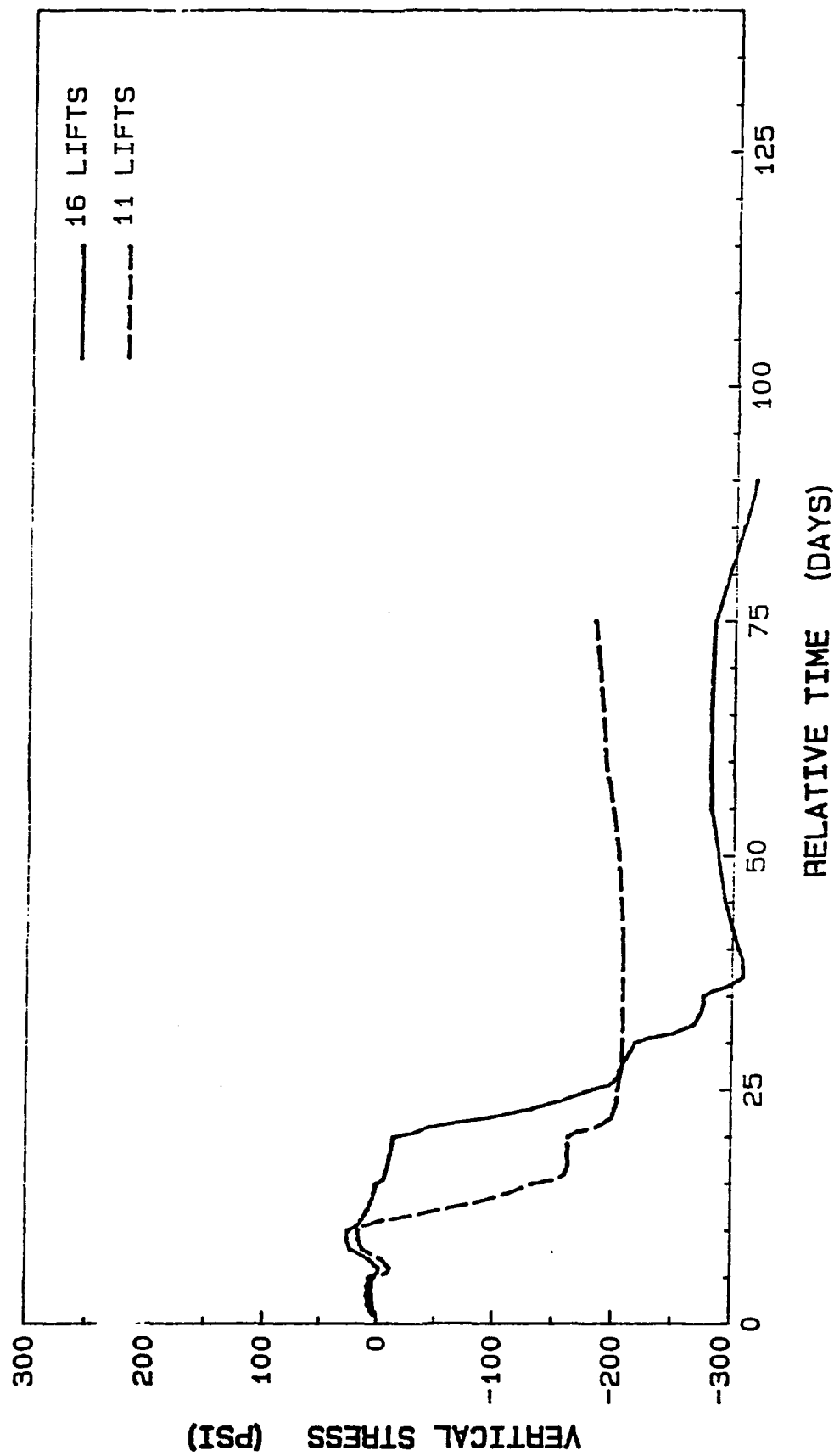


Figure 289. Vertical stress history at element 720, integration point 4

ELEM. 731 INT. PT. 3 - UA, LC, LS

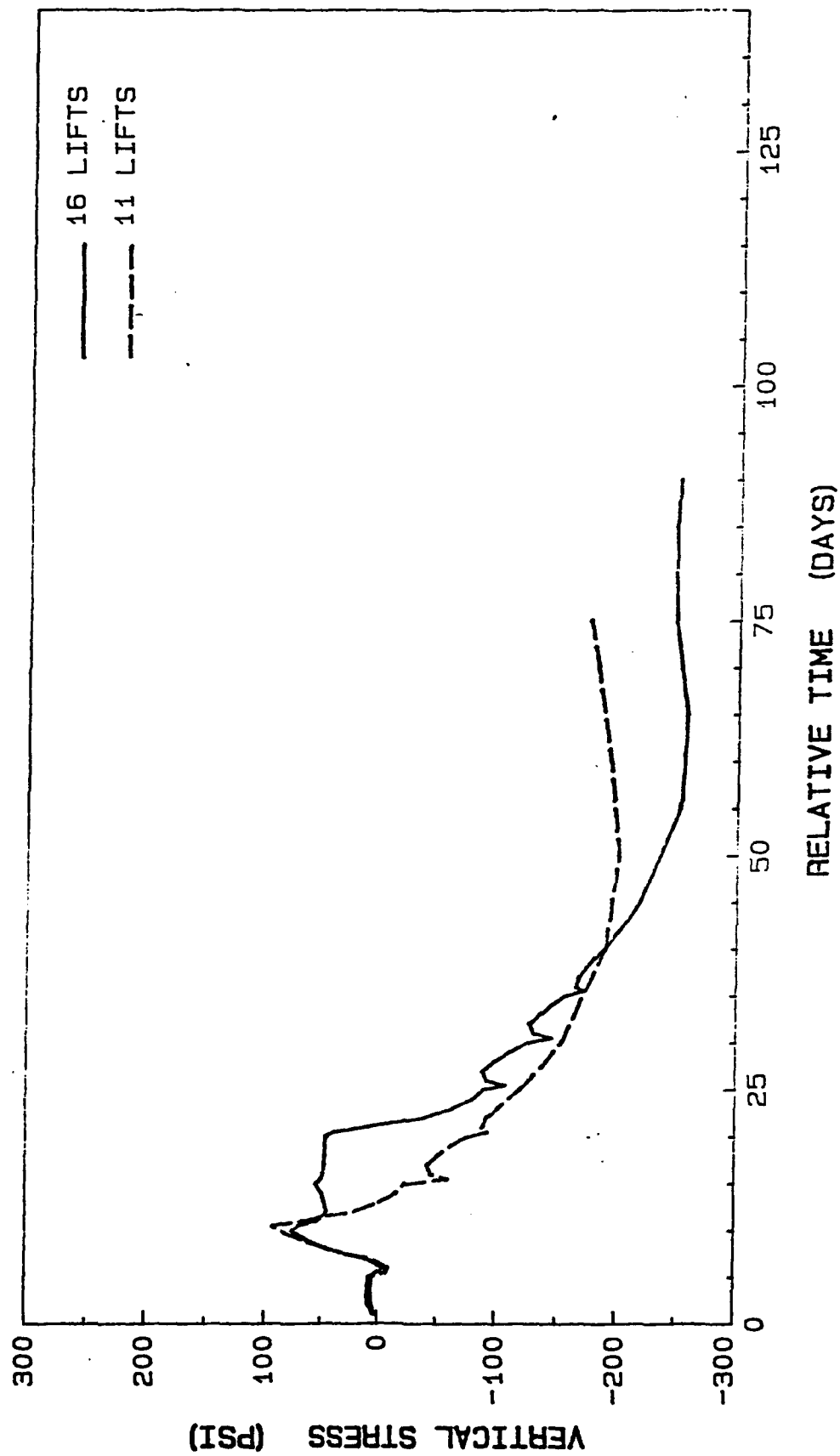


Figure 290. Vertical stress history at element 731, integration point 3

ELEM. 736 INT. PT. 2 - UA, LC, LS

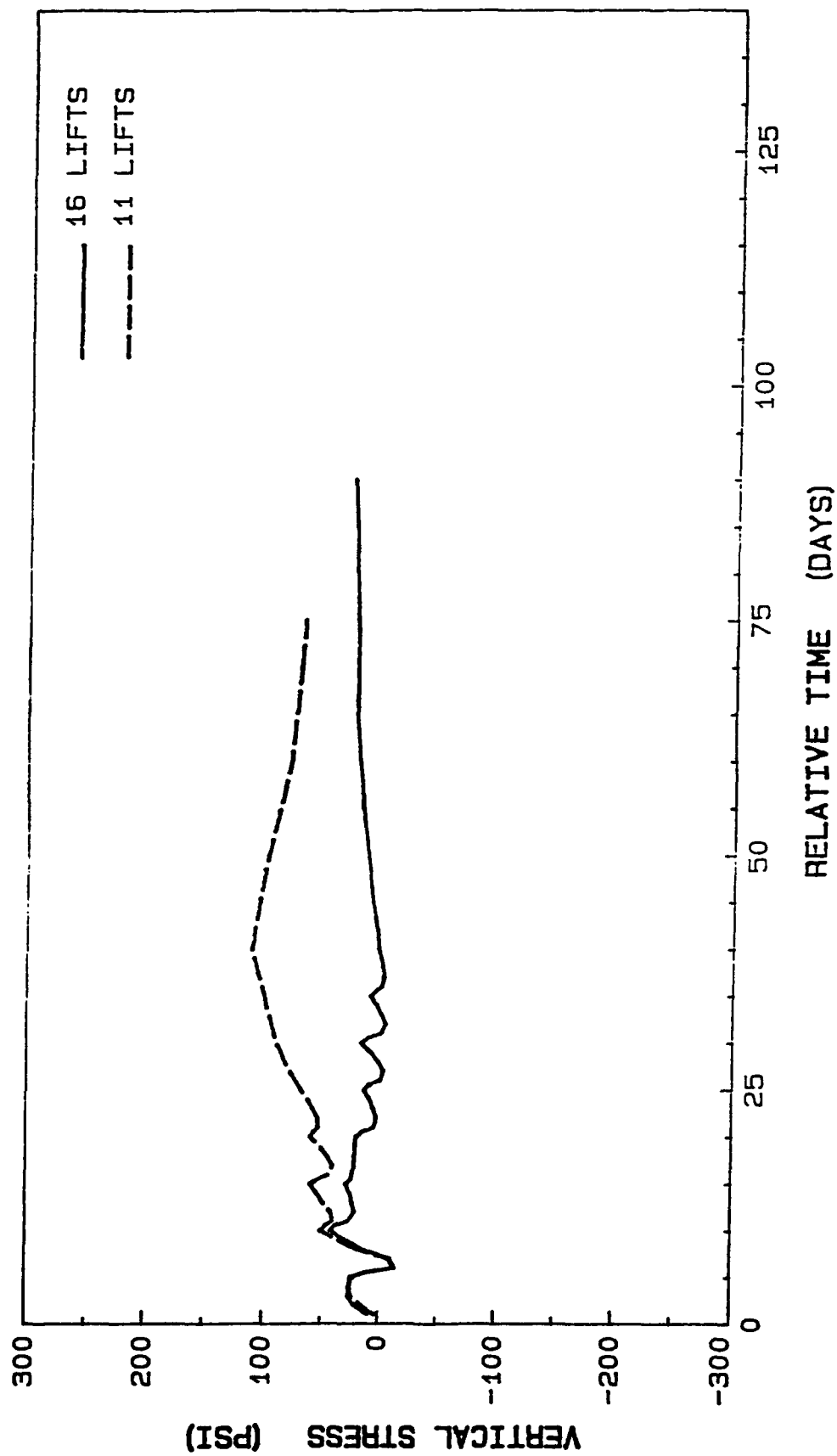


Figure 291. Vertical stress history at element 736, integration point 2

ELEM. 807 INT. PT. 1 - UA, LC, LS

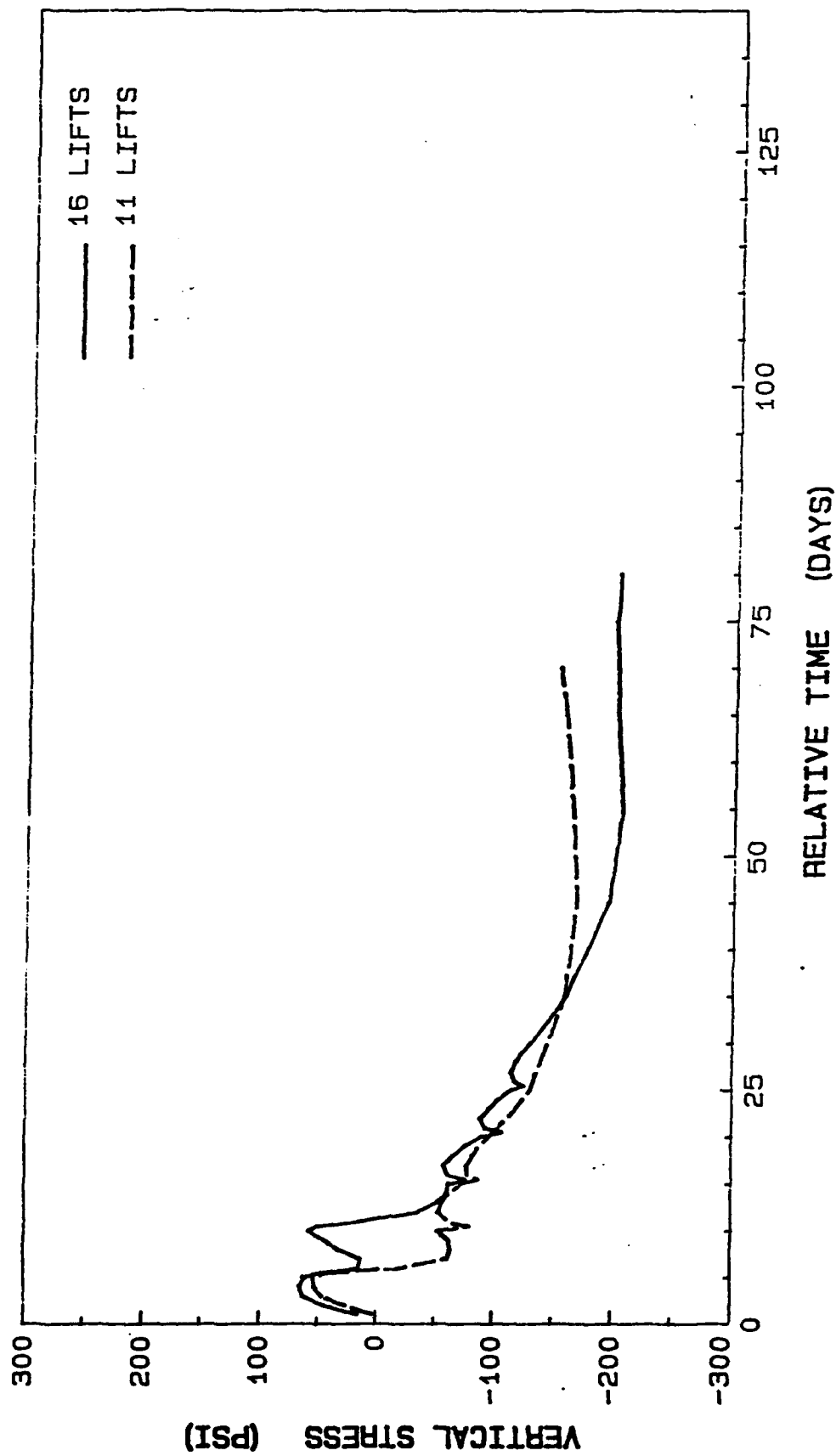


Figure 292. Vertical stress history at element 807, integration point 1

ELEM. 812 INT. PT. 2 - UA, LC, LS

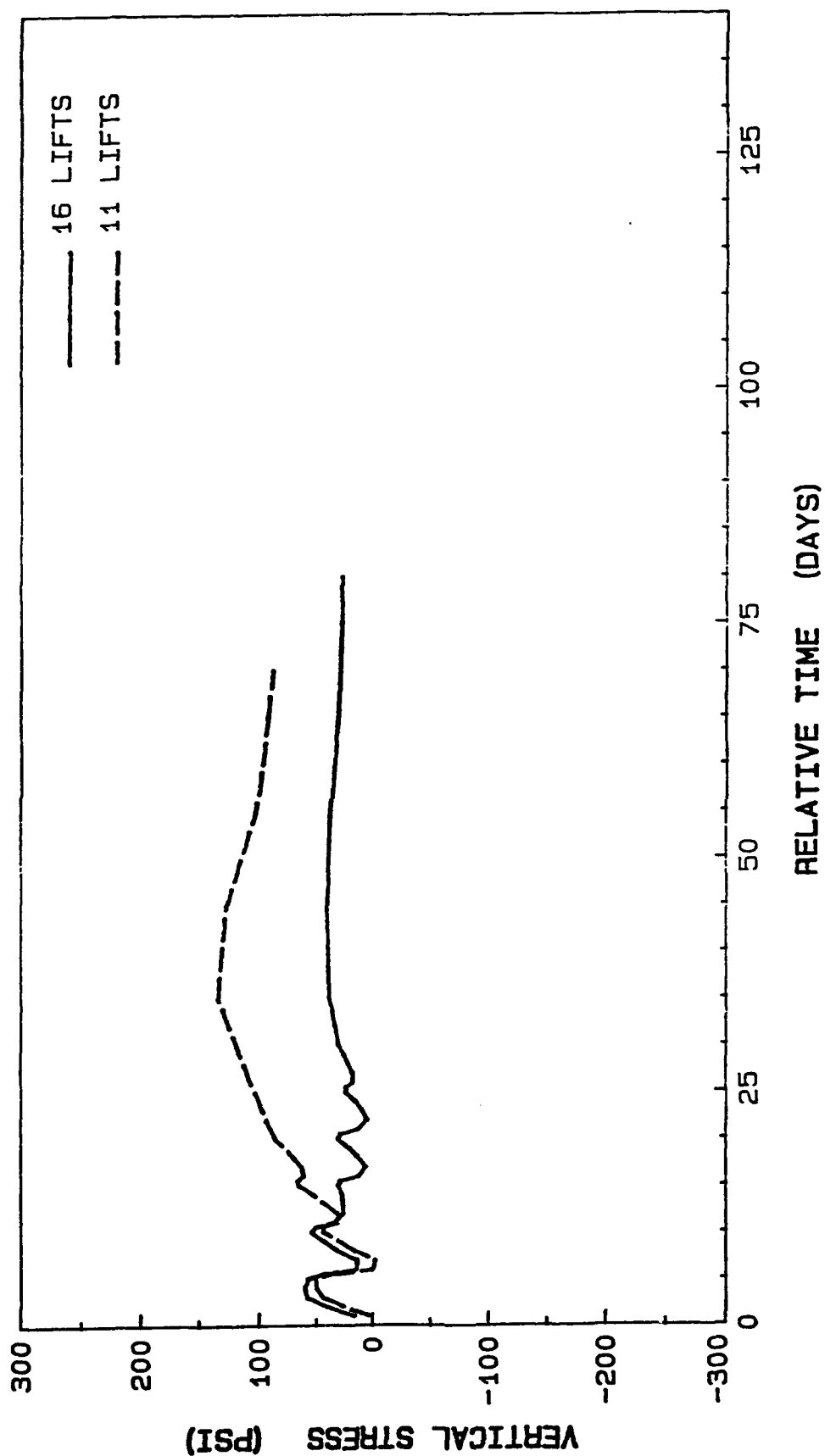


Figure 293. Vertical stress history at element 812, integration point 2

ELEM. 853 INT. PT. 2 - UA, LC, LS

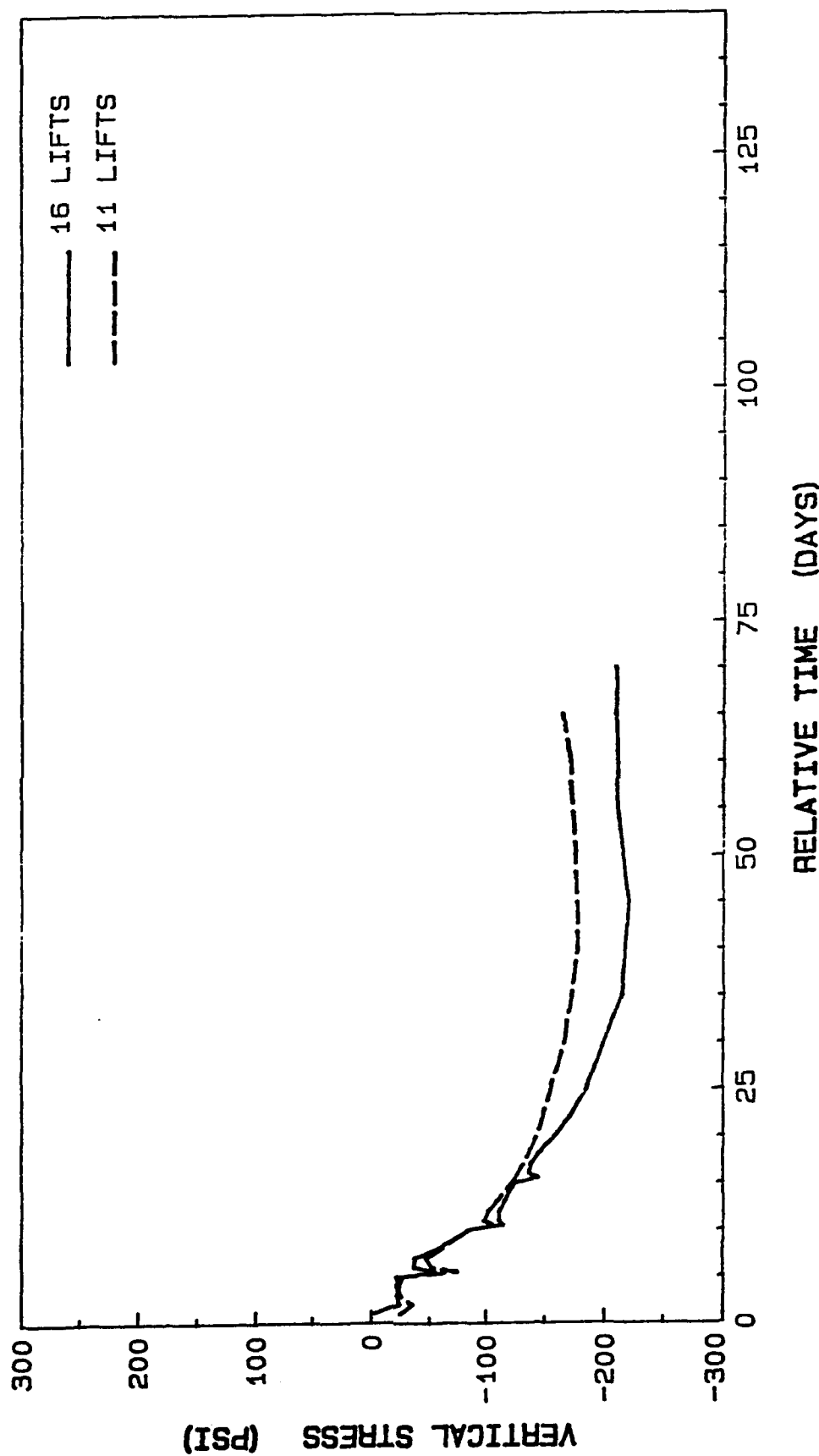


Figure 294. Vertical stress history at element 853, integration point 2

ELEM. 864 INT. PT. 1 - UA, LC, LS

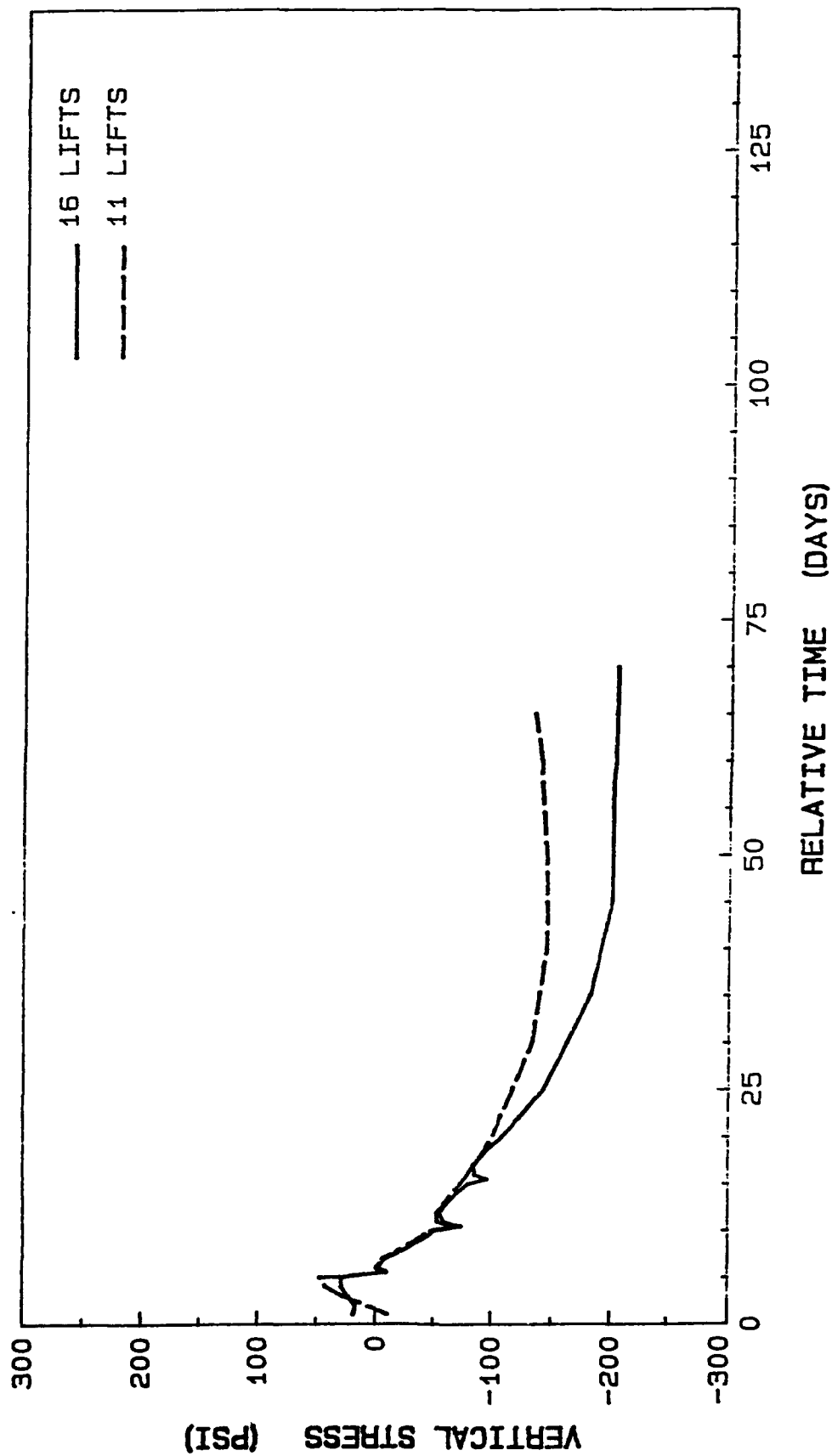


Figure 295. Vertical stress history at element 864, integration point 1

ELEM. 945 INT. PT. 2 - UA, LC, LS

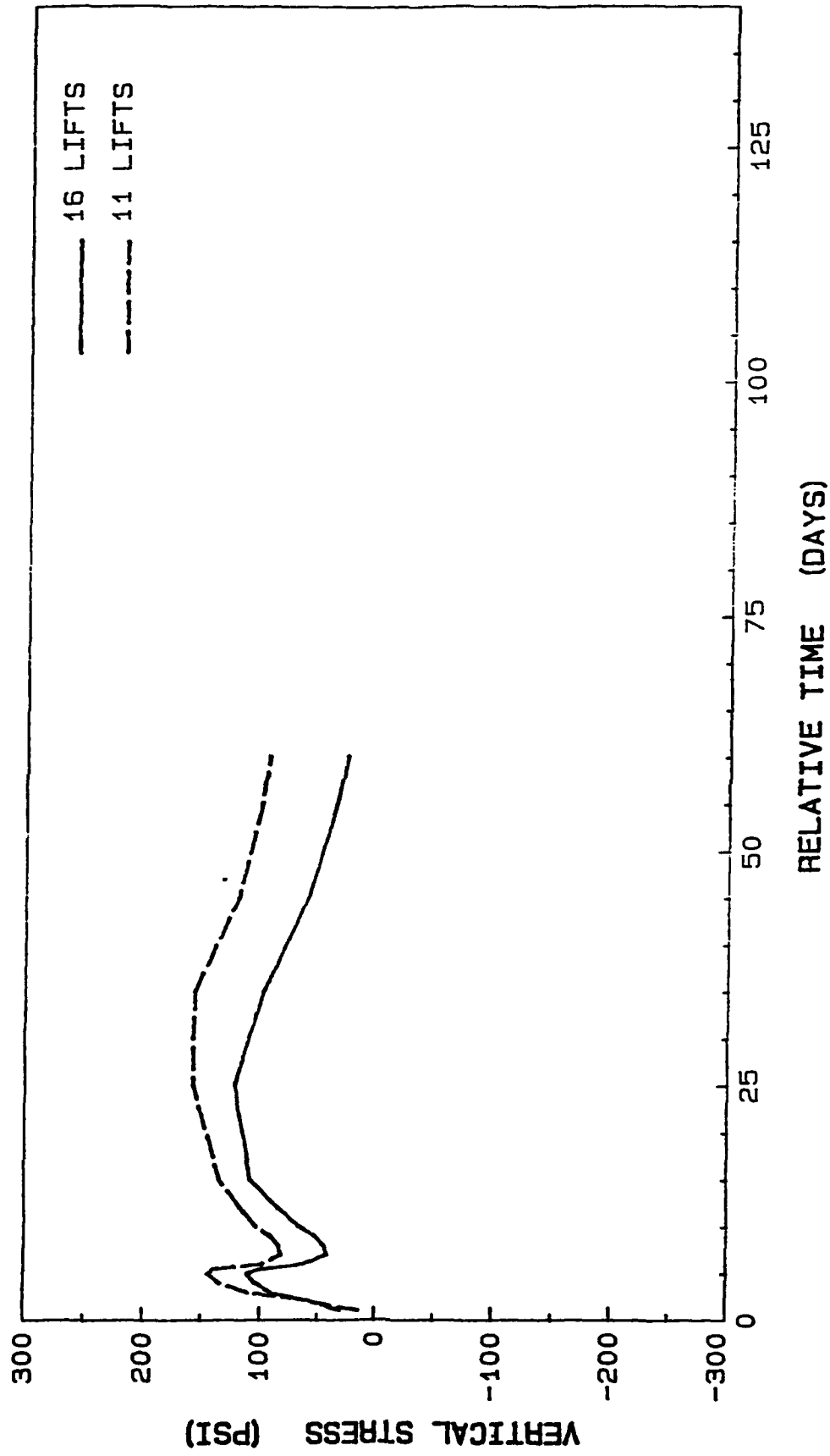


Figure 296. Vertical stress history at element 945, integration point 2

### Introduction

173. The significant findings from the previously discussed results will be restated. In addition, an assessment as to the meaning of these results and any pertinent conclusions will be discussed.

### Overview and Significance of the Results

174. First, the modelling procedure was explored both with respect to the heat transfer and stress analyses. (The material model was supplied through WES.) It was concluded that Equation 2 (limiting element size) could be violated in the horizontal direction in the slab and soil since the heat tended to flow perpendicular to that direction. In addition, the soil depth could be cut from 20 ft to 10 ft and still produce nearly identical results. This reduces the required number of elements by 20 percent.

175. The use of gap or interface elements was essential for the soil-concrete interface if the results at this location are needed. If the results near that interface or early time results are not required, interface elements would not be needed.

176. The use of air elements and multipoint constraints (MPC) should be analyzed further. The correct initial properties for the air elements are essential to produce reasonable results. The initial temperature for the air elements can greatly affect the rise or lowering of the surface temperature in the void. The MPC's are also of some concern, and more detailed study of the load transfer at the end nodes should be explored to ensure that correct results are being obtained at the upper corners of the openings.

177. The lower bound creep and shrinkage load case consistently produced the highest tensile stresses. The maximum tensile stress seen in the monolith AL-3 was approximately 180-200 psi for vertical stresses on the chamber face which is due to both thermal and mechanical effects. The other critical location is in the slab near the center of the chamber where the stresses reach approximately 250 psi just prior to placing the first lift in the wall section. Once the placement of the wall begins, the tensile stresses begin to reduce due to the bending of the slab. (Eventually, this location has a

stress of approximately 250 psi in compression.) Also, the top of the slab shows a stress of approximately 450 psi which is very large and undoubtedly would cause cracking, but this appears to be primarily due to the bending of the slab and could be controlled by placing tensile reinforcement in the top-center of the chamber floor. This high stress is identical for both the 11-lift and 16-lift schedules and is, therefore, independent of the construction plan.

178. The most significant result is that the 11-lift and 16-lift construction procedure produced nearly identical stresses and strains at most locations. The maximum deviation in stress between the two models occurred at the void floor surface and was 130 psi with the maximum stress being 180 psi at this location. A stress of 180 psi is well below what would be considered a critical tensile stress. The next worst case is a difference of 70 psi with a maximum of 150 psi for a location at the lift interface. It can be concluded that the 11-lift model produces no significant increase in the tensile stresses compared with the 16-lift construction. Therefore, the 11-lift construction should be used and could save a minimum of \$700,000 as demonstrated (US Army Corps of Engineers, St. Louis District 1988).

179. A three-dimensional model for a portion of AL-3 was developed. The intent was to verify the two-dimensional results and provide guidance in simulating the actual three-dimensional state with a two dimensional model. Due to the enormous physical disk space and other complications associated with the program ABAQUS and the three-dimensional material model, the analyses could not be completed. These problems are being addressed and large scale three-dimensional analyses of lock and dam monoliths will be possible in the near future.

## REFERENCES

- American Concrete Institute Committee 207 (Mass Concrete Committee). 1973. "Effect of Restraint, Volume Change and Reinforcement on Cracking of Massive Concrete."
- ANATECH Inc. 1987 (Oct). "Development of Two and Three Dimensional Aging and Creep Model for Concrete," US Army Engineer Waterways Experiment Station, Vicksburg, MS.
- Fehl, Barry. 1987 (May). "Analytical Prediction of Thermal Stresses in Mass Concrete," M.S. Thesis, University of Texas at Austin.
- Fintel, Mark, ed. 1974. Handbook of Concrete Engineering. Van Nostrand Reinhold Co., New York.
- Headquarters, US Army Corps of Engineers. 1983 (Sep). "Basic Pile Group Behavior," Technical Report K-83-1, Case Task Group on Pile Foundation, Washington, DC.
- \_\_\_\_\_. 1987. "ABAQUS - Structural and Heat Transfer Finite Element Code," User's Manual. Providence, RI.
- Hibbitt, Karlsson, and Sorenson, Inc. 1987. "ABAQUS - Structural and Heat Transfer Finite Element Code," Theoretical Manual, Providence, RI.
- Holman, J. P. 1981. Heat Transfer. Fifth Edition, McGraw-Hill Inc., New York.
- Hughes, B. P. and Ghunaim, F. 1982. "An Experimental Study of Early Thermal Cracking in Reinforced Concrete," Magazine of Concrete Research. Vol. 34, No. 118, pp. 18-24.
- Norman, C. D., Bombich, T., and Jones, W. 1987. "Thermal Stress Analysis of Mississippi River Lock and Dam 26(R)," US Army Engineer Waterways Experiment Station, Vicksburg, MS.
- Rawhouser, Clarence. 1945 (Feb). "Cracking and Temperature Control of Mass Concrete," Journal of American Concrete Institute. Vol. 16, No. 4, pp 305-346.
- Thompson, Obbie. 1987 (Dec). "EXTRACT - FORTRAN Source Code for Extracting Data from ABAQUS Post Files," US Army Corps of Engineers, St. Louis District.
- US Army Corps of Engineers, St. Louis District. 1988 (Sep). "Report to Lower Mississippi Valley Division on Thermal Stress Analysis on Monoliths AL-3 and AL-5 of the Auxiliary Lock and Dam No. 26 (Replacement)."

Table 1  
Thermal Analysis Material Properties  
and Convection Coefficients

<b>Material Properties: Concrete</b>	
Conductivity	2.3494 Btu-in./day-in. <sup>2</sup> , °F
Density	0.08714 lb/in. <sup>3</sup> (151 lb/ft <sup>3</sup> )
Specific heat	0.21 Btu/lb, °F
<b>Foundation (Soil)</b>	
Conductivity	1.584 Btu-in./day-in. <sup>2</sup> , °F
Density	0.0758 lb/in. <sup>3</sup> (131 lb/ft <sup>3</sup> )
Specific heat	0.45 Btu/lb, °F
<b>Air</b>	
Conductivity	24000. Btu-in./day-in. <sup>2</sup> , °F
Density	3.19E-07 lb/in. <sup>3</sup>
Specific heat	0.24 Btu/lb, °F
Gap Conductance	200. Btu-in./day-in. <sup>2</sup> , °F
<b>Convection Coefficient</b>	
<b>Outer walls</b>	
With forms in place	0.14112 Btu/day-in. <sup>2</sup> , °F
Without forms	0.6792 Btu/day-in. <sup>2</sup> , °F
<b>Inner walls (Inside Culvert and Access Void)</b>	
With forms in place	0.12528 Btu/day-in. <sup>2</sup> , °F
Without forms	0.4224 Btu/day-in. <sup>2</sup> , °F

Table 2  
Individual Pile Stiffness for Chamber Monolith

<u>Direction</u>	<u>Stiffness Pile kips/in.</u>
F <sub>x</sub> (horizontal, strong axis)	54.6
F <sub>y</sub> (horizontal, weak axis)	44.2
F <sub>z</sub> (axial)	896.4

Table 3

Spring (pile) Stiffnesses Used in Two-Dimensional Stress Analysis

(Stiffnesses are per 1.0 in. thickness)

<u>Distance Perpendicular to Flow Direction (ft)</u>	<u>0-15</u>	<u>25-55</u>	<u>65-80</u>
Spring spacing (ft)	5	10	5
No. of piles in row	15	8	15
Vertical stiffness	13.339	7.114	13.339
Horizontal stiffness	0.813	0.433	0.813

Table 4

Load Cases Examined for Stress Analyses to Select Adiabatic Curve

<u>Load Case</u>	<u>Adiabatic</u>	<u>Creep</u>	<u>Shrinkage</u>
1	None	Lower bound	Lower bound
2	Lower bound	Lower bound	Lower bound
3	Upper bound	Lower bound	Lower bound

---

Table 5

Load Cases Examined for Stress Analyses to Assess  
the Effect of Creep and Shrinkage

<u>Load Case</u>	<u>Adiabatic</u>	<u>Creep</u>	<u>Shrinkage</u>
3	Upper bound	Lower bound	Lower bound
4	Upper bound	Upper bound	Upper bound
5	Upper bound	Lower bound	Upper bound
6	Upper bound	Upper bound	Lower bound
7	Upper bound	Lower bound	None
8	Upper bound	None	Lower bound
9	Upper bound	None	None

---

Table 6  
Spring (Pile) Forces for Static and Parametric Analysis

<u>Node/Distance From Center Line</u>	Spring Forces			
	lb		Nonlinear, Incremental (load case 3)	
	<u>X-Comp.</u>	<u>Y-Comp.</u>	<u>X-Comp.</u>	<u>Y-Comp.</u>
1412 80 ft	-3.3	-2711.	104.	-2613.
1418 75 ft	-1.0	-2642.	99.1	-2590.
1423 70 ft	-1.6	-2536.	91.2	-2552.
1428 65 ft	-2.0	-2442.	83.6	-2542.
1438 55 ft	-1.0	-1210.	37.7	-1353.
1450 45 ft	-1.3	-1142.	31.1	-1319.
1458 35 ft	-0.5	-1084.	25.2	-1234.
1466 25 ft	0.5	-1013.	19.3	-1088.
1474 15 ft	1.1	-932.	12.8	-900.
1478 10 ft	1.8	-1675.	16.7	-1525.
1482 5 ft	1.0	-1631.	8.5	-1419.
1486 0 ft	0.0	-808.	0.0	-691.

Table 7  
Internal Equilibrium Check Results

<u>Time</u> <u>Days</u>	<u>Actual</u> <u>Force, lb</u>	<u>Applied</u> <u>Force, lb</u>	<u>Percent</u> <u>Difference</u>
25	1,244.	1,358.	8.4
30	2,690.	2,738.	1.8
35	3,920.	3,993.	1.8
40	4,570.	4,633.	1.4
62	4,733.	4,633.	2.2

Table 8  
External Equilibrium Check Results for Load  
Case 3 at Service Loads

---

$+\Sigma F_x$	
Applied forces, lb	
Hydrostatic chamber wall mo. side	-5253.6
Hydrostatic culvert right face	2437.1
Hydrostatic culvert left face	-2437.1
Hydrostatic Ill. side	2502.6
Backfill	966.1
Earthquake forces	-1238.6
0.1 Dead load	<u>-1911.7</u>
Total	-4935.2
Reaction forces from ABAQUS, lb	
Spring forces	- 529.2
Reaction forces at center line	<u>5455.2</u>
Total	4926.4
$+\Sigma F_y$	
Applied forces, lb	
Dead load	-19117.0
Hydrostatic chamber slab	-12890.0
Uplift chamber slab	12931.0
Hydrostatic culvert floor	- 2812.3
Uplift culvert roof	<u>2062.1</u>
Total	-19826.2
Reaction forces from ABAQUS, lb	
Spring forces	19826.0

---

Table 9

Soil Initial Temperature Used in Transient Heat Transfer Analysis

<u>Soil Depth, in.</u>	<u>Temperature, °F</u>
0.0	76.57
7.5	73.98
15	71.56
22.5	69.33
30	67.3
37.5	65.47
45	63.83
52.5	62.38
60	61.1
67.5	59.98
75	59
82.5	58.14
90	57.39
97.5	56.72
105	56.11
112.5	55.54
120	55

---

Table 10  
Surface Heat Transfer Coefficients in Btu/day in.<sup>2</sup> °F

	<u>Exterior</u>	<u>Interior (not closed)</u>	<u>Interior (closed)</u>
With forms	0.14112	0.12528	0.165
Without forms	0.6792	0.4224	0.0857

Table 11  
Thermal Material Properties Used in the  
Transient Heat Transfer Analysis

	<u>Concrete</u>	<u>Soil</u>	<u>Air</u>
Conductivity, Btu in./in. <sup>2</sup> day °F	2.34936	1.584	24000
Density, lb/in. <sup>3</sup>	0.08714	0.0758	0.000046
Specific heat, Btu/lb °F	0.21	0.45	0.24

APPENDIX A: DEVELOPMENT OF TWO- AND THREE-DIMENSIONAL AGING  
AND CREEP MODEL FOR CONCRETE (ANATECH, INC. 1987)

Purpose

1. The purpose of this work is to develop a computationally robust constitutive model for aging concrete, considering creep, shrinkage, and cracking for use in the ABAQUS code. The model parameters are quantified from laboratory data for the elastic modulus as function of age, creep strain versus time, and shrinkage strain versus time. Two versions of this model are considered: a two-dimensional version which can be applied to problems involving plane stress, plane strain, and axisymmetric stress states; and an unrestricted version for general three-dimensional stress states. The modeling of the cracking in both of these versions differ significantly from one another--the three-dimensional case being far more complex in the computational details than its two-dimensional counterpart. This brief report describes the main features of the constitutive model with respect to aging, creep, and cracking.

Aging Effects in Concrete Creep

2. Figure A1 shows a typical compliance curve (specific strain) for a concrete cylinder loaded at age  $\tau_0$  with stress  $\sigma_0$ . The vertical segment of this curve represents the elastic strain per unit stress which is the inverse of the elastic modulus. The curve represents the time-dependent response of the cylinder which consists of a purely creep component (visco-elastic) and a much smaller elastic component which is due to the aging elastic recovery. It is impossible to separate these two components in the same experiment; however, separate experiments for  $E(\tau)$  can be conducted and then used to identify the purely creep part from the creep experiments. This, however, is not usually done in practice, which becomes a source of error in the predicted versus measured data. The measured curve  $J(t-\tau_0)$  is usually used directly in analysis for the creep component  $\epsilon^c$  in the strain decomposition formula, which can be written as follows for the creep test:

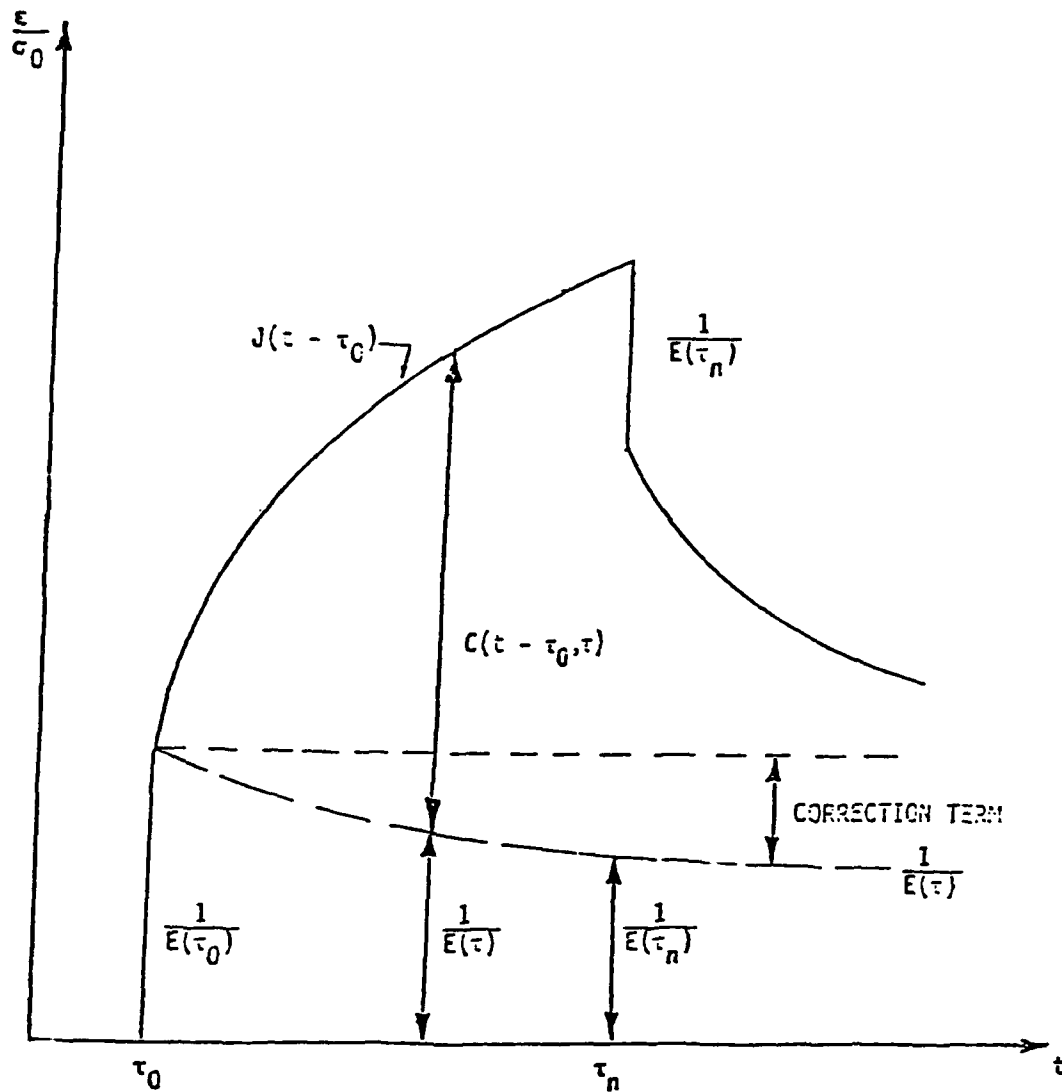


Figure A1. Compliance curve for concrete

$$\epsilon = \epsilon^e + \epsilon^c + \frac{\sigma_0}{E} + \sigma_0 J(t - \tau_0) \quad (A1)$$

where

$\epsilon^e$  = the elastic strain

$\epsilon^c$  = the creep strain

In strict terms, the creep strain  $\epsilon^c$  should be  $C(t - \tau_0)\sigma_0$ , so that the total specific creep strain becomes

$$\frac{\epsilon}{\sigma} = \frac{1}{E(\tau_0)} + J(t-\tau_0) = \frac{1}{E(\tau)} + C(t-\tau_0, \tau) \quad (A2)$$

As can be easily determined,  $J$  and  $C$  are the same for non-aging materials and are nearly equal (within data scatter) for mature concrete. However, they may differ significantly for very young concrete and, hence should be treated separately.

3. If one plots in the same figure several creep curves for different ages of loading, one obtains Figures A2 and A3. These curves differ from one another in the elastic portion as well as the slope, as is illustrated in Figure A3. Both of these differences are strictly due to aging, i.e., the four curves shown in Figure A3 become one for nonaging materials and would approach each other as the concrete's age increases.

#### Temperature Effects in Concrete Creep

4. Temperature affects concrete in a manner that is characteristic of the so-called thermo-rheologically-simple material, but with the added effects of aging. Thermo-rheologically-simple material is assumed to be nonaging. For such material a creep curve at any temperature  $T$ , when plotted as function of  $\log t$ , can be obtained from the creep curve at a base temperature  $T_0$  by a simple shift along the  $\log t$  axis as shown in Figure A4. The shift  $\phi(t)$  is usually referred to as the shift factor, and the log of  $\phi(t)$  is called the shift function.

5. The concept of thermo-rheologically-simple behavior is useful in two respects: first, as a means to linearize the highly nonlinear strain-stress hereditary integral; and second, as an extrapolation scheme to cover a wide range of temperatures using only a few tests. It should be noted that, in age of computer-based numerical analysis, numerical integration of nonlinear integral equations can be accomplished just as easily in any form. However, the time-temperature equivalence principle can help explain the physical behavior by illustrating the well-practiced concept of accelerated creep tests in which long range creep data can be obtained by conducting creep tests at higher temperature, but for a much shorter time.

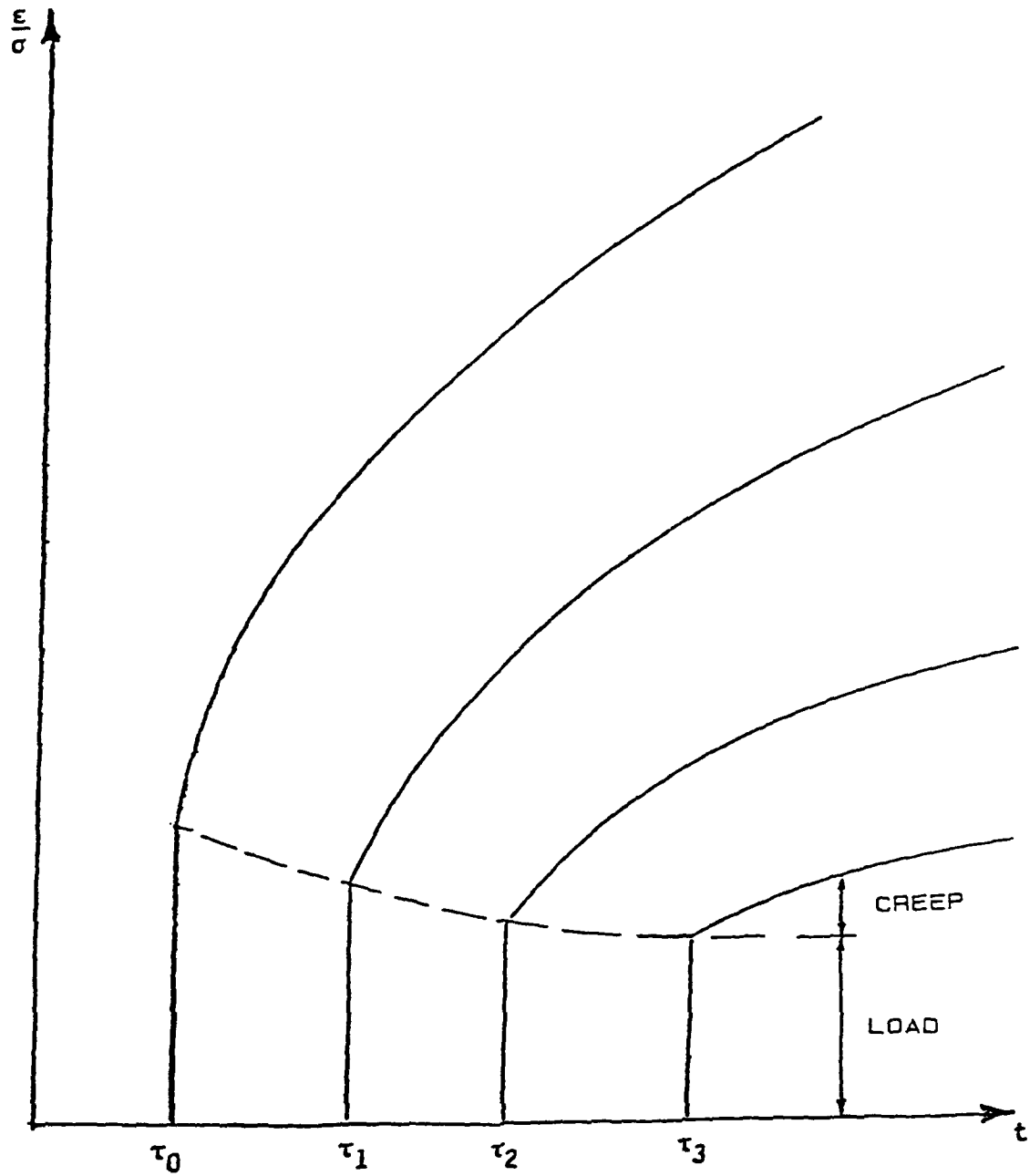


Figure A2. Concrete compliance curves at different ages

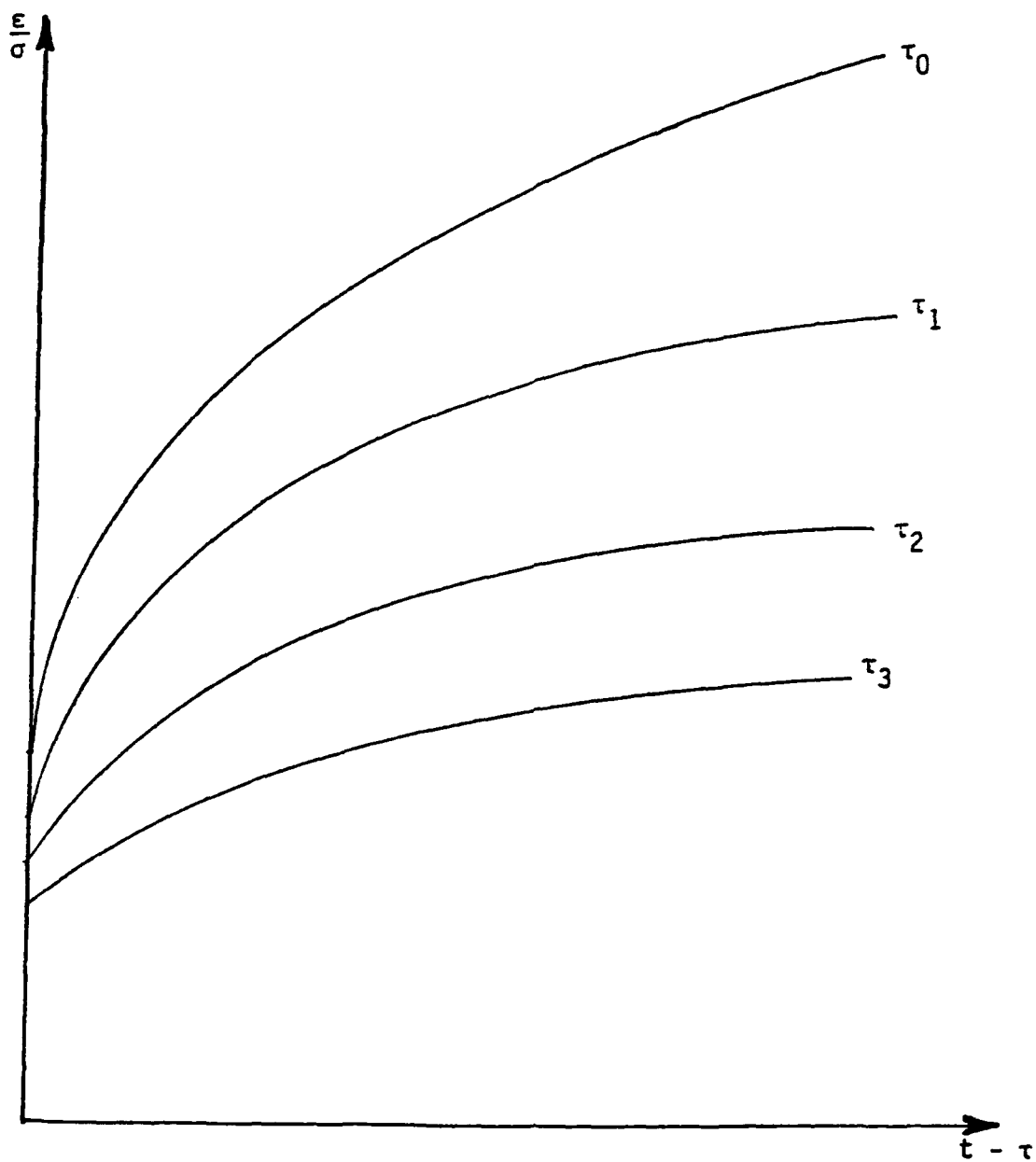


Figure A3. Concrete compliance curves as function of duration of load

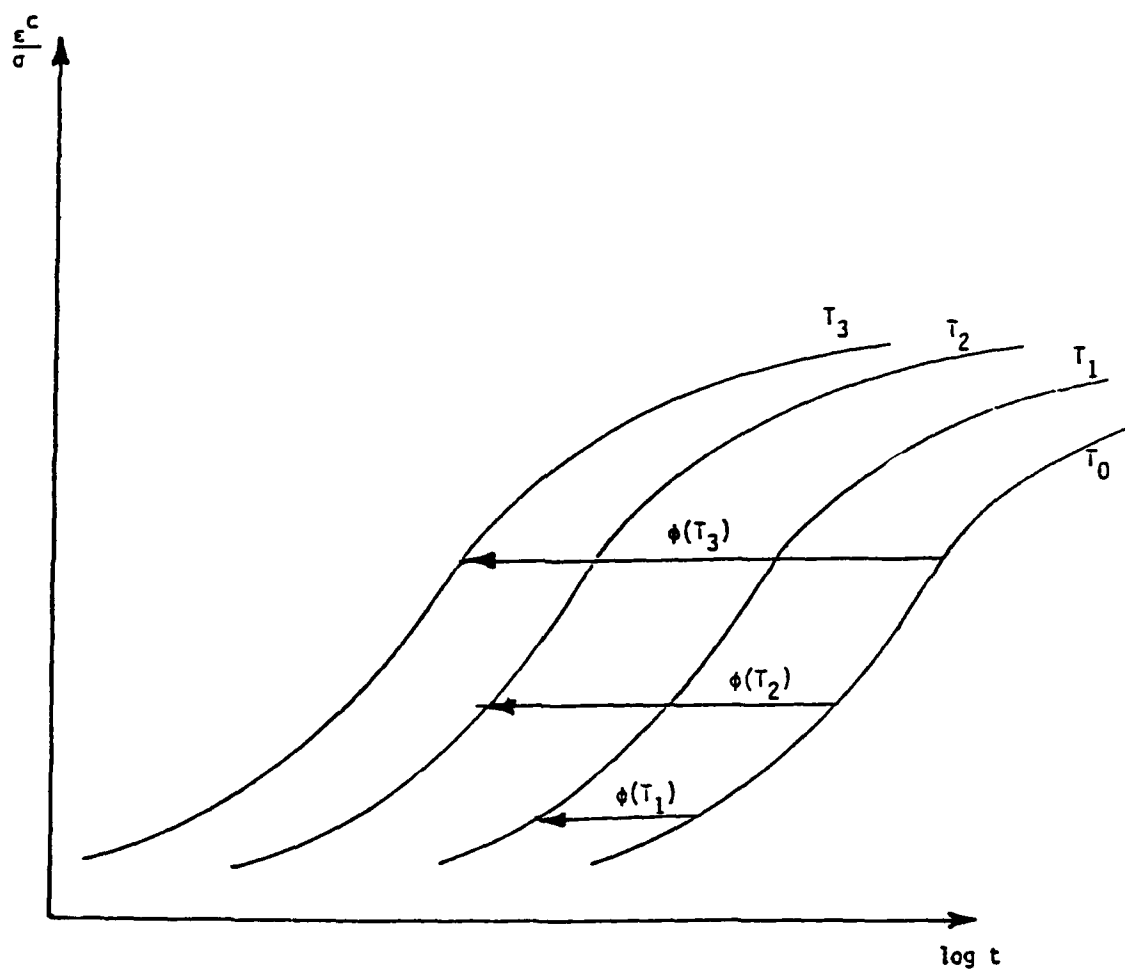


Figure A4. Time-temperature equivalence for linear viscoelastic material

6. Mathematically, the creep compliance for nonaging thermorheologically-simple material can be represented as follows. At temperature  $T_0$ , we have

$$J(t) = J(\log t) = J(\xi) \quad (A3)$$

where  $\xi = \log t$ .

7. In order to apply the shift principle, we replace  $t$  by  $\phi t$  and then

$$\xi = \log(\phi t) = \log t + \log \phi \quad (A4)$$

with  $\phi$  being the shift needed to go from the creep curve at temperature  $T_0$  to the creep curve at temperature  $T$ . In general

$$\xi = \log t + \int_0^t \phi[T(\lambda)] d\lambda \quad (A5)$$

where in this equation  $T$  is allowed to vary continuously in time. Using this expression for  $\xi$ , the creep compliance for any temperature  $T$  becomes  $J(\xi)$ . This is to say that the same mathematical expression for  $J(t)$  at  $T_0$  can be used for any  $T$  by simply replacing  $t$  by  $\xi$  and then evaluating the data. Thus, if

$$J(t) = A(1 - e^{-rt}) \text{ for } T_0 \quad (A6)$$

then

$$J(\xi) = a(1 - e^{-r\xi}) \text{ for any } T \quad (A7)$$

where

$$\xi = \int_0^t \phi[T(\lambda)] d\lambda \quad (\text{A8})$$

and  $\phi$  is obtained graphically from plots such as shown in Figure A4. This process is not so straightforward for aging materials because the creep strain depends not only on the duration of loading but also on the time at which the load is applied. This implies that the shift factor becomes a function of temperature and age.

8. Recalling the fact that temperature has a softening effect on creep, which is akin to the rejuvenation of concrete, the time-temperature equivalence principle can be extended to include the age of the material. Assuming that aging of concrete is a logarithmically decreasing effect, we introduce the concept of double shift: first shifting the base curve for aging, and then shifting it again for temperatures. This is done as follows. Let the base curve be  $J(t, \tau_0)$  for temperature  $T_0$ . If we plot this curve on the  $\log t$  axis, we have

$$J(t, \tau_0) = J[\log \eta] \quad (\text{A9})$$

where  $\eta = \eta(t - \tau_0)$ .

9. We have now introduced the time shift factor  $\eta$ . Now introducing the temperature shift factor, we have

$$J(t, \tau_0, T) = J[\log \eta(t - \tau_0) + \log \phi(T)] = J[\xi(t, \tau_0)] \quad (\text{A10})$$

where

$$\xi(t, \tau_0) = \eta(t - \tau_0) \phi(T) \quad (\text{A11})$$

In general, for time varying temperature,

$$\xi(t, \tau) = \int_0^t \phi[T(\lambda)] \frac{\partial \eta(\lambda - \tau)}{\partial \lambda} d\lambda \quad (A12)$$

and the creep compliance becomes

$$J(t, \tau, T) = J[\xi(t, \tau)] \quad (A13)$$

The way to determine the time and temperature shift factor is: first place the base curve obtained at age  $\tau_0$  on the log  $t - \tau$  axis: the curves for  $\tau_1$ ,  $\tau_2$ ,  $\tau_3$  ... plot below the base curve, as shown in Figure A5. The time shift factor  $\eta(t - \tau)$  can then be determined by simply plotting the values of  $\eta(t - \tau)$ , obtained graphically, versus  $\tau$  then fitting a formula to the curve. Consider for example the formula:

$$J(t, \tau) = A(\tau)(1 - e^{-rt}) \quad (A14)$$

Then the curve for age  $\tau_1$  becomes

$$J(t, T_1) = A(\tau_0)(1 - e^{-r\xi(t, \tau_1)}) \quad (A15)$$

where  $\xi(t, \tau_1) = \eta(t - \tau_1)$ .

10. The next step is to determine the temperature shift factor  $\phi(T)$  in the manner described previously. However, the assumption has to be made that the temperature shift is independent of age, i.e.,  $\phi(T)$  is the same for all ages.

#### WES Creep Relation

11. The creep relation for WES concrete is given below.

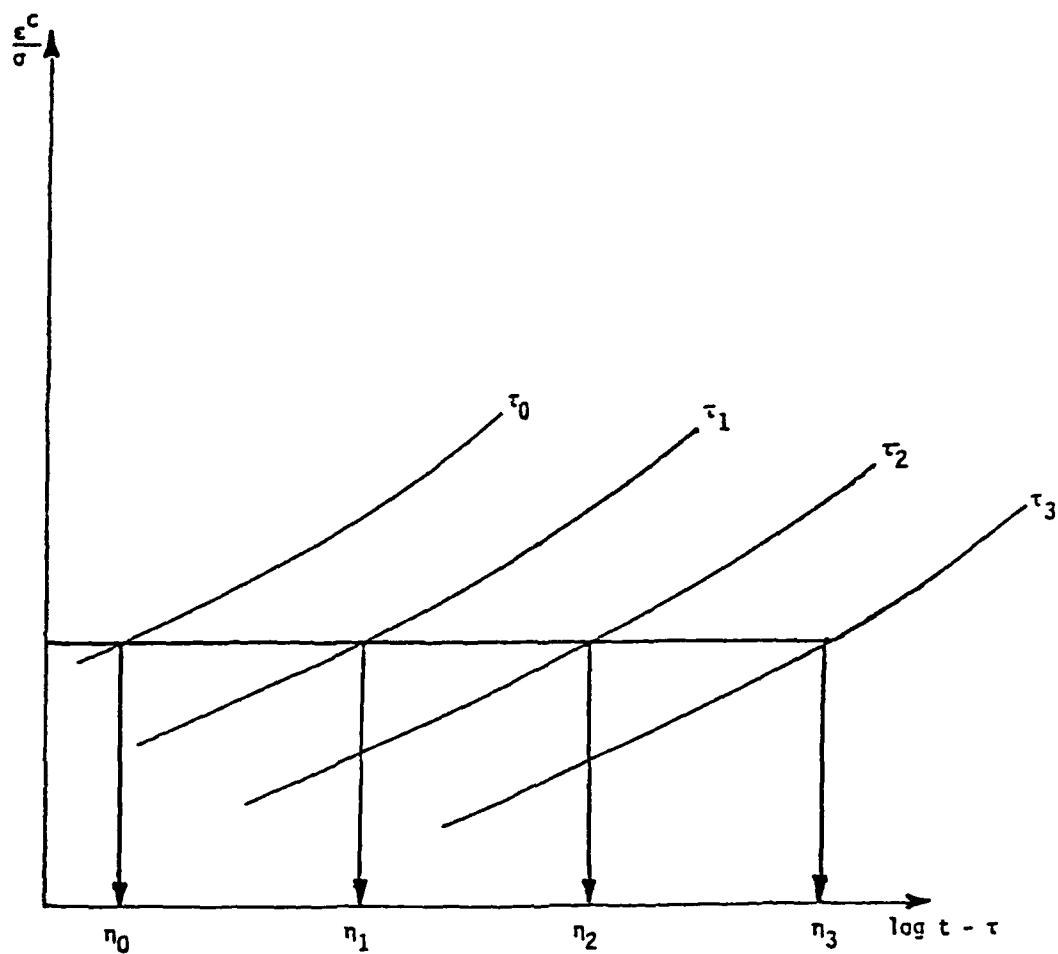


Figure A5. Concrete creep curves shifted with age

$$J(t, \tau, T) = \sum_{i=1}^2 A_i(\tau, T) (1 - e^{-x_i(t-\tau)}) + D(\tau, T) [t - \tau] \quad (A16)$$

where

$$A_i(\tau, T) = A_{0i} e^{-Q/RT} \left[ \frac{E(3)}{E(\tau)} \right]^2 \quad (A17)$$

$$E(\tau) = E_0 + E_1(1 - e^{-\sigma_1(\tau-1)}) + E_2(1 - e^{-\sigma_2(\tau-1)}) \quad (A19)$$

Shrinkage is expressed as follows:

$$\epsilon^s = C_1(1 - e^{-S_1 t}) + C_2(1 - e^{-S_2 t}) \quad (A20)$$

The uniaxial strain-stress relation becomes

$$\epsilon(t) = \int_0^t \left[ \frac{1}{E(\tau)} + J(t, \tau, T) \right] \frac{\partial \sigma(\tau)}{\partial \tau} d\tau + \alpha T + \epsilon^s \quad (A21)$$

The main features of the above relations are discussed below.

- a. The creep formula is not the traditional logarithmic function, but it matches the available data. The linear term in Equation A16 implies the presence of a viscous element which characterizes long term creep for metals. Its inclusion here is motivated by accurate data fitting, not by physical considerations. Furthermore, the objection to this term is that it is nonaging. This is true only if the coefficient  $D$  is a constant, which is not the case here. The logarithmic formula found its way in concrete creep because the term  $\log(t - \tau + 1)$  has a continuously decreasing slope; thus, it exhibits an aging phenomenon. The slope of the logarithmic formula is proportional to  $1/(t - \tau + 1)$ , which is a decreasing function of time. In our case, the slope of the linear term is proportional to  $1/E^2$  (see Equation 19), which is an exponentially decreasing function of time. However, Equation 21 gives a long-term strain that exhibits aging. It might be interesting in this regard to discuss Bazant's point and other workers in the field who are similarly attached to the logarithmic formula. If we go back to Figure A1, we see that the measured creep compliance is  $J(t - \tau_0)$ , which is not the true creep curve, although it is the curve that is usually plotted on semi-log scale. However, as we discussed earlier, the true creep compliance  $C(t - \tau_0)$ , which is usually ignored by experimentalists, has an aging correction term as shown in the figure. Notice that  $C(t - \tau_0, \tau)$  is larger than  $J(t - \tau_0)$ , and the difference between the two curves become wider and wider with time. Therefore, if  $J(t - \tau_0)$  is a log function, then  $C(t - \tau_0, \tau)$  cannot be a log function any may in fact be closer to a linear function at long time. Also, there is evi-

dence that temperature eliminates the effect of aging, and at certain temperatures concrete behaves like polymers. Therefore, it boils down to how one looks at the data. It should be noted further that the present analysis is not limited by the linear term in the creep formula and a third exponential term can be used instead. For example, the term  $(1 - e^{-0.00038t})$  can replace the linear term  $3.8 \times 10^{-4}t$  with little loss in accuracy in the range of the data.

- b. The first term in the series in Equation 16 governs the short-term creep for the first day; the second governs the intermediate-term creep, up to 30 days; and the last governs the creep behavior beyond 30 days.
- c. Aging is determined from the elastic modulus data and is represented as an inverse square function, i.e., the creep strain is proportional to the square of the inverse of the elastic modulus. This was determined by trial and error because of lack of data.

### Cracking

12. Cracking is assumed to occur when a cracking criterion is satisfied. This criterion consists of the following elements: (a) it is strain driven but is modified by the stress, as will be shown later; (b) the crack surface normal is in the direction of the principal strain; and (c) the cracking criterion is interactive.

13. This criterion is implemented as follows. Consider a trace of the two-dimensional failure surface shown in Figure A6 in principal stress space. The  $f'_t$  and  $f'_c$  have the usual meaning, namely tensile and compressive strength, respectively. For isotropic material, which describes concrete prior to cracking, the principal strain and principal stress direction coincide. Therefore, one could also express the cracking criterion in terms of the principal strains. It is important to do so for concrete if we were to predict cracking correctly. Consider, for example, a cube of material pressure loaded with  $\sigma_2$ . The cube will split, in the direction of the load, under the effect of the  $\epsilon_1$  strain. The  $\sigma_1$  stress will be a small

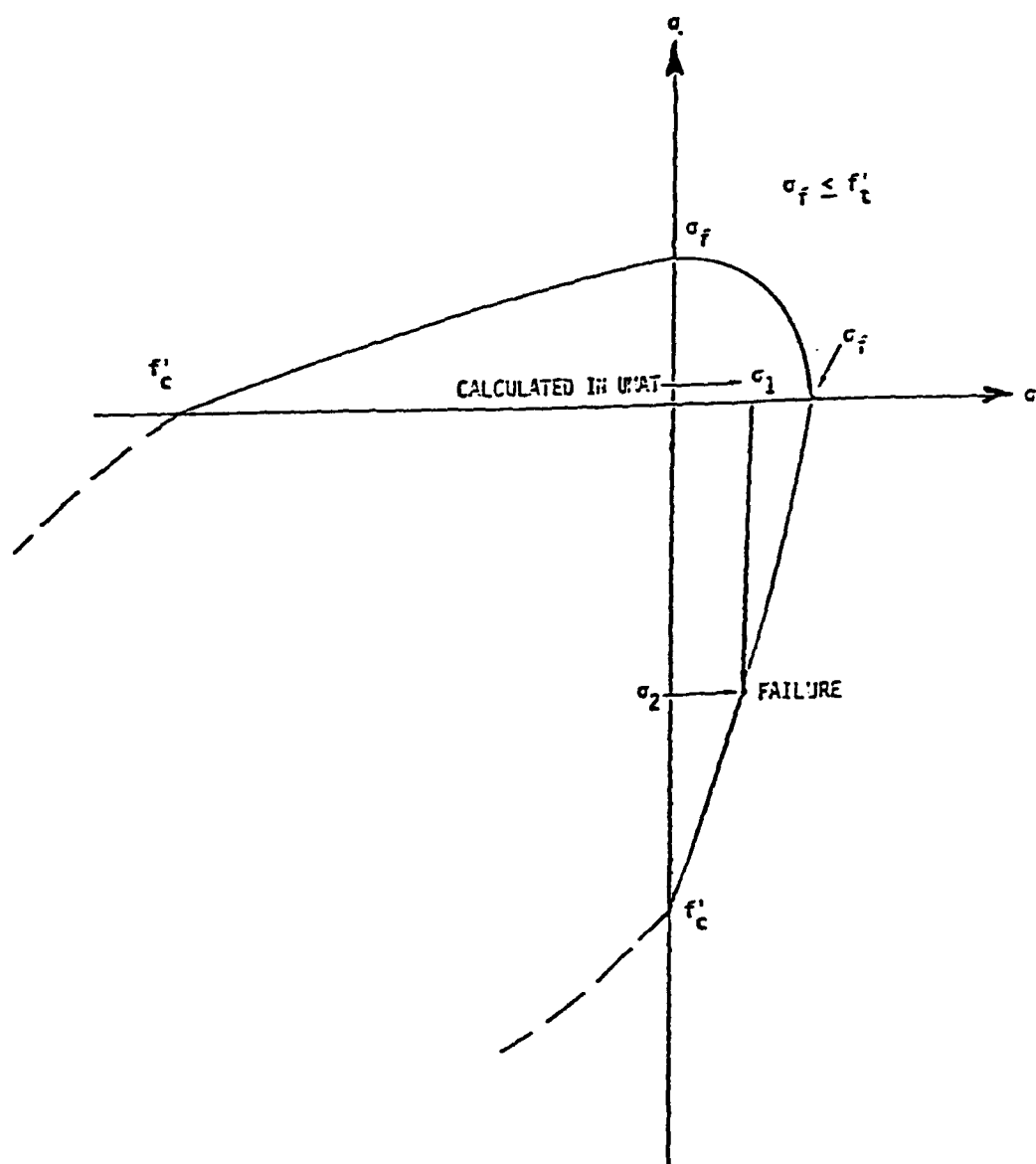


Figure A6. Concrete failure surface

positive, actually zero in a finite element plane stress analysis. If the cracking criterion is a function of the stress only, then from Figure A6 cracking occurs when  $\sigma_2$  approaches the ultimate uniaxial compressive strength. The  $\epsilon_1$  strain is  $-\nu \epsilon_2 = -\nu \sigma_2/E$ . If  $\sigma_2 = f'_c$ , then the cracking strain is calculated to be 20 percent of the uniaxial ultimate compressive strain, or twice the value usually assumed.

14. One concludes from this example that a strain-dependent cracking criterion is more appropriate. Now let us consider the same example, but with sufficiently small  $\sigma_2$  so as not to cause immediate cracking. If  $\sigma_2$  is sustained for long enough time, cracking could eventually occur as a result of the added creep strain  $\epsilon_1^c$ . The total cross strain becomes  $\epsilon_1 = -\nu \sigma_2/E + \epsilon_1^c$ .

15. We see, therefore, that the material shows higher tensile strain capacity under creep. We may conclude from this that the cracking criterion ought to be time dependent.

16. We seen then that a stress-alone or strain-alone cracking criterion will not be general enough for time-dependent analysis. However, we lack time-dependent cracking data. Therefore, in order to accommodate the creep and relaxation effect together with elastic stress and strain states, without new experiments, we adopt an interactive criterion. This is illustrated in Figure A7 which describes a linear relationship between the cracking stress and cracking strain. The uniaxial tension test is the midpoint of the straight line that crosses the  $\epsilon$  and  $\sigma$  axes at  $2f'_t/E$  and  $2f'_t$ , respectively. Several familiar test conditions are indicated in the figure. The actual interaction curve is shown in dashed line. Note that cracking under zero strain is physically impossible for compressive materials (with Poisson's ratio  $< 0.5$ ). The shape of the curve in Figure A7 is obviously data dependent, but for simplicity, we assume it to be a straight line. The factor of 2 is arbitrary but it used to expand the curve above and below the midpoint in order to accommodate cracking at high stress but low strain and low or zero stress but high strain, as well as creep-induced cracking. Although creep cracking data are scarce, there is some evidence that creep cracking strain is about twice that of the uniaxial tensile strength. Implementation of this criterion in the model is as follows:

- a. Calculate the maximum principal strain  $\epsilon_1$  in UMAT.
- b. Enter Figure A7 with  $\epsilon_1$  and calculate  $\sigma_f$ .

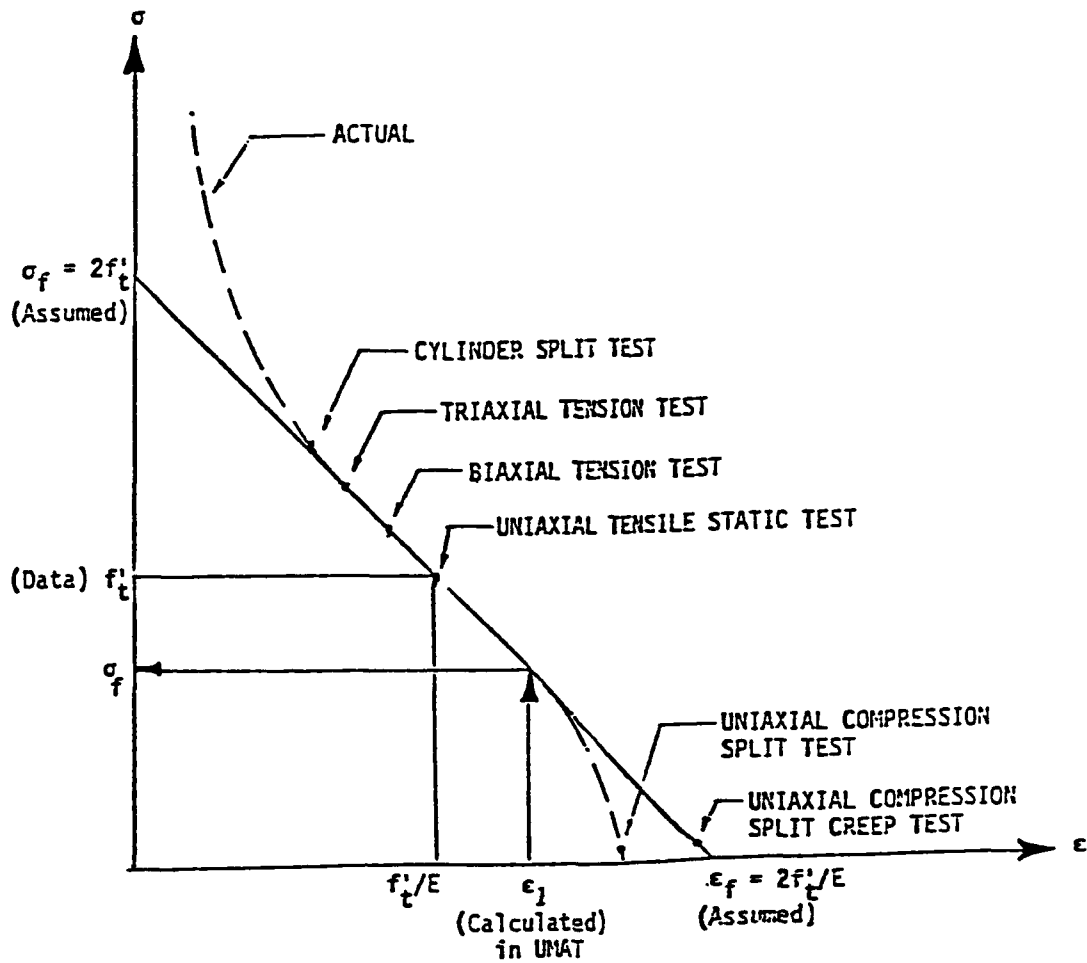


Figure A7. Interactive fracture criterion for concrete

- c. Adjust the failure surface (Figure A6 amplitude, using  $\sigma_f$  as the intercept, instead of  $f'_t$ ).
- d. Enter Figure A6 using the principal stresses  $\sigma_1$  and  $\sigma_2$  calculated in UMAT, and calculate whether the  $(\sigma_1, \sigma_2)$  point penetrates the failure surface. If so, introduce a crack whose normal is in the principal strain direction and formulate the constitutive matrix in the principal coordinate system.
- e. Rotate the precracking stresses to the same coordinate system and adjust these stresses to reflect the new cracking state.
- f. Rotate the constitutive matrix and the stresses back to the coordinate system of the structure.
- g. The new constitutive matrix and stresses are then used by ABAQUS to calculate the nodal forces and the tangent stiffness matrix in the next step.

#### **Waterways Experiment Station Cataloging-In-Publication Data**

Truman, Kevin Z.

Evaluation of thermal and incremental construction effects for monoliths AL-3 and AL-5 of the Melvin Price Locks and Dam / by Kevin Z.

Truman, David J. Petruska, Abdelkader Ferhi ; prepared for Department of the Army, US Army Corps of Engineers.

382 p : ill. ; 28 cm. -- (Contract report ; ITL-92-3)

Includes bibliographical references.

1. Structural optimization -- Data processing. 2. Melvin Price Locks and Dam (Ill.) 3. Concrete -- Expansion and contraction. 4. Concrete -- Creep. I. Petruska, David J. II. Ferhi, Abdelkader. III. United States Army. Corps of Engineers. IV. U.S. Army Engineer Waterways Experiment Station. V. Computer-aided Structural Engineering Project. VI. Title. VII. Series: Contract report (U.S. Army Engineer Waterways Experiment Station) ; ITL-92-3.

TA7 W34c no.ITL-92-3

# WATERWAYS EXPERIMENT STATION REPORTS PUBLISHED UNDER THE COMPUTER-AIDED STRUCTURAL ENGINEERING (CASE) PROJECT

	Title	Date
Technical Report K-78-1	List of Computer Programs for Computer-Aided Structural Engineering	Feb 1978
Instruction Report O-79-2	User's Guide: Computer Program with Interactive Graphics for Analysis of Plane Frame Structures (CFRAME)	Mar 1979
Technical Report K-80-1	Survey of Bridge-Oriented Design Software	Jan 1980
Technical Report K-80-2	Evaluation of Computer Programs for the Design/Analysis of Highway and Railway Bridges	Jan 1980
Instruction Report K-80-1	User's Guide: Computer Program for Design/Review of Curvilinear Conduits/Culverts (CURCON)	Feb 1980
Instruction Report K-80-3	A Three-Dimensional Finite Element Data Edit Program	Mar 1980
Instruction Report K-80-4	A Three-Dimensional Stability Analysis/Design Program (3DSAD)	
	Report 1: General Geometry Module	Jun 1980
	Report 3: General Analysis Module (CGAM)	Jun 1982
	Report 4: Special-Purpose Modules for Dams (CDAMS)	Aug 1983
Instruction Report K-80-6	Basic User's Guide: Computer Program for Design and Analysis of Inverted-T Retaining Walls and Floodwalls (TWDA)	Dec 1980
Instruction Report K-80-7	User's Reference Manual: Computer Program for Design and Analysis of Inverted-T Retaining Walls and Floodwalls (TWDA)	Dec 1980
Technical Report K-80-4	Documentation of Finite Element Analyses	
	Report 1: Longview Outlet Works Conduit	Dec 1980
	Report 2: Anchored Wall Monolith, Bay Springs Lock	Dec 1980
Technical Report K-80-5	Basic Pile Group Behavior	Dec 1980
Instruction Report K-81-2	User's Guide: Computer Program for Design and Analysis of Sheet Pile Walls by Classical Methods (CSHTWAL)	
	Report 1: Computational Processes	Feb 1981
	Report 2: Interactive Graphics Options	Mar 1981
Instruction Report K-81-3	Validation Report: Computer Program for Design and Analysis of Inverted-T Retaining Walls and Floodwalls (TWDA)	Feb 1981
Instruction Report K-81-4	User's Guide: Computer Program for Design and Analysis of Cast-in-Place Tunnel Linings (NEWTUN)	Mar 1981
Instruction Report K-81-6	User's Guide: Computer Program for Optimum Nonlinear Dynamic Design of Reinforced Concrete Slabs Under Blast Loading (CBARCS)	Mar 1981
Instruction Report K-81-7	User's Guide: Computer Program for Design or Investigation of Orthogonal Culverts (CORTCUL)	Mar 1981
Instruction Report K-81-9	User's Guide: Computer Program for Three-Dimensional Analysis of Building Systems (CTABS80)	Aug 1981
Technical Report K-81-2	Theoretical Basis for CTABS80: A Computer Program for Three-Dimensional Analysis of Building Systems	Sep 1981
Instruction Report K-82-6	User's Guide: Computer Program for Analysis of Beam-Column Structures with Nonlinear Supports (CBEAMC)	Jun 1982

(Continued)

# WATERWAYS EXPERIMENT STATION REPORTS PUBLISHED UNDER THE COMPUTER-AIDED STRUCTURAL ENGINEERING (CASE) PROJECT

(Continued)

	Title	Date
Instruction Report K-82-7	User's Guide: Computer Program for Bearing Capacity Analysis of Shallow Foundations (CBEAR)	Jun 1982
Instruction Report K-83-1	User's Guide: Computer Program with Interactive Graphics for Analysis of Plane Frame Structures (CFRAME)	Jan 1983
Instruction Report K-83-2	User's Guide: Computer Program for Generation of Engineering Geometry (SKETCH)	Jun 1983
Instruction Report K-83-5	User's Guide: Computer Program to Calculate Shear, Moment, and Thrust (CSMT) from Stress Results of a Two-Dimensional Finite Element Analysis	Jul 1983
Technical Report K-83-1	Basic Pile Group Behavior	Sep 1983
Technical Report K-83-3	Reference Manual: Computer Graphics Program for Generation of Engineering Geometry (SKETCH)	Sep 1983
Technical Report K-83-4	Case Study of Six Major General-Purpose Finite Element Programs	Oct 1983
Instruction Report K-84-2	User's Guide: Computer Program for Optimum Dynamic Design of Nonlinear Metal Plates Under Blast Loading (CSDOOR)	Jan 1984
Instruction Report K-84-7	User's Guide: Computer Program for Determining Induced Stresses and Consolidation Settlements (CSETT)	Aug 1984
Instruction Report K-84-8	Seepage Analysis of Confined Flow Problems by the Method of Fragments (CFRAG)	Sep 1984
Instruction Report K-84-11	User's Guide for Computer Program CGFAG, Concrete General Flexure Analysis with Graphics	Sep 1984
Technical Report K-84-3	Computer-Aided Drafting and Design for Corps Structural Engineers	Oct 1984
Technical Report ATC-86-5	Decision Logic Table Formulation of ACI 318-77, Building Code Requirements for Reinforced Concrete for Automated Constraint Processing, Volumes I and II	Jun 1986
Technical Report ITL-87-2	A Case Committee Study of Finite Element Analysis of Concrete Flat Slabs	Jan 1987
Instruction Report ITL-87-1	User's Guide: Computer Program for Two-Dimensional Analysis of U-Frame Structures (CUFRAM)	Apr 1987
Instruction Report ITL-87-2	User's Guide: For Concrete Strength Investigation and Design (CASTR) in Accordance with ACI 318-83	May 1987
Technical Report ITL-87-6	Finite-Element Method Package for Solving Steady-State Seepage Problems	May 1987
Instruction Report ITL-87-3	User's Guide: A Three Dimensional Stability Analysis/Design Program (3DSAD) Module	Jun 1987
	Report 1: Revision 1: General Geometry	Jun 1987
	Report 2: General Loads Module	Sep 1989
	Report 6: Free-Body Module	Sep 1989

(Continued)

# WATERWAYS EXPERIMENT STATION REPORTS PUBLISHED UNDER THE COMPUTER-AIDED STRUCTURAL ENGINEERING (CASE) PROJECT

(Continued)

	Title	Date
Instruction Report ITL-87-4	User's Guide: 2-D Frame Analysis Link Program (LINK2D)	Jun 1987
Technical Report ITL-87-4	Finite Element Studies of a Horizontally Framed Miter Gate Report 1: Initial and Refined Finite Element Models (Phases A, B, and C), Volumes I and II Report 2: Simplified Frame Model (Phase D) Report 3: Alternate Configuration Miter Gate Finite Element Studies--Open Section Report 4: Alternate Configuration Miter Gate Finite Element Studies--Closed Sections Report 5: Alternate Configuration Miter Gate Finite Element Studies--Additional Closed Sections Report 6: Elastic Buckling of Girders in Horizontally Framed Miter Gate Report 7: Application and Summary	Aug 1987
Instruction Report GL-87-1	User's Guide: UTEXAS2 Slope-Stability Package; Volume I, User's Manual	Aug 1987
Instruction Report ITL-87-5	Sliding Stability of Concrete Structures (CSLIDE)	Oct 1987
Instruction Report ITL-87-6	Criteria Specifications for and Validation of a Computer Program for the Design or Investigation of Horizontally Framed Miter Gates (CMITER)	Dec 1987
Technical Report ITL-87-8	Procedure for Static Analysis of Gravity Dams Using the Finite Element Method -- Phase 1a	Jan 1988
Instruction Report ITL-88-1	User's Guide: Computer Program for Analysis of Planar Grid Structures (CGRID)	Feb 1988
Technical Report ITL-88-1	Development of Design Formulas for Ribbed Mat Foundations on Expansive Soils	Apr 1988
Technical Report ITL-88-2	User's Guide: Pile Group Graphics Display (CPGG) Post-processor to CPGA Program	Apr 1988
Instruction Report ITL-88-2	User's Guide for Design and Investigation of Horizontally Framed Miter Gates (CMITER)	Jun 1988
Instruction Report ITL-88-4	User's Guide for Revised Computer Program to Calculate Shear, Moment, and Thrust (CSMT)	Sep 1988
Instruction Report GL-87-1	User's Guide: UTEXAS2 Slope-Stability Package; Volume II, Theory	Feb 1989
Technical Report ITL-89-3	User's Guide: Pile Group Analysis (CPGA) Computer Group	Jul 1989
Technical Report ITL-89-4	CBASIN--Structural Design of Saint Anthony Falls Stilling Basins According to Corps of Engineers Criteria for Hydraulic Structures; Computer Program X0098	Aug 1989

(Continued)

# WATERWAYS EXPERIMENT STATION REPORTS PUBLISHED UNDER THE COMPUTER-AIDED STRUCTURAL ENGINEERING (CASE) PROJECT

(Continued)

	Title	Date
Technical Report ITL-89-5	CCHAN—Structural Design of Rectangular Channels According to Corps of Engineers Criteria for Hydraulic Structures; Computer Program X0097	Aug 1989
Technical Report ITL-89-6	The Response-Spectrum Dynamic Analysis of Gravity Dams Using the Finite Element Method; Phase II	Aug 1989
Contract Report ITL-89-1	State of the Art on Expert Systems Applications in Design, Construction, and Maintenance of Structures	Sep 1989
Instruction Report ITL-90-1	User's Guide: Computer Program for Design and Analysis of Sheet Pile Walls by Classical Methods (CWALSHT)	Feb 1990
Technical Report ITL-90-3	Investigation and Design of U-Frame Structures Using Program CUFRBC Volume A: Program Criteria and Documentation Volume B: User's Guide for Basins Volume C: User's Guide for Channels	May 1990
Instruction Report ITL-90-6	User's Guide: Computer Program for Two-Dimensional Analysis of U-Frame or W-Frame Structures (CWFRAM)	Sep 1990
Instruction Report ITL-90-2	User's Guide: Pile Group—Concrete Pile Analysis Program (CPGC) Preprocessor to CPGA Program	Jun 1990
Technical Report ITL-91-3	Application of Finite Element, Grid Generation, and Scientific Visualization Techniques to 2-D and 3-D Seepage and Groundwater Modeling	Sep 1990
Instruction Report ITL-91-1	User's Guide: Computer Program for Design and Analysis of Sheet-Pile Walls by Classical Methods (CWALSHT) Including Rowe's Moment Reduction	Oct 1991
Instruction Report ITL-87-2 (Revised)	User's Guide for Concrete Strength Investigation and Design (CASTR) in Accordance with ACI 318-89	Mar 1992
Technical Report ITL-92-2	Finite Element Modeling of Welded Thick Plates for Bonneville Navigation Lock	May 1992
Technical Report ITL-92-4	Introduction to the Computation of Response Spectrum for Earthquake Loading	Jun 1992
Instruction Report ITL-92-3	Concept Design Example, Computer Aided Structural Modeling (CASM) Report 1: Scheme A Report 2: Scheme B Report 3: Scheme C	Jun 1992 Jun 1992 Jun 1992
Instruction Report ITL-92-4	User's Guide: Computer-Aided Structural Modeling (CASM) - Version 3.00	Apr 1992
Instruction Report ITL-92-5	Tutorial Guide: Computer-Aided Structural Modeling (CASM) - Version 3.00	Apr 1992

(Continued)

**WATERWAYS EXPERIMENT STATION REPORTS  
PUBLISHED UNDER THE COMPUTER-AIDED  
STRUCTURAL ENGINEERING (CASE) PROJECT**

(Concluded)

	Title	Date
Contract Report ITL-92-1	Optimization of Steel Pile Foundations Using Optimality Criteria	Jun 1992
Technical Report ITL-92-7	Refined Stress Analysis of Melvin Price Locks and Dam	Sep 1992
Contract Report ITL-92-2	Knowledge-Based Expert System for Selection and Design of Retaining Structures	Sep 1992
Contract Report ITL-92-3	Evaluation of Thermal and Incremental Construction Effects for Monoliths AL-3 and AL-5 of the Melvin Price Locks and Dam	Sep 1992